Optical-fiber-based distributed dosimetry for space applications

Arnaud Meyer

No. d'ordre NNT : **2023STET050**

THÈSE DE DOCTORAT
DE L'UNIVERSITÉ JEAN MONNET SAINT-ÉTIENNE

Membre de l'Université de LYON

opérée au sein du
Laboratoire Hubert Curien

École Doctorale No. 488
(SCIENCES, INGÉNIERIE, SANTÉ)

Specialité / discipline de doctorat :
Optique, Photonique et Hyperfréquences

Soutenue publiquement le 08/12/2023, par :
Arnaud MEYER

Optical-fiber-based distributed dosimetry for space applications

---

Dosimétrie répartie par fibre optique pour les applications spatiales

Devant le jury composé de :

Christophe CAUCHETEUR	Professeur	Université de Mons	Rapporteur
Frédéric WROBEL	Professeur	Université de Montpellier	Rapporteur
Sylvain GIRARD	Professeur	Université Jean Monnet	Examinateur
Jochen KUHNHENN	Docteur	Fraunhofer INT	Examinateur
Damien LAMBERT	Docteur	CEA DAM DIF	Examinateur
Julien MEKKI	Docteur	CNES	Examinateur
Adriana MORANA	Maîtresse de conférences	Université Jean Monnet	Examinatrice
Aziz BOUKENTER	Professeur	Université Jean Monnet	Directeur de thèse
André CHAMPAVÈRE	Ingénieur	GuidOptix	Invité

Optical-fiber-based distributed dosimetry for space applications

Dosimétrie répartie par fibre optique pour les applications spatiales

Remerciements – Thanks and acknowledgements

Cette thèse est une étape importante d'un long projet de reconversion professionnelle, qui a débuté avec la reprise de mes études dans les sciences physiques et qui se poursuivra encore, je l'espère, au service de la production et de la diffusion des savoirs scientifiques.

Dans le cadre de ce projet peu conventionnel qui est le mien, je tiens donc tout d'abord à remercier les institutions et personnes qui ont permis de le mener à bien, à commencer par l'Université Jean Monnet Saint-Étienne, sa Faculté des Sciences et Techniques et ses équipes pédagogiques, mais également son Service Universitaire de Formation Continue qui m'a aiguillé et permis de faire de mon projet une réalité. Je remercie également Pôle Emploi pour avoir financé ma formation jusqu'à mon entrée en doctorat.

Ces trois années de travail de thèse menées au sein de l'équipe MOPERE du Laboratoire Hubert Curien m'ont permis de faire mes premiers pas dans le monde de la recherche. Je remercie ici toute l'équipe, à commencer par mon directeur de thèse Aziz BOUKENTER, ainsi que Sylvain GIRARD et Adriana MORANA pour leur accompagnement compétent et exigeant. Je n'oublie pas l'ensemble des enseignants, post-doctorants, doctorants et personnels du laboratoire qui m'ont prêté support pendant cette période, en espérant avoir également pu leur rendre la pareille. J'adresse des remerciements supplémentaires à Martin ROCHE, Nourdine KERBOUB et Luca WENINGER pour leur participation à certains des résultats expérimentaux présentés ici.

Les travaux de thèse exposés dans ce manuscrit sont également l'illustration de partenariats forts entre différents acteurs scientifiques et techniques, qui ont chacun contribué au succès de ces travaux. Je remercie donc d'abord l'entreprise iXblue (maintenant Exail) pour la fourniture des fibres optiques, et plus particulièrement Gilles MÉLIN pour ses précieuses indications sur les fibres testées dans cette thèse. La fourniture des appareils OTDR embarqués a également été rendue possible par la collaboration de la société VIAVI Solutions, ainsi que d'André CHAMPAVÈRE de GuidOptix et du CNES. Les essais sous radiation ont été le fruit d'un partenariat très apprécié avec l'équipe RADIAC de l'IES de l'Université de Montpellier, ainsi qu'avec le centre canadien TRIUMF, associés dans le cadre du projet européen RADNEXT.

Les données de simulation présentes dans ce manuscrit sont le résultat de nombreuses séances de travail menées avec Damien LAMBERT du CEA DAM DIF, que je remercie copieusement pour la qualité de nos travaux communs et l'étendue des connaissances qu'il a su m'y transmettre. Dans une relation plus indirecte mais fortement liée à la rédaction de ce manuscrit, je me dois également de remercier Giovanni SANTIN de l'ESA pour son excellent *Short Course* donné à la conférence

NSREC 2022, qui a été pour moi non seulement une fenêtre vers une meilleure compréhension des phénomènes physiques en jeu dans les effets des radiations, mais également une source de bibliographie de très grande qualité sur l'environnement radiatif spatial.

Enfin, je remercie les membres du jury pour leur temps consacré à évaluer mon travail de thèse sous la forme du présent manuscrit et lors de la soutenance, et plus particulièrement les rapporteurs Christophe CAUCHETEUR de l'Université de Mons et Frédéric WROBEL de l'Université de Montpellier pour leur relecture attentive du manuscrit.

Pour conclure sur une note plus personnelle, je souhaite remercier mon entourage de m'avoir accompagné sur cette période où tout n'a pas toujours été facile, et j'ai énormément apprécié les moments passés avec eux qui m'ont donné l'énergie nécessaire afin de mener mon projet à bien.

Je dois bien sûr une dernière volée de remerciements toute particulière à la MJC de Saint-Chamond et à son club Astro.Uranie, dont j'ai poussé la porte il y a bientôt trente ans. C'est à eux que je dois cette passion pour les sciences et cette culture du partage de la connaissance qui sont précisément ce qui m'ont porté jusqu'ici, et, je n'en doute pas, qui continueront à porter ma carrière scientifique dans les années qui viennent.

Contents

List of acronyms

ADC	Analog/digital converter
CERN	*Centre Européen pour la Recherche Nucléaire*, European Organization for Nuclear Research
CHARM	Cern High energy AcceleRator Mixed field facility
CME	Coronal Mass Ejection
CMOS	Complementary Metal-Oxide Semiconductor
CPU	Central Processing Unit
CSDA	Continuous Slowing-Down Approximation
DC	Direct Current
DDD	Displacement Damage Dose
DESY	Deutsches Elektronen-SYnchrotron
DOFRS	Distributed Optical Fiber Radiation Sensing
EEO	Extremely Elliptical Orbit
EPR	Electron Paramagnetic Resonance
ESR	Electron Spin Resonance
FBG	Fiber Bragg Grating
FWHM	Full Width at Half Maximum
GCR	Galactic Cosmic Rays
GEO	Geostationary(/Geosynchronous) Earth Orbit
HEO	Highly Elliptical Orbit
IR	Infrared (typically $\lambda > 800\,\text{nm}$)
IP	Internet Protocol
LEO	Low Earth Orbit
LET	Linear Energy Transfer
LHC	Large Hadron Collider
MC	Monte Carlo
MEO	Medium Earth Orbit
MOS	Metal-Oxide Semiconductor
NANF	Nested Antiresonant Nodeless Fiber
NBOHC	Non-Bridging Oxygen Hole Center
NIR	Near-Infrared (typically $800\,\text{nm} < \lambda < 2000\,\text{nm}$)

NIST National Institute of Standards and Technology
ODC Oxygen-Deficient Center
OFDR Optical Frequency-Domain Reflectometry
OSL Optically-Stimulated Luminescence
OTDR Optical Time-Domain Reflectometry
PIF Proton Irradiation Facility
POHC Phosphorus-Oxygen Hole Center
RAM Random Access Memory
RIA Radiation-Induced Attenuation
RIE Radiation-Induced Emission
RIRIC Radiation-Induced Refractive Index Change
SEE Single-Event Effect
SEFI Single-Event Functional Interrupt
SEL Single-Event Latchup
SCPI Standard Commands for Programmable Instruments
SI *Système International d'unités*, International System of Units
SNR Signal-to-Noise Ratio
SPE Solar Particle Event
SSH Secure Shell protocol
STH Self-Trapped Hole
TID Total Ionizing Dose
TCP Transmission Control Protocol
USB Universal Serial Bus
UV Ultraviolet (typically $\lambda < 400\,\mathrm{nm}$)
VNC Virtual Network Computing

Chapter 0:

Introduction

0. Introduction

Optical fiber technology encompasses a wide range of applications, starting from the prominent field of telecommunications, for which hundreds of millions of kilometers of optical fiber are produced each year. Other approaches to the use of optical fibers can be found in the field of optical fiber sensing, enabling measurement of a variety of environmental properties using optical fibers not only as transmission media, but mainly as sensing elements. A particular feature of optical fiber sensing is the ability, using appropriate interrogation techniques, to perform *distributed* measurements, i.e. to retrieve the value of a measurand at virtually any location along the sensing fiber.

Dosimetry, i.e. measurement of ionizing radiation, is one of the many types of measurands available to optical fiber sensing, and one that has seen consequent research interest in the last years. Optical fiber-based dosimetry, involving detection of the point defects induced by ionizations in the fiber material, has been shown to enable radiation monitoring in a variety of environments, including radiotherapy, particle accelerators, nuclear reactors, or inertial confinement fusion facilities.

Distributed dosimetry, combining the two concepts presented here above, enables spatially-resolved radiation measurements while using a single optical fiber and interrogator. This technology, mainly documented in the literature in the context of radiation monitoring for particle accelerators, has a promising potential to assist in the characterization of radiation environments or to complement arrays of point dosimeters in large architectures.

This Ph.D. thesis aims to explore the possibility offered by commercial, off-the-shelf, embedded interrogators coupled with size-reduced, radiosensitive optical fiber to provide distributed dosimetry in the context of space missions, which offer a complex radiation environment coupled with strict environmental and operational constraints.

This thesis work was operated from October 2020 to September 2023 in the Laboratoire Hubert Curien of Université Jean Monnet Saint-Étienne (France), among the MOPERE (*Matériaux pour l'Optique et la Photonique en Environnements Radiatifs Extrêmes*) team, which is specialized in the behavior of optical materials in radiation environments. The experimental work was carried out in numerous irradiation facilities: X-ray irradiators in Laboratoire Hubert Curien, γ ray irradiator in Université de Montpellier (France), and proton irradiator in the TRIUMF center (Canada).

While the present manuscript is dedicated to the subject of distributed dosimetry, other works were performed during these three years. One of these topics explored in parallel was radioluminescence

dosimetry, experimented for a variety of optical fibers, and subject of a dedicated publication (cf. **Article A.1** in appendix).

The first chapter of this manuscript introduces the various concepts across which this thesis work stands, as they are currently developed in the scientific literature. The space radiation environment is presented, as well as the basic interaction mechanisms of ionizing radiation with materials. Then, optical fibers and their documented applications for dosimetry are introduced, with a focus on the phosphorus-doped fibers used in the experimental part of this thesis. Finally, distributed optical fiber sensing techniques are presented, along with, more specifically, a review of applications of distributed dosimetry documented in the literature to this date.

The second chapter focuses on the material and software means used in this thesis work. The main experimented components – optical fibers and embedded interrogators – are presented, as well as the irradiation facilities involved in the experimental work. The software used for the simulation work are also introduced in this part, with a small introduction to the concept of Monte Carlo simulations.

The third chapter presents the experimental work and discusses its results. A first, metrological approach was performed using repeated measurements with different types of interrogators to evaluate the measurement accuracy in the absence of radiation. Then, the main radiation tests, involving different combinations of interrogators and optical fibers irradiated under γ and X-rays, are presented with their results. A final experiment, dedicated to Single-Event Effects (SEE) testing of the interrogator devices under high-energy protons, is reported at the end of this chapter.

The fourth chapter focuses on simulation work, to bring further insights on the dose deposition process in optical fibers irradiated in different environments. Results of Monte Carlo simulations of deposited dose in optical fibers are presented for photons, protons, electrons and neutrons of different energies. Moreover, a combination of simulation software is used to predict results of X-ray irradiations, considering several parameters that are specific to the operation of X-ray tubes.

Chapter 1:

Theoretical framework and state of the art

1. Theoretical framework and state of the art

Contents of this chapter

1.1. The space radiation environment

Discovery of high-energy radiation by the end of the 19th century, through cathode rays [1] then X-rays [2] gave birth to many new fields of research, focused on the nature, the effects, the applications, and also the hazards of these new physical objects showing particular properties [3–5].

Another topic of interest literally gained altitude when, in the turn of the 20th century, two different types of observations converged towards the presence of high-energy radiation in regions outside of the Earth's atmosphere. On one side, early research on ground-based cosmic ray detection emerged after the report of anomalous ionization events in closed vessels, observed between 1900 and 1901 by German scientists Julius Elster and Hans Geitel and simultaneously by Scottish scientist Charles Thomson Rees Wilson[1] [6]. On the other side, the Norwegian scientist Kristian Birkeland observed

[1] Nobel Prize in Physics 1927.

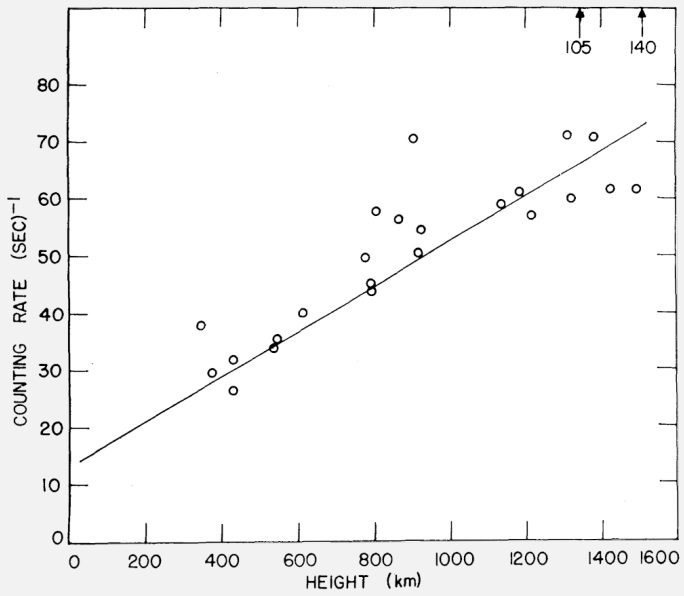

Figure 1.1. – Evolution of the count rate of a Geiger-Müller counter with the altitude of the Explorer-I satellite launched in 1958 above California. (from [12])

correlation between the appearance of sunspots and aurorae borealis sighted during his polar expeditions [7], inducing questioning in the scientific community about the nature of the radiation connecting these events [8].

The first scientific proof of the increased presence of high-energy particles in high altitude dates from the pioneer measurements made in 1912 by the Austrian scientist Victor Franz Hess[2,3] with an electroscope installed onboard of a balloon, reaching altitudes as high as 5350 m [9]. Subsequent observations performed by other teams, including German physicist Werner Kolhörster who reached an altitude of 9300 m in 1914 [6], further confirmed this tendency. The term *cosmic rays* was itself introduced by American physicists Robert Millikan[4] and G. Harvey Cameron once the extraterrestrial origin of these radiations was evidenced by their very high measured energy, which could only be the result of nuclear reactions taking place inside stars [10].

The next breakthrough in the measurement and characterization of the radiation environment above the atmosphere was performed in 1947 by the American scientists James A. Van Allen and H. E. Tatel, who used Geiger-Müller counters placed onboard a V-2 rocket to evaluate the radiation flux at altitudes up to 161 km [11]. In the following years, along with the development of space flight, more extensive and precise measurements were performed at increased altitudes (cf. **Figure 1.1**).

With increased awareness of the presence of ionizing radiation in space came eventually the question

[2]Nobel Prize in Physics 1936.
[3]The fact that Hess received the Nobel prize as late as 24 years after his discovery highlights the reluctance of the scientific community of this time to acknowledge the spacial origin of such radiation. Incidentally, Kolhörster and Millikan were clearly not convinced of Hess's findings until their own experiments proved otherwise [6].
[4]Nobel Prize in Physics 1923.

of safety, both regarding electronic instrumentation on board of satellites and protection of human life in the prospect of future space flights [13]. For those reasons, a more complete characterization of the type and quantity of radiation encountered in space became a topical issue with implications far beyond pure scientific curiosity, and in the prospect of manned space exploration, more and more scientific missions were launched in order to fully characterize the diversity of particle types, energies and locations that weave the complexity of the space radiation environment [14].

1.1.1. Sources of radiation in space

Current knowledge of the space radiation environment usually classifies radiation sources in three categories, distinct in origin, nature and intensities: Galactic Cosmic Rays (GCRs) produced by far-away stellar events, Solar events originating from our Sun, and trapped particles found inside planetary magnetospheres [15].

Galactic Cosmic Rays (GCRs)

Cosmic rays, in general, refer to extraterrestrial, high-energy radiation, but special attention is given to *galactic* cosmic rays, often referred to as GCRs, because of their peculiar origin and properties.

The fact that cosmic rays could be observed and indirectly measured from the ground made this topic of research thrive ever since the beginning of the 20$^{\text{th}}$ century, with various implications about their nature and origins [16]. Cosmic ray detection on Earth typically involves large arrays of sensors, able to sense the numerous secondary particles produced in the showers phenomena happening when cosmic rays interact with Earth's atmosphere [17]. As more measurements were performed in altitude as well as on the surface of Earth, it became clear that this radiation was of omnidirectional, isotropic nature, and was not affected by diurnal variations [18]. Such cosmic rays could therefore originate not only from a near object such as the Sun, but rather from virtually every direction, hinting at galactic, or even extra-galactic, origins [16].

Even though the whole range of astrophysical processes producing GCRs is still not completely clear, especially for the highest energy kind, this type of radiation is nowadays assumed to originate from multiple sources, ranging from our Solar system to outside the Milky Way galaxy [16]. In particular, the very high energies obtained by GCR particles are assumed to be the result of an acceleration process powered by scattering from the interstellar medium, as first suggested by the Italian-American physicist Enrico Fermi[5] [19–21].

GCRs are primarily composed of charged particles, with protons and alpha particles as its main components (respectively ~85 % and ~12 % of particle abundance) and a significantly lower amount

[5] Nobel Prize in Physics 1938.

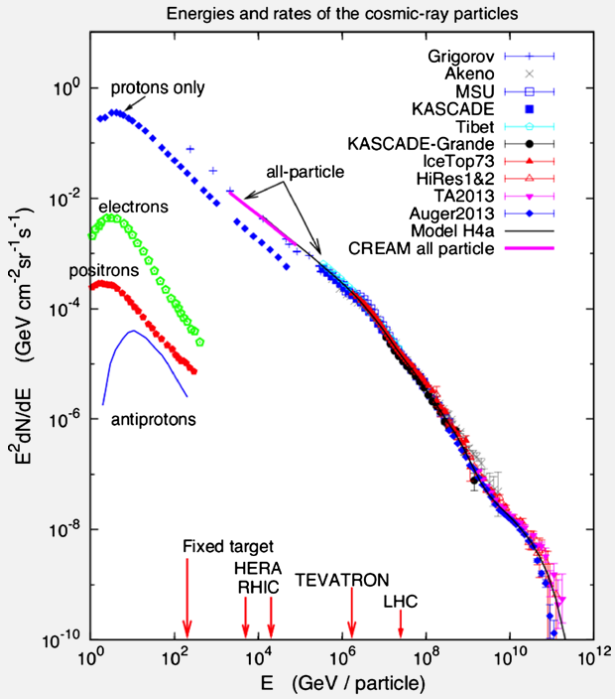

Figure 1.2. – Energy spectra of Galactic Cosmic Rays (GCRs), along with the contribution of individual particle types at lower energies. (from [20])

of electrons or positrons (2 %) and heavy ions (1 %) [22, 23]. Uncharged particles are also included in GCRs, although in very low quantity. In particular, cosmic γ rays, theorized to be secondary particles produced by charged primaries [24], opened a wide topic of astronomical research, highlighted for instance by the map of steady γ sources produced by the Fermi Gamma-ray Space Telescope [25].

The energy spectrum of GCRs is extremely broad, and spans over twelve decades, from the GeV to roughly 10^{12} GeV, with the highest ever recorded energy to date for a single particle being detected in 1991 from a cosmic-ray proton estimated to an energy of 3.2×10^{14} MeV, equivalent to 51 J [26]. However, as shown in **Figure 1.2**, such extremely-high-energy events are also extremely improbable, with an energy radiance reaching 10^{-10} GeV m^{-2} s^{-1} sr^{-1} for particles around 10^{12} GeV, that translates roughly to 1 km$^{-2} \cdot$ century^{-1}.

GCRs are also considered to be one of the main sources of high-energy heavy ions [27] that, despite their relatively low abundance compared to other types of particles found in GCRs, cover the whole elemental spectrum as demonstrated by several in-situ measurements [28]. **Figure 1.3** compares abundances of elements with atomic number $1 \leq Z \leq 28$ in GCRs with the ones of our solar system. It illustrates that elements of all types can be found in GCRs, and highlights that elements such as lithium, beryllium and boron are distinctively more abundant in GCRs than in the solar system.

The reference model for simulation of GCRs fluxes is the Badhwar-O'Neill (BON) model, which is periodically updated with new experimental data [29]. This environmental model is combined with known models of radiation damage to electronics in the CREME96 software, which simulates the

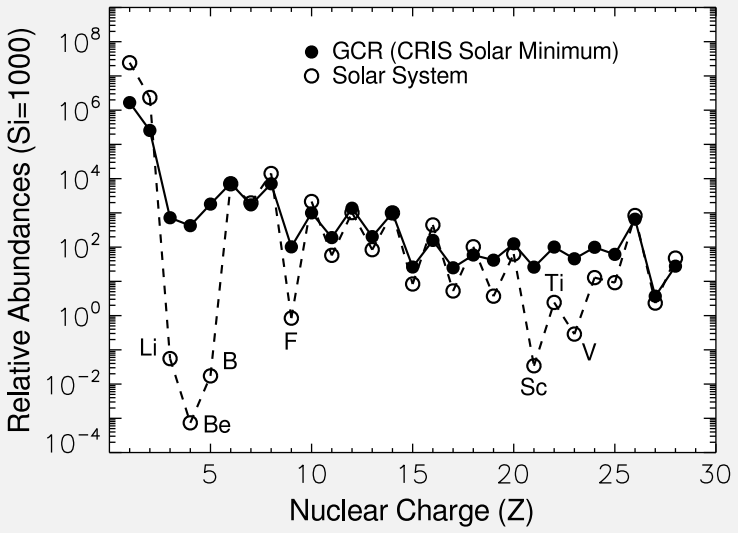

Figure 1.3. – Relative elemental abundances of heavy ions with energy 160 MeV/nucleon in GCRs (solid line), compared to abundances in the Solar System (dashed line). Reference is silicon (Si), associated to a value of 1000. (adapted from [28])

consequences of particle interaction with spacecraft electronics in the form of Single-Event Upsets (SEUs, cf/ **Section 1.1.3**) [30]. A more modern implementation is the CRÈME software suite, which includes CREME96 along with additional environmental models (such as the simulation of neutrons emitted by the Moon), and Monte Carlo capabilities [31].

Secondary particles produced from interaction of GCRs with the Earth's atmosphere are also a topic of interest, defining a radiation environment encountered in atmospheric flights such as commercial airplanes [32]. Noticeable sub-products of these interactions are the so-called *atmospheric* neutrons [33] as well as several radioisotopes used for radiometric dating, such as ^{14}C, ^{210}Pb and ^{137}Cs [34].

The spectrum of atmospheric neutrons at ground level is documented in the JEDEC JESD89 standard [35–37]. More complete models, that simulate fluences of multiple types of secondary particles at different altitudes, include the EPOS model [38], as well as the recent RAMSEES model [39].

Solar events

The Sun is the main source of energy of the Solar system, and the amount of radiation it delivers to Earth over the whole electromagnetic spectrum (also known as the *solar constant*) sums to an average irradiance of 1367 W/m^2, with a small annual variation of $\pm$0.1 W/m^2 [40].

The energy spectrum covered by solar radiation is extremely broad, and ranges from meter waves (around 10^{-6} eV) to high-energy particles in the GeV range, and includes many types of particles, such as photons, protons, ions, neutrons, neutrinos and energetic neutral atoms. This diversity in nature and energy reflects the various processes assumed to be at their source [41, 42].

The presence of a continuous stream of particles originating from the Sun was first evidenced in the 1950s by the observation of the tail of comets [43], and was named *solar wind* due to its hydrodynamic origins [44]. Solar wind is known to be emitted from the Sun's outer atmosphere, named *corona*, which extends up to ten solar radii while having a temperature on the order of 10^6 K, which is paradoxically higher than the Sun's surface [45]. Solar wind spreads throughout the whole solar system until its farthest extents, as measured by the Pioneer 10 probe [46], and causes an average solar mass loss of $2 \times 10^{-14}\,\mathrm{M}_\odot/\mathrm{yr}$ [47] (with $M_\odot \approx 1.988 \times 10^{30}$ kg the solar mass [48]) , which is roughly equivalent to 10^9 kg/s.

In practice, two different kinds of solar winds can be identified, as evidenced by the differences in solar wind speed observed by the Mariner 2 probe in 1962 [49]: the steady *slow solar wind* travelling between 250 and 400 km/s, originating from interfaces between coronal regions of opposed magnetic polarities; and the more transient *fast solar wind* travelling between 400 and 800 km/s, originating from coronal holes [50, 51]. These two different origins and processes highlight the complex structure of the solar corona from which they are generated.

However, as the Sun hosts intense thermonuclear reactions at its core and is essentially composed of extremely-high-temperature plasma, its emissions are anything but steady [52], and events such as the apparition of sunspots are very common. The occurrence of such events, named *solar activity*, is known to follow a 11-year cycle of increasing, then decreasing number of events, called the Schwabe cycle, itself linked to the 22-year Hale cycle that reflects the intrinsic solar magnetic state [53].

Solar events are usually categorized in two types: *solar flares* are burst of electromagnetic radiation, effectively observed as a sudden increase of brightness on the surface of the Sun in the form of luminous, intense filaments (cf. **Figure 1.4a**); *coronal mass ejections* (CMEs) are releases of massive amounts of plasma from the Sun's corona, and can reach several solar radii (cf. **Figure 1.4b**). These two kinds of events are not always associated, except in the case of very large CME events [22, 46].

Solar flares are the most iconic, and arguably spectacular, type of observable solar events and manifest as a burst of electromagnetic radiation (including visible light) appearing in the Sun's atmosphere. They were first observed in 1859 by English amateur astronomers Richard Carrington and Richard Hodgson, and were linked to the occurrence of a powerful magnetic storm observed on Earth the day after [54, 55], hinting at the fact that these visual events were accompanied by a burst of high-velocity, charged particles. These intense *solar particle events* (SPEs) are mainly composed of electrons and can be observed for several hours, although they generate in total relatively low amount of particle fluence (between 10^7 and 10^8 cm^{-2} for a single SPE) [22].

On the other hand, particle events arising from CMEs usually span longer than solar flare events, and can emit streams of particles for several days. They mainly include protons, have a wide angular coverage and can reach large amounts of fluence (on the order of 10^9 cm^{-2}) [22].

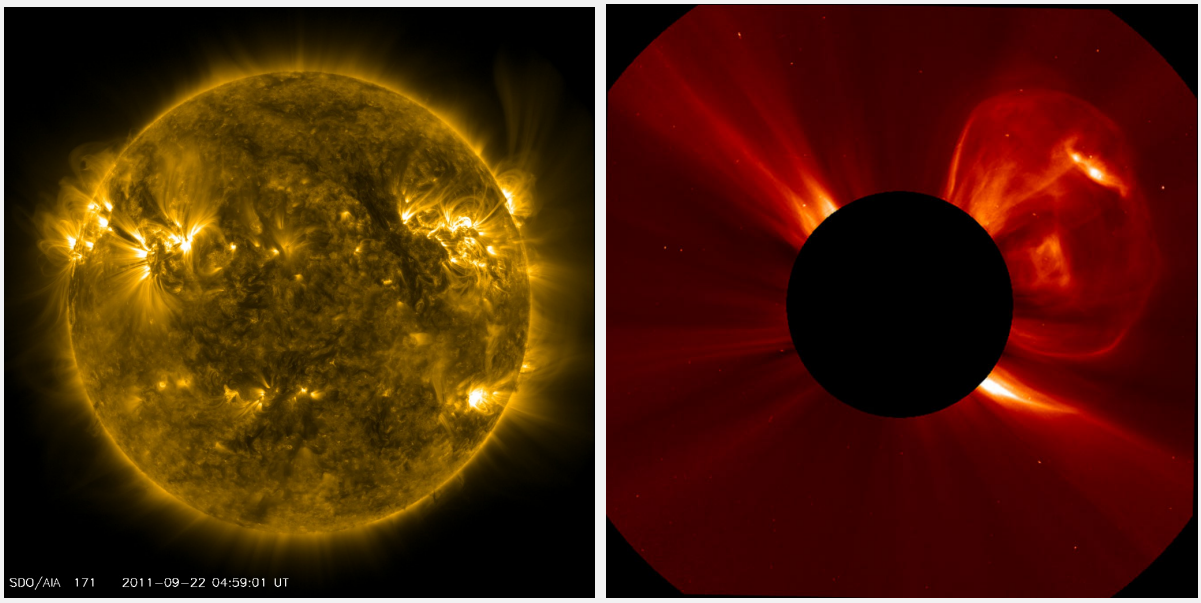

(a) Ultraviolet (170 nm) image of the surface taken by AIA instrument of satellite SDO. (NASA/SDO, AIA, EVE, and HMI science teams.)

(b) White light image of the corona from 1.5 to 6 $R_\odot$ taken by the LASCO C2 instrument of satellite SOHO. (ESA/NASA/SOHO/Jhelioviewer)

Figure 1.4. – Satellite observations of an intense solar event in September 21-22, 2011.

Figure 1.5 illustrates the intensity of such SPEs, which generate bursts of high-energy photons several hours after the observation of a solar flare (cf. **Figure 1.5a**). The emitted protons can reach fluences on the order of $3 \times 10^{10}\,\mathrm{cm}^{-2}$ for the most massive events, and cover a large energy spectrum (cf. **Figure 1.5b**), typically up to 200 MeV and exceptionally up the GeV range, as for the burst of fast-travelling particles observed in 2005 which are believed to have been accelerated in the Sun's coronal region [56].

Several models have been developed to simulate the long term cumulative fluence of protons, as well as other energetic particles such as heavy ions, received from SPEs. A model of reference is the ESP-PSYCHIC model [27], which is an improvement of the ESP model [59], itself derived from the historical JPL91 [60] and King [61] models. The Moscow State University (MSU) has also proposed a model for SPE fluxes [62]. Finally, the more recent SAPPHIRE model aims to include the sporadic nature of SPEs, which results in a greater accuracy compared to other models, especially for energies higher than 10 MeV [63].

Trapped particles and radiation belts

As introduced in the previous sections, the vast majority of energetic particles originating from GCRs or SPEs, such as protons, electrons, alpha particles and heavy ions, are of charged nature. This property leads to a great coupling potential, via Coulomb or Lorentz forces, of these particles with

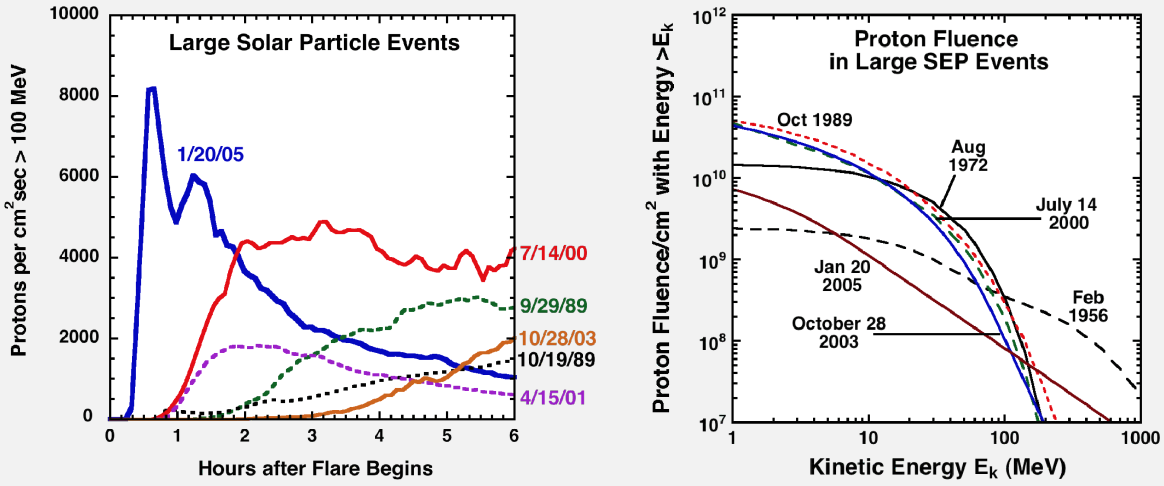

(a) Time profile of > 100 MeV protons. (from [57])

(b) Proton energy spectrum, compared with neutron data from 1956. (adapted from [57])

Figure 1.5. – Time profile and energy spectrum of protons detected during noticeably large SPEs between 1972 and 2003 [56, 57]. The 1956 data was taken from ground neutron monitors [58].

electromagnetic fields. One of such fields is the Earth's magnetic field (also called *geomagnetic* field), which is especially significant in the context of space radiation.

The geomagnetic field originates from electric currents, i.e. motion of charged particles, within the Earth's environment. The main geological process contributing to the geomagnetic field is the convection motion of molten iron in the outer region of Earth's core, producing a self-exciting dynamo process that generates the *core field* [64, 65]. The magnetic field resulting from this main generation process can reach intensities up to 30 000 nT at the equator and 60 000 nT at the poles [64]. Its structure is described in a first approximation by a dipolar field tilted 10.3° relative to Earth's rotation axis [66], but a more realistic representation also includes additional multipolar components as well and a slow evolution on the century scale [64]. Other processes also contribute to the geomagnetic field, among which the motion of magnetized rocks in the Earth's crust (the *crustal field*), the movement of charged particles in the ionosphere or magnetosphere, and tidal motions [64, 67].

The interaction between the geomagnetic field and solar winds constitutes the *magnetosphere*, a cavity shaped by the interaction of the Earth's magnetic field and the constant stream of charged particles originating from the Sun [66]. The outer limit of the magnetosphere is called *magnetopause*, and its extents are typically measured in mean Earth radii ($R_E \approx 6371.2$ km [68]), with about $10\,R_E$ in direction of the Sun and hundreds of R_E in the opposite direction [69, 70]. **Figure 1.6** gives a schematic representation of the shape and extents of Earth's magnetosphere.

Most charged particles from solar winds are deflected by the Earth's magnetosphere, forming a deflection surface called *bow shock* (cf. **Figure 1.6**) located at a distance between 2 and $3\,R_E$ in front of the magnetopause, on which solar particles are slown down to sub-magnetosonic velocities [66]. However, the complex structure of the magnetosphere generates several weaknesses in this protec-

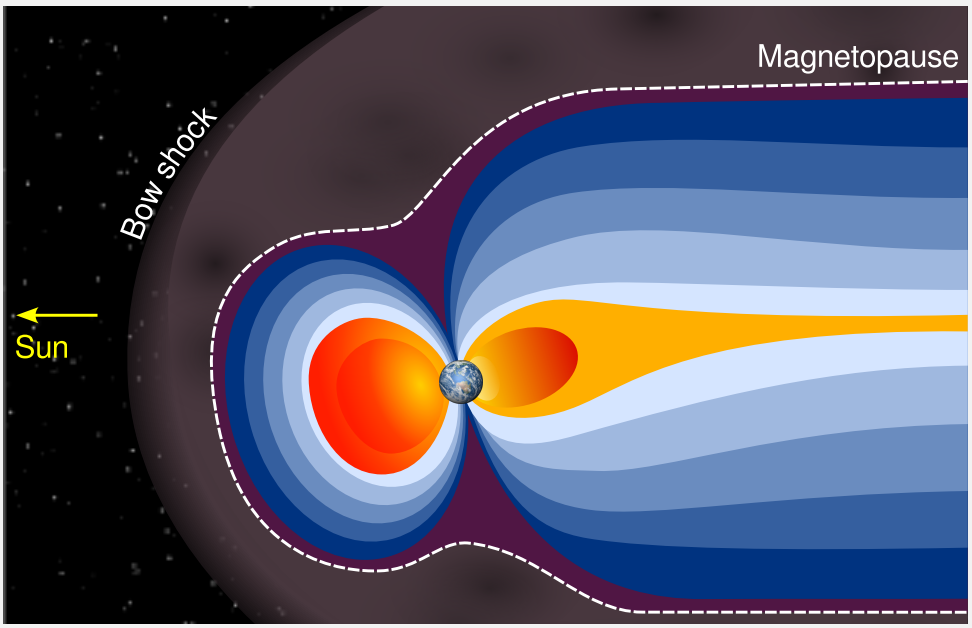

Figure 1.6. – Illustration of Earth's magnetosphere and its layers. Orange color symbolizes the plasmasphere, in where the two radiation belts are located. (adapted from NASA/Wikimedia Commons)

tive barrier, in the form of open field lines through which a fraction of the solar wind particles can cross the magnetopause, and eventually exit though the tail of the magnetosphere, through a process called *magnetic reconnection* [71]. In strong solar events, the intense stream of energetic particles penetrating the magnetosphere is the cause of various large-scale phenomena observed on Earth, such as aurorae [72], geomagnetic storms [73], or even blackouts in the most exceptional cases [74].

While most of the particles entering the magnetosphere are ejected to the magnetotail, part of them can be trapped through an adiabatic process described by three distinct motions, illustrated in **Figure 1.7**: *drift*, causing particles to rotate in the equatorial plane; *bouncing*, causing a back-and-forth motion between northern and southern hemispheres; and *gyration*, causing a very fast spinning movement along these trajectories [66, 75–78]. The frequency of these motions varies typically between the order of a millihertz for drift to several hundred kilohertz for gyration [76]. As the adiabatic nature of this process implies that the energy of the incoming particles is conserved, it contributes to building a reservoir of permanently trapped, energetic particles known as the *radiation belts* [66, 77, 79].

Radiation belts were first discovered experimentally by the Explorer I satellite [80] and followed by numerous other missions [81–83]. These pioneer measurements revealed the existence of two distinct radiation belts [84]: an inner belt including both protons and electrons [85], and an outer belt mainly consisting of electrons [86]. These radiation belts are often called the *Van Allen belts*, after James A. Van Allen, who lead the pioneering research on this field [87]. The inner belt extends typically from the immediate outer atmosphere to about $2\,R_E$ (altitudes from ~100 km to ~12 000 km), while the outer belt extends from $3\,R_E$ to about $10\,R_E$ [79, 84, 88]. These limits are not fixed, as the actual structure of the radiation belts follows a complex, dynamic process which is the subject of a whole

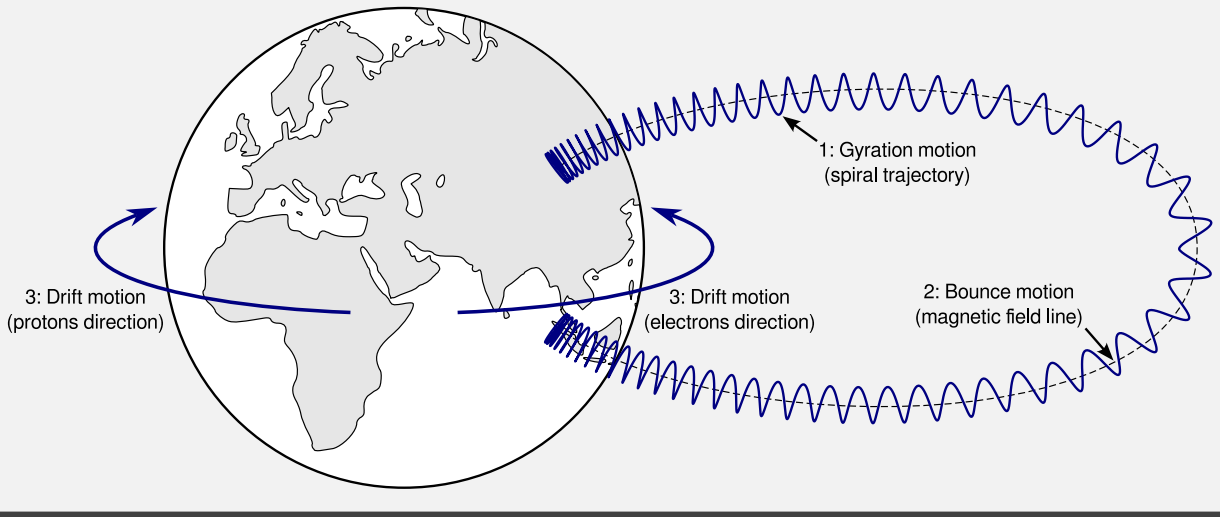

Figure 1.7. – Illustration of the three types of motion of particles trapped in the geomagnetic field: gyration and bounce motions are shown combined (blue line), and the drift motion causes this combination to rotate around the Earth in a direction that depends on the particle charge sign. (adapted from [77])

field of research [89].

Although most of these trapped particles are believed to originate from solar winds through the magnetic reconnection process cited here above, other sources are also considered. A significant part of the protons confined in the inner belt are believed to be the product of the decay of so-called *albedo neutrons*, created from the interaction of GCRs with atoms in the outer atmosphere [79]. Moreover, migration processes have been observed between particles of outer and inner belts, especially during large solar events [90].

Finally, artificial factors can also influence the structure and the population of radiation belts [77, 91, 92], such as high-altitude nuclear explosions [93], high-frequency radiowave heating [94], and release of easily ionizing chemicals [95]. These so-called *artificial radiation belts* were especially observed after the Argus and Starfish nuclear detonations which took place around 1960 [96], with the release of a large amount of high-energy electrons in the inner radiation belt, causing dramatic radiation damage that was documented for at least 11 satellites [92]. However, these artificial perturbations were not established to be permanent, because of processes such as atmospheric scattering and radial diffusion that cause the electron population to decay with time [97]. Recent data acquired in 2015 by the Van Allen probes [98] show no trace of the high electron population observed in the inner belt in the 1960s [99], as illustrated in **Figure 1.8**.

Several models are available for the trapped radiation belt particles. The two models of reference are AP-8 for trapped protons between 0.1 MeV and 400 MeV [100], and AE-8 for trapped electrons between 0.04 MeV and 7 MeV [101]. Each model comes with two variants, one for minimal solar activity (AP-8MIN and AE-8MIN) and one for maximal solar activity (AP-8MAX and AE-8MAX). A large amount of new experimental data was acquired since the development of these models between

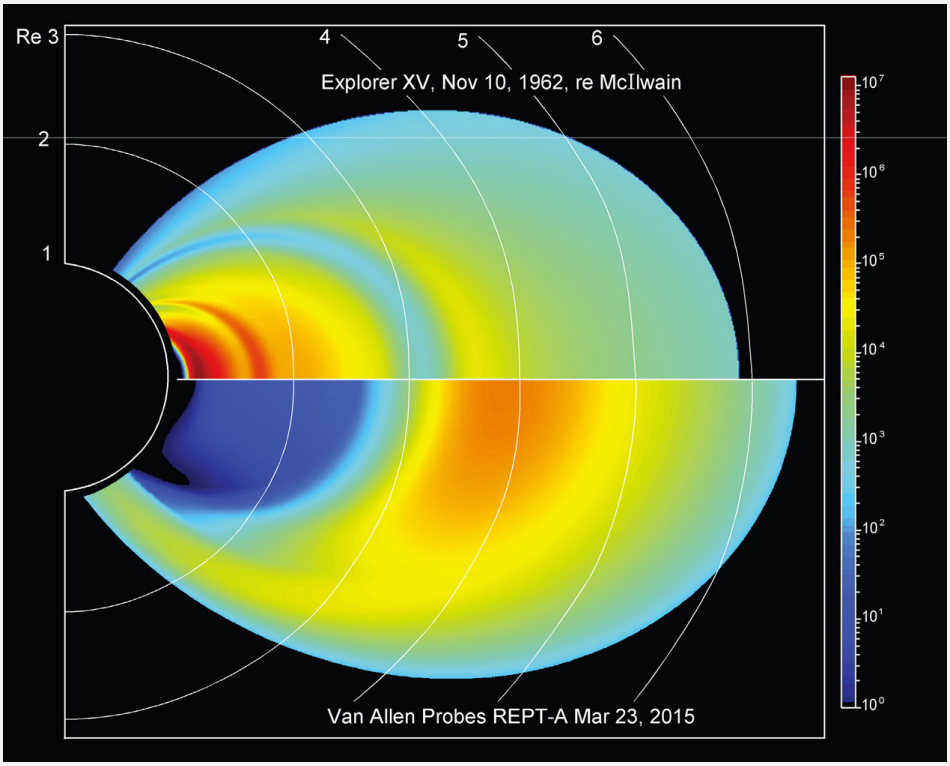

Figure 1.8. – Comparison of $> 5\,\text{MeV}$ electrons fluence rates (in $\text{cm}^{-2}\,\text{s}^{-1}$) measured by Explorer XV in 1962 [99] (above) and REPT-A in 2015 [98] (below), highlighting changes in belts structure. (from [92])

the 1960s and the 1980s, highlighting several discrepancies that called for their refinement; these new generation models are AE9 for electrons between 40 keV and 10 MeV, AP9 for protons between 100 keV and 2 GeV, and an additional model named SPM that handles low-energy electrons and protons, as well as helium and oxygen ions [102, 103]. Other models, such as MERLIN [104], focus on the prediction of radiation belt dynamics due to solar events, paving the way for a multi-scale, dynamic modeling suitable for specification of the radiation environment in defined orbits [105].

Figure 1.9 shows the predictions of the AP9 and AE9 models [102, 103] as a function of altitude for different proton and electron energies, which give an overview of the current knowledge of the radiation environment encountered in Earth's radiation belts.

Finally, the trapping mechanisms presented here also apply to the magnetosphere of objects other than Earth. The radiation belts of Jupiter and Saturn have been studied by several probes and have revealed to host large quantities of trapped particles at very high energies, with unique features compared to Earth such as their faster rotation speed as well as the presence of many natural satellites within their magnetospheres [106–108]. In particular, the jovian radiation belts are so intense that they are considered as an electron source near Earth during low solar activity [109, 110].

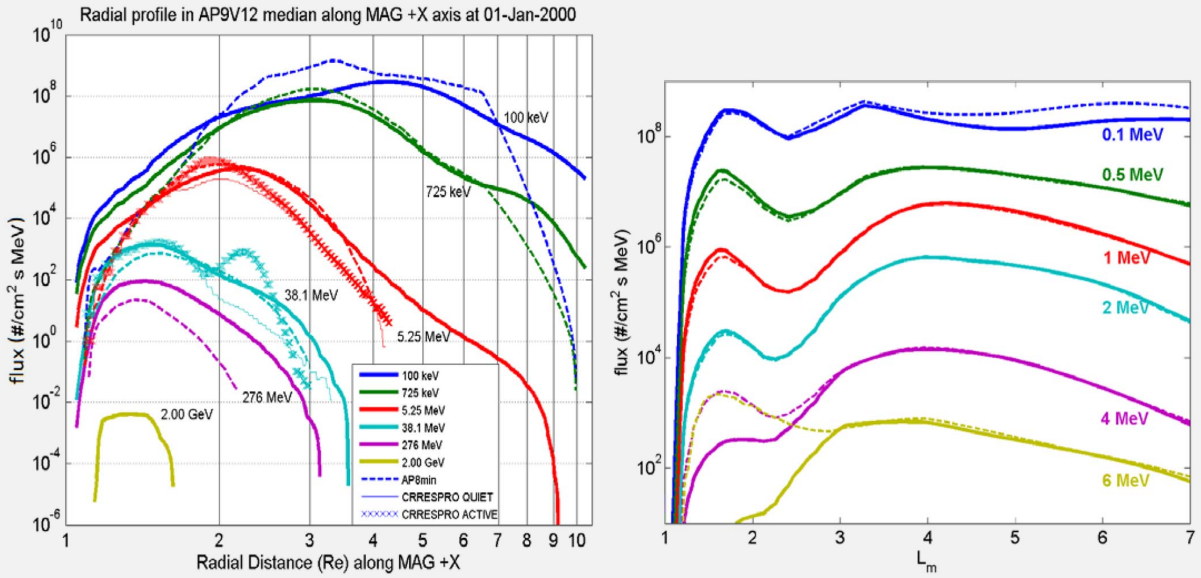

(a) Protons from 100 keV to 2 GeV. **(b)** Electrons from 0.1 MeV to 6 MeV ($L_m \approx R/R_E$).

Figure 1.9. – Evolution with altitude of the mean differential particle fluence rates simulated by the AP9 and AE9 models. Dashed lines are comparisons with other models. (from [103])

1.1.2. Locations of interest for radiation study

The combination of the three main space radiation sources presented in **Section 1.1.1**, as well as the specific needs of space equipment and missions, result in several typical radiation environments which are a subject of interest because of their direct consequences on the radiation protection design of spacecrafts. The following sections will present and define these locations of interest, as well as their radiation environment as currently understood and measured.

Low Earth Orbit (LEO)

The LEO is typically located between altitudes of 300 km, below which the atmospheric drag affects the stability of the orbit, and 1500 km, beyond which numerous technical and cost issues arise, including the need for powerful launchers and increased communication path loss and latency [111, 112]. A further distinction is sometimes made between the lower and upper LEO, with a separation around ~600 km altitude [113].

Being comparatively easier and cheaper to access, the LEO is the most populated satellite orbit, with an estimated total of about 10 000 orbiting satellites in 2020; this number has been rapidly increasing recently due to the launch of massive small satellite constellations including several tens of thousands of units [113, 114]. The LEO is also noticeably the orbit of choice for most manned scientific missions, among which the International Space Station (ISS) [115].

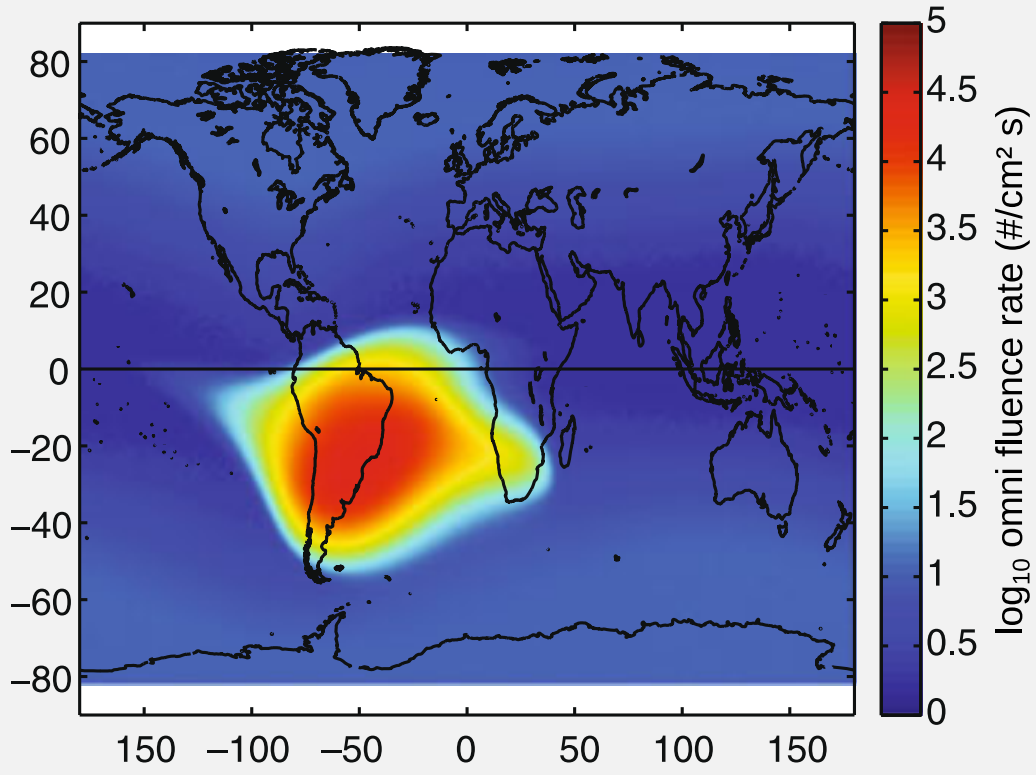

Figure 1.10. – Mapping of the median $>$ 36 MeV proton omnidirectional fluence rate measured over 13 years by the satellite POES N15, at an altitude of ~840 km. The outstanding area of high intensity located above South America is the *South Atlantic Anomaly* (SAA). (adapted from [102])

The LEO radiation environment is a mixture of trapped protons and electrons from the inner belt, as well as protons, helium ions and heavier ions originating from GCR [116–118]. Additionally, spacecraft structures, while reducing the overall amount of radiation received inside the spacecraft, also convert part of these charged particles to secondary radiation [22, 119], through physical processes such as bremsstrahlung [120] or atomic fragmentation [121].

Low-energy ($\leq$ 10 keV) electrons, while not energetic enough to penetrate spacecraft structures, also play an important role in satellite mission design because of a surface charge accumulation process known as *spacecraft charging* [122, 123].

The local structure of the radiation belts also plays an important role in LEOs. In particular, the geographical variation of the particle fluence rate is very significant at low altitudes, especially because of the *South Atlantic Anomaly* (SAA), a region mostly located above the South American continent and featuring a sharp increase of radiation intensity, as illustrated in **Figure 1.10**. The anomalous levels of radiation observed in this area are believed to originate from a local weakening of the geomagnetic field, down to 22 500 nT at ground level [124], causing the migration of inner radiation belt particles to lower altitudes [88]. The SAA was discovered during the first satellite missions in the late 1950s, and has been observed ever since to follow a slow expansion [125].

Apart from radiation, another environmental constraint that can significantly affect the function and

design of spacecrafts is temperature. The temperature of a spacecraft element is the result of the equilibrium of a complex set of parameters, some environmental [126] and some linked to the satellite architecture and materials [127]. This balance between incoming and outgoing power is neither homogeneous through the whole body of the spacecraft nor constant along the orbit, and is especially affected by the exposition to the Sun [128]. The temperature of a LEO satellite can range between $-100\,^{\circ}\mathrm{C}$ and $+100\,^{\circ}\mathrm{C}$ for solar panels and $-40\,^{\circ}\mathrm{C}$ to $+85\,^{\circ}\mathrm{C}$ for the inner electronic elements [129].

Medium Earth Orbit (MEO)

The MEO is usually defined as the region located between altitudes of 2000 km, above the LEO range, and 35 800 km, the altitude of geosynchronous orbits [130]. Because of its higher access cost while lacking the advantages of geostationary satellites, the MEO is much less populated than the LEO [130], and hosts mainly two kinds of spacecrafts: GNSS satellites for positioning services [131], or geosynchronous satellites in transit to their final orbit [132].

Geostationary/Geosynchronous Earth Orbit (GEO)

The GEO is a special orbit located at an altitude of ~35 800 km, at which the satellite orbital speed matches the Earth's rotational speed, effectively keeping the satellite at the same longitude [111, 112, 133]. As a result, a geostationary satellite is always located in the same position in the sky when viewed from the ground, which was identified as early as 1945 by science fiction author Arthur C. Clarke to be a very promising solution for wireless communication [134]. In practice, the influence of the Moon causes geosynchronous orbits to wobble on the North-South direction with an amplitude of several degrees, which can be compensated by satellites at the cost of propulsion energy [112].

Highly/Extremely Elliptical Orbits (HEO/EEO)

HEO, EEO and other orbits of the same kind (Molinya, Loopus…) are defined by a very elongated shape, oscillating between low altitude (~1000 km at periapsis) and very high altitude (~40 000 km at apoapsis) [111, 112, 133]. These orbits are mainly used by communication satellites that need to access high-latitude regions that are more difficult to cover with GEO satellites [111], as well as a workable alternative to GEO, because their long stay in apoapsis (~6 to 8 hours) makes them stand in a quasi-fixed position when viewed from the ground [112]).

Interplanetary missions

Space missions are not only limited to Earth's vicinity, and further destinations in the Solar system are also targeted by space agencies, because of their high scientific interest [135]. While historically restricted to high-budget missions, interplanetary missions are also expanding through the competition between national space agencies [136–138], use of small satellites [137, 139, 140] and emergence of private space industry actors [141, 142].

Interplanetary missions are characterized by long transfer times (on the order of 200–300 days for Mars, 800–1200 days for Jupiter and 1800–3400 days for Saturn [143]), most of which is spent outside the protection given by the Earth's magnetosphere. In addition to the radiation encountered during the trip to their destination, interplanetary spacecrafts are also exposed to the local radiation environment of the body they are visiting, for the whole duration of the mission.

In the case of the Moon and Mars, which lack a magnetic field of significant intensity, the main sources of radiation are GCRs and SPEs [144]. In these environments, the dose rate is estimated to ~200 µGy/d [144, 145].

In contrast, the gas giants Jupiter and Saturn host a magnetosphere of their own, which reduces the influence of GCRs and SPEs, but is also the location of intense and energetic radiation belts in a same manner than in Earth's orbit [146]. An evaluation of the dose received by the Galileo probe as it passed through 34 different orbits in little more than 6 years gave an average dose rate of ~2.7 Gy(Si)/d behind 2.2 g/cm^2 aluminum shielding [147], and numerical simulation on the moons of Jupiter and Saturn has estimated dose rates from ~10 mGy(Si)/d on Callisto and Enceladus to ~100 Gy(Si)/d on Europa with an equivalent shielding thickness [148].

1.1.3. Effects of radiation on devices and living beings

Basic mechanisms of radiation effects

Particles interact with matter through a wide range of physical processes, and, in some cases, the results of these processes may alter the irradiated material. The interaction processes involved, as well as their outcome in terms of material alteration, depend on the type of incoming particles, their level of energy, and the interaction susceptibility of the irradiated sample.

The intensity of these interactions is given by their *interaction cross section* σ, which expresses the probability of a given physical process to occur. This is linked to the stochastic nature of quantum mechanics, and such cross sections can be computed from quantum theories [149]. In nuclear physics, σ has the dimension of a surface area, and is often expressed in barns/atom (with 1 b = 10^{-24} cm^2).

Quantity	Flux	Fluence	Energy-Fluence	Fluence rate
Symbol	$\dot{N}$	ϕ	ψ	$\dot{\phi}$
Definition	$\frac{\mathrm{d}N}{\mathrm{d}t}$	$\frac{\mathrm{d}N}{\mathrm{d}a}$	$E\phi(E)$	$\frac{\mathrm{d}\phi}{\mathrm{d}t}$
SI Unit	s^{-1}	m^{-2}	$\mathrm{J}\cdot\mathrm{m}^{-2}$	$\mathrm{m}^{-2}\cdot\mathrm{s}^{-1}$
Usual unit	s^{-1}	cm^{-2}	$\mathrm{J}\cdot\mathrm{cm}^{-2}$	$\mathrm{cm}^{-2}\cdot\mathrm{s}^{-1}$

Table 1.1. – Usual quantities for qualifying the **amount of incoming particles**. N is the count of incoming particles, E their energy, t the time, and a the cross-sectional area of a sphere through which the particles are counted [151]. The last rows mentions units usually employed in radiation effects literature [152].

In radiation physics, σ is often normalized by the atomic mass of the material, resulting in a practical unit of cm^2/g [150].

The quantity of particles irradiating a material (or a location in space) can be defined in several ways, and the main physical quantities used in literature – flux, fluence, energy-fluence, fluence rate – are defined in **Table 1.1**.

Charged particles, like electrons and protons, interact strongly with matter because of Coulomb interactions that mainly take place with atomic electrons. As a result, an atomic electron may be imparted an energy greater than its binding energy, allowing it to leave the nuclear bond and become a secondary electron; the remaining atomic components with one electron less form an ion, resulting in an *ionization* event. Two other, non-ionizing interaction processes can also be considered between charged particles and atoms: bremsstrahlung, producing a secondary photon; and atomic recoil, producing atomic displacement [153].

In a microscopic scale, there is a certain probability of interaction for each individual event encountered by a charged particle travelling inside matter, with different outcomes in terms of outgoing particle energy and direction. However, on a macroscopic scale, these individual interactions can be summarized as a continuum, resulting in the incoming particle losing energy for each length unit traversed in the material [154]. This approximation is known as the *Continuous Slowing-Down Approximation* (CSDA), which involves the parameter S, named *stopping power*, also often normalized by the material density ρ in the *mass stopping power* S/ρ [152].

Another common quantity linked to this approach is the *Linear Energy Transfer* (LET), which expresses the linear energy loss through electronic interaction. LET can be associated with an energy threshold Δ, to consider only interactions that produce secondary electrons of an energy $E \leq \Delta$, enabling to filter out secondary particles that are too energetic to fully transfer their energy in a region of interest [152]. If $\Delta = \infty$ or not specified, this quantity is called *unrestricted LET* L_∞ (or simply L) and is equal to the part of the stopping power due only to electronic interactions [151].

Quantity	Stopping power	Mass stopping power	LET
Symbol	S	S/ρ	L_Δ
Definition	$\frac{\mathrm{d}E}{\mathrm{d}l}$	$\frac{1}{\rho}\frac{\mathrm{d}E}{\mathrm{d}l}$	$\frac{\mathrm{d}E_\Delta}{\mathrm{d}l}$
SI Unit	$\mathrm{J}\cdot\mathrm{m}^{-1}$	$\mathrm{J}\cdot\mathrm{m}^{2}\cdot\mathrm{kg}^{-1}$	$\mathrm{J}\cdot\mathrm{m}^{-1}$
Usual unit	$\mathrm{MeV}\cdot\mathrm{cm}^{-1}$	$\mathrm{MeV}\cdot\mathrm{cm}^{2}\cdot\mathrm{g}^{-1}$	$\mathrm{MeV}\cdot\mathrm{cm}^{-1}$

Table 1.2. – Usual quantities for qualifying **linear energy loss of charged particles**. $\mathrm{d}E$ is the energy lost by the particle traversing a length $\mathrm{d}l$ inside a material of density ρ. Δ is a threshold energy above which secondary electrons are not considered [151]. The last rows mentions units usually employed in radiation effects literature [152].

Quantity	Energy imparted	Absorbed dose	Absorbed dose rate
Symbol	ϵ	D	$\dot{D}$
Definition	$\sum_i (\epsilon_{\mathrm{in}} - \epsilon_{\mathrm{out}} + Q)_i$	$\frac{\mathrm{d}\bar{\epsilon}}{\mathrm{d}m}$	$\frac{\mathrm{d}D}{\mathrm{d}t}$
SI Unit	J	$\mathrm{J}\cdot\mathrm{kg}^{-1}$	$\mathrm{J}\cdot\mathrm{kg}^{-1}\cdot\mathrm{s}^{-1}$
Usual unit	MeV	Gy (or rad)	$\mathrm{Gy}\cdot\mathrm{s}^{-1}$ (or $\mathrm{rad}\cdot\mathrm{s}^{-1}$)

Table 1.3. – Usual **dosimetric** quantities. i is a single ionization event, ϵ_{in} is the energy of the incoming particle, ϵ_{out} the sum of energies of all outgoing particles, Q the decrease of rest energy of all particles and nuclei of a single ionization event. $\bar{\epsilon}$ is the mean energy imparted by particles in a sample of mass m, and t is the time [151]. The last rows mentions units usually employed in radiation effects literature, with $1\,\mathrm{Gy} = 100\,\mathrm{rad} = 1\,\mathrm{J\,kg^{-1}}$ [152].

The three main quantities for qualifying the linear energy loss of charged particles – stopping power, mass stopping power and LET – are described in **Table 1.2**.

The energy transferred by such charged particles causes alteration of the target material, either through the multiple ionizations produced in the track of the particle, or through atomic displacements. Therefore, the measurement of this transferred energy is of key importance to quantify the reaction of a material under radiation. The physical quantity used for this purpose is the *absorbed dose*, which describes the amount of energy transferred by ionizing particles to a material, normalized by the mass of the material sample. Absorbed dose is expressed in the special unit Gray (Gy), which is equal to J/kg [151]. Another, more ancient unit, is the *radiation-absorbed dose* (rad) [155] which is equal to 0.01 Gy and still very widely used in the radiation effects literature [152]. A more precise definition of the different quantities used for calculation of absorbed dose is presented in **Table 1.3**.

Additionally, because of the complex chain of interactions involved in dose deposition, absorbed dose in a given radiation environment is specific to every material; therefore, it is preferred to specify in the unit the material for which dose is applicable, such as Gy(material) or Gy(mat) [152].

Photons, which are the components of X-ray and γ ray beams, have for energies greater than 1 MeV a lower interaction cross-section with matter than charged particles [156]. However, they can cause a chain of interactions that effectively results in ionizations, causing these types of radiation to be sometimes referred to as *indirectly* ionizing radiation [157]. Three interactions processes, described hereafter, are mainly considered between photons and atoms [158].

The first process, called *photoelectric effect* [159, 160], sees an atomic electron of binding energy E_b totally absorb the incoming photon of energy E_γ, resulting in the liberation of this now-called *photoelectron* with a kinetic energy $E_{\text{pe}} = E_\gamma - E_b$. Additionally, as another atomic electron replaces the vacancy, a secondary fluorescence photon or Auger electron can also be emitted [161].

The second process, called *Compton scattering*, has the incoming photon transfer only part of its energy to an atomic electron, which is released as a secondary particle while the incident photon changes direction [162–164].

The third process, called *pair production* [165–167], has the photon interacting with a Coulomb field and converting part of its energy into the production of an electron-positron pair. If the interaction happens within the field of an atomic electron, this electron is also released, producing an electron-electron-positron triplet (*triplet production*) [168]. Both these processes can only happen if the photon energy is greater than a threshold of $2m_e c^2 \approx 1.022\,\text{MeV}$, with m_e the electron mass [152, 158].

These three ionization processes have different influences depending on the photon energy and the type of material. Photoelectric effect is typically dominant for low photon energies (< ~100 keV), and pair production typically dominates for high photon energies (> ~10 MeV). Between these two areas, Compton scattering is typically the dominant effect. An illustration of the influence of these three processes with photon energy is shown in **Figure 1.11** for bulk silica (SiO_2).

There are other physical processes involving high-energy photons, but considered as negligible because of their high threshold energies and very small cross sections, compared to the processes cited here above. These typically include photonuclear reactions (the average binding energy of a nucleon being between 7 MeV and 9 MeV), photofission and meson production [170].

Electrons released through these photonic processes interact with matter as described previously, resulting in ionizations from these secondary electrons; because of this chain of events, a special attention is given on the generation of secondary electrons by incoming photons. This conversion of photon to secondary electron energy is expressed by the physical quantity *kerma*, which stands for *kinetic energy released per mass*, and equals to the mean sum of kinetic energies of all secondary charged particles released by an uncharged particle, divided by the mass of the material sample. The concept of kerma can also be applied to other uncharged particles such as neutrons [171, 172].

A summary of the main processes and quantities used for dosimetry with photon beams is illustrated in **Figure 1.12**. The incoming number of photons per surface area is characterized by the fluence ϕ,

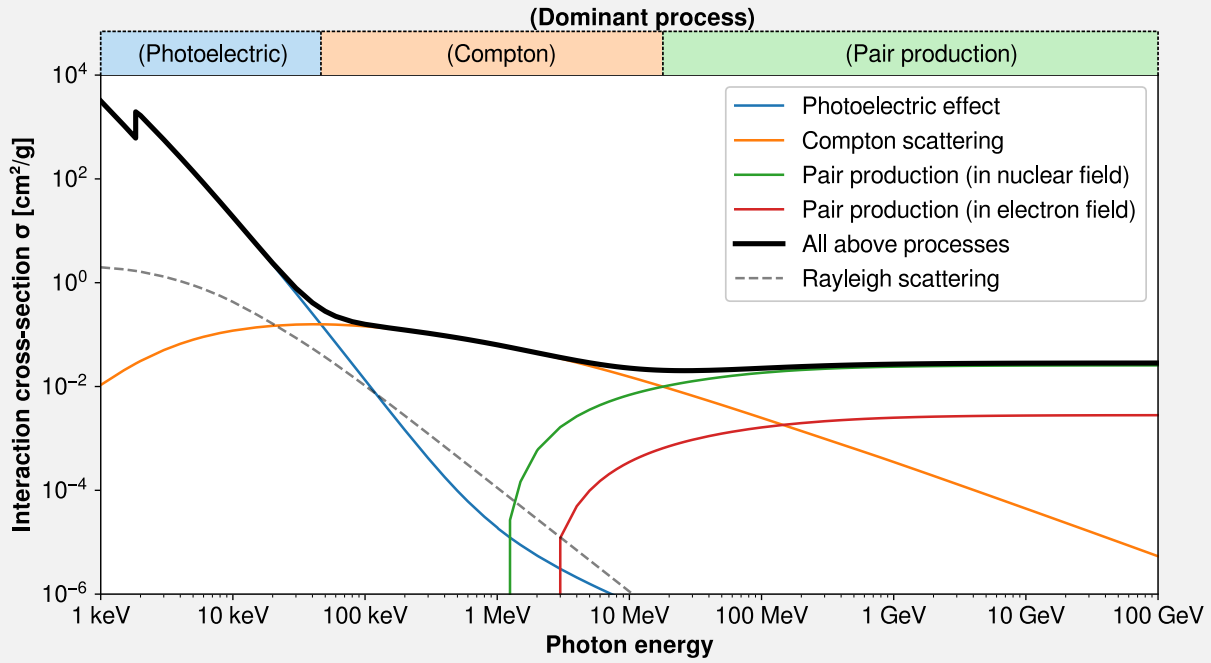

Figure 1.11. – Interaction cross-sections of photons in bulk silica (SiO_2) as a function of their energy, through the three main photonic ionization processes: photoelectric effect, Compton scattering and pair production (within nucleus or electron field). The black solid line indicates the sum of all these three processes, and the grey dashed line shows the interaction cross-section of Rayleigh scattering, for reference. The discontinuity at 1.839 keV is due to the K-shell transition of silicon. Data are from NIST XCOM [169].

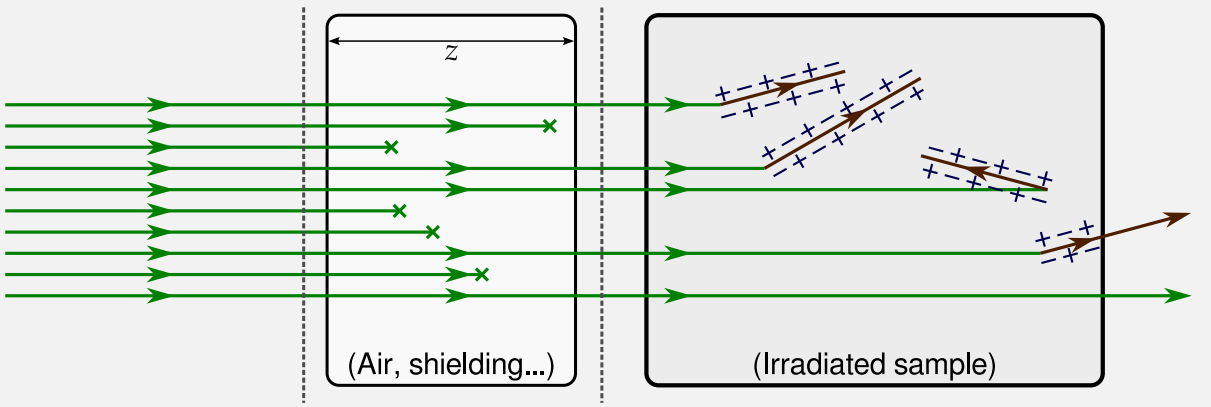

Incoming photons	Attenuation	e⁻ liberation	Dose deposition
Fluence ϕ [cm^{-2}]	Fluence ϕ [cm^{-2}]	Kerma K [Gy(mat)]	Absorbed dose D [Gy(mat)]
Inverse square law: $\phi_B = \phi_A \frac{d_A^2}{d_B^2}$	Mass attenuation coefficient μ/ρ: $\phi(z) = \phi_0 \exp\left(-\frac{\mu}{\rho} z \rho\right)$	Mass-energy transfer coefficient μ_{tr}/ρ: $K = \frac{\mu_{tr}}{\rho} \phi E$	(Monte Carlo simulations)

Figure 1.12. – Summary of main processes, quantities and formulae used for dosimetry with photon beams. For reading clarity, the photons are here considered monoenergetic with energy E.

which, in the common case of an isotropic source, decreases with the distance d from the source in an inverse-square law [152]. Part of these photons are scattered or absorbed during their travel, which is expressed by the *mass attenuation coefficient* μ/ρ; this factor is itself calculated from the sum of cross-sections σ of all interactions mentioned above, along with Rayleigh scattering [173, 174]. Inside the material, the photons release secondary electrons characterized by the kerma K; a quantity associated with this process is the *mass-energy absorption coefficient* μ_{en}/ρ, which is tabulated for most elements [174]. Finally, these secondary electrons cause ionizations as they traverse the material, resulting in dose deposition D; this quantity is always lesser or equal to K because some secondary electrons can leave the material before depositing all their energy.

Being the constituents of atomic nuclei, protons and neutrons can also be captured by a nucleus, resulting in a new atom or isotope. These newly created nuclei are usually unstable, and release energy in the form of secondary particles different types according to the nuclear reaction involved. In this context, the resulting secondary particles are usually categorized under α (helium nucleus), β (electron or positron) or γ (photon) radiation [175].

Radiation effects on electronic devices

Literature on radiation effects often separates absorbed dose in two categories: *total ionizing dose* (TID) refers to the absorbed dose due to ionizations; while *displacement damage dose* (DDD) refers to the absorbed dose due to atomic displacement. The distinction between these two quantities is due to the different observed effects on electronic devices [176].

TID affects electronic devices through different processes, the most common of which is charge trapping in the oxide volume (typically SiO_2 in the case of silicon semiconductors) of MOS or CMOS devices, which degrades the DC drain current [177], causing effects such as the increase in of dark current of image sensors pixels illustrated in **Figure 1.13**. Other processes, such a border and interface traps, are also well studied in this context [178]. The lower dimensions of modern electronic devices, following the tendency predicted by G. E. Moore in 1965 [179], have however reduced the sensitive volume of electronic devices to TID, and resulted in higher tolerance to these effects, at least in the case of silicon-based devices [180].

DDD creates defects in the crystalline structure of the semiconductor, resulting in the creation of additional, parasitic levels in the semiconductor bandgap [182]. This leads to several measurable effects on the devices, among which an increase of the leakage current [183].

Electronic devices are also significantly affected by transient events called *Single-Event Effects* (SEE) that are the results of localized, ephemeral ionizations that can however affect the functioning in major ways, especially in digital devices [184]. Such SEEs are usually declined in the literature through more specific phenomena: for instance, in *Single-Event Upsets* (SEU), microelectronic cells change

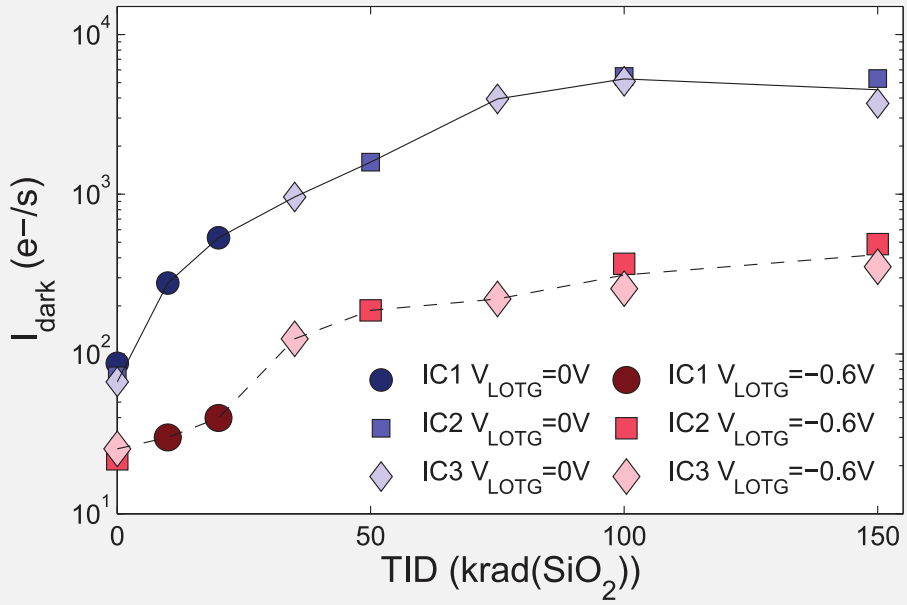

Figure 1.13. – Evolution with TID of the dark current of the reference pixel on different types of CMOS image sensors. (from [181])

state (from 0 to 1 or vice versa) [185], with side-effects ranging from none to memory corruption or execution of wrong instructions [186]. Another SEE phenomenon specific to CMOS technologies is called *Single-Event Latch-up* (SEL), in which a parasitic transistor is created in the device, causing an auto-regenerative, low-resistance path that can only be cleared by switching off the device power supply [187, 188]. A more dramatic version of this effect is the *Single-Event Burnout* (SEB), in which the current density in the parasitic transistor becomes so intense that it permanently damages the device if not stopped promptly [189, 190]

Mitigation and hardening techniques to protect electronic devices under radiation have been studied for several decades [191], and typically take a multi-scale approach. On the component level, design of transistor architectures that prevent charge build-up or limit the ability of leakage current to flow are several examples of the so-called *hardness by design* approach [192]. On the system level, hardware or software redundancies are often implemented to counteract the effects of SEUs [186, 193], as well as periodical resets to eliminate SELs build-up [194]. Simulation tools, such as Technology Computer-Aided Design (TCAD) for semiconductor architecture and Simulation Program with Integrated Circuit Emphasis (SPICE), are also commonly used to assist the design of such radiation-hardened devices [195].

Moreover, the packaging of individual components as well as additional shielding of the whole system can also be considered to reduce their overall exposition to radiation [196]. Finally, radiation testing of massive batches of components is also standard practice in radiation assurance procedures, and components databases built from experimental data can be used to assess their risk of failure in the context of a given mission [197].

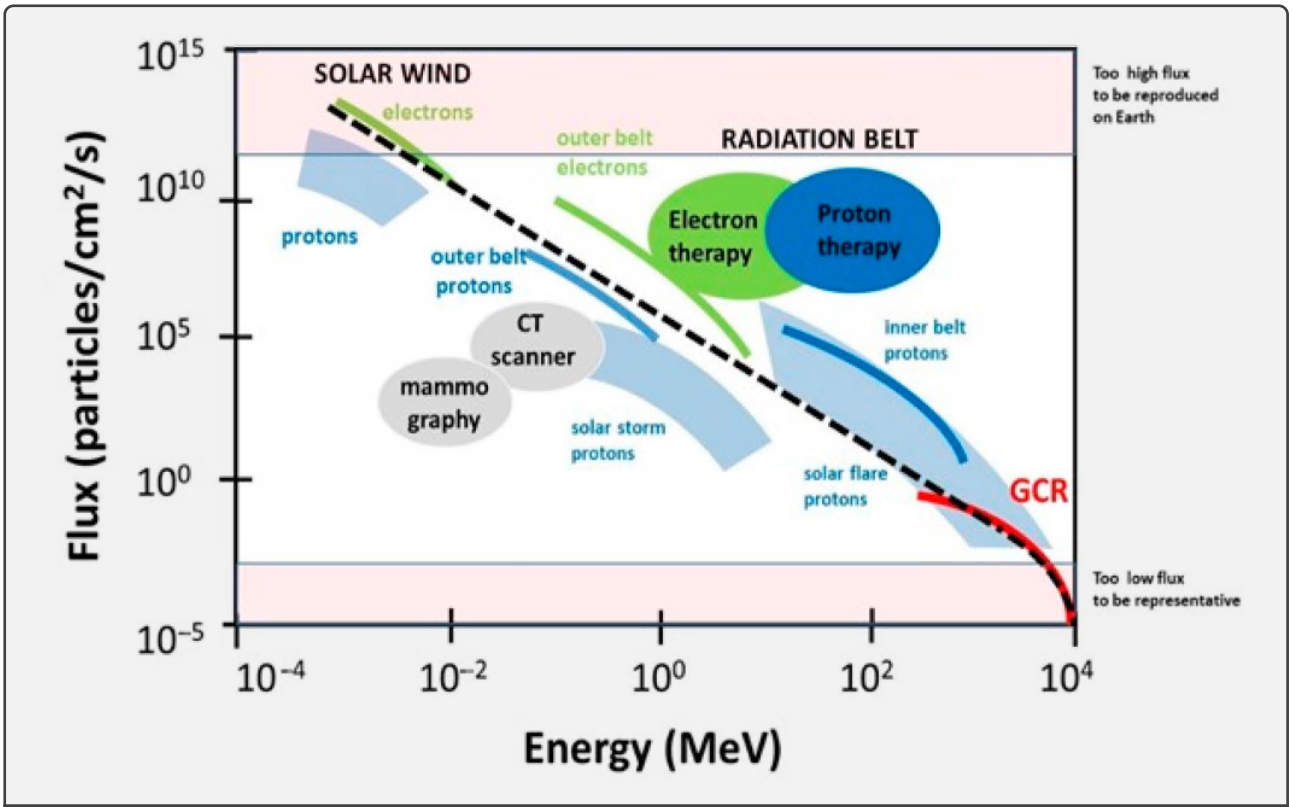

Figure 1.14. – Comparison between spatial radiation environments and typical medical radiation conditions. (from [119]).

Radiation effects on living beings

Ionizing radiation is known to induce negative biological effects on living beings, through many physical and chemical, direct and indirect processes [198]. While these negative effects are usually undesirable, they can also be applied in very controlled conditions to treat cancerous tumours with very high accuracy, using for example high-energy proton beams [199]. A comparison between radiation environments encountered in space and in medical applications is shown in **Figure 1.14**.

Effects of ionizing radiation on human beings have been thoroughly studied in the medical literature, and have revealed many adverse consequences of radiation exposure, including damage to tissues, carcinogenesis, degradation of the central nervous system, or immune system suppression [200].

For these reasons, the measurement of radiation exposure of human personnel operating space missions is essential, and radiation protection dosimetry for space missions has been documented for large space stations such as Mir [201] and ISS [202]. A particular quantity linked to the biological effects of radiation exposure is the *effective dose* H, expressed in sieverts (Sv), which takes into account the biological function and radiation sensitivity of specific areas in the human body through a quality factor Q, which is multiplied by the absorbed dose D [203]:

$$H = D \times Q \tag{1.1}$$

Radiation exposure of living beings is therefore a challenge for potential future interplanetary missions, because of the large amounts of total dose received as well as several aggravating factors such as individual radiosensitivity [119]. Several countermeasures are being designed for this purpose, including reinforced shielding of collective areas or shelters [204, 205], active electromagnetic shielding [205, 206] or specifically designed portable clothing [207, 208].

1.2. Radiation effects on optical fibers

Optical fibers are circular dielectric waveguides that are optimized for conducting light. Their initial development in the late 1960s was heavily linked to the expansion of telecommunications [209] and the increasing bandwidth requirements of these technologies [210]. Electrical cables are restricted in bandwidth because they suffer from high attenuation at very high signal frequencies due to the *skin effect*, confining electrical current to the very surface of the conductor and therefore increasing its resistance [211]. Optical communication, not suffering from the same physical limitations, was thus seen as a promising alternative, especially following the discovery of the laser [212, 213]. However, a practical solution to guide light without intense attenuation, or without needing an unrealistic amount of material and precision manufacturing, was lacking at that time [214].

Whereas the whole theory of optical fibers, adapted from existing knowledge on millimeter waveguides, was already established at the time [215], the first optical fibers suffered from high attenuation, on the order of ~1000 dB/km, that made them impractical for telecommunications [211]. The first breakthrough came from Charles Kuen Kao[6], who identified material impurities as the prime responsible for such attenuation [216], leading the way to further improvements. A result of 20 dB/km at 632.8 nm was first reported in 1970 [217], and later refinements in manufacturing, as well as the use of infrared wavelengths, have enabled the current figure of ~0.2 dB/km which is commonly observed for single-mode, telecommunication-grade optical fibers operating at 1550 nm [218].

Today, while telecommunication remains the overwhelmingly dominant market for optical fibers with an estimated annual global supply of 511 million kilometers of telecom-grade fiber in 2019 [219], many other applications involve optical fiber for a variety of purposes. Optical signal amplifiers [220, 221] are an essential component of long-distance optical networks, while fiber laser amplifiers [222, 223] are used for many applications, including industrial, multi-kilowatt laser cutting or welding systems in which optical fibers are also used to transport this high optical power to its destination [224]. Another very significant application is the whole domain of optical fiber point or distributed, which involves the use of such fibers – either telecommunication-grade or so-called *specialty* optical fibers, for a wide range of sensing and monitoring applications that includes temperature [225], strain [226], vibration [227], rotation [228], liquid level [229], refractive index [230], magnetic field [231], and ionizing radiation, which measurement is the main subject of this thesis.

This whole diversity of applications of optical fibers has lead to their use in environments beyond their original telecommunication purpose, and optical fiber-based devices can be found nowadays in harsh, radiation-affected environments such as space [232], nuclear reactors [233], nuclear waste repositories [234], medical applications [235], particle accelerators [236] or even experimental nuclear

[6] Nobel Prize in Physics 2009.

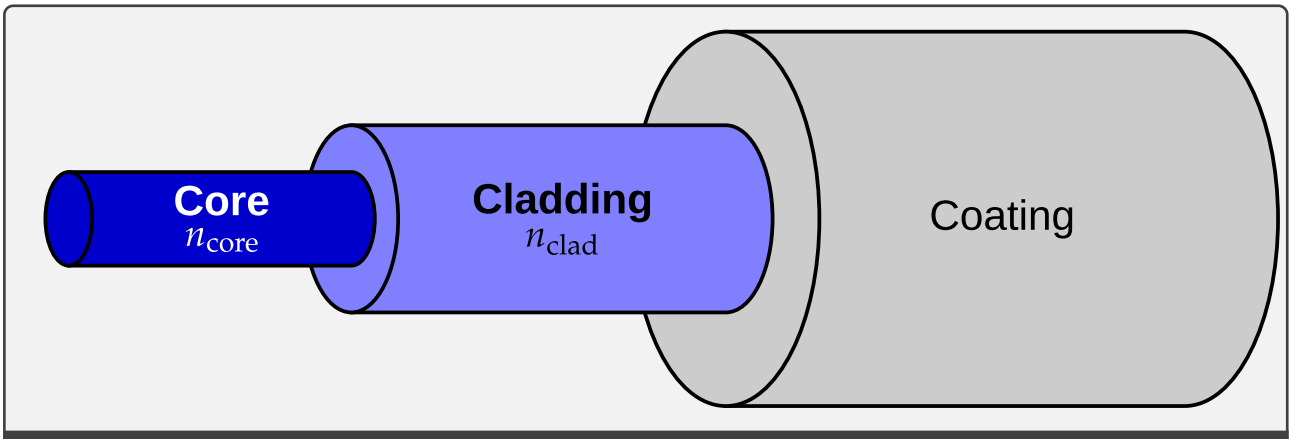

Figure 1.15. – Illustration of the three main components of a step-index optical fiber: core, cladding and coating. n_{core} and n_{clad} represent the refractive indices of, respectively, core and cladding.

fusion facilities [237, 238]. Therefore, a proper understanding of the effects of ionizing radiation on optical fibers and their applications is essential to assess their suitability to such environments.

1.2.1. Composition and geometry of optical fibers

Silica-based optical fibers nowadays are not all made after a single design, but the term instead encompasses a family of many different variations of circular, dielectric optical waveguides, dictated by a variety of applications [239]. However, the basic structure of an optical fiber usually revolves around the three main components illustrated in **Figure 1.15**: *core*, *cladding* and *coating*.

The main role of the coating is to mechanically protect the inner components from moisture and stress that can considerably affect fiber lifetime [240]. This part is however not devoid of engineering interest, and design of the coating can be of vital importance, especially in sensing applications; either because it acts an interface between the inner waveguide and the outside environment, or because of its influence on enabling or attenuating cladding modes [241, 242].

The main functionality of the optical fiber, namely to guide light, is performed by the two inner elements: the core and the cladding. To ensure suitable functionality for its target application, the design of an optical fiber includes the choice of a functional waveguide architecture, with proper materials and an appropriate engineering of refractive indices.

Material and losses

The base of an optical fiber is a dielectric material which is transparent, i.e. has low optical absorption, at the range of wavelengths for which it is designed. The typical material used for this application is glass based on amorphous silica (SiO_2), which presents both advantages to be inexpensive [211] and transparent in the ultraviolet, visible and near-infrared ranges, with at least 10 % transmission

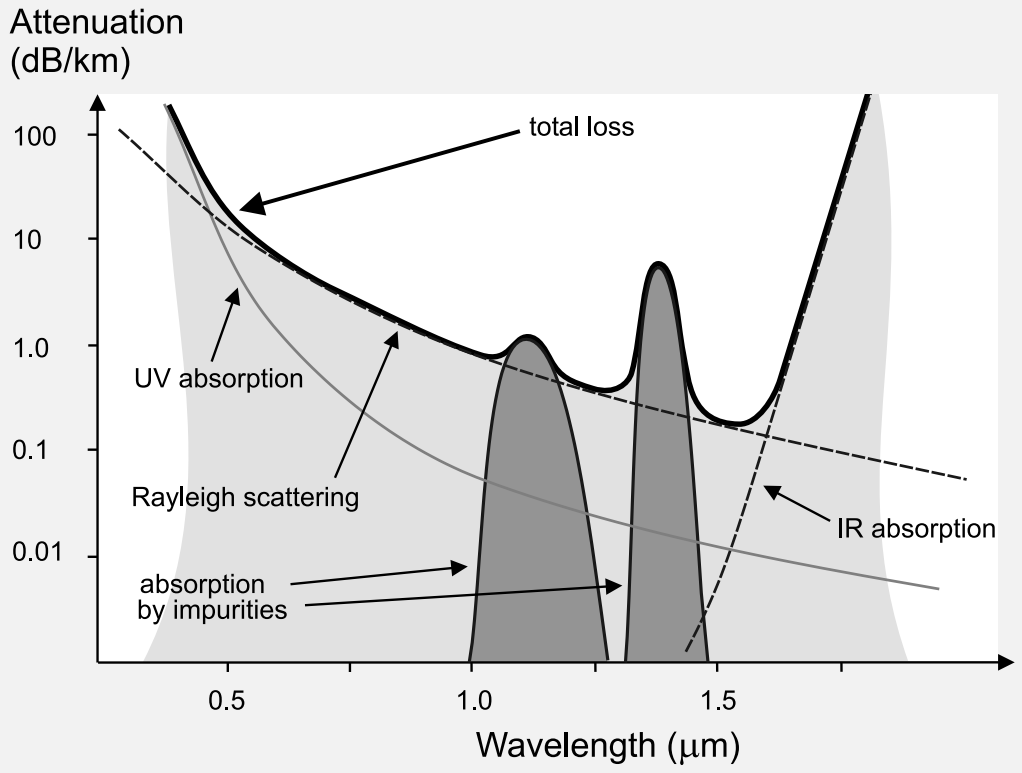

Figure 1.16. – devicesverview of the loss mechanisms in a typical optical fiber-grade silica, as a function of the wavelength. The low-loss window can be identified around 1550 nm. (from [244])

between 160 nm and 4000 nm for 2 mm thickness [243]. Other kinds of glasses, such as fluorides, chalcogenides and halides, have also been considered for their extremely low attenuation in the infrared domain, but have so far not met these expectations in practice, due to their high chemical reactivity and inferior mechanical properties [244]. Polymer materials are another alternative, being cheap and easy to manufacture into fibers, but also provide more attenuation than silica in the visible to near-infrared range [245].

In the typical application range of optical fibers, at wavelengths between 300 nm and 2000 nm, losses in silica are mainly explained by four concurrent phenomena, illustrated in **Figure 1.16**. The two first contributions are due to electronic and molecular absorption of silica, inducing two absorption tails from ultraviolet and infrared [244]. Other, additional absorption bands come from impurities embedded in the glass during manufacturing, such as hydroxyl (OH) which induces a distinctive absorption band centered around 1385 nm associated with the first OH-stretching overtone vibrations [246, 247]. A final, important contributor to material-induced losses is Rayleigh scattering (introduced in more detail in **Section 1.3.1**), which evolves in a inverse, fourth-power law with the wavelength. Scattering losses are linked to fluctuations of the material density, which are reflected by a quantity known as *fictive temperature* in materials science [248, 249]. Through engineering of a low fictive temperature on a pure-silica-core optical fiber, an attenuation as low as 0.1419 dB/km at 1550 nm has been reached in 2018 [250], with a lowest theoretical limit estimated to 0.114 dB/km [244].

The minimum of these material-induced losses is located at a wavelength of ~1550 nm, and therefore the optical domain of choice for long-distance telecommunication networks, called *C-band*, is located between 1530 nm and 1565 nm [251]. This range is also called *third telecommunication window*, for historical reasons linked to the availability of inexpensive lasers at these wavelengths [252]. Another optical domain of interest for the present thesis is the *long wavelength band*, or *L-band*, defined between 1565 nm and 1625 nm, and used both to extend data transmission capacity of existing lines [253] and for network diagnostic [254].

In addition to these losses solely linked to the base material, other sources of attenuation can be identified for optical fibers: guiding losses, due to coupling with so-called *leaky modes* [255] and/or induced by curvature [256]; coupling losses, applicable for injecting or retrieving signal [257]; and splicing losses, in the case multiple optical fibers segments are welded together [258]. Finally, additional defects can be created in the fiber material, which cause additional losses in the form of optical absorption [259]; this latter subject, of prime importance in the study of the effects of ionizing radiation on optical fibers, is discussed in more detail in **Section 1.2.2**.

Waveguide architecture and properties

Considering light as an electromagnetic wave[7], its propagation in vacuum and in matter is described by Maxwell's equations. Particular solutions of these equations, known as *guided modes*, can be calculated from a set of conditions leading to constructive phase matching, so that light propagates through the waveguide. The detailed handling of these calculations is amply covered in the literature [261–265] and the following paragraphs will give the main results relevant to the present work.

In the case of a simple, step-index fiber design (cf. **Figure 1.15**), the main parameters used for mode calculation are the operating wavelength λ, the radii r_{core} and r_{clad} of the core and cladding, and their refractive indices n_{core} and n_{clad}. For this type of fiber, we have typically $n_{\text{core}} > n_{\text{clad}}$.

A first key parameter is the refractive index contrast between core and cladding, which can expressed by a few quantities: *numerical aperture* NA (which also gives the fiber half-angle of acceptance θ) and *relative refractive index difference* Δ:

$$\text{NA} = \sin(\theta) = \sqrt{{n_{\text{core}}}^2 - {n_{\text{clad}}}^2} \qquad \Delta = \frac{{n_{\text{core}}}^2 - {n_{\text{clad}}}^2}{2{n_{\text{core}}}^2} = \frac{\text{NA}^2}{2{n_{\text{core}}}^2} \approx \frac{n_{\text{core}} - n_{\text{clad}}}{n_{\text{core}}} \tag{1.2}$$

A guided mode is associated with an effective refractive index n_{eff}, such as $n_{\text{clad}} < n_{\text{eff}} < n_{\text{core}}$. From

[7] Even though electromagnetism can be considered as an approximation to the quantum nature of light, the optical fiber waveguide design is experimentally valid down to single photons [260].

this value can be deduced the *propagation constant* β and two normalized parameters u and w:

$$\beta = \frac{2\pi}{\lambda} n_{\text{eff}} \qquad u = \frac{2\pi}{\lambda} r_{\text{core}} \sqrt{{n_{\text{core}}}^2 - {n_{\text{eff}}}^2} \qquad w = \frac{2\pi}{\lambda} r_{\text{core}} \sqrt{{n_{\text{eff}}}^2 - {n_{\text{clad}}}^2} \tag{1.3}$$

To determine the guided modes of an optical fiber, Maxwell's equations are applied in the core and cladding. Accounting for the rotational symmetry of the fiber, treatment of these equations in cylindrical coordinates yields an expression in the form of Bessel's differential equation. Because of this, solutions are expressed according to the Bessel function of first kind J_m in the core, and the modified Bessel function of second kind K_m in the cladding.

An important, practical approximation known as *weakly guiding approximation* is performed by considering $\Delta \ll 1$, and therefore $n_{\text{core}} \approx n_{\text{clad}}$. In this condition, which is commonly encountered in practice, we obtain the following eigenvalue equation of parameter m [266]:

$$\frac{J_m(u)}{uJ_{m+1}(u)} = \frac{K_m(w)}{wK_{m+1}(w)} \tag{1.4}$$

For a given value of m, only a finite number of modes are solutions of this equation. In the weakly guiding approximation, the transverse electric/magnetic modes are degenerated, and called *linearly polarized* (LP); the denomination of optical fiber modes under this approximation is therefore LP_{mn} (with m as above and n another index to discriminate multiple solutions with the same value of m), and the fundamental mode is named LP_{01} [266].

A key parameter for mode calculation is the *normalized frequency* V, which is linked to the number of guided modes permitted in a given fiber. If $V < 2.405$ (the first zero of the Bessel J_0 function), then the optical fiber can guide only the fundamental mode and is therefore called *single-mode* at this value of λ. If $V \geq 2.405$, then more than one mode can be guided, and the fiber is called *multimode*. This property is also reflected in the *cutoff wavelength* λ_c: if $\lambda > \lambda_c$, then the fiber is single-mode.

$$V = \sqrt{u^2 + w^2} = \frac{2\pi}{\lambda} r_{\text{core}} \sqrt{{n_{\text{core}}}^2 - {n_{\text{clad}}}^2} \qquad \lambda_c \approx \frac{2\pi}{2.405} r_{\text{core}} \sqrt{{n_{\text{core}}}^2 - {n_{\text{clad}}}^2} \tag{1.5}$$

Many other designs exist beyond the step-index architecture presented here above; an overview of some commonly used refractive index profiles – step-index, gradient-index and double-clad – is shown in **Figure 1.17**, along with a more complex example of a photonic crystal fiber.

Calculation of the guided modes and field characteristics of optical fiber with arbitrary refractive index profiles usually involves numerical computation. Some models used for static evaluation of the modes are Beam Propagation Method (BPM) [267], Multilayer approximation [268] or generic Finite Element Method (FEM), used for instance by the software COMSOL [269]. Time-resolved

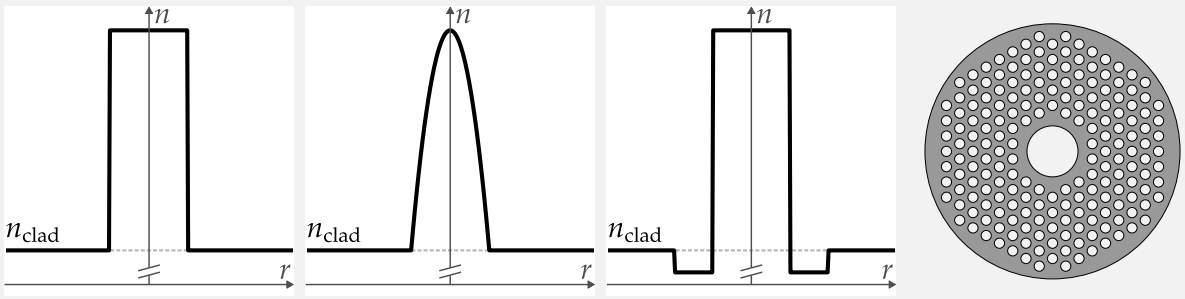

(a) Step-index profile. **(b)** Gradient-index profile. **(c)** Double-clad profile. **(d)** Photonic crystal fiber.

Figure 1.17. – **(a–c)** Several typical refractive index profiles for rotation-symmetric optical fibers, giving the evolution of the refractive index n as a function of the radius coordinate r. The refractive index of the cladding n_{clad} is indicated in dashed line. **(d)** Cross-sectional layout of a photonic crystal fiber, where dark areas are pure silica and light areas are air.

models, such as the Finite-Difference Time-Domain (FDTD) method [270, 271] can also be used for specific application such as modeling the propagation of ultrashort pulses [272].

Engineering of refractive indices using dopants

As illustrated by the waveguide considerations presented in the previous section, one the main aspects that governs the function of an optical fiber is the refractive index contrast between the cladding and other regions of the fiber (such as the core).

To obtain the desired refractive index in specific locations of an optical fiber, a usual solution is to mix silica with other molecules, known as *dopants*, in varying proportions [275]. As shown in **Figure 1.18**, the refractive index can increase or decrease depending on the dopant involved, and evolves mostly linearly with dopant concentration, enabling fine tuning of the refractive index through precise stoichiometry of the dopant material during manufacturing.

Some of the main types of dopants used for optical fibers are listed hereafter:

- Germanium (Ge) is the most commonly used core dopant for telecom-grade optical fibers [276], and is also known for its photosensitive properties, which makes it a dopant of choice for ultraviolet inscription of Fiber Bragg Gratings (FBGs) [277].

- Fluorine (F) is used to decrease the refractive index of the material, either to produce double-clad fiber profiles (cf. **Figure 1.17c**), or *pure silica core* fibers with very low losses [250, 278].

- Phosphorus (P) is used to soften the glass material, and therefore decrease its drawing temperature [279]. Another application of this dopant is in fiber amplifiers, in which phosphorus reduces the clustering of rare-earth ions [280].

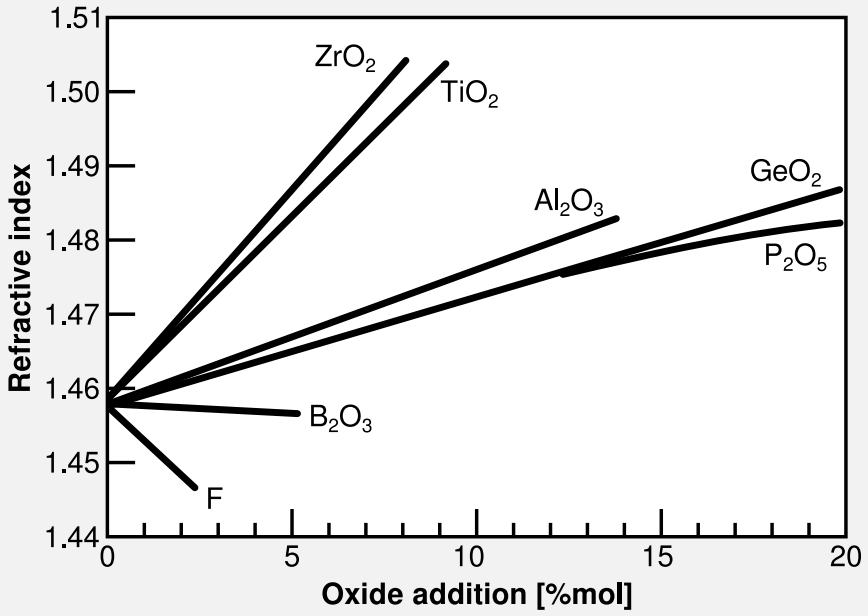

Figure 1.18. – Overview of the refractive index at 587.6 nm (n_d) of silica (SiO_2) with different dopant concentrations. Seven types of dopants are represented here: alumina Al_2O_3, boron trioxide B_2O_3, fluorine F, germanium dioxide GeO_2, phosphorus pentoxide P_2O_5, titania TiO_2 and zirconium dioxide ZrO_2. (adapted from [273, 274])

- Aluminum (Al) is another component that prevents clustering of rare-earth ions, and therefore also commonly used in fiber amplifiers [281, 282].
- Cerium (Ce) is used to prevent the formation of color centers in silica glasses [283]. Its ionization properties under radiation are also exploited in radioluminescence applications [284].
- Other rare-earth elements such erbium (Er) and ytterbium (Yb) are commonly used in fiber amplifier applications, especially in telecommunications because of the amplification properties of Er in the ~1550 nm range, which efficiency is enhanced by the addition of Yb [220, 285].

Several manufacturing techniques exist in order to obtain the desired profile of dopant concentrations, and therefore refractive index, along the radius of the optical fiber. The most common method is the Modified Chemical Vapor Deposition (MCVD), in which materials are vaporized and deposited as a succession of thin films in a rotating, hollow tube [286]. This process can be refined to be compatible with a wider range of dopants, such as in Surface Plasma Chemical Vapor Deposition (SPCVD) which involve plasmas to enable deposition of low vapor pressure materials [287]. The *preform* obtained from this process is then heated and drawn to the desired thickness and length [288].

Photonic crystals fibers (also called *hollow core fibers*) involve only pure silica and air, and rely on complex architectures (cf. **Figure 1.17d**) co-designed by numerical simulation to define and shape guided modes. These fibers can enable innovative sensing applications, either using the fiber design [289], or functionalized by injecting gas [290] or nanoparticles [291] to further increase their sensitivity to a designed measurand. Recent refinements in the design of such fibers, especially through the

inclusion of nested structures in so-called *Nested Antiresonant Nodeless Fibers* (NANFs) [292], have also enabled a dramatic decrease of the high losses usually observed with photonic crystal fibers [293]. NANFs have been the object of an intense publication activity in the recent years, with reports of low attenuations at telecom wavelengths on par with classical step-index architectures [294].

1.2.2. Radiation-induced physical processes in silica-based optical fibers

Silica (SiO_2) is an amorphous material, with a local structure in the form of $SiO_{4/2}$ tetrahedrons connected jointly at the corners [295]. It is most commonly found in nature under one of its crystalline forms, called quartz, which is very abundant in most types of crustal rocks on Earth [296]. Other, rarer forms of crystalline SiO_2, such as cristobalite, tridymite and coesite can also be formed in conditions of high temperature or pressure [297]. While fine crystalline SiO_2 powder is known to induce a lung cancer type called *silicosis*, amorphous silica is estimated to be less toxic [298].

Production of silica is performed by fusion of natural quartz, through a variety of processes that lead to different qualities of material, with varying amounts of metallic impurities and OH contents. Type IV silica, produced from $SiCl_4$ through water-vapor free plasma fusion, has the lowest amount of impurities [299, 300]. Silica with high OH content is sometimes called *wet*, while silica with low OH is called *dry* [301].

Impurities in materials, as well as localized ionizations or alterations of the material arrangement, create local structures known synonymously as *defects*, *point defects* or *color centers*. Whereas some of these defects are already present in the material after manufacturing [297], ionizing radiation induces the appearance of new defects, through ionization or displacement damage, as summarized in **Figure 1.19**.

Study of defects and their generation processes in pure silica as well as its doped variants has been extensively performed since the 1950s [303, 304], and a variety of characterization techniques, such as Electron Paramagnetic Resonance (EPR), also called Electron Spin Resonance (ESR) [305], have been used to establish an abundant literature on the different types of defects encountered in silica-based materials [306].

Defects in bulk silica

The E′ defect results from the trapping of a hole at an oxygen vacancy site [302]. Even though three distinct variants of this defect (E'_α, E'_β and E'_γ) have been identified using EPR, they exhibit a common optical absorption band located at 5.8 eV with a FWHM of 0.7 eV [307]

Oxygen vacancies, in a neutral state, cause the occurrence of the *Oxygen-Deficient Center* (ODC) species of defects, which are found in two types. ODC(I) is the most frequently occurring type,

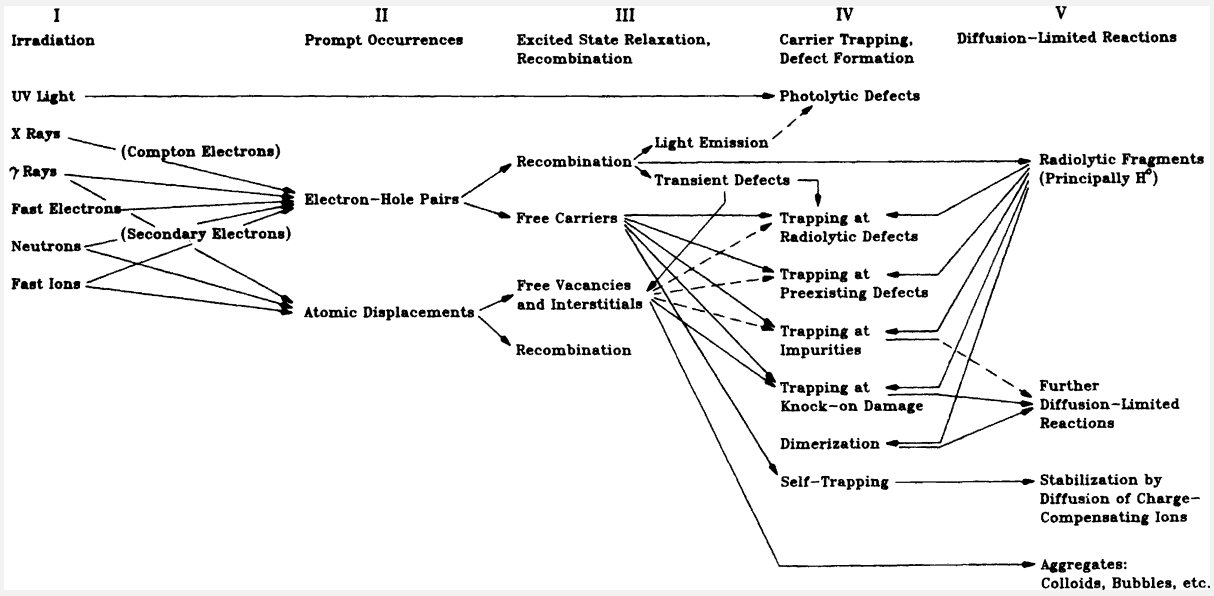

Figure 1.19. – Overview of the different mechanisms of defects creation in bulk silica exposed to ionizing radiation. (from [302])

and has an optical absorption band centered at 7.6 eV with a FWHM between 0.5 eV and 0.6 eV [307]. ODC(II) is believed to originate from a metastable vacancy, and exhibits an absorption band with a maximum at 5.03 eV and a FWHM of 0.4 eV; however, due to the lesser appearance probability of this state, this band has a much weaker intensity, typically 10^4 lower than ODC(I) [307].

Breakage of an Si — O bond results in a *Non-Bridging Oxygen Hole Center* (NBOHC) type of defect. It is characterized by an asymmetric optical absorption spectrum, which can be approximated by three Gaussian bands centered respectively at 1.95 eV, 2.04 eV and 2.21 eV in the visible range [308, 309], and five Gaussian bands between 4.706 eV and 7.29 eV in the ultraviolet range [310].

Holes resulting of ionizations can also be *self-trapped*, i.e. prevented to recombine because they stand in a low-potential region of the material from where they cannot escape [311]. These types of defects are called *Self-Trapped Holes* (STH), which, despite their very high instability [312] are the main contributors to RIA of pure-silica-core fibers under steady [313] or short pulse irradiations [314]. Two types of STH can be distinguished: STH_1 are inherent to the material, and characterized by optical absorption bands centered at 1.88 eV and 2.6 eV; STH_2 are assisted by bond strains and give optical absorption bands of lower energies, centered at 1.63 eV and 2.16 eV [306].

Moreover, impurities brought by the manufacturing process also cause a variety of defects. In particular, chlorine-related defects are well studied in the literature, with an optical absorption band centered at 3.8 eV associated with interstitial, atomic Cl^0 defects. Another absorption band located at 3.26 eV is believed to be associated with molecular Cl_2 defects [315].

Finally, materials based on doped silica, because they include additional elements to the basic silica matrix, are the source of very wide range of material-specific defects. Germanium-doped silica, in

particular, has been the object of numerous studies on its specific defects [316–320], which are of key importance to understand and model the behavior of telecom-grade optical fibers under radiation [321, 322]. Defects linked to other doping materials, such as aluminum [323, 324], have also been studied. The main dopant of interest in the context of this thesis work is phosphorus, and defects of phosphorus-doped silica are described in more detail in **Section 1.2.3**.

Several simulation methods are used to model such defects and their properties, such as *Molecular Dynamics* [325] used in the free software LAMMPS [326], or *First Principle* (FP) (also called *ab initio*) method, which models molecule interactions down to the quantum level [327–329]

Radiation-induced attenuation (RIA)

Defects created or converted during irradiation induce optical absorption, around defined energy bands that are specific to each defect, as explained here above. The increase of the defect population is linked to an increase of the optical absorption intensity [330], causing the measurable phenomenon known as RIA.

The theoretical framework of RIA measurement streams from modeling by a Beer-Lambert law the intensity $I(z)$ of an optical signal measured after travelling through a homogeneous segment of length z in an optical fiber:

$$I(z) = I_0\, e^{-\alpha z} \tag{1.6}$$

where I_0 is the signal intensity at $z = 0$, and α an attenuation coefficient that reflects all different types of losses induced by the optical fiber and its material (see also **Section 1.2.1**).

If we consider that α has two main components: α_0, representing the intrinsic fiber losses before irradiation, and α_{RIA}, representing the additional losses caused by the defects created under radiation, then (1.6) becomes:

$$I(z) = I_0\, e^{-(\alpha_0+\alpha_{\text{RIA}})z} \tag{1.7}$$

RIA is typically measured by a setup with a source placed at one end of the fiber and a detector placed at the other end [331]. In this case, it can be calculated from the intensities I_{init} and I_{irrad} measured at the detector, respectively before and after irradiation, for a same optical fiber length L:

$$\text{RIA} = -\frac{10}{L}\log_{10}\left(\frac{I_{\text{irrad}} - I_{\text{dark}}}{I_{\text{init}} - I_{\text{dark}}}\right) = \frac{10}{\ln(10)}\alpha_{\text{RIA}} \tag{1.8}$$

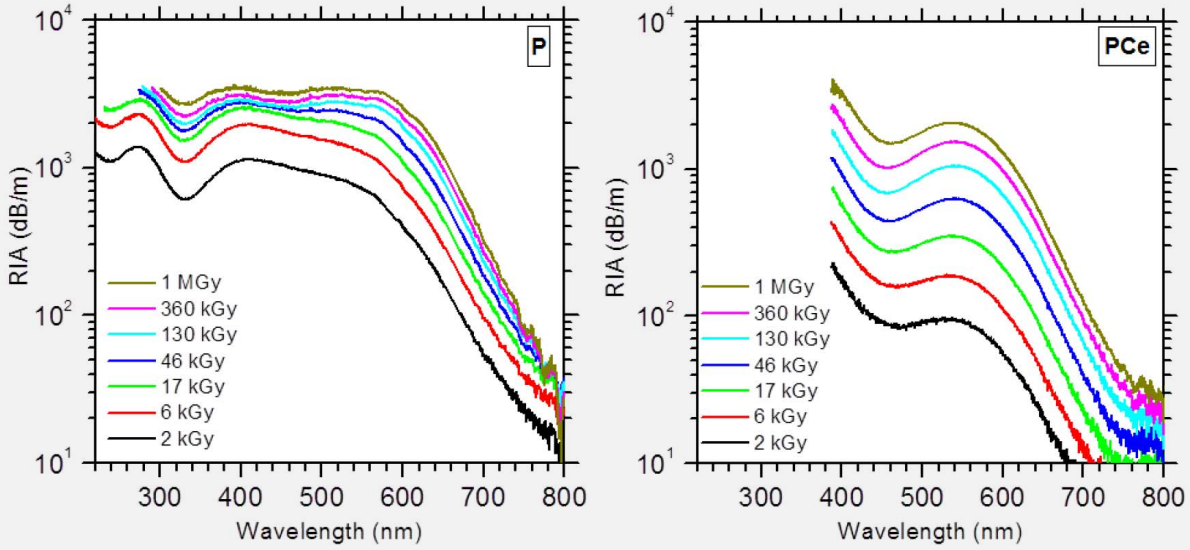

(a) Phosphorus (P)-doped. **(b)** Phosphorus (P) and cerium (Ce) co-doped.

Figure 1.20. – RIA spectrum in the visible range of multimode optical fibers with two different types of dopants, irradiated under X-rays at different doses. (from [334])

where I_{dark} is the dark signal of the detector, measured with the light source switched off. The unit of RIA as calculated in (1.8) is given in dB/m. The radiation-induced loss coefficient α_{RIA}, which is less commonly used in the literature, is given in m^{-1}.

Because both components of α are dependent on the wavelength, spectral measurements can also be performed to evaluate the RIA spectrum of an optical fiber. The setup used in this case involves a broad-spectrum light source, typically a black-body source such as an halogen lamp, launching light at one end of the fiber, and a spectrometer at the other end of the fiber [332]. In this case, RIA calculation is performed by applying (1.8) for each wavelength given by the spectrometer.

Finally, RIA can be measured *a posteriori* by using a destructive method called *cutback* [333], which also enables measuring the intrinsic losses of an optical fiber. This measurement setup involves a broad-spectrum source and a spectrometer as described here above; in the case of cutback, two transmission spectra are acquired: I_{long} and I_{short}, measured respectively before and after removing a known length ΔL by cutting the optical fiber. The intrinsic attenuation for each wavelength is then obtained by applying (1.8) for each wavelength as described above. As the cutback method cannot distinguish initial material losses from radiation-induced losses, measurement of the RIA spectrum in this context involves comparing the attenuation spectrum between irradiated and non-irradiated samples of a same fiber.

An example of such attenuation spectra is shown in **Figure 1.20** for two different types of multimode optical fibers irradiated under X-rays. The increase of attenuation with the received dose is clearly visible, as well as the material-specific structure of the absorption spectrum, which is the signature of the underlying radiation-induced defects [334].

Another RIA measurement setup, involving Optical Time-Domain Reflectometry (OTDR) (cf. **Section 1.3.2**), is the main subject of this thesis and is further developed in **Section 1.4**.

Radiation-induced emission (RIE)

In addition to optical absorption, several materials can also exhibit the inverse effect, namely the emission of light, either spontaneously or when excited by temperature or an optical probe.

A first emission process, named *radioluminescence*, comes from the radiation-induced excitation of impurities, dopants or defects, that spontaneously relax within a characteristic time that is proper to each kind of center [306]. The difference in energy between the excited and fundamental (or intermediate) states is emitted in the form of a photon, which, provided its energy stands in the forbidden energy band of the material, is allowed to propagate and be ultimately detected [335].

As a consequence, radioluminescence causes the irradiated material to convert the high energy received from the irradiating particles to a lower-energy optical signal, in a process that can be compared to fluorescence, even though there are differences in excitation and relaxation processes [335]. This behavior makes radioluminescence a useful tool to detect and quantify radiation, and measurement devices using this phenomenon are called *scintillators* [336].

Optical fiber materials also produce radioluminescence, which is both considered as an adverse effect as it generates a parasitic signal when coupled to calibrated scintillators [337], and a desirable effect as it enables to perform dosimetry using the optical fiber both as a sensitive element and to transport the generated signal to an external measuring device [338]. Many types of optical fiber dopants exhibit measurable radioluminescence, as illustrated in **Figure 1.21** (see also **Article A.1**), but some of the most sensitive dopants for such applications are cerium [284], gadolinium [339], nitrogen [340] and germanium [341].

Another phenomenon causing emission of light under radiation is the Cherenkov radiation[8] [343] which is produced when a charged particle travels through a medium of refractive index $n = c/v_p$ with a speed greater than the local phase velocity of light v_p [344]. This condition implies a minimum, threshold energy E_{min} below which this speed is not achieved, and given by the following relativistic expression [345]:

$$E_{\text{min}} = m_0\, c^2 \left(\frac{1}{\sqrt{1-\beta^2}} - 1 \right) \tag{1.9}$$

where m_0 is the rest mass of the charged particle, $c = 299\,792\,458\,\text{m/s}$ the speed of light in vacuum [346] and $\beta = v_p/c = 1/n$ the speed fraction. For electrons ($m_e \approx 0.511\,\text{MeV/c}^2$ [346]) in silica-based optical fibers ($n \approx 1.4$), this threshold energy E_{min} is on the order of 200 keV.

[8] Named after Pavel Alekseyevich Cherenkov (1904–1990), Nobel Prize in Physics 1958.

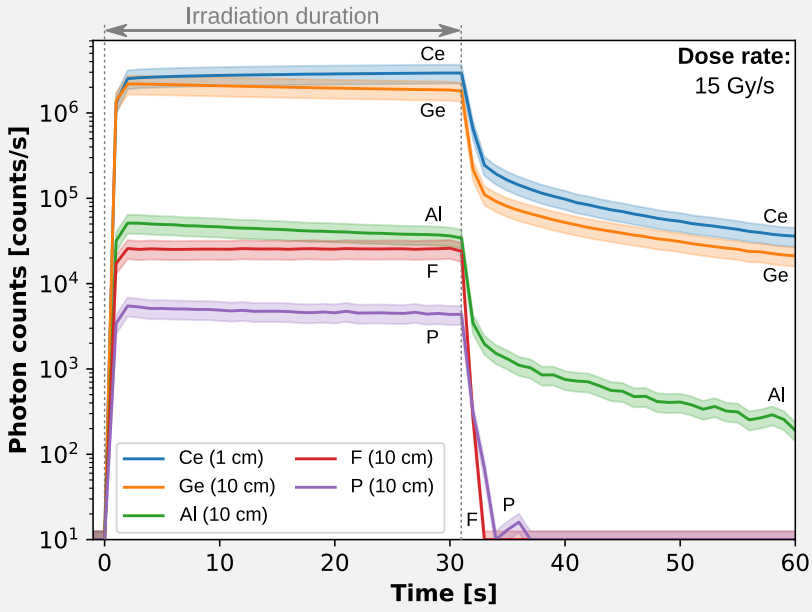

Figure 1.21. – Comparison of X-ray radioluminescence signal of multimode optical fibers with different dopants: cerium (Ce), germanium (Ge), aluminum (Al), fluorine (F) and phosphorus (P). The Ce-doped sample is ten times shorter than the others, which reduces its signal by a factor of ~10. Filled areas show uncertainties at ±25 %. (from [342])

Investigation of luminescent defects can also be conducted without ionizing radiation, but instead by radiation at optical wavelengths. This technique, called *Photoluminescence* (PL), enables to selectively excite defects by selecting the excitation wavelength, making it possible to perform a finer analysis of the different defect species present in a material [347].

Other techniques causing emission of light are typically used after irradiation.

Thermoluminescence (TL) involves heating the irradiated material at a controlled rate. As the temperature increases, the radiation-induced defects are relaxed and produce a luminescent signal [348], which intensity depends on the dose absorbed by the material, enabling dosimetry applications [349]. Because the temperature is linked to the relaxation energy of defects, this method enables other means to characterize defects created under radiation [350].

Optically-Stimulated Luminescence (OSL) consists in injecting a light signal at a particular wavelength in an irradiated material and to measure its emission spectrum, minus the stimulation wavelength. This process also results in relaxing some of defects created under radiation, and produces a signal that can be correlated to the dose received by the material [351].

Radiation-induced refractive index change (RIRIC)

Ionizing radiation produce density change in materials [352–354], either due to displacement damage [355] or to structural reorganization of matter as a result of ionizations [356]. This change of density

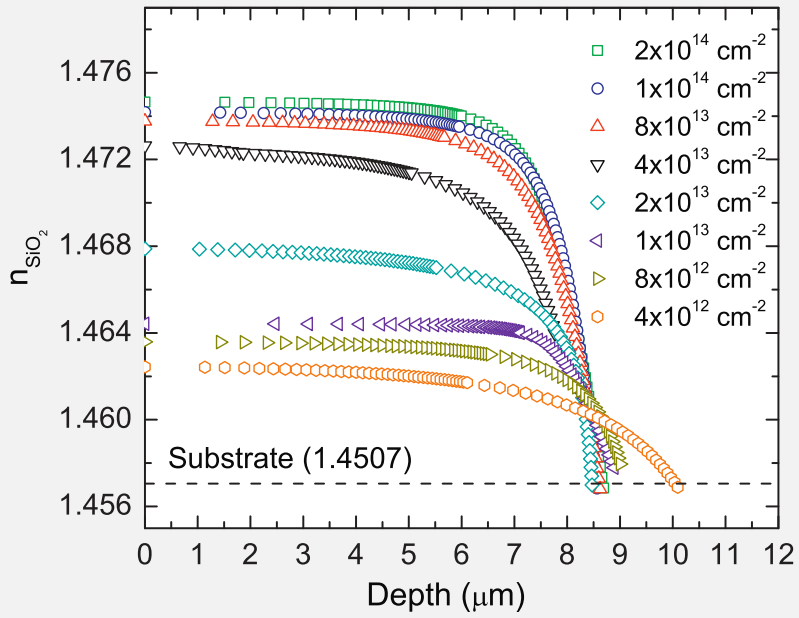

Figure 1.22. – Evolution of the refractive index n_{SiO_2} of pure silica as a function of the depth in bulk samples irradiated with a combination of 25 MeV bromine (Br) and 10 MeV chlorine (Cl) ions at different fluences. Refractive index measurement was performed using ellipsometry. (from [362])

is linked to a change of the material refractive index, which has been evidenced under irradiation with particles of many different natures, such as X-rays [357], γ rays [358], protons [359], neutrons [360] and ions [361, 362]. An example is shown in **Figure 1.22** with measurements of the refractive index of pure silica irradiated at different heavy ion fluences.

Material density changes can also be caused by non-ionizing radiation, such as ultraviolet light [363] or femtosecond lasers [364]; such processes are widely exploited for the inscription of fiber Bragg gratings (FBGs) [365].

In terms of observable behavior of the material under radiation, RIRIC is usually considered as a secondary phenomenon compared to RIA and RIE; mostly because of its comparatively weak influence on the performance limits of optical fibers in radiation environments [330], but also because RIRIC only becomes significant at high dose levels [366], such phenomena being typically reported in the MGy range [358, 367, 368]. However, in certain applications such as imaging systems, the change of the refractive index of optical elements, such as lenses, can cause radiation-induced aberrations [369], even when using "radiation-hardened" glasses that are actually only resistant to RIA [370].

Modeling of RIRIC is usually deduced from RIA characteristics of a material by applying the Kramers-Kronig relations, which link together the integrals of the real and imaginary parts of the complex refractive index of a material over the whole spectrum [371]; this approach has however proved unsatisfactory to accurately reflect experimental results [359, 372, 373]. Another approach involves the Lorentz-Lorenz equation, linking refractive index change with compaction [374]. Finally, a model of X-ray RIRIC of a polymeric material has also been proposed [375].

Defect name	P_1	P_2	P_4	s-POHC	m-POHC
Schematic	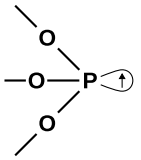	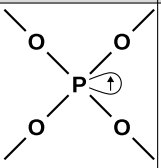	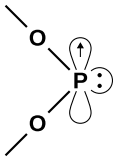	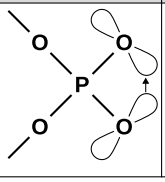	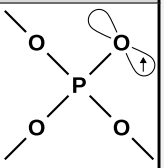
Absorption energy	0.79 eV	4.5 eV	4.8 eV	2.2 eV, 2.5 eV 3.1 eV, 5.3 eV	
Absorption wavelength	1569 nm	276 nm	258 nm	564 nm, 496 nm 400 nm, 234 nm	

Table 1.4. – Overview of the main defects in phosphorus-doped silica. **O** and **P** represent respectively oxygen and phosphorus atoms, arrows represent vacant electron orbits, colon represents a dangling bond. (schematics are adapted from [376])

1.2.3. Defects of interest in phosphorus-doped silica

Phosphorus (P)-doped fibers raised attention around the 1980s, starting from observations that Ge-P co-doped fibers showed resistance to transient RIA in pulsed, high-dose-rate irradiations with 0.5 MeV electrons, while displaying very stable long-term RIA behavior in comparison with other types of doping [377]. These experiments led to specific research on the identification and characterization of defects in P-doped silica, summarized in **Table 1.4**. Most of these defects are named with the letter P and a numerical index, following a convention set by an early study on crystalline phosphorus pentoxide P_2O_5 [378]; noticeably, the P_3 detected in this early work could not be observed in later studies, which makes this defect typically absent from listings found in the literature [306].

The P_1 defect is modeled by a three-coordinated P atom with an unpaired electron, comparable to the structure of SiE′ defects in pure silica [376]. It is characterized by an optical absorption band centered at 0.79 eV with a FWHM of 0.29 eV [379].

The P_2 defect is modeled by a four-coordinated P atom (also called *silicon-substituted phosphorus* because it replaces the role of Si in the SiO_4 tetrahedron), with an additional, unpaired electron [376]. It is characterized by an optical absorption band centered at 4.5 eV with a FWHM of 1.27 eV [379].

The P_4 defect is modeled from a three-coordinated P atom that receives an additional electron, causing the break of an oxygen bond [376]. It is characterized by an optical absorption band centered at 4.8 eV with a FWHM of 0.41 eV [379].

The *Phosphorus-Oxygen Hole Center* (POHC) is modeled from a four-coordinated P that receives an additional electron, resulting in an unpaired spin. Two variants of the POHC appear in the literature, depending on their stability at room temperature: the stable variant (s-POHC) in which the spin is shared between two non-bridging oxygen atoms [376], as well as a metastable variant (m-POHC) in which a non-bridging oxygen has an unpaired electron [306, 376]. These variants of POHC produce

a combined optical absorption spectrum with four bands located at 2.2 eV, 2.5 eV, 3.1 eV and 5.3 eV, making POHC the main contributor of P-doped fibers RIA in the visible range [380], although the attribution of each of these bands to one or the other variant is still unclear [381].

While none of these defects appear to be present in non-irradiated optical fibers [381, 382], correlations observed in the RIA and EPR signals of P-doped fibers under radiation have highlighted several creation and conversion processes. First, good correlation was observed between the intensities of the 4.5 eV RIA band and the sum of 2.3 eV and 3.0 eV bands under 10 keV X-rays for doses up to 2 kGy [381]. Also, evolution of the defect populations inferred from EPR measurements during high-temperature annealing also suggested the conversion of POHCs to P_1 defects [376, 382]. This conversion is believed to take place at the microsecond scale, causing an increase of RIA observed after pulsed irradiation [380].

1.2.4. Measurable effects of radiation on phosphorus-doped optical fibers

Following the early interest raised by Griscom's works in 1983 on phosphorus-doped silica [376], P-doped optical fibers as well as Ge-P co-doped fibers have been extensively investigated under ionizing radiation and reported in the scientific literature. This section highlights the main published results on P-doped optical fibers.

RIA of P-doped fibers

The optical absorption properties of P-doped silica were explored in the bulk material [376], then in optical fibers with 0.1 % P doping in the core [379], which characterized well the RIA properties of this type of fiber.

In the near-infrared range, RIA of P-doped fibers is mainly dictated by the P_1 defects. It results in a wide absorption band centered around 1569 nm, shown in **Figure 1.23b**, which has been repeatedly explored in the literature [383].

In the visible and UV ranges, RIA of P-doped fibers is mainly shaped by POHC defects [384], with a smaller contribution of other defects such as P_2 and P_4. Visible and UV RIA responses of P-doped fibers are remarkable by their very high intensity compared to near-infrared RIA, as illustrated in **Figure 1.23a**, which has suggested potential of this type of fibers for high-sensitivity dosimetry in this visible domain [385].

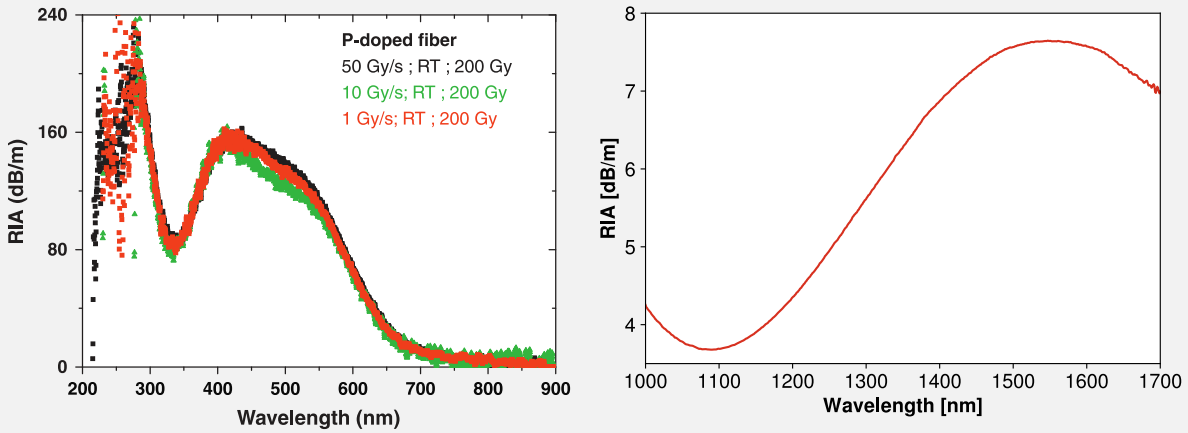

(a) Visible RIA spectrum of a ø62.5 µm multimode P-doped fiber irradiated under X-rays at 200 Gy, with different dose rates. (from [385])

(b) Infrared RIA spectrum of a single-mode P-doped fiber irradiated under X-rays at 3 kGy at a dose rate of 1 Gy/s. (data from [392])

Figure 1.23. – Visible and infrared RIA spectra of P-doped optical fibers as reported in the literature. Note that the dose on the right-hand data is 15 times higher than the left-hand one.

Stability of RIA

The RIA in P-doped fibers was already observed as remarkably stable with time as soon as the first studies on the radiation response at 820 nm of Ge-P co-doped optical fibers [377]. This topic was later explored for fibers doped only with phosphorus, which exhibited the same stable behavior between 670 nm and 1550 nm [386].

The temperature stability of P-doped fiber RIA at 1550 nm was throughly explored in a systematic study performed between $-80\,°C$ and $300\,°C$, which concluded to a variation $\pm 15\,\%$ of the RIA of this type of fiber in a large operating range of $-80\,°C$ to $+120\,°C$ [387].

Another phenomenon which affects stability of RIA is photobleaching, which causes light traversing the optical fiber to deplete a proportion of the radiation-induced defects [388]. Photobleaching was first investigated on Ge-P co-doped fibers at a wavelength of 850 nm both for RIA measurement and photobleaching signal, with mitigated results as exposition to low powers ($\leq$ ~1 mW) resulted in increasing RIA instead of decreasing it [389]. For P-doped fibers, photobleaching was shown to affect RIA response in the visible and UV ranges [390], as well as in the infrared range [391], offering the possibility to regenerate P-doped fiber-based dosimeters by injecting optical power.

Irradiation with different types of particles

P-doped fibers have been tested under steady-state X-rays [387], pulsed X-rays [393], high-energy (6 MeV) X-rays [394], γ rays [386], protons [395], electrons [396], neutrons [397]. They were also

tested in mixed particle environments, such as the TESLA TTF1 facility in DESY Hamburg [398] or the CHARM facility at CERN [399].

Several studies have matched the RIA response at 1550 nm of P-doped fibers between different types of particles with the actual ionizing dose position in the fiber, with the help of Monte Carlo simulations [395, 399, 400]. A RIA sensitivity factor of $4\,\mathrm{dB\,km^{-1}\,Gy^{-1}}$ was reported at 1550 nm for a single-mode, acrylate-coated, P-doped fiber manufactured by iXblue [395].

RIE and RIRIC measurement

P-doped fibers were studied as potential scintillation dosimeters [401, 402], although they exhibit a comparatively weak radioluminescence signal compared to other common types of fibers [342] (see also **Figure 1.21** and **Article A.1**).

No reports of RIRIC observed on P-doped fibers were found in the literature to this date. This absence of results can however be explained by the overall high sensitivity to radiation of this type of fibers, which are therefore not investigated under the very high doses at which such effects are typically observed, as exposed in **Section 1.2.2**.

1.3. Distributed optical fiber sensing

Sensing applications for optical fibers were developed in the late 1970s, less than a decade after the creation of this medium originally intended only for transmitting light [403]. Optical fiber sensors nowadays not only cover a wide range of measurands, but also interrogation techniques [404]. While some technologies, such as fiber-optic gyroscopes (FOGs), use the whole length of the fiber as a single sensing element [405], some others enable to spatially resolve the measurand along the available optical fiber length.

One of the most developed technologies for this purpose are Fiber Bragg Gratings (FBGs), which are periodical refractive index perturbations inscribed in the core of an optical fiber [406]. FBGs are sensitive to various external parameters such as temperature and strain, and enable localized measurement because of their small individual length, on the order of 1–20 mm [407]. Multiple FBGs can be inscribed in a same optical fiber, which, coupled to a multiplexed reading technology, enable to perform a measurement at many discrete points along the fiber [408].

Other interrogation technologies enable to perform so-called *distributed* measurements, i.e. capable of performing measurement at virtually any point of the optical fiber [409]. The physical and technological details of the devices enabling such distributed measurements will be presented hereafter.

1.3.1. Spontaneous scattering processes in optical fibers

Overview of spontaneous scattering processes

The electromagnetic theory of light describes light propagation in matter as a series of interactions of an incoming light wave with the molecules composing the medium: the molecules, polarized by this electromagnetic wave, form a dipole, and this dipole, called *scattering center*, emits an electromagnetic wave of same frequency (and therefore wavelength) in all directions. In an ideal, completely isotropic and homogeneous material, scattering of the incoming wave happens equally in all locations, such as all the scattered wave meets destructive interference everywhere but in its original propagation direction. This phenomenon is called *coherent forward scattering*, and explains the forward propagation of light in media as well as the existence of a refractive index [410, 411].

In real materials, however, exist local perturbations that break this principle: destructive interferences are not always produced with the same amplitude as the scattered wave, and as a result, part of the scattered wave is allowed to propagate in directions other than forward. When the optical properties of the medium are not significantly affected by the intensity of incident light, these processes are described as *spontaneous light scattering* (as opposed to *stimulated* scattering processes, that happen at very large intensities) [410].

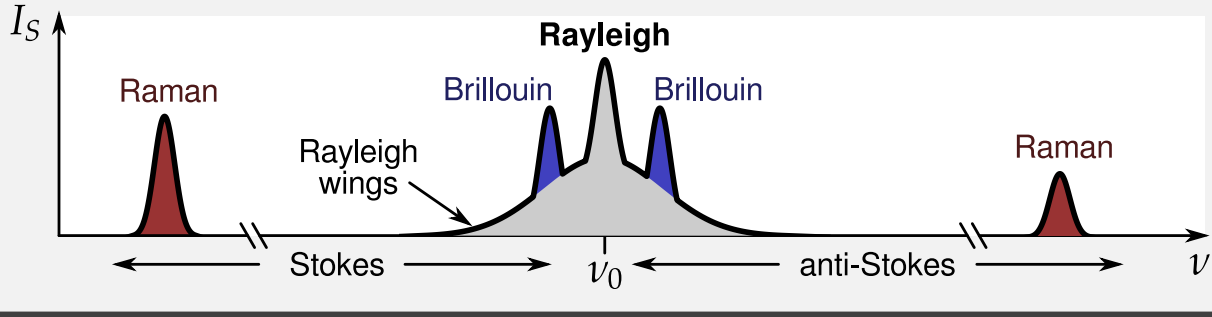

Figure 1.24. – Overview of optical scattering processes in matter and their (indicative) relative intensity I_S, as a function of the frequency ν of the scattered signal, compared to the frequency ν_0 of the incoming light. (adapted from [410])

These local perturbations come from various origins, that each produce a distinguishable scattering process, as illustrated in **Figure 1.24**.

Rayleigh[9] *scattering* originates from non-propagating density fluctuations in the material, which are linked to the degree of disorder created in the material during manufacturing. This is an *elastic* scattering process, and therefore the scattered signal has the same frequency as the incident signal.

Brillouin[10] *scattering* originates from light-excited pressure waves, i.e. sound waves, propagating in the material. This process is *inelastic*, and therefore the scattered signal has a different frequency than the incoming signal, through two different processes: the *Stokes*[11] shift sees part of the incoming signal energy $h\nu_0$ absorbed by a phonon $\hbar\Omega$, resulting in a scattered signal of reduced frequency $E_s = h\nu_0 - \hbar\Omega$; on the contrary, the *anti-Stokes* shift results in the phonon increasing the energy of the scattered signal $E_{as} = h\nu_0 + \hbar\Omega$ [410]. Brillouin spectroscopy, built upon these phenomena, is used as a characterization technique in materials science [412].

Raman[12] *scattering* originates from non-propagating vibrational modes of the molecules constituting the material. This is also an inelastic process, with Stokes and anti-Stokes components as described here above [410]. The Raman shift spectrum, often expressed as a function of the wavenumber $1/\lambda$ (unit: cm^{-1}), is a signature of the molecule, which makes Raman spectroscopy a very efficient material characterization technique [413].

In anisotropic materials such as crystals, an additional scattering process named *Rayleigh wings* originates from fluctuations in the orientation of anisotropic molecules. This phenomenon causes inelastic scattering around the original frequency ν_0, with a broad spectrum due to the very fast relaxation time of these reorientation processes [410].

[9] Named after the English scientist Lord Rayleigh (1842–1919), Nobel Prize in Physics 1904.
[10] Named after the French scientist Léon Brillouin (1889–1969).
[11] Named after the English scientist Sir George Gabriel Stokes (1819–1903).
[12] Named after the Indian scientist Chandrasekhara Venkata Raman (1888–1970), Nobel Prize in Physics 1930.

The Rayleigh scattering process

The core mechanic of the Rayleigh scattering processes is the polarization of material constituents (molecules or atom) by the incoming electromagnetic wave that is light [414]. In the case of Rayleigh scattering, the size of the polarized object is considered very small compared to the wavelength of the incoming signal; as a result, the electromagnetic field to which the molecule or atom is subjected can be seen as uniform. The electric part of the field, in particular, causes the movement of the electrons, which creates a spatial charge imbalance, and by consequence a dipole [415].

Because the incoming wave oscillates at an angular frequency $\omega = 2\pi c/\lambda$, with λ the wavelength and c the speed of light in vacuum, the dipoles formed in this process also oscillate at this same frequency. As a consequence of Maxwell's equations, these spatial and temporal variations of charges cause the emission of a secondary electromagnetic field, the scattered signal, which time-averaged radiated power P can be modeled as follows [416, 417]:

$$P = \frac{q^2 \omega^4 x_0^2}{12\pi\, \epsilon_0\, c^3} = \frac{4\pi^3 c\, x_0^2\, q^2}{3\epsilon_0\, \lambda^4} \tag{1.10}$$

with x_0 the oscillation amplitude, $q = 1.602\,176\,634\,\mathrm{C}$ the elementary charge, and $\epsilon_0 \approx 8.854\,188\,\mathrm{F/m}$ the vacuum electric permittivity.

A remarkable property of this classical model is the wavelength dependence of the intensity of Rayleigh scattered light which is proportional to $1/\lambda^4$, that explains the high intensity of Rayleigh-scattered signal at short wavelengths (such as scattering of sunlight by atmospheric molecules, producing the perceived blue color of the sky [418]), and the low intensity of this phenomenon at infrared wavelengths, contributing to the transparency window of optical fibers at 1550 nm that was illustrated in **Figure 1.16**.

More complete models of scattering can include resonances linked to molecular absorption levels [419], or thermodynamic considerations to represent the variation of density inside the material [420]. Other models of optical elastic scattering processes are also needed in the case of scattering particles of larger sizes, such as numerical computation from Maxwell's equations, or Mie[13] theory, which models scattered signal as a sum of spherical harmonics that can be efficiently computed and adjusted to an arbitrary level of precision [421, 422].

[13] Named after the german physicist Gustav Mie (1868–1957).

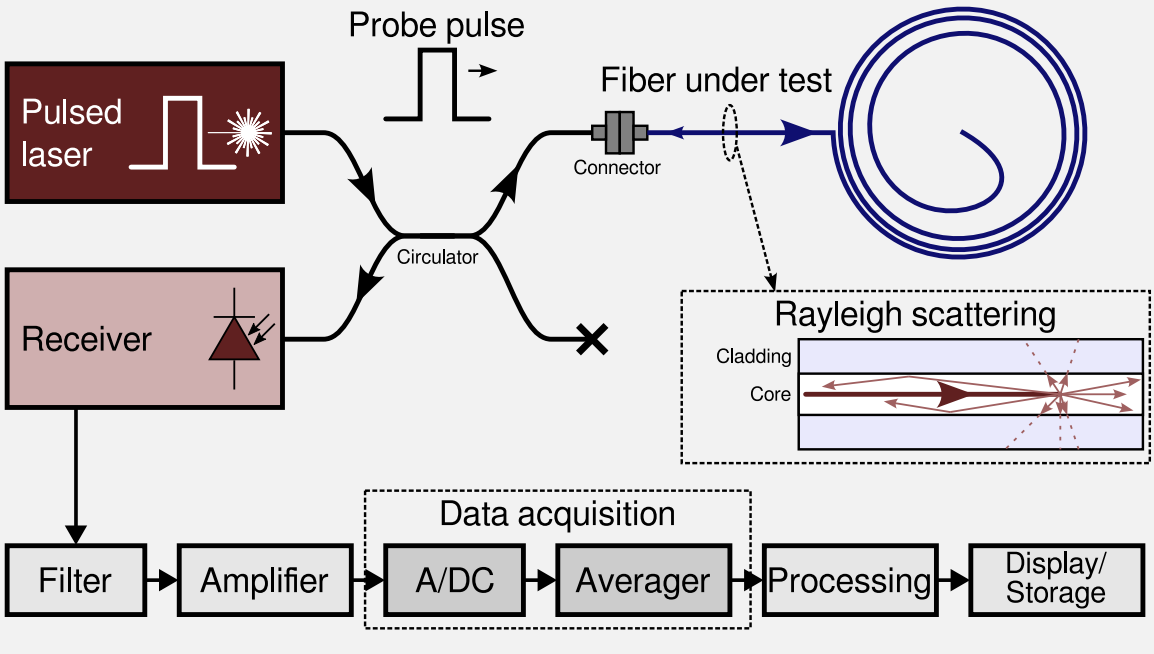

Figure 1.25. – Overview of the optical and functional architecture of a typical OTDR device. (adapted from [425])

1.3.2. Optical Time-Domain Reflectometry (OTDR)

Functioning principle and basic architecture

In optical fibers, Rayleigh scattering causes part of the transmitted signal to be scattered in all directions, from virtually every point of the fiber. A fraction of this scattered signal, called *backscattered signal*, has a direction opposite to the incoming signal, and meets the criteria to be coupled to a backward-propagating guided mode [423]. In practice, only about 0.1 % to 1 % of the scattered signal is actually guided, depending on the characteristics of the fiber [424].

The principle of OTDR devices is to sense this backscattered signal, along with a time-of-flight measurement that estimates the distance travelled by the signal, to obtain a linear map of the intensity backscattered by the optical fiber as a function of the length inside the fiber [424].

A typical architecture of an OTDR device is shown in **Figure 1.25**. A pulsed laser generates a very short laser pulse, called *probe pulse*, which is launched into the optical fiber under test. At every point along the optical fiber, the probe pulse generates a small amount of backscattered signal that travels back to reach the fiber entry. This backward propagating signal is then directed to a receiver, made of a photodiode or photomultiplier device, which measures the intensity of the backscattered signal at every instant. This measurement is sent to the signal processing part of the device, which performs the storage of this data and its mapping as a function of the distance in the optical fiber.

The position z from which was produced the backscattered signal measured at a time t after launching of the laser pulse can be easily deduced from knowledge of the group velocity v_g of the laser pulse inside the fiber:

$$z = \frac{v_g}{2} t \tag{1.11}$$

The factor 2 is introduced by the round-trip nature of this process: z is covered by the probe pulse in the forward direction, then z is covered again in the reverse direction by the backscattered signal.

Thus, a high time resolution on the sampling of the receiver signal enables a high spatial sampling for the mapping of the backscattered signal. In the commercial OTDR devices used for this thesis work, the maximum spatial sampling was on the order of 4 cm, which corresponds approximately to a receiver sampling frequency of 2.6 MHz; this value does however not necessarily reflect the real-time interrogation rate of the sample because of the possible use of signal acquisition techniques such as equivalent time sampling [426, 427].

However, this value of spatial sampling largely underestimates the actual spatial resolution of the device, which is impacted by a signal broadening phenomenon caused by the width of the probe pulse. Because the whole backscattering response of the fiber is convolved by the spatial extent $w = \tau\, v_g$ of the probe pulse of duration τ, this pulse width further limits the spatial resolution Δz of OTDR devices , which is therefore given by the relation [425]:

$$\Delta z = \frac{v_g}{2} \tau \tag{1.12}$$

For a typical pulse duration $\tau = 10\,\text{ns}$, Δz is on the order of 1 m [425].

In some specific setups, such as multimode fibers where a very high spatial resolution is targeted, the bandwidth of the optical fiber itself can also contribute to limiting the resolution [425].

Because the receiver is subjected to stochastic noise from different sources, including shot noise and thermal noise, an OTDR signal is typically averaged during a time interval to produce a result with considerably reduced noise. In this case, the signal-to-noise ratio (SNR) typically increases in proportion to $\sqrt{N}$, with N the number of averaged measurements [425].

As OTDR measures backscattered signal, OTDR devices typically need only one extremity of the fiber to operate, in so-called *single-ended* operation. This architecture offers many advantages, such as the ability to quickly diagnose very long telecommunication lines with a single device [428].

Double-ended architectures, which typically involve a single device interrogating sequentially both ends of an optical fiber through an optical switch, are less flexible but offer the possibility to retrieve the local backscattering parameters along the measurement line, which allows for more accurate attenuation measurements [425]. Another advantage of the double-ended architecture is the ability to

still perform measurements in case of a single breakage or high-attenuation event in the measurement line [429].

Hybrid architectures, such as folded-path OTDR which features a mirror installed at the end of the interrogated optical fiber [430], can provide the advantages of double-ended measurements with only one end of the fiber to be accessed, although these methods can present other limitations due to the very high power difference between backscattered and reflected signals [425].

Analysis of OTDR traces

The result of an OTDR measurement is a one-dimensional map of the intensity of the backscattered signal as a function of the distance inside the optical fiber.

The backscattered intensity I_{BS} measured by the receiver from a location placed at distance z in the optical fiber can be modeled as follows [425]:

$$I_{\mathrm{BS}}(t) = \frac{v_g}{2} I_0 \, \alpha_{\mathrm{Rayleigh}}(z) \, B(z) \, \exp\left(\int_0^z -2\alpha(u) \, \mathrm{d}u \right) \tag{1.13}$$

where v_g is the group velocity of the pulse inside the optical fiber, I_0 the intensity of the probe pulse as it enters the fiber, $\alpha_{\mathrm{Rayleigh}}$ the Rayleigh scattering-loss coefficient, B the capture fraction (i.e. the fraction of backscattered intensity that is guided by the optical fiber) and α the total loss coefficient. The factor 2 assumes that the backscattered signal encounters the same attenuation as the probe pulse, which is usually the case with Rayleigh scattering, where the backscattered wavelength is identical to the incoming wavelength.

An important consideration in this model is the fact that all factors affecting I_{BS} ($\alpha_{\mathrm{Rayleigh}}$, B and α) are not necessarily constant along the measurement line, but have each a local value at the location z. Therefore, the OTDR signal reflects these local values in the Rayleigh scattering factor, the capture fraction and the total attenuation of the scanned optical fiber as a function of the distance.

In the particular case of a fiber segment in which these parameters are constant, then the 10-base logarithm of I_{BS} has the following form:

$$\log_{10}(I_{\mathrm{BS}}) = \log_{10}\left(\frac{v_g}{2} \, I_0 \, \alpha_{\mathrm{Rayleigh}} \, B \right) - \frac{2\alpha}{\ln(10)} z = -\frac{2\alpha}{\ln(10)} z + K \tag{1.14}$$

which is a linear function of z with slope $-\frac{2}{\ln(10)}\alpha z$ and intercept K.

The typical OTDR trace of a single optical fiber, represented in a logarithmic scale, is therefore essentially a linear, decreasing function. This linear trend is combined with single reflective events along

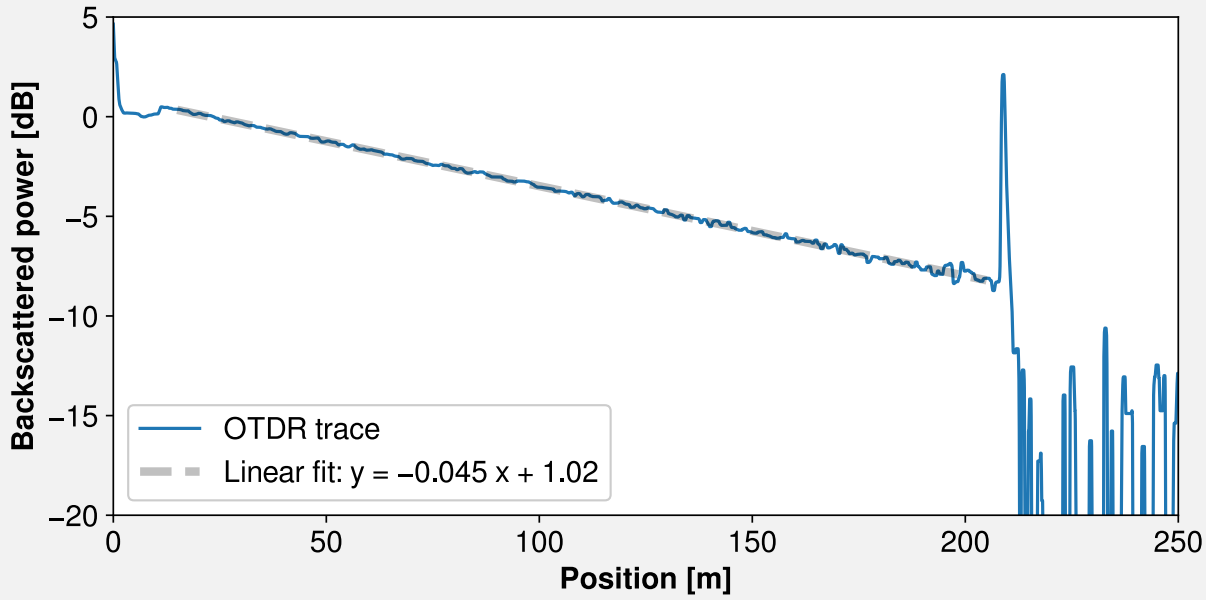

Figure 1.26. – OTDR trace at 1310 nm of a ~200 m sample of single-mode optical fiber with significant attenuation, spliced to a ~5 m connecting fiber. The pulse width was set to 5 ns and scan time to 10 s. A linear fit is used to evaluate the slope of the linear segment between 15 m and 205 m, which results in a calculated attenuation of ~45 dB/km.

the measurement line, which typically occur in air/glass interfaces because of the Fresnel reflection phenomenon [431] and produce a sharp, localized peak of high backscattered power.

Other single disturbance events, such as splice losses or change in the scattering coefficient or in the capture fraction, can also induce a sharp decrease or increase of the backscattered signal. An OTDR trace is therefore the combination of steady and more localized responses, as illustrated in **Figure 1.26**, and its accurate interpretation can be ambiguous without relying to double-ended measurement [425]. Finally, after the end of the measurement line, where no significant signal is backscattered, the OTDR trace typically returns a low-power noise that represents the noise floor of the system [432].

1.3.3. Other distributed sensing technologies

Optical Frequency-Domain Reflectometry (OFDR)

OFDR relies on Rayleigh scattering, but performs its measurement using a more complex process involving frequency sweep [425]. In its coherent version (C-OFDR), the device launches an optical signal with swept frequency into both arms of an interferometer, one of which is connected to the optical fiber under test.

The resulting signal is recorded under very high time resolution to build a frequency-based interferogram which, when Fourier transformed, produces a backscatter diagram of the same kind as the

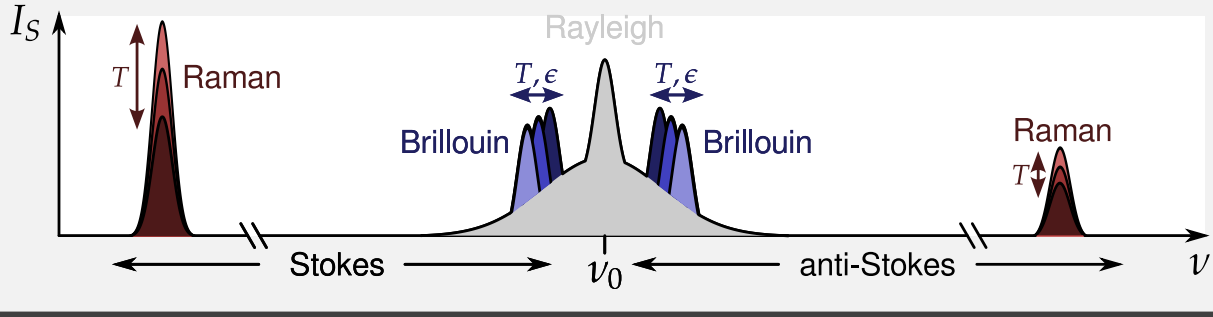

Figure 1.27. – Overview of the two main scattering processes used for distributed optical fiber sensing, showing the relative intensity I_S of the scattered signal as a function of its frequency ν, compared to the probe frequency ν_0. Arrows indicate the tendency of evolution of these signals with temperature T and strain ϵ.

one obtained with OTDR, but with a significantly increased spatial resolution that can go down to ~20 µm on commercial devices [433].

Sensing applications are also developed around OFDR technology, through measurement of relative optical path change that can be induced by factors such as temperature and strain [434]. Because of the very high spatial resolution offered by this technology, distributed sensing based on OFDR has seen interest for applications as diverse as silicon photonics [435], shape reconstruction of small objects [436] or monitoring of civil infrastructures [437].

Distributed sensing based on Brillouin or Raman scattering

Distributed sensing technologies are not limited to the sole spontaneous Rayleigh scattering described in the previous sections, but can involve a variety of scattering processes, summarized in **Figure 1.27**, which enable different possibilities in terms of measurands and performance [409].

Brillouin scattering enables measurement of temperature and strain through analysis of the frequency shift of both backscattered Stokes and anti-Stokes signals. Typical technologies include Brillouin Time-Domain Reflectometry (BOTDR), involving spontaneous Brillouin scattering in a single-ended architecture, and Brillouin Time-Domain Analysis (BOTDA), involving stimulated Brillouin scattering in a double-ended architecture [438, 439].

Raman scattering enables measurement of temperature only, through analysis of the intensity difference between Stokes and anti-Stokes signals. This process in used in Raman Distributed Temperature Sensing (R-DTS) devices, which involve spontaneous Raman scattering in a single-ended architecture [440].

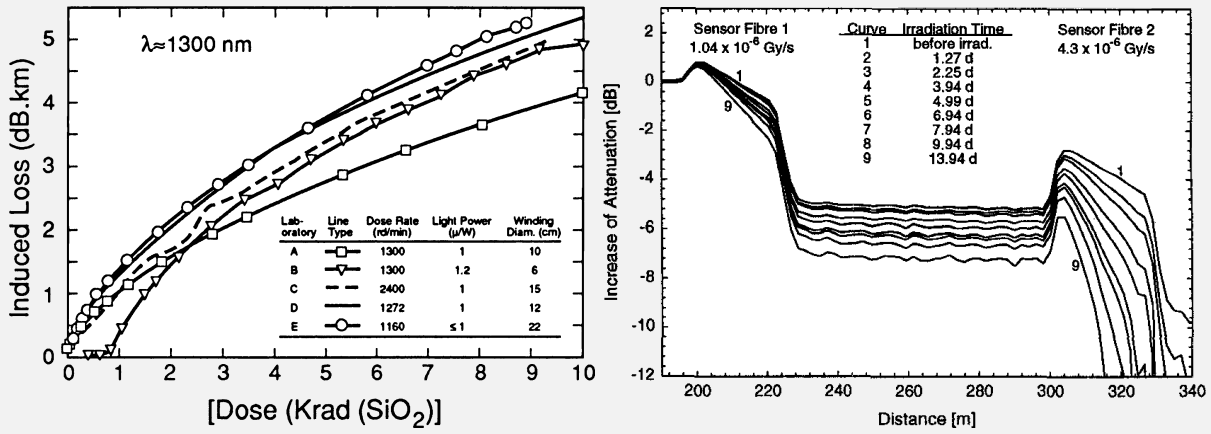

(a) RIA measured by OTDR at 1300 nm on a sample of unspecified single-mode optical fiber irradiated under ^{60}Co γ rays. Measurements were performed by five different laboratories. (from [451])

(b) OTDR traces over time of two rare-earth doped optical fibers samples irradiated with ^{60}Co γ rays. The first sample is located between ~200–220 m, and the second between ~300–330 m. (from [452])

Figure 1.28. – Early data on RIA measurement using OTDR and distributed dosimetry.

1.4. Distributed dosimetry

Because the effects of ionizing radiation on optical fibers are well known and studied (cf. **Section 1.2**), fiber-based dosimetry is a topic widely covered in the literature, with applications involving mainly RIA or RIE phenomena [441–443]. However, in most cases, these applications use the whole length of the optical fiber as a single sensing element, and are thus only able to supply a scalar measurement, averaged over the whole sensing line [444, 445].

Localized optical fiber-based dosimetry has been proposed using FBGs [446, 447] or Long-Period Gratings (LPGs) [448], although with limited accuracy, partly because of their high sensitivity to other environmental influences such temperature and strain [449, 450].

Distributed sensing techniques (cf. **Section 1.3**) provide a new set of interrogation methods to retrieve localized measurements from an optical fiber, at virtually any location along the fiber length. Such techniques, applied to dosimetry, could therefore provide a spatial mapping of dose or dose rate, enabling evaluation of a whole radiation environment using only a single optical fiber and interrogator. This section describes the most significant developments of this technology as reported in the scientific literature.

OTDR as a RIA measurement method

In the 1980s, several task groups, including the NATO Nuclear Effects Task Group and the United States Department of Defense, required standardization of RIA measurement methods on optical fibers [453]. In particular, OTDR measurements, while identified as a method worth exploring, had

no available data applied to RIA as of 1990 [451]. Several studies were thus performed in the early 1990s to circumvent this lack of published experimental data.

In 1990, five independent laboratories tested a 500 m sample of a single-mode optical fiber, of unspecified core doping, under ^{60}Co γ rays up to 100 $Gy(SiO_2)$. The RIA was measured by an OTDR device functioning at 1300 nm with a pulse width of 1 µs. While there was a significant spread of the results, as shown in **Figure 1.28a**, the conclusions highlighted the advantages of the OTDR method for RIA measurements, notably because of its single-ended architecture and stability of measurement [451].

Shortly after, a conference paper was also dedicated to RIA measurement using OTDR [454], followed by a synthesis article about the dosimetric properties of optical fibers that included this measurement method [386]. One of the main arguments raised by the authors in favor of OTDR characterization of RIA was the high stability of the measurement when performing long experiments [386].

An article published in 1994 was also solely dedicated to the use of OTDR for RIA measurement. The authors concluded on a high reliability and practicability of the device, but highlighted two drawbacks: the significant time required for a single measurement (~100 s in this article) and the potential photobleaching effect linked to the use of high-intensity pulses [455].

The first significant published results of distributed dosimetry were presented in the RADECS 1997 conference, in where the authors demonstrated the ability to detect dose evolution at different locations of rare-earth doped optical fiber in low dose rate conditions: 0.1 Gy/d, matching space environment conditions. In **Figure 1.28b**, the OTDR traces of the two irradiated optical fibers segments are shown with their slope decrease with irradiation time, while the central segment, shielded under lead (Pb), shows no change in its slope. [452].

Monitoring of the TTF1 linear accelerator in DESY Hamburg

The pioneer field experiment on the topic of optical-fiber based distributed dosimetry was performed by a German team who used a Ge-P co-doped optical fiber interrogated by OTDR to monitor the radiation emitted by the TESLA Test Facility phase 1 (TTF1) accelerator in the Deutsches Elektronen-Synchrotron (DESY) accelerator center in Hamburg, Germany. The experiment started in 1999, and its results were the subject of internal DESY reports [456–458], conference papers [236, 459] and a peer-reviewed article [398].

The TTF1 is a complex linear accelerator based on a radiofrequency laser and several acceleration and compression modules, enabling acceleration of electrons up to 230 MeV (as of 2004). Losses along this acceleration process create high-energy particle showers of a wide variety, including electrons, positrons, neutrons and X-rays [398].

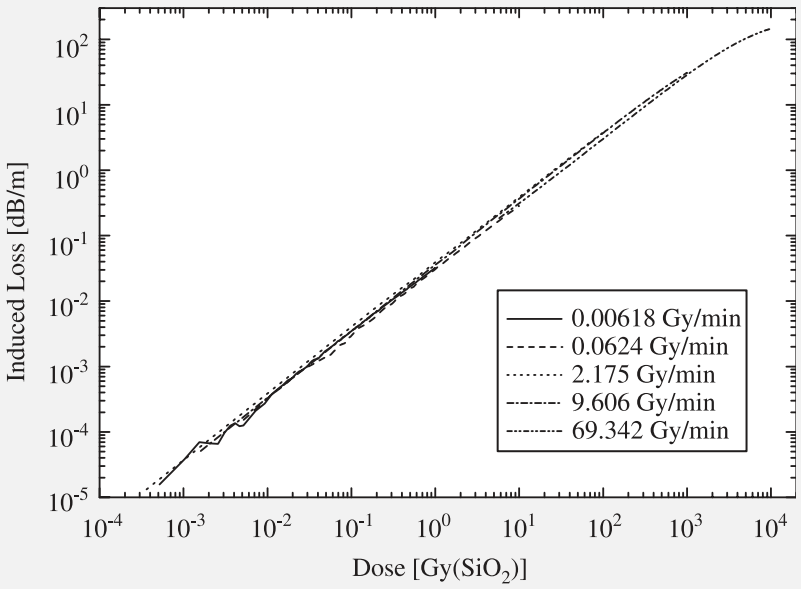

Figure 1.29. – Calibration curve under ^{60}Co γ rays of the Ge-P co-doped fiber selected for distributed dosimetry of the TTF1 facility in DESY Hamburg. Measurements were performed at room temperature with $\lambda = 678\,\text{nm}$ at five dose rates, indicated by different line styles. (from [398])

The aim of the distributed dosimeter was to evaluate the dose to which the electronics and the permanent magnet materials of the accelerator were subjected. Another idea was to be able to perform measurements in the very small (0.5 mm–1 mm) gap near the accelerator magnets, in which conventional online dosimetry systems could not access, whereas the small dimensions of optical fibers enable them to operate as near to the magnets as possible [398].

To this end, a commercial multimode, radiosensitive optical fiber was used, with a 50 µm diameter germanophosphosilicate (Ge-P) core, 125 µm diameter cladding, and a thick 500 µm coating. This fiber was qualified and calibrated by the research team, and chosen among others because of its high radiation sensitivity and stability [398][14].

Calibration of this Ge-P co-doped fiber was performed under ^{60}Co γ rays at five different dose rates from 0.3708 Gy/h to 4160.52 Gy/h, as illustrated in **Figure 1.29**. RIA was measured at 678 nm and 829 nm using a dedicated setup, and the fiber response was modeled by a power function:

$$\text{RIA}(D) = cD^f \tag{1.15}$$

with c the sensitivity coefficient, D the dose in Gy, and f an exponential factor. Measurements at 678 nm resulted in $c_{678\,\text{nm}} = 3.69\,\text{dB km}^{-1}\,\text{Gy}^{-1}$ and $f_{678\,\text{nm}} = 0.972$, while measurements at 829 nm yielded $c_{829\,\text{nm}} = 4.2\,\text{dB km}^{-1}\,\text{Gy}^{-1}$ and $f_{829\,\text{nm}} = 1.025$. The authors also state that a linear model suits these data acceptably up a dose of 1000 Gy [398].

[14]The paper makes a reference to an upcoming article: *Properties of (Ge+P)-doped dosimetry fibres*, that would have detailed the selection process of the optical fibers; the said article seems however to have never been published.

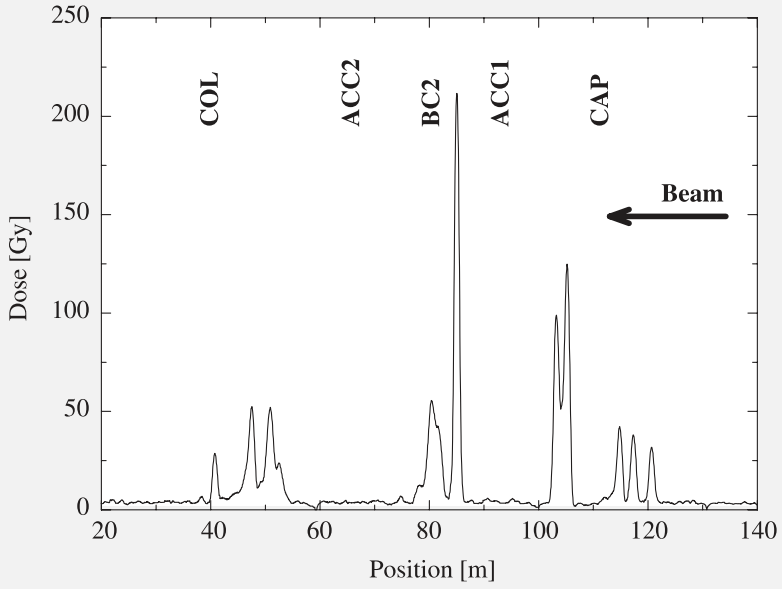

Figure 1.30. – Dose inferred from OTDR measurements as a function of the position along the TTF1 accelerator in DESY Hamburg between December 2001 and January 2002. The name of the different components of the accelerator are given on the graph, along with the direction of the accelerator beam. (from [398])

The distributed dosimetry setup involved an a high-accuracy, table-top OTDR device (Tektronix FiberMaster TFP2A), able to reach pulse widths down to 1 ns. The instrument was operated at a wavelength of 850 nm, selected because of its higher radiation sensitivity than infrared wavelengths (cf. **Section 1.2.4**), and a pulse width of 3 ns, to reach a good compromise between spatial resolution and measurement dynamics (cf. **Section 1.3.2**) [398].

Qualification of this dosimetry setup indicated a minimum spatial resolution of 1.5 m, and a minimum detectable dose of 3 Gy with the OTDR settings indicated here above. Given the dynamic range of 15 dB offered by the OTDR device with a pulse width of 3 ns, the maximum measurable dose with this setup was assumed to be 360 Gy over a length of 10 m, after which the measurement reaches the noise floor of the device. To work around this problem, an optical switch was used to enable double-ended interrogation of the measurement fiber [398].

The results of this setup are shown in **Figure 1.30** for a cumulated period of two months. The distributed nature of the measurement enables to perceive the difference in received dose for each element of the facility. This distributed dosimetry system was combined with a more conventional, power-meter based RIA measurement at a wavelength of 660 nm, with twelve different optical fiber lines installed near the most sensitive parts of the facility in order to obtain additional measurements on these locations. Thermoluminescence dosimeters, readable after irradiation, were also used as an additional measurement method [398].

The good accordance between the results obtained in these experiments between different dosimetry

systems led to the adoption of optical-fiber based dosimetry as a standard in future developments of the TESLA Test Facility [398]. In addition, the distributed dosimetry technique was also proposed later as a part of a multi-approach system to detect beam losses in particle accelerators [460].

Distributed Optical Fiber Radiation Sensing (DOFRS) at CERN

Very large physical instruments, such as the Large Hadron Collider (LHC) that covers a total length of ~26.7 km, present a considerable challenge for monitoring because of the sheer number of devices needed to ensure the required functionality within an acceptable spatial resolution. For instance, a 2014 magazine article reported that 1054 beam position monitors were installed in total on both sides of the accelerator, amounting to a space resolution of ~50 m; each sensor being connected by a radiation-hardened coaxial cable [461].

Optical fiber sensing presents multiple advantages in this context, such as high electromagnetic immunity and ability to multiplex measurements along a same optical fiber [462]. The first reported applications involved FBGs for temperature and strain measurement on the main instruments of the facility such as the CMS experiment [463]. Later communications reported the testing of a distributed temperature measurement system using Raman scattering [464].

Radiation monitoring of the LHC follows the same kind of requirements and challenges, and involves a sensor array called RadMon, based on electronic radiation sensors, that was reported to include ~400 units as of 2011 [465]. This complex sensor architecture is however difficult to maintain, and several updates of the RadMon sensors architecture were conducted in order to circumvent failures observed during their function [466].

For these reasons, distributed dosimetry was perceived as a promising alternative for radiation monitoring of CERN facilities, and was the object of a dedicated Ph.D. thesis [467]. The first reported study on this subject was focused on the characterization of a multimode optical fiber-based distributed dosimetry system in the mixed radiation field of the CHARM facility. The authors used a P-doped fiber with a core diameter of 50 µm and a portable OTDR device (EXFO FTB500) to measure RIA at 850 nm and 1300 nm, with two different pulse durations of 5 ns and 10 ns in different irradiation conditions. The optical fiber used for sensing was also calibrated under ^{60}Co γ rays, and the sensitivity coefficient of the fiber in the linear RIA range was reported to be ~3–3.5 dB km^{-1} Gy^{-1} at 830 nm, and ~1 dB km^{-1} Gy^{-1} at 1312 nm. Whereas some limiting factors were highlighted, such as a saturation of the system with relatively low doses (~20 kGy), this technology was concluded to be promising, especially if combined of an optical fiber designed for radiation sensing [466].

Stemmed from these conclusions, the development of a dedicated distributed dosimetry system for CERN, named DOFRS, was the object of two conference papers [468, 469] as well as six peer-reviewed articles [383, 390, 395, 399, 470, 471].

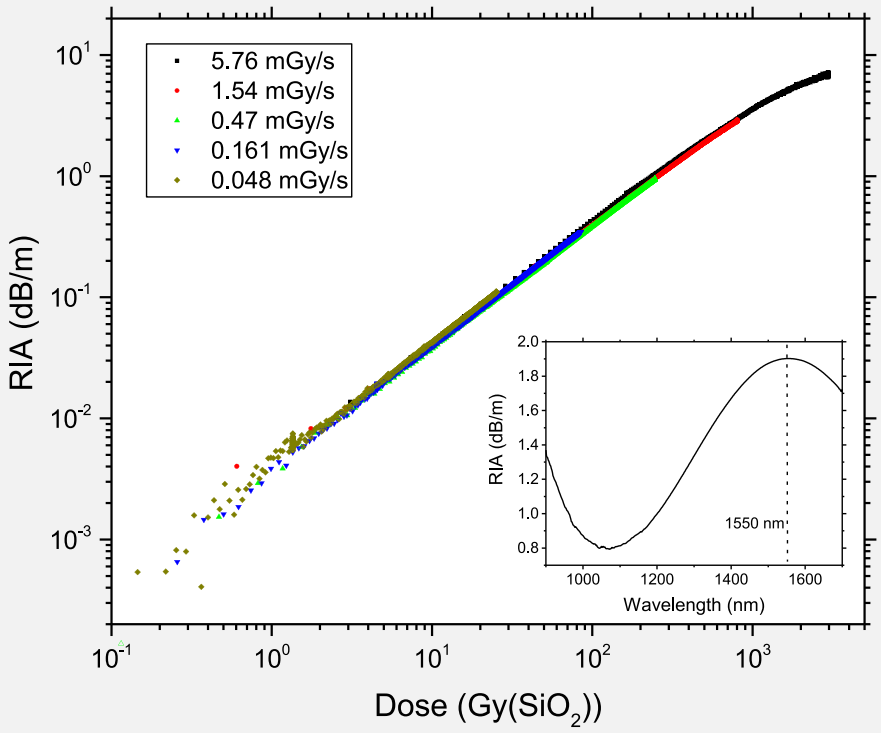

Figure 1.31. – Calibration curve under ^{60}Co γ rays of the P-doped fiber selected for the CERN DOFRS system. Measurements were performed at room temperature with $\lambda = 1550\,\text{nm}$ at five different dose rates, indicated by different colors. Inset shows the shape of the RIA spectrum of this fiber in the near-infrared range. (from [395])

A first aspect of this work was focused on the characterization of a single-mode, phosphorus-doped optical fiber designed specifically for this dosimetry application. The radiation response of the fiber was tested under ^{60}Co γ rays at five different dose rates from $0.1728\,\text{Gy}(\text{SiO}_2)/\text{h}$ to $20.736\,\text{Gy}(\text{SiO}_2)/\text{h}$, as illustrated in **Figure 1.31**, and measured by a portable OTDR device (Viavi MTS6000) at 1550 nm and a pulse width of 2 ns. The fiber RIA response was considered linear up to $500\,\text{Gy}(\text{SiO}_2)$ with $< 5\,\%$ error, and the sensitivity in this linear region was $4\,\text{dB}\,\text{km}^{-1}\,\text{Gy}(\text{SiO}_2)^{-1}$ with an uncertainty of $\pm 10\,\%$.

This characterization process demonstrated several interesting performances of this dosimetry system. First, as shown by the ^{60}Co data in **Figure 1.31**, the fiber response showed no significant dependence on the dose rate. Second, the time stability of the measurement was excellent, with no significant change of the RIA detected several days after switching off irradiation. Third, the photobleaching effect induced from the OTDR interrogation process was estimated to be negligible with sufficiently high RIA values (on the order of a few dB/m). Fourth, the RIA showed no significant dependence on the temperature between 20 °C and 45 °C, which is a reasonable operating range for this application [395].

Another aspect of the development of the DOFRS system was to demonstrate its capability to perform

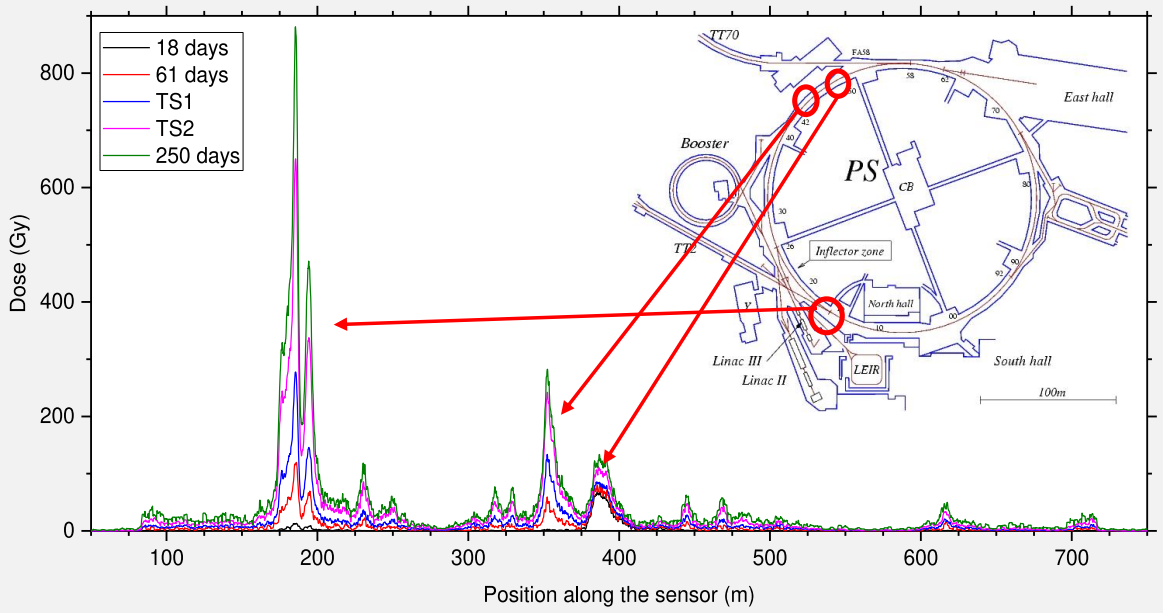

Figure 1.32. – Example of distributed dosimetry measurements on the CERN Proton Synchrotron (PS) during ~8 months in 2018. (from [473])

under the whole diversity of particle types that can be found in accelerator facilities. In addition to ^{60}Co γ rays, the system was also characterized under X-rays, allowing for higher dose rates [395]. Similar results were also obtained under 480 MeV protons, with a similar sensitivity coefficient of 4.1 dB km^{-1} Gy$(SiO_2)^{-1}$ at an uncertainty of $\pm$5 %, compatible with the value obtained under γ rays [395]. Finally, a dedicated article to the characterization of this system in the complex, mixed-field radiation environment of the CHARM facility has also shown consistent results with the dose predicted by Monte Carlo simulation, along with the ability to accurately map the radiation profile of the optical fiber using the distributed nature of the measurement [399].

Research of further improvements to this dosimetry system were also reported in the literature, through investigation of fibers with different dopants [383] or the potential of using photobleaching to regenerate the sensing fiber and extend its lifetime [390].

Finally, the actual implementation of this system on the various accelerators in CERN was reported. The first equipped accelerator was the Proton Synchrotron Booster (PSB), which is the second accelerator stage of the CERN with a circumference of 157 m [472]; the corresponding published results were performed with an earlier design involving a multimode, P-doped optical fiber interrogated by an OTDR at 850 nm. The third CERN accelerator stage, the Proton Synchrotron (PS) with a circumference of ~628 m [472], was also equipped with the DOFRS system since 2018 [469], but its results (cf. **Figure 1.32**) were not reported in the scientific literature, and only in internal publications [473, 474]. Instrumentation of the fourth accelerator stage, the Super Proton Synchrotron (SPS) with a circumference of ~6.91 km, began in 2021 and the corresponding results were documented in [471].

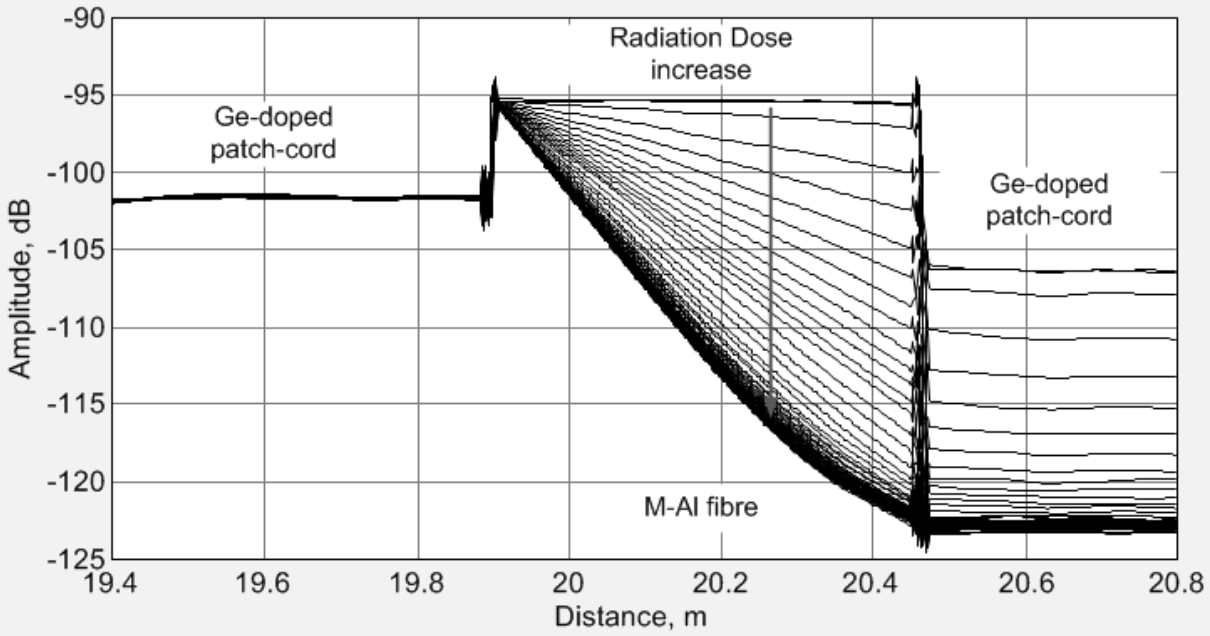

Figure 1.33. – OFDR amplitude trace of a measurement line including a ~50 cm segment of Al multimode optical fiber irradiated under ^{60}Co γ rays up to 73 kGy. (from [477])

Distributed dosimetry using Optical Frequency-Domain Reflectometry (OFDR)

OFDR (cf. **Section 1.3.3**) was also considered as an alternative to OTDR for distributed dosimetry systems because of the higher spatial resolution enabled by this technology. This higher accuracy and the capacity of this system to perform distributed dosimetry was demonstrated in many publications and a Ph.D. thesis [475], with many different types of optical fiber dopants including aluminum (Al) [476, 477], phosphorus (P) [478, 479], germanium (Ge) [480] and germanium-phosphorus (Ge-P) [481]. **Figure 1.33** shows an example of an OFDR amplitude trace in which an irradiated segment of ~50 cm of irradiated Al-doped fiber is clearly affected as the dose increases.

Other recent studies involving OFDR for remote dosimetry include a very preliminary proof-of-concept study involving a nanoparticle-doped enhanced-backscattering fiber [482] and an investigation of the sensitivity enhancing properties of metallic coatings on a P-doped optical fiber under 6 MeV and 10 MeV X-rays [483].

1.5. Objectives of the present thesis work

As introduced in **Section 1.1**, the space environment is a complex combination of radiation and temperature effects that significantly affect both electronic devices and living beings. Accurate sensing of the radiation received by spacecraft is of major interest in this context, both for the characterization of the radiation environment at a designated location and for the monitoring requirements of radiation protection in the case of manned missions.

The behavior of optical fibers under radiation has been thoroughly studied through various aspects, including attenuation (RIA), emission (RIE) and compaction (RIRIC), as exposed in **Section 1.2**. In particular, the time and temperature stability of the P_1 defects of phosphorus-doped optical fibers stand out in comparison to what is commonly observed on other types of radiation-induced defects found in common optical fiber types. The near-infrared RIA band associated with the P_1 defects, centered around 1550 nm, provides a very practical and convenient way to observe the evolution of the defect population in an irradiated optical fiber, and, as a consequence, offers the ability to estimate the amount of dose received by the fiber.

Optical-fiber based dosimetry combines the capability to measure radiation as described above with the other intrinsic advantages of optical fibers: small dimensions, low mass, relative immunity to outside electromagnetic effects, and capacity to act both as a sensing element and a means to transport signal to an outside reading device; all of which can provide an advantage for space missions.

Among the various interrogation techniques enabled by optical fiber, backscatter measurements (cf. **Section 1.3**) are of particular interest because of their ability to produce one-dimensional maps of a measurand along the optical fiber line, enabling so-called *distributed* sensing. OTDR, using Rayleigh scattering, provides a measurement from which the local attenuation of optical fibers can be determined at arbitrary positions with a spatial resolution usually limited by the pulse width, on the order of 1 m for a 10 ns pulse. The single-ended nature of the interrogation techniques allows for simple sensing architectures, although the limited dynamic range of the device restricts the maximum measurable attenuation.

The combination of optical fiber dosimetry with distributed interrogation techniques enabled the emerging application of distributed optical fiber-based dosimetry, presented in **Section 1.4**. This technology, first developed at the turn of the 21st century, was successfully tested in the complex, high-dose radiation environments provided by particle accelerators. The CERN DOFRS system, in particular, involves a *ad hoc*, phosphorus-doped optical fiber coupled with a commercial OTDR device operating at 1550 nm.

Bridging the gap between the current implementations of distributed dosimetry and the conditions of space missions provides several challenges: first, the dose and dose rates requirements are radically

Item	Objective	Means
Functionality	Assess the ability of the system to perform accurate dose measurement.	Testing of the dosimetry system in a controlled, standardized radiation environment, with a range of dose rates that matches the targeted application.
Performance	Assess the main performance figures and limits of the system.	Statistical analysis of large numbers of measurements taken in similar conditions, either at room temperature or in a defined, controlled temperature range.
Tolerance to TID	Assess the ability of the system to operate reliably within the typical Total Ionizing Dose exposition of a space mission.	Radiation testing of the OTDR device itself during its operation, in a range of doses and dose rates that match the targeted application, and analysis of hardware and software failures.
Tolerance to SEE	Assess the sensitivity of the system to Single Event Effects and its ability to mitigate them.	Radiation testing of the OTDR device under very energetic particles and analysis of hardware and software failures.

Table 1.5. – Main objectives of this thesis work.

lower in space than in the particle accelerators in which most of these technologies have been tested; second, the high cost of sending devices into space makes it impractical to use typical commercial OTDR devices, even their portable versions, onboard spacecrafts. Therefore, the use of so-called *embedded* devices, reduced in dimensions, comes as a necessary step to enable distributed sensing in this context. However, the ability of these devices to operate with the same performance as their large-sized counterparts was not fully demonstrated, although a 2020 study involving atmospheric neutrons showed promising results [400].

Another, critical issue that contrasts with existing distributed dosimetry applications is the fact that the interrogating device must fly with the sensing optical fiber, and, as a consequence, be exposed to the same harsh environment. A proper assessment of the ability of such embedded devices to perform in these conditions of radiation and temperature is therefore needed to validate the concept of porting such distributed dosimetry systems to space missions.

In regard to the statements made here above, the objective of this thesis work is to characterize and validate the performance of distributed dosimetry systems in space radiation environment. This main objective could be split into several items, presented in **Table 1.5**.

1.6. Summary of the theoretical part

English

The space radiation environment is characterized by a diversity of particle types and energies, combined with disparities in locations, from the radiation belts in Earth's orbit to direct exposure to solar events and GCRs in interplanetary missions.

Radiation effects on optical fibers have been extensively studied in the literature; phosphorus-doped fibers, in particular, have exhibited interesting dosimetric properties through measurement of their RIA in the near-infrared range.

Among the available technologies to measure this RIA, OTDRs offer both the ability to acquire measurements in real-time and to virtually access any segment of an optical fiber line, resulting in a so-called *distributed* measurement.

Combining this interrogation technology with radiosensitive optical fibers, distributed dosimetry has seen two main documented implementations, for particle accelerators, that have demonstrated experimentally the validity and interest of such measurements.

The objective of the present thesis work is to validate the concept of an optical-fiber-based, embedded and distributed dosimetry system suitable for space applications.

Français

L'environnement radiatif spatial se caractérise par des particules de divers types et énergies, ainsi que par des disparités locales, des ceintures de radiations dans l'orbite terrestre à l'exposition directe aux événements solaires et au rayonnement cosmique galactique lors des missions interplanétaires.

Les effets des radiations sur les fibres optiques ont été étudiées de manière étendue dans la littérature; les fibres dopées phosphore, notamment, ont montré des propriétés dosimétriques intéressantes par la mesure de leur atténuation radio-induite (RIA) dans le proche infrarouge.

Parmi les technologies disponibles pour mesurer cette RIA, les OTDRs offrent à la fois la capacité d'acquérir des mesures en temps réel et d'accéder virtuellement à n'importe quel segment d'une ligne de fibre optique, donnant des mesures dites *réparties*.

En combinant cette technologie d'interrogation avec des fibres optiques radiosensibles, la dosimétrie répartie a vu deux principales implémentations documentées, pour des accélérateurs de particules, qui ont démontré expérimentalement la validité et l'intérêt de telles mesures.

L'objectif du présent travail de thèse est de valider le concept d'un système de dosimétrie répartie par fibre optique et embarqué, convenant aux applications spatiales.

Chapter 2:

Materials and methods

2. Materials and methods

Contents of this chapter

2.1. Optical fibers

The optical fibers used in this work were phosphorus-doped, single-mode fibers manufactured by the French specialty fiber manufacturer iXblue (rebranded Exail since 2022). Two kinds of fibers were tested: a standard-sized fiber (called **A** for further purposes), for comparison with other published results, and a novel, size-reduced, P-doped optical fiber (called **B** for further purposes) tailored for dosimetry measurement in space applications. The size difference between these two fibers, which share the same core diameter, is illustrated in **Figure 2.1**.

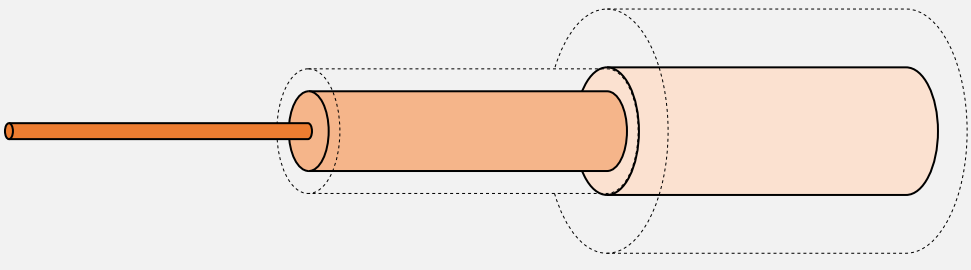

Figure 2.1. – Section view of the **B** fiber (in solid lines), compared to the same scale with fiber **A** (represented in dashed lines).

Fiber	A	B
Core diameter	8 µm	8 µm
Cladding diameter	125 µm	80 µm
Coating diameter	245 µm	128 µm
Core material	P-doped SiO_2 (6.6 wt%)	P-doped SiO_2 (6.6 wt%)
Cladding material	SiO_2	SiO_2
Coating material	Dual-coat acrylate	Dual-coat acrylate

Table 2.1. – Main characteristics of the two types of optical fiber used in this work.

The main characteristics of these fibers are presented in **Table 2.1**. They share the same core specifications, with the material of both cores being silica doped with phosphorus at 6.6 wt%, and a same core diameter of 8 µm. These fibers however differ in their cladding specifications: whereas the cladding material is pure silica in both cases, their cladding diameter is different, with 125 µm for fiber **A** and 80 µm for fiber **B**.

The coating material for both fibers is acrylate, which is able to sustain temperatures up to 85 °C [484]. Both fibers involve a dual coat design, commonly found in telecommunication fibers [485], in which an inner, softer acrylate is itself coated with an outer, harder acrylate [486], resulting in significantly lower microbending losses [487].

The radial electrical field profile of the guided mode at 1610 nm was simulated based on the refractive index profile of these fibers[1], using the software COMSOL Multiphysics v5.5.0.359. The results are shown in **Figure 2.2** for the one-dimensional radial profile, and in **Figure 2.3** for the two-dimensional profile in the fiber cross-sectional plane. In both cases, the simulation determined two guided modes for each fiber, with extremely close characteristics, which as per the weakly guiding fiber theory [266] corresponds to the two-fold degeneration of mode LP_{01}; only one of these solutions is therefore illustrated here.

Despite the dimensional differences between fibers **A** and **B**, they both share a very similar mode profile, for which respectively 96 % and 95 % of the optical intensity (square of the amplitude) is confined in the core. The size reduction of fiber **B** does therefore have little impact on the optical properties of the fiber, and theoretically enables it to perform as a single-mode, radiation-sensitive fiber, with the advantages of reduced volume and mass footprints.

These characteristics make fiber **B** a suitable candidate for distributed dosimetry for space applications, which is why an important amount of this thesis work is dedicated to assess the operational performance of this fiber in such setups.

[1] These refractive index profiles were supplied by the manufacturer and cannot be published in this thesis.

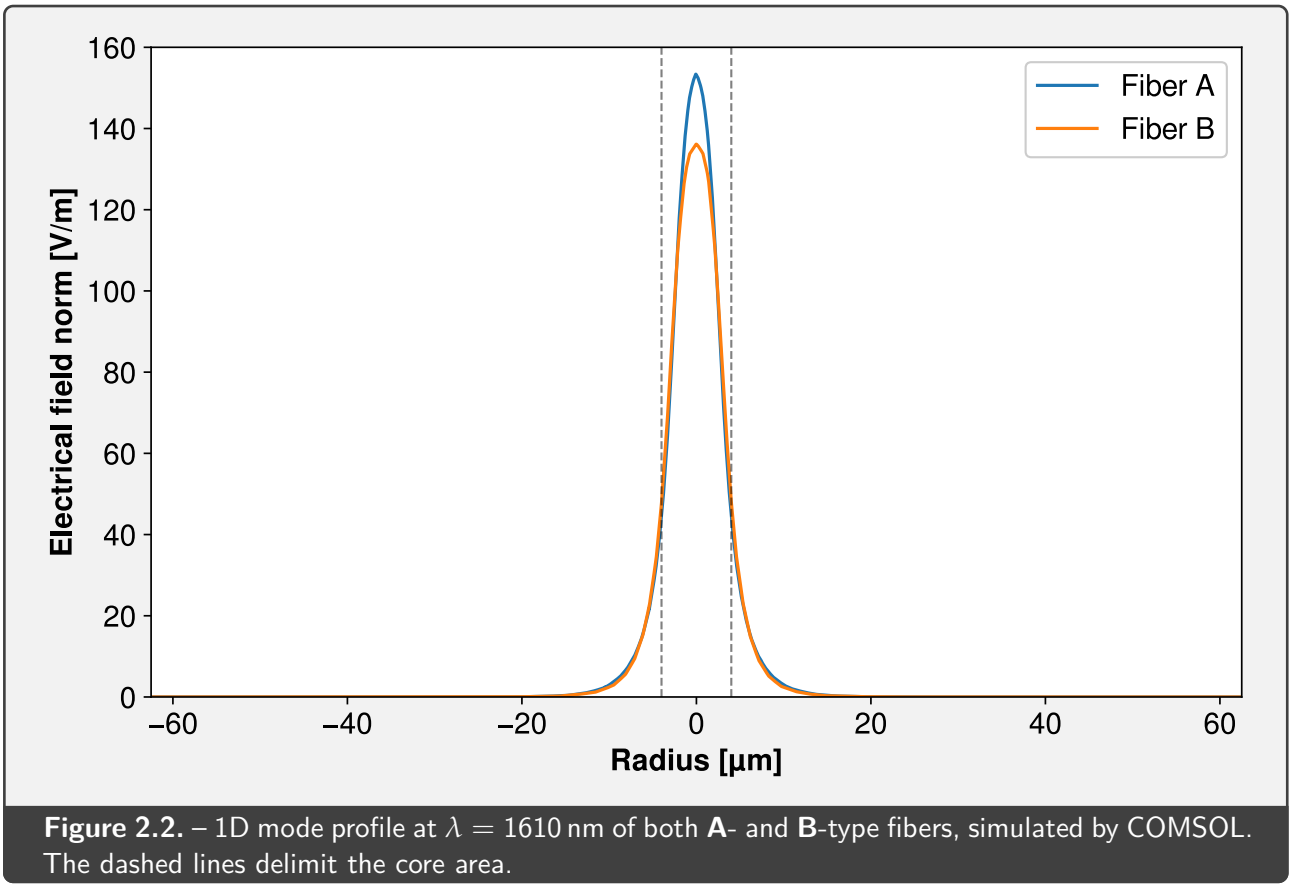

Figure 2.2. – 1D mode profile at $\lambda = 1610\,\text{nm}$ of both **A**- and **B**-type fibers, simulated by COMSOL. The dashed lines delimit the core area.

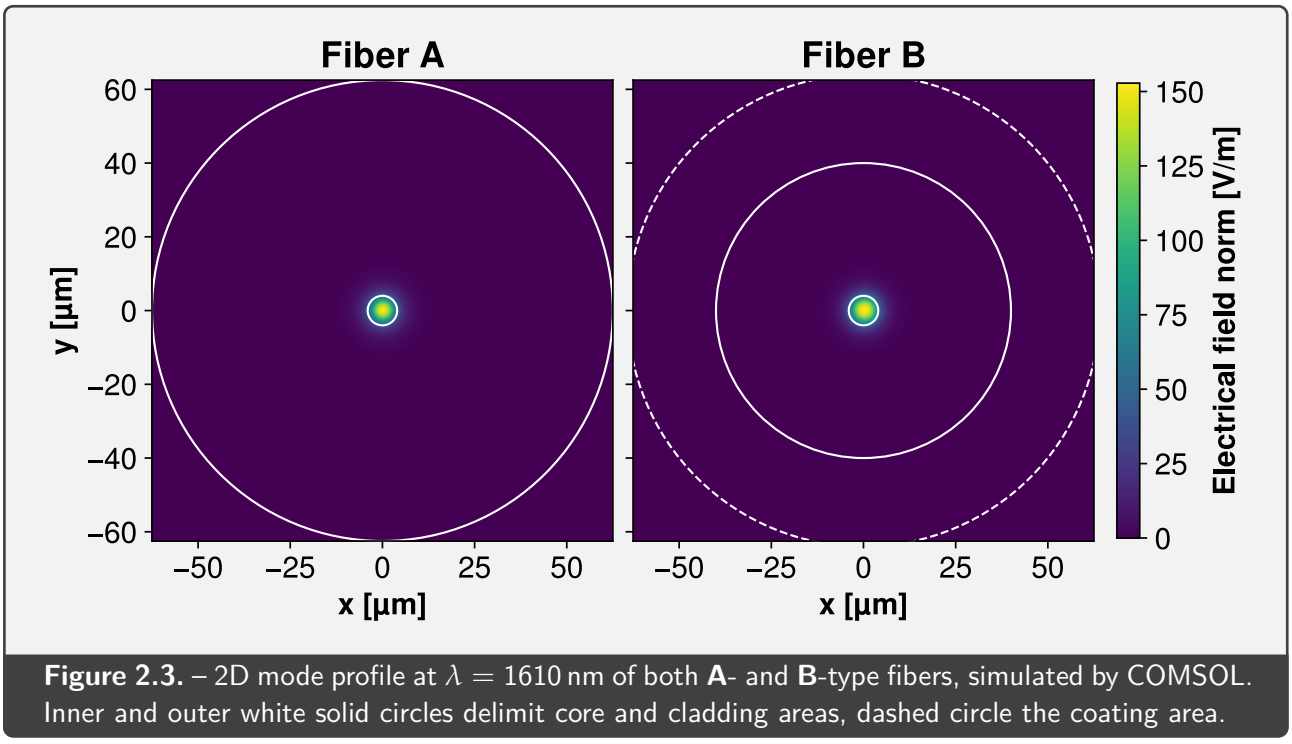

Figure 2.3. – 2D mode profile at $\lambda = 1610\,\text{nm}$ of both **A**- and **B**-type fibers, simulated by COMSOL. Inner and outer white solid circles delimit core and cladding areas, dashed circle the coating area.

Figure 2.4. – Photograph of the three types of OTDR devices used in this work: on the left, MTS 6000A from JDSU; on the middle, Micro iOTDR from VIAVI Solutions; on the right, Nano iOTDR from VIAVI Solutions. The ruler is 20 cm long.

2.2. OTDR devices

Three types of OTDR devices, illustrated in **Figure 2.4**, were used in this thesis work:

- MTS 6000A from JDSU (now VIAVI Solutions), equipped with a 8129 VLR OTDR module;
- Micro iOTDR from VIAVI Solutions;
- Nano iOTDR from VIAVI Solutions.

The first device is a standard, state-of-the art commercial OTDR device, with a portable, modular design. It is equipped with a single-mode, dual-wavelength interrogation module.

The two last devices are embedded OTDRs, with considerably reduced dimensions as shown in **Figure 2.4**, and are the main focus of this work.

2.2.1. Generalities on OTDR devices

All types of OTDR devices used in this thesis work are supplied by the same manufacturer (VIAVI Solutions) and therefore offer the advantage of sharing many common features and functionalities.

Interface

All three tested devices share a similar user interface, which includes a graphical interface for visualizing OTDR traces during and after acquisition, change the various acquisition and device settings, and manage the local file storage (if available). Interaction with this interface is usually performed

Figure 2.5. – Screenshot of the main results screen of a Micro iOTDR device, with a typical OTDR trace and analysis.

via a touch screen and hardware buttons, as it is the case with the MTS6000A device, but these features are notably absent from the embedded iOTDR versions. However, for all devices, this user interface can be accessed remotely, as explained here below.

As illustrated in **Figure 2.5**, the user interface also features an analysis of the measured OTDR trace, with indication of the start, length and attenuation of each detected segment. While this analysis, designed for telecommunication diagnostics, is useful for a quick overview of an unknown measurement line, it was ignored altogether in this thesis work, in favor of the raw OTDR trace data.

All devices also feature an Ethernet [488] interface, enabling communication through the TCP/IP [489] protocol. The IP address of the device can be either static or set automatically via transaction with a *Dynamic Host Configuration Protocol* (DHCP) [490] server; in the framework of this thesis work, all IP addresses were set statically, for simplicity and reliability concerns.

The Ethernet interface on each device provides several features:

- Access to the graphical user interface through a *Virtual Network Computing* (VNC) system [491] via TCP port 5900.
- File transfer through the *File Transfer Protocol* [492] via TCP port 21.

- Command interface through *Standard Commands for Programmable Instruments* (SCPI) [493], via TCP ports 8000 and 8002, used respectively for the system and OTDR functions.
- Proprietary access for device maintenance and update through *Secure Shell* (SSH) on TCP port 22 and *HyperText Transfer Protocol Secure* (HTTPS) on TCP port 443.

Both embedded OTDR devices (Micro and Nano iOTDRs) also feature a *Universal Serial Bus* (USB) [494] port that can be used simultaneously for power supply and software emulation of an Ethernet interface, providing the features listed above. However, our testing of these features revealed a low reliability of these USB interfaces, which are meant for initial configuration, as well as reduced capability to command several devices from a same computer.

In this work, the Ethernet interface of each OTDR device was used for controlling these devices by a remote computer, by issuing SCPI commands for parameter setting, acquisition control and data retrieval. The VNC interface was also used to provide a graphical view of the device operation to allow periodical monitoring of the measurement system.

Acquisition parameters

Each OTDR enables setting a variety of parameters, as illustrated in **Figure 2.6**, to adapt to different acquisition conditions. The main parameters that were used in this work are:

- **Wavelength**: selection of the laser wavelength. While the embedded OTDR devices only have one type of laser available, larger-sized units typically allow selection between several wavelengths (1550 nm and 1625 nm for the 8129 VLR board on the MTS 6000A).
- **Pulse width**: setting of the laser pulse duration. All tested devices enable a wide range of pulse widths – typically from 5 ns to 20 µs – with some differences between devices, notably regarding the lowest available pulse width: 3 ns for the 8129 VLR board on MTS 6000A, 5 ns for the Micro iOTDR and 10 ns for the Nano iOTDR.
- **Resolution**: setting of the spatial sampling. MTS 6000A and Micro iOTDR allow down to 4 cm, while Nano iOTDR only allows down to 8 cm. As explained in (cf. **Section 1.3.2**), spatial sampling is not the only parameter that affects the actual spatial resolution of the measurement; in our case, the pulse width is instead the limiting factor.
- **Scan time**: setting of the averaging time. All devices allow to set this time between 10 s and 180 s, allowing for a better SNR, especially for locations with low reflectivity, typically found at the end of the measurement line.
- **Index of refraction**: setting of the theoretical refractive index of the guided mode. This parameter is used to enable fine tuning of the position scale in the OTDR graph.

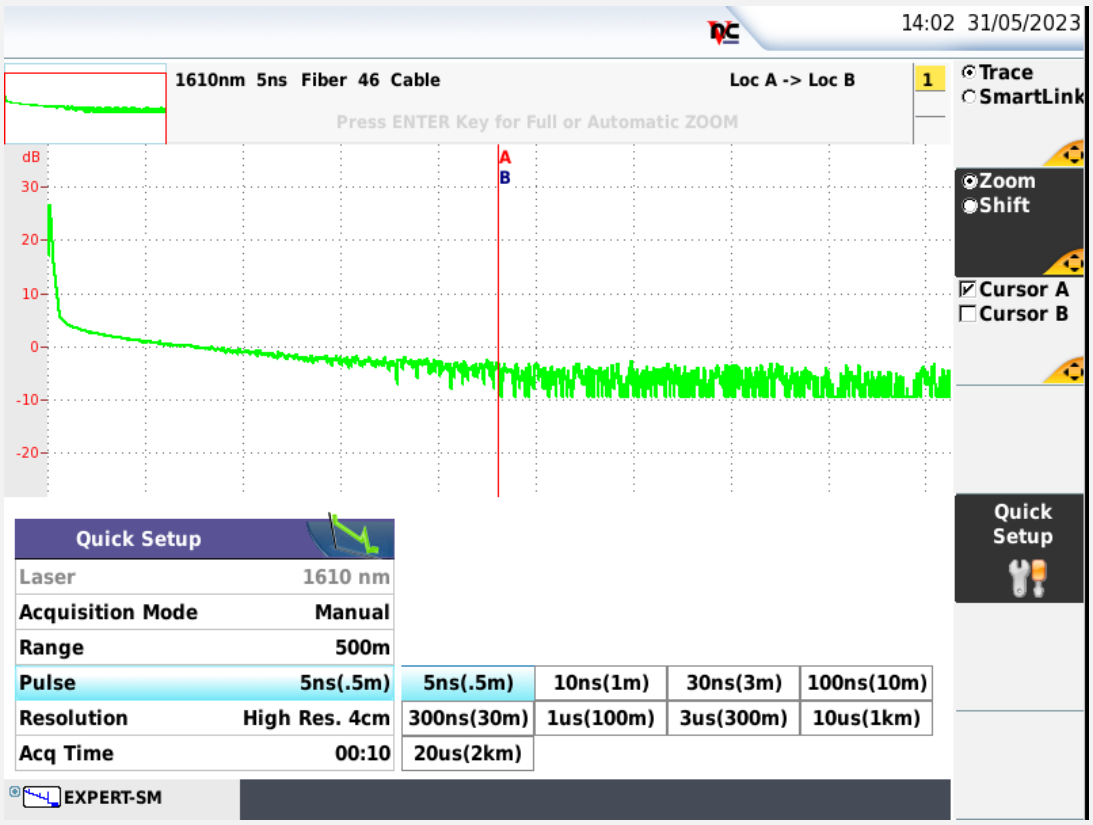

Figure 2.6. – Screenshot of the main parameter setting screen of a Micro iOTDR device. The highlighted choice is pulse width, and the list displayed to the right shows the available pulse widths selectable on this device, from 5 ns to 20 µs. The lengths indicated in parentheses are the theoretical spatial resolutions linked to each pulse width.

- **Scatter coefficient**: setting of the theoretical fraction of the probe pulse power that is backscattered. This value is given in dB and is typically on the order of −80 dB.

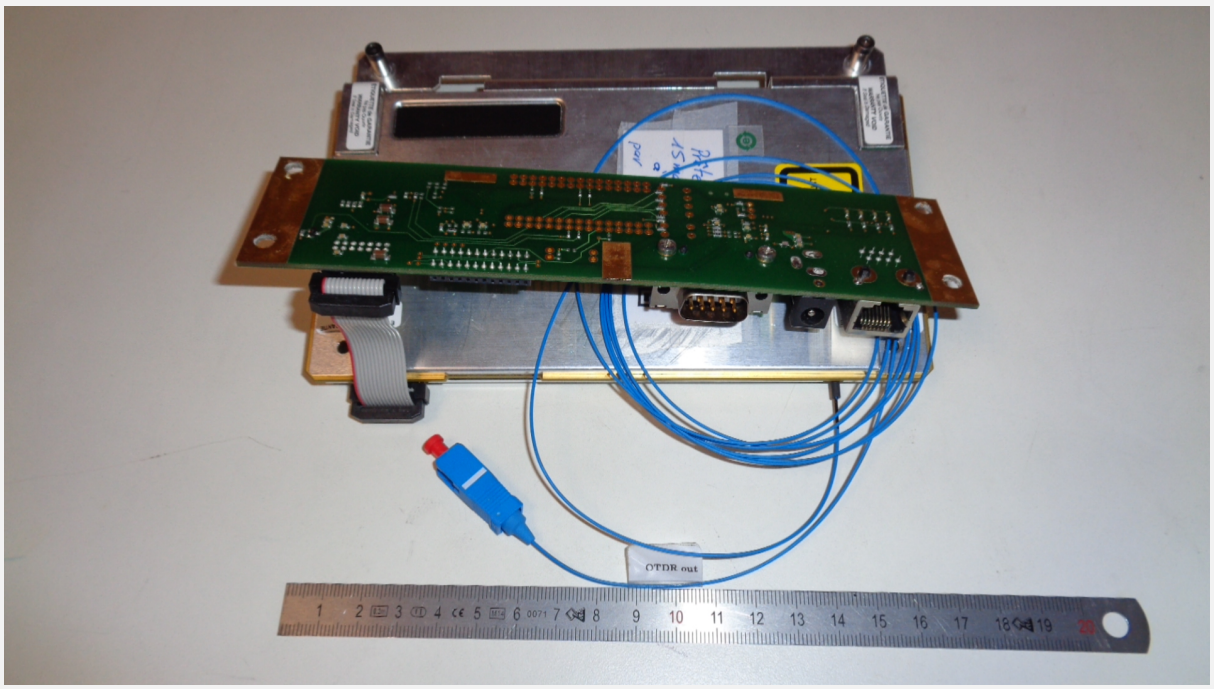

Figure 2.7. – Photograph of a Micro iOTDR device, with its optional interface card.

2.2.2. Micro iOTDR devices

The Micro iOTDR from VIAVI Solutions, illustrated in **Figure 2.7**, is an embedded OTDR device designed for in-service interrogation of optical fiber networks up to a range of ~260 km [495]. Its main technical characteristics are given in the datasheet excerpt shown in **Figure 2.8**.

Its dimensions are 91 mm × 170 mm × 16.5 mm and its mass 200 g, which makes it about 20 times smaller in volume and 13 times lighter than the MTS 6000A unit[2].

Its interfaces are:

- A single-mode fiber of length ~5 m, equipped with a SC/PC connector [496], for connection with the optical fiber to interrogate.
- A USB-C interface that can be used both as a 5 V power supply and software-emulated Ethernet communication for initial configuration.
- A 14-pin interface that provides connection for a 12 V power supply, a full 8-pin Ethernet connection and additional hardware reset and shutdown commands.

The devices that were tested in this work were equipped with an interface card, designed by the manufacturer, to link the 14-pin connector to both a ⌀2.5 mm circular connector for power supply and a RJ45 socket for Ethernet interface. To ease handling, transportation and installation of these

[2]Dimensions and mass of the MTS 6000A device: 280 mm × 200 mm × 95 mm, 2.620 kg.

Specifications Micro iOTDR card for Medium or Long Range integrated OTDR – (typical at 25°C)

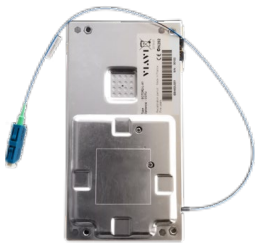

General		
Dimensions	91 x 170 x 16.5 mm	
Operating temperature	-5 to 65°C or 70°C according to the variant	
Storage temperature	–20 to 85°C	
Humidity	85% without condensing	
EMC	EN61326-1, EN6100-3-2	
Interfaces	Ethernet 10/100/1000	
Power consumption	5.1 W (Typical at 25°C) 10mW in standby mode	
OTDR		
Laser Safety	Class 1	
Number of data points	Up to 512,000	
Sampling resolution	From 4 cm	
Distance range	Up to 260 Km	
Distance accuracy	+/-1m +/- Sampling resolution +/- distance * 10-5	
OTDR Range Details	**Medium Range**	**Long Range**
Wavelength[1] (nm)	1625 nm	1610 or 1626 nm
Wavelength accuracy[1] (nm)	+/-3	+/-3
Dynamic range[2] (dB)	37	40
Pulse width	5 ns to 20 µs	5ns to 20 µs
Event dead zone[3] (m)	1	0.8
Attenuation dead zone[4] (m)	3.5	3

[1]Laser at 25°C and measured at 10 µs.

[2]The one way difference between the extrapolated backscattering level at the start of the fiber and the RMS noise level, after 3 minutes averaging and using the largest pulse width.

[3]Measured at ±1.5 dB down from the peak of an unsaturated reflective event using the shortest pulse width.

[4]Measured at ±0.5 dB from the linear regression using a -55dB type reflectance and using the shortest pulse width.

Figure 2.8. – Manufacturer datasheet of the Micro iOTDR device. (from [495])

devices with their interface card, customized supports in aluminum were designed to group these elements as a single unit, as shown in **Figure 2.4**.

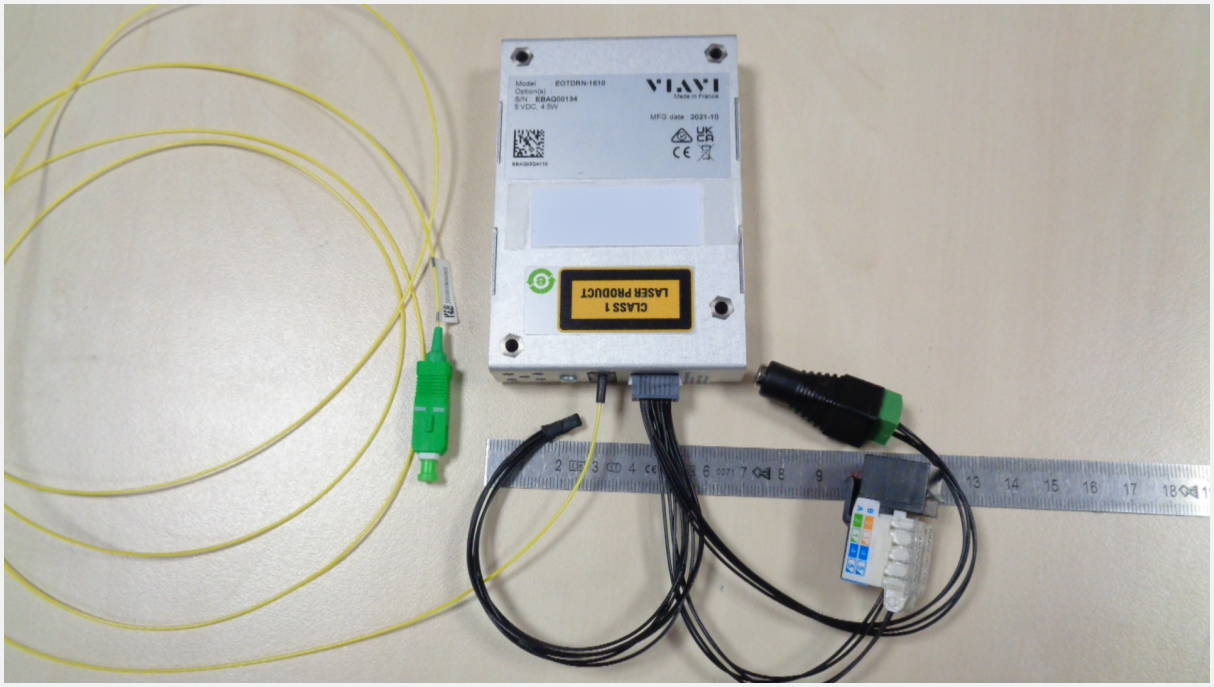

Figure 2.9. – Photograph of a Nano iOTDR device, with its interface adapter for power supply and Ethernet.

2.2.3. Nano iOTDR devices

The Nano iOTDR from VIAVI Solutions, illustrated in **Figure 2.9**, is an even smaller embedded OTDR device, compared to the Micro iOTDR, that enables optical network monitoring up to a medium range of ~160 km [495]. Its main technical characteristics are given in the datasheet excerpt shown in **Figure 2.10**.

Its dimensions are 98.5 mm × 67.5 mm × 16.5 mm and its mass 110 g, which correspond to a 48 times volume gain and 23 times mass gain compared to the MTS 6000A unit.

Its interfaces are:

- A single-mode fiber of length ~5 m, equipped with a SC/APC connector [496], for connection with the optical fiber to interrogate.
- A USB-C interface that can be used both as a 5 V power supply and software-emulated Ethernet communication for initial configuration.
- A 14-pin interface that provides connection for a 5 V power supply, a full 8-pin Ethernet connection and additional hardware reset and shutdown commands.

The devices that were tested in this work were equipped with a custom-made interface adapter, attached to the 14-pin connector and enabling connection of a 5 V supply through a ⌀2.5 mm circular connector and a RJ45 socket for Ethernet connection.

Specifications Nano iOTDR card for Medium Range integrated OTDR – (typical at 25°C)

General	
Dimensions	98.5 x 67.5 x 16.5 mm
Operating case temperature	-5 to 75°C
Storage temperature	-40 to 85°C
Humidity	5 to 85% without condensing
EMC	EN61326-1, EN6100-3-2
Interfaces	Ethernet 10/100
Power consumption	5.1 W (Typical at 25°C) 10mW in standby mode
OTDR	
Laser Safety	Class 1
Number of data points	Up to 512,000
Sampling resolution	From 4 cm
Distance range	Up to 160 Km
Distance accuracy	+/-1m +/- Sampling resolution +/- distance * 10-5
OTDR Range Details	**Medium Range**
Wavelength[1] (nm)	1610 nm
Wavelength accuracy[1] (nm)	+/-5
Dynamic range[2] (dB)	32
Pulse width	10 ns to 10 µs
Event dead zone[3] (m)	1.5
Attenuation dead zone[4] (m)	5

[1]Laser at 25°C and measured at 10 µs.

[2]The one way difference between the extrapolated backscattering level at the start of the fiber and the RMS noise level, after 3 minutes averaging and using the largest pulse width.

[3]Measured at ±1.5 dB down from the peak of an unsaturated reflective event using the shortest pulse width.

[4]Measured at ±0.5 dB from the linear regression using a -55dB type reflectance and using the shortest pulse width.

Figure 2.10. – Manufacturer datasheet of the Nano iOTDR device. (from [495])

2.3. Radiation facilities

The radiation tests reported in this work were performed in different facilities, each offering different capabilities in terms of particle type and energy, as well as accessible dose rates. This section will review the two types of irradiators used in this thesis work.

2.3.1. X-ray irradiators

Generalities on X-rays and X-ray tubes

X-rays denominates high-energy electromagnetic radiation, typically starting from 100 eV [497]. Since its discovery by the German physicist Wilhelm Röntgen[3], this type of radiation gained immense interest, first in the medical domain with the birth of radiology, then in material physics since the discovery of crystalline X-ray diffraction by Max von Laue[4] [498].

Means of production of such X-rays have consequently also been the subject of considerable interest and refinement, and many technologies of X-ray sources exist as of today, relying on physical phenomena such as braking radiation, synchrotron radiation or Cherenkov radiation [499].

Among these production technologies, X-ray tubes are the most commonly used, with an history of development dating more than a century [500], and applications in fields as diverse as medical imaging [501], material characterization [502], sterilization of medical material [503], food [504] or insects [505], and radiation testing of electronic devices [506].

A typical X-ray tube, illustrated in **Figure 2.11**, consists of the assembly under vacuum of a cathode, typically a filament through which an electrical current circulates, and an anode, typically a high-atomic-number material such as tungsten (W). A high electrical voltage V (on the order of ten or hundreds of kilovolts) is applied between the cathode and anode while an electrical current I (typically in the ampere range) circulates through the cathode, heating the filament and causing emission of electrons by thermionic effect. The resulting electron flow i is called *tube current*, and is typically in the milliampere range (with $1\,\text{mA} \approx 6.24 \times 10^{15}\,\text{electron/s}$) [501].

The very high potential difference V induces a strong electrical field, causing the released electrons to be accelerated to a high energy $E_{e^-} = Vq$, (with $q = 1.602\,176\,634 \times 10^{-19}\,\text{C}$ the elementary charge [346]). When expressed in electronvolts, E_{e^-} simply has the same numerical value as V, so a 100 kV potential leads an energy of 100 keV for each electron.

These high-energy primary electrons interact with the anode material, and produce secondary X-ray emission through two processes: bremsstrahlung (braking radiation) and characteristic emission.

[3] Nobel Prize in Physics 1901.
[4] Nobel Prize in Physics 1914.

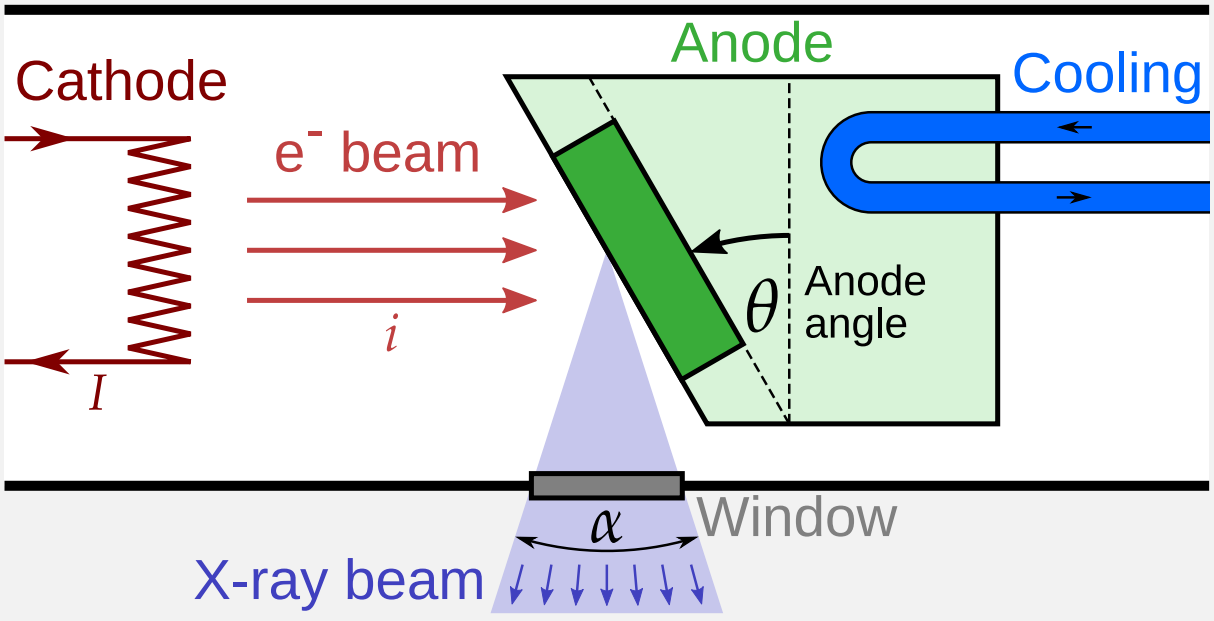

Figure 2.11. – Overview of the main components of a typical X-ray tube. (adapted from [392])

Bremsstrahlung (German word for "braking radiation") originates from a deviation of the incident electron trajectory caused by Coulomb interaction with the electric field of atomic nuclei; as the electron is deviated, it is decelerated by the electric field and the resulting energy difference is emitted in the form of photons [507]. The energy spectrum of the resulting radiation is continuous, with a maximum energy corresponding the incident electron energy. The stopping power of electrons due to bremsstrahlung, which is linked to its probability of occurrence, is proportional to the square of the atomic number Z of the material [508], and therefore the use of high-atomic-number materials is preferred in the anode for more efficient production of X-rays [501].

Characteristic emission is a fluorescence phenomenon caused by liberation of core electrons of the anode material: as these get replaced with electrons of lesser binding energy, a photon is emitted with a precisely defined energy, namely the difference between energy levels of the chased electron and its replacement [509]. The spectrum of characteristic emission is therefore composed of sharp peaks standing a defined energies, which are specific of the anode material, hence the *characteristic* nature of this radiation. X-ray characteristic emission was discovered in 1909 by the British physicist Charles Glover Barkla[5], and is commonly used as a method to produce narrow linewidth radiation for diffraction spectroscopy [510], as well as a material characterization technique, through the help of handbooks compiling lists of known characteristic lines for most elements [511].

While both these processes are able to convert electrons to X-ray photons, their overall efficiency is very low, due to the low cross-sections of these interactions, and a typical X-ray tube efficiency is usually considered to be lesser than 1 % [501].

[5]Nobel Prize in Physics 1917.

The resulting X-ray beam also exhibits particular angular features. Whereas the produced X-ray photons are theoretically emitted in all directions, the fact that the interactions mentioned here above take place inside the volume of the anode, and the fact that this anode is usually made of a high-density, high-attenuating material, cause the resulting X-ray beam to cover a privileged angular region, through which the path travelled inside the material is minimal. This phenomenon is called *heel effect*, and causes the X-ray beam to be emitted with a small angle that depends on the anode angle (θ on **Figure 2.11**) [512].

The vacuum tube, usually also made of a high-density material, is sealed with a window made, in the contrary, of a low-atomic-number element such as beryllium (Be), positioned under the anode so that most of the produced X-rays can leave the tube without significant absorption [513]. The positioning and size of the window also define the maximum angular range of the exiting beam.

X-ray tubes can be operated with short pulses, in applications such as radiography [501], or continuously in other applications such as thickness gauging in metallurgical production lines [514]. Because of the high amount of heat generated on the anode during this process, an additional cooling system is usually required to avoid damaging the anode material, and therefore significantly lengthen the lifetime of the X-ray tube [501].

MOPERIX and LabHX X-ray facilities in Université Jean Monnet Saint-Étienne

Two X-ray facilities, named MOPERIX and LabHX, were used in this thesis work, both located in Laboratoire Hubert Curien of Université Jean Monnet Saint-Étienne (France). Both are commercial X-ray irradiators involving a similar architecture. Their main characteristics are given in **Table 2.2** and **Figure 2.12**.

Each irradiator includes a X-ray tube inside an lead (Pb) enclosure with walls thick enough (6 mm for MOPERIX, 8 mm for LabHX) to ensure a safe radiation level for personnel operating outside when the tube operates at maximum voltage and current. Passage of cables and optical fibers is made through two dedicated openings with a labyrinth structure that are designed to reduce external radiation leakage to a minimum.

Both irradiators offer a wide range of dose rates, typically from 500 $\mu Gy(SiO_2)/s$ to more than 20 $Gy(SiO_2)/s$, which can be adjusted using several parameters, such as distance from the source, X-ray tube voltage and current, or additional shielding. In particular, adjustment of the tube voltage enables to change the energy spectrum, controlling the mean energy of photons [392], while adjustment of the tube current controls the intensity of the beam.

Before each irradiation, dosimetry is performed *in situ* at the desired position, voltage and current using a PTW 23344 plane-parallel ionization chamber, which features a ⌀3 cm sensitive element, connected to a PTW UNIDOS E reading device.

Facility	MOPERIX	LabHX
Picture	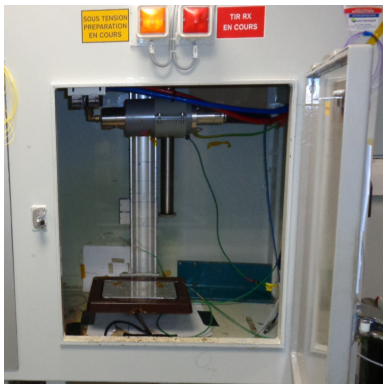	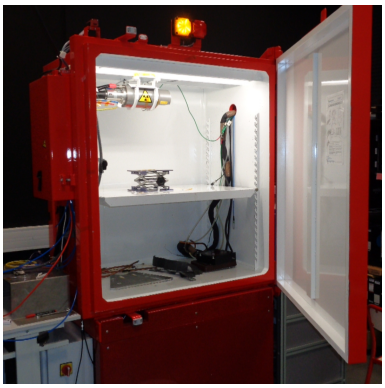
X-ray tube	COMET MXR 165 [515]	COMET MXR 225-26 [516]
Maximum voltage	160 kV	225 kV
Maximum current	45 mA	30 mA
Anode material	Tungsten (W)	Tungsten (W)
Anode angle	30°	30°
Beam coverage	50°	40°
Tube filtration	4 mm beryllium (Be)	2 mm beryllium (Be)

Table 2.2. – Main characteristics of the two X-ray facilities in Laboratoire Hubert Curien that were used in this thesis work.

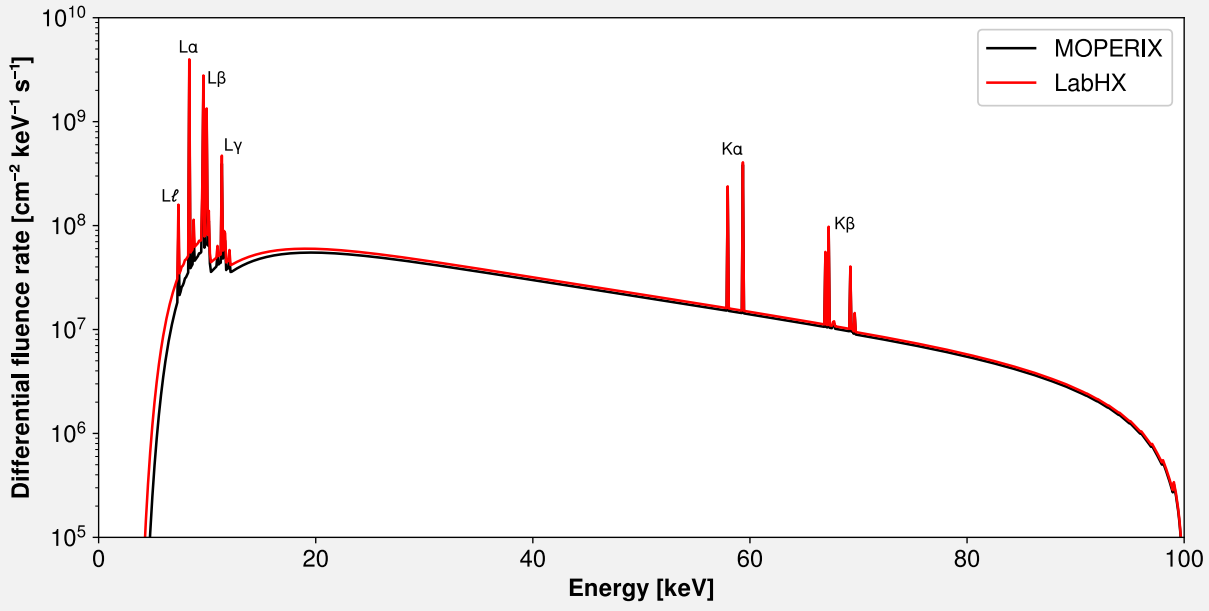

Figure 2.12. – SpekPy simulated fluence rate spectra of MOPERIX and LabHX X-ray tubes operated at a voltage of 100 kV and a current of 1 mA, from a location at a distance of 50 cm vertically from the anode center. Filtering from the beryllium window (different for each irradiator) and from the air layer are taken into account. The main tungsten characteristic X-ray lines [511] are also annotated.

Isotope	^{60}Co	^{131}I	^{137}Cs	^{222}Rn	^{238}U
Half-life	5.271 yr	8.025 d	30.08 yr	3.8235 d	4.468×10^9 yr
Emission	β^- 318 keV γ 1.173 MeV γ 1.332 MeV	γ 364 keV β^- 606 keV	β^- 514 keV γ 662 keV	α 5.489 MeV	α 4.151 MeV α 4.198 MeV

Table 2.3. – Summary data of five radionuclides commonly found in nature or in nuclear/radiation applications, with their half-lives and main emission type and energies. [517]

2.3.2. γ ray irradiator

Generalities on γ rays and radionuclides

Gamma (γ) rays are high-energy photons that are produced as the result of nuclear fission or transitions in energy levels of atomic nuclei [518]. The production of γ rays in controlled environments, such as irradiation facilities, is therefore ensured by radioactive elements called *radionuclides* (also called *radioisotopes*). Out of the 3338 different radionuclides identified as of 2022 [519], **Table 2.3** presents the summary data of five of the most commonly occurring of these radioactive elements.

Each radionuclide is associated with a *decay constant* λ, expressed in s^{-1}, which is proper to the isotope in question, and corresponds to the change by unit of time in the number of nuclides at a particular energy state. This decay constant is often converted to a macroscopic quantity known as *half-life* $T_{1/2} = \ln(2)/\lambda$, which corresponds to the expected period of time necessary to reduce by half the radionuclide population [151]. Because such half-lives are often measured in years (cf. **Table 2.3**), procurement, operation, storage and disposal of radionuclides are subject to strict regulation [520].

The quantity of radiation emitted by a radioactive source is often expressed in terms of *activity*, which reflects the number of disintegration events by unit of time in the whole volume of the source. The SI unit of activity is becquerel (Bq), which corresponds to s^{-1} [151], but a more macroscopic unit, often used in practice, is the curie[6] (Ci), which corresponds to 3.7×10^{10} Bq [521, 522]. Activity A, decay constant λ and number of radionuclides N are linked through the following equation [151]:

$$A = \lambda N \tag{2.1}$$

Among the various type of particles produced by radionuclides, γ rays are used in fields as diverse as medical surgery [523] or imaging [524], industrial nondestructive testing [525], sterilization [526], and radiation testing [527]. As shown in **Table 2.3**, not all radionuclides produce emission of significant γ ray radiation; a few selected isotopes are therefore involved for such applications.

[6] Named after Marie Skłodowska-Curie (1867–1934), Nobel Prize in Physics 1903 and Nobel Prize in Chemistry 1911.

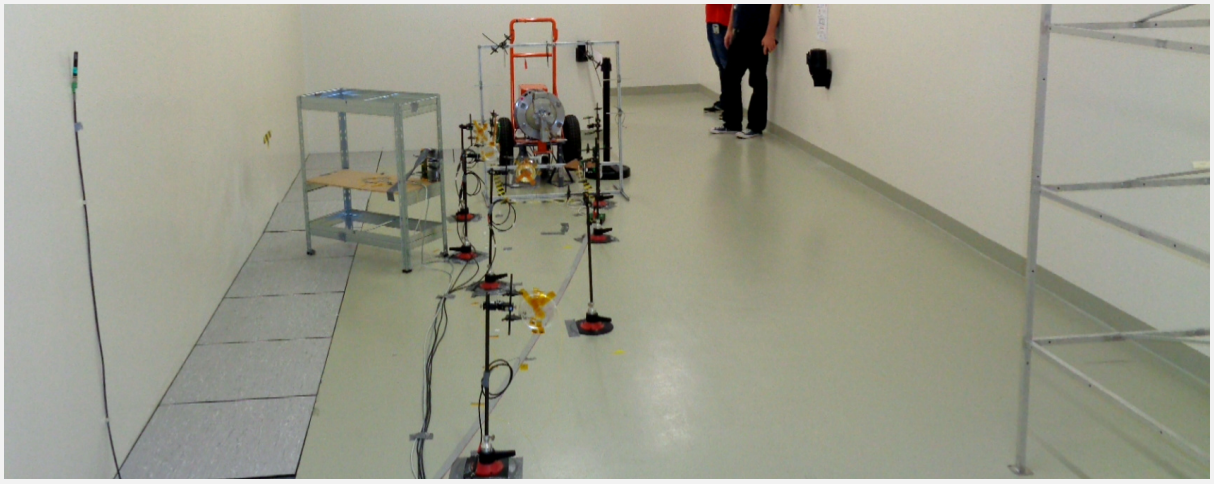

Figure 2.13. – Photograph of the PRESERVE γ ray irradiation facility in 2021. The ^{60}Co source is installed at the center of the picture, on the orange structure.

Cobalt-60 (^{60}Co) is of special interest in γ ray applications, because of its main γ emission of two sharp, equally intense lines at 1.173 MeV and 1.332 MeV [517], resulting in a mean energy of 1.25 MeV. ^{60}Co is produced by irradiation of stable ^{59}Co in nuclear reactors [528], and is typically sealed inside steel capsules, which often produce an additional secondary photon spectrum [529]. Emission of γ rays by ^{60}Co is performed in a two-step process: ^{60}Co decays into an excited ^{60}Ni atom through a beta decay process, then ^{60}Ni undergoes transition from energy level 2.505 748 MeV to 1.332 508 MeV then to the stable level at 0 MeV, releasing at each step a photon with an energy corresponding to the energy level difference [530].

PRESERVE facility in Université de Montpellier

The PRESERVE facility in Institut d'Électronique et des Systèmes of Université de Montpellier (France) is a γ ray irradiator involving a ^{60}Co source, emitting photons at 1.17 MeV and 1.33 MeV.

The source is installed in a large 9 m × 4 m area (cf. **Figure 2.13**), enabling a wide range of available dose rates due to the inverse-square distance law [152], which predicts a ~300 fluence ratio between locations at 0.5 m and 9 m in front of the source. At the distance of ~4 m at which our irradiations were performed, the dose rate is on the order of 10 µGy(Air)/s.

The irradiation area is enclosed by thick concrete walls that absorb radiation down to a safe level in the outside rooms. Passage of cables and fibers is ensured by dedicated openings running through the concrete wall delimiting the irradiation room from the nearby instrumentation room.

Dosimetry is performed *in situ* before each irradiation, using a PTW TM30013 cylindrical Farmer chamber with a ø6 mm sensitive element, connected to a PTW UNIDOS E reading device.

(a) Beam line 1B entrance. **(b)** Beam line 1B sample holder.

Figure 2.14. – Photographs of the TRIUMF PIF facility. (courtesy of Martin Roche)

2.3.3. Proton irradiator

The Proton Irradiation Facility (PIF) in the TRIUMF particle accelerator center in Vancouver (Canada) is a high-energy proton irradiator, able to supply protons with a broad range of energies, ranging from 20 MeV to 480 MeV.

These protons are extracted from the main cyclotron of the TRIUMF center, and their energy can be selected through the use of stripping foils placed at variable radial locations in the cyclotron. Two beam lines are extracted from the cyclotron for use in the PIF facility.

Beam line 1B (BL1B) provides high-energy protons (350 MeV or 480 MeV) with low intensities (up to 2 nA at the maximum energy) [531]. These characteristics makes BL1B suitable for SEE testing of electronic devices for space applications [532], and the facility provides vertical, adjustable sample holders (cf. **Figure 2.14**) that can precisely position target components of the tested device in the center of the proton beam.

Beam line 2C (BL2C) provides lower energy protons (from 63 MeV to 105 MeV) with higher intensities (up 10 nA at the minimum energy) [531]. Its energy range can be further extended by placing materials in front of the beam, reducing the available energies down to 20 MeV [533], although at the cost of a larger energy spread due to straggling [534]. BL2C is used for component testing with higher proton intensities, and was also involved in research toward proton therapy for the treatment of ocular melanomas [199].

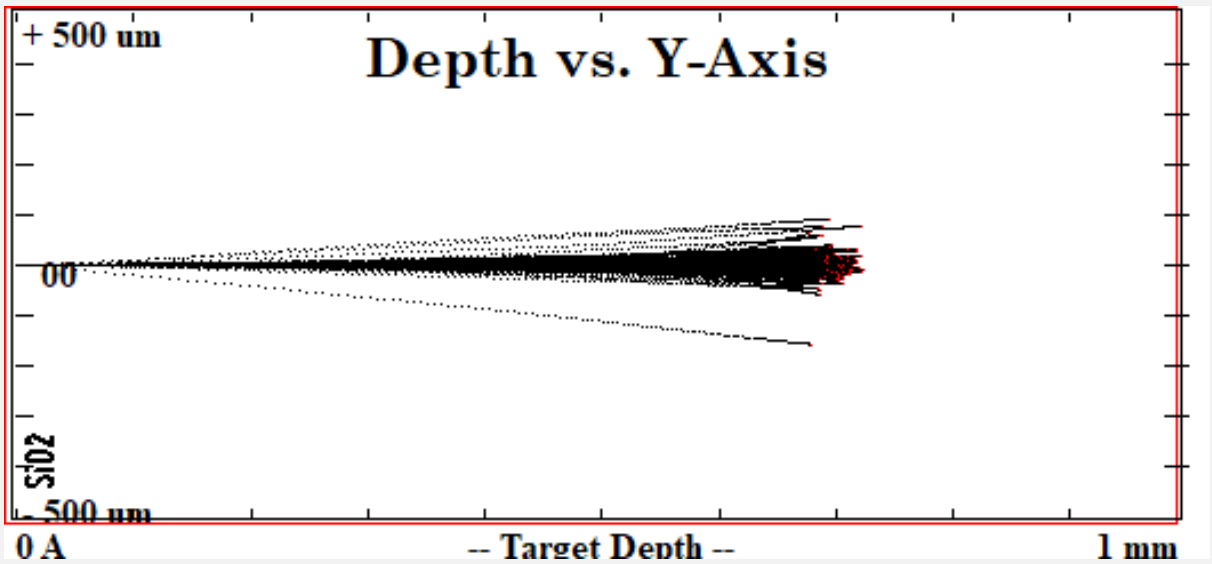

Figure 2.15. – Monte Carlo simulation of 10 MeV proton tracks inside a SiO_2 sample, using the software SRIM. ~200 particle events are represented here.

2.4. Simulation tools

In addition to the experimental work performed in this thesis, a consequent amount of simulation was performed to understand and model the interactions between ionizing radiation and optical fibers in different radiation environments.

Two categories of simulation tools were mainly used: Monte Carlo codes, which simulate particle interactions down to the individual level, and X-ray models, which predict the spectrum produced by X-ray sources. This section presents two of such software that were used in this thesis work: Geant4 for Monte Carlo simulation of particle physics, and SpekPy for modeling of X-ray spectra.

2.4.1. Principles of Monte Carlo (MC) simulation

Particle interaction models revolve around the quantity *cross-section*, which expresses the probability of occurrence of a given interaction (cf. **Section 1.1.3**). On the microscopic scale, this intrinsically probabilistic nature of interations makes it possible, given a same initial particle and conditions, to obtain very different event chains depending on the occurrence and the result of such interactions, as illustrated by the proton trajectories shown in **Figure 2.15**. On the macroscopic scale, however, the mean result of a very large number of interactions is usually observed.

Whereas, in the case of very simple geometries and conditions, this mean result can be determined analytically, more complex situations require numerical simulation of a large number of particles events. This is the concept of *Monte Carlo*[7] (MC) codes, which involve simulation of single particles,

[7]Named by Stanislav Ulam and John Von Neumann in the 1940s, in reference to the Monte Carlo casino in Monaco [535].

for which the occurrence and result of each possible interaction is determined by the outcome of a random number generator [536].

MC methods apply to various integration [537] and probability [538] problems, and are used in domains as diverse as optical tolerancing [539], climatology [540], computer graphics [541], finance [542] and artificial intelligence [543]. However, particle simulation in physics remains the main domain of application of such methods [544].

After simulation of the complete event chains of n independent particles, the mean value $\bar{x}$ and standard deviation s of a quantity of interest x (particle flux, dose deposition, track length…) are given by the following descriptive statistics [545]:

$$\bar{x} = \frac{1}{n}\sum_i x_i \qquad\qquad s = \sqrt{\frac{1}{n-1}\sum_i (x_i - \bar{x})^2} \tag{2.2}$$

As s is roughly proportional to $1/\sqrt{n}$, the uncertainty on the results will decrease as the number of simulated particle increases. Therefore, a very high number of independent particles is usually simulated, so that the uncertainty on the results is low enough to be acceptable. In MC simulation of particle physics, it is therefore not uncommon to simulate millions or billions of particle events to obtain a result of satisfactory accuracy [546].

A common operation scheme is also to run MC simulations in *batches*, each batch including a same, large number of particles. After running a number N of batches, the mean $\overline{X}$ and standard deviation S of the investigated value are calculated using the same descriptive statistics as in (2.2). From these, the confidence interval u about $\overline{X}$, at a level of confidence of p%, can be estimated as follows:

$$u = t_p \frac{S}{\sqrt{N}} \tag{2.3}$$

with t_p the p^{th} percentile of the bilateral Student's t distribution at $N-1$ degrees of freedom, i.e. such as t takes p% of its values in the interval $[-t_p, t_p]$. Because of the properties of the t distribution, t_p approaches the confidence interval at p% of the normal distribution for high values of N [547].

This high requirement in number of calculations make Monte Carlo codes very resource-heavy [548], although the fact that each simulated particle is independent make them extremely well suited to parallelization [549], and therefore to use on dedicated computer clusters, provided the code properly handles the various data synchronisations required for such parallel execution [550].

Other advanced methods can be used to reduce the overall number of MC calculations while keeping low uncertainty on the results. These *variation reduction* methods aim to reduce the amount of unnecessary calculation, through diverse strategies such as weighing factors on the source or interactions to bias the simulation towards a desired phenomenon (e.g. bremsstrahlung emission) [551].

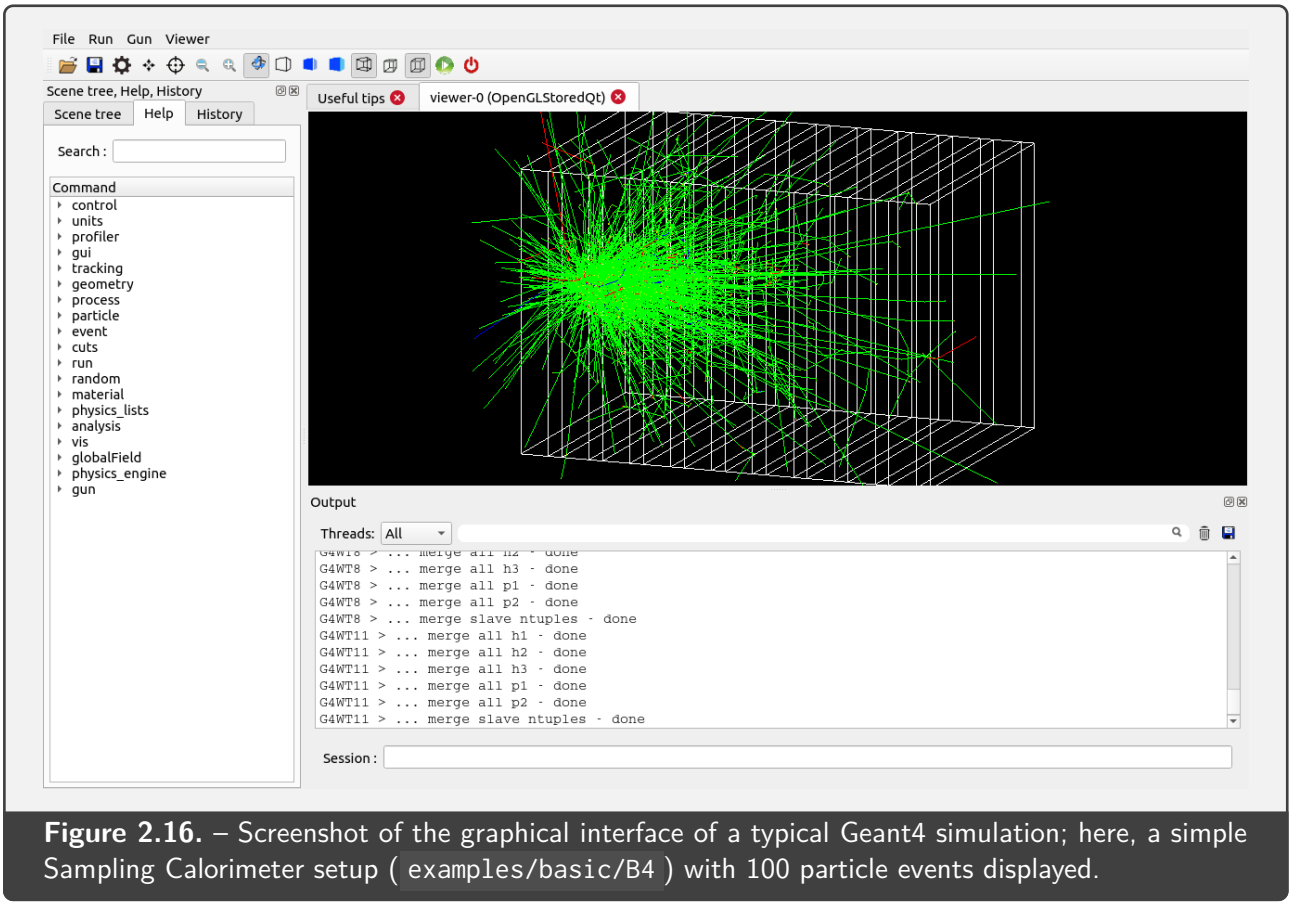

Figure 2.16. – Screenshot of the graphical interface of a typical Geant4 simulation; here, a simple Sampling Calorimeter setup (`examples/basic/B4`) with 100 particle events displayed.

Many different MC codes are available for simulation of particle interaction. The most commonly used general-purpose codes are MCNP [552], FLUKA [553, 554], Geant4 (cf. **Section 2.4.2**) and PHITS [555]. Other, more specialized codes include, for simulation of low-energy electrons, positrons and photons, PENELOPE [556] (50 eV to 1 GeV) and EGSnrc [557] (1 keV to 10 GeV); for simulation of charged particles, SRIM [558] is also one of the reference codes.

2.4.2. Geant4: simulation of particle physics

Geant4 [559–561] is a C++ toolkit for building MC codes dedicated to the simulation of particle physics. It is developed by an international collaboration and published by CERN under an *ad hoc* open source[8] license. The first version of Generation of Events And Tracks (GEANT) was created by CERN in the 1970s [563], and further developed with versions 2 and 3 released in the 1980s [564]. The current major version 4 was first released in 2003 [559], and marked the beginning of an international collaboration outside CERN to maintain and implement new features in this toolkit.

Whereas Geant4 is originally designed for simulation of high-energy physics, up to the TeV scale, in the context of particle accelerators [565], it includes numerous physical models that provide it with a very versatile range of particle types and energies.

[8]The Geant4 software license authorizes modification and redistribution of the source code and binaries, but forbids related patent registration and restricts the use of the Geant4 name [562].

A number of these available physics models were reviewed in the literature to be suitable for simulation of space radiation effects [566]. In particular, the physics package `QBBC_EMZ` stands as the recommended setup in the context of space applications [567]. This package includes the electromagnetic library `G4EmStandardPhysics_option4`, which automatically selects the most accurate models for electromagnetic interactions and tracking of charged particles [568], and the `QBBC` library that includes hadronic and neutronic interaction models suited for medical and space applications [566].

Additional packages that extend the functionality of Geant4 are the Geant4-DNA project for finely modeling cellular radiobiological effects [569, 570], Geant4-MicroElec for microdosimetry [571, 572], GATE for nuclear-based imaging systems [573] and GRAS for simulation of space environment effects [574].

Programming of a Geant4-based simulation involves creation of several C++ classes, inherited from the virtual classes supplied by the toolkit, handling important definitions such as geometry, physics models, tallying and program interface. This modular, configurable nature, along with the fact that the whole toolkit source code is readable, enables to control the behavior of the simulation in a great level of detail, but at the cost of programming complexity.

After compilation, the resulting simulation software can either be run in command-line mode, for output on the terminal or in files, or in a graphical interface mode, which uses renderers provided in the Geant4 toolkit to draw the geometry of the simulation and enable to control various parameters as well as to visualize the results of particle events, as illustrated in **Figure 2.16**.

2.4.3. SpekPy: simulation of X-ray tube spectrum

SpekPy [575, 576] is a Python library for modeling spectra of X-ray tubes. It was designed in the 2010s by a team of Swedish physicists [577, 578], and released in 2019 under a free software license[9].

SpekPy is the successor of the stand-alone software SpekCalc released in 2009 [579], which itself was based on a X-ray spectrum model established by Poludniowski et al. [580, 581]. In 2020, this model was considerably refined [582, 583] with the subsequent release of SpekPy.

As of version 2.09 (released in June 2023), SpekPy can simulate tungsten (W) anodes with operating voltage from 10 kV to 500 kV and molybdenum (Mo) or rhodium (Rh) anodes from 20 kV to 50 kV. It also enables to simulate the effects of filtering, with a large mass-attenuation coefficient database that includes elements with atomic number up to 100 and definition of many compound materials. Spectra simulated by SpekPy with a tungsten anode at a variety of voltages and filtrations were validated against standard NIST data [575].

[9] SpekPy is licensed under the MIT license, that solely requires to keep the license notice in all distributed versions.

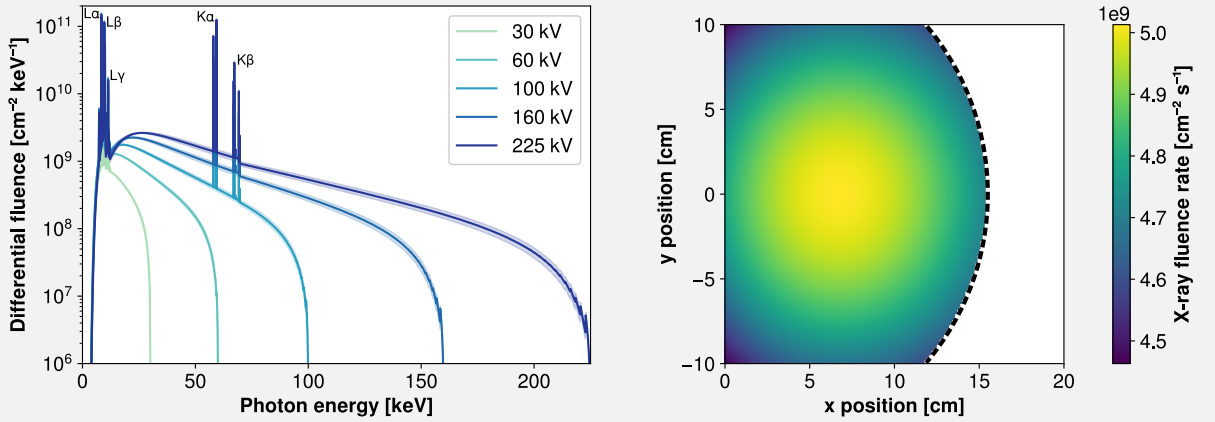

(a) Differential fluence spectra for five voltages. The main tungsten characteristic X-ray lines [511] are also annotated.

(b) Map of the fluence rate at 100 kV in the xy plane. The dashed line indicates the 40° angular limit of the considered tube.

Figure 2.17. – Examples of SpekPy simulation of a tungsten (W) anode with a inherent filtration of 2 mm beryllium (Be), and an operating current of 20 mA. The z distance is 42.5 cm, and air filtering of the same thickness was entered in the simulation. (from [392])

The spatial evolution of the produced X-ray spectrum is also modeled by SpekPy, by inputting the anode angle and the x, y and z coordinates of the point at which the spectrum is to be simulated: the origin is located at the center of the anode surface, the z central axis oriented in the beam propagation direction, the x axis oriented in the anode to cathode direction, and y determined using the right-hand rule [392].

The decrease in fluence according to the inverse-square law with distance from the source is taken into account, as well as the oblique increase of filtering paths, causing an effective increase of the filtering in case of off-axis estimations. The heel effect described in **Section 2.3.1**, which causes the beam to be tilted in the positive x direction, is also simulated by SpekPy, but the authors recommend in this case using the high-accuracy, but slower option `kqp` that models more completely the anisotropy of bremsstrahlung emission [576].

In addition to spectra, SpekPy can also calculate various quantities such as fluence (integral of the differential fluence spectrum), half-value layer (HVL) thickness for various materials, mean energy, effective energy and air kerma.

Some results of SpekPy calculations are shown in **Figure 2.17a** for spectra of a tungsten anode at different voltages, and **Figure 2.17b** for the mapping of the fluence rate in a configuration typical to the LabHX irradiator introduced in **Section 2.3.1**.

2.5. Summary of the materials and method part

English

Two kinds of radiosensitive, phosphorus-doped optical fibers are tested in this thesis work: fiber **A** matches the dimensions of standard, telecom-grade fibers, while fiber **B** offers the same specifications with lower dimensions, enabling reduced volume and mass footprints suitable for space applications.

These fibers were connected to embedded OTDR devices of two different types: VIAVI Solutions Micro iOTDR and Nano iOTDR, the latter offering the smallest dimensions. A standard-sized portable OTDR device, MTS 6000A, was also used for comparison.

Three type of irradiation facilities were used in the course of this thesis: X-ray irradiators, enabling high dose rates at low photon energies, a γ ray facility producing photons of 1.25 MeV mean energy with a very low dose rate, and a 480 MeV proton facility for SEE testing.

Finally, physics simulation software were also used in complement to the experimental tools. The Monte Carlo code Geant4 is able to simulate particle transport and dose deposition in arbitrary geometries, while SpekPy enables simulation of the spectrum and fluence produced by an X-ray tube.

Français

Deux types de fibres radiosensibles, dopées phosphore, sont évaluées dans ce travail de thèse: la fibre **A** correspond aux dimensions standards des fibres télécom, tandis que la fibre **B** fournit les mêmes spécifications avec des dimensions plus petites, permettant des empreintes réduites de volume et de masse convenant aux applications spatiales.

Ces fibres ont été connectées à des OTDRs embarqués de deux types différents : les Micro iOTDR et Nano iOTDR de VIAVI Solutions, ce dernier offrant les dimensions les plus réduites. Un OTDR portable de taille standard, le MTS 6000A, a également été utilisé pour comparaison.

Trois types d'installations d'irradiation ont été utilisés au cours de cette thèse : les irradiateurs à rayons X, permettant des débits de dose élevés à de basses énergies de photons, un irradiateur γ produisant des photons de 1,25 MeV d'énergie moyenne avec un très faible débit de dose, et un irradiateur proton à 480 MeV pour les essais d'effets singuliers (SEE).

Enfin, des logiciels de simulation physique ont également été utilisés en complément des outils expérimentaux. Le code Monte-Carlo Geant4 permet de simuler le transport de particules et le dépôt de dose dans des géométries arbitraires, tandis que SpekPy permet la simulation du spectre et de la fluence produits par un tube à rayons X.

Chapter 3:

Characterization of the dosimetry system

3. Characterization of the dosimetry system

Contents of this chapter

3.1. Metrological properties of the dosimetry system

The reduced dimensions of embedded OTDR devices, such as the Micro and Nano iOTDRs introduced in **Section 2.2**, are the result of design compromises that can affect the performance of these devices in certain fields of application.

This section relates the experiments that were conducted in order to evaluate the main performance figures of these devices for distributed dosimetry applications.

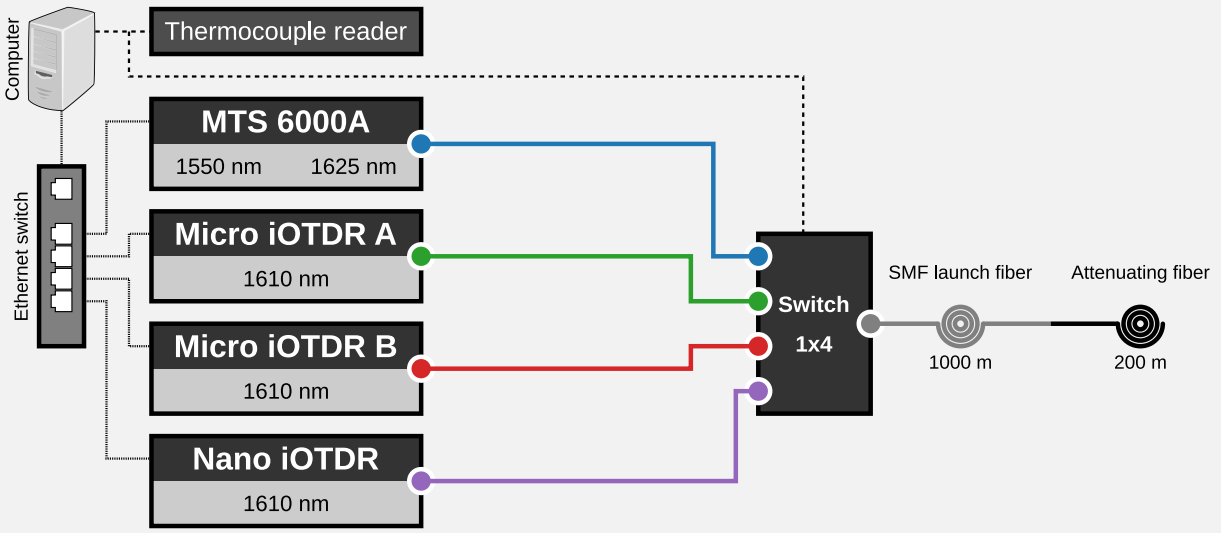

Figure 3.1. – Experimental setup for the characterization of metrological properties of the three different types of OTDR devices.

3.1.1. Experimental setup

To compare the properties of the three types of OTDR devices investigated in this thesis work, the setup illustrated in **Figure 3.1** was run with different parameters, for a total duration of 1 month. The experiment was conducted at room temperature, with daily and weekly variations amounting to a temperature range of 24 °C to 32 °C.

Four devices were tested: a standard-sized MTS 6000A device operating at both 1550 nm and 1625 nm, two Micro iOTDR devices operating at 1610 nm, and one Nano iOTDR device operating at 1610 nm.

The output of these OTDR devices was connected to a same measurement line, made of the succession of two samples of optical fiber. The first sample is a 1 km-long single mode, telecom-grade fiber, designed to be used as a launch fiber to compensate the dead zone at the beginning of OTDR measurement lines [584]. The second fiber is a 200 m-long sample of fiber **B** after irradiation with γ rays at a dose of 12.97 $Gy(SiO_2)$ (cf. **Section 3.2**), which results in a total attenuation of ~12 dB at 1610 nm. To enable all OTDR devices to access this measurement line while optimizing their optical budget, a 1-to-4 optical switch (LEONI eol 1x4) connects each OTDR output to the common line.

For each OTDR device, two parameters were investigated: scan time, either 10 s or 180 s, and pulse width (spatial resolution), ranging from the minimum value allowed by the device: 3 ns (0.3 m) for MTS 6000A, 5 ns (0.5 m) for Micro iOTDR, 10 ns (1 m) for Nano iOTDR, up to 1 µs (1000 m). In the case of the MTS 6000A device, both wavelengths of 1550 nm and 1625 nm were investigated.

The scatter coefficient was set to −81 dB on all devices, however they were configured with different settings for the index of refraction. Therefore, this difference was taken into account in the data

analysis, and the data shown here below have been corrected to ensure a homogeneous position scaling between all investigated devices.

To allow unattended and reliable acquisition, all devices were connected to an embedded computer (Raspberry Pi 4 model B), enabling OTDR device control and data retrieval through Ethernet connection, and switch control through serial connection. A simple Python script running on the acquisition computer looped through all investigated settings on all devices, running an acquisition and saving data for each of these setting. At the change from one device to the other, the script also commanded the switch to change to the corresponding channel.

In addition to the OTDR measurements, an additional measurement of the room temperature was performed by a K-type thermocouple connected to a USB thermocouple reader (Pico Technology TC-08), and recorded using a dedicated acquisition software.

3.1.2. Overview of the data

Most measurements were acquired with the minimum available scan time of 10 s, in order to test the performance of the tested OTDR devices at their maximum temporal resolution. In these conditions, ~1200 similar measurements were collected for each combination of device, wavelength and pulse width, enabling statistical analysis of the influence of each of these parameters.

Example OTDR traces of the complete measurement line are shown in **Figure 3.2**, for the minimum pulse width and scan time enabled by each investigated device. The long, flat segment between ~0 m and ~1000 m is the 1 km launch fiber, and the decreasing segment between ~1000 m and ~1200 m is the attenuating fiber. The three intense peaks correspond to reflection events caused by, respectively, the connection between the OTDR and the launch fiber at ~0 m, the connection between launch fiber and attenuating fiber at ~1000 m, and the end of the attenuating fiber at ~1200 m.

The attenuating fiber segment is shown in more detail in **Figure 3.3**, again for all devices at minimum pulse width and scan time. These sample data show an overall good accordance between measurements acquired by all investigated devices, along with a visible increase of the noise level as the backscattered signal decreases. A first difference between these different devices can be spotted in the precise location at which the two reflection peaks, corresponding to the beginning and the end of the attenuating fiber segment, are represented. This difference in positioning can be explained by the different lengths of internal and external optical fibers on each device, as the Micro and Nano iOTDR devices feature a ~5 m connector fiber, whereas the testing fiber is directly connected on the OTDR card of the MTS 6000A device.

The increase of the noise level as the scattered signal decreases can however be compensated, to a degree, by averaging a large number of measurements. Two methods can be used for such post-

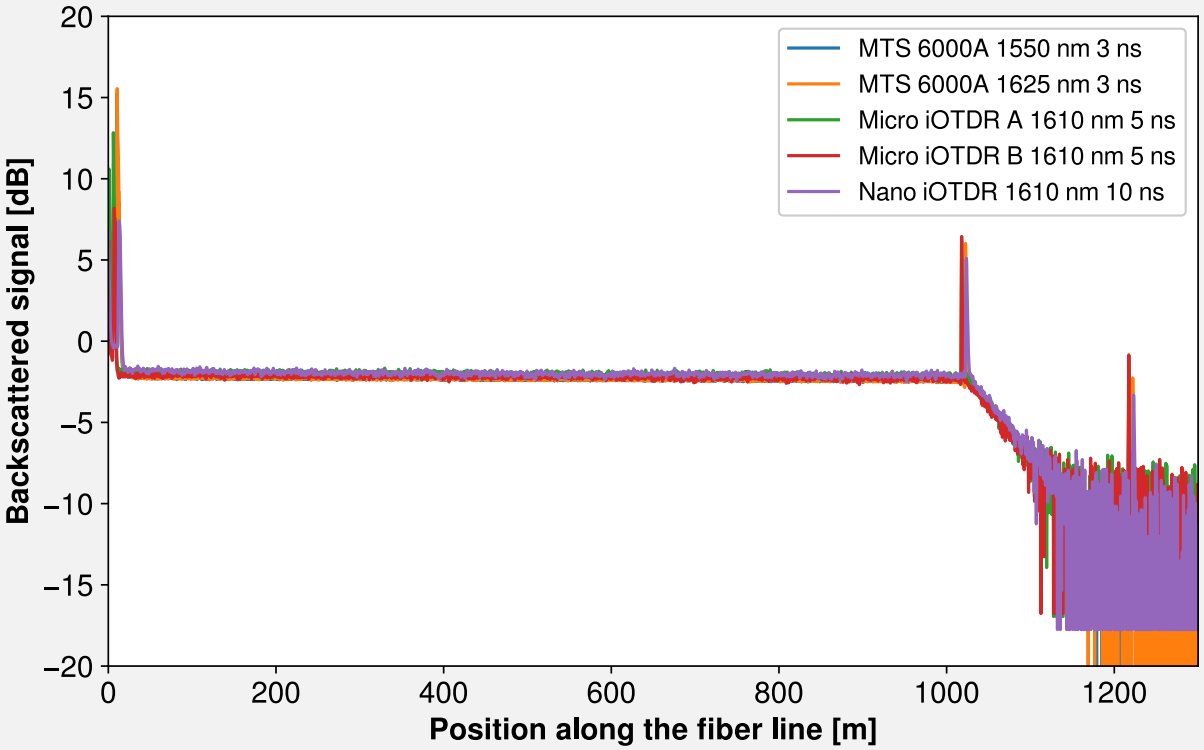

Figure 3.2. – Sample data for the metrological characterization of investigated OTDR devices. Device name, wavelength and pulse width are shown in the legend, and the common scan time was 10 s.

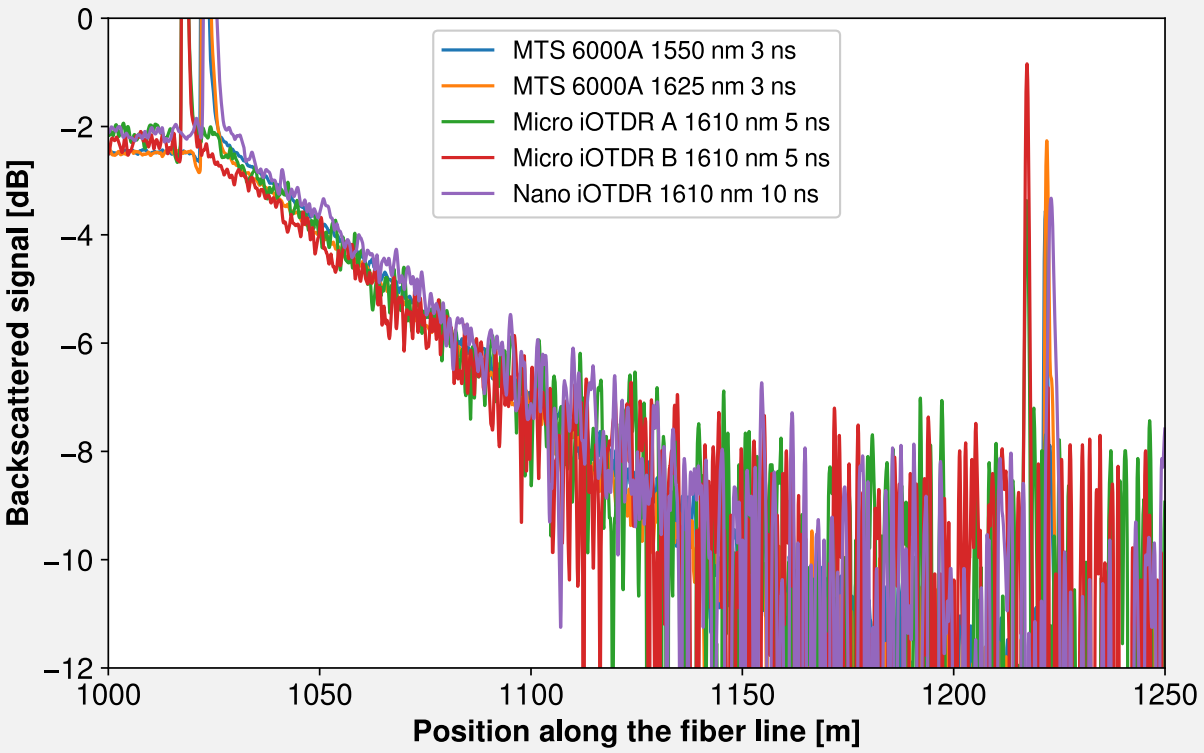

Figure 3.3. – Sample data of a region of interest (attenuating fiber). Device name, wavelength and pulse width are shown in the legend, with a common scan time of 10 s.

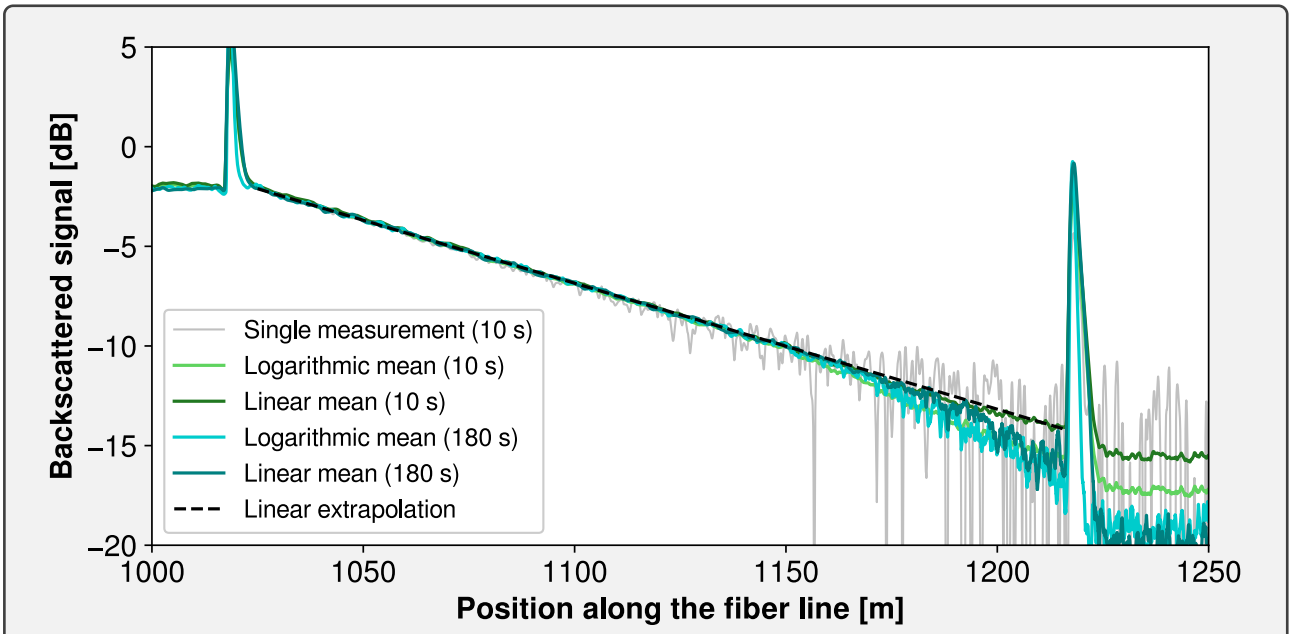

Figure 3.4. – Averaged traces of Micro iOTDR A on the irradiated fiber segment, acquired at a scan time of either 10 s or 180 s. Two processing methods are compared here: averaging in a logarithmic space or in a linear space. The trace in light gray shows a single 10 s measurement in these conditions, for comparison. The dashed line shows an extrapolation of the linear fit of the trace from 1025 m to 1100 m.

processing of the data: a first method averages the OTDR traces in their original, logarithmic scale in dB; a second method converts the traces to a linear scale ($I_{\text{linear}} = 10^{I_{\text{dB}}/10}$), then averages them, before converting these averaged values back to dB ($I_{\text{dB}} = 10\log_{10}(I_{\text{linear}})$).

Such averaging methods are compared in **Figure 3.4** for Micro iOTDR A traces, using the mean of ~1200 measurements performed with a scan time of 10 s, and ~70 measurements performed with a scan time of 180 s (so as to obtain comparable total acquisition times). To facilitate comparison on this figure, all data were slightly offset in order to superimpose their reflection peaks. Comparison of these averaged measurements with **Figure 3.3** highlights a very reduced noise and an overall better linearity of the trace corresponding to the irradiated fiber segment.

The linearity of these averaged traces is not perfect, however, and comparison with the linear extrapolation drawn in dashed line reveals some differences between the four averaged set of data shown in **Figure 3.4**. Both traces averaged in a logarithmic scale have their value decreasing faster than the linear extrapolation, which is especially visible below a value of ~−11.5 dB. On the other hand, traces averaged in a linear scale suffer less deviation from the linear extrapolation, but show different features between data acquired at different scan times: while 10 s are in very good accordance with the linear extrapolation, 180 s data below ~−11.5 dB are considerably more noisy and end up standing in average between linear extrapolation and logarithmic mean values.

These non-linearities occurring at very low signal levels could be linked to the noise floor of the devices, combined with the thresholding of low values (observable on the right of **Figure 3.2**) that

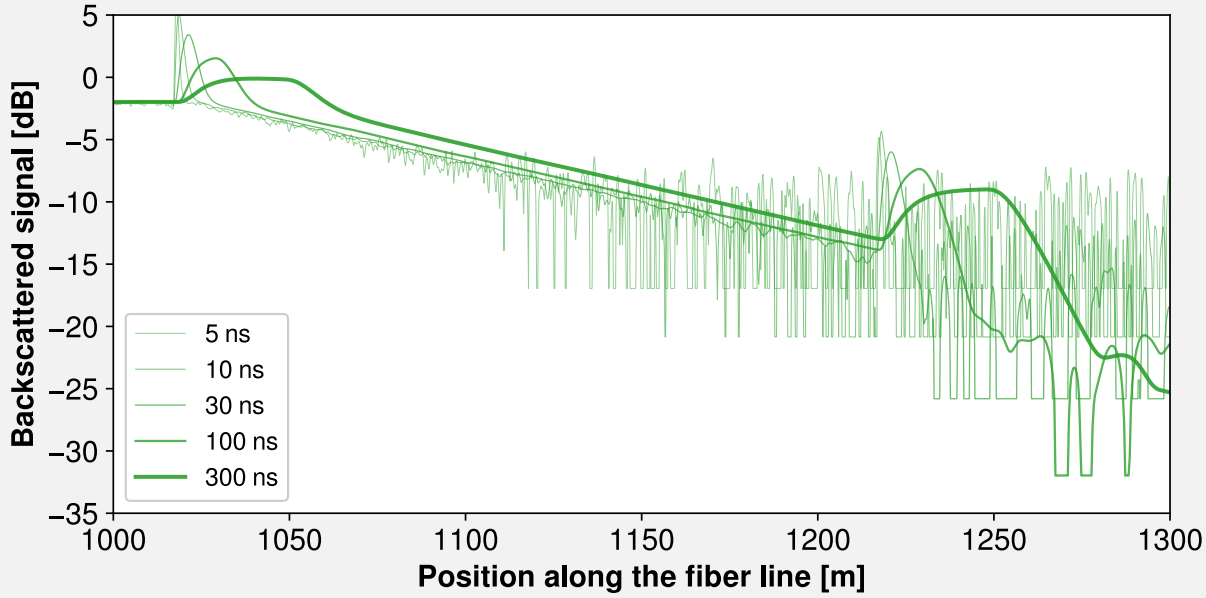

Figure 3.5. – Sample data of a region of interest (attenuating fiber) acquired by the Micro iOTDR A with different pulse widths and a scan time of 10 s.

skew the distribution of measurement points around the true value of the measurand and therefore decrease the efficiency of the mean calculation to act as an accurate estimator. Therefore, averaging OTDR traces in post-processing can only improve the signal quality to a limited degree.

Finally, the effects of adjusting pulse width are demonstrated in **Figure 3.5**, for the same attenuating segment measured by Micro iOTDR A with different pulse widths and a scan time of 10 s. A first observable consequence is a spread of the reflection peaks, located at ~1010 m and 1210 m: as the pulse width increases, each reflection peak becomes smaller in intensity, but wider in position, although the location of the left side of the peak is less affected by changes in pulse width. This effect is directly linked to the dependence of OTDR measurement accuracy on the pulse width, as described in **Section 1.3.2**. A second consequence of increasing pulse width is a decrease of the measurement noise, especially at lower signal levels; this is explained by the fact that more energy is being injected in the fiber, resulting in a much higher backscattered signal compared to the noise level of the receiver.

3.1.3. Dynamic range

The term *dynamic range*, applied to OTDR devices, can encompass a number of different definitions linked to different usages [585], among which the capability to detect strong reflecting events linked to line breakage [586], such as the observed peaks at ~1220 m in **Figure 3.3**. The definition of dynamic range applicable to distributed dosimetry, however, is linked to the ability to accurately measure the optical fiber attenuation at low signal levels.

Although the difference between the highest and lowest measurable value is on the order of 30 dB for

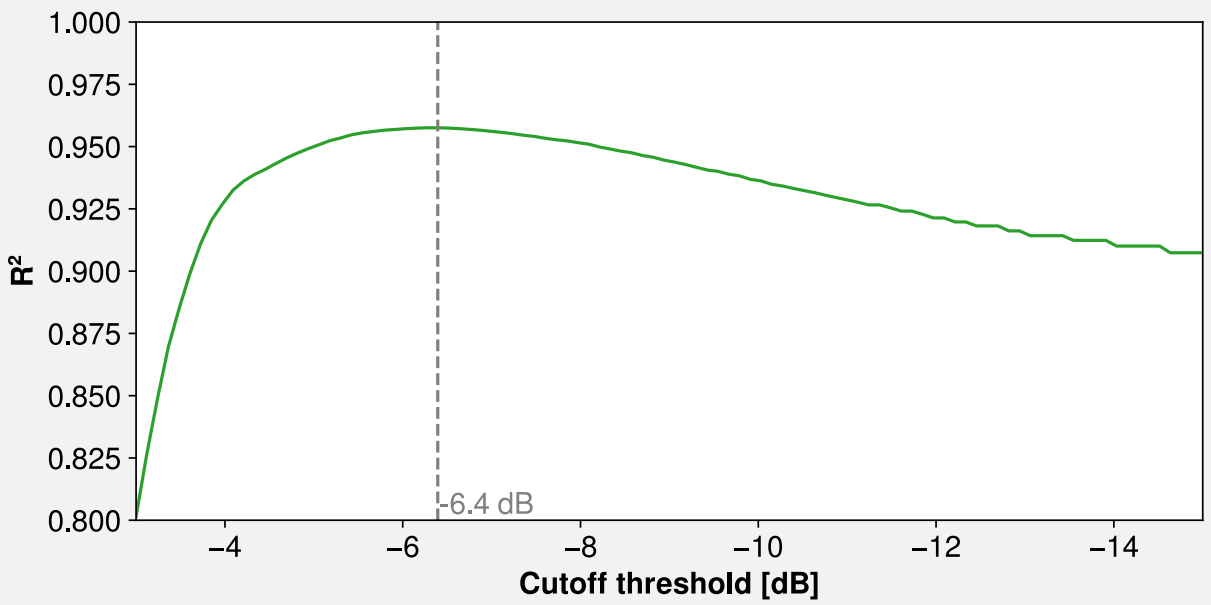

Figure 3.6. – Evolution of the coefficient of determination R^2 of the linear fit on the device Micro iOTDR A with 5 ns pulse width and 10 s scan time, as a function of the cutoff threshold C. The dashed vertical line indicates the location C_{max} of the maximum value of R^2.

the investigated devices, this range cannot be fully exploited for dosimetry measurements because a significant part must be reserved for detecting bright reflection spikes without overloading the sensitive receiver of the device [425].

To estimate the exploitable dynamic range of both Micro and Nano iOTDR devices, we employed the statistical metric *coefficient of determination* R^2 (with $0 \leq R^2 \leq 1$), that evaluates the fraction of variability in the data that are explained by a given model [587]. In the case of linear regression, a value of R^2 close to unity means that the experimental data are well described by a linear model.

We applied linear regression on segments of increasing length in the section of the OTDR traces corresponding to the attenuating fiber. The considered segments were automatically calculated between the start of the attenuating section (at a fixed position, determined manually for each configuration), and the first occurrence of a backscattered signal value below C, with C a cutoff threshold. By evaluating the value of R^2 for decreasing values of C, a trend such as the one pictured in **Figure 3.6** is obtained, which features a maximum at the cutoff threshold C_{max}.

The determined value of C_{max} for all investigated devices and pulse widths is shown in **Figure 3.7** for a scan time of 10 s. It highlights that increasing the pulse width significantly decreases the linearity threshold of all investigated devices, enabling to measure accurately lower signal intensities. As exposed from the previous discussion on **Figure 3.5**, this behavior is expected because of the higher amount of energy injected into the optical fiber for larger pulse widths.

However, this decrease of the optimal cutoff threshold appears to reach a minimum for a pulse width between 100 ns and 300 ns depending on the device; the linearity threshold actually increases, in all

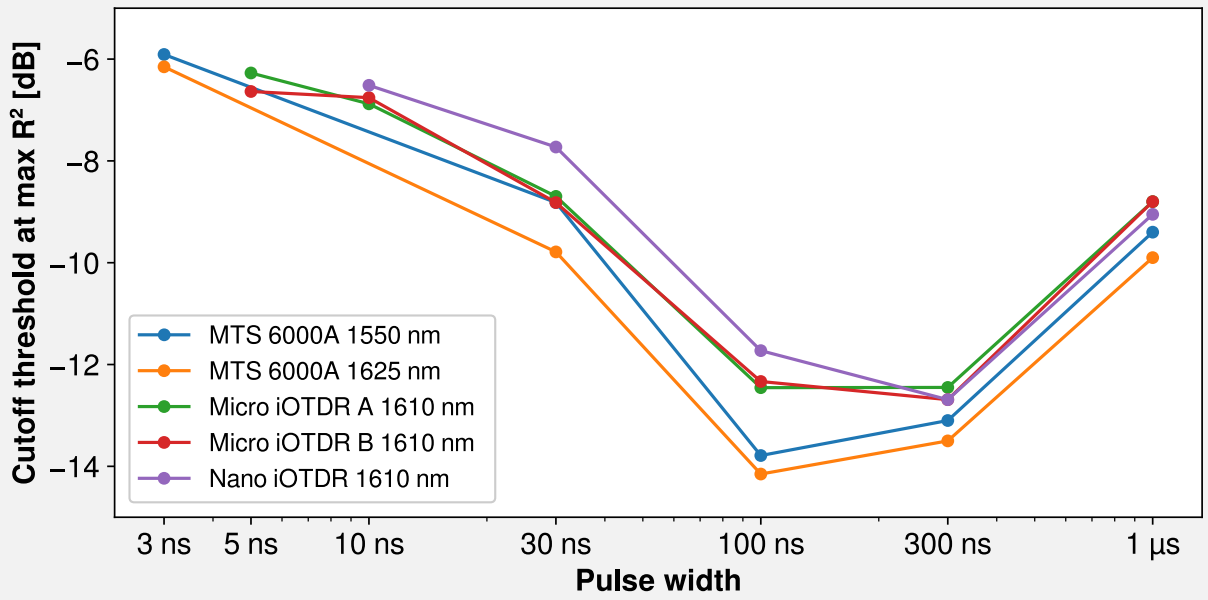

Figure 3.7. – Optimal cutoff threshold C_{max} determined as a function of pulse width for all investigated OTDR devices, with a scan time of 10 s.

cases, for the largest investigated pulse width of 1 µs. These counter-intuitive results can be linked to the comparatively short sampling length used for this study, considering the reduced spatial sampling applied automatically by the devices on larger pulse widths (respectively 0.64 m for 300 ns and 1.28 m for 1 µs), and the broadening of the reflection peaks which reduces the amount of available signal for analysis. The results exposed here for larger ($\geq$ 300 ns) pulse widths can therefore be less relevant when interrogating longer ($\geq$ 1 km) samples.

These data also show a good consistency between results of the three types of investigated devices. The MTS 6000A has overall the highest dynamic, for both its wavelengths, compared to the other devices, except for the pulse width of 3 ns which is not accessible to the iOTDR devices. Results of both Micro iOTDR models are in excellent accordance for all investigated pulse widths, with a threshold of −6.5 dB at the minimum pulse width of 5 ns. Finally, the Nano iOTDR has overall the least dynamic, and reaches a threshold of −6.5 dB at its minimum pulse width of 10 ns.

3.1.4. Measurement accuracy and repeatability

Because of the large number of data acquired in similar conditions for each set of parameters on each device, the accuracy and repeatability of the measurement can be estimated using a statistical analysis of these results. In order to calculate the attenuation measured by the device in each acquisition, a linear fit is applied separately on each segment – launch fiber and attenuating fiber – between positions determined manually for each combination of wavelength and pulse width. In the case of the attenuating segment, the end position was determined by a cutoff intensity value, as described

in **Section 3.1.3**. The applied threshold value was the optimal C_{max} value calculated for each setting as described here above.

The statistical evaluation of the measurements performed on the launch fiber segment is presented in the form of histograms in **Figure 3.8**, and evolution of the mean value and standard deviation in **Figure 3.9**. For both figures, the scan time was set to the minimum value of 10 s, to test performances at the maximum temporal resolution, and displayed data are up to a pulse width of 300 ns.

Regarding measurement accuracy, a noticeable feature of these data is the significant difference on the mean attenuation value measured through all investigated devices and settings. This behavior can be explained by a variety of causes: first, the different interrogation wavelengths, especially between the MTS 6000A and the iOTDR devices, are physically linked to different optical fiber losses, as illustrated in **Section 1.2.1**. In particular, the data acquired at 1550 nm by the MTS 6000A shows a systematically lower measured attenuation, on the order of 0.19–0.20 dB/km, which is consistent with the usual performance of telecom-grade optical fibers [218].

Another cause of this deviation in mean measured values comes from the different pulse widths used for interrogation, which are linked to different group velocities v_g, and therefore different refractive indices and effective wavelengths as they propagate through the optical fiber [588], affecting their attenuation because of the wavelength-dependent losses of the material. A consistent behavior between wavelength, pulse width and mean attenuation could however not generally be observed on these launch fiber data, as illustrated for instance by the different results obtained between Micro iOTDR A and B shown in **Figure 3.8**; these discrepancies could be explained by different calibration settings between devices.

The spread of measured data around the mean value, which is expressed by the width of histograms in **Figure 3.8** and the standard deviation data in **Figure 3.9**, enables to evaluate the repeatability of the measurement. For pulse widths up to 100 ns, the general tendency is an increased repeatability of the measured attenuation value with increasing pulse width. This tendency is not totally consistent with larger pulse widths, such as the 300 ns pulse displayed on these figures which, in most cases, features a larger standard deviation than the 100 ns data measured on a same device. The lesser repeatability of these measurements at 300 ns is explained by the comparatively less linear OTDR trace observed at this setting, possibly as an effect of the reflection peak at the start of the line which is broadened by these large pulse widths (cf. **Figure 3.5**). This behavior is also present in the data taken at a pulse width of 1 µs, not displayed in these figures, which features a much larger standard deviation.

Relating to the comments made here above, the Nano iOTDR data stand out, both in the evolution of the mean attenuation value and the spread of measurements according to pulse width. We observe a very high spread of the data acquired for all investigated settings on this device, and a mean attenuation value which systematically stands higher than all other investigated devices for comparable

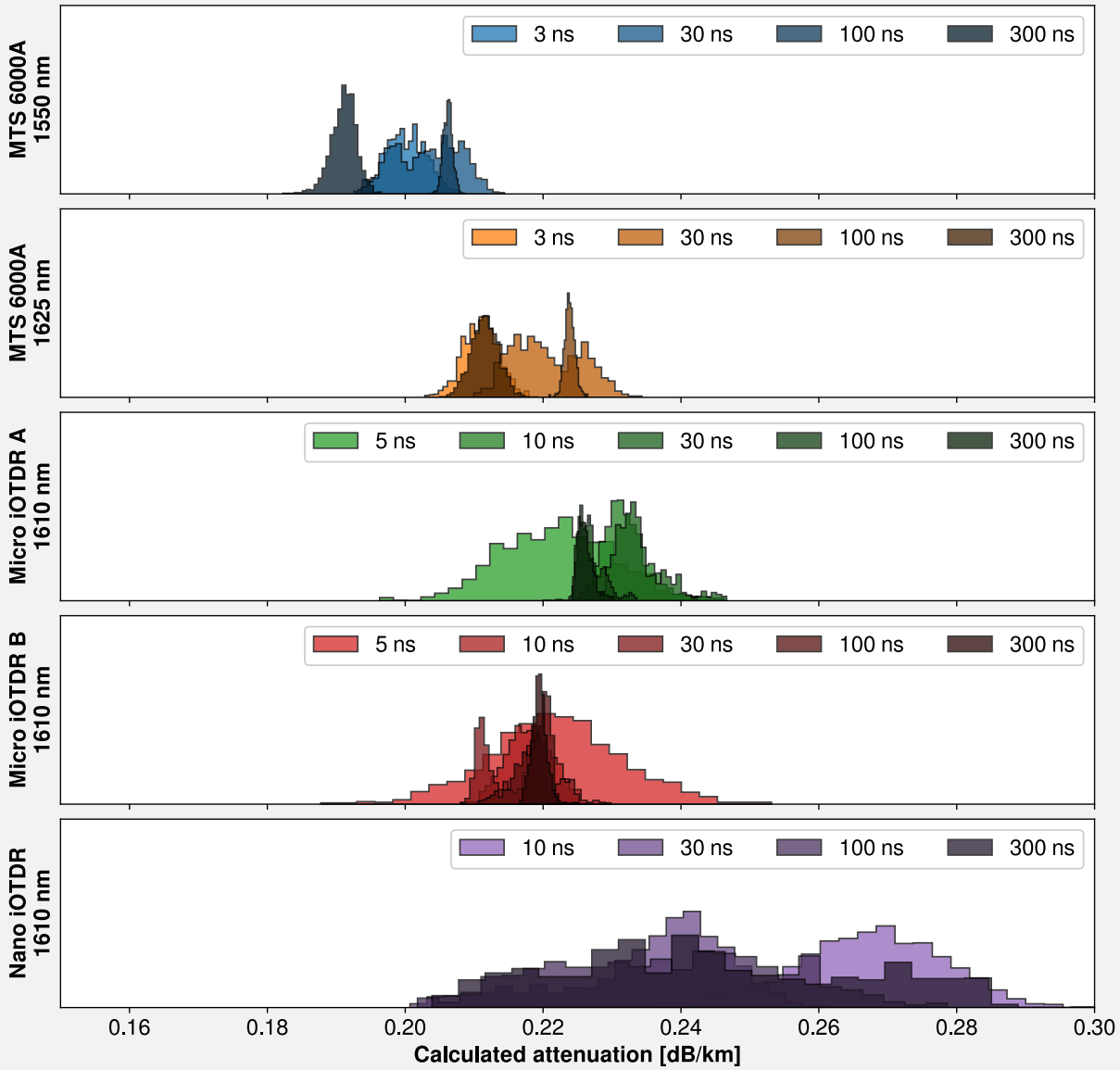

Figure 3.8. – Histograms of calculated attenuation values of the launch fiber segment over ~1200 measurements for all investigated devices and pulse widths, using a scan time of 10 s.

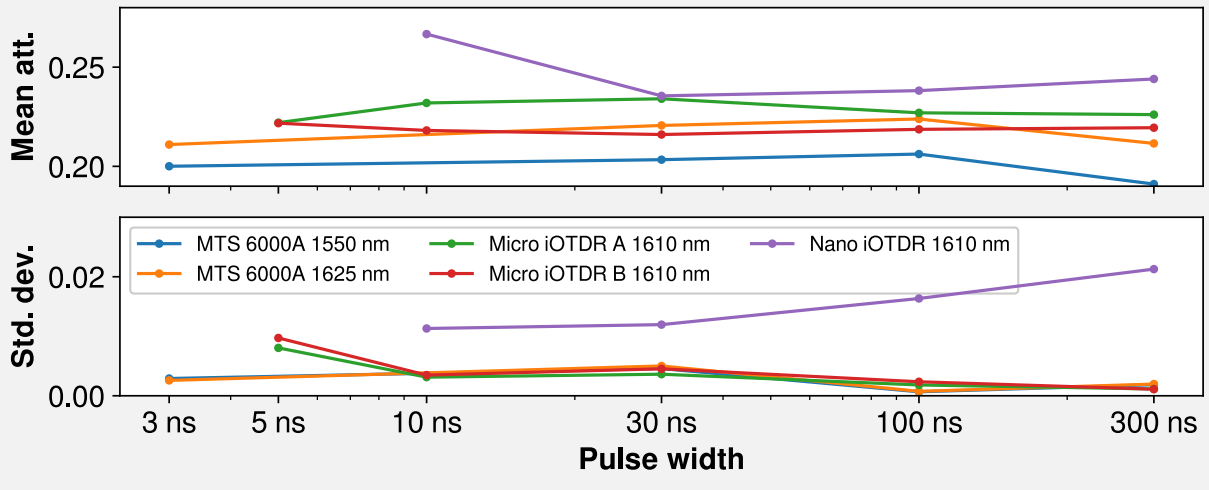

Figure 3.9. – Mean attenuation and standard deviation (in dB/km) of the launch fiber segment.

pulse widths.

These observations on the launch fiber segment are however mitigated by the data taken on the attenuating fiber segment, which are shown as histograms in **Figure 3.10** and as graphs of mean attenuation and standard deviation in **Figure 3.11**.

The evolution of mean measured attenuation as a function of the pulse width follows, on this segment, a more consistent behavior across devices, with a shift towards larger attenuation values as the pulse width increases. For pulse widths of 30 ns and 100 ns, all devices are in good accordance with a mean attenuation of ~64 dB/km. More deviation can be observed for other pulse widths, mainly because of value spreading.

The repeatability of this attenuating fiber measurement is also highly dependent on the pulse width, with a decreased spread of the values as the pulse width increases. Both Micro iOTDRs reach notably the lowest standard deviation observed in these data, even compared to the MTS 6000A device, for pulse widths of 30 ns and 100 ns. However, the value spreading of all three iOTDR devices at their smallest pulse widths (5 ns for the Micro iOTDRs and 10 ns for the Nano iOTDR) is comparatively very large, especially compared to the MTS 6000A device. This difference can be explained by a comparatively higher noise level on these embedded devices, therefore decreasing the SNR and increasing the uncertainty, especially given the low signal levels to be measured in such highly attenuating samples.

The Nano iOTDR device, in particular, systematically yields a lower repeatability than both Micro iOTDR devices for equivalent pulse widths. This high spread in values can stem from several origins, including an overall higher noise level in this device, but also a possible dependence on the temperature, given the ~8 °C span encountered in this experiment. An evaluation of the temperature dependence of these devices, explored in **Section 3.1.6**, is therefore necessary to complement these observations.

A summary of this statistical analysis is presented in **Table 3.1**, with the values of the mean attenuation measured by each device on each segment, accompanied by their relative uncertainties at a 95 % confidence interval. These data also exhibit a significant difference between uncertainties estimated on the launch and attenuating fiber segments, the former always yielding larger or equal uncertainties to the latter.

In the case of measurement on high-attenuating fibers, and when using the maximum available length, these data indicate an uncertainty on the attenuation measurement on the order of ±6 % for Micro iOTDRs operating at a pulse width of 5 ns, and ±5 % for the Nano iOTDR operating at a larger pulse width of 10 ns.

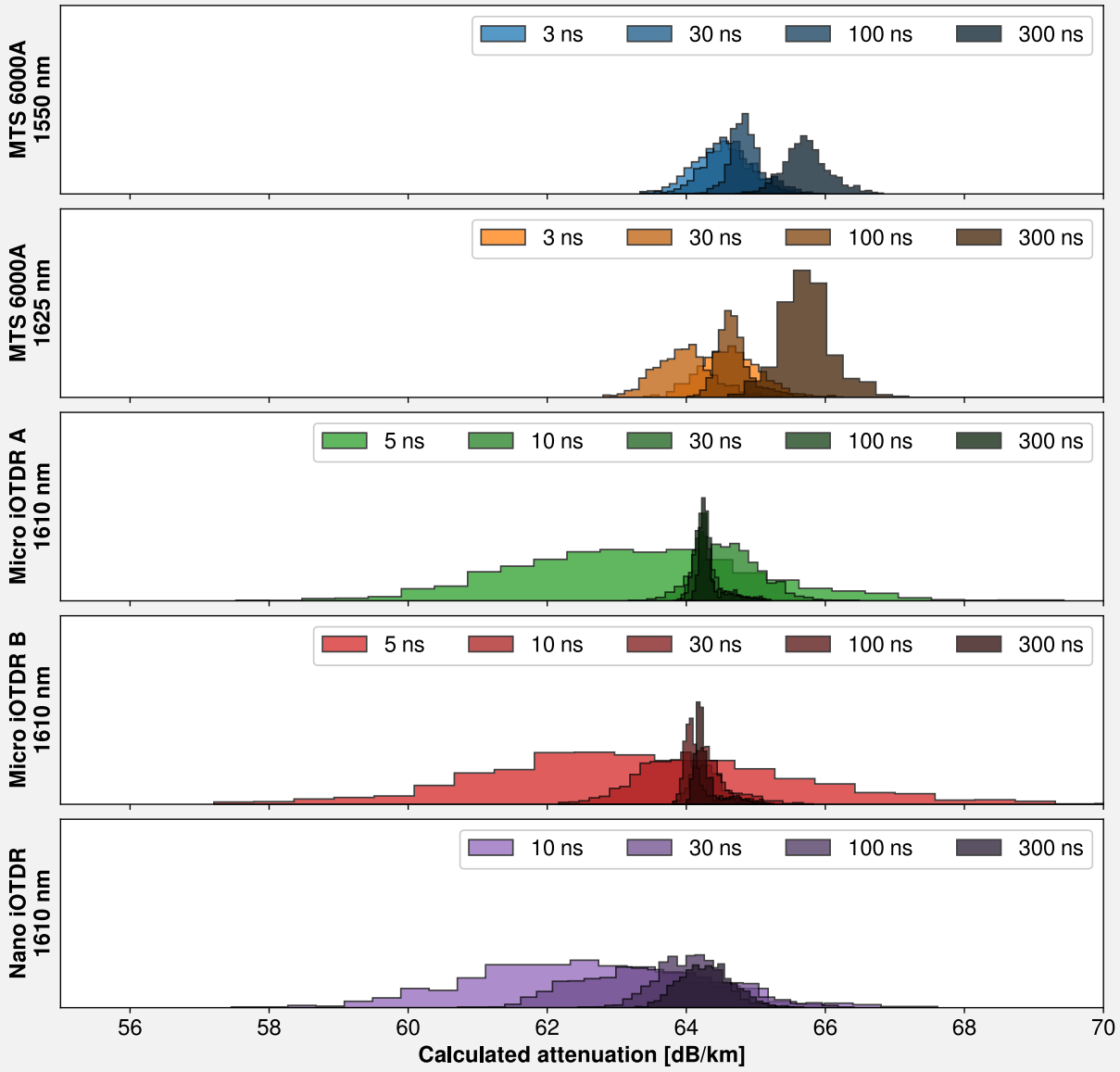

Figure 3.10. – Histograms of calculated attenuation values of the attenuating fiber segment over ~1200 measurements for all investigated devices and pulse widths, using a scan time of 10 s.

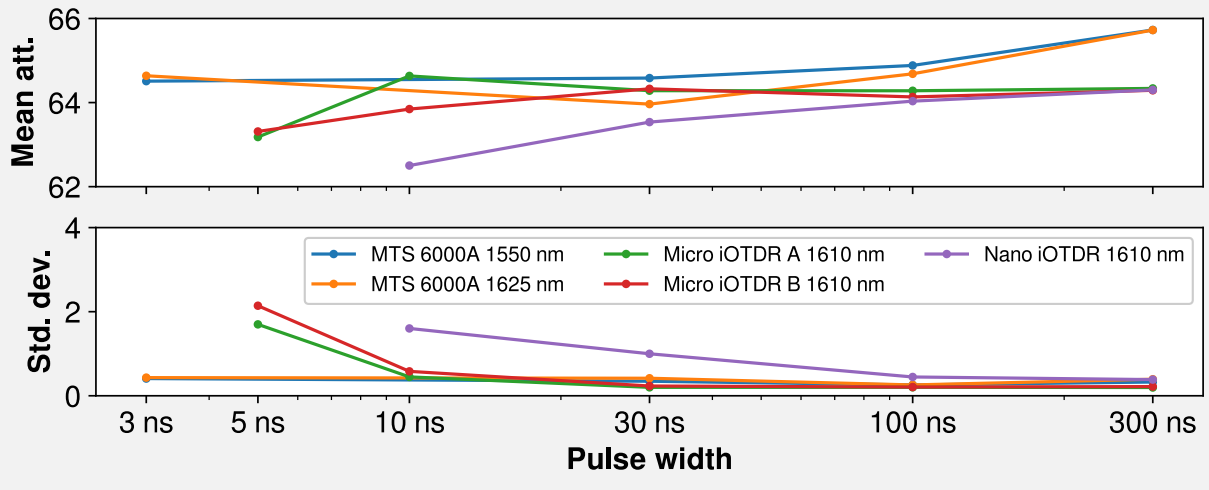

Figure 3.11. – Mean attenuation and std. deviation (in dB/km) of the attenuating fiber segment.

Device	Wavelength	Pulse	Launch fiber	Attenuating fiber
MTS 6000A	1550 nm	3 ns	0.200 dB/km ± 2.8 %	64.51 dB/km ± 1.2 %
		30 ns	0.203 dB/km ± 4.4 %	64.58 dB/km ± 1.0 %
		100 ns	0.206 dB/km ± 0.6 %	64.88 dB/km ± 0.8 %
		300 ns	0.191 dB/km ± 1.9 %	65.73 dB/km ± 1.0 %
	1625 nm	3 ns	0.211 dB/km ± 2.4 %	64.64 dB/km ± 1.3 %
		30 ns	0.221 dB/km ± 4.5 %	63.96 dB/km ± 1.3 %
		100 ns	0.224 dB/km ± 0.7 %	64.68 dB/km ± 0.8 %
		300 ns	0.212 dB/km ± 1.8 %	65.72 dB/km ± 1.2 %
Micro iOTDR A	1610 nm	5 ns	0.222 dB/km ± 7.1 %	63.18 dB/km ± 5.3 %
		10 ns	0.232 dB/km ± 2.6 %	64.63 dB/km ± 1.4 %
		30 ns	0.234 dB/km ± 3.0 %	64.28 dB/km ± 0.6 %
		100 ns	0.227 dB/km ± 1.6 %	64.28 dB/km ± 0.6 %
		300 ns	0.226 dB/km ± 1.0 %	64.34 dB/km ± 0.6 %
Micro iOTDR B	1610 nm	5 ns	0.222 dB/km ± 8.6 %	63.31 dB/km ± 6.6 %
		10 ns	0.218 dB/km ± 3.1 %	63.85 dB/km ± 1.8 %
		30 ns	0.216 dB/km ± 4.1 %	64.33 dB/km ± 0.7 %
		100 ns	0.219 dB/km ± 2.1 %	64.13 dB/km ± 0.6 %
		300 ns	0.219 dB/km ± 1.0 %	64.29 dB/km ± 0.7 %
Nano iOTDR	1610 nm	10 ns	0.267 dB/km ± 8.3 %	62.50 dB/km ± 5.0 %
		30 ns	0.236 dB/km ± 10.0 %	63.54 dB/km ± 3.1 %
		100 ns	0.238 dB/km ± 13.5 %	64.03 dB/km ± 1.4 %
		300 ns	0.244 dB/km ± 17.1 %	64.30 dB/km ± 1.2 %

Table 3.1. – Mean measured attenuations and their relative uncertainty at a confidence interval of 95 % for all investigated OTDR devices at different pulse widths and a scan time of 10 s.

Length	**MTS 6000A** 1550 nm 3 ns (0.3 m)	**MTS 6000A** 1625 nm 3 ns (0.3 m)	**Micro iOTDR A** 1610 nm 5 ns (0.5 m)	**Micro iOTDR B** 1610 nm 5 ns (0.5 m)	**Nano iOTDR** 1610 nm 10 ns (1.0 m)
1 m	111.4 %	56.5 %	133.4 %	286.5 %	450.1 %
2 m	36.6 %	38.2 %	82.5 %	241.7 %	157.8 %
5 m	14.3 %	14.2 %	43.5 %	78.9 %	57.5 %
10 m	6.5 %	8.3 %	21.7 %	29.2 %	42.2 %
20 m	2.6 %	2.8 %	10.5 %	12.8 %	16.5 %
50 m	1.2 %	1.4 %	5.3 %	6.6 %	5.4 %
100 m	1.2 %	1.3 %	5.3 %	6.6 %	5.0 %

Table 3.2. – Relative uncertainty at a confidence interval of 95 % of the attenuation measured by all investigated OTDR devices on segments of different lengths of the attenuating fiber. All measurements are performed with a scan time of 10 s, and the minimum pulse width (and associated spatial resolution) available to the device, indicated in the column header.

3.1.5. Influence of the sampling length

In distributed dosimetry systems, the spatial resolution of the measurement is determined by the sampling length of the fiber segment from which the attenuation is to be extracted, ranging from the minimum resolution allowed by the OTDR pulse width to the maximum length of the measurement line. Although using very short sampling lengths increases the spatial resolution, this improvement is counterbalanced by a significant decrease of the available measurement points on which to evaluate the attenuation, which could theoretically result in an increase of measurement uncertainty.

A comparison for all devices of the measurement uncertainties at a confidence level of 95 % with increasing sampling lengths on the attenuating fiber is shown in **Table 3.2**. Each device was considered with its minimum pulse width (indicated in the table) and a scan time of 10 s, and the whole available data (~1200 measurements) were considered in each case to extract these statistics.

These data highlight the major influence of sampling length on the measurement repeatability, ranging from extremely large uncertainties observed for the shortest sampling lengths up to the percent-scale uncertainties observed in **Table 3.1** for the maximum available length. For very short lengths ($\leq$ 5 m), the very high uncertainties can be linked to the short-scale signal fluctuations observed on OTDR traces (cf. **Figure 3.3**), which, in extreme cases, even leads in the linear fit algorithm yielding a slope of the wrong sign. For larger values, the decrease in uncertainty with the sampling length ℓ roughly follows a $1/\ell$ trend, until reaching the minimum value around 50 m. The apparent lack of effect of increasing sampling length from 50 m to 100 m is explained by the application of the thresholding algorithm described in **Section 3.1.3** for calculating these data, as the cutoff threshold of ~ -6 dB in these sets of parameters is already reached after the first 50 m of the irradiated sample.

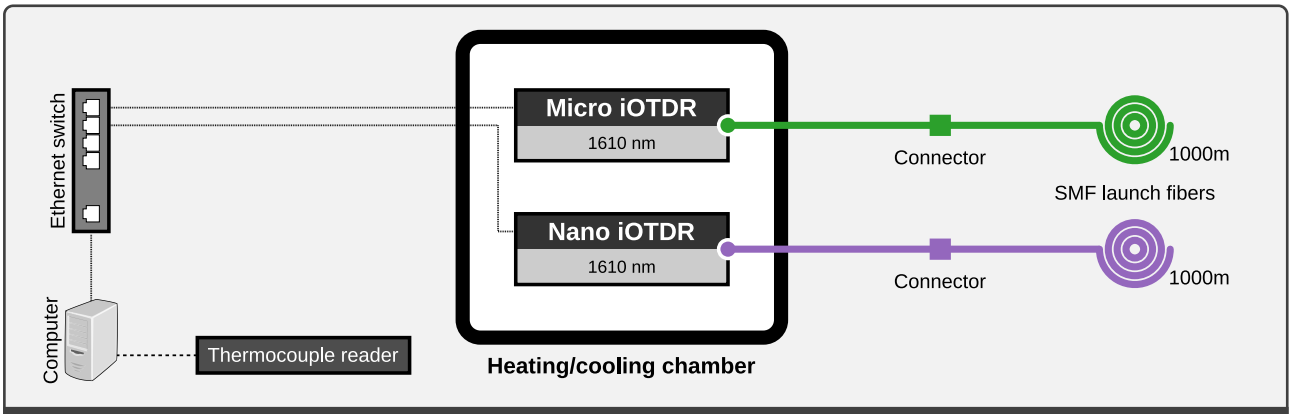

Figure 3.12. – Experimental setup for the characterization of temperature dependence of Micro and Nano iOTDR devices.

3.1.6. Temperature dependence

To assess the sensitivity of both Micro and Nano iOTDR devices to ambient temperature, we performed a series of measurements in a temperature-controlled environment as illustrated in **Figure 3.12**. Both iOTDR devices were placed in a heating and cooling chamber (BINDER MK 115), and connected to 1 km-long samples of telecom-grade launch fibers. The devices were controlled by a setup similar to the one described in **Section 3.1.1** to automatically acquire OTDR data and record temperature. The pulse width was set to the minimum available value (5 ns for Micro iOTDR, 10 ns for Nano iOTDR), and the scan time set to 10 s.

The temperature of the heating/cooling chamber was controlled between $-5\,^{\circ}\mathrm{C}$ and $40\,^{\circ}\mathrm{C}$. As illustrated in **Figure 3.13**, this temperature was adjusted by increments of $\pm 5\,^{\circ}\mathrm{C}$, and maintained constant in plateaux of 2 h each, between which a slow ramp of 1 h ensured a smooth transition from one temperature setpoint to the other. The surface temperatures of the iOTDR devices, measured by additional thermocouples, are also shown in comparison to the setpoint, and stand systematically higher (~3.5 °C for the Micro iOTDR, ~4.5 °C for the Nano iOTDR) because of the heat generated by these devices during their operation.

The Nano iOTDR device noticeably failed after ~100 h of functioning, which results in slightly less data collected for this device, although it does not impact the final results significantly, as all temperature plateaux are properly explored. This device resumed normal operation after a power cycling, indicating that it did not suffer from permanent damage.

Analysis of the attenuation measured by these devices was performed by manually identifying the start and end of the launch fiber on the OTDR traces, and applying a linear fit on this portion of the acquired data. An overview of the resulting measurements, as a function of the device temperature, is shown in **Figure 3.14**. From this qualitative overview, it clearly appears that the Nano iOTDR measurements are significantly influenced by the device temperature, whereas measurements performed by the Micro iOTDR appear to be more stable over the range of investigated temperatures.

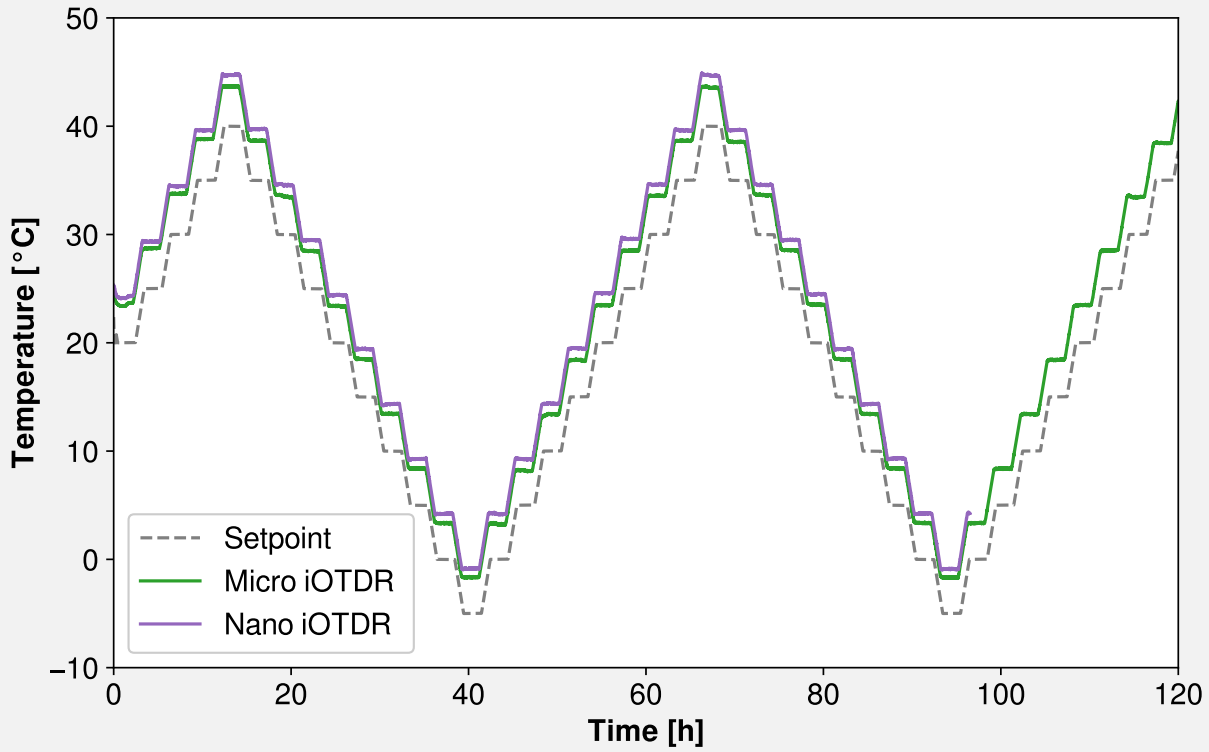

Figure 3.13. – Evolution of the heating/cooling chamber temperature setpoint (in dashed line), along with the temperature measured by thermocouples on the surface of the iOTDR devices (in solid lines), for the duration of the experiment.

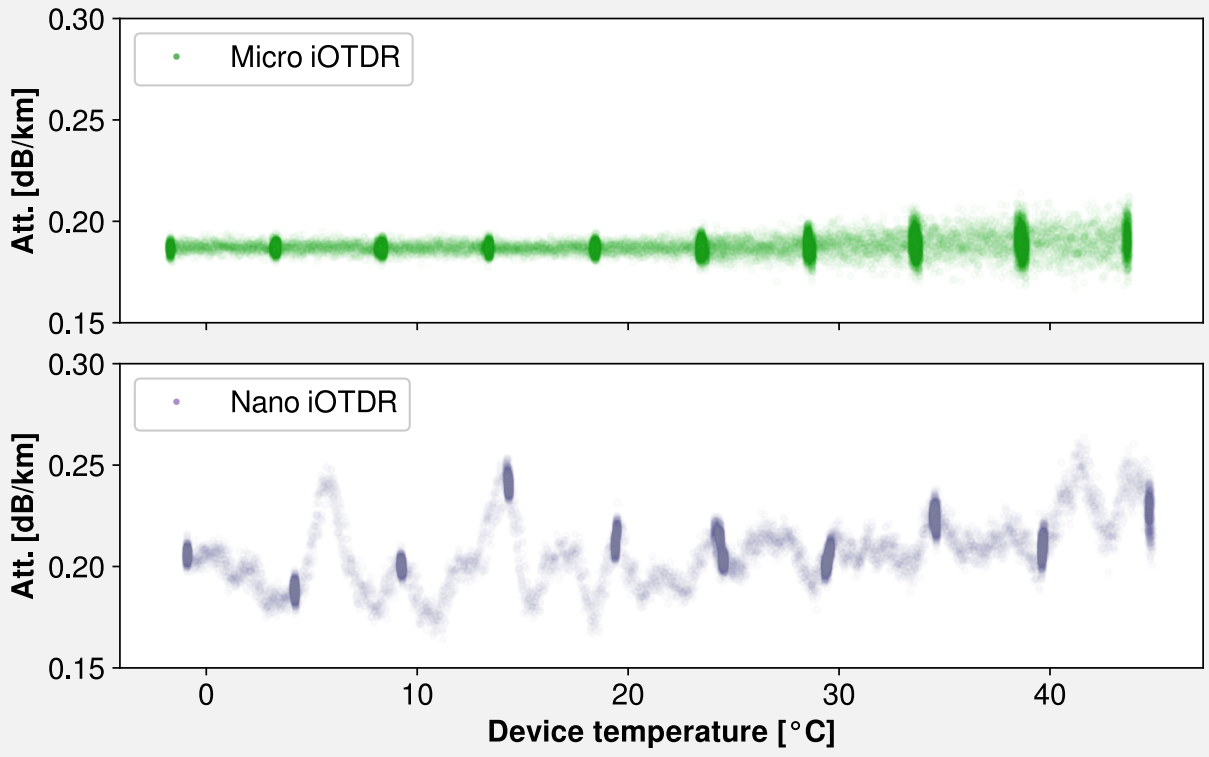

Figure 3.14. – Measured attenuation as a function of device temperature, for all acquired data on Micro and Nano iOTDR devices.

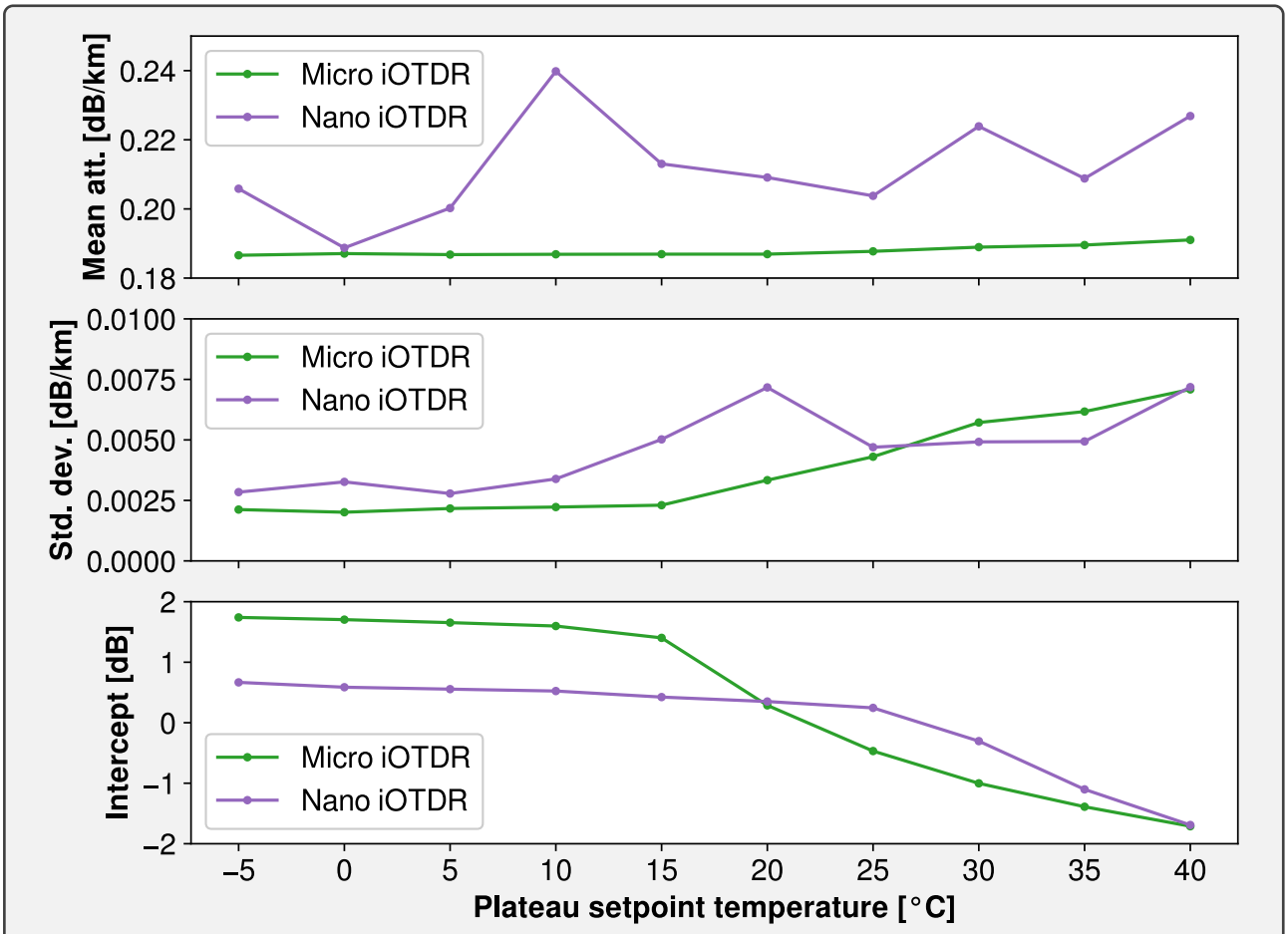

Figure 3.15. – Statistics of linear fit parameter estimation for all measurements taken at a given temperature plateau: top graph shows the mean attenuation, middle graph shows the standard deviation of measured attenuation, and bottom graph shows the mean intercept of the linear fit.

A more quantitative approach is proposed in **Figure 3.15**, in which three relevant statistics are computed for each device from the data corresponding to each temperature plateau (~300 data points per plateau). The evolution of the mean measured attenuation shows a very slight increase of this value with increasing temperature for the Micro iOTDR, whereas no simple description could be made of the large variations of the Nano iOTDR measurements with temperature, although this behavior appears to be very reproducible through multiple cycles, as illustrated in **Figure 3.14**.

A possible explanation to these results are the intrinsic temperature dependence of both receiver and emitter of OTDR devices. In the case of the receiver, sources of temperature dependence can originate from photodiode dark current [589] or, for avalanche photodiodes, noise [590] or breakdown voltage [591]. In the case of the emitter, the wavelength of laser diodes is also temperature-dependent [592], and their temperature are affected Joule heating when driving the laser, making it also dependant on the operating pulse width. Therefore, the complex temperature response exhibited by the Nano iOTDR could be linked to an incomplete compensation of these phenomena.

For the whole investigated temperature range of $-5\,°C$ to $40\,°C$, this statistical analysis indicates

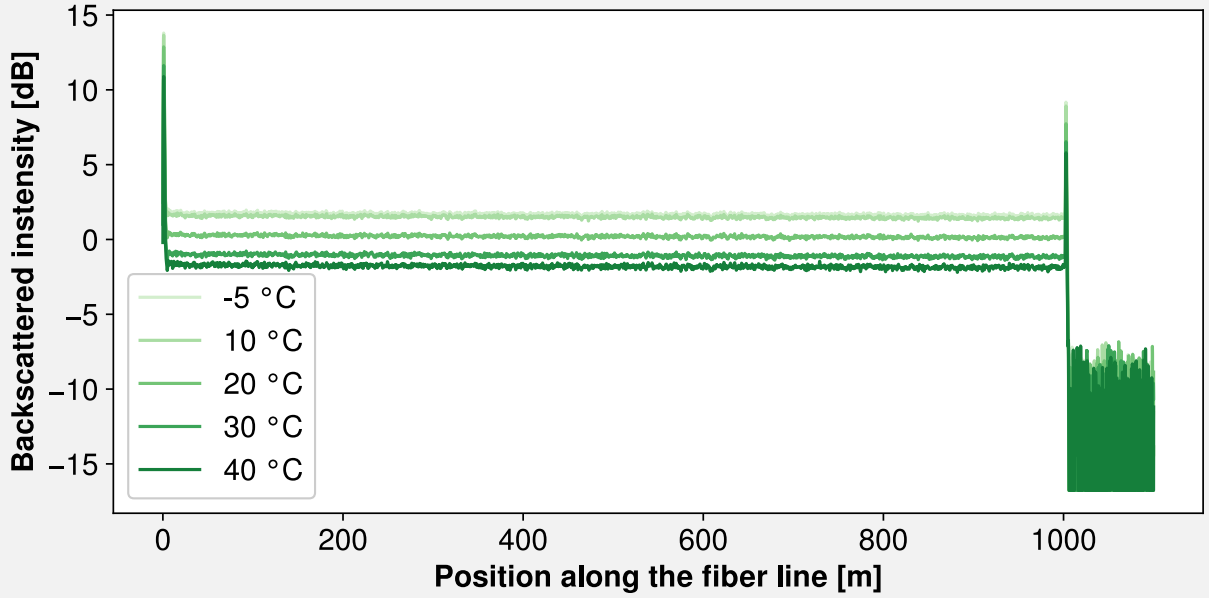

Figure 3.16. – Samples of complete Micro iOTDR traces represented at different plateau setpoint temperatures (indicated in legend). A vertical shift can be observed between traces acquired at different temperatures.

a relative deviation of the mean measured attenuation of ±1.2 % around 0.188 dB/km for the Micro iOTDR device, and ±12 % around 0.212 dB/km for the Nano iOTDR device, although the non-monotonic nature of the Nano iOTDR temperature dependence can result in very large deviations from small temperature changes; for instance, the whole scale of ±12 % is explored between 10 °C and 15 °C as shown in **Figure 3.14**.

The standard deviation of the attenuation measurement is, in both cases, generally increasing with temperature, which is in good accordance with the occurrence of thermal noise in electronics [593]. The Nano iOTDR device also features an uncommon behavior on this topic, as the uncertainty at 20 °C appears to be, only on this device, higher than the one observed at other temperatures.

Finally, another parameter worth of interest is the intercept of the linear fit algorithm, which indicates the attenuation value given at the position 0 m by the linear model. The evolution of this parameter is noticeably correlated with temperature, and decreases with increasing temperature for both devices. This behavior can be linked to an observed variation in the backscattered intensity at the start of the launch fiber segment, which is illustrated in **Figure 3.16**. This vertical shift cannot be explained by the effect of temperature on the optical fiber connectors between the iOTDR devices and the sample fibers, as these connectors were installed outside of the chamber in this experiment.

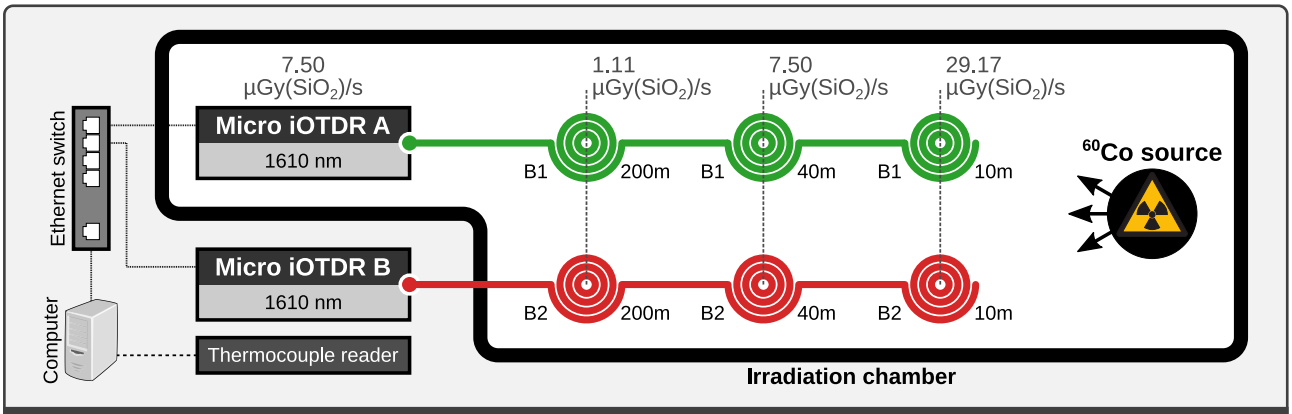

Figure 3.17. – Experimental setup of the γ ray irradiation of Micro iOTDR devices. The dose rate of irradiated elements is indicated in gray above each position.

3.2. Radiation testing of the Micro iOTDR system

To assert the functionality of the Micro iOTDR device to operate as a distributed dosimetry system for space radiation measurements, a series of radiation tests was performed with this type of device and radiosensitive fiber samples of type **B**.

This characterization was staged in two parts, involving different radiation facilities: the first part involved γ ray irradiation, with a range of low doses and dose rates that approaches the requirements for the space environment; the second part involved an X-ray irradiation under higher dose rates, in order to extend the range of investigated doses and dose rates.

The results presented in this section were the object of a conference presentation [594] and the publication **Article A.2** [595]; most figures presented hereafter are therefore adapted from these works.

3.2.1. Experimental setup of γ ray irradiation

Two distributed dosimetry systems, based on Micro iOTDR devices and radiosensitive fibers of type **B**, (cf. **Section 2.1**) were tested in the γ ray irradiator at the PRESERVE facility (cf. **Section 2.3.2**).

The setup of these measurements is illustrated in **Figure 3.17**. Each Micro iOTDR device was connected to a series of optical fiber samples of varying lengths placed at different dose rates, spliced together to form a measurement line.Three different dose rates were investigated: 1.11 $\mu Gy(SiO_2)/s$, 7.50 $\mu Gy(SiO_2)/s$ and 29.17 $\mu Gy(SiO_2)/s$, as determined by the local dosimetry system before irradiation of the samples. These different dose rates were obtained by placing the samples at different distances from the source, as illustrated in **Figure 3.18**. The length of the optical fiber samples was selected for each dose rate to deliver a total attenuation on the order of 3 dB after one month of irradiation, as per the sensitivity figure of 4 $dB\,km^{-1}\,Gy(SiO_2)^{-1}$ previously reported for such phosphorus-doped fibers [395].

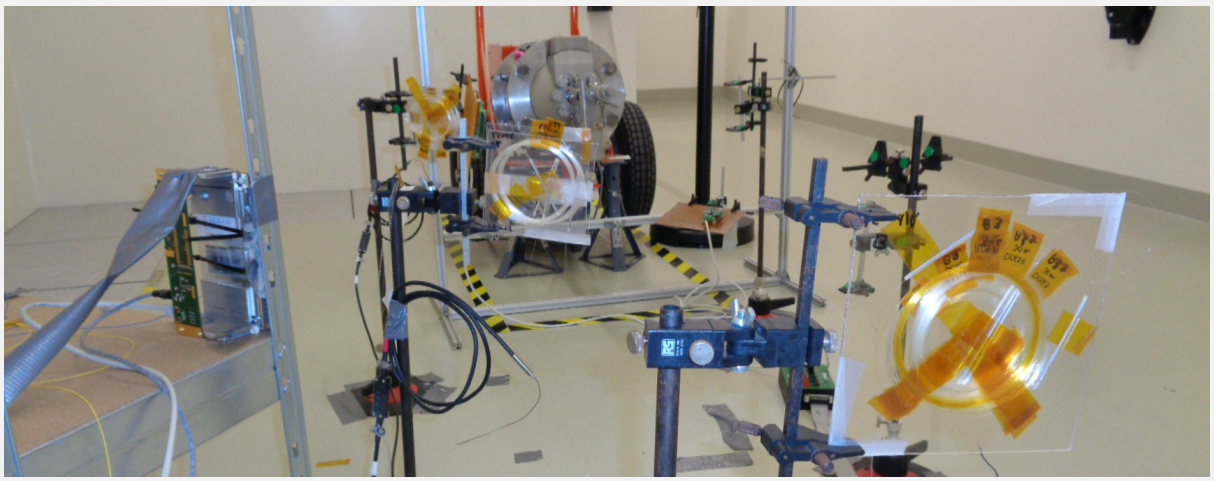

Figure 3.18. – Photograph of the Micro iOTDR γ ray irradiation setup. The irradiated Micro iOTDR device is on the left, and several optical fiber samples installed on transparent vertical supports can be seen at different distances from the source in the middle.

Although very similar, the two tested measurement lines feature two important differences. First, one of the OTDR devices (Micro iOTDR A) was also put inside the irradiation chamber during the whole duration of the experiment, at a dose rate of $7.50\,\mu Gy(SiO_2)/s$, in order to assess the ability of Micro iOTDR devices to sustain TID levels matching requirements of space missions. Second, in order to evaluate the batch-to-batch variability of optical fiber samples, each measurement line featured one of two types of fibers **B1** and **B2**, each drawn from a different preform manufactured under the general specifications of fiber **B**.

The OTDR devices were configured with a pulse width of 5 ns and a scan time of 180 s in order to maximize the SNR at low signal levels. They were interrogated in sequence through Ethernet by an automatic acquisition script running on an embedded computer (Raspberry Pi 4 model B). In addition, K-type thermocouples were installed at the location of each sample to monitor their temperature, acquired through a thermocouple reader (Pico Technology TC-08) and automatically recorded on the embedded computer. The temperature thus recorded over the duration of the experiment ranged from 19 °C to 25 °C.

The complete measurement lines shown in **Figure 3.17** were irradiated for a duration of one month, then only the 200 m samples were kept, along with the Micro iOTDR devices, for an additional duration of three months. This setup therefore underwent a grand total of 138 days of irradiation.

3.2.2. Results of γ ray irradiation

An overview of the evolution of the OTDR traces of the Micro iOTDR A measurement line during the first month of irradiation is shown in **Figure 3.19**. The overall increase of the slope with accumulated time, and therefore dose, can be observed for the three segments corresponding to the three irradiated

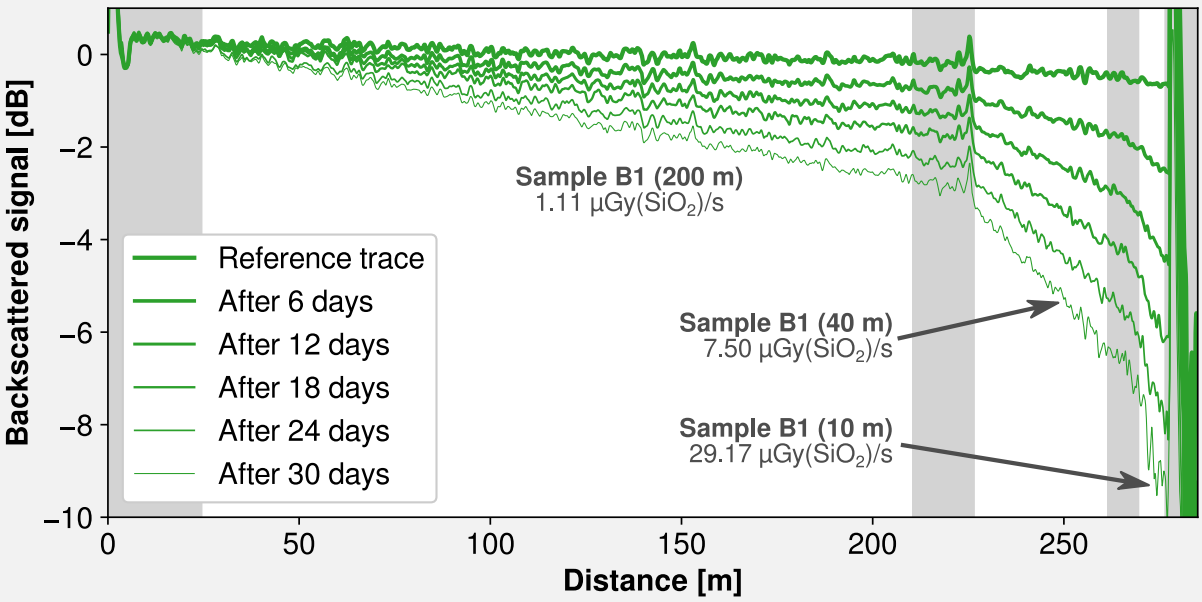

Figure 3.19. – Evolution of the OTDR traces acquired by Micro iOTDR A during the first month of irradiation. The segments considered for RIA calculation are shown in a white background.

samples. The different rates of increase can be linked to the dose rate received by each sample, a higher dose rate leading to a steeper increase of the slope with time.

The evolution of attenuation over time was then extracted from these OTDR traces by applying a linear fit and retrieving the parameter corresponding to the slope. The dose values were deduced from the irradiation time and the dose rate applied to each segment. Because of the long duration of this experiment, two additional parameters were taken into account for the dose calculation: first, all irradiation shutdown periods were logged and deduced from the effective irradiation time; second, the decay characteristic of ^{60}Co, and therefore of the effective dose rate, was also considered using a half-life of (1925.20 ± 0.25) d as reported by NIST [596].

The RIA graphs resulting of this analysis are shown in **Figure 3.20** for the Micro iOTDR A line during the first month of acquisition. The visible gap in data on the left-hand side of each graph is due to a splice breakage that was repaired a few days after its occurrence. Each of these data set was fit with an homogeneous linear function ($f(x) = ax$) to evaluate the linearity of the corresponding measurements as well as to determine their sensitivity. Comparison with these linear fits show a very good linearity of all measurements, as well as similar calculated sensitivity coefficients between $4.20\,\mathrm{dB\,km^{-1}\,Gy(SiO_2)^{-1}}$ and $4.53\,\mathrm{dB\,km^{-1}\,Gy(SiO_2)^{-1}}$.

A visible difference between these different graphs is the measurement noise, which is significantly larger for the data set corresponding to the $29.17\,\mu\mathrm{Gy(SiO_2)/s}$ segment. This behavior is explained by multiple parameters, such as the comparatively short length of this sample, as well as the very low signal level obtained as the combined result of its higher dose rate and the cumulative decrease of signal caused by samples located upstream on the measurement line.

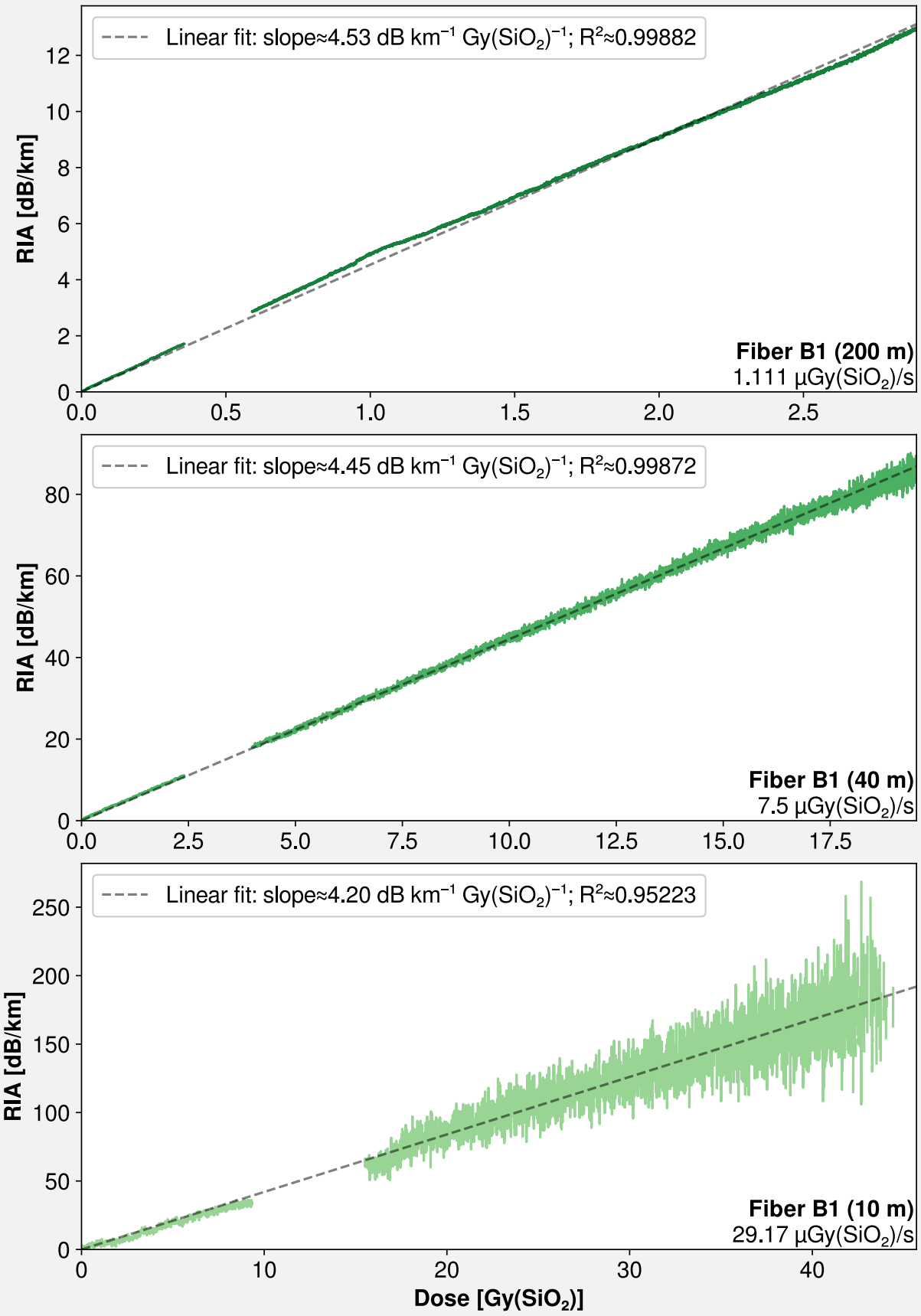

Figure 3.20. – RIA at 1610 nm as a function of dose for each segment on the measurement line connected to Micro iOTDR A, during the first month of irradiation. Linear fit of each of these data sets is shown in dashed line.

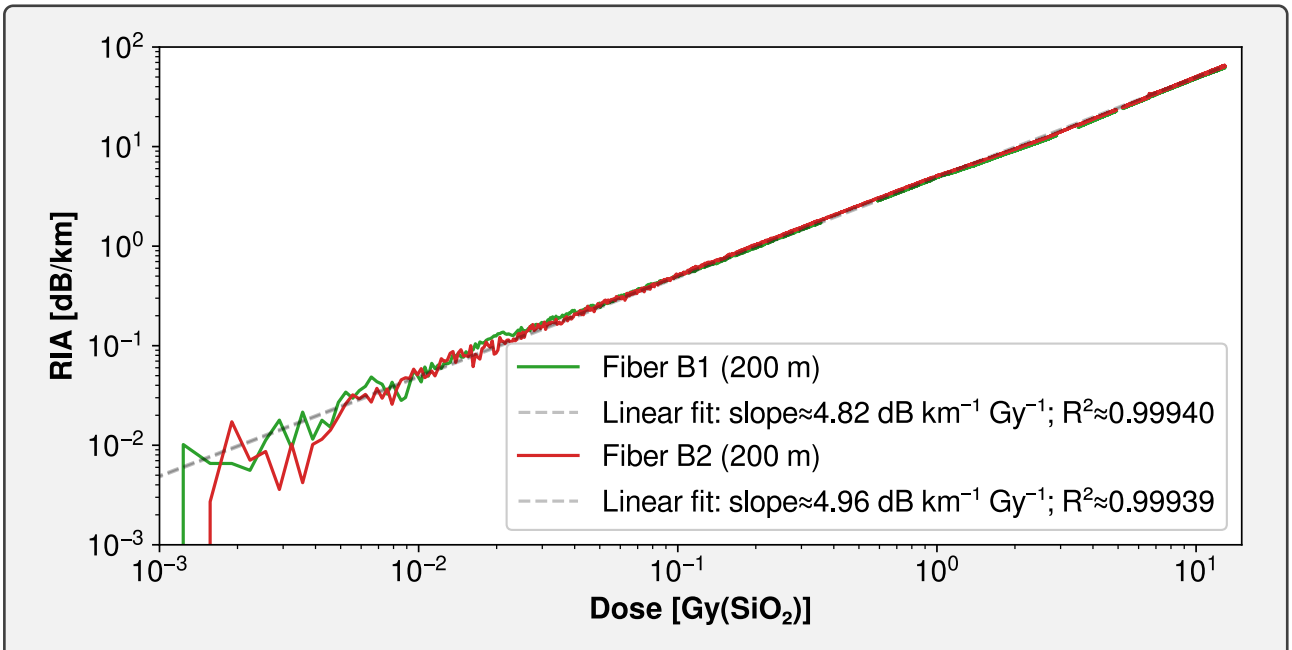

Figure 3.21. – Log-log plot of the evolution of RIA at 1610 nm of 200 m-long samples of fibers **B1** and **B2** irradiated under γ rays at 1.11 µGy(SiO$_2$)/s, during the complete irradiation period. Dashed lines show the linear fits applied to each data set.

Comparison between both 200 m-long samples of fibers **B1** and **B2**, for the complete duration of irradiation, is shown in **Figure 3.21**. These data highlight a very good accordance between the results acquired by both measurement lines, by two different devices and two different optical fiber samples. Both measurements show very good linearity up to the maximum reached dose of 12.97 Gy(SiO$_2$), and yield very close sensitivity characteristics, using an homogeneous linear fit as described here above, with 4.82 dB km^{-1} Gy(SiO$_2$)$^{-1}$ for line A (noticeably larger than in **Figure 3.20**, which is calculated up to a lower dose) and 4.96 dB km^{-1} Gy(SiO$_2$)$^{-1}$ for line B. Considering the measurement uncertainty of ±6 % reported in **Section 3.1.4**, both these values stand in very good accordance.

Finally, these log-log data also hint at a minimum detectable dose of ~10^{-3} Gy(SiO$_2$).

3.2.3. Reliability of the Micro iOTDR devices

Both Micro iOTDR devices were continuously operated during the complete duration of the γ ray irradiation. No noticeable difference was observed between the performances of Micro iOTDR devices A and B, neither in the quality of delivered measurement, nor in their ability to communicate with the acquisition computer.

The Micro iOTDR A device, in particular, operated without failure during the 138 days of the experiment, while being irradiated at a dose rate of 7.50 µGy(SiO$_2$)/s up to a total dose of 81.05 Gy(SiO$_2$). The Micro iOTDR B device only suffered a single software freeze in the same period of time, which was resolved by a power cycling.

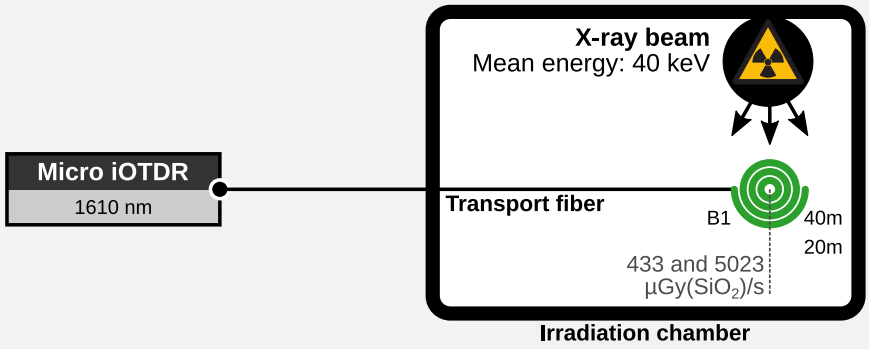

Figure 3.22. – Experimental setup of X-ray irradiation of **B1** fiber samples interrogated by a Micro iOTDR device.

3.2.4. Comparison with X-ray irradiation

In order to further assess the performance of these dosimetry systems, additional data were collected on samples of fiber **B1** irradiated under X-rays in the MOPERIX irradiator (cf. **Section 2.3.1**), over a larger range of doses and dose rates. The X-ray source was driven with an anode voltage of 100 kV, corresponding to a mean energy-fluence of ~40 keV, and the anode current was adjusted to reach the desired dose rates. The temperature range for these experiments was between 20 °C and 22 °C.

Two measurements were performed in this setup, as illustrated in **Figure 3.22**: a first sample of 40 m was irradiated at 433 $\mu Gy(SiO_2)/s$, and a second sample of 20 m was irradiated at 5023 $\mu Gy(SiO_2)/s$. Each sample was spliced to a radiation-hard transport fiber, connecting it to the OTDR device placed outside the irradiation chamber.

In these X-ray runs, the iOTDR device was not irradiated, because of the low photon energy of this irradiation setup compared to the ^{60}Co γ source, which would not ensure enough penetration in the electronic devices to properly match the conditions of space radiation [506]. For the same reasons, both optical fiber samples were coiled in a flat spiral to avoid any possible screening effect from overlapping fiber segments.

The sensitivities measured in these two X-ray irradiations, determined by fitting an homogeneous linear function to data acquired up to 100 $Gy(SiO_2)$, were respectively 3.97 $dB\,km^{-1}\,Gy(SiO_2)^{-1}$ for dose rate 433 $\mu Gy(SiO_2)/s$ and 3.86 $dB\,km^{-1}\,Gy(SiO_2)^{-1}$ for dose rate 5023 $\mu Gy(SiO_2)/s$, as shown in **Figure 3.23**. Both these values are lower than sensitivities measured under γ rays; this can be explained by several factors, such as different total doses and differences in dosimetry between irradiation facilities.

A comparison of the resulting X-ray data with the γ ray results is shown in **Figure 3.24**. These data indicate a very good accordance between the two sets of experiments, in a range of five decades of dose, from $10^{-3}\,Gy(SiO_2)$ to $3 \times 10^{2}\,Gy(SiO_2)$, and three decades of dose rate, from $10^{-6}\,Gy(SiO_2)/s$ to $5 \times 10^{-3}\,Gy(SiO_2)/s$.

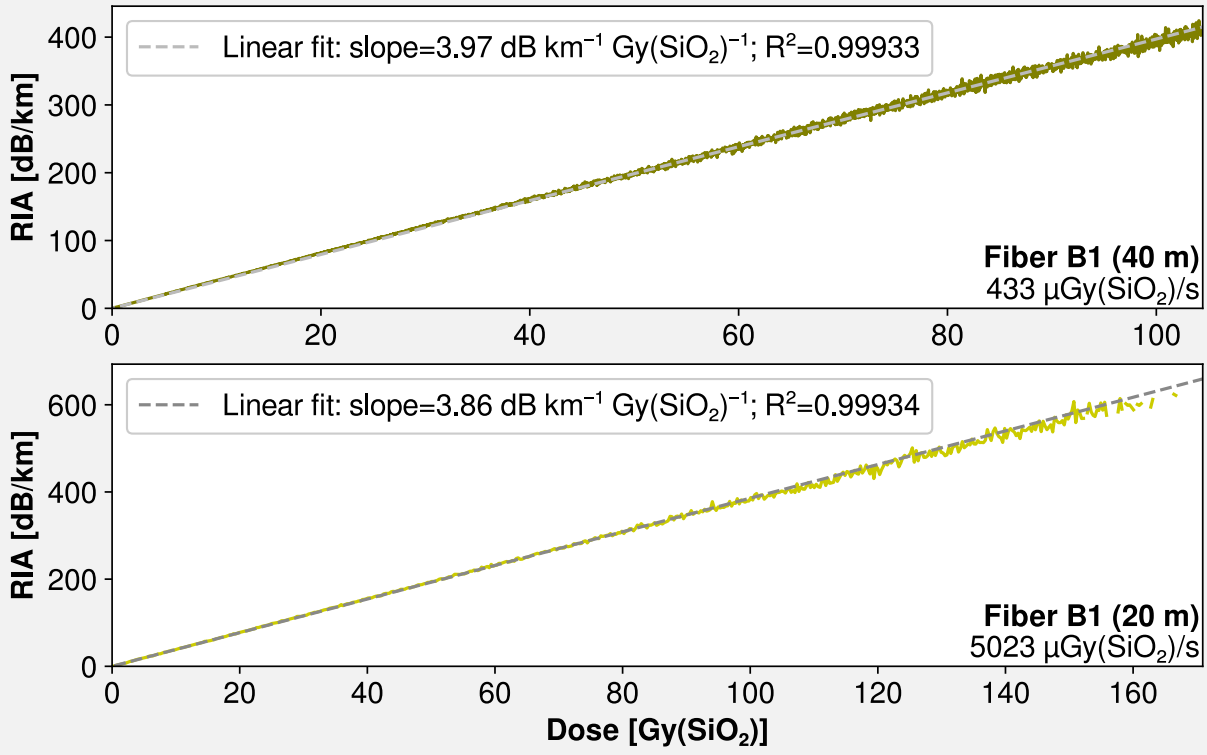

Figure 3.23. – RIA at 1610 nm measured by Micro iOTDR as a function of dose, for each sample irradiated in X-rays. Linear fit of each of these data is shown in dashed line.

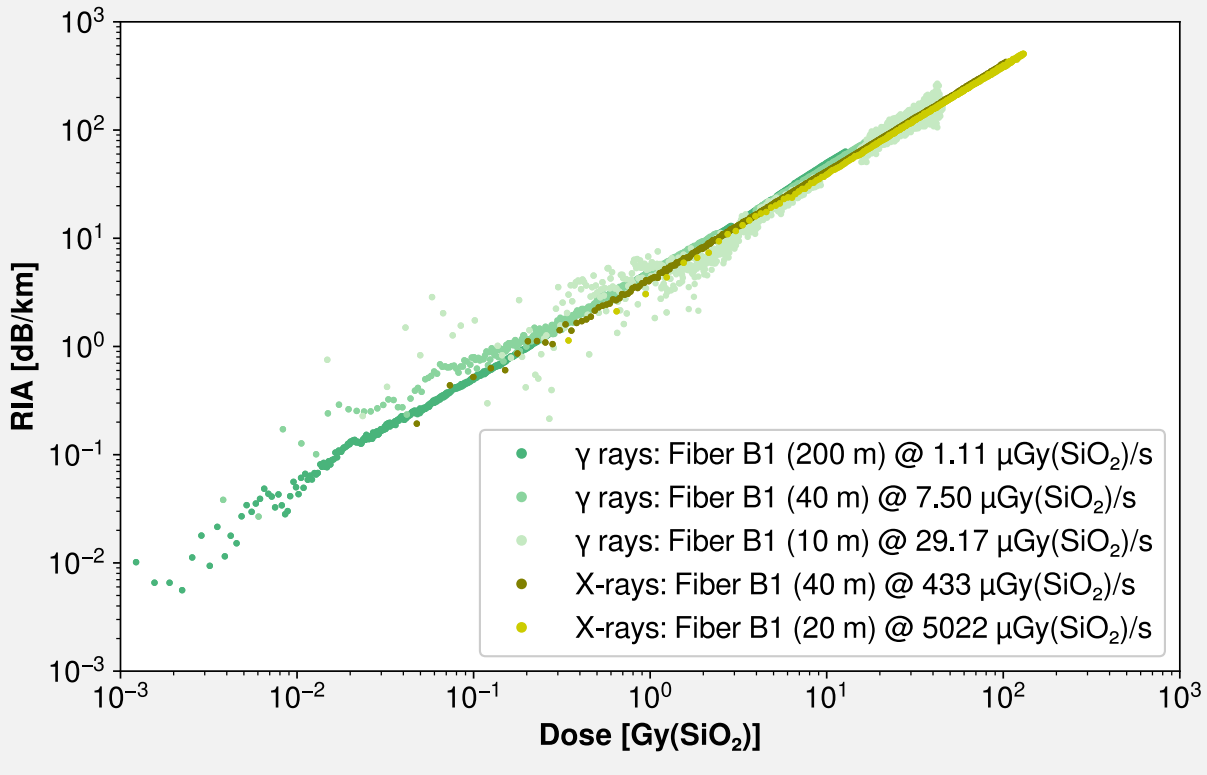

Figure 3.24. – Log-log plot of the evolution of RIA at 1610 nm of all **B1** samples under γ and X-rays. γ data are shown in a lighter color to ease comparison with X-ray data.

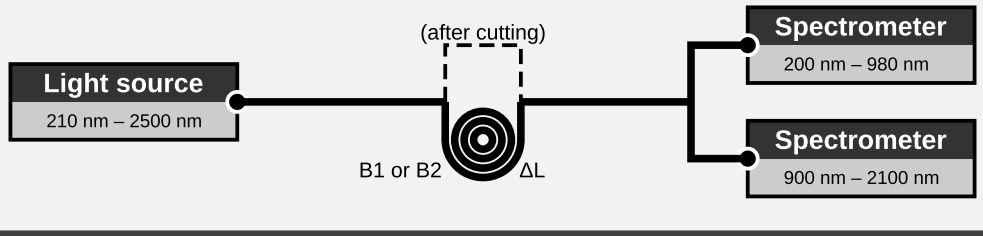

Figure 3.25. – Experimental setup of spectral RIA measurement with the cutback method.

3.2.5. Analysis of the spectral RIA characteristic

As the Micro iOTDR devices used in these experiments are only capable of a single interrogation wavelength of 1610 nm, a more complete analysis of the spectral RIA characteristic of the irradiated fiber samples was performed using a *cutback* method. This destructive characterization method consists in the analysis of the transmitted spectra before and after removal of a known length ΔL from the sample [597]. The intrinsic spectral attenuation $A(\lambda)$ of the sample can be deduced from these transmitted spectra, I_{long} and I_{short}, through the following formula:

$$A(\lambda) = -\frac{10}{\Delta L}\log_{10}\left(\frac{I_{\text{short}}(\lambda) - I_{\text{dark}}(\lambda)}{I_{\text{long}}(\lambda) - I_{\text{dark}}(\lambda)}\right) \tag{3.1}$$

with $I_{\text{dark}}(\lambda)$ the dark signal spectrum, measured with the light source switched off.

This method was applied to measure the spectral RIA of the 200 m samples irradiated under γ rays, using the setup shown in **Figure 3.25**. A halogen-deuterium light source (Ocean Optics DH-2000-BAL), emitting on a continuous spectrum from 210 nm to 2500 nm, was used to inject light in the samples, and the transmitted signal was analyzed using two spectrometers: one for the visible range (Ocean Optics QE65000) and one for the NIR range (Ocean Optics NIRQuest). These measurements were performed separately, with different removed lengths (~1 m for visible, ~200 m for NIR).

The resulting values were subtracted from the ones acquired on a pristine fiber (~1 dB/km at 1550 nm), yielding the spectral RIA graphs for a dose of 12.97 $\text{Gy}(\text{SiO}_2)$ shown in **Figure 3.26** for the visible domain and **Figure 3.27** for the NIR domain. These data show similar RIA values for both types of fiber, especially in the NIR range used for OTDR measurements; the sensitivities at a wavelength of 1610 nm are 4.72 $\text{dB km}^{-1}\,\text{Gy}(\text{SiO}_2)^{-1}$ for fiber **B1**, and 4.70 $\text{dB km}^{-1}\,\text{Gy}(\text{SiO}_2)^{-1}$ for fiber **B2**; both these values are in good agreement with the results reported in **Section 3.2.2**, considering the measurement uncertainties (cf. **Section 3.1.4**) and the difference between measuring setups.

These results are also in very good accordance with the literature on phosphorus-doped fibers (cf. **Section 1.2.4**), with a distinctive, broad absorption band in the NIR range due to P_1 defects and multiple, very intense bands in the visible range, mainly due to POHCs. The small peaks featured around 1100 nm are measurement artifacts due to the cutoff wavelengths of the fibers (cf. **Section 1.2.1**), which are typically featured in cutback results [333].

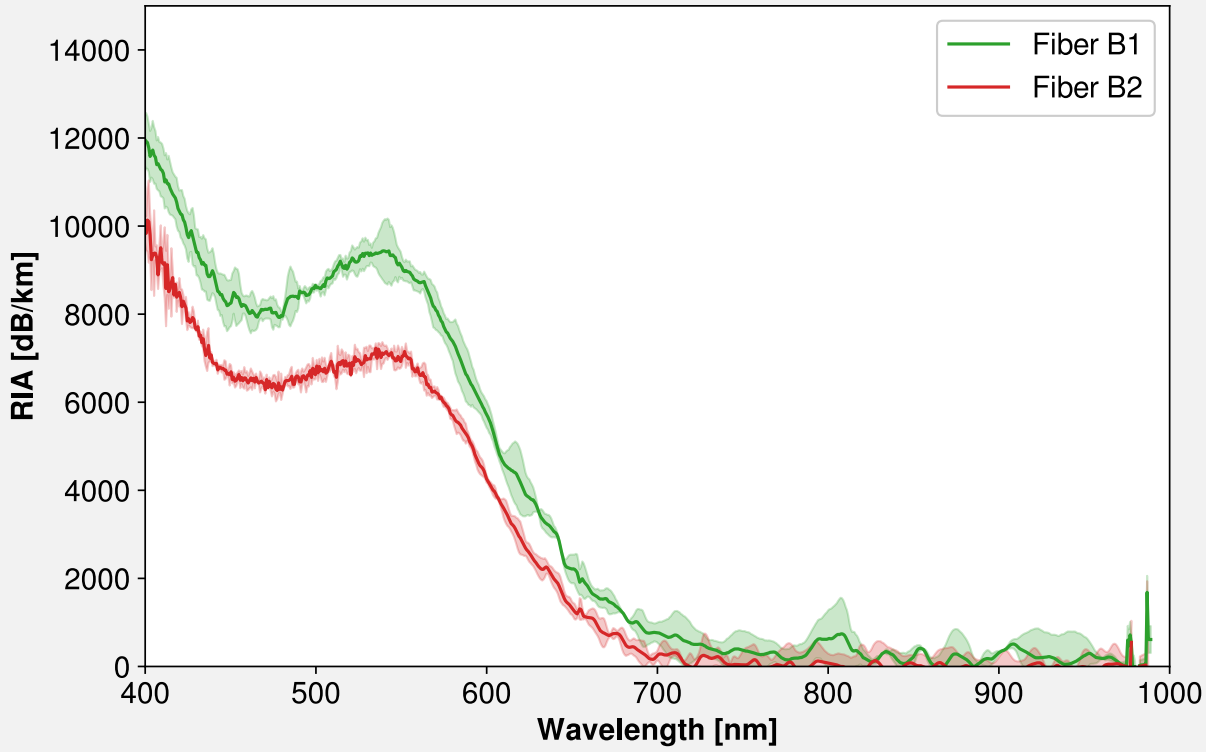

Figure 3.26. – Spectral RIA, in the visible domain, of the **B1** and **B2** samples irradiated under γ rays at a dose of 12.9 Gy(SiO_2). Filled areas in lighter color show uncertainties at $\pm 2\sigma$.

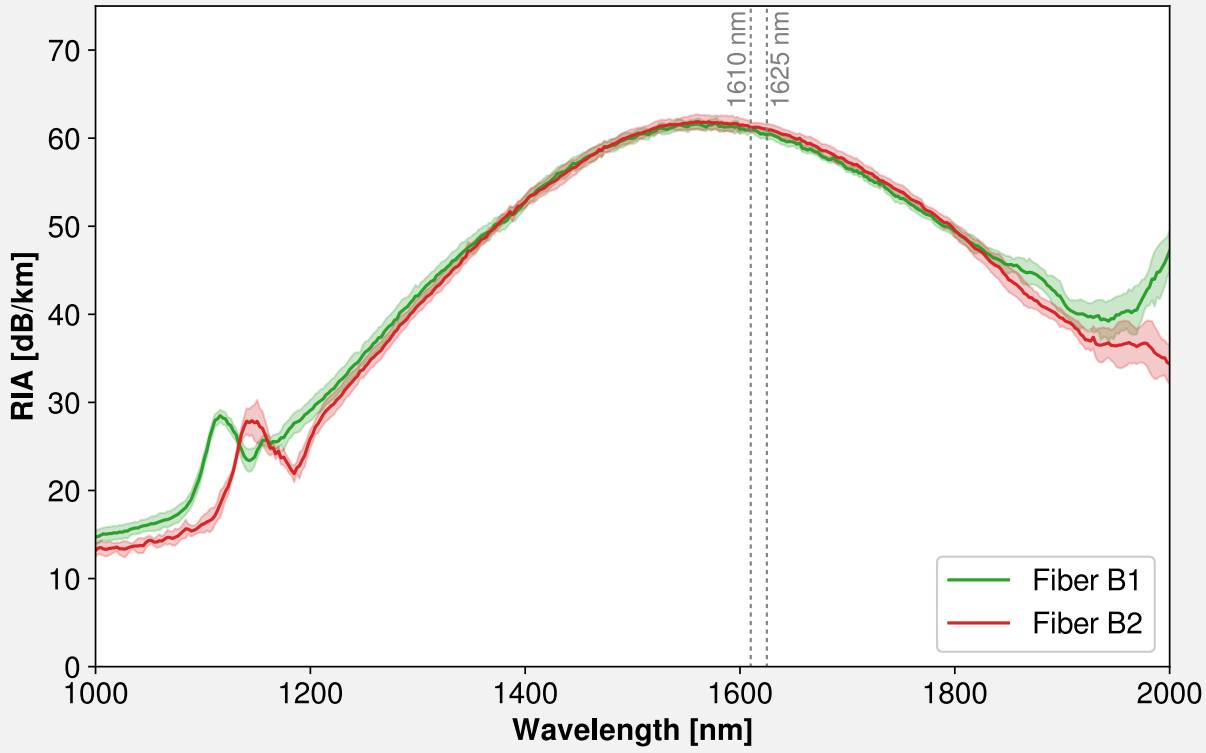

Figure 3.27. – Spectral RIA, in the near-infrared domain, of the **B1** and **B2** samples irradiated under γ rays at a dose of 12.9 Gy(SiO_2). Filled areas in lighter color show uncertainties at $\pm 2\sigma$. Position of wavelengths 1610 nm and 1625 nm are indicated in dashed lines for further reference.

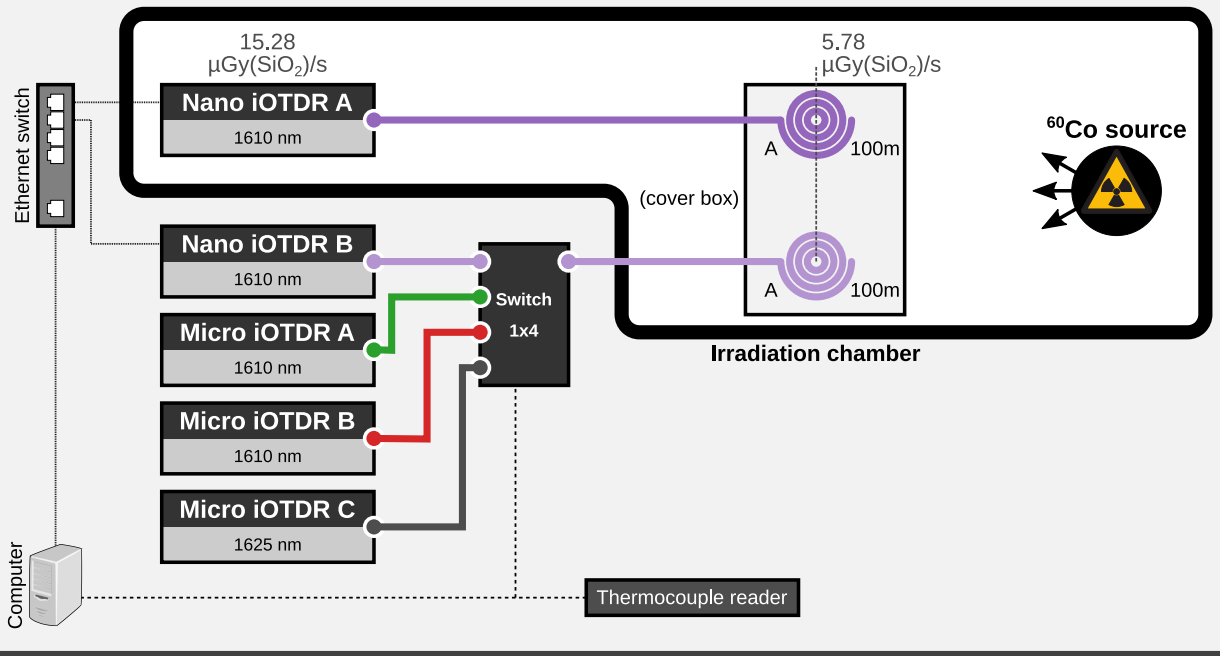

Figure 3.28. – Experimental setup of the γ ray irradiation of Nano iOTDR devices. The dose rate of irradiated elements is indicated in gray above each position.

3.3. Radiation testing of the Nano iOTDR system

Characterization of the Nano iOTDR devices followed a similar approach as described here above for the Micro iOTDRs (cf. **Section 3.2**), through testing of the complete dosimetry system under γ and X-rays, with different target doses and dose rates.

3.3.1. Experimental setup of γ ray irradiation

In a comparable way to the experiment described in **Section 3.2**, two distributed dosimetry systems based on Nano iOTDR devices and fibers of type **A** were tested in the γ ray irradiator at the PRESERVE facility (cf. **Section 2.3.2**).

A schematic of the measurement setup is proposed in **Figure 3.28**. Both measurement lines were completely identical in this case, each consisting of a single, 100 m-long sample of fiber **A**, installed at a dose rate of 5.78 $\mu Gy(SiO_2)/s$. The samples were also enclosed in a custom 3D printed cover box, depicted in **Figure 3.29**, in order to isolate them from ambient lighting and avoid possible extrinsic photobleaching effects that had been highlighted from previous irradiation campaigns in other facilities, although with different types of optical fibers [598].

This complete setup was irradiated for a total duration of 84 days. One of the two Nano iOTDR devices was also irradiated, at a dose rate of 15.28 $\mu Gy(SiO_2)/s$, for the whole duration of the experiment, while the other devices remained in the instrumentation room for comparison.

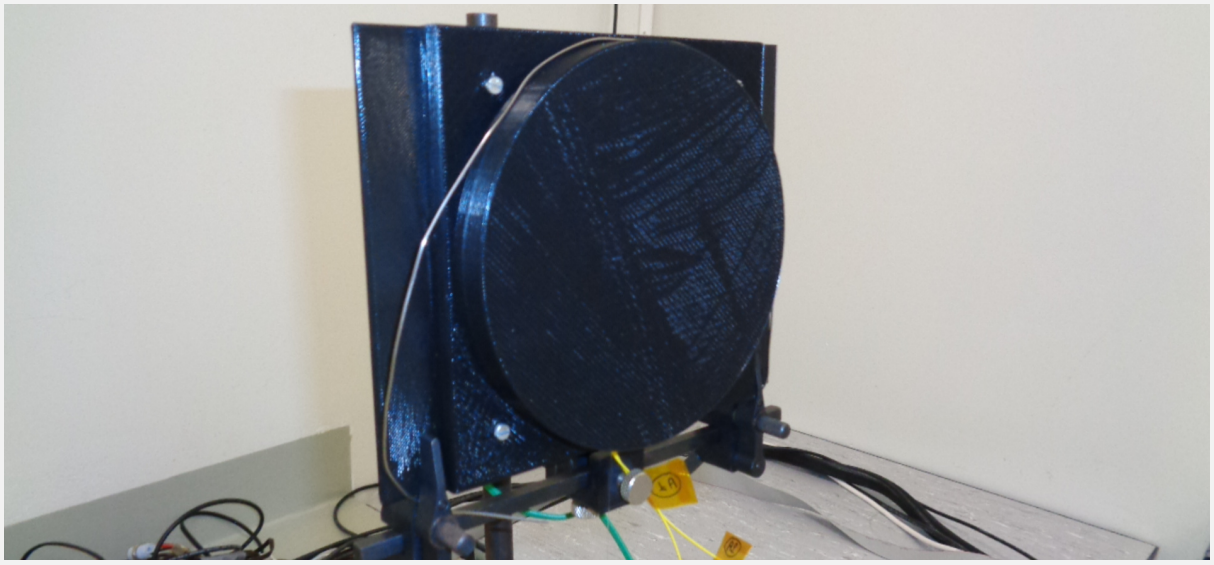

Figure 3.29. – Photograph of the cover box used to isolate optical fibers from ambient lighting in the γ ray irradiation experiment involving Nano iOTDR.

A particular feature of this experiment, compared to **Section 3.2**, is the involvement of four different iOTDR devices on the second measurement line, coupled together to the optical fiber sample through a 1-to-4 optical switch (LEONI eol 1x4). In addition to the Nano iOTDR B device, three Micro iOTDR devices – two of which operating at 1610 nm and one operating at 1625 nm – were also interrogating the second measurement line; the Micro iOTDR A used here was the one irradiated to a TID of 81.05 $\mathrm{Gy(SiO_2)}$ in the previous γ ray experiment (cf. **Section 3.2**). Measurements on this line were performed in a sequence (one device after the other), whereas measurements on the first line were performed continuously by the Nano iOTDR A device only.

The OTDR devices were configured with their minimum pulse width (10 ns for Nano iOTDRs, 5 ns for Micro iOTDRs), and a scan time of 10 s, to check performances at the maximum temporal resolution. Their data were recorded automatically by an embedded computer (Raspberry Pi 4 model B). Additional temperature measurements were performed by J-type thermocouples, connected to a thermocouple reader (Pico Technology TC-08), recording a temperature range from 14 °C to 21 °C for the total duration of the experiment.

3.3.2. Results of γ ray irradiation

An overview of the evolution of the OTDR traces acquired by the Nano iOTDR A for a significant part of the irradiation is shown in **Figure 3.30**. It features a clear increase of the OTDR trace slope with irradiation time, as previously observed in **Figure 3.19** for the Micro iOTDR. A noticeable feature of these Nano iOTDR data is a visible increase of the noise as the signal level decreases due to attenuation, until reaching a level at ~−9 dB, below which data cannot be distinguished from noise.

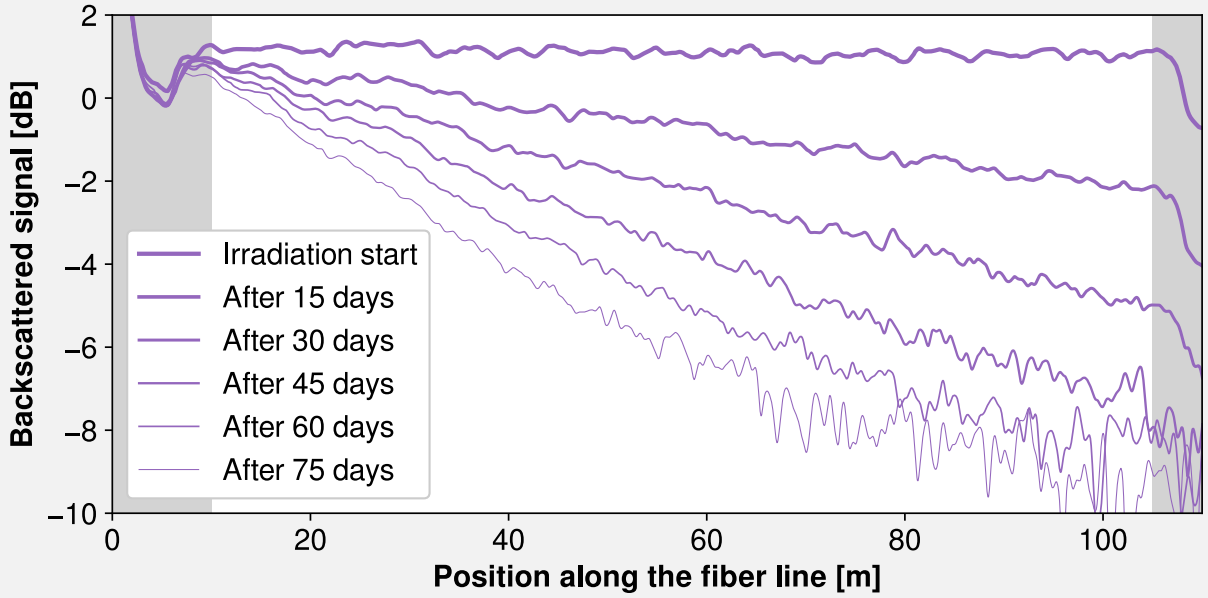

Figure 3.30. – Evolution of OTDR traces acquired by Nano iOTDR A for the first 75 days of irradiation. The segment considered for RIA calculation is shown as a white background.

This decreased SNR for low signal values, compared to the previous Micro iOTDR data, can be interpreted as a consequence of both the decreased scan time applied in this experiment (10 s for this experiment, compared to 180 s for the Micro iOTDR experiment), as well as the overall increased noise and reduced dynamic that was observed for the Nano iOTDR device in **Section 3.1.3**.

Analysis of the results was also performed as described in **Section 3.2** to compute the values of dose and RIA. Dose was calculated from irradiation time and the known dose rate received by the samples; this calculation also took into account downtimes of the facility and decay of the ^{60}Co source. Attenuation was extracted from the OTDR traces by applying a linear fit with a cutoff threshold of -6.5 dB, corresponding to the optimal setting for this device and set of parameters, as described in **Section 3.1.3**. Attenuation was then converted to RIA by subtracting every attenuation value from the attenuation measured at irradiation start.

The results of RIA measurements under γ rays are summarized in **Figure 3.31**, until the maximum dose of 40.16 $\mathrm{Gy(SiO_2)}$ reached by both samples. In the same way as for Micro iOTDR devices, both Nano iOTDR measurements stand in good accordance, with a very similar trend toward higher dose values. The sensitivities calculated from applying an homogeneous linear fit on these data are also in very good accordance with each other, with 3.87 $\mathrm{dB\,km^{-1}\,Gy(SiO_2)^{-1}}$ measured on device A and 3.77 $\mathrm{dB\,km^{-1}\,Gy(SiO_2)^{-1}}$ measured on device B.

A significant deviation from this linear trend can however be observed in both Nano iOTDR devices for doses lesser than 3×10^{-2} $\mathrm{Gy(SiO_2)}$, for which the measured RIA stands almost consistently above the linear fit of the complete data. These results can be explained by the high uncertainties observed on all iOTDR devices for low attenuation values (cf. **Section 3.1.4**), along with the shorter

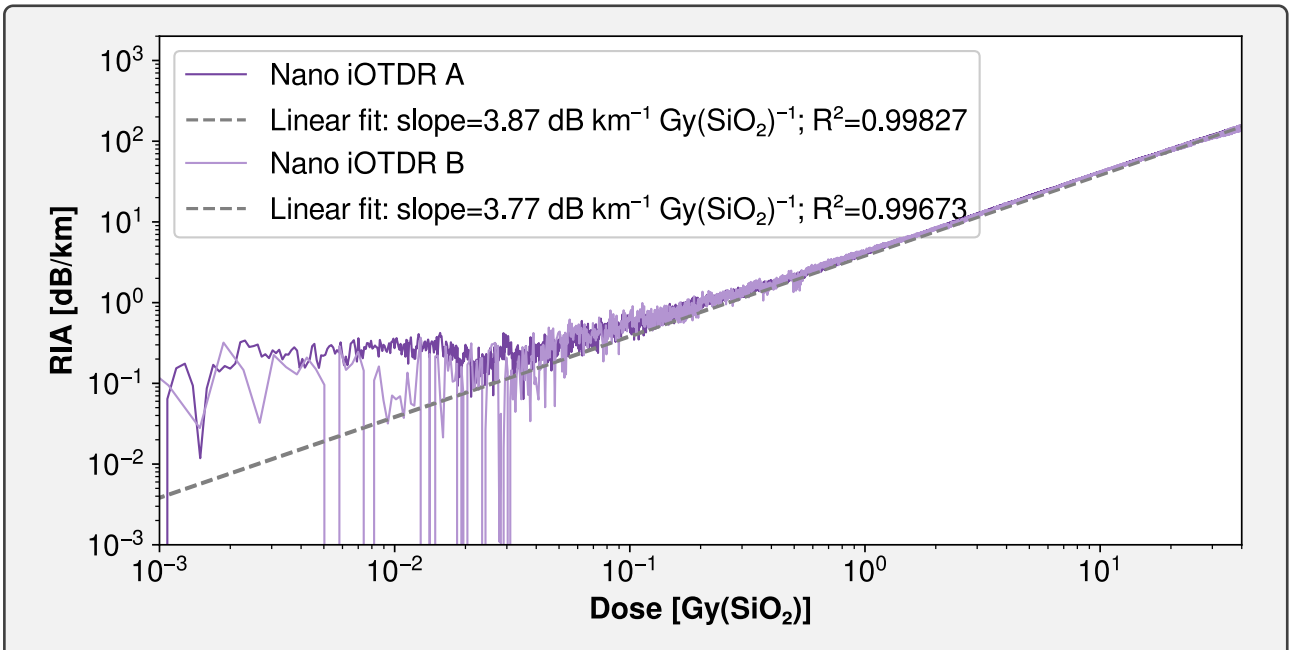

Figure 3.31. – Log-log plot of the evolution of RIA at 1610 nm of samples of fiber **A** irradiated under γ rays at 5.78 µGy(SiO$_2$)/s, during the complete irradiation period. Dashed lines show the linear fits applied to each data set.

sampling lengths involved in this experiment compared to Micro iOTDR γ irradiation, causing this phenomenon to be more evident on this graph as compared to **Figure 3.21**.

3.3.3. Reliability of the Nano iOTDR devices

In the same way as the γ ray irradiation of Micro iOTDR devices, the Nano iOTDRs were continuously operated during the whole duration of the γ ray irradiation. Neither software nor hardware failure was observed on any of the two devices during the 84 days of irradiation, nor any significant difference in the quality of measurement between the irradiated and the non-irradiated devices.

The Nano iOTDR A, irradiated during the whole experiment at a dose rate of 15.28 µGy(SiO$_2$)/s, underwent a TID of 106.20 Gy(SiO$_2$) without perceivable effects during or after irradiation.

3.3.4. Comparison between Micro and Nano iOTDR devices

RIA data computed from the OTDR traces recorded by all devices involved in this experiment (two Nano iOTDRs and three Micro iOTDRs) are compared in **Figure 3.32**. In all cases, measurements were performed on 100 m samples of fiber **A**, although the actual measurement lines were distinct between Nano iOTDR A and all other devices (cf. **Section 3.3.1**).

Comparison between these results highlights a great similarity in the shape and range of measurements acquired by these five different devices on two similar samples. All RIA data exhibit good

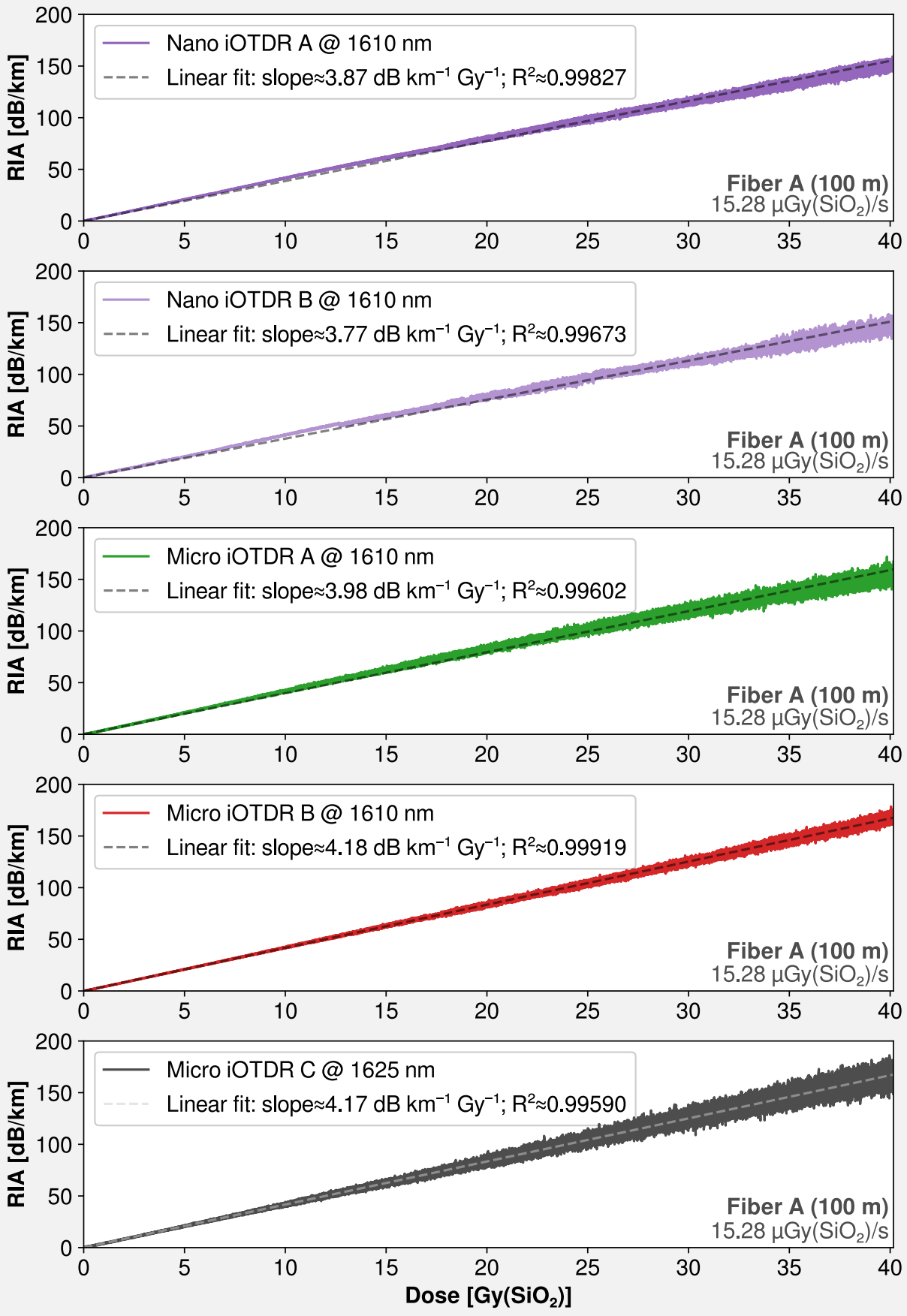

Figure 3.32. – RIA as a function of dose, measured on 100 m samples of fiber **A** with five different interrogating devices. Each data set includes a linear fit shown in dashed line.

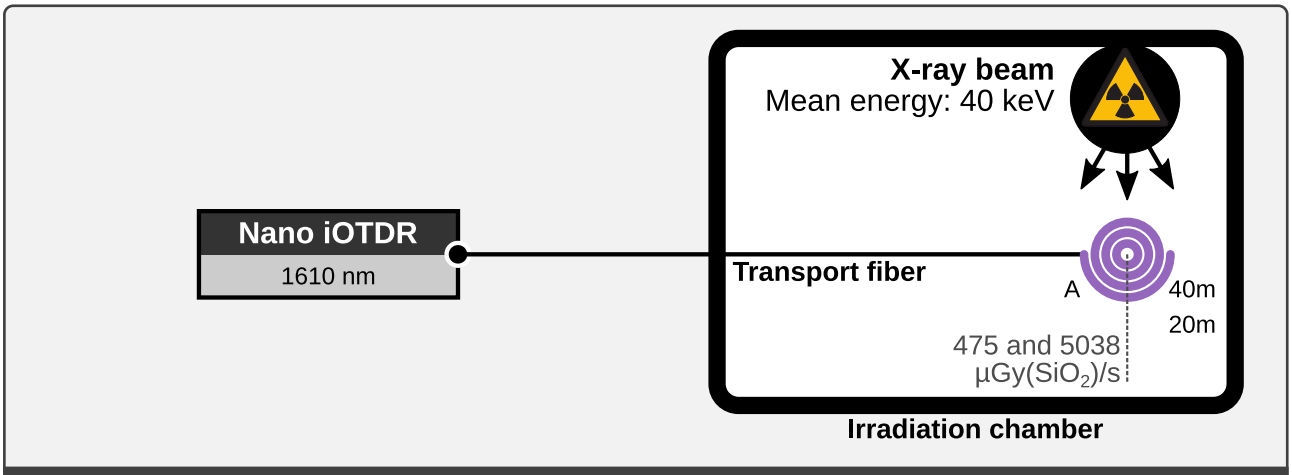

Figure 3.33. – Experimental setup of X-ray irradiation of samples of fiber **A** interrogated by a Nano iOTDR device.

linearity up to the maximum investigated dose of 40.16 $\mathrm{Gy(SiO_2)}$, with a coefficient of determination R^2 always greater than 0.99 in all cases.

The sensitivity coefficient, determined by the slope of the linear fit applied to RIA data, is also consistent between these five dosimetry systems. This parameter mean value is 3.99 $\mathrm{dB\,km^{-1}\,Gy(SiO_2)^{-1}}$, with a relative uncertainty of $\pm 12.4\,\%$ at a 95 % confidence level. This significant spread between devices can be explained by the presence of noise in the measurements, which can be a combined result of lesser exploitable signal at higher dose rates as illustrated in **Figure 3.30**, as well as the significant measurement uncertainty observed at short pulse widths for all iOTDRs in **Section 3.1.4**.

The difference in wavelength between Micro iOTDR C, operating at 1625 nm, and all other shown devices, operating at 1610 nm, only yields an insignificant difference of 0.01 $\mathrm{dB\,km^{-1}\,Gy(SiO_2)^{-1}}$, which is consistent with the spectral RIA data measured on a phosphorus-doped fiber in **Section 3.2.5**, indicating a difference lesser than 1 % in RIA levels measured between these two wavelengths.

The overall increased noise level observed on the 1625 nm device, however, can be explained by the comparatively lower signal level observed on the traces acquired by this device, probably due to connector losses.

3.3.5. Comparison with X-ray irradiation

In complement to the measurements performed under γ rays, additional measurements were performed under X-rays in the MOPERIX irradiator (cf. **Section 2.3.1**) to evaluate the performance of the Nano iOTDR and fibers of type **A** for larger values of dose and dose rate. The experimental setup, illustrated in **Figure 3.33**, involved a 40 m sample irradiated at 475 $\mathrm{\mu Gy(SiO_2)/s}$ up to a dose of 100 $\mathrm{Gy(SiO_2)}$ and a 20 m sample irradiated at 5038 $\mathrm{\mu Gy(SiO_2)/s}$ up to a dose of 344 $\mathrm{Gy(SiO_2)}$. The temperature range for these experiments was between 20 °C and 25 °C.

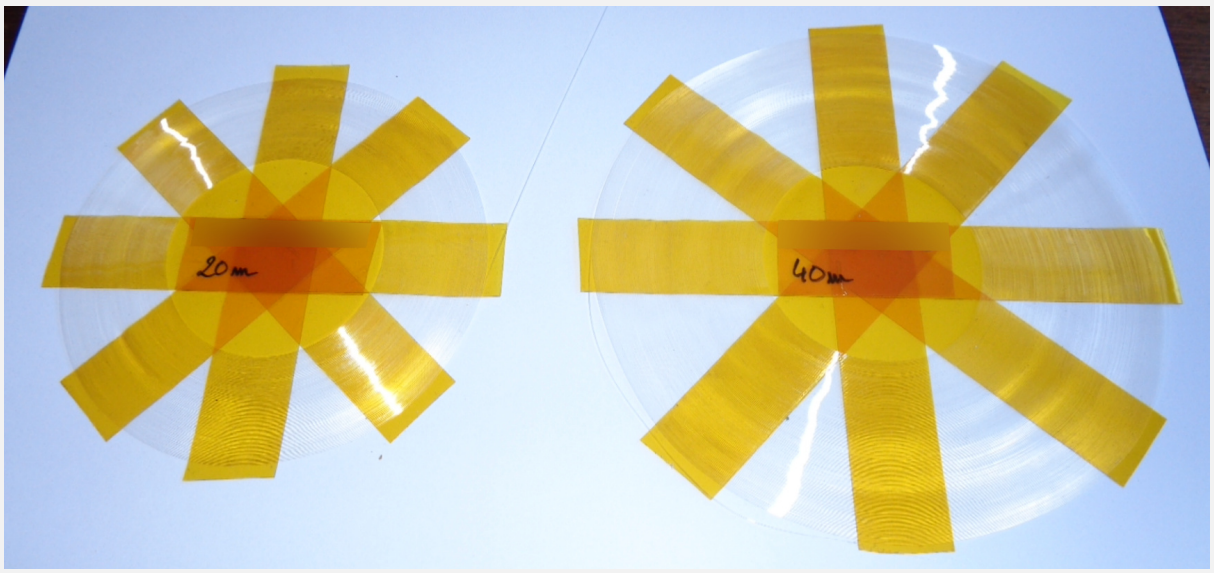

Figure 3.34. – Photograph of the 20 m and 40 m flat coil samples of fiber **A** used for X-ray irradiation.

In a similar way to the Micro iOTDR tests under X-rays, the anode voltage was set to 100 kV, amounting to a mean energy-fluence of 40 keV on the X-ray beam, and the current was adjusted to reach the desired dose rate. To ensure homogeneous irradiation of their whole length, the fibers were also coiled as flat spirals, as illustrated in **Figure 3.34**. These samples were positioned in the X-ray irradiator and spliced to a radiation-hard transport fiber, connected to the Nano iOTDR device placed outside of the irradiation chamber.

RIA data acquired during the 475 $\mu Gy(SiO_2)/s$ irradiation are shown in **Figure 3.35**, along with the data recorded during recovery, after completely switching off the X-ray source. These data show a good linearity of the measurement up to the maximum reached dose of 100 $Gy(SiO_2)$, with a sensitivity coefficient of 3.55 $dB\,km^{-1}\,Gy(SiO_2)^{-1}$. The significant difference between this value and the one measured in γ ray irradiation is partially explained by the fact that RIA evolution with dose is not entirely linear [599]; linear fit up to a dose of 40 $Gy(SiO_2)$ on the same data yields a sensitivity coefficient of 3.80 $dB\,km^{-1}\,Gy(SiO_2)^{-1}$, which stands in very good accordance with γ ray data. The recovery data collected after X-ray irradiation show no significant evolution of the RIA in an interval of 60 h, which highlights the great stability of NIR RIA of phosphorus-doped fibers at room temperature [395].

A compilation of the data acquired under γ rays and X-rays for the combination of Nano iOTDR and fiber **A** is shown in **Figure 3.36**. In the same way as observed in **Figure 3.31** for the γ ray data, all shown measurements are in very good accordance at high dose values, but deviate from this linear characteristic at lower doses. This deviation is also observed on the X-ray data, however at higher dose levels as compared to γ ray data. This difference between γ ray and X-ray data can be the result of the comparatively shorter length of the X-ray samples, which increases the measurement uncertainties as observed in **Section 3.1.5**.

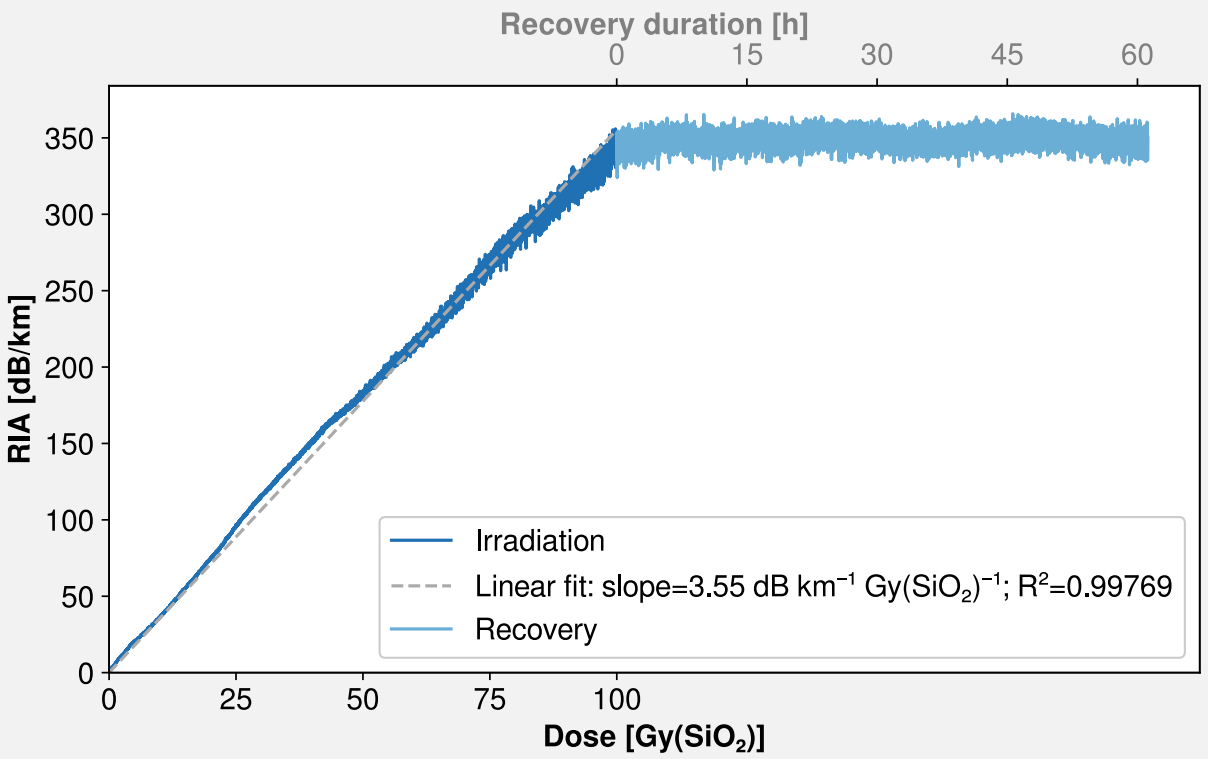

Figure 3.35. – Evolution of 1610 nm RIA of fiber **A** irradiated under X-rays at 475 µGy(SiO$_2$)/s. Recovery data are indicated in a lighter color. Dashed line indicates the linear fit applied to RIA data during irradiation.

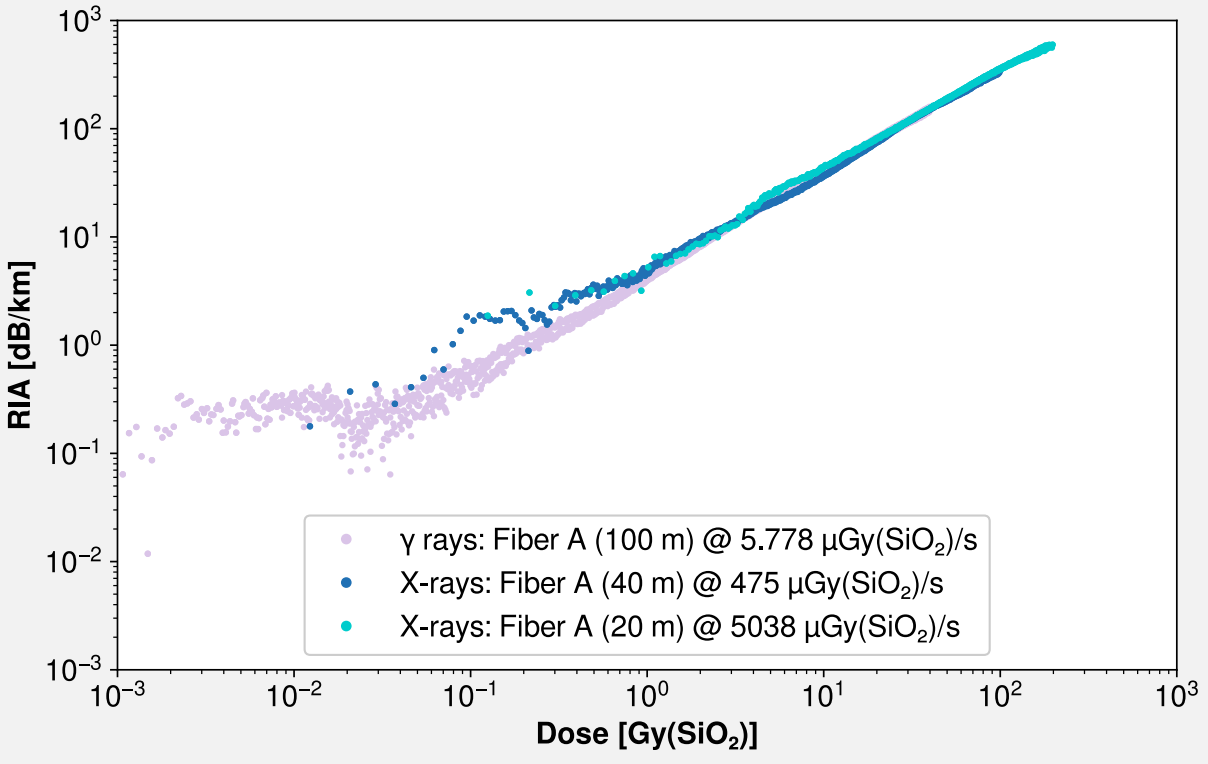

Figure 3.36. – Log-log plot of the evolution of RIA at 1610 nm of **A** samples under γ and X-rays. γ data are shown in a lighter color to ease comparison with X-ray data.

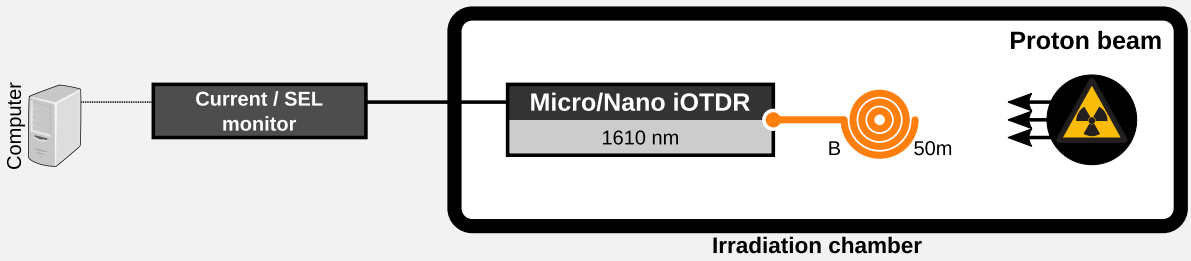

Figure 3.37. – Experimental setup of proton irradiation for Micro or Nano iOTDR devices.

3.4. SEE testing of embedded OTDRs

As introduced in **Section 1.1.3**, TID is not the only factor affecting operation of electronic devices in radiation environments: SEE are another major concern that can lead to significant loss of functionality, even at very low dose levels.

Qualification of SEE tolerance is therefore an important step toward space qualification of the dosimetry system proposed in this thesis work. For this purpose, a proton irradiation campaign was conducted in order to evaluate SEE behavior of both Micro and Nano iOTDR devices.

3.4.1. Experimental setup of proton irradiation

Proton irradiations were performed with the beam line 1B in the TRIUMF PIF facility, producing protons from 350 MeV to 480 MeV (cf. **Section 2.3.3**).

As illustrated in **Figure 3.37**, for each irradiation, one OTDR device (Micro or Nano iOTDR) was connected to a 50 m sample of fiber **B**, arranged as a coil; both elements were placed in the trajectory of the proton beam, as shown in **Figure 3.38**. Because of the low cross-section of the beam (7 cm $\times$ 7 cm), it was possible to target specific electronic components of the irradiated devices, using component layouts provided by the manufacturer for each type of OTDR[1].

To investigate the possible occurrence of single-event latchups (SELs, cf. **Section 1.1.3**), a current monitor was installed upstream of the OTDR power supply. This monitor was programmed both to record the current consumption over time and to automatically power cycle the OTDR in case of a detected overconsumption.

For each run, the proton beam was switched on while the irradiated OTDR was continuously performing acquisition on the fiber sample, and maintained until a failure was detected on the device. The supply current of the device was also continuously monitored during each run. Proton fluence, measured using a radiation monitor, was recorded at occurrence of each failure.

[1]These component location data cannot be published in this thesis.

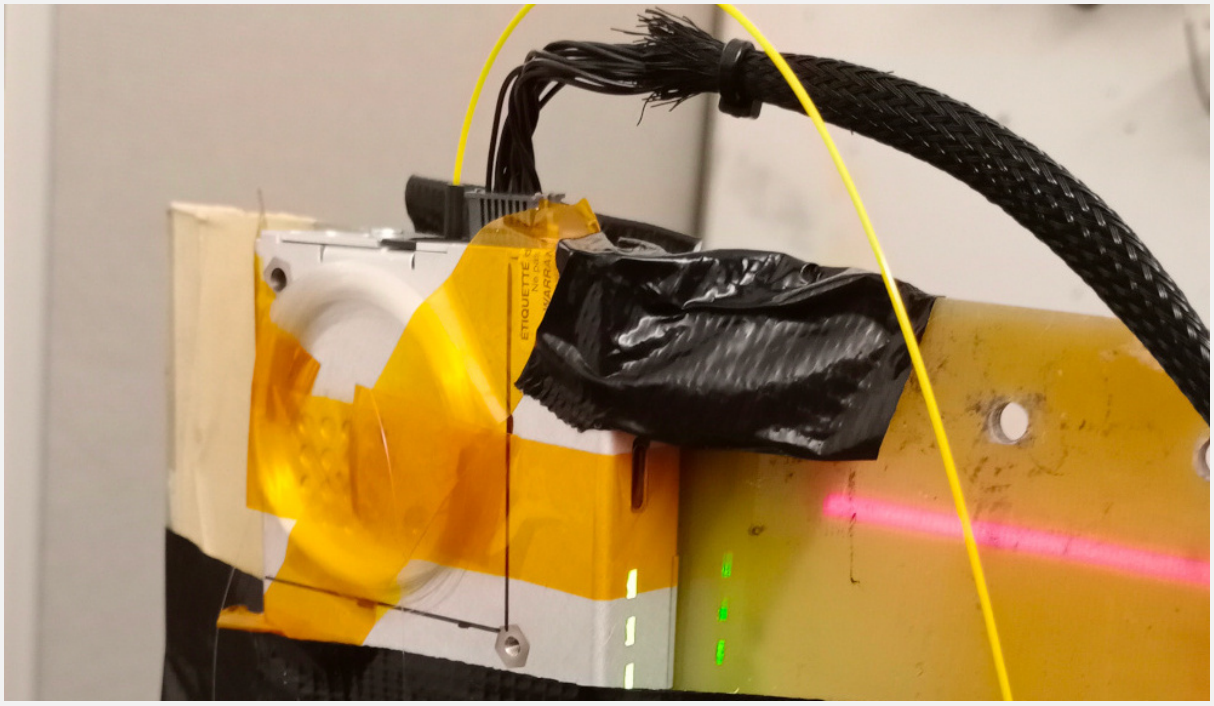

Figure 3.38. – Photograph of a Nano iOTDR placed on the sample holder of the proton beam with a 50 m coil of fiber **B**. (courtesy of Martin Roche)

The total allotted beam time was 24 h, during which several device placements and beam energies were tested on both Micro and Nano iOTDR devices.

3.4.2. Results of proton irradiation

Single-event latchups (SELs)

The power supply current monitoring did not show any anomalous power consumption on either OTDR device, and therefore no SELs were detected for the duration of the irradiation campaign.

The corresponding received total proton fluences by each device, totalized through all runs, were 2.921×10^{10} cm^{-2} at 355 MeV and 4.212×10^{9} cm^{-2} at 480 MeV for the Micro iOTDR; 1.406×10^{10} cm^{-2} at 480 MeV for the Nano iOTDR.

Single-event functional interrupts (SEFIs)

SEFIs [600], in the form of software failures, were however detected during irradiation runs.

For the Micro iOTDR, SEFIs were observed through communication loss with the device, which resumed normal operation after a power cycle. These failure data, according to the proton fluence, are shown in **Figure 3.39**. The targeted components on this device were its CPU, RAM, Flash memory,

DC/DC converter, analog/digital converter (ADC) and USB controller. Two additional runs, indicated at the top of the figure, were performed with aluminum (Al) shielding: one targeting the CPU and the DC/DC converter through a 13 mm-thick shielding, and the other targeting only the CPU through a 19 mm-thick shielding.

Comparison between these different components indicate a higher sensitivity of the CPU compared to other parts, and, on the opposite, a lesser sensitivity of the analog/digital converter and DC/DC converter. Also, comparison between the different beam energies of 355 MeV and 480 MeV highlights a higher sensitivity of the Micro iOTDR to higher-energy protons, which is expected because of their higher penetration. Irradiation of the whole device yields a median proton fluence until failure of ~2×10^8 cm^{-2} at 355 MeV and ~1×10^8 cm^{-2} at 480 MeV. Finally, additional shielding does not appear to significantly influence these results.

For the Nano iOTDR, SEFIs were also observed through communication failures; although, after a few runs, the device systematically issued a warning "Signal detected in the fiber under test", which requires manual acknowledgment after each acquisition. This error was not recoverable after power cycling, and hindered automatic acquisition, making further testing difficult on this device.

Nano iOTDR failure data are shown in **Figure 3.40**. Because of the smaller dimensions of this device, it was more difficult to target its individual components, and only two configurations were tested: first, CPU, RAM, Flash memory and USB controller; then CPU and RAM only. Only one beam energy, of 480 MeV, was tested. These results show a larger data dispersion when irradiating more components, but are globally in good agreement with a figure of ~2×10^8 cm^{-2} until failure.

Expected failure rate in low Earth orbit (LEO)

Considering an application in Low Earth Orbit (LEO), the fluence rate of unshielded protons with energy ~300 MeV can be evaluated to ~10^2 cm^{-2} s^{-1} (cf. **Figure 1.9a** in **Section 1.1.1**), although these values can greatly vary according to parameters such as the altitude and inclination of the considered spacecraft orbit [601].

Using this fluence rate value, the total fluence received by each device without observation of SELs would correspond to a duration in orbit of respectively ~10.6 yr for the Micro iOTDR and ~4.46 yr for the Nano iOTDR. Accordingly, the median fluence of 10^8 cm^{-2} until occurrence of a SEFI would correspond to one failure every ~11.5 d.

This failure rate appears very reasonable to allow operation of the dosimetry system in a space environment, especially if we consider that the observed failures are non-permanent in the case of the Micro iOTDR, which resumes normal operation after power cycling.

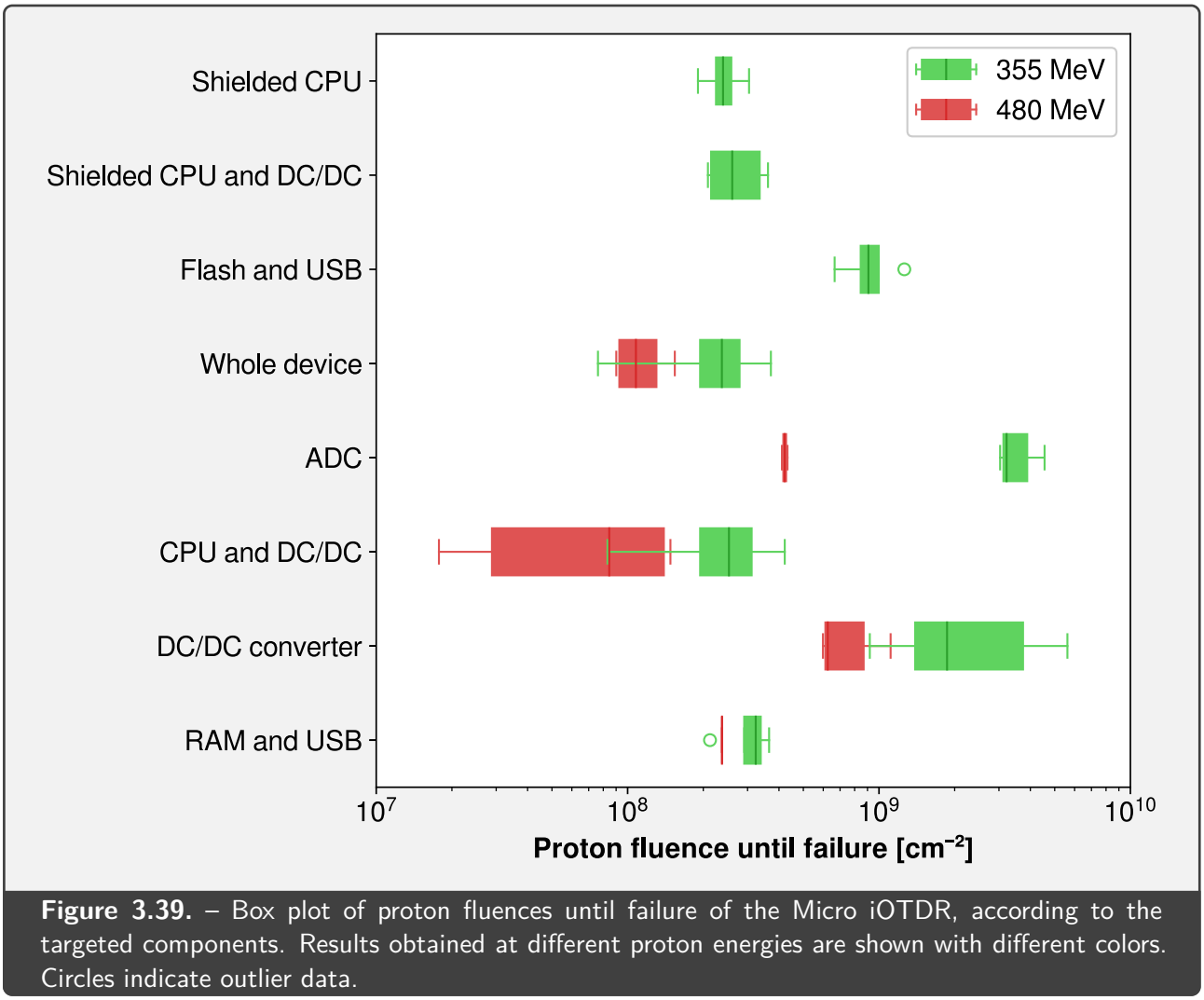

Figure 3.39. – Box plot of proton fluences until failure of the Micro iOTDR, according to the targeted components. Results obtained at different proton energies are shown with different colors. Circles indicate outlier data.

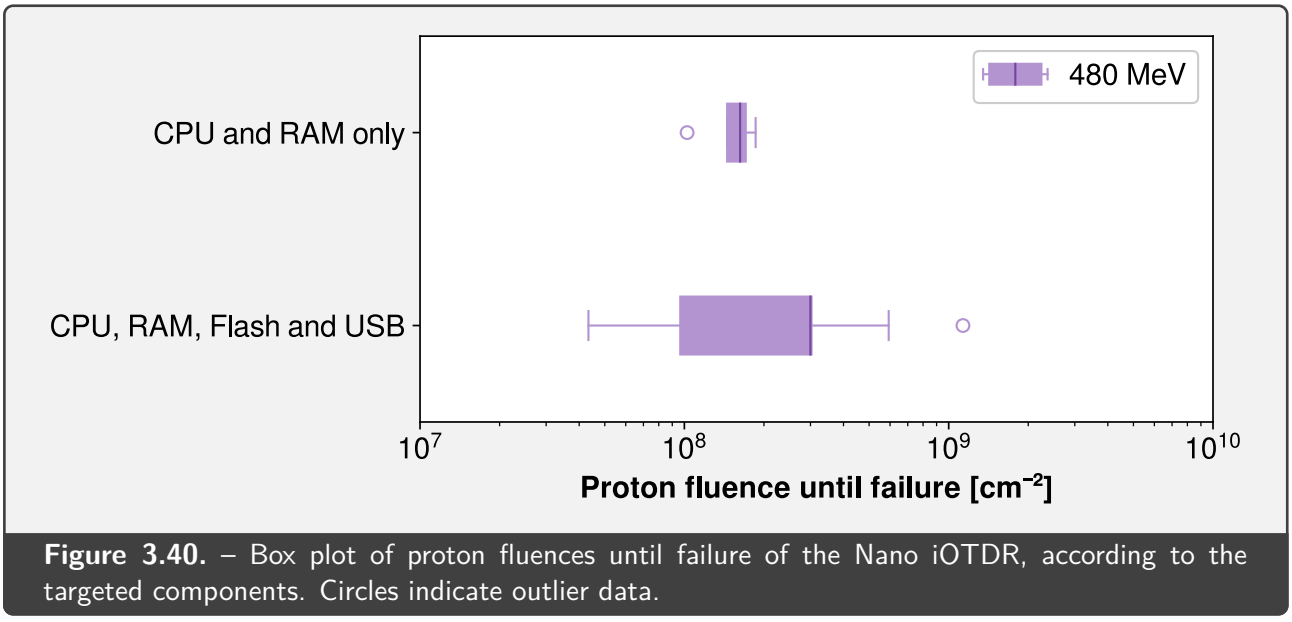

Figure 3.40. – Box plot of proton fluences until failure of the Nano iOTDR, according to the targeted components. Circles indicate outlier data.

3.5. Conclusion of the experimental part

Distributed dosimetry systems based on Micro and Nano iOTDR devices, coupled with radiosensitive fibers of type **A** and **B**, were evaluated for their metrological performance as well as their ability to perform dosimetry measurements in controlled irradiation conditions.

Metrological properties of embedded OTDR devices

The metrological evaluation compared the three different types of OTDR devices investigated in this thesis work – MTS 6000A, Micro iOTDR and Nano iOTDR – over a large set of measurements performed in similar conditions on two optical fiber samples of different attenuations. Investigations on the dynamic range of these devices showed a decreased capability of Micro and Nano iOTDRs to perform reliable measurement at low signal values, as compared to the MTS 6000A device, because of comparatively higher noise levels. These results also suggested the use of a thresholding algorithm to analyze only the portion of available data that stands before the first occurrence of a cutoff value C, which optimal value was determined to be on the order of $-6.5\,\mathrm{dB}$ for both Micro and Nano iOTDR devices operating at their lowest available pulse width and scan time.

Accuracy and repeatability of these devices were also evaluated for a wide range of parameters, including pulse width and sampling length. These data showed a small spread of mean measured values across tested configurations, attributed both to different group velocities resulting of different pulse widths, and potential calibration issues at very low attenuation values. An expected increase of repeatability with increasing pulse width was also observed, until reaching a maximum at 100 ns for most devices, which can be explained by the limited length of samples used in this experiment. The relative uncertainty on measurements performed on an attenuating fiber segment, with the lowest scan time of 10 s, was evaluated to $\pm 6\,\%$ for the Micro iOTDR at 5 ns pulse width and $\pm 5\,\%$ for the Nano iOTDR at 10 ns pulse width.

The influence of sampling length was also shown to be very significant in the measurement uncertainty. Measurements performed on samples $\leq 5\,\mathrm{m}$ resulted in extremely high, and impractical, uncertainties because of the small-scale fluctuations observed on OTDR traces. For longer samples, the uncertainties evaluated for sampling lengths of 10 m, 20 m and 50 m were respectively $\pm 25\,\%$, $\pm 10\,\%$ and $\pm 5\,\%$ for Micro iOTDR; $\pm 40\,\%$, $\pm 15\,\%$ and $\pm 5\,\%$ for the Nano iOTDR, each device operating at its shortest pulse width.

Temperature tests between $-5\,^{\circ}\mathrm{C}$ and $40\,^{\circ}\mathrm{C}$ also revealed very different responses from both types of embedded OTDRs, with the Micro iOTDR showing only a $\pm 1.2\,\%$ deviation of its measurement over this temperature range, whereas the Nano iOTDR suffered a $\pm 12\,\%$ deviation in a complex, but repeatable, pattern. Increasing temperature also caused an increase of measurement uncertainty,

explainable by thermal noise, although the Nano iOTDR here again presented uncommon features. Another significant effect linked to the temperature was also a vertical shift of the OTDR trace, shifting toward lower values as the temperature increases.

γ and X-ray testing of the distributed dosimetry systems

Two main configurations of distributed dosimetry systems were tested under γ and X-ray irradiation: Micro iOTDR coupled with fiber of type **B**, and Nano iOTDR coupled with fiber of type **A**.

γ ray irradiations with ^{60}Co exhibited a continuous, linear evolution of the RIA measured by the dosimetry system, with a sensitivity coefficient of ~4.9 $\mathrm{dB\,km^{-1}\,Gy(SiO_2)^{-1}}$ for fiber **B** irradiated up to 12.97 $\mathrm{Gy(SiO_2)}$, and ~3.8 $\mathrm{dB\,km^{-1}\,Gy(SiO_2)^{-1}}$ for fiber **A** irradiated up to 40.16 $\mathrm{Gy(SiO_2)}$. Spectral RIA measurement of irradiated samples of fiber **B** shown that the RIA measured at 1610 nm by these dosimetry systems was caused by the absorption band linked to P_1 defects of phosphorus-doped, silica-based optical fibers.

The minimum detectable dose for the Nano iOTDR experiment was $3 \times 10^{-2}\,\mathrm{Gy(SiO_2)}$, which is in good accordance with the $\pm 5\,\%$ repeatability figure presented here above: the minimum detectable attenuation in a pristine optical fiber of 0.20 dB/km attenuation would be 0.01 dB/km, yielding a lower theoretical detectable dose of ~25 $\mathrm{mGy(SiO_2)}$ with a fiber sensitivity of ~4 $\mathrm{dB\,km^{-1}\,Gy(SiO_2)^{-1}}$. In the case of the Micro iOTDR experiment, this minimum detectable dose was much lower, on the order of $10^{-3}\,\mathrm{Gy(SiO_2)}$, although the scan time was considerably longer.

Comparison of γ ray results with X-ray irradiations performed at doses up to 344 $\mathrm{Gy(SiO_2)}$ showed good accordance with each other, although the linearity of RIA evolution with dose significantly decreases at high dose levels, causing a decrease of the observed sensitivity coefficient between γ rays and X-rays experiments.

Finally, irradiation of the interrogating devices themselves under γ rays, during their operation, revealed neither signs of failure nor decrease in performance on both types of embedded OTDRs, up to a TID of 81.05 $\mathrm{Gy(SiO_2)}$ for the Micro iOTDR and 106.20 $\mathrm{Gy(SiO_2)}$ for the Nano iOTDR.

SEE testing of embedded OTDRs

Micro and Nano iOTDR were tested for SEE using protons of 355 MeV and 480 MeV, while targeting specific electronic components. Results showed no occurrence of SELs on the Micro iOTDR up to a fluence of $2.921 \times 10^{10}\,\mathrm{cm^{-2}}$ for 355 MeV protons and a median fluence on the order of ~$10^8\,\mathrm{cm^{-2}}$ for the occurrence of a SEFI, which corresponds to respectively ~8.95 yr and ~11.5 d in LEO.

A small dependence on the targeted components was observed, the most sensitive component being the CPU and less sensitive being the DC/DC converter and the analog/digital converter.

Français

Les performances métrologiques, ainsi que la capacité à réaliser des mesures dosimétriques dans des conditions contrôlées d'irradiation, ont été évaluées pour des systèmes de dosimétrie répartie basés sur les Micro et Nano iOTDR, couplés à des fibres radiosensibles de type **A** et **B**.

L'évaluation métrologique a comparé trois types d'OTDR – le MTS 6000A, le Micro iOTDR et le Nano iOTDR – sur un grand nombre de mesures réalisées dans des conditions similaires. L'analyse des régressions linéaires utilisées pour analyser la pente des traces OTDR ont déterminé une valeur de signal seuil de $-6{,}5\,\mathrm{dB}$ en dessous de laquelle l'exploitation de la pente n'est plus optimale. La précision de mesure a été déterminée à $\pm 6\,\%$ pour le Micro iOTDR opérant à une largeur d'impulsion de 5 ns et $\pm 5\,\%$ pour le Nano iOTDR opérant à 10 ns. La longueur d'échantillonnage influence également sur cette précision, avec respectivement, pour des longueurs interrogées de 10 m, 20 m et 50 m, des précisions de $\pm 25\,\%$, $\pm 10\,\%$ et $\pm 5\,\%$ pour le Micro iOTDR, et $\pm 40\,\%$, $\pm 15\,\%$ et $\pm 5\,\%$ pour le Nano iOTDR, chaque appareil opérant à sa largeur d'impulsion la plus courte.

La dépendance à la température de ces appareils a également été mise en évidence entre $-5\,^{\circ}\mathrm{C}$ et $40\,^{\circ}\mathrm{C}$, avec une très faible déviation de $\pm 1{,}2\,\%$ observée sur le Micro iOTDR, et une valeur beaucoup plus importante de $\pm 12\,\%$ sur le Nano iOTDR, qui présente une réponse non monotone.

Les essais d'irradiation sous rayons X et γ ont principalement testé deux systèmes de dosimétrie : le Micro iOTDR couplé à la fibre **B**, et le Nano iOTDR couplé à la fibre **A**.

Les irradiations γ au $^{60}\mathrm{Co}$ ont mis en évidence une évolution linéaire et continue de la RIA, avec des coefficients de sensibilité de ~4,9 $\mathrm{dB\,km^{-1}\,Gy(SiO_2)^{-1}}$ pour la fibre **B** irradiée jusqu'à 12,97 $\mathrm{Gy(SiO_2)}$, et ~3,8 $\mathrm{dB\,km^{-1}\,Gy(SiO_2)^{-1}}$ pour la fibre **A** irradiée jusqu'à 40,16 $\mathrm{Gy(SiO_2)}$. Les mesures spectrales réalisées sur la fibre **B** ont montré que la RIA mesurée à 1610 nm est causée par la bande d'absorption du défaut $\mathrm{P_1}$ des fibres dopées au phosphore.

La dose minimale détectée lors de ces expériences était de $3.10^{-2}\,\mathrm{Gy(SiO_2)}$ pour le Nano iOTDR opérant à un temps d'acquisition de 10 s, et $10^{-3}\,\mathrm{Gy(SiO_2)}$ pour le Micro iOTDR opérant à 180 s.

Les résultats γ ont été comparés à ceux acquis sous rayons X jusqu'à une dose de 344 $\mathrm{Gy(SiO_2)}$, qui ont montré un bon accord malgré la perte de linéarité de la réponse RIA à des doses importantes, réduisant les coefficients de sensibilité observés sous rayons X.

La tenue des interrogateurs aux radiations a également été évaluée. Premièrement, au cours des irradiations γ, un appareil de chaque type a été irradié, atteignant une dose de 81,05 $\mathrm{Gy(SiO_2)}$ pour le Micro iOTDR et 106,20 $\mathrm{Gy(SiO_2)}$ pour le Nano iOTDR, sans qu'aucun appareil n'ait montré de défaillance. Deuxièmement, les essais d'effets singuliers sous protons de 355 MeV et 480 MeV ont indiqué l'absence de latchup et une fluence médiane de ~$10^8\,\mathrm{cm^{-2}}$ avant l'observation d'une erreur logicielle, qui se traduit par une durée moyenne entre erreurs de ~11,5 jours en orbite basse terrestre.

Chapter 4:

Simulation of dose deposition in various radiation environments

4. Simulation of dose deposition in various radiation environments

Contents of this chapter

In addition to the experimental work presented in **Chapter 3**, simulation tools can be used to gain insights on the behavior of the radiosensitive fibers investigated in this thesis when they are subjected to various radiation environments.

This chapter exposes the results of two simulation cases: first, the dose deposited by a variety of primary particle types (photon, electron, proton, neutron) inside fibers of type **A** and **B**, according to their fluence and energy; second, in the case of X-ray irradiation with an X-ray tube, the influence of tube voltage, and therefore energy, on the dose deposited in such optical fibers.

Part of the contents presented in this chapter was published in **Article A.3** [392], which also features additional experimental work, and most figures hereafter are thus adapted from this publication.

4.1. Dose deposition under different particle types

Space radiation is characterized by a variety of particle types and energies, that can vary greatly from one location to another, as introduced in **Section 1.1**. These various radiation environments are defined by the fluence of each particle type as a function of their energy (cf. **Figure 1.9**).

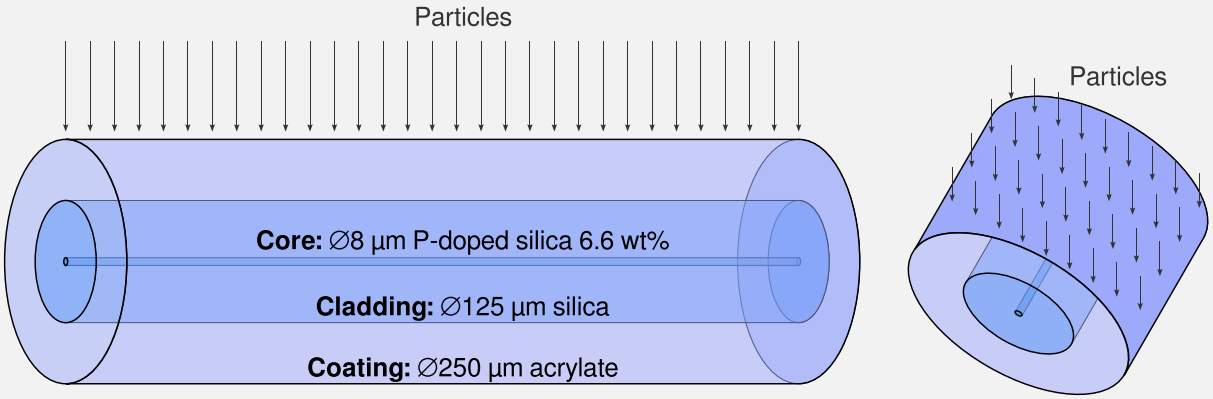

Figure 4.1. – Simulation setup of dose deposition by an arbitrary particle type in fiber **A**.

As exposed in **Section 1.4**, the distributed dosimetry systems tested in this thesis work involves the measurement of fiber RIA, which, in the case of phosphorus-doped fibers operating in the near-infrared range, is linked to P_1 defects (cf. **Section 1.2.4**), resulting from ionizations (cf. **Section 1.2.3**).

The amount of ionizations caused by radiation in a material is reflected by the absorbed dose (cf. **Section 1.1.3**), and therefore estimation of this quantity for different particle types and energies is a key element to the prediction of the optical fiber response in a given radiation environment.

4.1.1. Simulation details

To evaluate the dose deposited in the two types fibers investigated in this thesis work, we used the Monte Carlo code Geant4[1] (cf. **Section 2.4.2**), which is able to simulate and track particles, down to their complete interaction histories, in arbitrarily complex geometries.

Each type of optical fiber was modeled as three concentric cylinders (`G4Tubs` objects) of various diameters and materials, and with a common length of 1 mm, as illustrated in **Figure 4.1** in the case of fiber **A**. Fiber **B** was handled in a similar way, with its corresponding cladding and coating diameters (cf. **Table 2.1**). Silica material was modeled as SiO_2 with a density of $2.20\,g/cm^2$, and acrylate as $C_5H_3N_1$ with a density of $1.18\,g/cm^2$.

In each simulation, the fiber sample was irradiated with particles incoming vertically, as shown in **Figure 4.1**. In order to properly account for the geometry of these samples, the particles were generated in a random position within a rectangular area corresponding to the projection of the fiber sample on a horizontal plane: 250 µm × 1 mm for fiber **A**, and 128 µm × 1 mm for fiber **B**. The Geant4 module `G4GeneralParticleSource` was used to set up a particle generator with such properties.

The collection of physics models used for particle transport and interactions was `QBBC_EMZ` (cf. **Section 2.4.2**). These models provide the quantity *deposited energy* from the various interactions of the

[1]The version used in this work was Geant4 v11.1, released in December 2022.

incoming particle and its secondaries. Simulation of energy deposition is performed in discrete steps, set by a *cut in range* of 1 nm in our case, and is assumed to be continuous between these steps [559, 561]. Calculation of absorbed dose is then performed by the *primitive scorer* `G4PSDoseDeposition`, which divides this deposited energy by the product of material density and volume of the considered part [602]; in our case, this considered part was either the core, cladding or coating of the fiber.

Each simulation was run in 100 batches (ran with different random number generator seeds) of 1 million particles each. Considering the rectangular surface area of the particle generator as described here above, the particle fluence of each batch was therefore $4 \times 10^8\,\mathrm{cm}^{-2}$ for fiber **A**, and $7.81 \times 10^8\,\mathrm{cm}^{-2}$ for fiber **B**.

4.1.2. Dose deposited by photons in the core, cladding and coating

To analyze in more detail the intrinsic behavior of optical fibers when irradiated with photons, such as the γ and X-rays used in **Chapter 3**, the simulation procedure described in **Section 4.1.1** was ran with monoenergetic photons from 1 keV to 10 GeV. 100 energy values were considered in this range, spaced equally within a logarithmic scale.

The corresponding simulation results, in terms of dose/fluence ratio in the core, cladding and coating of the optical fibers, are shown in **Figure 4.2** for fiber **A** and **Figure 4.3** for fiber **B**. The uncertainties at 2σ are shown in these figures as a filled areas around the curves, although their low relative values make them mostly indistinguishable from the graph lines.

A first noticeable feature of these data is the lower dose deposition in the coating of both fiber types, compared to the dose deposited in the core and cladding, for almost all investigated energies. This behavior is explained by two properties of the acrylate material constituting this coating: first, its density is lesser than the one of silica present in the core and cladding (cf. **Section 4.1.1**); second, its interaction cross-section with photons is also lesser or equal to the one of silica over the whole investigated energy range [169].

The response of the inner components, core and cladding, can be further analyzed using the mass-energy absorption coefficient μ_{en}/ρ of silica, which gives the theoretical kerma, i.e. the total energy of generated secondary electrons divided by the material mass (cf. **Section 1.1.3**). For a material irradiated with monoenergetic photons, kerma at the corresponding energy constitutes the upper limit of absorbed dose. This quantity, given by NIST between 1 keV and 20 MeV for all elements with atomic number up to 92 [174], can be calculated for any material of known chemical composition, using the approximation formula [603]:

$$\left(\frac{\mu_{en}}{\rho}\right)_{SiO_2} \approx w_{Si}\left(\frac{\mu_{en}}{\rho}\right)_{Si} + w_O\left(\frac{\mu_{en}}{\rho}\right)_O \tag{4.1}$$

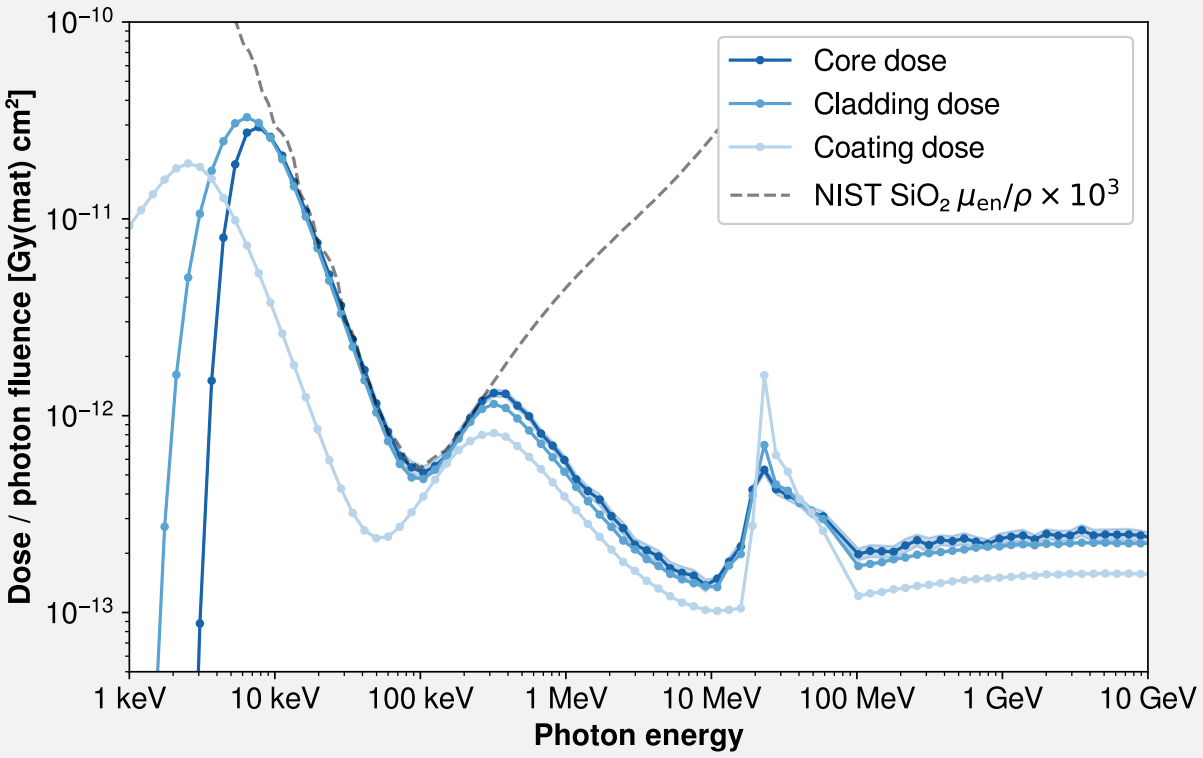

Figure 4.2. – Geant4 simulated dose/fluence of the different components of fiber **A** irradiated with photons. The mass-energy absorption coefficient for silica is plotted in dashed line, for comparison.

with w_{Si} and w_O the weight fraction of silicon and oxygen in SiO_2; respectively 0.467 435 and 0.532 565 [169]. On the graphs, the obtained value was multiplied by 10^3 to take into account the difference in mass units between NIST data (using grams) and definition of the Gray unit (using kilograms).

For photon energies between ~10 keV and ~200 keV, the simulated dose deposition matches the theoretical kerma, meaning that all electrons released in the core and cladding at these energies end up inducing ionizations within these same areas. Outside of this energy range, the absorbed dose stands systematically lower than the corresponding kerma.

At energies lesser than 10 keV, photons have a very high probability of interaction, and are therefore being absorbed by the outside elements of the fiber (coating then cladding), which also explains the higher value of dose deposition in the coating at these low energies. Above 200 keV, the decrease of absorbed dose compared to kerma is explained by the high kinetic energy of secondary electrons, which are able to leave the fiber volume before depositing their total amount of energy.

This influence of the geometrical parameters is evidenced further in **Figure 4.4**, which compares the dose response in the core of fibers **A** and **B**, as simulated both by Geant4 (cf. **Section 4.1.1**) and PHITS (cf. next **Section 4.1.3**). Below 10 keV, the reduced coating and cladding thicknesses of fiber **B** cause slightly more dose to be absorbed in the core. Above 200 keV, the larger core dimensions of **A** cause secondary electrons to deposit more dose: at the mean ^{60}Co γ ray energy of 1.25 MeV, the geometry of fiber **A** causes its core to absorb 1.7 times more dose than fiber **B**.

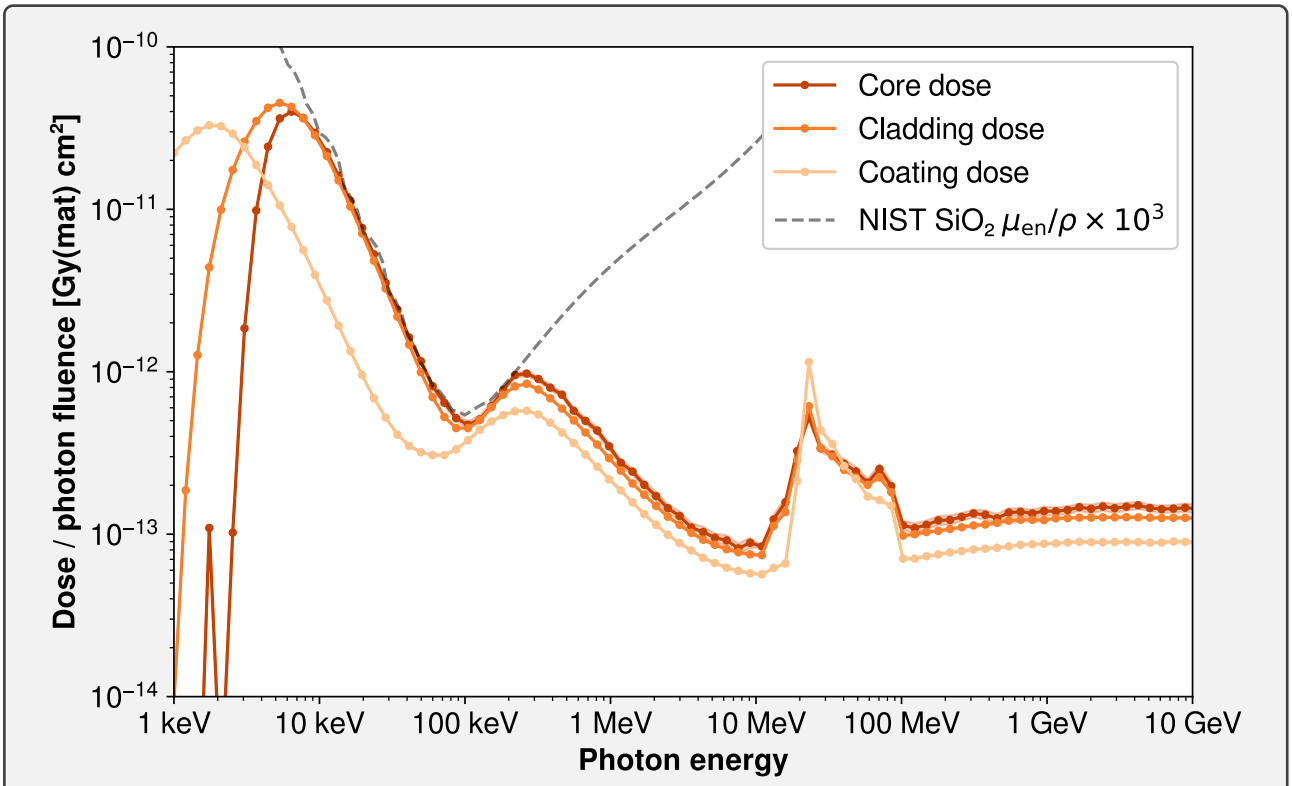

Figure 4.3. – Geant4 simulated dose/fluence of the different components of fiber **B** irradiated with photons. The mass-energy absorption coefficient for silica is plotted in dashed line, for comparison.

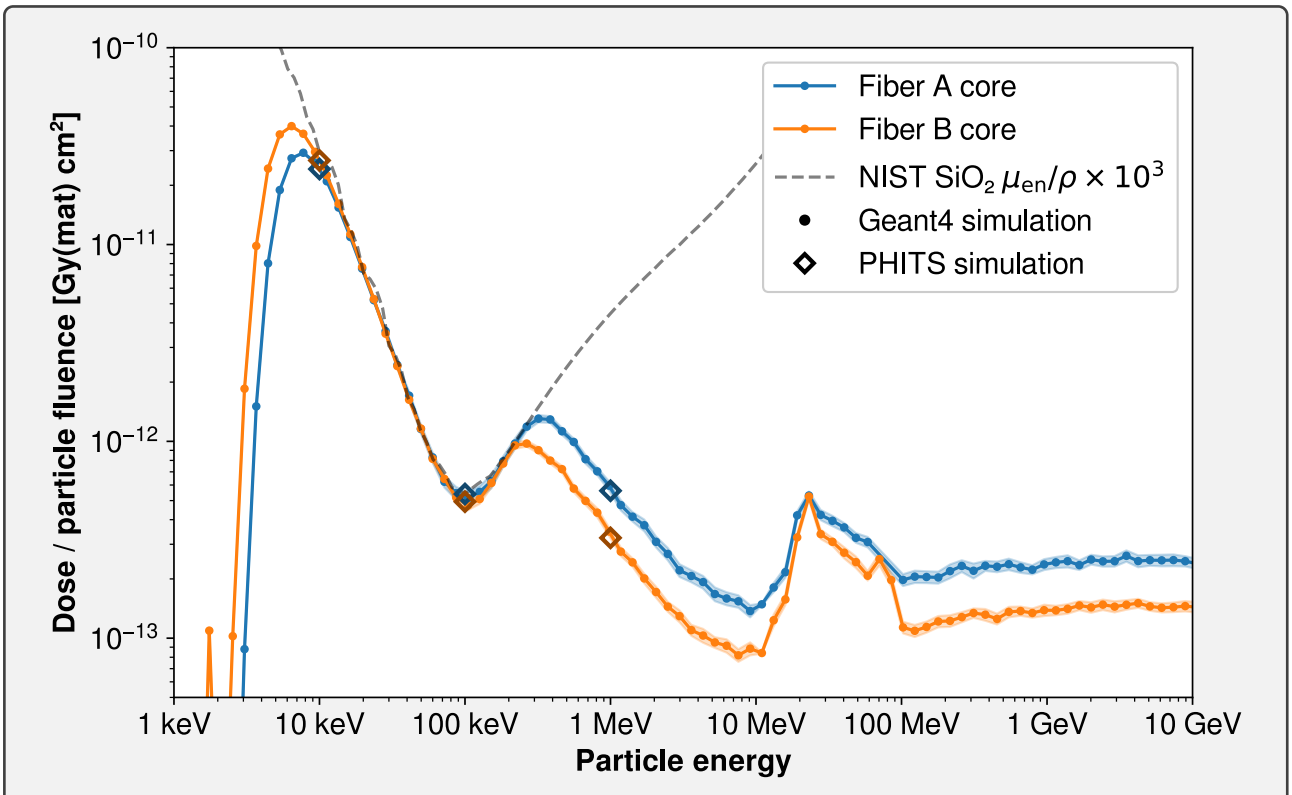

Figure 4.4. – Comparison of dose deposited by photons in the cores of fibers **A** and **B**. The mass-energy absorption coefficient for silica is plotted in dashed line. Geant4 data are indicated by dots, and PHITS data by diamonds.

Another particular feature of these simulated data lies in the range between 10 MeV and 100 MeV, with a sharp increase of the deposited dose, peaking at ~20 MeV. In this energy range, the number of simulated particles had to be increased (from 1 million to 100 million photons per energy value) in order to keep uncertainties down to a satisfactory value. Therefore, this increase appears to be linked to events that are relatively rare, but cause deposition of a large amount of energy; for instance, the generation of large amounts of charged secondary particles through pair or triplet production.

4.1.3. Two-dimensional maps of dose deposited by photons

A further, more graphical, analysis of the dose deposition by photons in optical fibers can be performed from two-dimensional maps of the simulated dose. Such maps are obtained by dividing the optical fiber sample into small cells of interest, inside which the dose is totalized independently during the simulation run.

Because of the relative complexity of use of the Geant4 toolkit, these 2D calculations were performed using the Monte Carlo software PHITS [555], which enables relatively easy configuration, visualisation and retrieval of such multi-dimensional data. Here, we configured a 200 × 200 rectangular pixel mesh spanning over the whole cross-sectional area of fiber **A**, i.e. a 250 µm × 250 µm square area. The same mesh parameters were set for fiber **B** to ease comparison of the results.

Simulation details were similar to the ones introduced here above in **Section 4.1.1**, and a total of 100 million photons were generated in each run. Although no detailed physics configuration is available in PHITS for photons, the parameter `negs=1` was set to enable photon and electron transport, and the cutoff energy was configured to the available minimum of 1 keV.

The resulting 2D dose/fluence maps are shown in **Figure 4.5** for fibers **A** and **B** irradiated with photons of 10 keV, 100 keV and 1 MeV. These results are in very good accordance, both in terms of absolute values and interpretation of the intrinsic phenomena of dose deposition, with the Geant4 simulations presented in **Section 4.1.2**. As shown previously in **Figure 4.4**, PHITS data, obtained from averaging 2D results within the core area of each fiber, perfectly match Geant4 data for the three simulated energies of 10 keV, 100 keV and 1 MeV.

While fibers **A** and **B** display similar behavior at same photon energies, with respect to their scale, these three different investigated energies illustrate different dose depositions processes.

At 10 keV, most of the dose is deposited in the cladding, which corresponds to the point of entrance of photons after traversing the coating. Therefore, at such low energies, the cladding absorbs most of the incoming radiation before it can reach the core, with a very high efficiency due to the high interaction probability of low-energy photons.

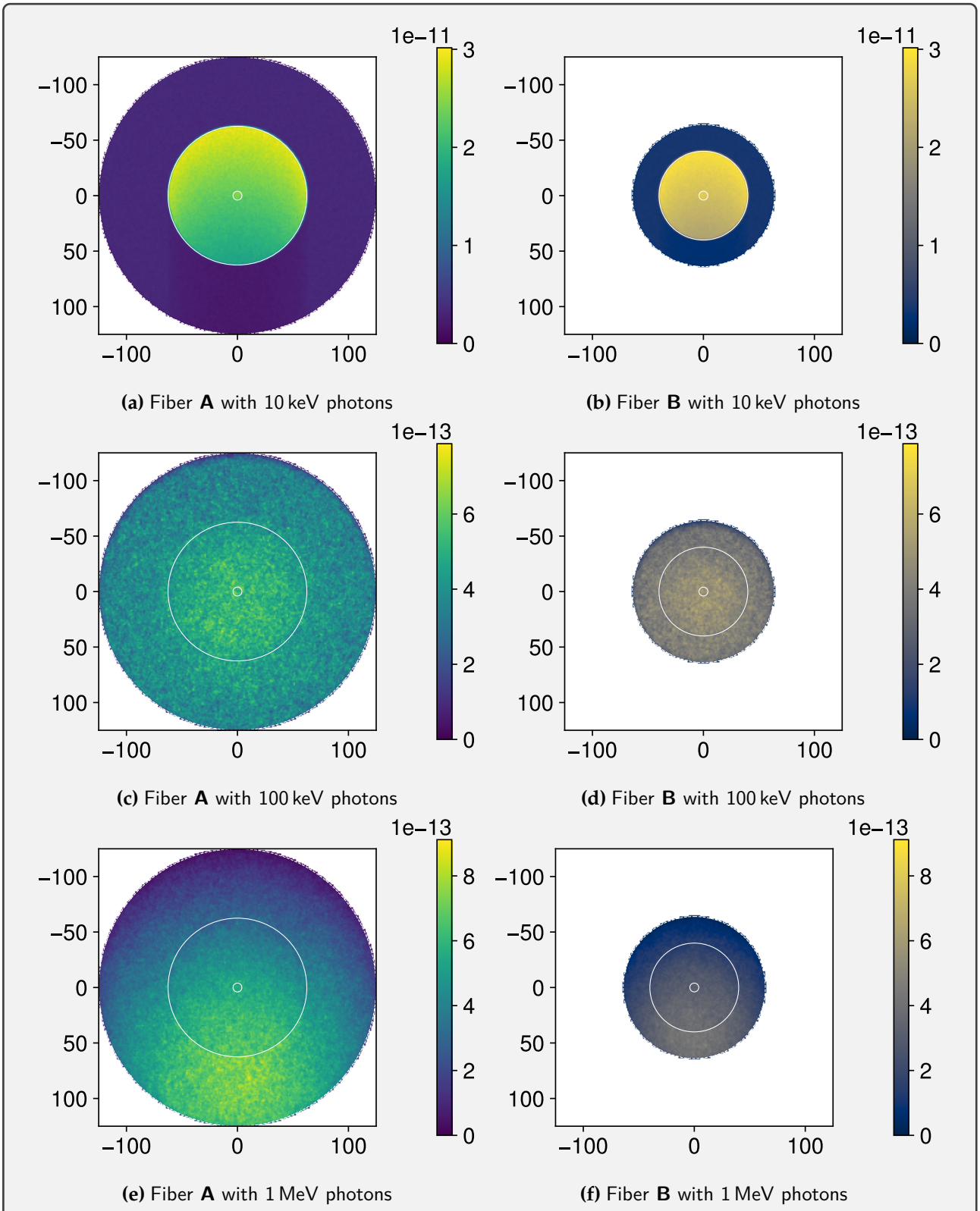

(a) Fiber **A** with 10 keV photons

(b) Fiber **B** with 10 keV photons

(c) Fiber **A** with 100 keV photons

(d) Fiber **B** with 100 keV photons

(e) Fiber **A** with 1 MeV photons

(f) Fiber **B** with 1 MeV photons

Figure 4.5. – Two-dimensional dose/fluence maps (in Gy(mat) cm^2) for fibers **A** and **B** irradiated with monoenergetic photons of different energies. Dimensions (x horizontally and z vertically) are in µm, and photons are incoming from above, i.e. toward positive z values. White circles delimit the coating (dashed lines), cladding and core areas.

Then, at 100 keV, the absorbed dose is much lesser in absolute value, but more equally spread into the fiber volume, although with a slight increase in the cladding and core regions. This relative homogeneity indicates that photons traverse the whole material, but mostly cause dose deposition at the location where they interact.

Finally, at 1 MeV, more dose is deposited in the bottom part of the fiber, indicating that the secondary electrons travel far within the material, preventing them from depositing their whole energy in the area where they were released. The bottom part of the coating, in particular, appears to absorb the most dose, as it is located on the exit trajectory of electrons released in the core and cladding. However, despite this local increase, the overall dose of the coating, averaged over its whole volume, remains lesser than the one absorbed in the other areas of the fiber. In terms of absolute value, the deposited dose in all areas is in the same order of magnitude as for 100 keV photons.

4.1.4. Dose deposited in the core by different particle types

In order to determine the optical fiber sensitivity to ionizing particles other than photons, the simulation process described for photons in **Section 4.1.2** can be generalized to other particle types, such as protons, electrons and neutrons.

The resulting dose/fluence values of these simulations, performed with Geant4 for particle energy between 1 keV and 10 GeV (with 100 energy values spaced evenly in a logarithmic scale), are shown in **Figure 4.6** for fiber **A** and **Figure 4.7** for fiber **B**.

Proton response is characterized by a sharp increase observed at an energy of ~3.5 MeV for fiber **A** and ~2.5 MeV for fiber **B**. This increase also corresponds to the maximum amount of dose deposition, and can be interpreted as the occurrence of a Bragg peak [604] in the core area at this energy. Protons of an energy lower than this threshold cannot reach the core area, and therefore do not deposit any significant amount of dose. On the contrary, protons of higher energies go through the core causing ionizations, but are not braked enough to deplete their whole energy within this area, resulting in a decrease of the deposited dose with increasing energy until reaching an asymptote at ~1 GeV, with a dose/fluence value of ~2.5×10^{-10} Gy(mat) cm^2 for both fiber types.

Electrons, being also charged particles, display a similar response to protons, but start depositing dose in the core at lower energies: respectively ~180 keV for fiber **A** and ~125 keV for fiber **B**. Their response also stabilizes more quickly, from electron energies larger than ~1 MeV, to an asymptote value similar to that of protons.

Finally, neutrons do not appear to yield any significant dose deposition in the core below an energy of ~200 keV. However, the `QBBC` model used for neutron interaction has been shown to largely underestimate dose deposition at energies lesser or equal to 100 keV [605], and neutron data presented

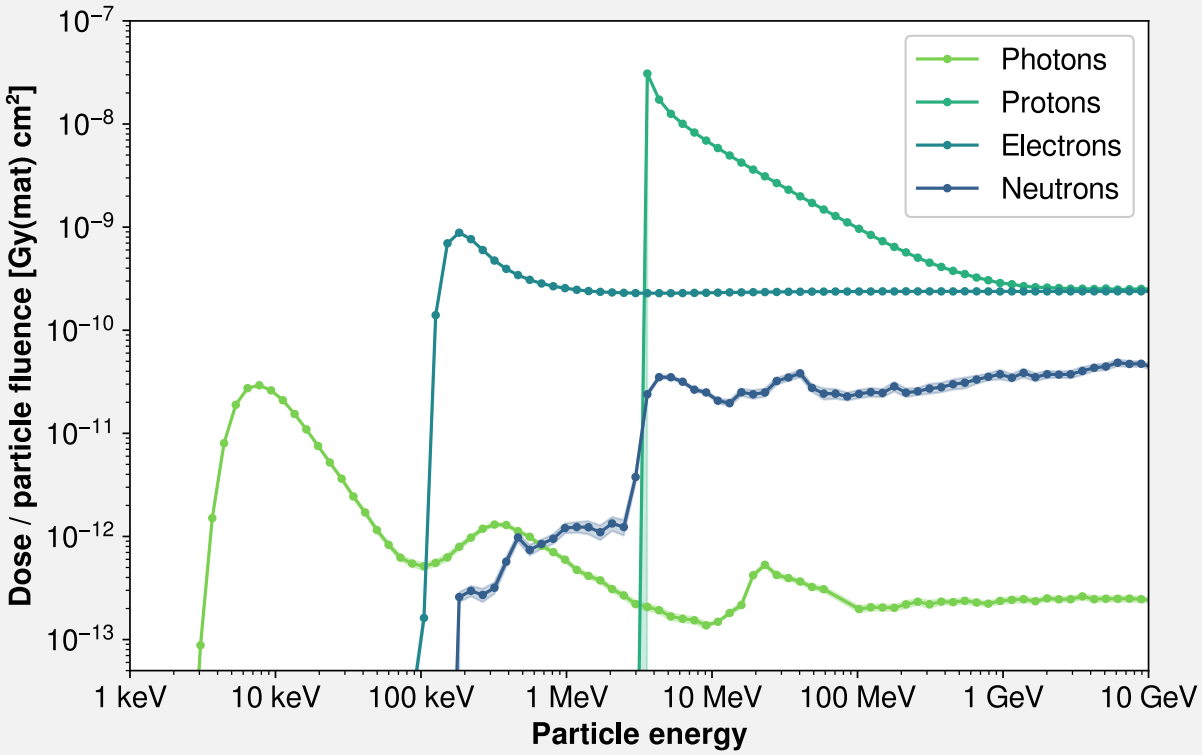

Figure 4.6. – Simulated dose/fluence in the core of fiber **A** irradiated with different particle types.

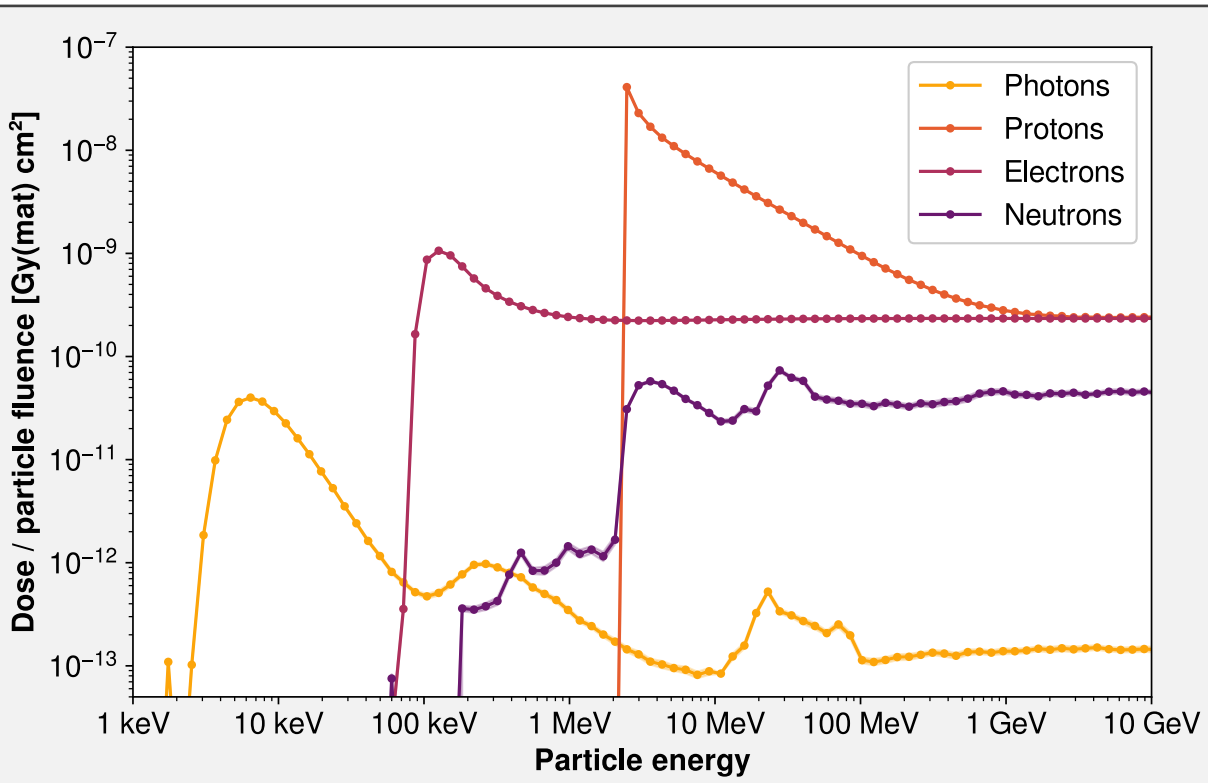

Figure 4.7. – Simulated dose/fluence in the core of fiber **B** irradiated with different particle types.

here might therefore be unreliable for low energies. For higher energies, the neutron dose response appears to feature two phases: first, between ~200 keV and ~2 MeV, the dose/fluence is in the same order of magnitude as photons; then, above ~2 MeV, the response suddenly increases then stabilizes up to ~5×10^{-11} Gy(mat) cm^2 for both fibers. Neutron response also noticeably features a small increase between 10 MeV and 100 MeV, in the same way as observed with photons in **Section 4.1.2**.

Overall, these data highlight a much higher sensitivity of optical fibers to charged particles, and especially high-energy protons. However, these charged particles cannot reach the core below a given threshold energy (~200 keV for electrons, ~5 MeV for protons), which render these fibers insensitive to charged particles at low energies. On the contrary, photons (and possibly neutrons) can deposit dose in the core even at low energies ($\geq$ 10 keV), making these fibers very suitable for detection of uncharged particles in a wide range of energies.

4.2. Dose deposition under X-rays at different energies

X-ray irradiators, because of their commercial availability, relative safety and ease of operation (compared to radionuclide sources for instance), provide a convenient way to perform radiation tests on materials and devices.

However, while these sources mainly emit photons, their energy spectrum is not discrete, but continuous and complexly shaped because of the combined effects of bremsstrahlung and characteristic emission (cf. **Section 2.3.1**). Also, the limited photon energy produced by these devices, linked to their operating tube voltage, can prevent to reproduce the intrinsic interaction phenomena expected in the target environment, such as Compton scattering in electronic devices [506].

This section presents the simulation work combined between SpekPy[2] (cf. **Section 2.4.3**) and Geant4 in order to describe the interaction of such X-rays on the irradiation of optical fibers. A particular topic explored here is the influence of modifying the source voltage on the irradiation conditions and the resulting dose deposition in the optical fiber core.

4.2.1. Simulation of the anode heel effect

The *anode heel effect*, introduced in **Section 2.3.1**, is a phenomenon that causes the radiation cone emitted by an X-ray tube to be skewed at a small angle instead of being centered on an axis perpendicular to the tube (cf. **Section 2.3.1**).

Whereas the heel effect is commonly linked to the anode angle, which is fixed during manufacturing in the case of MOPERIX and LabHX facilities, the fact this effect takes root from the conversion of electrons to X-rays within the volume of the anode makes it also dependant on the energy of primary electrons. Therefore, as a result, adjustment of an X-ray tube voltage can also cause an angular displacement of the beam.

In order to evaluate the dependence of the beam angle to the tube voltage, we performed SpekPy simulations of the beam fluence on a line following the x axis (in SpekPy coordinates, cf. **Section 2.4.3**) at a fixed vertical location centered on the origin ($y = 0$ and $z = 42.5$ cm). Tube parameters, including the anode angle, were set to match the LabHX facility (cf. **Table 2.2**).

The resulting graph in **Figure 4.8** shows the simulated fluence according to the position along the x-axis for five tube voltages between 30 kV and 225 kV. The values are normalized by their maximum to ease visual comparison. As the voltage increases, the beam is shifted away from the center axis, spanning a total of ~5 cm between the minimum and maximum investigated voltages of 30 kV and 225 kV. This shift however appears to be stabilized at higher voltages, and only a very small difference can be observed between the curves at 160 kV and 225 kV.

[2]The version used in this work was SpekPy v2.0.10, released in June 2023.

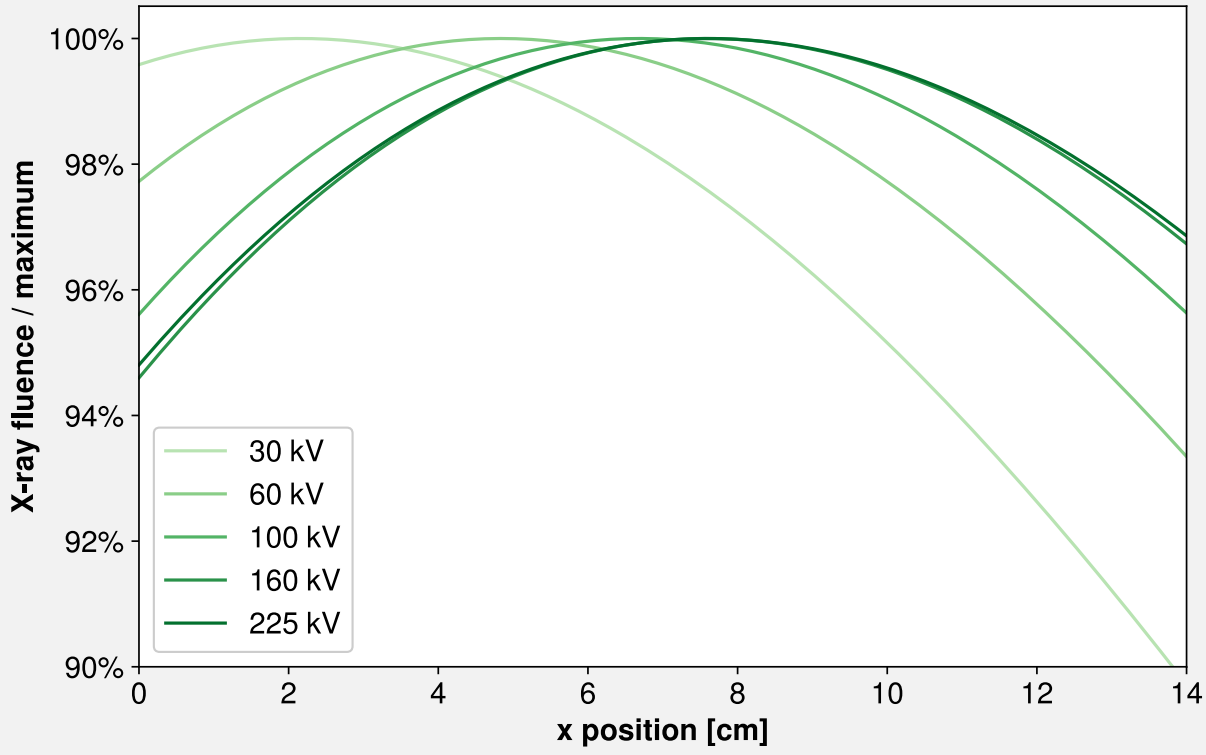

Figure 4.8. – Simulated fluence (normalized by maximum) of the X-ray beam at different tube voltages, along the x-axis at the position $y = 0$ and $z = 42.5\,\text{cm}$.

This tendency is further confirmed in **Figure 4.9**, which depicts the evolution of the x position of the beam maximum as a function of the tube voltage between 30 kV and 225 kV. This position evolves quickly between 30 kV and ~100 kV, then stabilizes for the higher voltage values, with much less evolution between 160 kV and 225 kV. Moreover, this evolution appears to be reversed at energies larger than ~190 kV; this can be explained by the lesser interaction cross-section of photons at higher energies [169], potentially alleviating the heel effect.

4.2.2. Dose deposited by X-rays at different tube voltages

To simulate the dose deposited by X-rays in the various parts of optical fiber samples, the Monte Carlo approach described in **Section 4.1.1** can be adapted to generate photons according to a given spectrum, instead of a constant energy.

For this purpose, X-ray tube spectra were generated using SpekPy, matching the parameters of the LabHX facility, for X-ray tube voltages between 30 kV and 225 kV by steps of 5 kV. These spectra were produced to match the effective spectrum received by an optical fiber sample coiled as a spiral of 5 cm radius and centered at the coordinates (x_{max}, $y = 0$, $z = 42.5\,\text{cm}$), with x_{max} the x position of the beam maximum at the corresponding voltage (cf. **Figure 4.9**).

Accordingly, spectra were generated at four locations (A, B, C and D in **Article A.3**) at a distance of

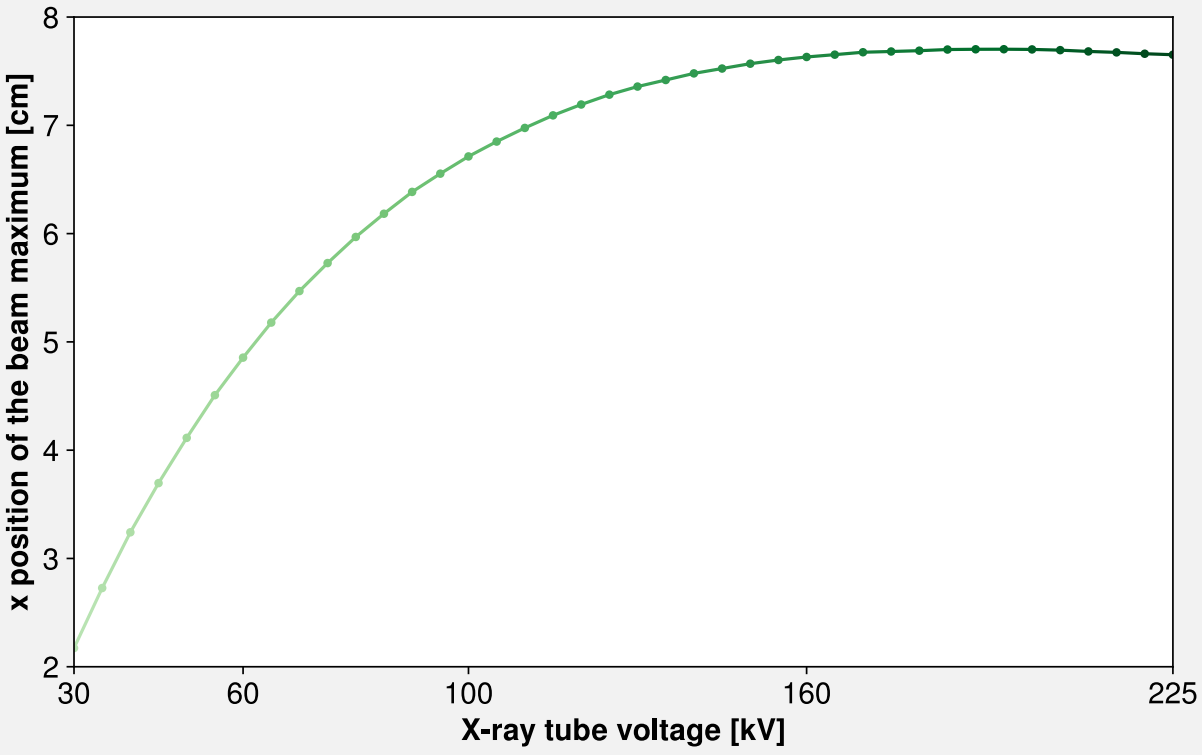

Figure 4.9. – Simulated evolution of the position of the beam maximum along the x-axis, at the position $y = 0$ and $z = 42.5\,\text{cm}$, according to X-ray tube voltage.

5 cm around this central point; then, for each investigated voltage, these four spectra were averaged to produce the final spectra supplied to the Monte Carlo simulations, and illustrated in **Figure 4.10**.

The exposure was set to $20\,\text{mA} \cdot \text{s}$; as 20 mA is the maximum tube current enabled by the LabHX facility over its complete voltage range, the resulting spectra therefore match the differential fluence generated during one second and can thus be considered as differential fluence *rate* spectra.

Integration of these spectra therefore returns a fluence rate, which is given in **Figure 4.11** for all investigated voltages. As illustrated by these data, in this setup and voltage range, the fluence increases with voltage in an almost linear relation.

Then, Monte Carlo simulations were performed with Geant4, using the procedure described in **Section 4.1.1**. In this case, the photon spectra corresponding to each X-ray tube voltage were supplied to the simulation using the `/gps/hist/file` command of the `G4GeneralParticleSource` module of Geant4: as a result, each generated photon was given a random energy, according to a probability density function matching the supplied spectra.

The dose/fluence graphs resulting from these simulations are given in **Figure 4.12** for fiber **A** and **Figure 4.13** for fiber **B**. For both fibers, core and cladding responses are very similar between each other, and the coating response is significantly lower; both these behaviors match the monoenergetic data given in **Section 4.1.2** for the corresponding mean photon energies.

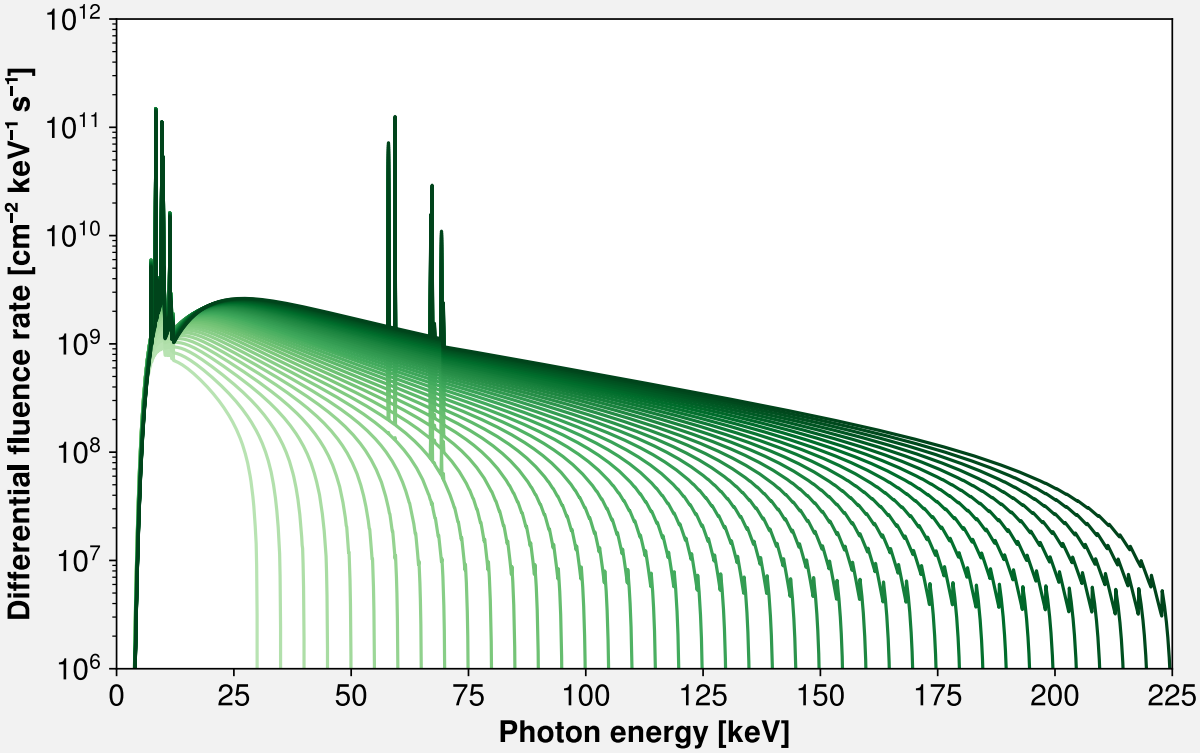

Figure 4.10. – SpekPy simulated spectra of X-rays irradiating an optical fiber coil placed around the beam maximum at a position $y = 0$ and $z = 42.5\,\text{cm}$. The 40 investigated voltages between 30 kV and 225 kV are illustrated here.

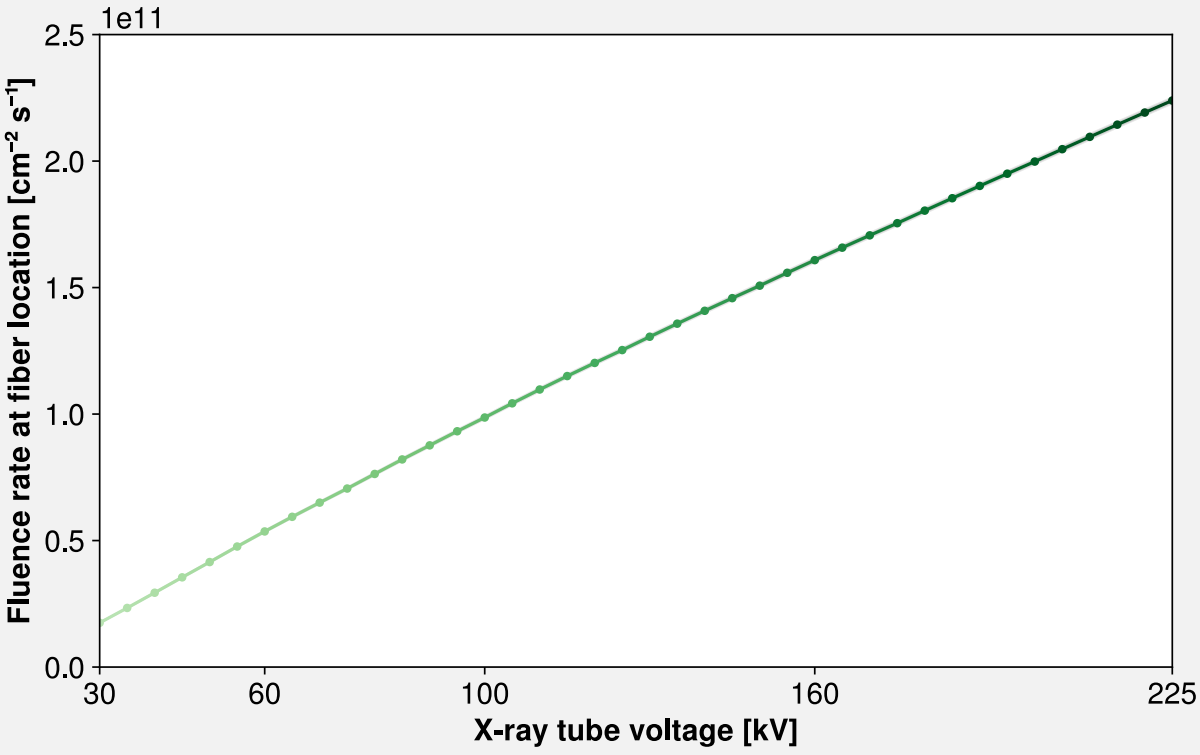

Figure 4.11. – SpekPy simulated fluence rate of X-rays irradiating an optical fiber coil placed around the beam maximum at a position $y = 0$ and $z = 42.5\,\text{cm}$, for all investigated voltages.

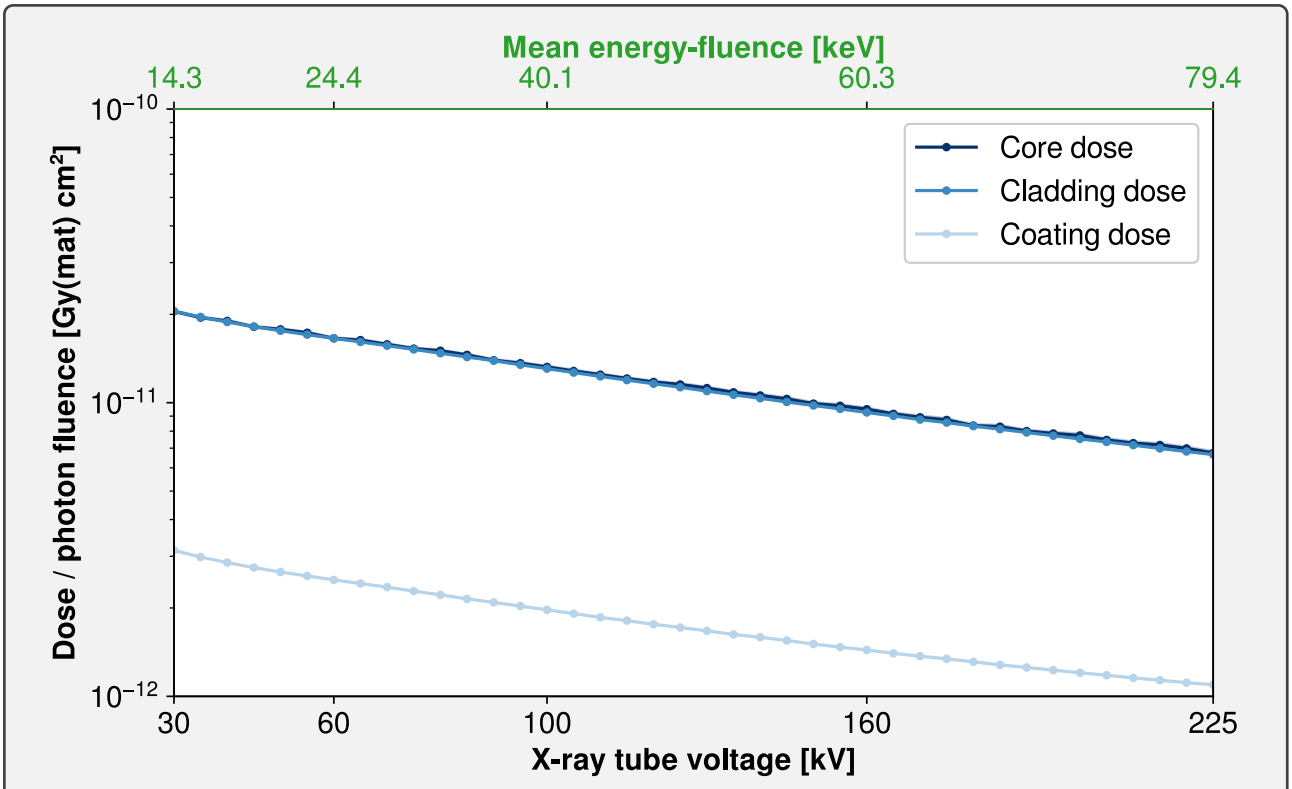

Figure 4.12. – Geant4 simulated dose/fluence of the different components of fiber **A** irradiated under X-rays with different tube voltages. Corresponding mean energy-fluences are given for reference.

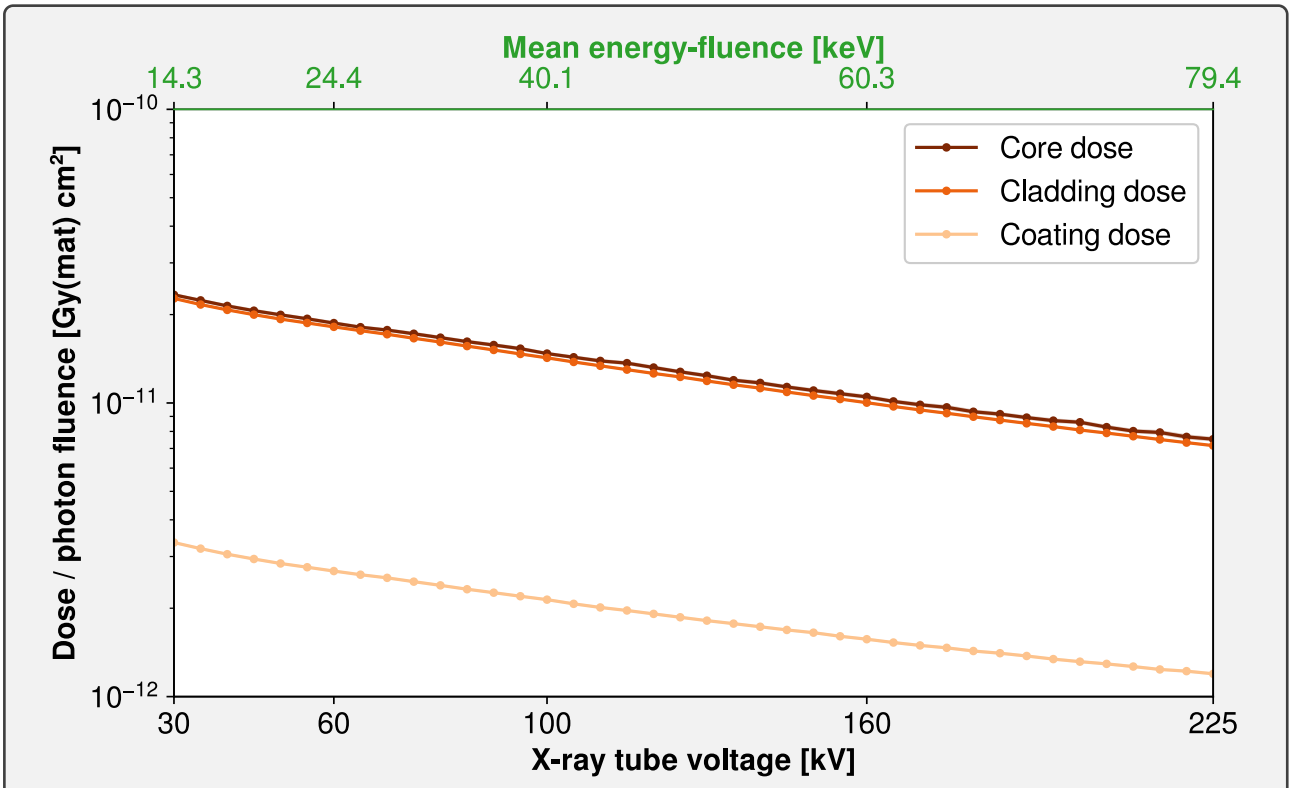

Figure 4.13. – Geant4 simulated dose/fluence of the different components of fiber **B** irradiated under X-rays with different tube voltages. Corresponding mean energy-fluences are given for reference.

4.2.3. Sensitivity of optical fibers to the features of X-ray spectra

To understand the comparative influence of the particular features of X-ray spectra on the dose deposition in optical fibers, as well as the influence of X-ray tube voltage on these processes, a combined simulation approach was performed using Geant4 and SpekPy.

First, the photon dose/fluence spectrum in the core of both fibers **A** and **B** was simulated using Geant4 through the simulation procedure described in **Section 4.1.1**, for monoenergetic photons between 1 keV and 225 keV with a linear step of 0.1 keV. The resulting data are similar to **Figure 4.4**, with a much increased energy resolution within the considered range.

Second, the X-ray differential fluence rate spectrum was calculated by SpekPy from the tube parameters of the LabHX facility, with an energy resolution of 0.1 keV, so that the energy values match exactly the Geant4 simulations described here above. These spectra were generated at the position $y = 0$, $z = 42.5$ cm, and an x coordinate corresponding to the position of the beam maximum according to the simulations of anode heel effect performed in **Section 4.2.1**.

Finally, the Geant4 dose/fluence spectrum was multiplied by the SpekPy differential fluence rate spectrum for each tube voltage, resulting in the differential dose rate spectra shown in **Figure 4.14** for fiber **A**, and in **Figure 4.16** for fiber **B**. These spectra illustrate the efficiency of each point of the X-ray energy spectrum to deposit dose in the core of an optical fiber of type **B**.

The influence of tube voltage is clearly distinguishable within the five investigated values between 30 kV and 225 kV. Increase of the tube voltage not only causes an extension of the photon energy spectrum toward larger energies, but also result in a significant increase of the amount of deposited dose at lower energies; this behavior is mainly due to the overall increase of fluence spectrum when increasing tube voltage, as illustrated previously in **Figure 4.10**. Therefore, increasing tube voltage, while ensuring that the irradiated sample stays in a position corresponding to the beam maximum at this voltage, generally increases the dose deposited in the optical fiber sample.

The characteristic X-ray emission lines of tungsten also stand out prominently in these data, and their relative influence, compared to the background bremsstrahlung spectrum of the X-ray tube, can be evaluated in the stacked bar plots displayed in **Figure 4.15** for fiber **A** and in **Figure 4.17** for fiber **B**. These graphs illustrate the overwhelming importance of the low-energy part of the X-ray spectrum on the effective dose deposition in the optical fiber core, as well as the importance of the L characteristic lines, with 48 % (at 30 kV) to 58 % (at 160 kV) of the total deposited dose being solely performed by $L\alpha$ and $L\beta$ lines.

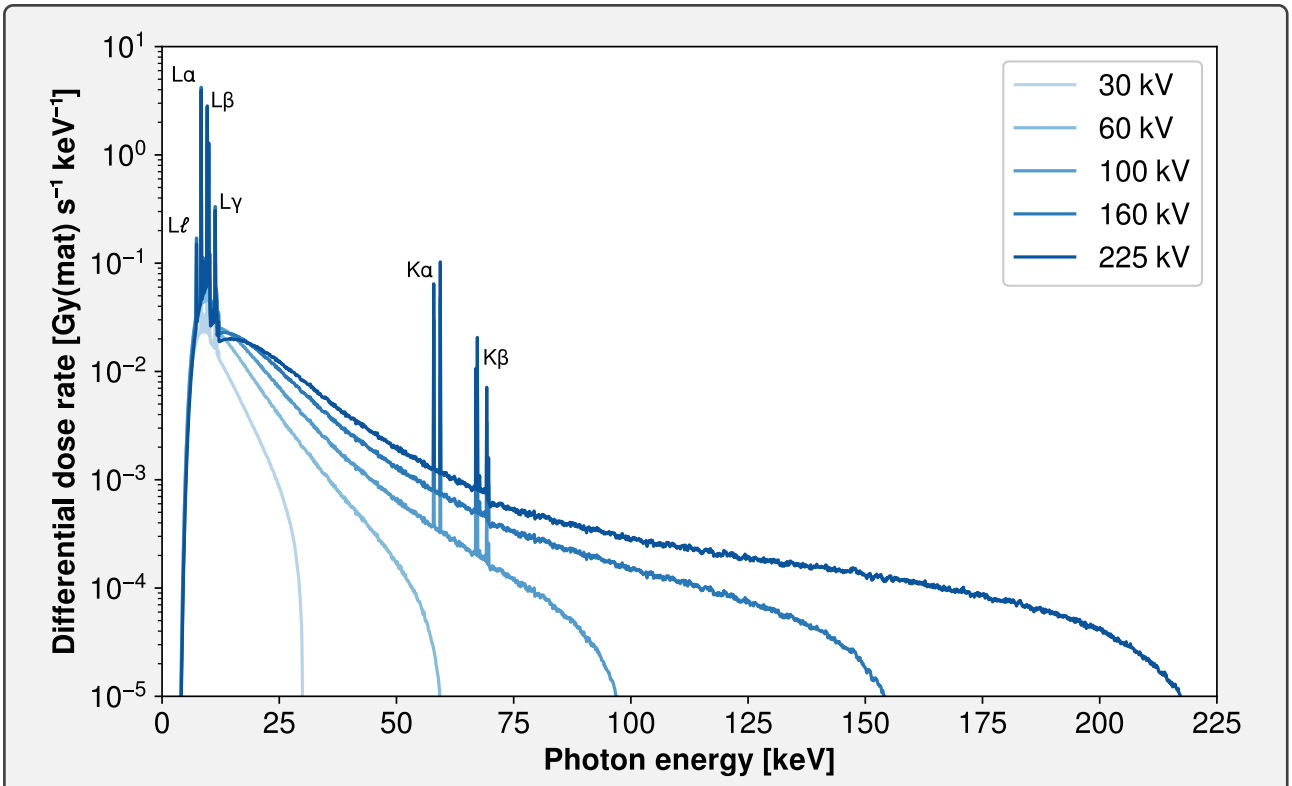

Figure 4.14. – Simulated differential dose response spectrum in the core of fiber **A** irradiated under X-ray with different tube voltages. The main tungsten characteristic X-ray lines are also annotated.

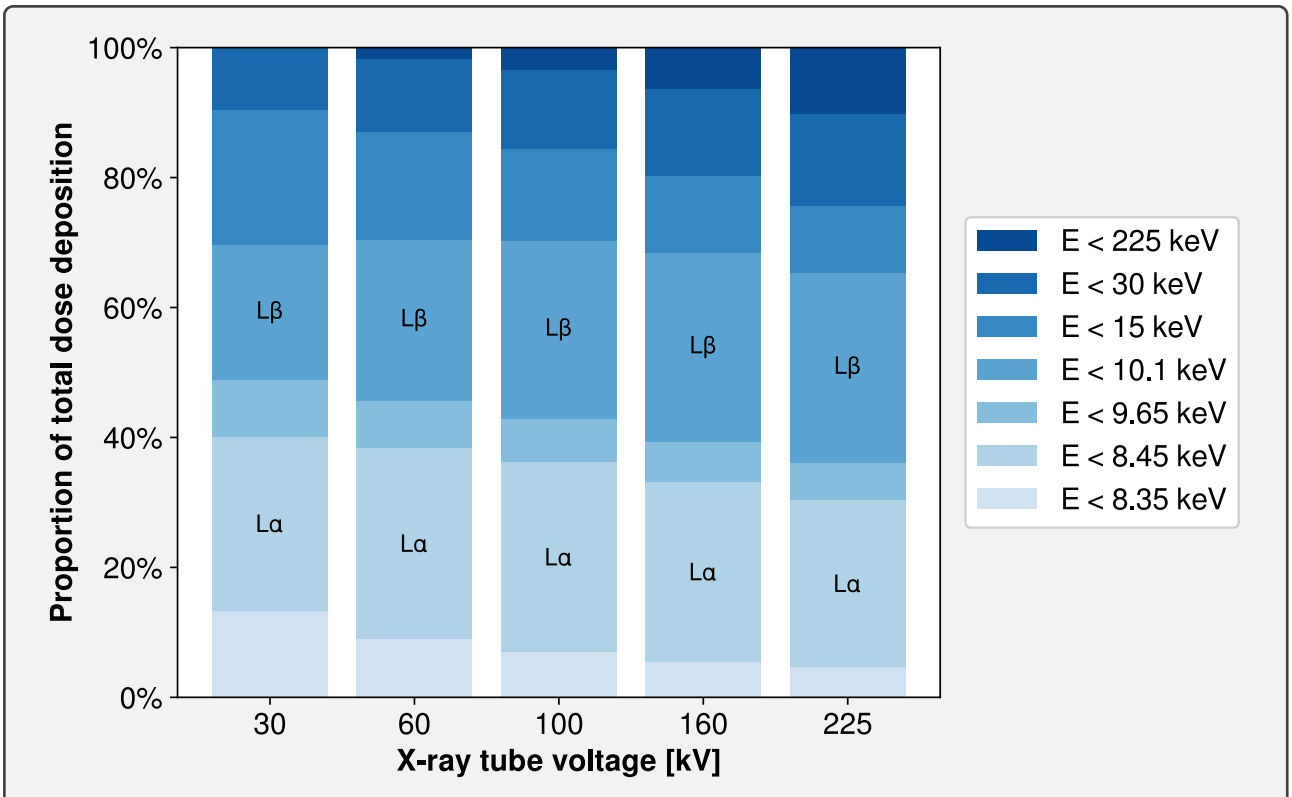

Figure 4.15. – Stacked bar plot of the simulated cumulative dose response in the core of fiber **A** irradiated under X-rays with different tube voltages. Contributions due only to tungsten characteristic X-ray lines $L\alpha$ and $L\beta$ are also annotated.

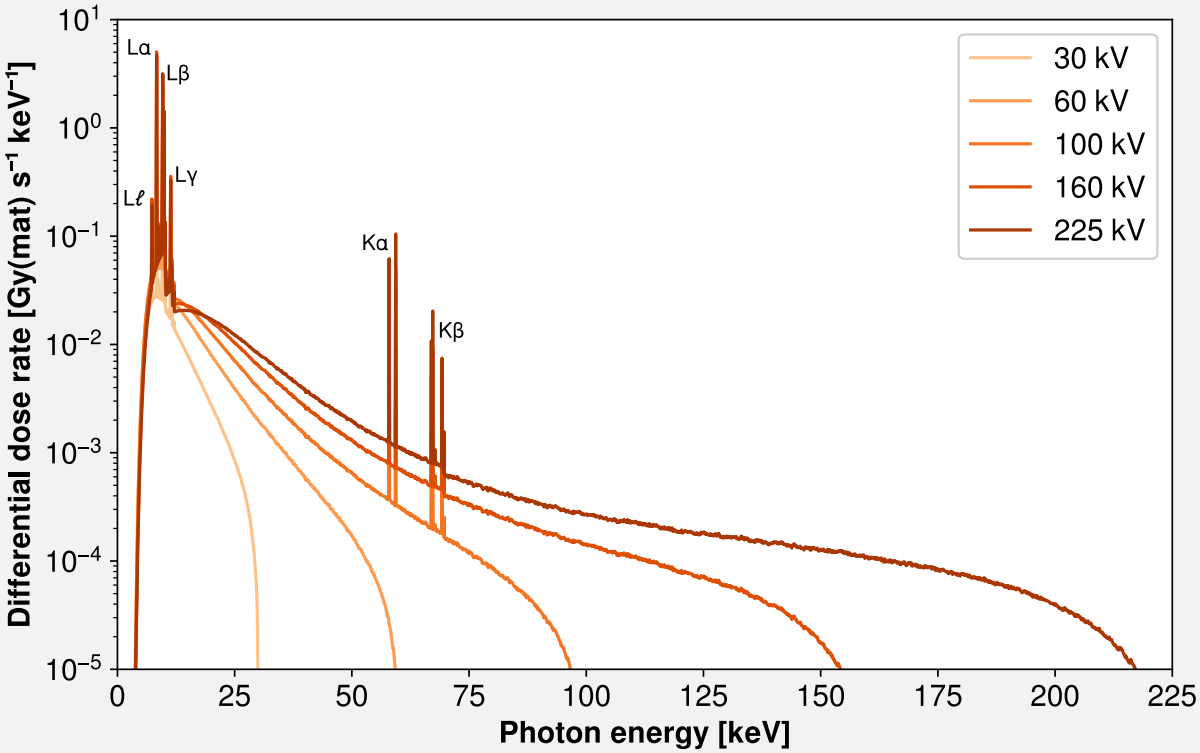

Figure 4.16. – Simulated differential dose response spectrum of in the core fiber **B** irradiated under X-ray with different tube voltages. The main tungsten characteristic X-ray lines are also annotated.

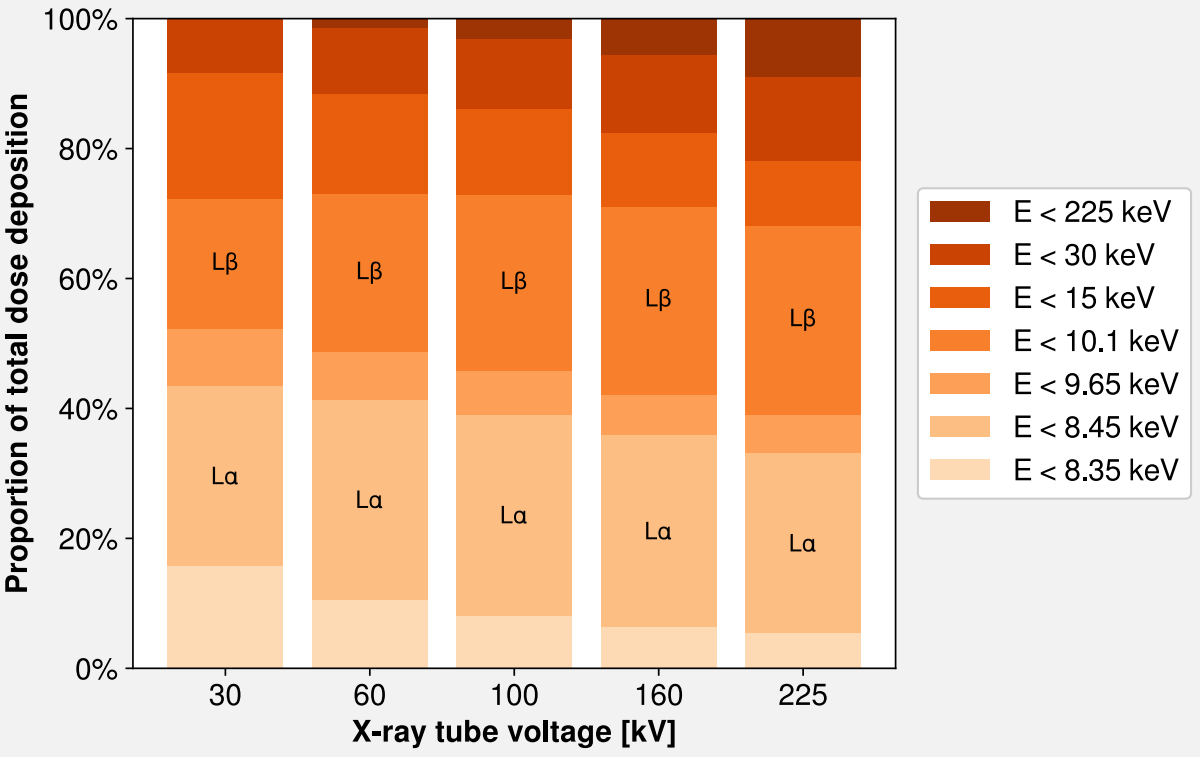

Figure 4.17. – Stacked bar plot of the simulated cumulative dose response in the core of fiber **B** irradiated under X-rays with different tube voltages. Contributions due only to tungsten characteristic X-ray lines $L\alpha$ and $L\beta$ are also annotated.

4.2.4. Prediction of the dose rate by simulation

To evaluate the ability of simulation tools to predict the dose received by optical fibers in X-ray irradiations at different tube voltages, simulation data presented in the previous sections were combined to evaluate the dose rate received by optical fiber samples, and compared with additional experimental data on phosphorus-doped optical fiber RIA.

Although these experimental data were strictly identical to the ones used in [392] (**Article A.3**), all simulation data in this chapter were recalculated with a more recent version of SpekPy, which results in slightly different values from the mentioned publication.

Simulation data

Multiplying the simulated dose/fluence in the core of fiber **A** (cf. **Figure 4.12**) by the corresponding simulated fluence rate (cf. **Figure 4.11**) at the same position, for each X-ray tube voltage between 30 kV and 225 kV, results in a dose rate estimated by simulation.

However, to compensate for a possible deviation between fluence rates simulated by SpekPy and the ones actually delivered by the LabHX irradiator, additional measurements were performed with an ionization chamber and compared with water kerma simulation (cf. **Article A.3**). These measurements resulted in a factor $k_{\text{simul}} = 0.84(\pm 10\,\%)$ between observed and simulated fluence rates.

RIA data

Additional RIA experiments were performed to obtain the experimental dose rates observed on a phosphorus-doped optical fiber. For this purpose, 1 m-long samples of fiber **A** were irradiated in the LabHX facility at five tube voltages between 30 kV and 225 kV.

The samples were coiled in flat spirals of radius 5 cm and centered at the location (x_{max}, $y = 0$, $z = 42.5$ cm), with x_{max} the x position of the beam maximum at the corresponding voltage (cf. **Section 4.2.1**). More details of this experimental setup are given in **Article A.3**.

Each sample was irradiated for a duration of 900 s, and RIA was measured at 1532 nm and 1550 nm using laser and photodiode setups. The resulting RIA data as a function of time, for each investigated tube voltage, are shown in **Figure 4.18**.

By fitting a linear function to the RIA data acquired in the first 100 s, the corresponding RIA rates (in $\text{dB}\,\text{m}^{-1}\,\text{s}^{-1}$) can be extracted for each investigated wavelength and voltage. These values can be converted to a dose rate, using a calibration factor $k_{\text{calib}} = 250\,\text{Gy(fiber)}\,\text{dB}^{-1}\,\text{m}$, determined from the value of $4.0\,\text{dB}\,\text{km}^{-1}\,\text{Gy}(\text{SiO}_2)^{-1}$ cited the literature for a same type of optical fiber under γ rays with comparable doses [395].

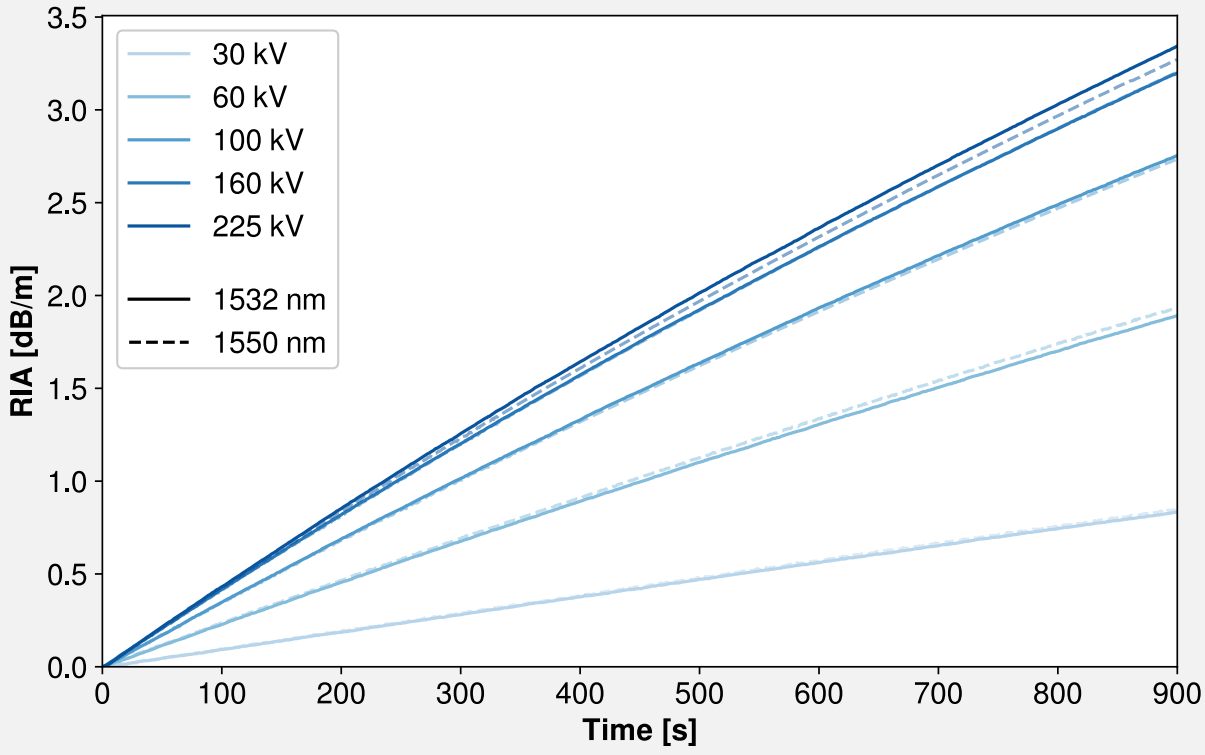

Figure 4.18. – Evolution of fiber **A** RIA at 1532 nm and 1550 nm according to irradiation time, at different X-ray tube voltages.

Ionization chamber data

A second set of experiments involved a PTW 23344 ionization chamber (cf. **Section 2.3.1**), placed at a position corresponding to the center of the irradiated fiber sample at each investigated voltage.

The dose rate measured by this device, given in $\mathrm{Gy(H_2O)/s}$, was compared to the one obtained using fiber RIA data described here above, and a linear relation was observed between these two quantities, with a constant scaling factor $k_{\mathrm{ioni}} = 2.14\,\mathrm{Gy(fiber)/Gy(H_2O)}$ for all investigated voltages.

Comparison between simulated and experimental dose rates

A summary of the various dose rate data presented here above is shown in **Figure 4.19**, which compares simulated dose rates at different X-ray tube voltages with experimental results. By taking into account the various scaling factors k_{simul}, k_{calib} and k_{ioni} introduced previously, these results show globally a good agreement.

Experimental data stand in excellent agreement between each other, with an insignificant difference between data acquired at 1532 nm and 1550 nm that matches the characteristics of the P_1 defect absorption band (cf. **Section 3.2.5** and **Article A.3**). The fact that ionization chamber data display the same absolute values is caused by the calculation of k_{ioni} as described here above, but superposition

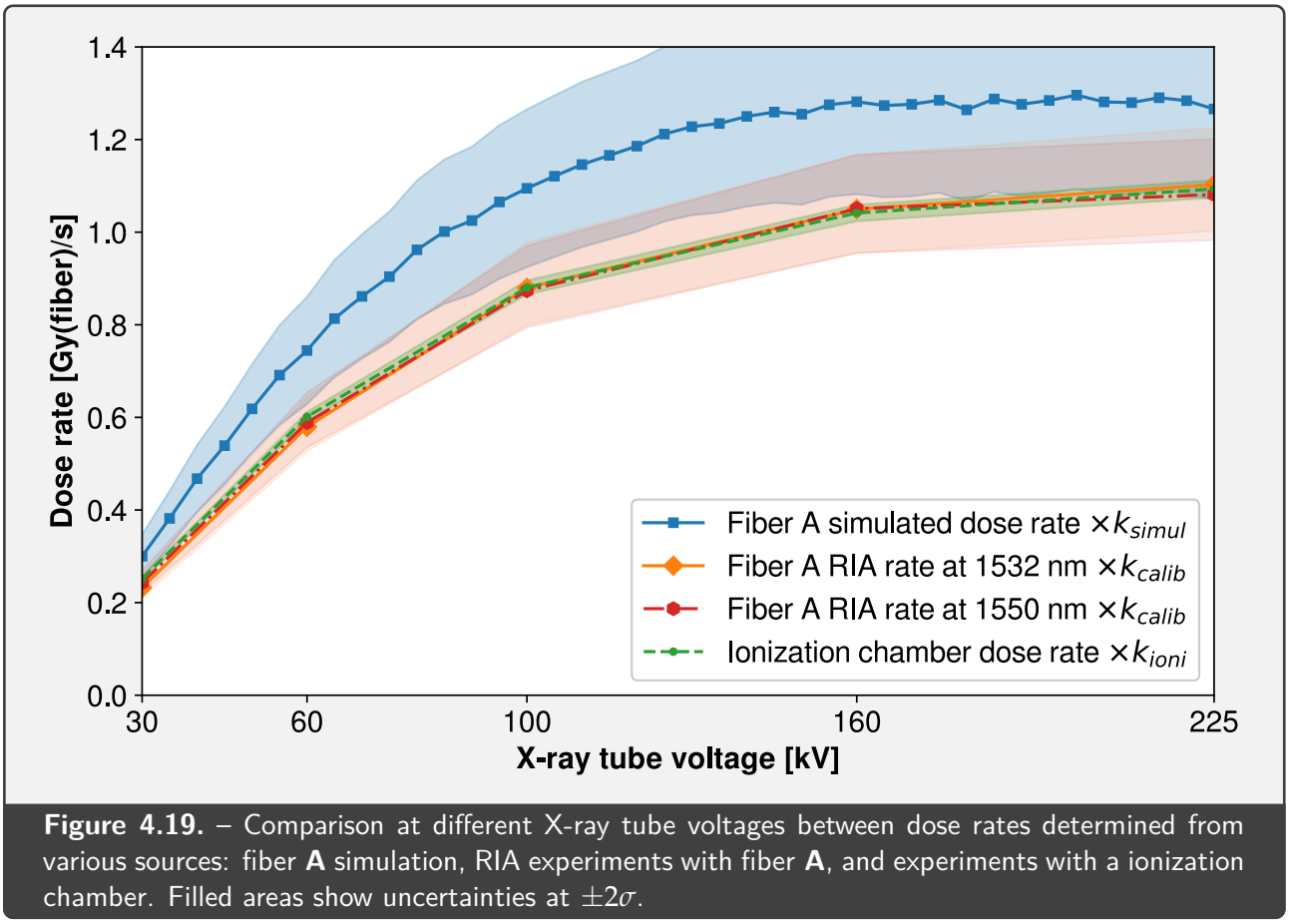

Figure 4.19. – Comparison at different X-ray tube voltages between dose rates determined from various sources: fiber **A** simulation, RIA experiments with fiber **A**, and experiments with a ionization chamber. Filled areas show uncertainties at $\pm 2\sigma$.

of these data show that the dose rate measured by this device closely follows the same evolution as the optical fiber RIA.

Compared to these experimental data, the simulated dose rates, while globally standing in the same order of magnitude and following the same evolution with voltage as experimental data, appear however to systematically overestimate the experimental dose rate by a factor ~1.25. At voltages greater than 160 kV, the simulated evolution of the dose rates also appears to reach a plateau, while the experimental data still show a slight increase. This difference could be explained by the uncertainties on sample positioning evidenced in **Article A.3**.

Multiple reasons have been proposed to explain these systematic deviations between simulated and experimental, such as uncertainties on the positioning, dimensions and composition of the samples, as well as of the specifications of the X-ray tube. In medical dosimetry, the use of correction factors for compensating various sources of experimental or environmental uncertainties is very common [606, 607], and such an approach could therefore lead to improvement of the present analysis.

4.3. Summary of the simulation part

English

As absorbed dose is linked to the observable effects of radiation on optical fibers, the simulation of this quantity in various environments enables further understanding of the processes involved, as well as possible predictions of irradiation results.

Monte Carlo simulations, performed with Geant4 on monoenergetic photons, protons, electrons and neutrons from 1 keV to 10 GeV, have quantified the sensitivity of the core of fibers **A** and **B**. Dose deposition by photons between 10 keV and 1 MeV has also been reviewed in more detail, with a great influence of the dimensions of fiber components on the dose absorbed by the core.

Simulations of dose deposition in X-ray irradiators are also possible with the additional X-ray spectrum and fluence data provided by SpekPy. Such simulations have highlighted an overwhelming influence of the low-energy part of the X-ray spectrum on dose deposition in optical fiber cores, as well as a major contribution of the *L* characteristic lines in the case of irradiation with a tungsten anode. These simulations can predict the dose rate received by optical fiber samples at different X-ray tube voltages from 30 kV to 225 kV, although comparison with experimental data highlight that this dose rate is overestimated by our simulation with a factor ~1.25.

Français

Étant donné que la dose absorbée est liée aux effets observables des radiations sur les fibres optiques, la simulation de cette grandeur dans divers environnements permet une meilleure compréhension des procédés mis en œuvre, ainsi que de possibles prédictions des résultats d'irradiation.

Les simulations Monte-Carlo, réalisées avec Geant4 sur des photons, protons, électrons et neutrons monoénergétiques de 1 keV à 10 GeV, ont quantifié la sensibilité du cœur des fibres **A** et **B**. Le dépôt de dose par des photons entre 10 keV et 1 MeV a également été revu plus en détail, avec une grande influence des dimensions des composants de la fibre sur la dose absorbée par le cœur.

La simulation du dépôt de dose dans des irradiateurs à rayons X est également possible grâce aux données supplémentaires de spectre X et de fluence fournies par SpekPy. Ces simulations ont mis en évidence une influence dominante de la partie basse énergie du spectre de rayons X sur le dépôt de dose dans le cœur des fibres optiques, ainsi qu'une contribution majeure des raies caractéristiques *L* dans le cas d'irradiations avec une anode au tungstène. Ces simulations peuvent prédire le débit de dose reçu par des échantillons de fibre optique à différentes tensions de tube à rayons X de 30 kV à 225 kV, bien que la comparaison avec les données expérimentales mette en évidence que ce débit de dose est surestimé par notre simulation d'un facteur de ~1,25.

Chapter 5:

Conclusion and perspectives

5. Conclusion and perspectives

Contents of this chapter

5.1. Interest of optical fiber-based dosimetry for space applications

The omnipresence of radiation in all aspects of space missions, from the terrestrial orbit to interplanetrary exploration (cf. **Section 1.1**), has induced the need for more research on the characterization of the space radiation environment, as well as toward the design of suitable devices for operation in these conditions.

Dosimetry technologies for space applications stand at the junction of these two needs, and require both a satisfactory accuracy when measuring radiation of different types and energies, while also being able to operate in the harsh conditions of the space environment, including, between many other factors, exposition to the radiation themselves.

Optical fibers, through various radiation-induced phenomena (cf. **Section 1.2.2**), have been demonstrated to be suitable sensitive elements for radiation sensing and measurement (cf. **Section 1.2.4**), not only as an alternative to existing dosimetry technologies, but also offering new possibilies such as distributed sensing (cf. **Section 1.3**) to enable dose measurement at virtually any given segment of an optical fiber.

Such distributed dosimetry systems, originating from the use of OTDR devices to measure RIA along optical fibers, were first introduced at the turn of the 21st century, and are still developed nowadays, especially in the context of radiation monitoring in large accelerator facilities (cf. **Section 1.4**).

Continuous development of OTDR devices since the introduction of this technology in the 1970s [608] has enabled design and commercialization of miniaturized, embedded devices that offer greatly reduced mass and volume footprints while providing similar functionalities (cf. **Section 2.2**), although with potentially reduced performance.

Combination of these embedded devices with radiosensitive fibers, which dimensions can also be further reduced compared to standard telecom-size fibers (cf. **Section 2.1**), offer the opportunity to design distributed dosimetry systems fit for the basic volume and mass requirements of space applications. However, prior to enabling the testing of such systems in space missions, their performance need to evaluated, both regarding their capacity to accurately perform dose measurement with the variety of particle types and energies that constitute the space radiation environment, and regarding their ability to operate safely within this same environment.

5.2. Experimental characterization of the dosimetry system

Both investigated devices – Micro and Nano iOTDRs – were first evaluated for their metrological properties, in the absence of radiation, to assess the capabilities and limitations of these embedded devices to perform attenuation measurements on optical fibers (cf. **Section 3.1**). A first limitation is the noise floor of these devices, preventing to perform accurate measurements below a threshold estimated at $-6.5\,\mathrm{dB}$ for both types of devices, when operating at their minimum pulse width and scan time (cf. **Section 3.1.3**). Then, their pure metrological performance were evaluated through statistical analysis of ~1200 similar measurements for each parameter set, yielding a measurement accuracy on the order of $\pm 5\,\%$ for both devices at their minimum scan time and pulse width (cf. **Section 3.1.4**).

The pulse width parameter was shown to be very important, both in terms of measurement accuracy – with the higher value of 100 ns being the most accurate in these experiments – and because of its influence on the spatial resolution, increased at lower pulse widths. Whereas the theoretical resolution is on the order of 1 m for a pulse width of 10 ns, the analysis performed with different sample lengths in **Section 3.1.5** showed measurement accuracy on such very short segments to be extremely low; acceptable uncertainties are obtained starting from a sampling length of 10 m, with $\pm 25\,\%$ accuracy, up to 50 m where the accuracy of $\pm 5\,\%$ matches the one of the whole available segment.

Influence of ambient temperature was also evaluated for both devices, between $-5\,^{\circ}\mathrm{C}$ and $40\,^{\circ}\mathrm{C}$. While the Micro iOTDR measurements exhibited a good temperature stability, with only $\pm 1.2\,\%$ deviation over the investigated temperature range, the Nano iOTDR was shown to be more sensitive with $\pm 12\,\%$ deviation in the same range, along with a non-monotonic temperature dependence. In both cases, the resulting OTDR traces were also shown to suffer a vertical shift correlated to the temperature, which could in unfavorable cases lower even further the dynamic range of these devices.

γ ray radiation tests were performed for dosimetry systems based on both devices, with similar setups involving irradiation at a controlled dose rate of a segment of radiosensitive fiber, as well as of the interrogating device itself. In both cases, the irradiated devices performed without noticeable failure during the several months of irradiation, totalizing a TID of $81.05\,\mathrm{Gy}(\mathrm{SiO_2})$ for Micro iOTDR and $106.20\,\mathrm{Gy}(\mathrm{SiO_2})$ for Nano iOTDR.

Real-time measurements performed by these devices on the irradiated fiber samples showed a linear evolution of RIA, with a coefficient of ~4.9 dB km^{-1} Gy(SiO$_2$)$^{-1}$ measured by Micro iOTDR on fiber **B** irradiated up to 12.97 Gy(SiO$_2$) (cf. **Section 3.2.2**), and ~3.8 dB km^{-1} Gy(SiO$_2$)$^{-1}$ measured by Nano iOTDR on fiber **A** irradiated up to 40.16 Gy(SiO$_2$). Additional spectral measurements showed that the RIA measured by these devices operating at 1610 nm was caused by the absorption band of the P_1 defects of phosphorus-doped optical fibers (cf. **Section 3.2.5**).

The minimum detectable dose in these γ ray irradiations was 10^{-3} Gy(SiO$_2$) with the Micro iOTDR interrogating 200 m of fiber **B** at a scan time of 180 s, and 3×10^{-2} Gy(SiO$_2$) with the Nano iOTDR interrogating 100 m of fiber **A** at a scan time of 10 s.

The range of investigated doses and doses rates was extended by complementary X-ray irradiations of the fiber samples, up to 340.6 Gy(SiO$_2$). These results were in good accordance with the ones obtained under γ rays, despite the reduced linearity of RIA at high dose levels (cf. **Section 3.3.5**).

Finally, SEE testing of the embedded OTDRs, performed with protons of 355 MeV and 480 MeV, has highlighted the capability of these devices to operate reliably under radiation. In the case of the Micro iOTDR irradiated with 355 MeV protons, no SELs were observed up to a fluence of 2.921×10^{10} cm^{-2}, and the median fluence for occurrence of a SEFI was ~10^8 cm^{-2}, which corresponds to respectively ~8.95 yr and ~11.5 d in LEO.

5.3. Simulation insights on the radiation response of optical fibers

Monte Carlo simulations of the dose deposited by photons were performed for both types of fiber, for photon energies from 1 keV to 10 GeV (cf. **Section 4.1.2**). These results showed the influence of the layered geometry of optical fibers, preventing photons of energy lesser than 10 keV to reach the core, and causing photons of energy greater than 200 keV to release secondary electrons of too high a velocity to entirely deposit their energy in the core area, given its small dimensions.

Comparison between fibers **A** and **B** showed similar photon sensitivities between 10 keV and 200 keV, but a higher sensitivity of fiber **A** for higher photon energies, with a factor of 1.7 at 1.25 MeV. This theoretical difference is only due to the differing dimensions between both fibers, as all other parameters were kept identical in the simulations; noticeably, the phosphorus concentration is the same in both fiber cores.

However, the higher experimental sensitivity of fiber **B** observed with ^{60}Co γ ray results obtained at this same mean energy has to be explained by additional parameters that counterbalance its geometrical disadvantage. A possible explanation can be linked to different concentration of P_1 defects precursors between both fibers, due to different manufacturing and drawing conditions. Similar differences between phosphorus-doped fibers of same specifications were already reported in [387].

Generalization of these simulation for protons, electrons and neutrons in the same energy range of 1 keV to 10 GeV (cf. **Section 4.1.4**) demonstrated a higher sensitivity of both fiber types to charged particles, and especially to protons at energies higher than 5 MeV. However at lower energies, the layered geometry of optical fibers also prevent these charged particles to reach their core. In this regard, the lower dimensions of fiber **B** enable detection of charged particles of a slightly lower energy than fiber **A**, with cutoff values on the order of 100 keV for electrons and 2.5 MeV for protons.

Simulation of dose deposition by X-rays (cf. **Section 4.2**) showed an overwhelming influence of the low-energy part of the photon spectrum generated by X-ray tubes in the dose deposition in the core of optical fibers. The characteristic X-ray emission lines $L\alpha$ and $L\beta$ of tungsten, located respectively at 8.4 keV and 9.7 keV [511], account for ~50 % of the deposited dose at all investigated tube voltages between 30 kV and 225 kV. Increase of this tube voltage was shown to increase the fluence over the whole energy spectrum, effectively causing an increase of dose deposition in the fiber, but also to tilt the X-ray beam angle due to its influence on the anode heel effect.

Combining Monte Carlo simulations and X-ray spectrum and fluence data provided by SpekPy, simulations can predict, to an extent, the actual dose rate on an optical fiber sample irradiated under X-rays at tube voltages between 30 keV and 225 keV (cf. **Section 4.2.4**). In their current state, however, these simulations still overestimate the dose rate determined experimentally by a factor ~1.25.

5.4. Toward distributed dosimetry for space applications

The experimental and simulation work performed in this thesis demonstrated the potential of distributed dosimetry systems including embedded OTDR devices and phosphorus-doped fibers to perform accurate and reliable dose measurement in a range of doses and dose rates suitable for space missions. Radiosensitive fibers of reduced dimensions (type **B**) were also shown to deliver dosimetric performance on par with standard-sized fibers (type **A**) previously characterized and qualified for distributed dosimetry in ground applications [395].

Whereas the radiation tests performed in the course of this thesis were only performed with photons, results reported in the literature with similar phosphorus-doped fibers subjected to various types of particles and energies (cf. **Section 1.2.4**) indicate that this technology can be suitable for dosimetry in the space radiation environment.

These first results can be consolidated with additional experimental data involving different types of particles. On the topic of simulation, a complementary approach would be to shift from the component simulation explored in this thesis to more general, system-oriented simulations featuring the different electronic components of the embedded OTDRs and their effects on the dosimetry system according to TID or SEE. In such complex geometries offered by electronic systems, simulation of

omnidirectional fluxes, which better matches the actual space radiation environment, is another improvement that could be considered.

Apart from radiation and temperature, other constraints of the space environment need to be further assessed, such as the ability of these systems to operate in vacuum, both regarding their outgassing properties and their ability to regulate heat when operating in the absence of air, conditions for which these commercial, off-the-shelf devices were not originally designed for.

Overall, distributed dosimetry systems based on embedded OTDRs offer promising applications for optical fiber-based space dosimetry, which has also seen recent developments toward the high-sensitivity measurement of radiation inside the International Space Station [609].

Bibliography

[1] J. J. Thomson, "Cathode Rays," *The London, Edinburgh, and Dublin Philosophical Magazine and Journal of Science*, vol. 44, no. 269, pp. 293–316, Oct. 1, 1897, ISSN: 1941-5982. DOI: 10.1080/14786449708621070.

[2] W. C. Röntgen, "On a New Kind of Rays," *Science*, vol. 3, no. 59, pp. 227–231, Feb. 14, 1896. DOI: 10.1126/science.3.59.227.

[3] B. Lindell, "A History of Radiation Protection," *Radiation Protection Dosimetry*, vol. 68, no. 1-2, pp. 83–95, Nov. 1, 1996, ISSN: 0144-8420. DOI: 10.1093/oxfordjournals.rpd.a031856.

[4] J. M. Slater, "From X-Rays to Ion Beams: A Short History of Radiation Therapy," in *Ion Beam Therapy: Fundamentals, Technology, Clinical Applications*, ser. Biological and Medical Physics, Biomedical Engineering, U. Linz, Ed., Berlin, Heidelberg: Springer, 2012, pp. 3–16, ISBN: 978-3-642-21414-1. DOI: 10.1007/978-3-642-21414-1_1.

[5] M. Walter, "From the Discovery of Radioactivity to the First Accelerator Experiments," in *From Ultra Rays to Astroparticles: A Historical Introduction to Astroparticle Physics*, B. Falkenburg and W. Rhode, Eds., Dordrecht: Springer Netherlands, 2012, pp. 17–47, ISBN: 978-94-007-5422-5. DOI: 10.1007/978-94-007-5422-5_2.

[6] V. L. Ginzburg, "Cosmic ray astrophysics (history and general review)," *Physics-Uspekhi*, vol. 39, no. 2, p. 155, Feb. 28, 1996, ISSN: 1063-7869. DOI: 10.1070/PU1996v039n02ABEH000132.

[7] K. Birkeland, *Recherches Sur Les Taches Du Soleil Et Leur Origine*. 1899.

[8] L. Vegard, "The Radiation Producing Aurora Borealis," *Nature*, vol. 86, no. 2163, pp. 212–213, 2163 Apr. 1911, ISSN: 1476-4687. DOI: 10.1038/086212a0.

[9] V. Hess, "On the Observations of the Penetrating Radiation during Seven Balloon Flights," 1912. DOI: 10.48550/arXiv.1808.02927.

[10] R. A. Millikan and G. H. Cameron, "High Frequency Rays of Cosmic Origin III. Measurements in Snow-Fed Lakes at High Altitudes," *Physical Review*, vol. 28, no. 5, pp. 851–868, Nov. 1, 1926. DOI: 10.1103/PhysRev.28.851.

[11] J. A. Van Allen and H. E. Tatel, "The Cosmic-Ray Counting Rate of a Single Geiger Counter from Ground Level to 161 Kilometers Altitude," *Physical Review*, vol. 73, no. 3, pp. 245–251, Feb. 1, 1948. DOI: 10.1103/PhysRev.73.245.

[12] J. A. Van Allen, G. H. Ludwig, E. C. Ray, and C. E. McIlwain, "Observation of High Intensity Radiation by Satellites 1958 Alpha and Gamma," *Journal of Jet Propulsion*, vol. 28, no. 9, pp. 588–592, 1958. DOI: 10.2514/8.7396.

[13] W. K. Sinclair, "History of the development of radiation protection standards for space activities," National Council on Radiation Protection and Measurements, Bethesda, MD (United States), CONF-960562-, Apr. 30, 1997.

[14] J. Barth, C. Dyer, and E. Stassinopoulos, "Space, atmospheric, and terrestrial radiation environments," *IEEE Transactions on Nuclear Science*, vol. 50, no. 3, pp. 466–482, Jun. 2003, ISSN: 1558-1578. DOI: 10.1109/TNS.2003.813131.

[15] J.-C. Boudenot, "Radiation Space Environment," in *Radiation Effects on Embedded Systems*, R. Velazco, P. Fouillat, and R. Reis, Eds., Dordrecht: Springer Netherlands, 2007, pp. 1–9, ISBN: 978-1-4020-5646-8. DOI: 10.1007/978-1-4020-5646-8_1.

[16] M. Bertolotti, "The Origin of Cosmic Rays," in *Celestial Messengers: Cosmic Rays: The Story of a Scientific Adventure*, ser. Astronomers' Universe, M. Bertolotti, Ed., Berlin, Heidelberg: Springer, 2013, pp. 291–317, ISBN: 978-3-642-28371-0. DOI: 10.1007/978-3-642-28371-0_13.

[17] T. Abu-Zayyad *et al.*, "The prototype high-resolution Fly's Eye cosmic ray detector," *Nuclear Instruments and Methods in Physics Research Section A: Accelerators, Spectrometers, Detectors and Associated Equipment*, vol. 450, no. 2, pp. 253–269, Aug. 11, 2000, ISSN: 0168-9002. DOI: 10.1016/S0168-9002(00)00307-7.

[18] M. Bertolotti, "The Confirmation: Millikan and the Birth Cry of Created Atoms," in *Celestial Messengers: Cosmic Rays: The Story of a Scientific Adventure*, ser. Astronomers' Universe, M. Bertolotti, Ed., Berlin, Heidelberg: Springer, 2013, pp. 45–59, ISBN: 978-3-642-28371-0. DOI: 10.1007/978-3-642-28371-0_3.

[19] E. Fermi, "On the Origin of the Cosmic Radiation," *Physical Review*, vol. 75, no. 8, pp. 1169–1174, Apr. 15, 1949. DOI: 10.1103/PhysRev.75.1169.

[20] P. Blasi, "The origin of galactic cosmic rays," *The Astronomy and Astrophysics Review*, vol. 21, no. 1, p. 70, Nov. 5, 2013, ISSN: 1432-0754. DOI: 10.1007/s00159-013-0070-7.

[21] D. Gaggero, "Cosmic Ray Diffusion in the Galaxy," in *Cosmic Ray Diffusion in the Galaxy and Diffuse Gamma Emission*, ser. Springer Theses, D. Gaggero, Ed., Berlin, Heidelberg: Springer, 2012, pp. 7–28, ISBN: 978-3-642-29949-0. DOI: 10.1007/978-3-642-29949-0_2.

[22] E. R. Benton and E. V. Benton, "Space radiation dosimetry in low-Earth orbit and beyond," *Nuclear Instruments and Methods in Physics Research Section B: Beam Interactions with Materials and Atoms*, Advanced Topics in Solid State Dosimetry, vol. 184, no. 1, pp. 255–294, Sep. 1, 2001, ISSN: 0168-583X. DOI: 10.1016/S0168-583X(01)00748-0.

[23] D. Gaggero, "Introduction," in *Cosmic Ray Diffusion in the Galaxy and Diffuse Gamma Emission*, ser. Springer Theses, D. Gaggero, Ed., Berlin, Heidelberg: Springer, 2012, pp. 1–5, ISBN: 978-3-642-29949-0. DOI: 10.1007/978-3-642-29949-0_1.

[24] D. Gaggero, "Diffuse Gamma Ray Emission from the Galaxy," in *Cosmic Ray Diffusion in the Galaxy and Diffuse Gamma Emission*, ser. Springer Theses, D. Gaggero, Ed., Berlin, Heidelberg: Springer, 2012, pp. 111–126, ISBN: 978-3-642-29949-0. DOI: 10.1007/978-3-642-29949-0_6.

[25] A. A. Abdo *et al.*, "Fermi/Large Area Telescope Bright Gamma-Ray Source List," *The Astrophysical Journal Supplement Series*, vol. 183, no. 1, p. 46, Jun. 2009, ISSN: 0067-0049. DOI: 10.1088/0067-0049/183/1/46.

[26] D. J. Bird *et al.*, "Detection of a Cosmic Ray with Measured Energy Well beyond the Expected Spectral Cutoff due to Cosmic Microwave Radiation," *The Astrophysical Journal*, vol. 441, p. 144, Mar. 1995, ISSN: 0004-637X. DOI: 10.1086/175344.

[27] M. A. Xapsos, C. Stauffer, T. Jordan, J. L. Barth, and R. A. Mewaldt, "Model for Cumulative Solar Heavy Ion Energy and Linear Energy Transfer Spectra," *IEEE Transactions on Nuclear Science*, vol. 54, no. 6, pp. 1985–1989, Dec. 2007, ISSN: 1558-1578. DOI: 10.1109/TNS.2007.910850.

[28] J. S. George *et al.*, "Elemental Composition And Energy Spectra Of Galactic Cosmic Rays During Solar Cycle 23," *The Astrophysical Journal*, vol. 698, no. 2, p. 1666, Jun. 2009, ISSN: 0004-637X. DOI: 10.1088/0004-637X/698/2/1666.

[29] T. C. Slaba and K. Whitman, "The Badhwar-O'Neill 2020 GCR Model," *Space Weather*, vol. 18, no. 6, e2020SW002456, 2020, ISSN: 1542-7390. DOI: 10.1029/2020SW002456.

[30] A. Tylka *et al.*, "CREME96: A Revision of the Cosmic Ray Effects on Micro-Electronics Code," *IEEE Transactions on Nuclear Science*, vol. 44, no. 6, pp. 2150–2160, Dec. 1997, ISSN: 1558-1578. DOI: 10.1109/23.659030.

[31] J. H. Adams *et al.*, "CRÈME: The 2011 Revision of the Cosmic Ray Effects on Micro-Electronics Code," *IEEE Transactions on Nuclear Science*, vol. 59, no. 6, pp. 3141–3147, Dec. 2012, ISSN: 1558-1578. DOI: 10.1109/TNS.2012.2218831.

[32] P. Goldhagen, J. M. Clem, and J. W. Wilson, "The energy spectrum of cosmic-ray induced neutrons measured on an airplane over a wide range of altitude and latitude," *Radiation Protection Dosimetry*, vol. 110, no. 1-4, pp. 387–392, Aug. 1, 2004, ISSN: 0144-8420. DOI: 10.1093/rpd/nch216.

[33] A. M. Preszler, S. Moon, and R. S. White, "Atmospheric neutrons," *Journal of Geophysical Research (1896-1977)*, vol. 81, no. 25, pp. 4715–4722, 1976, ISSN: 2156-2202. DOI: 10.1029/JA081i025p04715.

[34] U. S. Banerji, V. Goswami, and K. B. Joshi, "Quaternary dating and instrumental development: An overview," *Journal of Asian Earth Sciences: X*, vol. 7, p. 100 091, Jun. 1, 2022, ISSN: 2590-0560. DOI: 10.1016/j.jaesx.2022.100091.

[35] JEDEC, "Measurement And Reporting Of Alpha Particle And Terrestrial Cosmic Ray Induced Soft Errors In Semiconductor Devices," JESD89B, Sep. 2021.

[36] R. Baumann, "The new JEDEC JESD89A Test Standard How is it different than the old one and why should we use it?" In *2007 9th European Conference on Radiation and Its Effects on Components and Systems*, Sep. 2007, pp. 20–20. DOI: 10.1109/RADECS.2007.5205452.

[37] J. Baggio, D. Lambert, V. Ferlet-Cavrois, P. Paillet, C. Marcandella, and O. Duhamel, "Single Event Upsets Induced by 110 MeV Neutrons in Static-RAMs Using Mono-Energetic Neutron Sources," *IEEE Transactions on Nuclear Science*, vol. 54, no. 6, pp. 2149–2155, Dec. 2007, ISSN: 1558-1578. DOI: 10.1109/TNS.2007.910039.

[38] T. Pierog and K. Werner, "EPOS Model and Ultra High Energy Cosmic Rays," *Nuclear Physics B - Proceedings Supplements*, Proceedings of the XV International Symposium on Very High Energy Cosmic Ray Interactions (ISVHECRI 2008), vol. 196, pp. 102–105, Dec. 1, 2009, ISSN: 0920-5632. DOI: 10.1016/j.nuclphysbps.2009.09.017.

[39] H. Cintas *et al.*, "RAMSEES: A Model of the Atmospheric Radiative Environment Based on Geant4 Simulation of Extensive Air Shower," *Aerospace*, vol. 10, no. 3, p. 295, 3 Mar. 2023, ISSN: 2226-4310. DOI: 10.3390/aerospace10030295.

[40] V. M. Fedorov, "Interannual variability of the solar constant," *Solar System Research*, vol. 46, no. 2, pp. 170–176, Apr. 1, 2012, ISSN: 1608-3423. DOI: 10.1134/S0038094612020049.

[41] H. S. Hudson and A. L. MacKinnon, "Chapter 9 - High-Energy Solar Physics," in *The Sun as a Guide to Stellar Physics*, O. Engvold, J.-C. Vial, and A. Skumanich, Eds., Elsevier, Jan. 1, 2019, pp. 301–333, ISBN: 978-0-12-814334-6. DOI: 10.1016/B978-0-12-814334-6.00011-X.

[42] M. Pick and N. Vilmer, "Sixty-five years of solar radioastronomy: Flares, coronal mass ejections and SunEarth connection," *The Astronomy and Astrophysics Review*, vol. 16, no. 1, pp. 1–153, Oct. 1, 2008, ISSN: 1432-0754. DOI: 10.1007/s00159-008-0013-x.

[43] L. Biermann, "Kometenschweife und solare Korpuskularstrahlung," *Zeitschrift fur Astrophysik*, vol. 29, p. 274, Jan. 1, 1951, ISSN: 0372-8331.

[44] E. Parker, "Extension of the solar corona into interplanetary space," *Journal of Geophysical Research (1896-1977)*, vol. 64, no. 11, pp. 1675–1681, 1959, ISSN: 2156-2202. DOI: 10.1029/JZ064i011p01675.

[45] G. L. Withbroe, "The Temperature Structure, Mass, and Energy Flow in the Corona and Inner Solar Wind," *The Astrophysical Journal*, vol. 325, p. 442, Feb. 1, 1988, ISSN: 0004-637X. DOI: 10.1086/166015.

[46] J. L. Barth, "Space and Atmospheric Environments: From Low Earth Orbits to Deep Space," in *Protection of Materials and Structures from Space Environment*, J. I. Kleiman and Z. Iskanderova, Eds., ser. Space Technology Proceedings, Dordrecht: Springer Netherlands, 2003, pp. 7–29, ISBN: 978-1-4020-2595-2. DOI: 10.1007/1-4020-2595-5_2.

[47] O. Cohen, "The independency of stellar mass-loss rates on stellar X-ray luminosity and activity level based on solar X-ray flux and solar wind observations," *Monthly Notices of the Royal Astronomical Society*, vol. 417, no. 4, pp. 2592–2600, Nov. 11, 2011, ISSN: 0035-8711. DOI: 10.1111/j.1365-2966.2011.19428.x.

[48] NASA. "Sun Fact Sheet." (Nov. 17, 2022), [Online]. Available: https://nssdc.gsfc.nasa.gov/planetary/factsheet/sunfact.html (visited on 08/28/2023).

[49] C. W. Snyder, M. Neugebauer, and U. R. Rao, "The solar wind velocity and its correlation with cosmic-ray variations and with solar and geomagnetic activity," *Journal of Geophysical Research (1896-1977)*, vol. 68, no. 24, pp. 6361–6370, 1963, ISSN: 2156-2202. DOI: 10.1029/JZ068i024p06361.

[50] R. Benacquista, "Impact des structures du vent solaire sur les ceintures de radiation Terrestres," Thèse de doctorat, Toulouse, ISAE, Nov. 23, 2017.

[51] R. Schwenn, "Solar Wind: Global Properties," in *Encyclopedia of Astronomy & Astrophysics*, CRC Press, 2000.

[52] M. Faurobert, "Solar and Stellar Variability," in *The Sun as a Guide to Stellar Physics*. Elsevier Science, 2018, pp. 267–299, ISBN: 978-0-12-814334-6.

[53] I. G. Usoskin, "A history of solar activity over millennia," *Living Reviews in Solar Physics*, vol. 14, no. 1, p. 3, Mar. 4, 2017, ISSN: 1614-4961. DOI: 10.1007/s41116-017-0006-9.

[54] R. C. Carrington, "Description of a Singular Appearance seen in the Sun on September 1, 1859," *Monthly Notices of the Royal Astronomical Society*, vol. 20, pp. 13–15, Nov. 1, 1859, ISSN: 0035-8711. DOI: 10.1093/mnras/20.1.13.

[55] R. Hodgson, "On a curious Appearance seen in the Sun," *Monthly Notices of the Royal Astronomical Society*, vol. 20, pp. 15–16, Nov. 1, 1859, ISSN: 0035-8711. DOI: 10.1093/mnras/20.1.15.

[56] R. A. Mewaldt *et al.*, "Solar-Particle Energy Spectra during the Large Events of October-November 2003 and January 2005," vol. 1, p. 111, Jan. 1, 2005.

[57] R. A. Mewaldt *et al.*, "Radiation risks from large solar energetic particle events," *AIP Conference Proceedings*, vol. 932, no. 1, pp. 277–282, Aug. 28, 2007, ISSN: 0094-243X. DOI: 10.1063/1.2778975.

[58] P. Meyer, E. N. Parker, and J. A. Simpson, "Solar Cosmic Rays of February, 1956 and Their Propagation through Interplanetary Space," *Physical Review*, vol. 104, no. 3, pp. 768–783, Nov. 1, 1956. DOI: 10.1103/PhysRev.104.768.

[59] M. Xapsos, C. Stauffer, G. Gee, J. Barth, E. Stassinopoulos, and R. McGuire, "Model for solar proton risk assessment," *IEEE Transactions on Nuclear Science*, vol. 51, no. 6, pp. 3394–3398, Dec. 2004, ISSN: 1558-1578. DOI: 10.1109/TNS.2004.839159.

[60] J. Feynman, G. Spitale, J. Wang, and S. Gabriel, "Interplanetary proton fluence model: JPL 1991," *Journal of Geophysical Research: Space Physics*, vol. 98, no. A8, pp. 13 281–13 294, 1993, ISSN: 2156-2202. DOI: 10.1029/92JA02670.

[61] J. H. King, "Solar Proton Fluences for 1977-1983 Space Missions," *Journal of Spacecraft and Rockets*, vol. 11, no. 6, pp. 401–408, 1974, ISSN: 0022-4650. DOI: 10.2514/3.62088.

[62] R. A. Nymmik, "Some problems with developing a standard for determining solar energetic particle fluxes," *Advances in Space Research*, vol. 47, no. 4, pp. 622–628, Feb. 15, 2011, ISSN: 0273-1177. DOI: 10.1016/j.asr.2010.11.004.

[63] P. Jiggens, D. Heynderickx, I. Sandberg, P. Truscott, O. Raukunen, and R. Vainio, "Updated Model of the Solar Energetic Proton Environment in Space," *Journal of Space Weather and Space Climate*, vol. 8, A31, 2018, ISSN: 2115-7251. DOI: 10.1051/swsc/2018010.

[64] G. Hulot, T. J. Sabaka, N. Olsen, and A. Fournier, "The Present and Future Geomagnetic Field," in *Treatise on Geophysics : Volume 5 Geomagnetism Ed. 2*, Elsevier Science, 2015, ISBN: 978-0-444-53802-4.

[65] E. Friis-Christensen, H. Lühr, and G. Hulot, "Swarm: A constellation to study the Earths magnetic field," *Earth, Planets and Space*, vol. 58, no. 4, pp. 351–358, Apr. 1, 2006, ISSN: 1880-5981. DOI: 10.1186/BF03351933.

[66] M. Schulz, "Magnetosphere," in *Handbook of the Solar-Terrestrial Environment*, Y. Kamide and A. Chian, Eds., Berlin, Heidelberg: Springer, 2007, pp. 155–188, ISBN: 978-3-540-46315-3. DOI: 10.1007/978-3-540-46315-3_7.

[67] D. J. Knecht and B. M. Shuman, "The Geomagnetic Field," in *Handbook of Geophysics and the Space Environment, 4th Edition*, Dec. 1, 1985.

[68] H. Moritz, "Geodetic Reference System 1980," *Journal of Geodesy*, vol. 74, no. 1, pp. 128–133, Mar. 1, 2000, ISSN: 1432-1394. DOI: 10.1007/s001900050278.

[69] J. G. Lyon, "The Solar Wind-Magnetosphere-Ionosphere System," *Science*, vol. 288, no. 5473, pp. 1987–1991, Jun. 16, 2000. DOI: 10.1126/science.288.5473.1987.

[70] E. W. Hones Jr. *et al.*, "Structure of the magnetotail at 220 RE and its response to geomagnetic activity," *Geophysical Research Letters*, vol. 11, no. 1, pp. 5–7, 1984, ISSN: 1944-8007. DOI: 10.1029/GL011i001p00005.

[71] A. Nishida, "Magnetic Reconnection," in *Handbook of the Solar-Terrestrial Environment*, Y. Kamide and A. Chian, Eds., Berlin, Heidelberg: Springer, 2007, pp. 279–310, ISBN: 978-3-540-46315-3. DOI: 10.1007/978-3-540-46315-3_11.

[72] B. Hultqvist, "The Aurora," in *Handbook of the Solar-Terrestrial Environment*, Y. Kamide and A. Chian, Eds., Berlin, Heidelberg: Springer, 2007, pp. 333–354, ISBN: 978-3-540-46315-3. DOI: 10.1007/978-3-540-46315-3_13.

[73] Y. Kamide and Y. P. Maltsev, "Geomagnetic Storms," in *Handbook of the Solar-Terrestrial Environment*, Y. Kamide and A. Chian, Eds., Berlin, Heidelberg: Springer, 2007, pp. 355–374, ISBN: 978-3-540-46315-3. DOI: 10.1007/978-3-540-46315-3_14.

[74] D. H. Boteler, "Geomagnetic Hazards to Conducting Networks," *Natural Hazards*, vol. 28, no. 2, pp. 537–561, Mar. 1, 2003, ISSN: 1573-0840. DOI: 10.1023/A:1022902713136.

[75] T. G. Northrop, "Adiabatic Theory of Charged Particle Motion," in *Radiation Trapped in the Earths Magnetic Field*, B. M. McCormac, Ed., ser. Astrophysics and Space Science Library, Dordrecht: Springer Netherlands, 1966, pp. 26–44, ISBN: 978-94-010-3553-8. DOI: 10.1007/978-94-010-3553-8_3.

[76] M. Schulz and L. J. Lanzerotti, *Particle Diffusion in the Radiation Belts* (Physics and Chemistry in Space), red. by J. G. Roederer. Berlin, Heidelberg: Springer, 1974, vol. 7, ISBN: 978-3-642-65677-4 978-3-642-65675-0. DOI: 10.1007/978-3-642-65675-0.

[77] W. N. Spjeldvik and P. L. Rothwell, "The Radiation Belts," in *Handbook of Geophysics and the Space Environment, 4th Edition*, Dec. 1, 1985.

[78] M. Kelley, *The Earth's Ionosphere : Plasma, Physics and Electrodynamics Ed. 2*. Elsevier Science, 2009, ISBN: 978-0-12-088425-4.

[79] W. Li and M. Hudson, "Earth's Van Allen Radiation Belts: From Discovery to the Van Allen Probes Era," *Journal of Geophysical Research: Space Physics*, vol. 124, no. 11, pp. 8319–8351, 2019, ISSN: 2169-9402. DOI: 10.1029/2018JA025940.

[80] L. H. Meredith, M. B. Gottlieb, and J. A. Van Allen, "Direct Detection of Soft Radiation above 50 Kilometers in the Auroral Zone," *Physical Review*, vol. 97, no. 1, pp. 201–205, Jan. 1, 1955. DOI: 10.1103/PhysRev.97.201.

[81] V. I. Krassovsk, "Exploration of the Upper Atmosphere with the Help of the Third Soviet Sputnik," *Proceedings of the IRE*, vol. 47, no. 2, pp. 289–296, Feb. 1959, ISSN: 2162-6634. DOI: 10.1109/JRPROC.1959.287296.

[82] J. A. Van Allen and L. A. Frank, "Radiation Measurements to 658,300 Km. with Pioneer IV," *Nature*, vol. 184, no. 4682, pp. 219–224, 4682 Jul. 1959, ISSN: 1476-4687. DOI: 10.1038/184219a0.

[83] J. A. Van Allen, C. E. McIlwain, and G. H. Ludwig, "Radiation observations with satellite 1958," *Journal of Geophysical Research (1896-1977)*, vol. 64, no. 3, pp. 271–286, 1959, ISSN: 2156-2202. DOI: 10.1029/JZ064i003p00271.

[84] J. A. Van Allen, "The geomagnetically trapped corpuscular radiation," *Journal of Geophysical Research (1896-1977)*, vol. 64, no. 11, pp. 1683–1689, 1959, ISSN: 2156-2202. DOI: 10.1029/JZ064i011p01683.

[85] R. S. Selesnick *et al.*, "Observations of the inner radiation belt: CRAND and trapped solar protons," *Journal of Geophysical Research: Space Physics*, vol. 119, no. 8, pp. 6541–6552, 2014, ISSN: 2169-9402. DOI: 10.1002/2014JA020188.

[86] X. Li and M. A. Temerin, "The Electron Radiation Belt," *Space Science Reviews*, vol. 95, no. 1, pp. 569–580, Jan. 1, 2001, ISSN: 1572-9672. DOI: 10.1023/A:1005221108016.

[87] J. A. Van Allen, "Energetic Particles in the Earth's External Magnetic Field," in *Discovery of the Magnetosphere*. American Geophysical Union Washington D. C, 1997, vol. 7.

[88] "Radiation Belts and Their Environment," in *Physics of Earths Radiation Belts: Theory and Observations*. Springer Nature, 2022, ISBN: 978-3-030-82167-8. DOI: 10.1007/978-3-030-82167-8.

[89] J.-F. Ripoll *et al.*, "Particle Dynamics in the Earth's Radiation Belts: Review of Current Research and Open Questions," *Journal of Geophysical Research: Space Physics*, vol. 125, no. 5, e2019JA026735, 2020, ISSN: 2169-9402. DOI: 10.1029/2019JA026735.

[90] D. N. Baker, S. G. Kanekal, X. Li, S. P. Monk, J. Goldstein, and J. L. Burch, "An extreme distortion of the Van Allen belt arising from the Hallowe'en solar storm in 2003," *Nature*, vol. 432, no. 7019, pp. 878–881, 7019 Dec. 2004, ISSN: 1476-4687. DOI: 10.1038/nature03116.

[91] J. A. V. Allen, C. E. McIlwain, and G. H. Ludwig, "Satellite observations of electrons artificially injected into the geomagnetic field," *Proceedings of the National Academy of Sciences*, vol. 45, no. 8, pp. 1152–1171, Aug. 1959. DOI: 10.1073/pnas.45.8.1152.

[92] T. I. Gombosi, D. N. Baker, A. Balogh, P. J. Erickson, J. D. Huba, and L. J. Lanzerotti, "Anthropogenic Space Weather," *Space Science Reviews*, vol. 212, no. 3, pp. 985–1039, Nov. 1, 2017, ISSN: 1572-9672. DOI: 10.1007/s11214-017-0357-5.

[93] M. Walt, "From Nuclear Physics to Space Physics by Way of High Altitude Nuclear Tests," in *Discovery of the Magnetosphere*. American Geophysical Union Washington D. C, 1997, vol. 7.

[94] T. R. Pedersen and E. A. Gerken, "Creation of visible artificial optical emissions in the aurora by high-power radio waves," *Nature*, vol. 433, no. 7025, pp. 498–500, 7025 Feb. 2005, ISSN: 1476-4687. DOI: 10.1038/nature03243.

[95] R. Lüst, "Barium cloud experiments in the upper atmosphere," in *The Century of Space Science*, J. A. M. Bleeker, J. Geiss, and M. C. E. Huber, Eds., Dordrecht: Springer Netherlands, 2001, pp. 179–187, ISBN: 978-94-010-0320-9. DOI: 10.1007/978-94-010-0320-9_6.

[96] M. Walt, "The effects of atmospheric collisions on geomagnetically trapped electrons," *Journal of Geophysical Research (1896-1977)*, vol. 69, no. 19, pp. 3947–3958, 1964, ISSN: 2156-2202. DOI: 10.1029/JZ069i019p03947.

[97] R. S. Selesnick, "Atmospheric scattering and decay of inner radiation belt electrons," *Journal of Geophysical Research: Space Physics*, vol. 117, no. A8, 2012, ISSN: 2156-2202. DOI: 10.1029/2012JA017793.

[98] D. N. Baker *et al.*, "Highly relativistic radiation belt electron acceleration, transport, and loss: Large solar storm events of March and June 2015," *Journal of Geophysical Research: Space Physics*, vol. 121, no. 7, pp. 6647–6660, 2016, ISSN: 2169-9402. DOI: 10.1002/2016JA022502.

[99] C. E. McIlwain, "The Radiation Belts, Natural and Artificial," *Science*, vol. 142, no. 3590, pp. 355–361, Oct. 18, 1963. DOI: 10.1126/science.142.3590.355.

[100] D. Sawyer and J. Vette, "AP-8 Trapped Proton Environment for Solar Maximum and Solar Minimum," United States, 1976, p. 176.

[101] J. I. Vette, "The AE-8 trapped electron model environment," NSSDC/WDC-A-RS-91-24, Nov. 1, 1991.

[102] G. P. Ginet *et al.*, "AE9, AP9 and SPM: New Models for Specifying the Trapped Energetic Particle and Space Plasma Environment," in *The Van Allen Probes Mission*, N. Fox and J. L. Burch, Eds., Boston, MA: Springer US, 2014, pp. 579–615, ISBN: 978-1-4899-7433-4. DOI: 10.1007/978-1-4899-7433-4_18.

[103] W. R. Johnston, T. P. O'Brien, S. L. Huston, T. B. Guild, and G. P. Ginet, "Recent Updates to the AE9/AP9/SPM Radiation Belt and Space Plasma Specification Model," *IEEE Transactions on Nuclear Science*, vol. 62, pp. 2760–2766, Dec. 1, 2015, ISSN: 0018-9499. DOI: 10.1109/TNS.2015.2476470.

[104] A. G. Smirnov *et al.*, "Medium Energy Electron Flux in Earth's Outer Radiation Belt (MERLIN): A Machine Learning Model," *Space Weather*, vol. 18, no. 11, e2020SW002532, 2020, ISSN: 1542-7390. DOI: 10.1029/2020SW002532.

[105] A. Brunet, A. Sicard, N. Balcon, and R. Ecoffet, "Multiscale Dynamic Modeling for Spatial Radiation Environment Specification Models," *IEEE Transactions on Nuclear Science*, vol. 70, no. 8, pp. 1555–1563, Aug. 2023, ISSN: 1558-1578. DOI: 10.1109/TNS.2023.3260837.

[106] I. Jun, H. B. Garrett, and R. W. Evans, "Trapped Particle Environments of the Outer Planets," *IEEE Transactions on Plasma Science*, vol. 47, no. 8, pp. 3923–3930, Aug. 2019, ISSN: 1939-9375. DOI: 10.1109/TPS.2019.2907069.

[107] E. Roussos and P. Kollmann, "The Radiation Belts of Jupiter and Saturn," in *Magnetospheres in the Solar System*, American Geophysical Union (AGU), 2021, pp. 499–514, ISBN: 978-1-119-81562-4. DOI: 10.1002/9781119815624.ch32.

[108] Q. Nénon, A. Sicard, and S. Bourdarie, "A new physical model of the electron radiation belts of Jupiter inside Europa's orbit," *Journal of Geophysical Research: Space Physics*, vol. 122, no. 5, pp. 5148–5167, 2017, ISSN: 2169-9402. DOI: 10.1002/2017JA023893.

[109] N. E. Engelbrecht, A. Vogt, K. Herbst, R. D. T. Strauss, and R. A. Burger, "Revisiting the Revisited Palmer Consensus: New Insights from Jovian Electron Transport," *The Astrophysical Journal*, vol. 929, no. 1, p. 8, Apr. 2022, ISSN: 0004-637X. DOI: 10.3847/1538-4357/ac58f5.

[110] J. G. Mitchell *et al.*, "First Measurements of Jovian Electrons by Parker Solar Probe/ISIS within 0.5 au of the Sun," *The Astrophysical Journal*, vol. 933, no. 2, p. 171, Jul. 2022, ISSN: 0004-637X. DOI: 10.3847/1538-4357/ac75ce.

[111] O. Montenbruck and E. Gill, "Around the World in a Hundred Minutes," in *Satellite Orbits: Models, Methods and Applications*, O. Montenbruck and E. Gill, Eds., Berlin, Heidelberg: Springer, 2000, pp. 1–13, ISBN: 978-3-642-58351-3. DOI: 10.1007/978-3-642-58351-3_1.

[112] J. N. Pelton, "Satellite Orbits for Communications Satellites," in *Handbook of Satellite Applications*, J. N. Pelton, S. Madry, and S. Camacho-Lara, Eds., New York, NY: Springer, 2013, pp. 93–114, ISBN: 978-1-4419-7671-0. DOI: 10.1007/978-1-4419-7671-0_5.

[113] J. C. McDowell, "The Low Earth Orbit Satellite Population and Impacts of the SpaceX Starlink Constellation," *The Astrophysical Journal Letters*, vol. 892, no. 2, p. L36, Apr. 2020, ISSN: 2041-8205. DOI: 10.3847/2041-8213/ab8016.

[114] B. Bastida Virgili *et al.*, "Risk to space sustainability from large constellations of satellites," *Acta Astronautica*, Space Flight Safety, vol. 126, pp. 154–162, Sep. 1, 2016, ISSN: 0094-5765. DOI: 10.1016/j.actaastro.2016.03.034.

[115] E. Messerschmid and R. Bertrand, "History and Current Development," in *Space Stations: Systems and Utilization*, E. Messerschmid and R. Bertrand, Eds., Berlin, Heidelberg: Springer, 1999, pp. 7–56, ISBN: 978-3-662-03974-8. DOI: 10.1007/978-3-662-03974-8_2.

[116] G. D. Badhwar, "The Radiation Environment in Low-Earth Orbit," *Radiation Research*, vol. 148, S3–S10, 5s Nov. 1, 1997, ISSN: 0033-7587. DOI: 10.2307/3579710.

[117] W. Furnell, A. Shenoy, E. Fox, and P. Hatfield, "First results from the LUCID-Timepix spacecraft payload onboard the TechDemoSat-1 satellite in Low Earth Orbit," *Advances in Space Research*, vol. 63, no. 5, pp. 1523–1540, Mar. 1, 2019, ISSN: 0273-1177. DOI: 10.1016/j.asr.2018.10.045.

[118] G. Reitz, "Characteristic of the radiation field in low earth orbit and in deep space," *Zeitschrift für Medizinische Physik*, Schwerpunkt: Space Radiation Research, vol. 18, no. 4, pp. 233–243, Dec. 1, 2008, ISSN: 0939-3889. DOI: 10.1016/j.zemedi.2008.06.015.

[119] J. Restier-Verlet *et al.*, "Radiation on Earth or in Space: What Does It Change?" *International Journal of Molecular Sciences*, vol. 22, no. 7, p. 3739, 7 Jan. 2021, ISSN: 1422-0067. DOI: 10.3390/ijms22073739.

[120] K. Wilson and H. Schaub, "Prospects and challenges of bremsstrahlung-based electrostatic potential and material composition determination for spacecraft," in *Proceedings of the 15th Spacecraft Charging Technology Conference*, 2018.

[121] C. Zeitlin and C. La Tessa, "The Role of Nuclear Fragmentation in Particle Therapy and Space Radiation Protection," *Frontiers in Oncology*, vol. 6, 2016, ISSN: 2234-943X.

[122] H. B. Garrett, "The charging of spacecraft surfaces," *Reviews of Geophysics*, vol. 19, no. 4, pp. 577–616, 1981, ISSN: 1944-9208. DOI: 10.1029/RG019i004p00577.

[123] S. T. Lai, "Fundamentals of Spacecraft Charging: Spacecraft Interactions with Space Plasmas," in *Fundamentals of Spacecraft Charging*, Princeton University Press, Oct. 17, 2011, ISBN: 978-1-4008-3909-4. DOI: 10.1515/9781400839094.

[124] F. J. Pavón-Carrasco and A. De Santis, "The South Atlantic Anomaly: The Key for a Possible Geomagnetic Reversal," *Frontiers in Earth Science*, vol. 4, 2016, ISSN: 2296-6463.

[125] C. C. Finlay *et al.*, "The CHAOS-7 geomagnetic field model and observed changes in the South Atlantic Anomaly," *Earth, Planets and Space*, vol. 72, no. 1, p. 156, Oct. 20, 2020, ISSN: 1880-5981. DOI: 10.1186/s40623-020-01252-9.

[126] B. J. Anderson, C. G. Justus, and G. W. Batts, "Guidelines for the Selection of Near-Earth Thermal Environment Parameters for Spacecraft Design," NASA/TM-2001-211221, Oct. 1, 2001.

[127] H. K. Kim and C. Y. Han, "Analytical and numerical approaches of a solar array thermal analysis in a low-earth orbit satellite," *Advances in Space Research*, vol. 46, no. 11, pp. 1427–1439, Dec. 1, 2010, ISSN: 0273-1177. DOI: 10.1016/j.asr.2010.08.023.

[128] M. F. Diaz-Aguado, J. Greenbaum, W. T. Fowler, and E. G. Lightsey, "Small satellite thermal design, test, and analysis," in *Modeling, Simulation, and Verification of Space-based Systems III*, vol. 6221, SPIE, May 31, 2006, pp. 74–85. DOI: 10.1117/12.666177.

[129] B. Moffitt, "Predictive Thermal Analysis of the Combat Sentinel Satellite," presented at the 16th AIAA/USU Conference on Small Satellites, Aug. 14, 2002.

[130] D. K. Skoulidou, A. J. Rosengren, K. Tsiganis, and G. Voyatzis, "Medium Earth Orbit dynamical survey and its use in passive debris removal," *Advances in Space Research*, vol. 63, no. 11, pp. 3646–3674, Jun. 1, 2019, ISSN: 0273-1177. DOI: 10.1016/j.asr.2019.02.015.

[131] G. X. Gao and P. Enge, "How Many GNSS Satellites are Too Many?" *IEEE Transactions on Aerospace and Electronic Systems*, vol. 48, no. 4, pp. 2865–2874, Oct. 2012, ISSN: 1557-9603. DOI: 10.1109/TAES.2012.6324666.

[132] T. Paulmier, D. Lazaro, B. Dirassen, R. Rey, J.-C. Matéo-Velez, and D. Payan, "Internal Charging Issues Met During Electric Orbit Raising and in GPS-Like MEO Environment," *IEEE Transactions on Plasma Science*, vol. 47, no. 8, pp. 3776–3782, Aug. 2019, ISSN: 1939-9375. DOI: 10.1109/TPS.2019.2922256.

[133] W. Emery and A. Camps, "Orbital Mechanics, Image Navigation, Map Projections," in *Introduction to Satellite Remote Sensing : Atmosphere, Ocean, Land and Cryosphere Applications*, Elsevier Science, 2017, ISBN: 978-0-12-809254-5.

[134] A. C. Clarke, "Extra-terrestrial relays," *Wireless World*, vol. 119, no. 1924, pp. 14–19, 1945.

[135] E. Seedhouse, "Potential Destinations," in *Interplanetary Outpost: The Human and Technological Challenges of Exploring the Outer Planets*, ser. Springer Praxis Books, E. Seedhouse, Ed., Boston, MA: Springer US, 2012, pp. 1–21, ISBN: 978-1-4419-9748-7. DOI: 10.1007/978-1-4419-9748-7_1.

[136] K. A. Farley *et al.*, "Mars 2020 Mission Overview," *Space Science Reviews*, vol. 216, no. 8, p. 142, Dec. 3, 2020, ISSN: 1572-9672. DOI: 10.1007/s11214-020-00762-y.

[137] A. Klesh *et al.*, "MarCO: Early Operations of the First CubeSats to Mars," *Small Satellite Conference*, Aug. 5, 2018.

[138] Y. Zou *et al.*, "Scientific objectives and payloads of Tianwen-1, Chinas first Mars exploration mission," *Advances in Space Research*, vol. 67, no. 2, pp. 812–823, Jan. 15, 2021, ISSN: 0273-1177. DOI: 10.1016/j.asr.2020.11.005.

[139] B. A. Cohen, P. O. Hayne, B. Greenhagen, D. A. Paige, C. Seybold, and J. Baker, "Lunar Flashlight: Illuminating the Lunar South Pole," *IEEE Aerospace and Electronic Systems Magazine*, vol. 35, no. 3, pp. 46–52, Mar. 2020, ISSN: 1557-959X. DOI: 10.1109/MAES.2019.2950746.

[140] T. R. Lockett *et al.*, "Near-Earth Asteroid Scout Flight Mission," *IEEE Aerospace and Electronic Systems Magazine*, vol. 35, no. 3, pp. 20–29, Mar. 2020, ISSN: 1557-959X. DOI: 10.1109/MAES.2019.2958729.

[141] B. Donahue and M. Duggan, "The 2033 Crew Mars Flyby Mission," in *2022 IEEE Aerospace Conference (AERO)*, Mar. 2022, pp. 01–16. DOI: 10.1109/AERO53065.2022.9843408.

[142] B. Westphala and V. Maiwaldb, "Critical Analysis and Review of Current Mars Mission Scenarios for SpaceX Starship," presented at the 25th IAA Symposium on Human Exploration of the Solar System, 2022.

[143] "Interplanetary missions," in *Interplanetary Mission Analysis and Design*, ser. Springer Praxis Books, S. Kemble, Ed., Berlin, Heidelberg: Springer, 2006, pp. 1–71, ISBN: 978-3-540-37645-3. DOI: 10.1007/3-540-37645-3_1.

[144] D. M. Hassler *et al.*, "Mars Surface Radiation Environment Measured with the Mars Science Laboratorys Curiosity Rover," *Science*, vol. 343, no. 6169, p. 1 244 797, Jan. 24, 2014. DOI: 10.1126/science.1244797.

[145] G. Reitz, T. Berger, and D. Matthiae, "Radiation exposure in the moon environment," *Planetary and Space Science*, Scientific Preparations For Lunar Exploration, vol. 74, no. 1, pp. 78–83, Dec. 1, 2012, ISSN: 0032-0633. DOI: 10.1016/j.pss.2012.07.014.

[146] B. H. Mauk and N. J. Fox, "Electron radiation belts of the solar system," *Journal of Geophysical Research: Space Physics*, vol. 115, no. A12, 2010, ISSN: 2156-2202. DOI: 10.1029/2010JA015660.

[147] P. Fieseler, S. Ardalan, and A. Frederickson, "The radiation effects on Galileo spacecraft systems at Jupiter," *IEEE Transactions on Nuclear Science*, vol. 49, no. 6, pp. 2739–2758, Dec. 2002, ISSN: 1558-1578. DOI: 10.1109/TNS.2002.805386.

[148] W. Atwell, B. Reddell, and P. Boeder, "A Comparison of the Radiation Environments in Deep Space," SAE International, Warrendale, PA, SAE Technical Paper 2007-01-3114, Jul. 9, 2007. DOI: 10.4271/2007-01-3114.

[149] H. Cheng and Y. C. Lee, "Quantum Theory of Photon Interaction in a Plasma," *Physical Review*, vol. 142, no. 1, pp. 104–114, Feb. 4, 1966. DOI: 10.1103/PhysRev.142.104.

[150] J. H. Hubbell, "Review of photon interaction cross section data in the medical and biological context," *Physics in Medicine & Biology*, vol. 44, no. 1, R1, Jan. 1999, ISSN: 0031-9155. DOI: 10.1088/0031-9155/44/1/001.

[151] S. M. Seltzer *et al.*, "Fundamental quantities and units for ionizing radiation," *ICRU Journal*, vol. 11, no. 1, p. 1, 2011, ISSN: 1742-3422.

[152] F. Ravotti, "Dosimetry Techniques and Radiation Test Facilities for Total Ionizing Dose Testing," *IEEE Transactions on Nuclear Science*, vol. 65, no. 8, pp. 1440–1464, Aug. 2018, ISSN: 1558-1578. DOI: 10.1109/TNS.2018.2829864.

[153] V. Valkovic, "Measurements of radioactivity," in *Radioactivity in the Environment Ed. 2*, Elsevier Science, 2019, pp. 123–280, ISBN: 978-0-444-64146-5.

[154] H. S. Porter and A. E. S. Green, "Comparison of Monte Carlo and continuous slowingdown approximation treatments of 1keV proton energy deposition in N2," *Journal of Applied Physics*, vol. 46, no. 11, pp. 5030–5038, 1975, ISSN: 0021-8979. DOI: 10.1063/1.321493.

[155] L. H. Gray, "II. The Transition from Röntgen to Rad," *The British Journal of Radiology*, Jul. 1956. DOI: 10.1259/0007-1285-29-343-355.

[156] W. C. Roesch and F. H. Attix, "Basic Concepts of Dosimetry," in *Radiation Dosimetry, Volume I: Fundamentals*, F. H. Attix and W. C. Roesch, Eds., 2nd ed., Academic Press, 1968, pp. 1–41, ISBN: 0-12-066401-1.

[157] E. B. Podgorak, "Introduction to Modern Physics," in *Radiation Physics for Medical Physicists*, ser. Biological and Medical Physics, Biomedical Engineering, E. B. Podgorsak, Ed., Berlin, Heidelberg: Springer, 2010, pp. 1–75, ISBN: 978-3-642-00875-7. DOI: 10.1007/978-3-642-00875-7_1.

[158] M. F. L'annunziata, "Electromagnetic Radiation: Photons," in *Radioactivity : Introduction and History, From the Quantum to Quarks Ed. 2*, Elsevier Science, 2016, ISBN: 978-0-444-63489-4.

[159] A. Einstein, *Über einen die Erzeugung und Verwandlung des Lichtes betreffenden heuristischen Gesichtspunkt*, Albert Einstein-Gesellschaft, 1905.

[160] R. H. Pratt, A. Ron, and H. K. Tseng, "Atomic Photoelectric Effect Above 10 keV," *Reviews of Modern Physics*, vol. 45, no. 2, pp. 273–325, Apr. 1, 1973. DOI: 10.1103/RevModPhys.45.273.

[161] R. Murray and K. E. Holbert, "Radiation and Materials," in *Nuclear Energy : An Introduction to the Concepts, Systems, and Applications of Nuclear Processes Ed. 8*, Elsevier Science, 2019, pp. 81–99, ISBN: 978-0-12-812881-7.

[162] A. H. Compton, "A Quantum Theory of the Scattering of X-rays by Light Elements," *Physical Review*, vol. 21, no. 5, pp. 483–502, May 1, 1923. DOI: 10.1103/PhysRev.21.483.

[163] A. H. Compton, "The Spectrum of Scattered X-Rays," *Physical Review*, vol. 22, no. 5, pp. 409–413, Nov. 1, 1923. DOI: 10.1103/PhysRev.22.409.

[164] R. H. Pratt, L. A. LaJohn, V. Florescu, T. Suri, B. K. Chatterjee, and S. C. Roy, "Compton scattering revisited," *Radiation Physics and Chemistry*, Special Issue on Future Directions in Atomic and Condensed Matter Research and Applications, vol. 79, no. 2, pp. 124–131, Feb. 1, 2010, ISSN: 0969-806X. DOI: 10.1016/j.radphyschem.2009.04.035.

[165] C. D. Anderson and S. H. Neddermeyer, "Positrons from Gamma-Rays," *Physical Review*, vol. 43, no. 12, pp. 1034–1034, Jun. 15, 1933. DOI: 10.1103/PhysRev.43.1034.

[166] P. M. S. Blackett, G. P. S. Occhialini, and E. Rutherford, "Some photographs of the tracks of penetrating radiation," *Proceedings of the Royal Society of London. Series A, Containing Papers of a Mathematical and Physical Character*, vol. 139, no. 839, pp. 699–726, Mar. 3, 1933. DOI: 10.1098/rspa.1933.0048.

[167] J. W. Motz, H. A. Olsen, and H. W. Koch, "Pair Production by Photons," *Reviews of Modern Physics*, vol. 41, no. 4, pp. 581–639, Oct. 1, 1969. DOI: 10.1103/RevModPhys.41.581.

[168] D. C. Gates, R. W. Kenney, and W. P. Swanson, "Electron Triplet Production by High-Energy Photons in Hydrogen," *Physical Review*, vol. 125, no. 4, pp. 1310–1318, Feb. 15, 1962. DOI: 10.1103/PhysRev.125.1310.

[169] "XCOM: Photon Cross Sections Database," NIST. (Sep. 17, 2009), [Online]. Available: https://www.nist.gov/pml/xcom-photon-cross-sections-database (visited on 04/14/2023).

[170] R. D. Evans, "X-Ray and -Ray Interactions," in *Radiation Dosimetry, Volume I: Fundamentals*, F. H. Attix and W. C. Roesch, Eds., 2nd ed., Academic Press, 1968, pp. 93–155, ISBN: 0-12-066401-1.

[171] J. Alsmiller and J. Barish, "Neutron kerma factors for H, C, N, O, and tissue in the energy range of 20 to 70 MeV," Oak Ridge National Lab. (ORNL), Oak Ridge, TN (United States), ORNL/TM-5702, Dec. 1, 1976. DOI: 10.2172/7320828.

[172] R. S. Caswell, J. J. Coyne, and M. L. Randolph, "Kerma Factors for Neutron Energies below 30 MeV," *Radiation Research*, vol. 83, no. 2, pp. 217–254, Aug. 1, 1980, ISSN: 0033-7587. DOI: 10.2307/3575276.

[173] J. H. Hubbell, "Photon mass attenuation and energy-absorption coefficients," *The International Journal of Applied Radiation and Isotopes*, vol. 33, no. 11, pp. 1269–1290, Nov. 1, 1982, ISSN: 0020-708X. DOI: 10.1016/0020-708X(82)90248-4.

[174] J. H. Hubbell and S. M. Seltzer, "X-Ray Mass Attenuation Coefficients," *NIST*, Sep. 17, 2009. DOI: 10.18434/T4D01F.

[175] J. Konya and N. M. Nagy, "Nuclear Reactions," in *Nuclear and Radiochemistry Ed. 2*, Elsevier Science, 2018, pp. 133–158, ISBN: 978-0-12-813643-0.

[176] C. Virmontois *et al.*, "Total Ionizing Dose Versus Displacement Damage Dose Induced Dark Current Random Telegraph Signals in CMOS Image Sensors," *IEEE Transactions on Nuclear Science*, vol. 58, no. 6, pp. 3085–3094, Dec. 2011, ISSN: 1558-1578. DOI: 10.1109/TNS.2011.2171005.

[177] H. J. Barnaby, "Total-Ionizing-Dose Effects in Modern CMOS Technologies," *IEEE Transactions on Nuclear Science*, vol. 53, no. 6, pp. 3103–3121, Dec. 2006, ISSN: 1558-1578. DOI: 10.1109/TNS.2006.885952.

[178] D. M. Fleetwood *et al.*, "Effects of oxide traps, interface traps, and border traps on metaloxidesemiconductor devices," *Journal of Applied Physics*, vol. 73, no. 10, pp. 5058–5074, May 15, 1993, ISSN: 0021-8979. DOI: 10.1063/1.353777.

[179] G. E. Moore, "Lithography and the future of Moore's law," in *Integrated Circuit Metrology, Inspection, and Process Control IX*, vol. 2439, SPIE, May 22, 1995, pp. 2–17. DOI: 10.1117/12.209195.

[180] D. M. Fleetwood, "Evolution of Total Ionizing Dose Effects in MOS Devices With Moores Law Scaling," *IEEE Transactions on Nuclear Science*, vol. 65, no. 8, pp. 1465–1481, Aug. 2018, ISSN: 1558-1578. DOI: 10.1109/TNS.2017.2786140.

[181] V. Goiffon *et al.*, "Identification of Radiation Induced Dark Current Sources in Pinned Photodiode CMOS Image Sensors," *IEEE Transactions on Nuclear Science*, vol. 59, no. 4, pp. 918–926, Aug. 2012, ISSN: 1558-1578. DOI: 10.1109/TNS.2012.2190422.

[182] J. R. Srour and J. W. Palko, "Displacement Damage Effects in Irradiated Semiconductor Devices," *IEEE Transactions on Nuclear Science*, vol. 60, no. 3, pp. 1740–1766, Jun. 2013, ISSN: 1558-1578. DOI: 10.1109/TNS.2013.2261316.

[183] M. Moll, "Displacement Damage in Silicon Detectors for High Energy Physics," *IEEE Transactions on Nuclear Science*, vol. 65, no. 8, pp. 1561–1582, Aug. 2018, ISSN: 1558-1578. DOI: 10.1109/TNS.2018.2819506.

[184] D. Kobayashi, "Scaling Trends of Digital Single-Event Effects: A Survey of SEU and SET Parameters and Comparison With Transistor Performance," *IEEE Transactions on Nuclear Science*, vol. 68, no. 2, pp. 124–148, Feb. 2021, ISSN: 1558-1578. DOI: 10.1109/TNS.2020.3044659.

[185] E. L. Petersen, P. Shapiro, J. H. Adams, and E. A. Burke, "Calculation of Cosmic-Ray Induced Soft Upsets and Scaling in VLSI Devices," *IEEE Transactions on Nuclear Science*, vol. 29, no. 6, pp. 2055–2063, Dec. 1982, ISSN: 1558-1578. DOI: 10.1109/TNS.1982.4336495.

[186] K. LaBel and M. Gates, "Single-event-effect mitigation from a system perspective," *IEEE Transactions on Nuclear Science*, vol. 43, no. 2, pp. 654–660, Apr. 1996, ISSN: 1558-1578. DOI: 10.1109/23.490908.

[187] A. Johnston, "The influence of VLSI technology evolution on radiation-induced latchup in space systems," *IEEE Transactions on Nuclear Science*, vol. 43, no. 2, pp. 505–521, Apr. 1996, ISSN: 1558-1578. DOI: 10.1109/23.490897.

[188] J. Schwank *et al.*, "Effects of particle energy on proton-induced single-event latchup," *IEEE Transactions on Nuclear Science*, vol. 52, no. 6, pp. 2622–2629, Dec. 2005, ISSN: 1558-1578. DOI: 10.1109/TNS.2005.860672.

[189] H. Becker, T. Miyahira, and A. Johnston, "Latent damage in CMOS devices from single-event latchup," *IEEE Transactions on Nuclear Science*, vol. 49, no. 6, pp. 3009–3015, Dec. 2002, ISSN: 1558-1578. DOI: 10.1109/TNS.2002.805332.

[190] A. F. Witulski *et al.*, "Single-Event Burnout Mechanisms in SiC Power MOSFETs," *IEEE Transactions on Nuclear Science*, vol. 65, no. 8, pp. 1951–1955, Aug. 2018, ISSN: 1558-1578. DOI: 10.1109/TNS.2018.2849405.

[191] R. Lacoe, J. Osborn, R. Koga, S. Brown, and D. Mayer, "Application of hardness-by-design methodology to radiation-tolerant ASIC technologies," *IEEE Transactions on Nuclear Science*, vol. 47, no. 6, pp. 2334–2341, Dec. 2000, ISSN: 1558-1578. DOI: 10.1109/23.903774.

[192] R. C. Lacoe, "Improving Integrated Circuit Performance Through the Application of Hardness-by-Design Methodology," *IEEE Transactions on Nuclear Science*, vol. 55, no. 4, pp. 1903–1925, Aug. 2008, ISSN: 1558-1578. DOI: 10.1109/TNS.2008.2000480.

[193] S. Kulis, "Single Event Effects mitigation with TMRG tool," *Journal of Instrumentation*, vol. 12, no. 01, p. C01082, Jan. 2017, ISSN: 1748-0221. DOI: 10.1088/1748-0221/12/01/C01082.

[194] V. Lalucaa, V. Goiffon, P. Magnan, C. Virmontois, G. Rolland, and S. Petit, "Single Event Effects in 4T Pinned Photodiode Image Sensors," *IEEE Transactions on Nuclear Science*, vol. 60, no. 6, pp. 4314–4322, Dec. 2013, ISSN: 1558-1578. DOI: 10.1109/TNS.2013.2287751.

[195] K. M. Warren *et al.*, "Monte-Carlo Based On-Orbit Single Event Upset Rate Prediction for a Radiation Hardened by Design Latch," *IEEE Transactions on Nuclear Science*, vol. 54, no. 6, pp. 2419–2425, Dec. 2007, ISSN: 1558-1578. DOI: 10.1109/TNS.2007.907678.

[196] W. Fan, C. Drumm, S. Roeske, and G. Scrivner, "Shielding considerations for satellite microelectronics," *IEEE Transactions on Nuclear Science*, vol. 43, no. 6, pp. 2790–2796, Dec. 1996, ISSN: 1558-1578. DOI: 10.1109/23.556868.

[197] J. Barth, K. LaBel, and C. Poivey, "Radiation assurance for the space environment," in *2004 International Conference on Integrated Circuit Design and Technology (IEEE Cat. No.04EX866)*, May 2004, pp. 323–333. DOI: 10.1109/ICICDT.2004.1309976.

[198] M. G. Stabin, "Biological Effects of Radiation," in *Radiation Protection and Dosimetry*, New York, NY: Springer, 2003, pp. 75–104, ISBN: 978-0-387-49982-6 978-0-387-49983-3. DOI: 10.1007/978-0-387-49983-3.

[199] C. Bélanger-Champagne *et al.*, "Delivery of proton FLASH at the TRIUMF Proton Therapy Research Centre," *Nuclear Instruments and Methods in Physics Research Section A: Accelerators, Spectrometers, Detectors and Associated Equipment*, vol. 1052, p. 168 243, Jul. 1, 2023, ISSN: 0168-9002. DOI: 10.1016/j.nima.2023.168243.

[200] J. C. Chancellor, G. B. I. Scott, and J. P. Sutton, "Space Radiation: The Number One Risk to Astronaut Health beyond Low Earth Orbit," *Life*, vol. 4, no. 3, pp. 491–510, 3 Sep. 2014, ISSN: 2075-1729. DOI: 10.3390/life4030491.

[201] E. R. Benton, E. V. Benton, and A. L. Frank, "Passive dosimetry aboard the Mir Orbital Station: Internal measurements," *Radiation Measurements*, Radiaiton on the MIR Space Station, vol. 35, no. 5, pp. 439–455, Oct. 1, 2002, ISSN: 1350-4487. DOI: 10.1016/S1350-4487(02)00075-6.

[202] T. Berger, "Radiation dosimetry onboard the International Space Station ISS," *Zeitschrift für Medizinische Physik*, Schwerpunkt: Space Radiation Research, vol. 18, no. 4, pp. 265–275, Dec. 1, 2008, ISSN: 0939-3889. DOI: 10.1016/j.zemedi.2008.06.014.

[203] C. H. McCollough and B. A. Schueler, "Calculation of effective dose," *Medical Physics*, vol. 27, no. 5, pp. 828–837, 2000, ISSN: 2473-4209. DOI: 10.1118/1.598948.

[204] M. R. Shavers *et al.*, "Implementation of ALARA radiation protection on the ISS through polyethylene shielding augmentation of the Service Module Crew Quarters," *Advances in Space Research*, Space Life Sciences: Radiation Risk Assessment and Radiation Measurements in Low Earth Orbit, vol. 34, no. 6, pp. 1333–1337, Jan. 1, 2004, ISSN: 0273-1177. DOI: 10.1016/j.asr.2003.10.051.

[205] P. Spillantini, "Manned exploration and exploitation of solar system: Passive and active shielding for protecting astronauts from ionizing radiationA short overview," *Acta Astronautica*, Future of Space Exploration: Towards the Stars, vol. 104, no. 2, pp. 509–515, Nov. 1, 2014, ISSN: 0094-5765. DOI: 10.1016/j.actaastro.2014.05.017.

[206] K. L. Ferrone, F. Guan, J. Ma, L. E. Peterson, C. E. Willis, and S. F. Kry, "Reducing space radiation cancer risk with magnetic shielding," *Advances in Space Research*, vol. 68, no. 1, pp. 153–160, Jul. 1, 2021, ISSN: 0273-1177. DOI: 10.1016/j.asr.2021.03.002.

[207] S. Nambiar and J. T. W. Yeow, "Polymer-Composite Materials for Radiation Protection," *ACS Applied Materials & Interfaces*, vol. 4, no. 11, pp. 5717–5726, Nov. 28, 2012, ISSN: 1944-8244. DOI: 10.1021/am300783d.

[208] R. Gaza *et al.*, "Orion EM-1 Internal Environment Characterization: The Matroshka AstroRad Radiation Experiment," presented at the Applied Space Environments Conference (ASEC 2019), 2019.

[209] S. E. Miller, "Photons in Fibers for Telecommunication," *Science*, vol. 195, no. 4283, pp. 1211–1216, Mar. 18, 1977. DOI: 10.1126/science.195.4283.1211.

[210] S. Cherry, "Edholm's law of bandwidth," *IEEE Spectrum*, vol. 41, no. 7, pp. 58–60, Jul. 2004, ISSN: 1939-9340. DOI: 10.1109/MSPEC.2004.1309810.

[211] F. Mitschke, "A Quick Survey," in *Fiber Optics: Physics and Technology*, F. Mitschke, Ed., Berlin, Heidelberg: Springer, 2010, pp. 3–12, ISBN: 978-3-642-03703-0. DOI: 10.1007/978-3-642-03703-0_1.

[212] T. H. Maiman, "Stimulated Optical Radiation in Ruby," *Nature*, vol. 187, no. 4736, pp. 493–494, 4736 Aug. 1960, ISSN: 1476-4687. DOI: 10.1038/187493a0.

[213] A. Javan, W. R. Bennett, and D. R. Herriott, "Population Inversion and Continuous Optical Maser Oscillation in a Gas Discharge Containing a He-Ne Mixture," *Physical Review Letters*, vol. 6, no. 3, pp. 106–110, Feb. 1, 1961. DOI: 10.1103/PhysRevLett.6.106.

[214] R. Kompfner, "Optical Communications," *Science*, vol. 150, no. 3693, pp. 149–155, Oct. 8, 1965. DOI: 10.1126/science.150.3693.149.

[215] E. Snitzer, "Cylindrical Dielectric Waveguide Modes," *JOSA*, vol. 51, no. 5, pp. 491–498, May 1, 1961. DOI: 10.1364/JOSA.51.000491.

[216] K. C. Kao and G. A. Hockham, "Dielectric-fibre surface waveguides for optical frequencies," *Proceedings of the Institution of Electrical Engineers*, vol. 113, no. 7, pp. 1151–1158, Jul. 1, 1966, ISSN: 2053-7891. DOI: 10.1049/piee.1966.0189.

[217] F. P. Kapron, D. B. Keck, and R. D. Maurer, "Radiation losses in glass optical waveguides," *Applied Physics Letters*, vol. 17, no. 10, pp. 423–425, Nov. 15, 1970, ISSN: 0003-6951. DOI: 10.1063/1.1653255.

[218] R. Lingle, D. W. Peckham, K. H. Chang, and A. McCurdy, "Single-Mode Fibers for Communication," in *Specialty Optical Fibers Handbook*. Academic Press, 2007, pp. 123–163, ISBN: 978-0-12-369406-5.

[219] T. Sasaki, T. Hasegawa, and H. Ishikawa, "Optical Fiber and Cables," in *Springer Handbook of Optical Networks*, ser. Springer Handbooks, B. Mukherjee, I. Tomkos, M. Tornatore, P. Winzer, and Y. Zhao, Eds., Cham: Springer International Publishing, 2020, ISBN: 978-3-030-16249-8 978-3-030-16250-4. DOI: 10.1007/978-3-030-16250-4_2.

[220] E. Desurvire, J. R. Simpson, and P. C. Becker, "High-gain erbium-doped traveling-wave fiber amplifier," *Optics Letters*, vol. 12, no. 11, pp. 888–890, Nov. 1, 1987, ISSN: 1539-4794. DOI: 10.1364/OL.12.000888.

[221] W. C. Wang, B. Zhou, S. H. Xu, Z. M. Yang, and Q. Y. Zhang, "Recent advances in soft optical glass fiber and fiber lasers," *Progress in Materials Science*, vol. 101, pp. 90–171, Apr. 1, 2019, ISSN: 0079-6425. DOI: 10.1016/j.pmatsci.2018.11.003.

[222] C. J. Koester and E. Snitzer, "Amplification in a Fiber Laser," *Applied Optics*, vol. 3, no. 10, pp. 1182–1186, Oct. 1, 1964, ISSN: 2155-3165. DOI: 10.1364/AO.3.001182.

[223] M. N. Zervas and C. A. Codemard, "High Power Fiber Lasers: A Review," *IEEE Journal of Selected Topics in Quantum Electronics*, vol. 20, no. 5, pp. 219–241, Sep. 2014, ISSN: 1558-4542. DOI: 10.1109/JSTQE.2014.2321279.

[224] C. Jauregui *et al.*, "Physical origin of mode instabilities in high-power fiber laser systems," *Optics Express*, vol. 20, no. 12, pp. 12 912–12 925, Jun. 4, 2012, ISSN: 1094-4087. DOI: 10.1364/OE.20.012912.

[225] H.-E. Joe, H. Yun, S.-H. Jo, M. B. Jun, and B.-K. Min, "A review on optical fiber sensors for environmental monitoring," *International Journal of Precision Engineering and Manufacturing-Green Technology*, vol. 5, no. 1, pp. 173–191, Jan. 1, 2018, ISSN: 2198-0810. DOI: 10.1007/s40684-018-0017-6.

[226] G. Gagliardi, M. Salza, S. Avino, P. Ferraro, and P. De Natale, "Probing the Ultimate Limit of Fiber-Optic Strain Sensing," *Science*, vol. 330, no. 6007, pp. 1081–1084, Nov. 19, 2010. DOI: 10.1126/science.1195818.

[227] N. J. Lindsey and E. R. Martin, "Fiber-Optic Seismology," *Annual Review of Earth and Planetary Sciences*, vol. 49, no. 1, pp. 309–336, 2021. DOI: 10.1146/annurev-earth-072420-065213.

[228] H. C. Lefèvre, "The fiber-optic gyroscope: Challenges to become the ultimate rotation-sensing technology," *Optical Fiber Technology*, Optical Fiber Sensors, vol. 19, pp. 828–832, 6, Part B Dec. 1, 2013, ISSN: 1068-5200. DOI: 10.1016/j.yofte.2013.08.007.

[229] C. A. R. Díaz *et al.*, "Optical Fiber Sensing for Sub-Millimeter Liquid-Level Monitoring: A Review," *IEEE Sensors Journal*, vol. 19, no. 17, pp. 7179–7191, Sep. 2019, ISSN: 1558-1748. DOI: 10.1109/JSEN.2019.2915031.

[230] F. Sequeira *et al.*, "Refractive Index Sensing with D-Shaped Plastic Optical Fibers for Chemical and Biochemical Applications," *Sensors*, vol. 16, no. 12, p. 2119, 12 Dec. 2016, ISSN: 1424-8220. DOI: 10.3390/s16122119.

[231] A. Dufour *et al.*, "Functionalized Microstructured Optical Fiber for Magnetic-Field Sensing in Radiation Environments," *IEEE Transactions on Nuclear Science*, vol. 70, no. 4, pp. 556–561, Apr. 2023, ISSN: 1558-1578. DOI: 10.1109/TNS.2023.3249299.

[232] S. Girard *et al.*, "Recent advances in radiation-hardened fiber-based technologies for space applications," *Journal of Optics*, vol. 20, no. 9, p. 093 001, Aug. 2018, ISSN: 2040-8986. DOI: 10.1088/2040-8986/aad271.

[233] F. Berghmans *et al.*, "Radiation hardness of fiber optic sensors for monitoring and remote handling applications in nuclear environments," in *Process Monitoring with Optical Fibers and Harsh Environment Sensors*, vol. 3538, SPIE, Jan. 11, 1999, pp. 28–39. DOI: 10.1117/12.335757.

[234] S. Delepine-Lesoille *et al.*, "Industrial Qualification Process for Optical Fibers Distributed Strain and Temperature Sensing in Nuclear Waste Repositories," *Journal of Sensors*, vol. 2012, e369375, Nov. 11, 2012, ISSN: 1687-725X. DOI: 10.1155/2012/369375.

[235] F. Baldini and A. G. Mignani, "Optical-Fiber Medical Sensors," *MRS Bulletin*, vol. 27, no. 5, pp. 383–387, May 2002, ISSN: 1938-1425, 0883-7694. DOI: 10.1557/mrs2002.123.

[236] H. Henschel, M. Koerfer, J. Kuhnhenn, U. Weinand, and F. Wulf, "Fibre optic sensor solutions for particle accelerators," in *17th International Conference on Optical Fibre Sensors*, vol. 5855, SPIE, May 23, 2005, pp. 515–518. DOI: 10.1117/12.624039.

[237] P. Moreau *et al.*, "Test of fiber optic based current sensors on the Tore Supra tokamak," *Fusion Engineering and Design*, Proceedings of the 26th Symposium of Fusion Technology (SOFT-26), vol. 86, no. 6, pp. 1222–1226, Oct. 1, 2011, ISSN: 0920-3796. DOI: 10.1016/j.fusengdes.2010.12.023.

[238] P. Paillet *et al.*, "Phosphosilicate Multimode Optical Fiber for Sensing and Diagnostics at Inertial Confinement Fusion Facilities," *IEEE Sensors Journal*, vol. 22, no. 23, pp. 22 700–22 706, Dec. 2022, ISSN: 1558-1748. DOI: 10.1109/JSEN.2022.3217436.

[239] H. Kanamori, "Optical fiber: Progress in half a century and recent trends," *JSAP Review*, vol. 2022, p. 220 101, 2022. DOI: 10.11470/jsaprev.220101.

[240] S. Schmid and A. F. Toussaint, "Optical Fiber Coatings," in *Specialty Optical Fibers Handbook*. Academic Press, 2007, pp. 95–122, ISBN: 978-0-12-369406-5.

[241] C. Li *et al.*, "A Review of Coating Materials Used to Improve the Performance of Optical Fiber Sensors," *Sensors*, vol. 20, no. 15, p. 4215, 15 Jan. 2020, ISSN: 1424-8220. DOI: 10.3390/s20154215.

[242] J.-M. Renoirt, C. Zhang, M. Debliquy, M.-G. Olivier, P. Mégret, and C. Caucheteur, "High-refractive-index transparent coatings enhance the optical fiber cladding modes refractometric sensitivity," *Optics Express*, vol. 21, no. 23, pp. 29 073–29 082, Nov. 18, 2013, ISSN: 1094-4087. DOI: 10.1364/OE.21.029073.

[243] M. Brinkmann *et al.*, "Optical Materials and Their Properties," in *Springer Handbook of Lasers and Optics*, ser. Springer Handbooks, F. Träger, Ed., Berlin, Heidelberg: Springer, 2012, pp. 253–399, ISBN: 978-3-642-19409-2. DOI: 10.1007/978-3-642-19409-2_5.

[244] F. Mitschke, "Losses," in *Fiber Optics: Physics and Technology*, F. Mitschke, Ed., Berlin, Heidelberg: Springer, 2010, pp. 75–84, ISBN: 978-3-642-03703-0. DOI: 10.1007/978-3-642-03703-0_5.

[245] Y. Koike and M. Asai, "The future of plastic optical fiber," *NPG Asia Materials*, vol. 1, no. 1, pp. 22–28, 1 Oct. 2009, ISSN: 1884-4057. DOI: 10.1038/asiamat.2009.2.

[246] J. Stone and G. E. Walrafen, "Overtone vibrations of OH groups in fused silica optical fibers," *The Journal of Chemical Physics*, vol. 76, no. 4, pp. 1712–1722, Feb. 15, 1982, ISSN: 0021-9606. DOI: 10.1063/1.443210.

[247] P. J. Lemaire, "Reliability of optical fibers exposed to hydrogen: Prediction of long-term loss increases," *Optical Engineering*, vol. 30, no. 6, pp. 780–789, Jun. 1991, ISSN: 0091-3286, 1560-2303. DOI: 10.1117/12.55865.

[248] K. Tsujikawa, K. Tajima, and M. Ohashi, "Rayleigh Scattering Reduction Method for Silica-Based Optical Fiber," *Journal of Lightwave Technology*, vol. 18, no. 11, p. 1528, Nov. 1, 2000.

[249] N. Shimodaira, K. Saito, N. Hiramitsu, S. Matsushita, and A. J. Ikushima, "Effects of fictive temperature and halogen doping on the boson peak in silica glass," *Physical Review B*, vol. 71, no. 2, p. 024 209, Jan. 28, 2005. DOI: 10.1103/PhysRevB.71.024209.

[250] Y. Tamura *et al.*, "The First 0.14-dB/km Loss Optical Fiber and its Impact on Submarine Transmission," *Journal of Lightwave Technology*, vol. 36, no. 1, pp. 44–49, Jan. 2018, ISSN: 1558-2213. DOI: 10.1109/JLT.2018.2796647.

[251] S. Pachnicke, "Fiber Optical Transmission Systems," in *Fiber-Optic Transmission Networks: Efficient Design and Dynamic Operation*, ser. Signals and Communication Technology, S. Pachnicke, Ed., Berlin, Heidelberg: Springer, 2012, pp. 11–29, ISBN: 978-3-642-21055-6. DOI: 10.1007/978-3-642-21055-6_2.

[252] G. P. Agrawal, "Optical Communication: Its History and Recent Progress," in *Optics in Our Time*, M. D. Al-Amri, M. El-Gomati, and M. S. Zubairy, Eds., Cham: Springer International Publishing, 2016, pp. 177–199, ISBN: 978-3-319-31903-2. DOI: 10.1007/978-3-319-31903-2_8.

[253] T. Hoshida *et al.*, "Ultrawideband Systems and Networks: Beyond C + L-Band," *Proceedings of the IEEE*, vol. 110, no. 11, pp. 1725–1741, Nov. 2022, ISSN: 1558-2256. DOI: 10.1109/JPROC.2022.3202103.

[254] M. Pellegatta, M. Monguzzi, A. Mazzarese, and A. Zucchetti, "Fiber networks maintenance in the all-optical network era," in *NOMS 2002. IEEE/IFIP Network Operations and Management Symposium. ' Management Solutions for the New Communications World'(Cat. No.02CH37327)*, Apr. 2002, pp. 855–868. DOI: 10.1109/NOMS.2002.1015629.

[255] R. Olshansky, "Leaky modes in graded index optical fibers," *Applied Optics*, vol. 15, pp. 2773–2777, Nov. 1, 1976, ISSN: 0003-6935. DOI: 10.1364/AO.15.002773.

[256] R. T. Schermer and J. H. Cole, "Improved Bend Loss Formula Verified for Optical Fiber by Simulation and Experiment," *IEEE Journal of Quantum Electronics*, vol. 43, no. 10, pp. 899–909, Oct. 2007, ISSN: 1558-1713. DOI: 10.1109/JQE.2007.903364.

[257] K. H. Yang and J. D. Kingsley, "Calculation of Coupling Losses Between Light Emitting Diodes and Low-Loss Optical Fibers," *Applied Optics*, vol. 14, no. 2, pp. 288–293, Feb. 1, 1975, ISSN: 2155-3165. DOI: 10.1364/AO.14.000288.

[258] J.-H. Chen, Y.-T. Sun, and L. A. Wang, "Reducing Splicing Loss Between a Silicon-Cored Optical Fiber and a Silica Optical Fiber," *IEEE Photonics Technology Letters*, vol. 28, no. 16, pp. 1774–1777, Aug. 2016, ISSN: 1941-0174. DOI: 10.1109/LPT.2016.2571729.

[259] D. L. Griscom, "Optical Properties and Structure of Defects in Silica Glass,", vol. 99, no. 1154, pp. 923–942, 1991. DOI: 10.2109/jcersj.99.923.

[260] C. Söller, O. Cohen, B. J. Smith, I. A. Walmsley, and C. Silberhorn, "High-performance single-photon generation with commercial-grade optical fiber," *Physical Review A*, vol. 83, no. 3, p. 031 806, Mar. 29, 2011. DOI: 10.1103/PhysRevA.83.031806.

[261] J.-P. Meunier, P. Nouchi, and E. Marin, "Propagation dans les fibres optiques," in *Physique et Technologie Des Fibres Optiques*, Hermes Science. Paris, France: Lavoisier, 2003, ISBN: 2-7462-0720-6.

[262] R. Lingle, D. W. Peckham, A. McCurdy, and J. Kim, "Light-Guiding Fundamentals and Fiber Design," in *Specialty Optical Fibers Handbook*, A. Méndez and T. F. Morse, Eds., Burlington: Academic Press, Jan. 1, 2007, pp. 19–68, ISBN: 978-0-12-369406-5. DOI: 10.1016/B978-012369406-5/50004-7.

[263] F. Mitschke, "Treatment with Wave Optics," in *Fiber Optics*, Berlin, Heidelberg: Springer, 2009, pp. 25–45, ISBN: 978-3-642-03702-3. DOI: 10.1007/978-3-662-52764-1.

[264] R. Noé, "Optical Waves in Fibers and Components," in *Essentials of Modern Optical Fiber Communication*, R. Noé, Ed., Berlin, Heidelberg: Springer, 2010, pp. 3–152, ISBN: 978-3-642-04872-2. DOI: 10.1007/978-3-642-04872-2_2.

[265] A. H. Hartog, "Optical Fibre Technology," in *An Introduction to Distributed Optical Fibre Sensors*, Boca Raton: CRC Press, Jun. 1, 2017, pp. 31–54, ISBN: 978-1-315-11901-4. DOI: 10.1201/9781315119014.

[266] D. Gloge, "Weakly Guiding Fibers," *Applied Optics*, vol. 10, no. 10, pp. 2252–2258, Oct. 1, 1971, ISSN: 2155-3165. DOI: 10.1364/AO.10.002252.

[267] M. D. Feit and J. A. Fleck, "Computation of mode properties in optical fiber waveguides by a propagating beam method," *Applied Optics*, vol. 19, no. 7, pp. 1154–1164, Apr. 1, 1980, ISSN: 2155-3165. DOI: 10.1364/AO.19.001154.

[268] C. Vassallo, *Optical Waveguide Concepts*, 1 vols. Elsevier, 1991, vol. 1, 322 pp., ISBN: 0-444-88684-2.

[269] D. F. Santos, A. Guerreiro, and J. M. Baptista, "Numerical investigation of a refractive index SPR D-type optical fiber sensor using COMSOL multiphysics," *Photonic Sensors*, vol. 3, no. 1, pp. 61–66, Mar. 1, 2013, ISSN: 2190-7439. DOI: 10.1007/s13320-012-0080-5.

[270] K. Yee, "Numerical solution of initial boundary value problems involving maxwell's equations in isotropic media," *IEEE Transactions on Antennas and Propagation*, vol. 14, no. 3, pp. 302–307, May 1966, ISSN: 1558-2221. DOI: 10.1109/TAP.1966.1138693.

[271] A. Taflove and S. C. Hagness, "Finite-Difference Time-Domain Solution of Maxwell's Equations," in *Wiley Encyclopedia of Electrical and Electronics Engineering*, John Wiley & Sons, Ltd, 2016, pp. 1–33, ISBN: 978-0-471-34608-1. DOI: 10.1002/047134608X.W8303.

[272] D. Sullivan, J. Liu, and M. Kuzyk, "Three-dimensional optical pulse simulation using the FDTD method," *IEEE Transactions on Microwave Theory and Techniques*, vol. 48, no. 7, pp. 1127–1133, Jul. 2000, ISSN: 1557-9670. DOI: 10.1109/22.848495.

[273] B. G. Bagley, C. R. Kurkjian, J. W. Mitchell, G. E. Peterson, and A. R. Tynes, "Materials, Properties and Choices," in *Optical Fiber Telecommunications*. 1979, pp. 167–231.

[274] P. Guenot, "Propriétés d'atténuation des fibres optiques, procédés d'élaboration," in *Physique et Technologie Des Fibres Optiques*, Hermes Science, Paris, France: Lavoisier, 2003, ISBN: 2-7462-0720-6.

[275] J. W. Fleming, "Material and Mode Dispersion in GeO2ůB2O3ůSiC2 Glasses," *Journal of the American Ceramic Society*, vol. 59, no. 11-12, pp. 503–507, 1976, ISSN: 1551-2916. DOI: 10.1111/j.1151-2916.1976.tb09418.x.

[276] D. Wood, K. Walker, J. MacChesney, J. Simpson, and R. Csencsits, "Germanium chemistry in the MCVD process for optical fiber fabrication," *Journal of Lightwave Technology*, vol. 5, no. 2, pp. 277–285, Feb. 1987, ISSN: 1558-2213. DOI: 10.1109/JLT.1987.1075496.

[277] D. P. Hand and P. S. J. Russell, "Photoinduced refractive-index changes in germanosilicate fibers," *Optics Letters*, vol. 15, no. 2, pp. 102–104, Jan. 15, 1990, ISSN: 1539-4794. DOI: 10.1364/OL.15.000102.

[278] H. Kanamori *et al.*, "Transmission characteristics and reliability of pure-silica-core single-mode fibers," *Journal of Lightwave Technology*, vol. 4, no. 8, pp. 1144–1150, Aug. 1986, ISSN: 1558-2213. DOI: 10.1109/JLT.1986.1074837.

[279] K. Tajima, M. Ohashi, K. Shiraki, M. Tateda, and S. Shibata, "Low Rayleigh scattering P2O5-F-SiO2 glasses," *Journal of Lightwave Technology*, vol. 10, no. 11, pp. 1532–1535, Nov. 1992, ISSN: 1558-2213. DOI: 10.1109/50.184889.

[280] B. J. Ainslie, "A review of the fabrication and properties of erbium-doped fibers for optical amplifiers," *Journal of Lightwave Technology*, vol. 9, pp. 220–227, Feb. 1, 1991, ISSN: 0733-8724. DOI: 10.1109/50.65880.

[281] K. Arai, H. Namikawa, K. Kumata, T. Honda, Y. Ishii, and T. Handa, "Aluminum or phosphorus codoping effects on the fluorescence and structural properties of neodymiumdoped silica glass," *Journal of Applied Physics*, vol. 59, no. 10, pp. 3430–3436, May 15, 1986, ISSN: 0021-8979. DOI: 10.1063/1.336810.

[282] W. Miniscalco, "Erbium-doped glasses for fiber amplifiers at 1500 nm," *Journal of Lightwave Technology*, vol. 9, no. 2, pp. 234–250, Feb. 1991, ISSN: 1558-2213. DOI: 10.1109/50.65882.

[283] J. L. Rygel and C. G. Pantano, "Synthesis and properties of cerium aluminosilicophosphate glasses," *Journal of Non-Crystalline Solids*, vol. 355, no. 52, pp. 2622–2629, Dec. 15, 2009, ISSN: 0022-3093. DOI: 10.1016/j.jnoncrysol.2009.09.004.

[284] A. Vedda *et al.*, "Ce3+-doped fibers for remote radiation dosimetry," *Applied Physics Letters*, vol. 85, no. 26, pp. 6356–6358, Dec. 17, 2004, ISSN: 0003-6951. DOI: 10.1063/1.1840127.

[285] J. T. Kringlebotn, J.-L. Archambault, L. Reekie, and D. N. Payne, "Er3+:Yb3+ codoped fiber distributed-feedback laser," *Optics Letters*, vol. 19, no. 24, pp. 2101–2103, Dec. 15, 1994, ISSN: 1539-4794. DOI: 10.1364/OL.19.002101.

[286] S. R. Nagel, J. B. Macchesney, and K. L. Walker, "An Overview of the Modified Chemical Vapor Deposition (MCVD) Process and Performance," *IEEE Transactions on Microwave Theory Techniques*, vol. 30, pp. 305–322, Jan. 1, 1982, ISSN: 0018-9480. DOI: 10.1109/TMTT.1982.1131071.

[287] A. Barnini *et al.*, "Rare-earth-doped optical-fiber core deposition using full vapor-phase SPCVD process," in *Optical Components and Materials XIV*, vol. 10100, SPIE, Feb. 16, 2017, pp. 59–68. DOI: 10.1117/12.2252448.

[288] S. R. Choudhury and Y. Jaluria, "Practical aspects in the drawing of an optical fiber," *Journal of Materials Research*, vol. 13, no. 2, pp. 483–493, Feb. 1998, ISSN: 2044-5326, 0884-2914. DOI: 10.1557/JMR.1998.0063.

[289] E. Liu and J. Liu, "Quasiperiodic photonic crystal fiber," *Chinese Optics Letters*, vol. 21, no. 6, p. 060 603, Jun. 10, 2023.

[290] B. Debord, F. Amrani, L. Vincetti, F. Gérôme, and F. Benabid, "Hollow-Core Fiber Technology: The Rising of Gas Photonics," *Fibers*, vol. 7, no. 2, p. 16, 2 Feb. 2019, ISSN: 2079-6439. DOI: 10.3390/fib7020016.

[291] A. Dufour *et al.*, "All-Fiber Magneto-Optical Effect Using Nanoparticles Doped Sol-Gel Thin Film Deposited Within Microstructured Fibers," *Journal of Lightwave Technology*, vol. 39, no. 17, pp. 5604–5610, Sep. 1, 2021. DOI: 10.1364/JLT.39.005604.

[292] F. Poletti, "Nested antiresonant nodeless hollow core fiber," *Optics Express*, vol. 22, no. 20, pp. 23 807–23 828, Oct. 6, 2014, ISSN: 1094-4087. DOI: 10.1364/OE.22.023807.

[293] K. Mukasa and T. Takagi, "Hollow core fiber cable technologies," *Optical Fiber Technology*, vol. 80, p. 103 447, Oct. 1, 2023, ISSN: 1068-5200. DOI: 10.1016/j.yofte.2023.103447.

[294] G. T. Jasion *et al.*, "0.174 dB/km Hollow Core Double Nested Antiresonant Nodeless Fiber (DNANF)," in *2022 Optical Fiber Communications Conference and Exhibition (OFC)*, Mar. 2022, pp. 1–3.

[295] T. Gerber and B. Himmel, "The structure of silica glass," *Journal of Non-Crystalline Solids*, vol. 83, no. 3, pp. 324–334, Jul. 1, 1986, ISSN: 0022-3093. DOI: 10.1016/0022-3093(86)90245-0.

[296] IARC Working Group on the Evaluation of Carcinogenic Risks to Humans, "Silica Dust, Crystalline, In The Form Of Quartz Or Cristobalite," in *Arsenic, Metals, Fibres and Dusts*, International Agency for Research on Cancer, 2012.

[297] G. M. Lo Piccolo, M. Cannas, and S. Agnello, "Intrinsic Point Defects in Silica for Fiber Optics Applications," *Materials*, vol. 14, no. 24, p. 7682, 24 Jan. 2021, ISSN: 1996-1944. DOI: 10.3390/ma14247682.

[298] K. Steenland and E. Ward, "Silica: A lung carcinogen," *CA: A Cancer Journal for Clinicians*, vol. 64, no. 1, pp. 63–69, 2014, ISSN: 1542-4863. DOI: 10.3322/caac.21214.

[299] R. Brückner, "Properties and structure of vitreous silica. I," *Journal of Non-Crystalline Solids*, vol. 5, no. 2, pp. 123–175, Nov. 1, 1970, ISSN: 0022-3093. DOI: 10.1016/0022-3093(70)90190-0.

[300] M. León, P. Martín, A. Ibarra, and E. R. Hodgson, "Gamma irradiation induced defects in different types of fused silica," *Journal of Nuclear Materials*, Fusion Reactor Materials, vol. 386–388, pp. 1034–1037, Apr. 30, 2009, ISSN: 0022-3115. DOI: 10.1016/j.jnucmat.2008.12.232.

[301] M. Stapelbroek, D. L. Griscom, E. J. Friebele, and G. H. Sigel, "Oxygen-associated trapped-hole centers in high-purity fused silicas," *Journal of Non-Crystalline Solids*, Electronic Properties and Structure of Amorphous Solids, vol. 32, no. 1, pp. 313–326, Feb. 1, 1979, ISSN: 0022-3093. DOI: 10.1016/0022-3093(79)90079-6.

[302] D. L. Griscom, "Nature Of Defects And Defect Generation In Optical Glasses," in *Radiation Effects on Optical Materials*, vol. 0541, SPIE, Dec. 12, 1985, pp. 38–59. DOI: 10.1117/12.975358.

[303] G. W. Arnold and W. D. Compton, "Radiation Effects in Silica at Low Temperatures," *Physical Review*, vol. 116, no. 4, pp. 802–811, Nov. 15, 1959. DOI: 10.1103/PhysRev.116.802.

[304] G. D. Watkins, J. W. Corbett, and R. M. Walker, "Spin Resonance in Electron Irradiated Silicon," *Journal of Applied Physics*, vol. 30, no. 8, pp. 1198–1203, 1959, ISSN: 0021-8979. DOI: 10.1063/1.1735293.

[305] D. L. Griscom, "Electron spin resonance in glasses," *Journal of Non-Crystalline Solids*, Proceedings of the Fifth University Conference on Glass Science, vol. 40, no. 1, pp. 211–272, Jul. 1, 1980, ISSN: 0022-3093. DOI: 10.1016/0022-3093(80)90105-2.

[306] S. Girard *et al.*, "Overview of radiation induced point defects in silica-based optical fibers," *Reviews in Physics*, vol. 4, p. 100 032, Nov. 1, 2019, ISSN: 2405-4283. DOI: 10.1016/j.revip.2019.100032.

[307] L. Skuja, "Optical Properties Of Defects In Silica," in *Defects in SiO2 and Related Dielectrics: Science and Technology*, ser. NATO Science Series, G. Pacchioni, L. Skuja, and D. L. Griscom, Eds., Dordrecht: Springer Netherlands, 2000, pp. 73–116, ISBN: 978-94-010-0944-7. DOI: 10.1007/978-94-010-0944-7_3.

[308] C. Campanella *et al.*, "Radiation Effects on Pure-Silica Multimode Optical Fibers in the Visible and Near-Infrared Domains: Influence of OH Groups," *Applied Sciences*, vol. 11, no. 7, p. 2991, 7 Jan. 2021, ISSN: 2076-3417. DOI: 10.3390/app11072991.

[309] S. Girard *et al.*, "Radiation responses of ultra-low loss pure-silica-core optical fibers in the visible to infrared domains," *Optical Materials: X*, vol. 16, p. 100 191, Oct. 1, 2022, ISSN: 2590-1478. DOI: 10.1016/j.omx.2022.100191.

[310] L. Skuja, K. Kajihara, M. Hirano, and H. Hosono, "Visible to vacuum-UV range optical absorption of oxygen dangling bonds in amorphous SiO2," *Physical Review B*, vol. 84, no. 20, p. 205 206, Nov. 14, 2011. DOI: 10.1103/PhysRevB.84.205206.

[311] R. T. Williams and K. S. Song, "The self-trapped exciton," *Journal of Physics and Chemistry of Solids*, vol. 51, no. 7, pp. 679–716, Jan. 1, 1990, ISSN: 0022-3697. DOI: 10.1016/0022-3697(90)90144-5.

[312] D. L. Griscom, "Self-trapped holes in pure-silica glass: A history of their discovery and characterization and an example of their critical significance to industry," *Journal of Non-Crystalline Solids*, Advances in Optical Materials, vol. 352, no. 23, pp. 2601–2617, Jul. 15, 2006, ISSN: 0022-3093. DOI: 10.1016/j.jnoncrysol.2006.03.033.

[313] S. Girard *et al.*, "Influence of Self-Trapped Holes on the Responses of Fluorine-Doped Multimode Optical Fibers Exposed to Low Fluences of Protons," *physica status solidi (a)*, vol. 216, no. 3, p. 1 800 547, 2019, ISSN: 1862-6319. DOI: 10.1002/pssa.201800547.

[314] S. Girard, D. L. Griscom, J. Baggio, B. Brichard, and F. Berghmans, "Transient optical absorption in pulsed-X-ray-irradiated pure-silica-core optical fibers: Influence of self-trapped holes," *Journal of Non-Crystalline Solids*, Advances in Optical Materials, vol. 352, no. 23, pp. 2637–2642, Jul. 15, 2006, ISSN: 0022-3093. DOI: 10.1016/j.jnoncrysol.2006.03.060.

[315] L. Skuja *et al.*, "Optical Absorption of Excimer Laser-Induced Dichlorine Monoxide in Silica Glass and Excitation of Singlet Oxygen Luminescence by Energy Transfer from Chlorine Molecules," *physica status solidi (a)*, vol. 218, no. 15, p. 2 100 009, 2021, ISSN: 1862-6319. DOI: 10.1002/pssa.202100009.

[316] A. Alessi, S. Agnello, S. Grandi, A. Parlato, and F. M. Gelardi, "Refractive index change dependence on Ge(1) defects in -irradiated Ge-doped silica," *Physical Review B*, vol. 80, no. 1, p. 014 103, Jul. 8, 2009. DOI: 10.1103/PhysRevB.80.014103.

[317] E. J. Friebele, D. L. Griscom, and G. H. Sigel, "Defect centers in a germaniumdoped silicacore optical fiber," *Journal of Applied Physics*, vol. 45, no. 8, pp. 3424–3428, Aug. 1, 1974, ISSN: 0021-8979. DOI: 10.1063/1.1663795.

[318] D. L. Griscom, "On the natures of radiation-induced point defects in GeO_2-SiO_2 glasses: Reevaluation of a 26-year-old ESR and optical data set," *Optical Materials Express*, vol. 1, no. 3, pp. 400–412, Jul. 1, 2011, ISSN: 2159-3930. DOI: 10.1364/OME.1.000400.

[319] L. Skuja, "Isoelectronic series of twofold coordinated Si, Ge, and Sn atoms in glassy SiO2: A luminescence study," *Journal of Non-Crystalline Solids*, vol. 149, no. 1, pp. 77–95, Oct. 2, 1992, ISSN: 0022-3093. DOI: 10.1016/0022-3093(92)90056-P.

[320] L. Skuja and A. Naber, "Site-selective luminescence study of defects. in gamma-irradiated glassy germanium dioxide," *Nuclear Instruments and Methods in Physics Research Section B: Beam Interactions with Materials and Atoms*, Radiation Effects in Insulators, vol. 116, no. 1, pp. 549–553, Aug. 2, 1996, ISSN: 0168-583X. DOI: 10.1016/0168-583X(96)00106-1.

[321] A. Morana *et al.*, "Temperature Dependence of Low-Dose Radiation-Induced Attenuation of Germanium-Doped Optical Fiber at Infrared Wavelengths," *IEEE Transactions on Nuclear Science*, vol. 69, no. 3, pp. 512–517, Mar. 2022, ISSN: 1558-1578. DOI: 10.1109/TNS.2021.3133421.

[322] I. Reghioua *et al.*, "O2 Loaded Germanosilicate Optical Fibers: Experimental In Situ Investigation and Ab Initio Simulation Study of GLPC Evolution under Irradiation," *Applied Sciences*, vol. 12, no. 8, p. 3916, 8 Jan. 2022, ISSN: 2076-3417. DOI: 10.3390/app12083916.

[323] A. Alessi *et al.*, "Radiation Effects on Aluminosilicate Optical Fibers: Spectral Investigations From the Ultraviolet to Near-Infrared Domains," *physica status solidi (a)*, vol. 216, no. 3, p. 1 800 485, 2019, ISSN: 1862-6319. DOI: 10.1002/pssa.201800485.

[324] C. Campanella *et al.*, "Temperature Dependence of Radiation Induced Attenuation of Aluminosilicate Optical Fiber," *IEEE Transactions on Nuclear Science*, vol. 69, no. 7, pp. 1515–1520, Jul. 2022, ISSN: 1558-1578. DOI: 10.1109/TNS.2022.3150870.

[325] S. Plimpton, "Fast Parallel Algorithms for Short-Range Molecular Dynamics," *Journal of Computational Physics*, vol. 117, no. 1, pp. 1–19, Mar. 1, 1995, ISSN: 0021-9991. DOI: 10.1006/jcph.1995.1039.

[326] A. P. Thompson *et al.*, "LAMMPS - a flexible simulation tool for particle-based materials modeling at the atomic, meso, and continuum scales," *Computer Physics Communications*, vol. 271, p. 108 171, Feb. 1, 2022, ISSN: 0010-4655. DOI: 10.1016/j.cpc.2021.108171.

[327] G. Pacchioni, "Ab Initio Theory Of Point Defects In SiO2," in *Defects in SiO2 and Related Dielectrics: Science and Technology*, ser. NATO Science Series, G. Pacchioni, L. Skuja, and D. L. Griscom, Eds., Dordrecht: Springer Netherlands, 2000, pp. 161–195, ISBN: 978-94-010-0944-7. DOI: 10.1007/978-94-010-0944-7_5.

[328] N. Richard *et al.*, "Coupled Theoretical and Experimental Studies for the Radiation Hardening of Silica-Based Optical Fibers," *IEEE Transactions on Nuclear Science*, vol. 61, no. 4, pp. 1819–1825, Aug. 2014, ISSN: 1558-1578. DOI: 10.1109/TNS.2014.2321480.

[329] L. Giacomazzi, L. Martin-Samos, A. Boukenter, Y. Ouerdane, S. Girard, and N. Richard, "Ge(2), Ge(1) and Ge-E centers in irradiated Ge-doped silica: A first-principles EPR study," *Optical Materials Express*, vol. 5, no. 5, pp. 1054–1064, May 1, 2015, ISSN: 2159-3930. DOI: 10.1364/OME.5.001054.

[330] S. Girard *et al.*, "Radiation Effects on Silica-Based Optical Fibers: Recent Advances and Future Challenges," *IEEE Transactions on Nuclear Science*, vol. 60, no. 3, pp. 2015–2036, Jun. 2013, ISSN: 1558-1578. DOI: 10.1109/TNS.2012.2235464.

[331] E. Taylor, E. Friebele, H. Henschel, R. West, J. Krinsky, and C. Barnes, "Interlaboratory comparison of radiation-induced attenuation in optical fibers. II. steady-state exposures," *Journal of Lightwave Technology*, vol. 8, no. 6, pp. 967–976, Jun. 1990, ISSN: 1558-2213. DOI: 10.1109/50.54517.

[332] C. M. Petrie, D. P. Hawn, W. Windl, and T. E. Blue, "Reactor radiation-induced attenuation in fused silica optical fibers heated up to 1000 C," *Journal of Non-Crystalline Solids*, vol. 409, pp. 88–94, Feb. 1, 2015, ISSN: 0022-3093. DOI: 10.1016/j.jnoncrysol.2014.11.003.

[333] W. Heitmann, "Precision Single-Mode Fiber Spectral Attenuation Measurements," *Journal of Optical Communications*, vol. 8, no. 1, pp. 2–8, Mar. 1, 1987, ISSN: 2191-6322. DOI: 10.1515/JOC.1987.8.1.2.

[334] D. Di Francesca *et al.*, "Radiation Response of Ce-Codoped Germanosilicate and Phosphosilicate Optical Fibers," *IEEE Transactions on Nuclear Science*, vol. 63, no. 4, pp. 2058–2064, Aug. 2016, ISSN: 1558-1578. DOI: 10.1109/TNS.2015.2507861.

[335] P. Lecoq, A. Annenkov, A. Gektin, M. Korzhik, and C. Pedrini, "Scintillation and Inorganic Scintillators," in *Inorganic Scintillators for Detector Systems: Physical Principles and Crystal Engineering*, ser. Particle Acceleration and Detection, Berlin, Heidelberg: Springer, 2006, pp. 1–34, ISBN: 978-3-540-27768-2. DOI: 10.1007/3-540-27768-4_1.

[336] G. Blasse, "Scintillator materials," *Chemistry of Materials*, vol. 6, no. 9, pp. 1465–1475, Sep. 1, 1994, ISSN: 0897-4756. DOI: 10.1021/cm00045a002.

[337] R. Nowotny, "Radioluminescence of some optical fibres," *Physics in Medicine and Biology*, vol. 52, no. 4, N67–N73, Jan. 2007, ISSN: 0031-9155. DOI: 10.1088/0031-9155/52/4/N01.

[338] A. Darafsheh, R. Taleei, A. Kassaee, and J. C. Finlay, "Proton therapy dosimetry using the scintillation of the silica fibers," *Optics Letters*, vol. 42, no. 4, pp. 847–850, Feb. 15, 2017, ISSN: 1539-4794. DOI: 10.1364/OL.42.000847.

[339] C. Hoehr *et al.*, "Novel Gd 3+ -doped silica-based optical fiber material for dosimetry in proton therapy," *Scientific Reports*, vol. 9, no. 1, p. 16 376, 1 Nov. 8, 2019, ISSN: 2045-2322. DOI: 10.1038/s41598-019-52608-5.

[340] J. Vidalot *et al.*, "Mirror-Assisted Radioluminescent Optical Fibers for X-Ray Beam Monitoring," *IEEE Transactions on Nuclear Science*, vol. 70, no. 4, pp. 575–582, Apr. 2023, ISSN: 1558-1578. DOI: 10.1109/TNS.2023.3248680.

[341] A. K. M. M. Rahman *et al.*, "Ge-doped silica optical fibres as RL/OSL dosimeters for radiotherapy dosimetry," *Sensors and Actuators A: Physical*, vol. 264, pp. 30–39, Sep. 1, 2017, ISSN: 0924-4247. DOI: 10.1016/j.sna.2017.07.038.

[342] A. Meyer *et al.*, "X-Ray Radioluminescence in Diversely Doped Multimode Silica-Based Optical Fibers," *IEEE Transactions on Nuclear Science*, vol. 69, no. 7, pp. 1625–1632, Jul. 2022, ISSN: 1558-1578. DOI: 10.1109/TNS.2022.3140392.

[343] P. A. Cherenkov, "Visible light from clear liquids under the action of gamma radiation," *Comptes Rendus (doklady) De L'Académie Des Sciences De L'URSS*, vol. 2, no. 8, 1934.

[344] J. Konya and N. M. Nagy, "Interaction of Radiation With Matter," in *Nuclear and Radiochemistry Ed. 2*, Elsevier Science, 2018, pp. 85–131, ISBN: 978-0-12-813643-0.

[345] J. Wolfenden *et al.*, "Cherenkov Radiation in Optical Fibres as a Versatile Machine Protection System in Particle Accelerators," *Sensors*, vol. 23, no. 4, p. 2248, 4 Jan. 2023, ISSN: 1424-8220. DOI: 10.3390/s23042248.

[346] E. Tiesinga, P. J. Mohr, D. B. Newell, and B. N. Taylor, "CODATA Recommended Values of the Fundamental Physical Constants: 2018," *Journal of Physical and Chemical Reference Data*, vol. 50, no. 3, p. 033 105, Sep. 23, 2021, ISSN: 0047-2689. DOI: 10.1063/5.0064853.

[347] A. Mooradian, "Photoluminescence of Metals," *Physical Review Letters*, vol. 22, no. 5, pp. 185–187, Feb. 3, 1969. DOI: 10.1103/PhysRevLett.22.185.

[348] A. J. J. Bos, "Theory of thermoluminescence," *Radiation Measurements*, The 2nd Summer School on Solid State Dosimetry: Concepts and Trends in Medical Dosimetry, vol. 41, S45–S56, Dec. 1, 2006, ISSN: 1350-4487. DOI: 10.1016/j.radmeas.2007.01.003.

[349] A. J. J. Bos, "High sensitivity thermoluminescence dosimetry," *Nuclear Instruments and Methods in Physics Research Section B: Beam Interactions with Materials and Atoms*, Advanced Topics in Solid State Dosimetry, vol. 184, no. 1, pp. 3–28, Sep. 1, 2001, ISSN: 0168-583X. DOI: 10.1016/S0168-583X(01)00717-0.

[350] A. Guttilla *et al.*, "Investigation by Thermoluminescence of the Ionization and Annealing Processes in Irradiated Ge-Doped Silica Fiber Preform," *IEEE Transactions on Nuclear Science*, vol. 68, no. 8, pp. 1556–1564, Aug. 2021, ISSN: 1558-1578. DOI: 10.1109/TNS.2021.3070695.

[351] E. G. Yukihara and S. W. S. McKeever, "Optically stimulated luminescence (OSL) dosimetry in medicine," *Physics in Medicine & Biology*, vol. 53, no. 20, R351, Sep. 2008, ISSN: 0031-9155. DOI: 10.1088/0031-9155/53/20/R01.

[352] W. Primak, L. H. Fuchs, and P. Day, "Effects of Nuclear Reactor Exposure on Some Properties of Vitreous Silica and Quartz," *Journal of the American Ceramic Society*, vol. 38, no. 4, pp. 135–139, 1955, ISSN: 1551-2916. DOI: 10.1111/j.1151-2916.1955.tb14916.x.

[353] R. A. B. Devine, "Macroscopic and microscopic effects of radiation in amorphous SiO2," *Nuclear Instruments and Methods in Physics Research Section B: Beam Interactions with Materials and Atoms*, vol. 91, no. 1, pp. 378–390, Jun. 1, 1994, ISSN: 0168-583X. DOI: 10.1016/0168-583X(94)96253-7.

[354] S. Rana, H. Subbaraman, A. Fleming, and N. Kandadai, "Numerical Analysis of Radiation Effects on Fiber Optic Sensors," *Sensors*, vol. 21, no. 12, p. 4111, 12 Jan. 2021, ISSN: 1424-8220. DOI: 10.3390/s21124111.

[355] W. Primak, "A review of the gross structural effects of energetic atomic particles on vitreous and crystalline silica," *Journal of Physics and Chemistry of Solids*, vol. 13, no. 3, pp. 279–286, Jun. 1, 1960, ISSN: 0022-3697. DOI: 10.1016/0022-3697(60)90012-3.

[356] W. Primak, "Mechanism for the Radiation Compaction of Vitreous Silica," *Journal of Applied Physics*, vol. 43, no. 6, pp. 2745–2754, 1972, ISSN: 0021-8979. DOI: 10.1063/1.1661588.

[357] W. Primak and R. Kampwirth, "Impurity Effect in the Ionization Dilatation of Vitreous Silica," *Journal of Applied Physics*, vol. 39, no. 13, pp. 6010–6017, 1968, ISSN: 0021-8979. DOI: 10.1063/1.1656106.

[358] B. Brichard, O. V. Butov, K. M. Golant, and A. Fernandez Fernandez, "Gamma radiation-induced refractive index change in Ge- and N-doped silica," *Journal of Applied Physics*, vol. 103, no. 5, p. 054 905, Mar. 7, 2008, ISSN: 0021-8979. DOI: 10.1063/1.2885116.

[359] A. I. Gusarov *et al.*, "Refractive-index changes caused by proton radiation in silicate optical glasses," *Applied Optics*, vol. 41, no. 4, pp. 678–684, Feb. 1, 2002, ISSN: 2155-3165. DOI: 10.1364/AO.41.000678.

[360] W. Primak, "Fast-Neutron-Induced Changes in Quartz and Vitreous Silica," *Physical Review*, vol. 110, no. 6, pp. 1240–1254, Jun. 15, 1958. DOI: 10.1103/PhysRev.110.1240.

[361] W. Primak and R. Kampwirth, "The Radiation Compaction of Vitreous Silica," *Journal of Applied Physics*, vol. 39, no. 12, pp. 5651–5658, 1968, ISSN: 0021-8979. DOI: 10.1063/1.1656029.

[362] O. Peña-Rodríguez, J. Manzano-Santamaría, J. Olivares, A. Rivera, and F. Agulló-López, "Refractive index changes in amorphous SiO2 (silica) by swift ion irradiation," *Nuclear Instruments and Methods in Physics Research Section B: Beam Interactions with Materials and Atoms*, Basic Research on Ionic-Covalent Materials for Nuclear Applications, vol. 277, pp. 126–130, Apr. 15, 2012, ISSN: 0168-583X. DOI: 10.1016/j.nimb.2011.12.057.

[363] R. E. Schenker and W. G. Oldham, "Ultraviolet-induced densification in fused silica," *Journal of Applied Physics*, vol. 82, no. 3, pp. 1065–1071, Aug. 1, 1997, ISSN: 0021-8979. DOI: 10.1063/1.365872.

[364] V. P. Veiko *et al.*, "Femtosecond laser-induced stress-free ultra-densification inside porous glass," *Laser Physics Letters*, vol. 13, no. 5, p. 055 901, Apr. 2016, ISSN: 1612-202X. DOI: 10.1088/1612-2011/13/5/055901.

[365] A. Martinez, M. Dubov, I. Khrushchev, and I. Bennion, "Photoinduced Modifications in Fiber Gratings Inscribed Directly by Infrared Femtosecond Irradiation," *IEEE Photonics Technology Letters*, vol. 18, no. 21, pp. 2266–2268, Nov. 2006, ISSN: 1941-0174. DOI: 10.1109/LPT.2006.884883.

[366] A. Morana *et al.*, "Structural and optical changes in silica-based optical fibers exposed to high neutron and gamma fluences," *Journal of Non-Crystalline Solids*, vol. 574, p. 121 150, Dec. 15, 2021, ISSN: 0022-3093. DOI: 10.1016/j.jnoncrysol.2021.121150.

[367] A. Fernandez Fernandez, B. Brichard, and F. Berghmans, "In situ measurement of refractive index changes induced by gamma radiation in germanosilicate fibers," *IEEE Photonics Technology Letters*, vol. 15, no. 10, pp. 1428–1430, Oct. 2003, ISSN: 1941-0174. DOI: 10.1109/LPT.2003.818247.

[368] R. Gutierrez, G. Swift, S. Dubovitsky, R. Bartman, C. Barnes, and L. Dorsky, "Radiation effects on fused biconical taper wavelength division multiplexers," *IEEE Transactions on Nuclear Science*, vol. 41, no. 6, pp. 1950–1957, Dec. 1994, ISSN: 1558-1578. DOI: 10.1109/23.340529.

[369] C. Muller *et al.*, "Investigations of the MGy dose level radiation effects on the photometric budget of a radiation-hardened CMOS-based camera," *Applied Optics*, vol. 58, no. 22, pp. 6165–6172, Aug. 1, 2019, ISSN: 2155-3165. DOI: 10.1364/AO.58.006165.

[370] D. Doyle, "Radiation hardness of optical materials," presented at the 3rd Instrument Workshop for the Europa Jupiter System Mission, Noordwijk, Netherlands, 2010.

[371] "Kramers-Kronig Relations and Sum Rules in Linear Optics," in *Kramers-Kronig Relations in Optical Materials Research*, ser. Springer Series in Optical Sciences, V. Lucarini, K.-E. Peiponen, J. J. Saarinen, and E. M. Vartiainen, Eds., Berlin, Heidelberg: Springer, 2005, pp. 27–48, ISBN: 978-3-540-27316-5. DOI: 10.1007/3-540-27316-6_4.

[372] M. J. F. Digonnet, "Kramers-Kronig analysis of the absorption change in fiber gratings," in *Doped Fiber Devices*, vol. 2841, SPIE, Nov. 20, 1996, pp. 109–120. DOI: 10.1117/12.258964.

[373] M. Fruit, A. I. Gusarov, D. B. Doyle, and G. J. Ulbrich, "Radiation impact on spaceborne optics: The dose coefficients approach," in *Photonics for Space and Radiation Environments*, vol. 3872, SPIE, Dec. 7, 1999, pp. 60–71. DOI: 10.1117/12.373286.

[374] A. Gusarov and S. K. Hoeffgen, "Radiation Effects on Fiber Gratings," *IEEE Transactions on Nuclear Science*, vol. 60, no. 3, pp. 2037–2053, Jun. 2013, ISSN: 1558-1578. DOI: 10.1109/TNS.2013.2252366.

[375] B. Andreas, I. Breunig, and K. Buse, "Modeling of X-ray-Induced Refractive Index Changes in Poly(methyl methacrylate)," *ChemPhysChem*, vol. 6, no. 8, pp. 1544–1553, 2005, ISSN: 1439-7641. DOI: 10.1002/cphc.200500068.

[376] D. L. Griscom, E. J. Friebele, K. J. Long, and J. W. Fleming, "Fundamental defect centers in glass: Electron spin resonance and optical absorption studies of irradiated phosphorusdoped silica glass and optical fibers," *Journal of Applied Physics*, vol. 54, no. 7, pp. 3743–3762, Jul. 1, 1983, ISSN: 0021-8979. DOI: 10.1063/1.332591.

[377] E. J. Friebele, G. H. Sigel, and M. E. Gingerich, "Radiation response of fiber optic waveguides in the 0.4 to 1.7 region," *IEEE Transactions on Nuclear Science*, vol. 25, no. 6, pp. 1261–1266, Dec. 1978, ISSN: 1558-1578. DOI: 10.1109/TNS.1978.4329522.

[378] R. A. Weeks and P. J. Bray, "Electron Spin Resonance Spectra of GammaRayIrradiated Phosphate Glasses and Compounds: Oxygen Vacancies," *The Journal of Chemical Physics*, vol. 48, no. 1, pp. 5–13, 1968, ISSN: 0021-9606. DOI: 10.1063/1.1667952.

[379] E. J. Friebele and D. L. Griscom, "Color Centers in Glass Optical Fiber Waveguides," *MRS Online Proceedings Library (OPL)*, vol. 61, 1985/ed, ISSN: 0272-9172, 1946-4274. DOI: 10.1557/PROC-61-319.

[380] S. Girard *et al.*, "Integration of Optical Fibers in Megajoule Class Laser Environments: Advantages and Limitations," *IEEE Transactions on Nuclear Science*, vol. 59, no. 4, pp. 1317–1322, Aug. 2012, ISSN: 1558-1578. DOI: 10.1109/TNS.2012.2199130.

[381] G. Origlio, F. Messina, S. Girard, M. Cannas, A. Boukenter, and Y. Ouerdane, "Spectroscopic studies of the origin of radiation-induced degradation in phosphorus-doped optical fibers and preforms," *Journal of Applied Physics*, vol. 108, no. 12, p. 123 103, Dec. 17, 2010, ISSN: 0021-8979. DOI: 10.1063/1.3517479.

[382] D. Di Francesca *et al.*, "Combined Temperature Radiation Effects and Influence of Drawing Conditions on Phosphorous-Doped Optical Fibers," *physica status solidi (a)*, vol. 216, no. 3, p. 1 800 553, 2019, ISSN: 1862-6319. DOI: 10.1002/pssa.201800553.

[383] G. Li Vecchi *et al.*, "Infrared radiation Induced attenuation of radiation sensitive optical fibers: Influence of temperature and modal propagation," *Optical Fiber Technology*, vol. 55, p. 102 166, Mar. 1, 2020, ISSN: 1068-5200. DOI: 10.1016/j.yofte.2020.102166.

[384] E. Regnier, I. Flammer, S. Girard, F. Gooijer, F. Achten, and G. Kuyt, "Low-Dose Radiation-Induced Attenuation at InfraRed Wavelengths for P-Doped, Ge-Doped and Pure Silica-Core Optical Fibres," *IEEE Transactions on Nuclear Science*, vol. 54, no. 4, pp. 1115–1119, Aug. 2007, ISSN: 1558-1578. DOI: 10.1109/TNS.2007.894180.

[385] S. Girard, Y. Ouerdane, C. Marcandella, A. Boukenter, S. Quenard, and N. Authier, "Feasibility of radiation dosimetry with phosphorus-doped optical fibers in the ultraviolet and visible domain," *Journal of Non-Crystalline Solids*, SiO2, Advanced Dielectrics and Related Devices, vol. 357, no. 8, pp. 1871–1874, Apr. 15, 2011, ISSN: 0022-3093. DOI: 10.1016/j.jnoncrysol.2010.11.113.

[386] H. Henschel, O. Köhn, and H. U. Schmidt, "Optical fibres as radiation dosimeters," *Nuclear Instruments and Methods in Physics Research Section B: Beam Interactions with Materials and Atoms*, vol. 69, no. 2, pp. 307–314, Jun. 2, 1992, ISSN: 0168-583X. DOI: 10.1016/0168-583X(92)96023-R.

[387] A. Morana *et al.*, "Operating Temperature Range of Phosphorous-Doped Optical Fiber Dosimeters Exploiting Infrared Radiation-Induced Attenuation," *IEEE Transactions on Nuclear Science*, vol. 68, no. 5, pp. 906–912, May 2021, ISSN: 1558-1578. DOI: 10.1109/TNS.2021.3053164.

[388] G. H. Sigel, E. J. Friebele, M. J. Marrone, and M. E. Gingerich, "An Analysis of Photobleaching Techniques for the Radiation Hardening of Fiber Optic Data Links," *IEEE Transactions on Nuclear Science*, vol. 28, no. 6, pp. 4095–4101, Dec. 1981, ISSN: 1558-1578. DOI: 10.1109/TNS.1981.4335681.

[389] E. J. Friebele and M. E. Gingerich, "Photobleaching effects in optical fiber waveguides," *Applied Optics*, vol. 20, no. 19, pp. 3448–3452, Oct. 1, 1981, ISSN: 2155-3165. DOI: 10.1364/AO.20.003448.

[390] G. Li Vecchi *et al.*, "In-situ regeneration of P-doped optical fiber dosimeter," *Optics Letters*, vol. 45, no. 18, pp. 5201–5204, Sep. 15, 2020, ISSN: 1539-4794. DOI: 10.1364/OL.402382.

[391] M. Roche *et al.*, "Combined Photobleaching and Temperature Effects on 1550 nm Radiation-Induced Attenuation of Germanosilicate Optical Fiber," *IEEE Transactions on Nuclear Science*, vol. 70, no. 8, pp. 1951–1957, Aug. 2023, ISSN: 1558-1578. DOI: 10.1109/TNS.2023.3263578.

[392] A. Meyer, D. Lambert, A. Morana, P. Paillet, A. Boukenter, and S. Girard, "Simulation and Optimization of Optical Fiber Irradiation with X-rays at Different Energies," *Radiation*, vol. 3, no. 1, pp. 58–74, 1 Mar. 2023, ISSN: 2673-592X. DOI: 10.3390/radiation3010006.

[393] S. Girard, J. Baggio, and J. Bisutti, "14-MeV Neutron, -Ray, and Pulsed X-Ray Radiation-Induced Effects on Multimode Silica-Based Optical Fibers," *IEEE Transactions on Nuclear Science*, vol. 53, no. 6, pp. 3750–3757, Dec. 2006, ISSN: 1558-1578. DOI: 10.1109/TNS.2006.886222.

[394] M. Gaillardin *et al.*, "Investigations on Ionizing Dose Deposition in Thin-Layered Devices: Sample-to-Sample Variability and Electronic Equilibrium Dependence," *IEEE Transactions on Nuclear Science*, vol. 70, no. 8, pp. 2027–2033, Aug. 2023, ISSN: 1558-1578. DOI: 10.1109/TNS.2023.3239950.

[395] D. Di Francesca *et al.*, "Qualification and Calibration of Single-Mode Phosphosilicate Optical Fiber for Dosimetry at CERN," *Journal of Lightwave Technology*, vol. 37, no. 18, pp. 4643–4649, Sep. 15, 2019.

[396] I. Reghioua *et al.*, "Cathodoluminescence Characterization of Point Defects in Optical Fibers," *IEEE Transactions on Nuclear Science*, vol. 64, no. 8, pp. 2318–2324, Aug. 2017, ISSN: 1558-1578. DOI: 10.1109/TNS.2016.2644981.

[397] J. Bisutti, S. Girard, and J. Baggio, "Radiation effects of 14MeV neutrons on germanosilicate and phosphorus-doped multimode optical fibers," *Journal of Non-Crystalline Solids*, SiO, Advanced Dielectrics and Related Devices 6, vol. 353, no. 5, pp. 461–465, Apr. 1, 2007, ISSN: 0022-3093. DOI: 10.1016/j.jnoncrysol.2006.10.013.

[398] H. Henschel, M. Körfer, J. Kuhnhenn, U. Weinand, and F. Wulf, "Fibre optic radiation sensor systems for particle accelerators," *Nuclear Instruments and Methods in Physics Research Section A: Accelerators, Spectrometers, Detectors and Associated Equipment*, vol. 526, no. 3, pp. 537–550, Jul. 1, 2004, ISSN: 0168-9002. DOI: 10.1016/j.nima.2004.02.030.

[399] D. Di Francesca *et al.*, "Dosimetry Mapping of Mixed-Field Radiation Environment Through Combined Distributed Optical Fiber Sensing and FLUKA Simulation," *IEEE Transactions on Nuclear Science*, vol. 66, no. 1, pp. 299–305, Jan. 2019, ISSN: 1558-1578. DOI: 10.1109/TNS.2018.2882135.

[400] S. Girard *et al.*, "Atmospheric Neutron Monitoring through Optical Fiber-Based Sensing," *Sensors*, vol. 20, no. 16, p. 4510, 16 Jan. 2020. DOI: 10.3390/s20164510.

[401] D. A. Bradley *et al.*, "Radioluminescence sensing of radiology exposures using P-doped silica optical fibres," *Applied Radiation and Isotopes*, vol. 141, pp. 176–181, Nov. 1, 2018, ISSN: 0969-8043. DOI: 10.1016/j.apradiso.2018.02.025.

[402] H. T. Zubair *et al.*, "Real-time radiation dosimetry using P-doped silica optical fiber," *Measurement*, vol. 146, pp. 119–124, Nov. 1, 2019, ISSN: 0263-2241. DOI: 10.1016/j.measurement.2019.06.010.

[403] T. Giallorenzi *et al.*, "Optical Fiber Sensor Technology," *IEEE Transactions on Microwave Theory and Techniques*, vol. 30, no. 4, pp. 472–511, Apr. 1982, ISSN: 1557-9670. DOI: 10.1109/TMTT.1982.1131089.

[404] B. Culshaw, "Optical Fiber Sensor Technologies: Opportunities and - Perhaps - Pitfalls," *Journal of Lightwave Technology*, vol. 22, no. 1, p. 39, Jan. 1, 2004.

[405] R. Bergh, H. Lefevre, and H. Shaw, "An overview of fiber-optic gyroscopes," *Journal of Lightwave Technology*, vol. 2, no. 2, pp. 91–107, Apr. 1984, ISSN: 1558-2213. DOI: 10.1109/JLT.1984.1073580.

[406] A. Othonos, "Fiber Bragg gratings," *Review of Scientific Instruments*, vol. 68, no. 12, pp. 4309–4341, Dec. 1, 1997, ISSN: 0034-6748. DOI: 10.1063/1.1148392.

[407] Y.-J. Rao, "Fiber Bragg grating sensors: Principles and applications," in *Optical Fiber Sensor Technology: Devices and Technology*, ser. Optoelectronics, Imaging and Sensing, K. T. V. Grattan and B. T. Meggitt, Eds., Boston, MA: Springer US, 1998, pp. 355–379, ISBN: 978-1-4615-5787-6. DOI: 10.1007/978-1-4615-5787-6_11.

[408] W. W. Morey, J. R. Dunphy, and G. Meltz, "Multiplexing fiber bragg grating sensors," *Fiber and Integrated Optics*, vol. 10, no. 4, pp. 351–360, Oct. 1, 1991, ISSN: 0146-8030. DOI: 10.1080/01468039108201715.

[409] X. Bao and L. Chen, "Recent Progress in Distributed Fiber Optic Sensors," *Sensors*, vol. 12, no. 7, pp. 8601–8639, 7 Jul. 2012, ISSN: 1424-8220. DOI: 10.3390/s120708601.

[410] R. W. Boyd, "Spontaneous Light Scattering and Acoustooptics," in *Nonlinear Optics*, 4e edition, London: Academic Press, 2020, pp. 381–417, ISBN: 978-0-12-811002-7 978-0-323-85057-5.

[411] R. Feynman, R. Leighton, and M. Sands, "The Origin of the Refractive Index," in *The Feynman Lectures on Physics Vol. I*, 1963.

[412] S. Kojima, "100th Anniversary of Brillouin Scattering: Impact on Materials Science," *Materials*, vol. 15, no. 10, p. 3518, 10 Jan. 2022, ISSN: 1996-1944. DOI: 10.3390/ma15103518.

[413] K. C. Doty, C. K. Muro, J. Bueno, L. Halámková, and I. K. Lednev, "What can Raman spectroscopy do for criminalistics?" *Journal of Raman Spectroscopy*, vol. 47, no. 1, pp. 39–50, 2016, ISSN: 1097-4555. DOI: 10.1002/jrs.4826.

[414] A. J. Cox, A. J. DeWeerd, and J. Linden, "An experiment to measure Mie and Rayleigh total scattering cross sections," *American Journal of Physics*, vol. 70, no. 6, pp. 620–625, Jun. 1, 2002, ISSN: 0002-9505. DOI: 10.1119/1.1466815.

[415] A. Lipson, S. G. Lipson, and H. Lipson, "Electromagnetic waves," in *Optical Physics*, 4th ed., Cambridge University Press, 2011, pp. 129–160, ISBN: 978-0-521-49345-1.

[416] R. Feynman, R. Leighton, and M. Sands, "Radiation Damping. Light Scattering," in *The Feynman Lectures on Physics Vol. I*, 1963.

[417] "Forced vibrations and origin of refractive index," in *Optics*, 2nd ed. Tata McGraw-Hill, 1992, pp. 149–168, ISBN: 0-07-460138-5.

[418] Lord Rayleigh, "On the transmission of light through an atmosphere containing small particles in suspension, and on the origin of the blue of the sky," *The London, Edinburgh, and Dublin Philosophical Magazine and Journal of Science*, vol. 47, no. 287, pp. 375–384, Apr. 1, 1899, ISSN: 1941-5982. DOI: 10.1080/14786449908621276.

[419] S. G. Stanton, R. Pecora, and B. S. Hudson, "Resonance enhanced dynamic Rayleigh scattering," *The Journal of Chemical Physics*, vol. 75, no. 12, pp. 5615–5626, Dec. 15, 1981, ISSN: 0021-9606. DOI: 10.1063/1.442000.

[420] I. L. Fabelinskii, "Theory of Molecular Light Scattering in Condensed Isotropic Media and Gases," in *Molecular Scattering of Light*, Boston, MA: Springer New York, 1968, pp. 19–79, ISBN: 978-1-4684-1740-1. DOI: 10.1007/978-1-4684-1740-1_2.

[421] G. Mie, "Beiträge zur Optik trüber Medien, speziell kolloidaler Metallösungen," *Annalen der Physik*, vol. 330, no. 3, pp. 377–445, 1908, ISSN: 1521-3889. DOI: 10.1002/andp.19083300302.

[422] H. Du, "Mie-scattering calculation," *Applied Optics*, vol. 43, no. 9, pp. 1951–1956, Mar. 19, 2004, ISSN: 2155-3165. DOI: 10.1364/AO.43.001951.

[423] M. Nakazawa, "Rayleigh backscattering theory for single-mode optical fibers," *JOSA*, vol. 73, no. 9, pp. 1175–1180, Sep. 1, 1983. DOI: 10.1364/JOSA.73.001175.

[424] A. H. Hartog, "Introduction," in *An Introduction to Distributed Optical Fibre Sensors*, CRC Press, Jun. 1, 2017, pp. 3–29, ISBN: 978-1-315-11901-4. DOI: 10.1201/9781315119014.

[425] A. H. Hartog, "Principles of Optical Time-Domain Reflectometry (OTDR) for Distributed Sensing," in *An Introduction to Distributed Optical Fibre Sensors*, CRC Press, Jun. 1, 2017, pp. 55–106, ISBN: 978-1-315-11901-4. DOI: 10.1201/9781315119014.

[426] J. Rettig and L. Dobos, "Picosecond time interval measurements," *IEEE Transactions on Instrumentation and Measurement*, vol. 44, no. 2, pp. 284–287, Apr. 1995, ISSN: 1557-9662. DOI: 10.1109/19.377832.

[427] Tektronix. "Real-Time Versus Equivalent-Time Sampling." (2023), [Online]. Available: https://www.tek.com/en/documents/application-note/real-time-versus-equivalent-time-sampling (visited on 08/31/2023).

[428] I. Sankawa, S. Furukawa, Y. Koyamada, and H. Izumita, "Fault location technique for in-service branched optical fiber networks," *IEEE Photonics Technology Letters*, vol. 2, no. 10, pp. 766–768, Oct. 1990, ISSN: 1941-0174. DOI: 10.1109/68.60785.

[429] L. El Hares, A. P. Strong, and P. Le Stanc, "Midstream & Subsea Pipeline Condition Monitoring," presented at the Offshore Technology Conference, OnePetro, May 2, 2011. DOI: 10.4043/21767-MS.

[430] M. P. Gold, A. H. Hartog, and D. N. Payne, "New approach to splice-loss monitoring using long-range OTDR," *Electronics Letters*, vol. 20, no. 8, pp. 338–340, Apr. 12, 1984, ISSN: 1350-911X. DOI: 10.1049/el:19840230.

[431] M. Hébert and R. D. Hersch, "Reflectance and transmittance model for recto-verso halftone prints," *JOSA A*, vol. 23, no. 10, pp. 2415–2432, Oct. 1, 2006, ISSN: 1520-8532. DOI: 10.1364/JOSAA.23.002415.

[432] A. Lipovac, V. Lipovac, M. Hamza, and V. Bato, "Extending OTDR Distance Span by External Front-End Optical Preamplifier," *Electronics*, vol. 10, no. 18, p. 2275, 18 Jan. 2021, ISSN: 2079-9292. DOI: 10.3390/electronics10182275.

[433] B. J. Soller, D. K. Gifford, M. S. Wolfe, and M. E. Froggatt, "High resolution optical frequency domain reflectometry for characterization of components and assemblies," *Optics Express*, vol. 13, no. 2, pp. 666–674, Jan. 24, 2005, ISSN: 1094-4087. DOI: 10.1364/OPEX.13.000666.

[434] D. K. Gifford, B. J. Soller, M. S. Wolfe, and M. E. Froggatt, "Distributed fiber-optic temperature sensing using Rayleigh backscatter," in *2005 31st European Conference on Optical Communication, ECOC 2005*, vol. 3, Sep. 2005, 511–512 vol.3. DOI: 10.1049/cp:20050584.

[435] M. Tokushima and J. Ushida, "Demonstration of in-depth analysis of silicon photonics circuits using OFDR: Waveguides with grating couplers," *Optics Letters*, vol. 47, no. 1, pp. 162–165, Jan. 1, 2022, ISSN: 1539-4794. DOI: 10.1364/OL.444876.

[436] A. Issatayeva, A. Amantayeva, W. Blanc, D. Tosi, and C. Molardi, "Design and analysis of a fiber-optic sensing system for shape reconstruction of a minimally invasive surgical needle," *Scientific Reports*, vol. 11, no. 1, p. 8609, 1 Apr. 21, 2021, ISSN: 2045-2322. DOI: 10.1038/s41598-021-88117-7.

[437] S. Abedin, A. M. Biondi, R. Wu, L. Cao, and X. Wang, "Structural Health Monitoring Using a New Type of Distributed Fiber Optic Smart Textiles in Combination with Optical Frequency Domain Reflectometry (OFDR): Taking a Pedestrian Bridge as Case Study," *Sensors*, vol. 23, no. 3, p. 1591, 3 Jan. 2023, ISSN: 1424-8220. DOI: 10.3390/s23031591.

[438] T. Horiguchi, K. Shimizu, T. Kurashima, M. Tateda, and Y. Koyamada, "Development of a distributed sensing technique using Brillouin scattering," *Journal of Lightwave Technology*, vol. 13, no. 7, pp. 1296–1302, Jul. 1995, ISSN: 1558-2213. DOI: 10.1109/50.400684.

[439] A. H. Hartog, "Brillouin-Based Distributed Temperature and Strain Sensors," in *An Introduction to Distributed Optical Fibre Sensors*, CRC Press, Jun. 1, 2017, pp. 161–229, ISBN: 978-1-315-11901-4. DOI: 10.1201/9781315119014.

[440] "Raman-Based Distributed Temperature Sensors (DTSs)," in *An Introduction to Distributed Optical Fibre Sensors*. CRC Press, Jun. 1, 2017, pp. 109–159, ISBN: 978-1-315-11901-4. DOI: 10.1201/9781315119014.

[441] A. L. Huston, B. L. Justus, P. L. Falkenstein, R. W. Miller, H. Ning, and R. Altemus, "Remote optical fiber dosimetry," *Nuclear Instruments and Methods in Physics Research Section B: Beam Interactions with Materials and Atoms*, Advanced Topics in Solid State Dosimetry, vol. 184, no. 1, pp. 55–67, Sep. 1, 2001, ISSN: 0168-583X. DOI: 10.1016/S0168-583X(01)00713-3.

[442] S. O'Keeffe, C. Fitzpatrick, E. Lewis, and A. AlShamma'a, "A review of optical fibre radiation dosimeters," *Sensor Review*, vol. 28, no. 2, J. Billingsley, Ed., pp. 136–142, Jan. 1, 2008, ISSN: 0260-2288. DOI: 10.1108/02602280810856705.

[443] H. Zubair *et al.*, "Recent Advances in Silica Glass Optical Fiber for Dosimetry Applications," *IEEE Photonics Journal*, vol. 12, no. 3, pp. 1–25, Jun. 2020, ISSN: 1943-0655. DOI: 10.1109/JPHOT.2020.2985857.

[444] M. Gottlieb and G. B. Brandt, "Temperature sensing in optical fibers using cladding and jacket loss effects," *Applied Optics*, vol. 20, no. 22, pp. 3867–3873, Nov. 15, 1981, ISSN: 2155-3165. DOI: 10.1364/AO.20.003867.

[445] A. Hartog, "A distributed temperature sensor based on liquid-core optical fibers," *Journal of Lightwave Technology*, vol. 1, no. 3, pp. 498–509, Sep. 1983, ISSN: 1558-2213. DOI: 10.1109/JLT.1983.1072146.

[446] C. Broadway *et al.*, "CYTOP Fibre Bragg Grating Sensors for Harsh Radiation Environments," *Sensors*, vol. 19, no. 13, p. 2853, 13 Jan. 2019, ISSN: 1424-8220. DOI: 10.3390/s19132853.

[447] M.-A. Lebel-Cormier, T. Boilard, M. Bernier, and L. Beaulieu, "Medical Range Radiation Dosimeter Based on Polymer-Embedded Fiber Bragg Gratings," *Sensors*, vol. 21, no. 23, p. 8139, 23 Jan. 2021, ISSN: 1424-8220. DOI: 10.3390/s21238139.

[448] H. Henschel, S. K. Hoeffgen, J. Kuhnhenn, and U. Weinand, "High Radiation Sensitivity of Chiral Long Period Gratings," *IEEE Transactions on Nuclear Science*, vol. 57, no. 5, pp. 2915–2922, Oct. 2010, ISSN: 1558-1578. DOI: 10.1109/TNS.2010.2059043.

[449] F. Esposito, A. Srivastava, S. Campopiano, and A. Iadicicco, "Radiation Effects on Long Period Fiber Gratings: A Review," *Sensors*, vol. 20, no. 9, p. 2729, 9 Jan. 2020, ISSN: 1424-8220. DOI: 10.3390/s20092729.

[450] A. Morana *et al.*, "Radiation Effects on Fiber Bragg Gratings: Vulnerability and Hardening Studies," *Sensors*, vol. 22, no. 21, p. 8175, 21 Jan. 2022, ISSN: 1424-8220. DOI: 10.3390/s22218175.

[451] L. D. Looney and P. B. Lyons, "Measurement of radiation-induced attenuation in optical fibers by optical-time-domain reflectometry," in *Optical Technology for Signal Processing Systems*, vol. 1474, SPIE, Sep. 1, 1991, pp. 132–137. DOI: 10.1117/12.44918.

[452] H. Henschel, O. Kohn, H. Schmidt, J. Kirchhof, and S. Unger, "Radiation-induced loss of rare earth doped silica fibres," in *RADECS 97. Fourth European Conference on Radiation and Its Effects on Components and Systems (Cat. No.97TH8294)*, Sep. 1997, pp. 439–444. DOI: 10.1109/RADECS.1997.698961.

[453] R. A. Greenwell and P. B. Lyons, "Development of radiation test procedures for fiber optic systems," in *Fibre Optics '90*, vol. 1314, SPIE, Sep. 1, 1990, pp. 218–222. DOI: 10.1117/12.21982.

[454] H. Henschel, O. Kohn, and H. Schmidt, "Radiation induced loss measurements of optical fibres with optical time domain reflectometers (OTDR) at high and low dose rates," in *RADECS 91 First European Conference on Radiation and Its Effects on Devices and Systems*, Sep. 1991, pp. 380–382. DOI: 10.1109/RADECS.1991.213571.

[455] R. H. West, H. Buker, E. J. Friebele, H. Henschel, and P. B. Lyons, "The use of optical time domain reflectometers to measure radiation-induced losses in optical fibers," *Journal of Lightwave Technology*, vol. 12, no. 4, pp. 614–620, Apr. 1994, ISSN: 0733-8724. DOI: 10.1109/50.285354.

[456] H. Henschel, M. Körfer, K. Wittenburg, and F. Wulf, "Fiber Optic Radiation Sensing Systems for TESLA," TESLA Report 2000-26, 2000, p. 2000.

[457] H. Henschel, O. Köhn, M. Körfer, T. Stegmann, and F. Wulf, "Preliminary Trials with Optical Fiber Dosimeters at TTF," TESLA Report 2000-25, 2000.

[458] H. Henschel, J. Kuhnhenn, M. Körfer, K. Wittenburg, and F. Wulf, "Light guide dosimeters and loss monitors," presented at the TTF2 Review Meeting (Salzau), Jan. 22, 2003.

[459] H. Henschel, M. Körfer, and F. Wulf, "Fibre optical radiation sensing system for TESLA," in *Proceedings DIPAC 2001ESRF*, 2001, pp. 73–75.

[460] F. Wulf, M. Körfer, W. Goettmann, and H.-J. Grabosch, "Beam loss monitors for FEL using optical fiber," in *2009 IEEE Nuclear Science Symposium Conference Record (NSS/MIC)*, Oct. 2009, pp. 1993–1997. DOI: 10.1109/NSSMIC.2009.5402133.

[461] O. R. Jones, "Beam instrumentation systems of the large hadron collider: Tutorial 50," *IEEE Instrumentation & Measurement Magazine*, vol. 17, no. 1, pp. 42–48, Feb. 2014, ISSN: 1941-0123. DOI: 10.1109/MIM.2014.6782996.

[462] A. Chiuchiolo *et al.*, "Structural Health Monitoring of Superconducting Magnets at CERN Using Fiber Bragg Grating Sensors," presented at the EWSHM - 7th European Workshop on Structural Health Monitoring, Jul. 8, 2014.

[463] Z. Szillási *et al.*, "One Year of FOS Measurements in CMS Experiment at CERN," *Physics Procedia*, Proceedings of the 2nd International Conference on Technology and Instrumentation in Particle Physics (TIPP 2011), vol. 37, pp. 79–84, Jan. 1, 2012, ISSN: 1875-3892. DOI: 10.1016/j.phpro.2012.02.360.

[464] I. Toccafondo *et al.*, "Raman distributed temperature measurement at CERN high energy accelerator mixed field radiation test facility (CHARM)," in *24th International Conference on Optical Fibre Sensors*, vol. 9634, SPIE, Sep. 28, 2015, pp. 528–531. DOI: 10.1117/12.2191551.

[465] G. Spiezia *et al.*, "The LHC radiation monitoring systemRadMon," *Proc. Sci*, vol. 143, pp. 1–12, 2011.

[466] G. Spiezia *et al.*, "A New RadMon Version for the LHC and its Injection Lines," *IEEE Transactions on Nuclear Science*, vol. 61, no. 6, pp. 3424–3431, Dec. 2014, ISSN: 1558-1578. DOI: 10.1109/TNS.2014.2365046.

[467] I. Toccafondo, "Distributed Optical Fiber Radiation and Temperature Sensing at High Energy Accelerators and Experiments," Sant'Anna School Adv. Studies, Pisa, 2015.

[468] D. Di Francesca, G. Li Vecchi, Y. Kadi, M. Brugger, S. Girard, and A. Alessi, "Implementation of Optical Fiber based Dosimetry at CERN," in *26th International Conference on Optical Fiber Sensors (2018), Paper WC1*, Optical Society of America, Sep. 24, 2018, WC1. DOI: 10.1364/OFS.2018.WC1.

[469] G. Li Vecchi *et al.*, "Distributed Optical Fiber Radiation Sensing at CERN," presented at the 9th International Particle Accelerator Conference (IPAC 2018), Apr. 29, 2018, WEPAF083. DOI: 10.18429/JACoW-IPAC2018-WEPAF083.

[470] D. Di Francesca *et al.*, "Distributed Optical Fiber Radiation Sensing in the Proton Synchrotron Booster at CERN," *IEEE Transactions on Nuclear Science*, vol. 65, no. 8, pp. 1639–1644, Aug. 2018, ISSN: 1558-1578. DOI: 10.1109/TNS.2018.2818760.

[471] K. Biko *et al.*, "CERN Super Proton Synchrotron Radiation Environment and Related Radiation Hardness Assurance Implications," *IEEE Transactions on Nuclear Science*, vol. 70, no. 8, pp. 1606–1615, Aug. 2023, ISSN: 1558-1578. DOI: 10.1109/TNS.2023.3261181.

[472] O. Brüning, H. Burkhardt, and S. Myers, "The large hadron collider," *Progress in Particle and Nuclear Physics*, vol. 67, no. 3, pp. 705–734, Jul. 1, 2012, ISSN: 0146-6410. DOI: 10.1016/j.ppnp.2012.03.001.

[473] D. Di Francesca, Y. Kadi, G. Li Vecchi, and K. Kandemir, "Optical Fiber Dosimetry," presented at the R2E Annual Meeting, Dec. 11, 2018.

[474] CERN, *EN Newsletter Issue #2 - 21 June 2021*, Jun. 21, 2021.

[475] A. Faustov, "Advanced fibre optics temperature and radiation sensing in harsh environments," Thèse de doctorat, Université de Mons, Belgium, 2014.

[476] A. V. Faustov, A. Gusarov, L. B. Liokumovich, A. A. Fotiadi, M. Wuilpart, and P. Mégret, "Comparison of simulated and experimental results for distributed radiation-induced absorption measurement using OFDR reflectometry," in *Fifth European Workshop on Optical Fibre Sensors*, vol. 8794, International Society for Optics and Photonics, May 20, 2013, 87943O. DOI: 10.1117/12.2026786.

[477] A. V. Faustov *et al.*, "Remote distributed optical fibre dose measuring of high gamma-irradiation with highly sensitive Al- and P-doped fibres," in *Optical Sensors 2013*, vol. 8774, SPIE, May 3, 2013, pp. 23–28. DOI: 10.1117/12.2017331.

[478] A. V. Faustov *et al.*, "The use of optical frequency-domain reflectometry in remote distributed measurements of the -radiation dose," *Technical Physics Letters*, vol. 41, no. 5, pp. 414–417, May 1, 2015, ISSN: 1090-6533. DOI: 10.1134/S1063785015050053.

[479] A. V. Faustov *et al.*, "Application of phosphate doped fibers for OFDR dosimetry," *Results in Physics*, vol. 6, pp. 86–87, Jan. 1, 2016, ISSN: 2211-3797. DOI: 10.1016/j.rinp.2016.02.001.

[480] A. V. Faustov *et al.*, "Comparison of Gamma-Radiation Induced Attenuation in Al-Doped, P-Doped and Ge-Doped Fibres for Dosimetry," *IEEE Transactions on Nuclear Science*, vol. 60, no. 4, pp. 2511–2517, Aug. 2013, ISSN: 1558-1578. DOI: 10.1109/TNS.2013.2273273.

[481] S. Rizzolo *et al.*, "Vulnerability of OFDR-based distributed sensors to high -ray doses," *Optics Express*, vol. 23, no. 15, pp. 18 997–19 009, Jul. 27, 2015, ISSN: 1094-4087. DOI: 10.1364/OE.23.018997.

[482] M. Olivero *et al.*, "Preliminary investigation of radiation dose sensors based on aluminum-doped silicate optical fibers," in *2020 IEEE International Symposium on Medical Measurements and Applications (MeMeA)*, Jun. 2020, pp. 1–5. DOI: 10.1109/MeMeA49120.2020.9137331.

[483] T. Qiu, C. Geng, R. Wu, and X. Tang, "Metal coating enhancement of optical fiber distributed radiation sensors based on optical frequency domain reflectometry technology," *Optical Fiber Technology*, vol. 73, p. 103 063, Oct. 1, 2022, ISSN: 1068-5200. DOI: 10.1016/j.yofte.2022.103063.

[484] G. Mélin *et al.*, "Radiation Resistant Single-Mode Fiber With Different Coatings for Sensing in High Dose Environments," *IEEE Transactions on Nuclear Science*, vol. 66, no. 7, pp. 1657–1662, Jul. 2019, ISSN: 1558-1578. DOI: 10.1109/TNS.2018.2885820.

[485] R. Janani *et al.*, "From acrylates to silicones: A review of common optical fibre coatings used for normal to harsh environments," *Progress in Organic Coatings*, vol. 180, p. 107 557, Jul. 1, 2023, ISSN: 0300-9440. DOI: 10.1016/j.porgcoat.2023.107557.

[486] Y. P. Michel, M. Lucci, M. Casalboni, P. Steglich, and S. Schrader, "Mechanical characterisation of the four most used coating materials for optical fibres," in *2015 International Conference on Photonics, Optics and Laser Technology (PHOTOPTICS)*, vol. 1, Mar. 2015, pp. 91–95.

[487] D. Gloge, "Optical-Fiber Packaging and Its Influence on Fiber Straightness and Loss," *Bell System Technical Journal*, vol. 54, no. 2, pp. 245–262, 1975, ISSN: 1538-7305. DOI: 10.1002/j.1538-7305.1975.tb02837.x.

[488] "IEEE Standard for Ethernet," Institute of Electrical and Electronics Engineers, IEEE 802.3-2022, Sep. 24, 2020.

[489] W. Eddy, "Transmission Control Protocol (TCP)," Internet Engineering Task Force, Request for Comments RFC 9293, Aug. 2022, 98 pp. DOI: 10.17487/RFC9293.

[490] R. Droms, "Dynamic Host Configuration Protocol," Internet Engineering Task Force, Request for Comments RFC 2131, Mar. 1997, 45 pp. DOI: 10.17487/RFC2131.

[491] T. Richardson, Q. Stafford-Fraser, K. Wood, and A. Hopper, "Virtual network computing," *IEEE Internet Computing*, vol. 2, no. 1, pp. 33–38, Jan. 1998, ISSN: 1941-0131. DOI: 10.1109/4236.656066.

[492] "File Transfer Protocol," Internet Engineering Task Force, Request for Comments RFC 959, Oct. 1985, 69 pp. DOI: 10.17487/RFC0959.

[493] "IEC/IEEE International - Standard Digital Interface for Programmable Instrumentation - Part 2: Codes, formats, protocols and common commands," IEC/IEEE, May 2004.

[494] "Universal serial bus interfaces for data and power - Part 2-1: Universal Serial Bus Specification, Revision 2.0," International Electrotechnical Commission, IEC 62680-2-1:2015, Sep. 15, 2015.

[495] Viavi Solutions. "Nano and Micro iOTDR Cards datasheets." (2022), [Online]. Available: https://www.viavisolutions.com/en-us/literature/nano-and-micro-iotdr-cards-data-sheets-en.pdf (visited on 05/31/2023).

[496] E. Sugita, R. Nagase, K. Kanayama, and T. Shintaku, "SC-type single-mode optical fiber connectors," *Journal of Lightwave Technology*, vol. 7, no. 11, pp. 1689–1696, Nov. 1989, ISSN: 1558-2213. DOI: 10.1109/50.45890.

[497] Y. Waseda, E. Matsubara, and K. Shinoda, "Fundamental Properties of X-rays," in *X-Ray Diffraction Crystallography: Introduction, Examples and Solved Problems*, Y. Waseda, E. Matsubara, and K. Shinoda, Eds., Berlin, Heidelberg: Springer, 2011, pp. 1–20, ISBN: 978-3-642-16635-8. DOI: 10.1007/978-3-642-16635-8_1.

[498] A. Hessenbruch, "A brief history of x-rays," *Endeavour*, vol. 26, no. 4, pp. 137–141, Dec. 1, 2002, ISSN: 0160-9327. DOI: 10.1016/S0160-9327(02)01465-5.

[499] E. B. Podgorak, "Production of X Rays," in *Radiation Physics for Medical Physicists*, ser. Biological and Medical Physics, Biomedical Engineering, E. B. Podgorsak, Ed., Berlin, Heidelberg: Springer, 2010, pp. 177–205, ISBN: 978-3-642-00875-7. DOI: 10.1007/978-3-642-00875-7_4.

[500] E. Ammann and W. Kutschera, "X-Ray Tubes-Continuous Innovative Technology," *The British Journal of Radiology*, vol. 70, S1–S9, Special-Issue-1 Nov. 1997, ISSN: 0007-1285. DOI: 10.1259/bjr.1997.0002.

[501] J. A. Seibert, "X-Ray Imaging Physics for Nuclear Medicine Technologists. Part 1: Basic Principles of X-Ray Production," *Journal of Nuclear Medicine Technology*, vol. 32, no. 3, pp. 139–147, Sep. 1, 2004, ISSN: 0091-4916, 1535-5675. pmid: 15347692.

[502] M. Ladd and R. Palmer, "X-Rays and X-Ray Diffraction," in *Structure Determination by X-ray Crystallography: Analysis by X-rays and Neutrons*, M. Ladd and R. Palmer, Eds., Boston, MA: Springer US, 2013, pp. 111–159, ISBN: 978-1-4614-3954-7. DOI: 10.1007/978-1-4614-3954-7_3.

[503] V. V. Rozanov, I. V. Matveichuk, A. P. Chernyaev, N. A. Nikolaeva, and S. A. Krasnov, "Current State and Lines of the Further Development of High-Tech Means of Radiation Sterilization," *Bulletin of the Russian Academy of Sciences: Physics*, vol. 84, no. 4, pp. 403–405, Apr. 1, 2020, ISSN: 1934-9432. DOI: 10.3103/S106287382004022X.

[504] B. Rajewsky, "X-ray equipment for food irradiation," in *Food Irradiation : Proceedings of an International Symposium on Food Irradiation / Jointly Organized by IAEA and FAO and Held in Karlsruhe, 6-10 June 1966*, Vienna : International Atomic Energy Agency, 1966., 1966.

[505] T. Mastrangelo *et al.*, "A New Generation of X Ray Irradiators for Insect Sterilization," *Journal of Economic Entomology*, vol. 103, no. 1, pp. 85–94, Feb. 1, 2010, ISSN: 0022-0493. DOI: 10.1603/EC09139.

[506] V. Girones *et al.*, "The Use of High-Energy X-Ray Generators for TID Testing of Electronic Devices," *IEEE Transactions on Nuclear Science*, vol. 70, no. 8, pp. 1982–1989, Aug. 2023, ISSN: 1558-1578. DOI: 10.1109/TNS.2023.3279626.

[507] W. Nakel, "The elementary process of bremsstrahlung," *Physics Reports*, vol. 243, no. 6, pp. 317–353, Jul. 1, 1994, ISSN: 0370-1573. DOI: 10.1016/0370-1573(94)00068-9.

[508] S. M. Seltzer and M. J. Berger, "Procedure for calculating the radiation stopping power for electrons," *The International Journal of Applied Radiation and Isotopes*, vol. 33, no. 11, pp. 1219–1226, Nov. 1, 1982, ISSN: 0020-708X. DOI: 10.1016/0020-708X(82)90245-9.

[509] A. Omar, P. Andreo, and G. Poludniowski, "A model for the emission of K and L x rays from an x-ray tube," *Nuclear Instruments and Methods in Physics Research Section B: Beam Interactions with Materials and Atoms*, vol. 437, pp. 36–47, Dec. 15, 2018, ISSN: 0168-583X. DOI: 10.1016/j.nimb.2018.10.026.

[510] J. Knoth, H. Schneider, and H. Schwenke, "Tunable exciting energies for total reflection X-ray fluorescence spectrometry using a tungsten anode and bandpass filtering," *X-Ray Spectrometry*, vol. 23, no. 6, pp. 261–266, 1994, ISSN: 1097-4539. DOI: 10.1002/xrs.1300230606.

[511] A. Thompson *et al.*, *X-Ray Data Booklet*. Lawrence Berkeley National Laboratory, 2009.

[512] K. K. Fung and W. B. Gilboy, ""Anode heel effect" on patient dose in lumbar spine radiography.," *The British Journal of Radiology*, vol. 73, no. 869, pp. 531–536, May 2000, ISSN: 0007-1285. DOI: 10.1259/bjr.73.869.10884750.

[513] T. Rogers, "High-Intensity Radiation from Beryllium-Window X-Ray Tubes," *Radiology*, vol. 48, no. 6, pp. 594–603, Jun. 1947, ISSN: 0033-8419. DOI: 10.1148/48.6.594.

[514] W. N. Lundahl, "X-ray thickness gauge for cold rolled strip steel," *Electrical Engineering*, vol. 67, no. 4, pp. 349–353, Apr. 1948, ISSN: 2376-7804. DOI: 10.1109/EE.1948.6444059.

[515] COMET. "MXR-165 datasheet." (2021), [Online]. Available: https://xray.comet.tech/getmedia/1ebeab27-fb14-42cf-9407-d8f49fb53347/mxr-165_single_sheet_en_v12.pdf?disposition=attachment (visited on 06/06/2023).

[516] COMET. "MXR-225/26 datasheet." (2022), [Online]. Available: https://xray.comet.tech/getmedia/32bf2ef7-5f5f-4083-a185-64e2d0217a93/mxr-225_26_single_sheet_en_v16.pdf?disposition=attachment (visited on 06/06/2023).

[517] R. Murray and K. E. Holbert, "Radioactivity," in *Nuclear Energy : An Introduction to the Concepts, Systems, and Applications of Nuclear Processes Ed. 8*, Elsevier Science, 2019, pp. 33–51, ISBN: 978-0-12-812881-7.

[518] Y. Katsumura and H. Kudo, "Radiations: Types and Sources," in *Radiation Applications*, ser. An Advanced Course in Nuclear Engineering, H. Kudo, Ed., vol. 07, Singapore: Springer, 2018, ISBN: 978-981-10-7349-6 978-981-10-7350-2. DOI: 10.1007/978-981-10-7350-2.

[519] M. Thoennessen, "2022 Update of the discoveries of nuclides," *International Journal of Modern Physics E*, vol. 32, no. 01, p. 2 330 001, Jan. 2023, ISSN: 0218-3013. DOI: 10.1142/S0218301323300011.

[520] C. Decristoforo, O. Neels, and M. Patt, "Emerging Radionuclides in a Regulatory Framework for Medicinal Products How Do They Fit?" *Frontiers in Medicine*, vol. 8, 2021, ISSN: 2296-858X.

[521] K. Debertin, "The art of realizing the Becquerel," *Applied Radiation and Isotopes*, vol. 47, no. 4, pp. 423–431, Apr. 1, 1996, ISSN: 0969-8043. DOI: 10.1016/0969-8043(95)00309-6.

[522] M. R. A. Pillai, "Preferred use of curie (ci) rather than becquerel (Bq) in nuclear medicine practice," *Nuclear Medicine and Biology*, vol. 45, pp. 51–52, Feb. 1, 2017, ISSN: 0969-8051. DOI: 10.1016/j.nucmedbio.2016.10.003.

[523] C. Lindquist, "Gamma knife radiosurgery," *Seminars in Radiation Oncology*, Stereotactic Radiosurgery, vol. 5, no. 3, pp. 197–202, Jul. 1, 1995, ISSN: 1053-4296. DOI: 10.1016/S1053-4296(05)80017-7.

[524] S. Bokhari, R. Shahzad, A. Castaño, and M. S. Maurer, "Nuclear imaging modalities for cardiac amyloidosis," *Journal of Nuclear Cardiology*, vol. 21, no. 1, pp. 175–184, Feb. 1, 2014, ISSN: 1532-6551. DOI: 10.1007/s12350-013-9803-2.

[525] L. Baranyai, "Industrial Applications of Radioisotopes," in *Nuclear and Radiochemistry Ed. 2*. Elsevier Science, 2018, pp. 335–367, ISBN: 978-0-12-813643-0.

[526] K. Mehta, "Gamma irradiators for radiation sterilization," International Atomic Energy Agency, 39101799, Jul. 15, 2008.

[527] D. Fleetwood, P. Winokur, L. Riewe, and R. Pease, "An improved standard total dose test for CMOS space electronics," *IEEE Transactions on Nuclear Science*, vol. 36, no. 6, pp. 1963–1970, Dec. 1989, ISSN: 1558-1578. DOI: 10.1109/23.45393.

[528] G. R. Malkoske, J. Slack, and J. L. Norton, "Cobalt-60 production in CANDU power reactors," presented at the SIEN 2003, International Symposium on Nuclear Energy, Nuclear Power - A New Challenge, Bucharest (Romania), Jul. 1, 2003.

[529] K. Han, D. Ballon, C. Chui, and R. Mohan, "Monte Carlo simulation of a cobalt-60 beam," *Medical Physics*, vol. 14, no. 3, pp. 414–419, 1987, ISSN: 2473-4209. DOI: 10.1118/1.596120.

[530] M.-M. Bé *et al.*, *Table of Radionuclides* (Monographie BIPM-5). Pavillon de Breteuil, F-92310 Sèvres, France: Bureau International des Poids et Mesures, 2006, vol. 3, ISBN: 92-822-2218-7.

[531] E. Blackmore, P. Dodd, and M. Shaneyfelt, "Improved capabilities for proton and neutron irradiations at TRIUMF," in *2003 IEEE Radiation Effects Data Workshop*, Jul. 2003, pp. 149–155. DOI: 10.1109/REDW.2003.1281368.

[532] C. Bélanger-Champagne, E. Blackmore, C. Lindsay, C. Hoehr, and M. Trinczek, "Simulation and Measurements of Collimator Effects in Proton and Neutron Radiation Testing for Single-Event Effects," *IEEE Transactions on Nuclear Science*, vol. 67, no. 1, pp. 161–168, Jan. 2020, ISSN: 1558-1578. DOI: 10.1109/TNS.2019.2952003.

[533] E. Blackmore, "Operation of the TRIUMF (20-500 MeV) proton irradiation facility," in *2000 IEEE Radiation Effects Data Workshop. Workshop Record. Held in Conjunction with IEEE Nuclear and Space Radiation Effects Conference (Cat. No.00TH8527)*, Jul. 2000, pp. 1–5. DOI: 10.1109/REDW.2000.896260.

[534] TRIUMF. "Proton Irradiation Facility (PIF) Overview," TRIUMF : Canada's particle accelerator centre. (2023), [Online]. Available: https://www.triumf.ca/proton-irradiation-facility (visited on 08/25/2023).

[535] D. D. McCracken, "The Monte Carlo Method," *Scientific American*, vol. 192, no. 5, pp. 90–97, 1955, ISSN: 0036-8733. JSTOR: 24944647.

[536] D. E. Raeside, "Monte Carlo principles and applications," *Physics in Medicine & Biology*, vol. 21, no. 2, p. 181, Mar. 1976, ISSN: 0031-9155. DOI: 10.1088/0031-9155/21/2/001.

[537] W. J. Morokoff and R. E. Caflisch, "Quasi-Monte Carlo Integration," *Journal of Computational Physics*, vol. 122, no. 2, pp. 218–230, Dec. 1, 1995, ISSN: 0021-9991. DOI: 10.1006/jcph.1995.1209.

[538] A. Lambert, D. Gruyer, and G. Saint Pierre, "A fast Monte Carlo algorithm for collision probability estimation," in *Robotics and Vision 2008 10th International Conference on Control, Automation*, Dec. 2008, pp. 406–411. DOI: 10.1109/ICARCV.2008.4795553.

[539] V. Genberg, G. Michels, and G. Bisson, "Optomechanical tolerancing with Monte Carlo techniques," in *Optomechanics 2011: Innovations and Solutions*, vol. 8125, SPIE, Sep. 24, 2011, pp. 86–94. DOI: 10.1117/12.892580.

[540] T. P. Barnett, "Monte Carlo Climate Forecasting," *Journal of Climate*, vol. 8, no. 5, pp. 1005–1022, May 1, 1995, ISSN: 0894-8755, 1520-0442. DOI: 10.1175/1520-0442(1995)008<1005:MCCF>2.0.CO;2.

[541] M. Zwicker *et al.*, "Recent Advances in Adaptive Sampling and Reconstruction for Monte Carlo Rendering," *Computer Graphics Forum*, vol. 34, no. 2, pp. 667–681, 2015, ISSN: 1467-8659. DOI: 10.1111/cgf.12592.

[542] D. Creal, "A Survey of Sequential Monte Carlo Methods for Economics and Finance," *Econometric Reviews*, vol. 31, no. 3, pp. 245–296, May 1, 2012, ISSN: 0747-4938. DOI: 10.1080/07474938.2011.607333.

[543] M. Swiechowski, K. Godlewski, B. Sawicki, and J. Madziuk, "Monte Carlo Tree Search: A review of recent modifications and applications," *Artificial Intelligence Review*, vol. 56, no. 3, pp. 2497–2562, Mar. 1, 2023, ISSN: 1573-7462. DOI: 10.1007/s10462-022-10228-y.

[544] D. W. O. Rogers, "Fifty years of Monte Carlo simulations for medical physics," *Physics in Medicine & Biology*, vol. 51, no. 13, R287, Jun. 2006, ISSN: 0031-9155. DOI: 10.1088/0031-9155/51/13/R17.

[545] D. C. Montgomery and G. C. Runger, "Descriptive Statistics," in *Applied Statistics and Probability for Engineers*, John Wiley & Sons, Mar. 22, 2010, pp. 199–238, ISBN: 978-0-470-05304-1.

[546] J.-F. Carrier, L. Archambault, L. Beaulieu, and R. Roy, "Validation of GEANT4, an object-oriented Monte Carlo toolkit, for simulations in medical physics," *Medical Physics*, vol. 31, no. 3, pp. 484–492, 2004, ISSN: 2473-4209. DOI: 10.1118/1.1644532.

[547] D. C. Montgomery and G. C. Runger, "Statistical Intervals for a Single Sample," in *Applied Statistics and Probability for Engineers*, John Wiley & Sons, Mar. 22, 2010, pp. 271–304, ISBN: 978-0-470-05304-1.

[548] E. Alerstam, T. Svensson, and S. Andersson-Engels, "Parallel computing with graphics processing units for high-speed Monte Carlo simulation of photon migration," *Journal of Biomedical Optics*, vol. 13, no. 6, p. 060 504, Nov. 2008, ISSN: 1083-3668, 1560-2281. DOI: 10.1117/1.3041496.

[549] C.-M. Ma, "Implementation of a Monte Carlo code on a parallel computer system," *Parallel Computing*, vol. 20, no. 7, pp. 991–1005, Jul. 1, 1994, ISSN: 0167-8191. DOI: 10.1016/0167-8191(94)90014-0.

[550] C. M. N. A. Pereira, A. C. A. Mól, A. Heimlich, S. R. S. Moraes, and P. Resende, "Development and performance analysis of a parallel Monte Carlo neutron transport simulation program for GPU-Cluster using MPI and CUDA technologies," *Progress in Nuclear Energy*, vol. 65, pp. 88–94, May 1, 2013, ISSN: 0149-1970. DOI: 10.1016/j.pnucene.2013.02.008.

[551] A. Haghighat and J. C. Wagner, "Monte Carlo variance reduction with deterministic importance functions," *Progress in Nuclear Energy*, vol. 42, no. 1, pp. 25–53, Jan. 1, 2003, ISSN: 0149-1970. DOI: 10.1016/S0149-1970(02)00002-1.

[552] M. E. Rising *et al.*, "MCNPő Code V.6.3.0 Release Notes," Los Alamos National Lab. (LANL), Los Alamos, NM (United States), LA-UR-22-33103, Jan. 10, 2023. DOI: 10.2172/1909545.

[553] C. Ahdida *et al.*, "New Capabilities of the FLUKA Multi-Purpose Code," *Frontiers in Physics*, vol. 9, 2022, ISSN: 2296-424X.

[554] G. Battistoni *et al.*, "Overview of the FLUKA code," *Annals of Nuclear Energy*, Joint International Conference on Supercomputing in Nuclear Applications and Monte Carlo 2013, SNA + MC 2013. Pluri- and Trans-disciplinarity, Towards New Modeling and Numerical Simulation Paradigms, vol. 82, pp. 10–18, Aug. 1, 2015, ISSN: 0306-4549. DOI: 10.1016/j.anucene.2014.11.007.

[555] T. Sato *et al.*, "Features of Particle and Heavy Ion Transport code System (PHITS) version 3.02," *Journal of Nuclear Science and Technology*, vol. 55, no. 6, pp. 684–690, Jun. 3, 2018, ISSN: 0022-3131. DOI: 10.1080/00223131.2017.1419890.

[556] F. Salvat, J. M. Fernandez-Varea, and J. Sempau, "PENELOPE2006, A Code System for Monte-Carlo Simulation of Electron and Photon Transport," Jul. 2008.

[557] National Research Council of Canada. Metrology Research Centre. Ionizing Radiation Standards and Conseil national de recherches du Canada. Centre de recherche en métrologie. Étalonnage de rayonnement ionisant, *EGSnrc: Software for Monte Carlo simulation of ionizing radiation*, National Research Council of Canada, 2021. DOI: 10.4224/40001303.

[558] J. F. Ziegler, M. D. Ziegler, and J. P. Biersack, "SRIM The stopping and range of ions in matter (2010)," *Nuclear Instruments and Methods in Physics Research Section B: Beam Interactions with Materials and Atoms*, 19th International Conference on Ion Beam Analysis, vol. 268, no. 11, pp. 1818–1823, Jun. 1, 2010, ISSN: 0168-583X. DOI: 10.1016/j.nimb.2010.02.091.

[559] S. Agostinelli *et al.*, "Geant4-a simulation toolkit," *Nuclear Instruments and Methods in Physics Research Section A: Accelerators, Spectrometers, Detectors and Associated Equipment*, vol. 506, no. 3, pp. 250–303, Jul. 1, 2003, ISSN: 0168-9002. DOI: 10.1016/S0168-9002(03)01368-8.

[560] J. Allison *et al.*, "Geant4 developments and applications," *IEEE Transactions on Nuclear Science*, vol. 53, no. 1, pp. 270–278, Feb. 2006, ISSN: 1558-1578. DOI: 10.1109/TNS.2006.869826.

[561] J. Allison *et al.*, "Recent developments in Geant4," *Nuclear Instruments and Methods in Physics Research Section A: Accelerators, Spectrometers, Detectors and Associated Equipment*, vol. 835, pp. 186–225, Nov. 1, 2016, ISSN: 0168-9002. DOI: 10.1016/j.nima.2016.06.125.

[562] "The Geant4 Software License," Geant4. (Jun. 28, 2006), [Online]. Available: https://geant4.web.cern.ch//download/license.html (visited on 06/07/2023).

[563] H. Nowak and W. Nowak, "Monte Carlo simulation of diffraction dissociation experiments with the BIS-2 spectrometer," USSR, 1980, p. 36.

[564] R. Brun, A. C. McPherson, P. Zanarini, M. Maire, and F. Bruyant, "GEANT 3 User's guide," CERN, Aug. 17, 1987.

[565] A. Schälicke *et al.*, "Geant4 electromagnetic physics for the LHC and other HEP applications," *Journal of Physics: Conference Series*, vol. 331, no. 3, p. 032 029, Dec. 2011, ISSN: 1742-6596. DOI: 10.1088/1742-6596/331/3/032029.

[566] A. V. Ivantchenko, V. N. Ivanchenko, J.-M. Q. Molina, and S. L. Incerti, "Geant4 hadronic physics for space radiation environment," *International Journal of Radiation Biology*, vol. 88, no. 1-2, pp. 171–175, Jan. 1, 2012, ISSN: 0955-3002. DOI: 10.3109/09553002.2011.610865. pmid: 21830895.

[567] V. Ivanchenko *et al.*, "Validation of Geant4 10.3 simulation of proton interaction for space radiation effects," *Experimental Astronomy*, vol. 44, no. 3, pp. 437–450, Dec. 1, 2017, ISSN: 1572-9508. DOI: 10.1007/s10686-017-9556-z.

[568] V. Ivanchenko *et al.*, "Progress of Geant4 electromagnetic physics developments and applications," *EPJ Web of Conferences*, vol. 214, p. 02 046, 2019, ISSN: 2100-014X. DOI: 10.1051/epjconf/201921402046.

[569] I. Kyriakou *et al.*, "Review of the Geant4-DNA Simulation Toolkit for Radiobiological Applications at the Cellular and DNA Level," *Cancers*, vol. 14, no. 1, p. 35, 1 Jan. 2022, ISSN: 2072-6694. DOI: 10.3390/cancers14010035.

[570] S. A. Zein *et al.*, "Monte Carlo simulations of electron interactions with the DNA molecule: A complete set of physics models for Geant4-DNA simulation toolkit," *Nuclear Instruments and Methods in Physics Research Section B: Beam Interactions with Materials and Atoms*, vol. 542, pp. 51–60, Sep. 1, 2023, ISSN: 0168-583X. DOI: 10.1016/j.nimb.2023.06.004.

[571] A. Valentin, M. Raine, J.-E. Sauvestre, M. Gaillardin, and P. Paillet, "Geant4 physics processes for microdosimetry simulation: Very low energy electromagnetic models for electrons in silicon," *Nuclear Instruments and Methods in Physics Research Section B: Beam Interactions with Materials and Atoms*, vol. 288, pp. 66–73, Oct. 1, 2012, ISSN: 0168-583X. DOI: 10.1016/j.nimb.2012.07.028.

[572] A. Valentin, M. Raine, M. Gaillardin, and P. Paillet, "Geant4 physics processes for microdosimetry simulation: Very low energy electromagnetic models for protons and heavy ions in silicon," *Nuclear Instruments and Methods in Physics Research Section B: Beam Interactions with Materials and Atoms*, vol. 287, pp. 124–129, Sep. 15, 2012, ISSN: 0168-583X. DOI: 10.1016/j.nimb.2012.06.007.

[573] D. Sarrut *et al.*, "Advanced Monte Carlo simulations of emission tomography imaging systems with GATE," *Physics in Medicine & Biology*, vol. 66, no. 10, 10TR03, May 2021, ISSN: 0031-9155. DOI: 10.1088/1361-6560/abf276.

[574] G. Santin, V. Ivanchenko, H. Evans, P. Nieminen, and E. Daly, "GRAS: A general-purpose 3-D Modular Simulation tool for space environment effects analysis," *IEEE Transactions on Nuclear Science*, vol. 52, no. 6, pp. 2294–2299, Dec. 2005, ISSN: 1558-1578. DOI: 10.1109/TNS.2005.860749.

[575] R. Bujila, A. Omar, and G. Poludniowski, "A validation of SpekPy: A software toolkit for modelling X-ray tube spectra," *Physica Medica*, vol. 75, pp. 44–54, Jul. 1, 2020, ISSN: 1120-1797. DOI: 10.1016/j.ejmp.2020.04.026.

[576] G. Poludniowski, A. Omar, R. Bujila, and P. Andreo, "Technical Note: SpekPy v2.0a software toolkit for modeling x-ray tube spectra," *Medical Physics*, vol. 48, no. 7, pp. 3630–3637, 2021, ISSN: 2473-4209. DOI: 10.1002/mp.14945.

[577] J. Ödén, J. Zimmerman, and G. Poludniowski, "Comparison of CT-number parameterization models for stoichiometric CT calibration in proton therapy," *Physica Medica*, vol. 47, pp. 42–49, Mar. 1, 2018, ISSN: 1120-1797. DOI: 10.1016/j.ejmp.2018.02.016.

[578] M. Persson *et al.*, "Upper limits of the photon fluence rate on CT detectors: Case study on a commercial scanner," *Medical Physics*, vol. 43, no. 7, pp. 4398–4411, 2016, ISSN: 2473-4209. DOI: 10.1118/1.4954008.

[579] G. Poludniowski, G. Landry, F. DeBlois, P. M. Evans, and F. Verhaegen, "SpekCalc: A program to calculate photon spectra from tungsten anode x-ray tubes," *Physics in Medicine and Biology*, vol. 54, no. 19, N433–N438, Sep. 2009, ISSN: 0031-9155. DOI: 10.1088/0031-9155/54/19/N01.

[580] G. G. Poludniowski and P. M. Evans, "Calculation of x-ray spectra emerging from an x-ray tube. Part I. Electron penetration characteristics in x-ray targets," *Medical Physics*, vol. 34, pp. 2164–2174, 6Part1 2007, ISSN: 2473-4209. DOI: 10.1118/1.2734725.

[581] G. G. Poludniowski, "Calculation of x-ray spectra emerging from an x-ray tube. Part II. X-ray production and filtration in x-ray targets," *Medical Physics*, vol. 34, pp. 2175–2186, 6Part1 2007, ISSN: 2473-4209. DOI: 10.1118/1.2734726.

[582] A. Omar, P. Andreo, and G. Poludniowski, "A model for the energy and angular distribution of x rays emitted from an x-ray tube. Part I. Bremsstrahlung production," *Medical Physics*, vol. 47, no. 10, pp. 4763–4774, 2020, ISSN: 2473-4209. DOI: 10.1002/mp.14359.

[583] A. Omar, P. Andreo, and G. Poludniowski, "A model for the energy and angular distribution of x rays emitted from an x-ray tube. Part II. Validation of x-ray spectra from 20 to 300 kV," *Medical Physics*, vol. 47, no. 9, pp. 4005–4019, 2020, ISSN: 2473-4209. DOI: 10.1002/mp.14360.

[584] R. J. Feuerstein, "Field Measurements of Deployed Fiber," in *Optical Fiber Communication Conference and Exposition and The National Fiber Optic Engineers Conference (2005), Paper NThC4*, Optica Publishing Group, Mar. 6, 2005, NThC4.

[585] A. Champavère, "Key OTDR Specification Relates to User's Real Needs," *Electrical Design News*, Dec. 1, 1999.

[586] D. Philen, I. White, J. Kuhl, and S. Mettler, "Single-Mode Fiber OTDR: Experiment and Theory," *IEEE Transactions on Microwave Theory and Techniques*, vol. 30, no. 10, pp. 1487–1496, Oct. 1982, ISSN: 1557-9670. DOI: 10.1109/TMTT.1982.1131282.

[587] D. C. Montgomery and G. C. Runger, "Simple Linear Regression and Correlation," in *Applied Statistics and Probability for Engineers*, John Wiley & Sons, Mar. 22, 2010, pp. 427–476, ISBN: 978-0-470-05304-1.

[588] R. W. Boyd and D. J. Gauthier, "Controlling the Velocity of Light Pulses," *Science*, vol. 326, no. 5956, pp. 1074–1077, Nov. 20, 2009. DOI: 10.1126/science.1170885.

[589] R. C. Dimick and G. J. Trezek, "Photodiode as a Sensitive Temperature Probe," *Review of Scientific Instruments*, vol. 34, no. 9, pp. 981–983, 1963, ISSN: 0034-6748. DOI: 10.1063/1.1718668.

[590] I. S. Amiri, F. M. A. M. Houssien, A. N. Z. Rashed, and A. E.-N. A. Mohammed, "Temperature effects on characteristics and performance of near-infrared wide bandwidth for different avalanche photodiodes structures," *Results in Physics*, vol. 14, p. 102 399, Sep. 1, 2019, ISSN: 2211-3797. DOI: 10.1016/j.rinp.2019.102399.

[591] L. J. J. Tan *et al.*, "Temperature Dependence of Avalanche Breakdown in InP and InAlAs," *IEEE Journal of Quantum Electronics*, vol. 46, no. 8, pp. 1153–1157, Aug. 2010, ISSN: 1558-1713. DOI: 10.1109/JQE.2010.2044370.

[592] M. Kondow, T. Kitatani, K. Nakahara, and T. Tanaka, "Temperature dependence of lasing wavelength in a GaInNAs laser diode," *IEEE Photonics Technology Letters*, vol. 12, no. 7, pp. 777–779, Jul. 2000, ISSN: 1941-0174. DOI: 10.1109/68.853497.

[593] A. Van Der Ziel, "Thermal Noise in Field-Effect Transistors," *Proceedings of the IRE*, vol. 8, no. 50, pp. 1808–1812, 1962, ISSN: 0096-8390. DOI: 10.1109/JRPROC.1962.288221.

[594] A. Meyer, "Towards an Embedded and Distributed Optical Fiber-based Dosimeter for Space Applications," presented at the IEEE Nuclear & Space Radiation Effects Conference (NSREC), in collab. with A. Morana *et al.*, Jul. 21, 2022.

[595] A. Meyer *et al.*, "Toward an Embedded and Distributed Optical Fiber-Based Dosimeter for Space Applications," *IEEE Transactions on Nuclear Science*, vol. 70, no. 4, pp. 583–589, Apr. 2023, ISSN: 1558-1578. DOI: 10.1109/TNS.2022.3226194.

[596] M. P. Unterweger, "Half-life measurements at the National Institute of Standards and Technology," *Applied Radiation and Isotopes*, Proceedings of the Conference on Radionuclide Metrology and Its A Pplications, ICRM'01, vol. 56, no. 1, pp. 125–130, Jan. 1, 2002, ISSN: 0969-8043. DOI: 10.1016/S0969-8043(01)00177-4.

[597] H. Sunak, "Single-mode fiber measurements," *IEEE Transactions on Instrumentation and Measurement*, vol. 37, no. 4, pp. 557–560, Dec. 1988, ISSN: 1557-9662. DOI: 10.1109/19.9812.

[598] C. Campanella *et al.*, "Influence of Ambient Light on the Radiation-Induced Attenuation of Germanosilicate Optical Fibers in the Visible and Near-Infrared Domains," *IEEE Transactions on Nuclear Science*, vol. 70, no. 4, pp. 562–567, Apr. 2023, ISSN: 1558-1578. DOI: 10.1109/TNS.2022.3228099.

[599] A. Gallet *et al.*, "Novel methodology for interpolation of radiation-induced attenuation in optical fibers," *Optical Fiber Technology*, vol. 80, p. 103 389, Oct. 1, 2023, ISSN: 1068-5200. DOI: 10.1016/j.yofte.2023.103389.

[600] R. Koga, S. Penzin, K. Crawford, and W. Crain, "Single event functional interrupt (SEFI) sensitivity in microcircuits," in *RADECS 97. Fourth European Conference on Radiation and Its Effects on Components and Systems (Cat. No.97TH8294)*, Sep. 1997, pp. 311–318. DOI: 10.1109/RADECS.1997.698915.

[601] J. ípa, G. Dilillo, R. Campana, and G. Galgóczi, "A comparison of trapped particle models in low Earth orbit," in *Space Telescopes and Instrumentation 2020: Ultraviolet to Gamma Ray*, vol. 11444, SPIE, Dec. 13, 2020, pp. 597–606. DOI: 10.1117/12.2561011.

[602] "G4PSDoseDeposit.cc source code, v11.0," CERN GitLab. (Jun. 25, 2021), [Online]. Available: https://gitlab.cern.ch/geant4/geant4/-/blob/geant4-11.0-release/source/digits_hits/scorer/src/G4PSDoseDeposit.cc (visited on 07/31/2023).

[603] F. H. Attix, "Energy-absorption coefficients for gamma-rays in compounds or mixtures," *Physics in Medicine & Biology*, vol. 29, no. 7, p. 869, Jul. 1984, ISSN: 0031-9155. DOI: 10.1088/0031-9155/29/7/009.

[604] A. Brown and H. Suit, "The centenary of the discovery of the Bragg peak," *Radiotherapy and Oncology*, vol. 73, no. 3, pp. 265–268, Dec. 1, 2004, ISSN: 0167-8140. DOI: 10.1016/j.radonc.2004.09.008.

[605] R. M. Ribeiro and D. Souza-Santos, "Comparison of the neutron ambient dose equivalent and ambient absorbed dose calculations with different GEANT4 physics lists," *Radiation Physics and Chemistry*, vol. 139, pp. 179–183, Oct. 1, 2017, ISSN: 0969-806X. DOI: 10.1016/j.radphyschem.2017.05.021.

[606] J. Seuntjens, H. Thierens, and U. Schneider, "Correction factors for a cylindrical ionization chamber used in medium-energy X-ray beams," *Physics in Medicine & Biology*, vol. 38, no. 6, p. 805, Jun. 1993, ISSN: 0031-9155. DOI: 10.1088/0031-9155/38/6/013.

[607] D. J. O'Brien, D. A. Roberts, G. S. Ibbott, and G. O. Sawakuchi, "Reference dosimetry in magnetic fields: Formalism and ionization chamber correction factors," *Medical Physics*, vol. 43, pp. 4915–4927, 8Part1 2016, ISSN: 2473-4209. DOI: 10.1118/1.4959785.

[608] M. K. Barnoski and S. M. Jensen, "Fiber waveguides: A novel technique for investigating attenuation characteristics," *Applied Optics*, vol. 15, no. 9, pp. 2112–2115, Sep. 1, 1976, ISSN: 2155-3165. DOI: 10.1364/AO.15.002112.

[609] D. Di Francesca *et al.*, "Low radiation dose calibration and theoretical model of an optical fiber dosimeter for the International Space Station," *Applied Optics*, vol. 62, no. 16, E43–E50, Jun. 1, 2023, ISSN: 2155-3165. DOI: 10.1364/AO.483560.

[610] A. Meyer, "X-Ray Radioluminescence in Diversely Doped Multimode Silica-based Optical Fibers," presented at the Radiation Effects on Components and Systems Conference (RADECS), in collab. with A. Morana *et al.*, Sep. 15, 2021.

[611] A. Meyer, "Influence of X-ray energy on dosimetry using phosphorus-doped optical fiber," presented at the Workshop on Radiation Effects on Optoelectronics and Photonics Technologies (RADOPT), in collab. with A. Morana, M. Roche, D. Lambert, and S. Girard, Nov. 16, 2021.

Appendix A:

Articles published as the main author

A. Articles published as the main author

Contents of this appendix

This appendix compiles the facsimilia of the published scientific articles written as the main author during the course of this thesis.

Article A.1, *X-Ray Radioluminescence in Diversely Doped Multimode Silica-Based Optical Fibers* [342], was published in July 2022 in the journal IEEE Transactions on Nuclear Science, in a special issue on the RADECS 2021 conference in which a presentation on the same topic was given [610]. This article was written in the early stage of the thesis, and focuses on a different topic, namely the radioluminescence properties of optical fibers (cf. **Section 1.2.2**). In this work, multimode optical fibers with five different types of dopants – cerium (Ce), germanium (Ge), aluminum (Al), fluorine (F) and phosphorus (P) – were compared for their radioluminescence properties.

Article A.2, *Toward an Embedded and Distributed Optical Fiber-Based Dosimeter for Space Applications* [595] was published in April 2023 in the journal IEEE Transactions on Nuclear Science, in a special issue on the NSREC 2022 conference in which a presentation on the same topic was given [594]. This article reports the results obtained with the Micro iOTDR in γ and X-ray irradiations **Section 3.2**.

Article A.3, *Simulation and Optimization of Optical Fiber Irradiation with X-rays at Different Energies* [392] was published in March 2023 in the journal MDPI Radiation, and follows up on a RADOPT 2021 conference presentation [611]. This article compares the results of SpekPy and Geant4 simulations (cf. **Chapter 4**) with additional experimental measurements to determine the influence of X-ray tube voltage on the dose deposition in single-mode, phosphorus-doped optical fibers.

IEEE TRANSACTIONS ON NUCLEAR SCIENCE, VOL. 69, NO. 7, JULY 2022 1625

X-Ray Radioluminescence in Diversely Doped Multimode Silica-Based Optical Fibers

Arnaud Meyer, *Student Member, IEEE*, Adriana Morana, *Member, IEEE*, Hicham El Hamzaoui, Bruno Capoen, Géraud Bouwmans, Mohamed Bouazaoui, Sylvain Girard, *Senior Member, IEEE*, Emmanuel Marin, Youcef Ouerdane, and Aziz Boukenter

***Abstract*— The radioluminescence (RL) response under X-rays is investigated for five different types of multimode silica-based optical fibers doped with Ge, P, Al, F, or Ce. The results indicate that all tested fibers show a measurable RL signal at dose rates from 0.1 to 15 Gy(SiO_2)/s, using 10-cm-long samples and a photomultiplier-based acquisition chain. Other influences of radiation, such as radiation-induced attenuation, are discussed in order to evaluate the potential of such fiber types for radiation detection or dosimetry applications.**

***Index Terms*— Dosimetry, optical fiber (OF), radiation, radioluminescence (RL), scintillators.**

I. Introduction

OPTICAL fibers (OFs) are waveguides well-suited for radiation monitoring because of their ability to act both as a sensing element and as a means of transporting measurement signal to devices located outside of the radiation area. Radiation effects on OFs can be mainly categorized into three different phenomena [1]: radiation-induced attenuation (RIA), which causes transmitted signal to decrease, radiation-induced emission (RIE), which consists of a measurable signal to be emitted during and/or after irradiation, and radiation-induced refractive index change (RIRIC), which causes a modification of the refractive index of either OF core or cladding material.

Amidst phenomena linked with RIE, radioluminescence (RL), i.e., emission induced by exciting, through irradiation, defects created during the fiber manufacturing and/or radiation-induced point centers, is particularly of interest, because the produced signal is conveniently transmitted by the OF producing the RL signal. The emitted light is then relatively easy to measure using conventional optical devices such as photomultiplier tubes.

Manuscript received 8 October 2021; revised 7 December 2021 and 17 December 2021; accepted 30 December 2021. Date of publication 5 January 2022; date of current version 18 July 2022.

Arnaud Meyer, Adriana Morana, Sylvain Girard, Emmanuel Marin, Youcef Ouerdane, and Aziz Boukenter are with the Université de Lyon, UJM-Saint-Etienne, CNRS, Institut d Optique Graduate School, Laboratoire Hubert Curien UMR 5516, 42023 Saint-Étienne, France (e-mail: arnaud.meyer@univ-st-etienne.fr; sylvain.girard@univ-st-etienne.fr).

Hicham El Hamzaoui, Bruno Capoen, Géraud Bouwmans, and Mohamed Bouazaoui are with CNRS, UMR 8523-PhLAM-Physique des Lasers Atomes et Molécules, Université de Lille, 59000 Lille, France (e-mail: mohamed.bouazaoui@univ-lille.fr).

Color versions of one or more figures in this article are available at https://doi.org/10.1109/TNS.2022.3140392.

Digital Object Identifier 10.1109/TNS.2022.3140392

TABLE I
OF Samples Used for This Experiment

Symbol	Core dopant	Core diameter	Manufacturer	Length ± 1 mm
Ge	Germanium	62 µm	iXblue	10 cm
P	Phosphorus	62 µm	iXblue	10 cm, 1 cm
Al	Aluminum	42 µm	iXblue	10 cm, 1 cm
F	Fluorine	50 µm	Draka	10 cm
Ce	Cerium	40 µm	FiberTech Lille	1 cm

OF-based scintillators have been widely studied and are commonly used for dosimetry purposes, especially in the medical area. Usual materials for this type of application typically involve specially engineered crystals or plastics [2], which yield a high RL signal, but are not designed to operate at high levels of total ionizing dose (TID) or high dose rates that could be encountered in severe environments such as space, nuclear or high-energy physics facilities.

Rods or OFs, optimized for dosimetry through measurement of RL signal, have been produced and studied, and typically involve dopants such as cerium (Ce) [3], [4], gadolinium (Gd) [5], or copper (Cu) [6], which are less commonly employed in commercially available OFs.

However, previous studies [7] have shown that OFs with more commonly available dopants may also show significant RL signal. We investigate in this study the RL properties of a panel of OFs, in order to assess their potential for dosimetry applications as sensing elements.

II. Materials and Methods

A. Choice of Samples

Five different types of multimode OFs, listed in Table I, were selected for this study, based on multiple criteria: their availability, to evaluate well-known kinds of fiber that are used on common applications, their already known properties under radiation, ranging from radiation-hardened to radiation-sensitive, and their composition. All samples share the same structure, with pure silica in the cladding (except for F-doped fiber) and pure silica doped with a single dopant in the core. Finally, multimode OFs were selected because of their

1626 IEEE TRANSACTIONS ON NUCLEAR SCIENCE, VOL. 69, NO. 7, JULY 2022

larger core diameter, and therefore, increased sensitive volume, compared to single-mode OFs.

Germanium (Ge) is amongst the most commonly available dopants for OFs, and the one primarily used for OF-based telecommunication. The sample chosen for this experiment is from a so-called "canonical" fiber [8], i.e., an OF designed for research, reflecting the manufacturing process and properties of commercially-available Ge-doped OFs. Previous studies of this fiber have highlighted a high cathodoluminescence (CL) signal [9], [10]. In particular, CL signal centered at ∼400 nm was associated with Germanium Lone Pair Centers (GLPC), known to be natively present in as-drawn Ge-doped fibers. Such GLPC centers can be converted to Ge (1) and Ge (2) defects during irradiation [1], when the core of the sample is irradiated with 10 keV electrons [10]. Ge-doped fibers are abundantly studied for dosimetry applications, through RL although at lower doses to fit requirements for medical applications [11]–[13], and through thermoluminescence at higher TIDs [14]–[16].

Phosphorus (P)-doped fibers are known to show high RIA response, especially in the visible domain [17]. The sample chosen for this experiment is from another canonical fiber, which presented a very weak CL emission band, centered at ∼410 nm and associated with P-related defects [10]. It should also be noted that a previous work showed that P-doped fibers could produce an RL signal exploitable for dosimetry under short (≤100 ms) X-ray pulses [18].

Aluminum (Al) is generally used as a codopant for Erbium-doped OF amplifiers as it prevents undesirable clustering of rare-earth ions [19]. Similar to P-doped OFs, Al-doped fibers also exhibit high RIA response [20]. A noticeable difference between P- and Al-doped fibers is their intrinsic, preirradiation transmission in the ultraviolet domain; the former being more transmitting whereas the latter is more absorbing. The Al-doped sample chosen for this experiment is a fiber sample designed by iXblue to study radiation response of Al-doped fiber without other dopants. CL measurements have shown an intense luminescence in the Al-doped core at ∼380 nm [21].

Fluorine (F), on the opposite, is a dopant mainly used in radiation-hardened OFs. It decreases the refractive index of silica and is, consequently, generally present in the fiber cladding and in lesser concentration, or absent, in the fiber core. F-doped silica fibers, along with pure silica-core fibers, are the most radiation-hardened OFs known to date for steady-state radiation environments up to 100 kGy [22]. The sample chosen for this experiment is a commercially available "rad-hard" OF, designed to yield very low RIA in both infrared and visible spectral regions. This same type of fiber is also used in our experiment as a transport fiber, to carry the RL signal of all tested samples outside of the irradiation chamber, to the acquisition system. CL measurements on this type of fiber show luminescence bands centered at ∼460, ∼560, and ∼650 nm, similar to the one recorded in the pure silica cladding of other fibers [10]. A comparable type of fiber, with a pure silica core and fluoropolymer cladding, was shown to exhibit under 100–225 MeV protons an RL signal with two bands also centered at ∼460 and ∼650 nm [23].

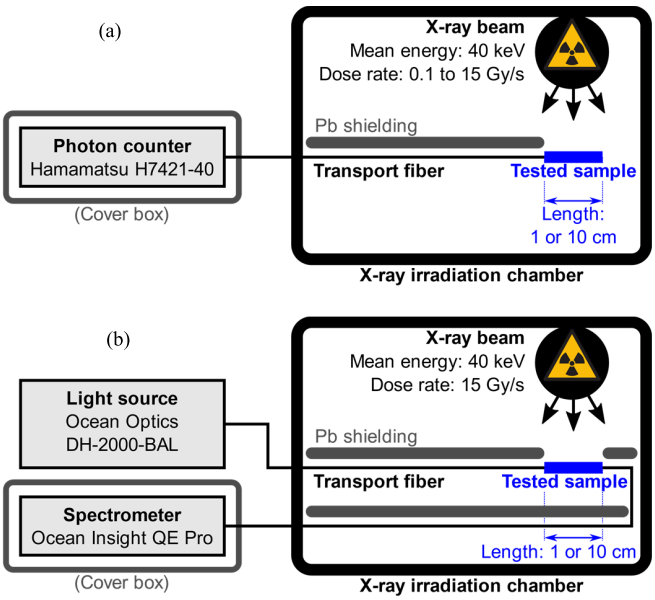

Fig. 1. Experimental setups. (a) Setup for RL measurements. (b) Setup for RIA measurements.

Finally, Cerium (Ce) doping was studied, since Ce-related centers present a strong RL signal at ∼500 nm, often investigated for dosimetry applications [3], [4], [24]–[26]. A Ce-doped fiber sample developed and supplied by FiberTech Lille was included in this experiment in order to compare performances of the other samples against fibers designed and optimized for RL.

B. Measurement Setup

All measurements were carried out at room temperature in the LabHX X-ray irradiator located in the Laboratoire Hubert Curien of Université Jean Monnet, Saint-Étienne, France.

The source of the irradiator is a COMET MXR 225/26 X-ray tube, using a tungsten anode driven at 100 kV, yielding X photons with a mean energy of ∼40 keV and an adjustable dose rate, set by varying the tube filament current.

The setup used for measuring RL signal is depicted in Fig. 1(a) and involves a Hamamatsu H7421-40 photon counting head, which uses internally a photomultiplier tube with a GaAsP photocathode and works in a spectral range from 380 to 720 nm. It was installed outside of the irradiation chamber, inside a box designed to screen most of ambient light. Its integration time was set to 1 ms for these experiments.

To measure RIA and RL spectra, another setup, shown in Fig. 1(b), involves an Ocean Optics DH-2000-BAL deuterium-halogen light source, covering a broad range of wavelengths from 210 to 2500 nm, and an Ocean Insight QE Pro spectrometer, operating between 250 and 1000 nm. The same setup, without switching on the light source, was used to acquire the RL spectra of each sample.

In order to transmit the RL signal emitted by the samples, a radiation-hardened OF was spliced to each of the samples, one at a time. This transport fiber was of the same type as F-doped samples investigated in this work.

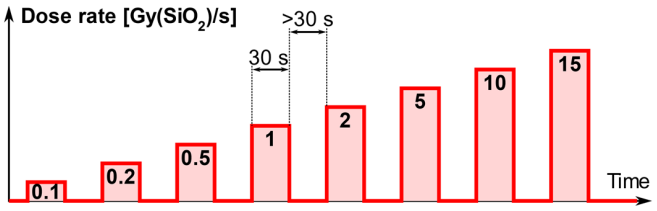

Fig. 2. Sequence of dose rates applied for irradiating each sample during RL measurements.

As preliminary results showed that this rad-hard fiber produces a nonnull RL signal when exposed to X-rays, the transport fiber was shielded using 3 mm thick lead (Pb) plates, covering most of the transport fiber length inside the irradiation chamber until the splicing point with the sample under test.

Each of these samples was prepared at the length specified in Table I. Because of the very high RL signal of this fiber type, the Ce-doped sample was cut to a length of 1 cm in order not to saturate the detector. In the same way, to stay within the dynamics of the measuring system, RIA measurements on the more radiosensitive Al- and P-doped fibers were performed on samples of 1 cm long.

For RL measurements, each sample was irradiated according to a sequence of irradiations with a duration of 30 s each, followed by a pause of at least 30 s, for eight values of dose rate from 0.1 to 15 Gy(SiO_2)/s ($\pm$10%), as shown in Fig. 2. The X-ray tube filament current was set from 0.15 to 25 mA in order to reach these dose rate values.

Total dose deposited on the sample is accumulated between subsequent dose rates and reaches $\sim$1.0 kGy at the end of the sequence. Therefore, the effects of TID must be considered along with dose rate, especially for radiation-sensitive OFs.

For RIA and spectral RL measurements, fresh samples were irradiated ten times for 30 s at a single dose rate value of 15 Gy(SiO_2)/s ($\pm$10%), with a pause of at least 30 s between each irradiation.

C. Data Analysis

For RL measurements, the measured photon counts during irradiation were summed in bins of 1 s and subtracted with the mean dark signal measured just before irradiation start, for each tested sample.

For spectral RL measurements, all spectra were subtracted with the dark signal measured prior to each run, and scaled using the spectral response of the whole measurement chain from a calibrated halogen source.

For RIA measurements, all transmission spectra were subtracted with the dark signal measured prior to each run, and parasitic signal in the UV domain was compensated by subtracting from each spectrum its mean value measured between 250 and 260 nm.

D. Repeatability of RL Measurements

In order to evaluate the uncertainties linked to our setup, four similar RL runs have been performed on 10 cm-long Al-doped samples, irradiated during 30 s at a dose rate of 10 Gy(SiO_2)/s ($\pm$10%). For each run, the new sample was positioned and spliced to the transport fiber, and the connection of the other end of transport fiber to the photon counting device was performed anew.

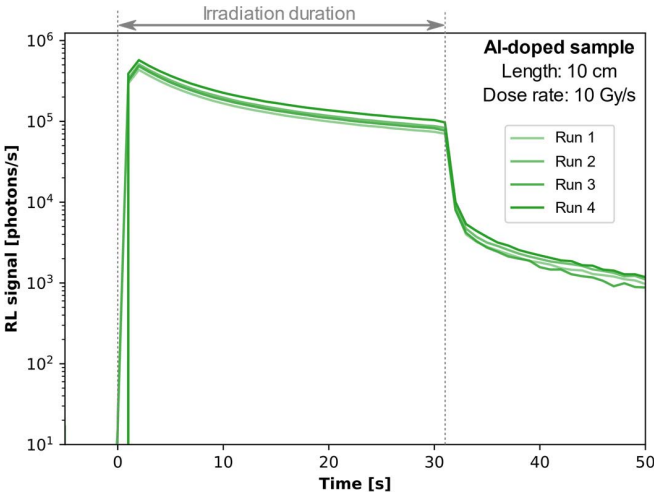

Fig. 3. RL signal over time recorded for four different pieces of Al-doped sample, irradiated each during 30 s at a dose rate of 10 Gy/s in order to check the variability of our measurement setup.

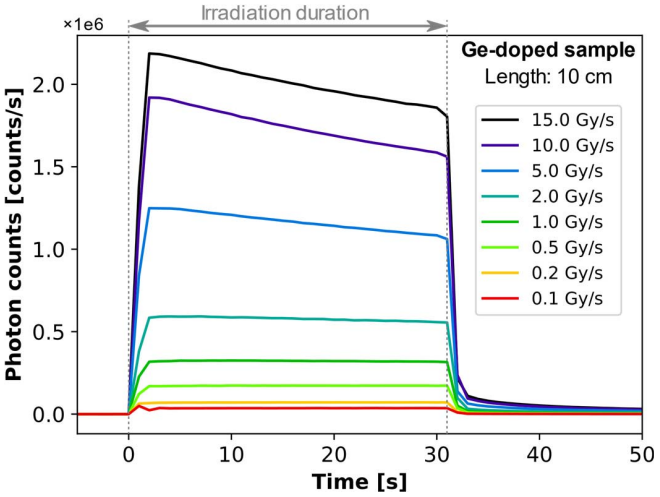

Fig. 4. Example of a dataset after dark subtraction, shown here for 10-cm-long Ge-doped sample. Time origin has been defined at irradiation start for each run.

By analyzing the difference in photon counts between these four runs, depicted in Fig. 3, we determined an overall uncertainty of $\pm$25% on the measured RL signal. This is explained by variabilities of sample length, splice quality between the sample and transport fiber, and quality of signal injection in the photon counting device.

III. Results and Discussion

A. RL Signal Against Time

An example of time traces of measured RL signal of a single sample, the 10-cm-long Ge-doped fiber, is shown in

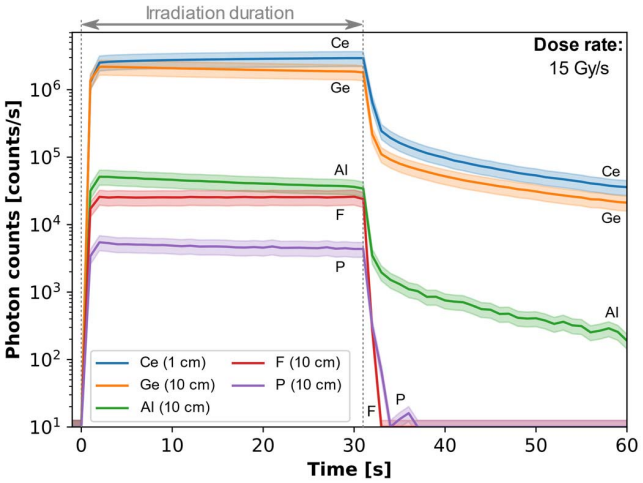

Fig. 5. Comparison of RL response of all tested fiber samples as a function of time, at the maximum dose rate of 15 Gy/s. Values lesser than 10^1 were clipped for clarity. Filled areas show the uncertainty range of ±25%.

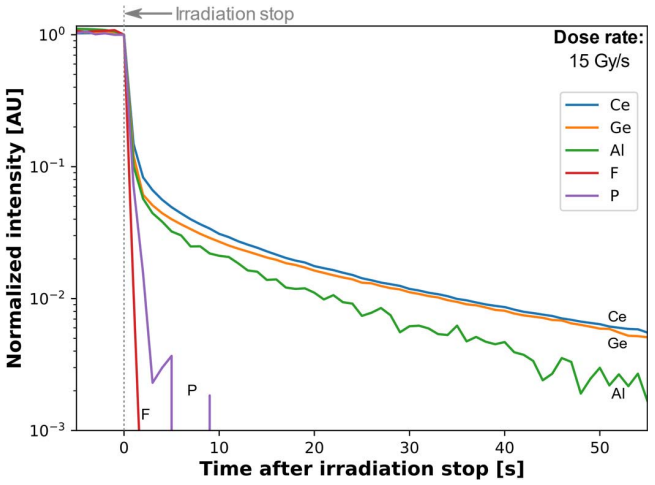

Fig. 6. Comparison of RL afterglow at 15 Gy/s of all tested fiber samples, normalized by the intensity measured at the end of irradiation. Values lesser than 10^3 were clipped for clarity.

Fig. 4. This type of graph clearly illustrates that the higher the dose rate, the higher the intensity of the measured RL signal. Moreover, in the case of radiosensitive samples, such as the depicted Ge-doped fiber, we can also observe that the RL signal intensity decreases with irradiation time, particularly at higher dose rates.

Because our setup involves low energy (≤100 keV) X rays, there is no significant occurrence of Cherenkov effect and therefore, its influence on the RL signal was not evaluated in the scope of our study.

Fig. 5 reports a comparison of all measured data at the highest investigated dose rate of 15 Gy/s. We can observe that the RL signal at this dose rate spreads roughly from 5×10^3 to 3×10^6 counts/s over the tested samples.

Out of all fibers tested in our panel, the Ce-doped sample, even with a length of only 1 cm and a smaller sensitive volume, still delivers the most intense RL signal, which also noticeably increases during irradiation. The 10-cm-long Ge-doped sample also delivers an intense RL signal comparable to the Ce-doped one, despite the size, and therefore, sensitive volume, difference of both samples.

On the other end of the range, the Al- and F-doped samples show a significant amount of RL, but at least one order of magnitude lower compared to previous samples at the highest tested dose rate. Finally, the P-doped sample stands out, as its measured RL signal is even lower than that of the F-doped fiber used for transport.

The afterglow, i.e., remaining RL signal after irradiation, is shown in greater detail in Fig. 6, normalized for all samples by their RL signal measured at the time of irradiation end. Afterglow is clearly identifiable for Ce-, Ge-, and Al-doped samples, whereas it appears to be either absent, or too low in comparison to measurement noise, for F- and P-doped samples. When normalized, it appears that the afterglow response is very similar among Ce-, Ge-, and Al-doped samples, decreasing to ∼10% and 1% of original value, respectively, after 1 and 30 s.

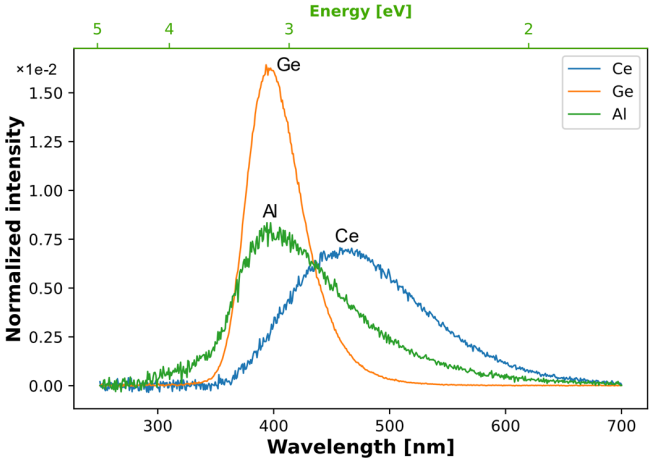

Fig. 7. RL spectra of Ce-, Ge-, and Al-doped samples, integrated during 1 s between 0 and 15 Gy at 15 Gy/s, normalized by integral.

It is interesting to note that these RL results are in good agreement with the ones previously observed under CL experiments [10], despite very different irradiation conditions (X-rays versus electrons and low versus high dose rate). Particularly, the case of F- and P-doped samples sharing the same afterglow features suggests that, also for RL, Si-related defects could be involved. One important difference between CL and RL results, however, involves the possible impact of RIA on the RL fibers, even for low probe lengths, which is negligible in CL measurements.

B. Spectral Features of RL Signal

Measured RL spectra of Ce-, Ge-, and Al-doped samples, calibrated as explained in Section II-C, are shown in Fig. 7, normalized by integral to compare their shapes. Because of the low RL signal delivered by F- and P-doped samples, our setup was unable to measure a significant RL spectrum for these two samples.

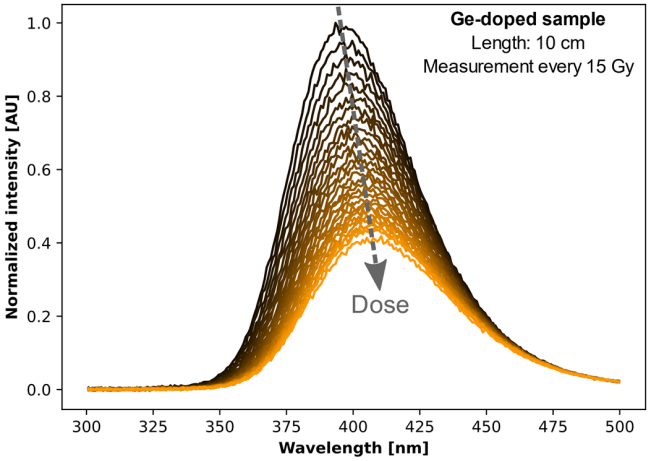

Fig. 8. Evolution of RL spectrum of Ge-doped fiber during irradiation. Each spectrum was acquired during 1 s at a dose rate of 15 Gy/s, amounting to a TID of 450 Gy at the end of the depicted sequence.

For the Ce-, Ge-, and Al-doped samples, at least 95% of the RL signal is emitted between 300 and 600 nm. The RL spectrum of the Ce-doped sample is centered at 2.6 eV and has been associated with 5d–4f transition of Ce^{3+} ions [3]. For the Ge-doped sample, the RL spectrum is centered as 3.2 eV, associated with GLPC [27], [28]. Finally, the underlying physical origins of the RL spectrum of Al-doped sample, centered at ∼3.1 eV, are still discussed [21], as different mechanisms for this emission have been proposed; some attributing it to electron–hole recombination near Al-M^+ centers [29], others associating it with charge-compensated substitutional Al^{3+} (Al^{3+}–M) [30].

Fig. 8 shows the evolution of Ge-doped sample RL spectrum during irradiation. It illustrates that two phenomena influence RL signal during irradiation: a decrease in amplitude, as well as a change of the spectral shape of the emitted signal. Although the former could be explained both by RIA and a decrease of the population of RL-inducing defects, such as GLPCs for the depicted Ge-doped sample, the latter could only be explained by a change in the spectral absorption of the fiber, and therefore, only to the occurrence of RIA. Similar spectral evolution was also observed for the two other samples; in these cases, RIA is assumed to be the main factor for RL decrease.

Also, because of the high sensitivity of Al-doped fiber to RIA, even more at shorter wavelengths as demonstrated in section 0, we may assume the Al spectrum shown in Fig. 7, acquired between 0 and 15 Gy, is affected by the occurrence of RIA and probably slightly shifted to the larger wavelengths.

C. Radiation-Induced Attenuation

Because of their different compositions, the samples under test exhibit very different levels of RIA. Fig. 9 reports the measured RIA of all samples. Fig. 9(a) shows the spectral RIA measured after a single run of 30 s at 15 Gy/s, totaling to a TID of 450 Gy. Fig. 9(b) shows the evolution of RIA at 450 nm wavelength over TID up to 4.5 kGy.

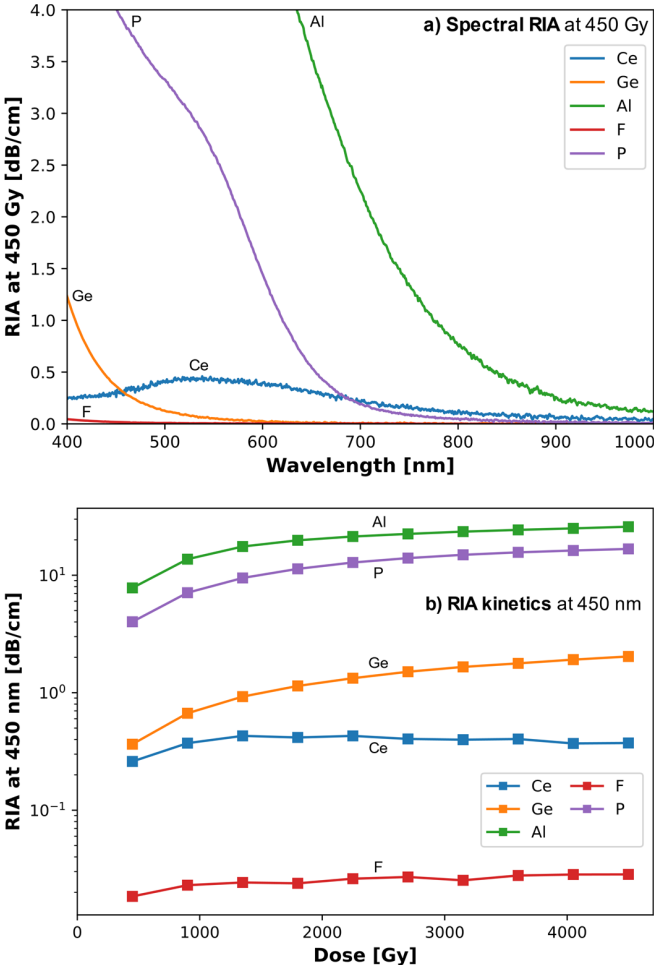

Fig. 9. RIA of all samples. (a) Spectral RIA recorded at a TID of 450 Gy. (b) Evolution of RIA at 450 nm as a function of TID.

The RIA response is very different amongst tested samples. Whereas, in Fig. 9(a), F- and Ce-doped samples exhibit a comparatively low level of RIA over the whole measured spectrum, Ge-, P-, and Al- doped samples yield a high RIA in the short wavelengths region, where most of the RL signal appears to be emitted, which explains the decrease in amplitude as observed in Fig. 8. The fact that the RIA is not flat over the whole spectrum also explains the change of spectral shape observed in Fig. 8.

RIA kinetics shown in Fig. 9(b) further elaborate on the ample difference in RIA response between samples. While Ce- and F- doped fibers show little increase and a comparatively low RIA, Ge-, P-, and Al-doped samples see a visible increase to high levels of RIA.

It is important to note that the decrease in RL signal cannot be directly deduced from the measured RIA level because each length element of the irradiated fiber emits an RL signal which travels through a different thickness of absorbing medium. A model taking into account these effects could be the goal of future studies and should allow one to optimize the design of dosimeters.

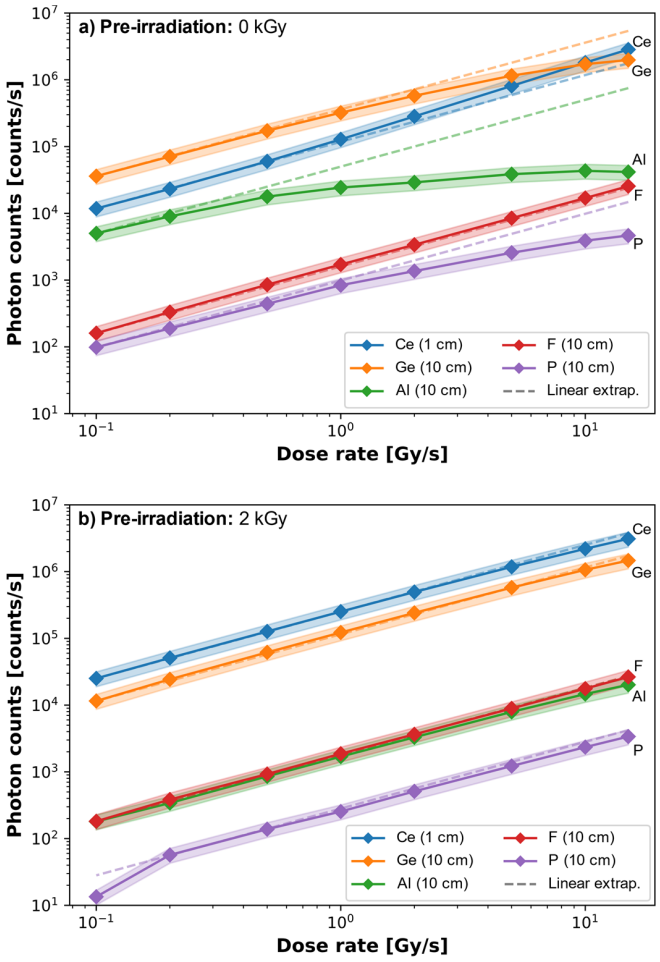

Fig. 10. Comparison of the mean value of RL signal of all tested fiber samples at different dose rates. Dashed lines show linear extrapolations from the first measurement points, in order to evaluate visually the linearity of each curve. (a) Results of the first run without preirradiation. (b) Results of the third run, totaling a preirradiation dose of ∼2 kGy. Filled areas show the uncertainty range of ±25%.

D. RL Signal Against Dose Rate

To assert the dosimetry performance of all tested samples, the mean value of the RL signal produced during irradiation was calculated for all samples at all dose rates and plotted in Fig. 10(a). We observe that all tested samples show a significantly measurable RL signal down to the lowest investigated dose rate of 0.1 Gy/s.

Whereas the characteristic of an ideal dosimeter would involve a delivered signal strictly proportional to the dose rate, comparison between data points and linear guidelines depicted in Fig. 10(a) shows that not all measured samples satisfy these requirements.

The Ge-doped sample shows excellent RL performances, as the signal delivered by the 10-cm-long Ge-doped sample is greater than the 1-cm-long Ce-doped sample at low dose rates. However, this behavior changes at higher dose rates and the amount of RL signal appears to be decreasing compared to an expected linear extrapolation. This can be explained by two phenomena: the occurrence of RIA at the emission wavelengths, and the decrease during irradiation of the population of preexisting GLPC defects, that are converted by radiation into Ge (1) and Ge (2) defects [27], [28].

The RIA effect is even more evident on the Al-doped sample, which high radiation sensitivity is well shown in Fig. 9. Because of the RIA increase with TID, dependence of RL signal of Al-doped sample with dose rate could not even be observed at the highest dose rates.

Similar conclusions can be drawn for the P-doped sample: although it appears to produce a signal comparable to F-doped fiber at low dose rates, its high RIA sensitivity results in a significantly decreased signal at higher dose rates.

On the opposite, the RL signal observed on the F-doped fiber sample presents a linear dependence on the dose rate, owing to its low RIA.

Finally, for the Ce-doped sample, the RL signal is noticeably increasing during irradiation, due to its RIA slowly decreasing with TID as shown in Fig. 9(b).

In an attempt to mitigate the observed effects of RIA on the linearity of RL response on radiosensitive samples, an identical series of measurements was performed on preirradiated samples, obtained by repeating three times in a row the irradiation sequence described in Fig. 2. The results shown in Fig. 10(b) were obtained during the third run, therefore, on samples preirradiated with a TID of 2 kGy.

As suggested by the RIA kinetics shown in Fig. 9(b), RIA stabilizes as TID increases, and therefore, the difference in attenuation between the start and end of the run becomes less and less important. This is observed on the RL signal measured on preirradiated samples shown in Fig. 10(b), where the nonlinearities observed for Ge-, Al-, and P-doped samples are significantly reduced, making these preirradiated samples more befitting for dosimetry applications. This increase in stability and reproducibility is, however, done at the expense of signal level, made evident by comparing Fig. 10(a) and (b), and therefore, a potentially degraded signal-over-noise ratio.

E. Potential for Dosimetry Applications

Whereas an ideal dose-rate meter would exhibit a constant ratio between dose rate and measured signal, the RL signal output by the fibers evaluated in this study depends on both dose rate and TID, as shown in Section III-D. Therefore, dosimetry applications involving these fibers would have to take into account this dependence on TID.

A first solution would be for the operating electronics to compensate for the effects of TID on the signal. This would involve either measuring a 2-D calibration function according to both dose rate and TID or establishing a model of the evolution of dose rate sensitivity according to TID. In both cases, the system would need to store a measurement of the TID received by the sensor, taken either by an external dosimeter or by integrating the measured dose rate after compensation (probably at the cost of a higher uncertainty level).

A second solution would be to preprocess the measuring elements in order to minimize the influence of TID on their sensitivity. This solution is explored in this study through the effects of preirradiation described in Section III-D.

The last solution would be to consider the actual requirements of the target dosimetry application. Not all applications involve the full range of dose rates, TID, and accuracy explored in this study. Medical imaging applications, for instance, usually involve much lower dose rates and TID than the ones we considered [31], resulting in a lesser influence of TID on the measurement that, if ignored, could result in an uncertainty range that may be acceptable.

IV. Conclusion

All multimode OFs tested in this study did show a significant, measurable RL signal in a range of dose rates from 0.1 to 15 Gy(SiO_2)/s.

The intensity of the RL signal was shown to be increasing with dose rate in all cases. However, depending on the doping, RL intensity does not depend linearly on dose rate because of RIA, as well as possible defects generation and recombination mechanisms.

Spectral measurements in Ce- and Ge-doped samples have shown that the origins of RL signal are well understood for these two kinds of fiber, but much less for Al-doped fiber. The low intensity of RL signal emitted by F- and P-doped samples did not enable its spectral measurement, and therefore, also makes it more difficult to reach a better understanding of the origins of such signal. However, the P-doped fiber noticeably delivers an RL signal significantly lower than the pure silica core F-doped fiber, hinting that P-doping may not be producing any kind of RL on its own in the UV-visible range of wavelengths that was explored in our study.

In particular, OFs sensitivity to RIA, such as Al- or P-doped fibers, yield an RL signal which is very dependent on the total amount of received dose. This dependence can be mitigated by preirradiating the samples, as shown here with a preirradiation TID of 2 kGy(SiO_2), however, at the cost of a decreased signal. Due to recovery over time of radiation-induced defects, the lifetime of such preirradiation need to be investigated.

In dosimetry applications, the preference would tend toward sensing elements with high sensitivity to dose rate, i.e., a strong RL signal, and low sensitivity to total dose, i.e., a low RIA and steady generation of RL-producing defects. Whereas OFs specifically designed for RL, such as the Ce-doped sample clearly show better suitability in both these parameters, we observe that Ge-doped fiber also yields a significant amount of RL signal, despite being more sensitive to total dose, and that F-doped fiber has very low RIA, which makes it reliable at higher doses, despite having a significantly weaker RL signal.

OFs producing a high RL signal, such as Ce-, Ge-, and Al-doped samples in our study, could also be suited for radiation monitoring applications such as beam loss monitoring for medical applications, were TID is typically much lower than the extents tested in this study. In applications demanding higher TID, occurrence of RIA could again be a factor limiting the performance of such fibers.

Also, we demonstrated that F-doped fibers, combining a low RIA sensitivity and a low production of RL signal, are well suited to be used as transport fibers for RL applications at high TID. The fact, however, that they deliver a nonnull RL signal still needs to be taken into account.

Further studies of the RL properties of OFs with commonly available dopants could include a more thorough study of the physical processes of generation or conversion of RL-producing defects as well as influence of temperature, in order to evaluate the sensitivity of these elements to duration and conditions of use.

Evaluation of changes in the RL properties of OFs under other sources of irradiations, such as gamma, protons or neutrons could also be investigated to assert whether they may be used as a reliable means to detect and quantify all kinds of radiation. In the particular case of protons, the effects of Cherenkov radiation on the signal could be evaluated.

Finally, a suitable modeling of RIA effects on RL may deliver more insights about the physical processes leading to the observed decrease of the RL signal at higher doses.

References

[1] S. Girard *et al.*, "Overview of radiation induced point defects in silica-based optical fibers," *Rev. Phys.*, vol. 4, Nov. 2019, Art. no. 100032, doi: 10.1016/j.revip.2019.100032.

[2] S. O'Keeffe, C. Fitzpatrick, E. Lewis, and A. I. Al-Shamma'a, "A review of optical fibre radiation dosimeters," *Sensor Rev.*, vol. 28, no. 2, pp. 136–142, Mar. 2008, doi: 10.1108/02602280810856705.

[3] N. Al Helou *et al.*, "Radioluminescence and optically stimulated luminescence responses of a cerium-doped sol-gel silica glass under X-ray beam irradiation," *IEEE Trans. Nucl. Sci.*, vol. 65, no. 8, pp. 1591–1597, Aug. 2018, doi: 10.1109/TNS.2017.2787039.

[4] A. Vedda *et al.*, "Ce^{3+}-doped fibers for remote radiation dosimetry," *Appl. Phys. Lett.*, vol. 85, no. 26, pp. 6356–6358, Dec. 2004, doi: 10.1063/1.1840127.

[5] C. Hoehr *et al.*, "Potential of novel optical fibers for proton therapy dosimetry," in *Proc. IEEE Nucl. Sci. Symp. Med. Imag. Conf. (NSS/MIC)*, Oct. 2017, pp. 1433–1434, doi: 10.1109/NSSMIC.2017.8532703.

[6] J. Bahout *et al.*, "Cu/Ce-Co-Doped silica glass as radioluminescent material for ionizing radiation dosimetry," *Materials*, vol. 13, no. 11, p. 2611, Jun. 2020, doi: 10.3390/ma13112611.

[7] D. A. Bradley *et al.*, "Towards the development of doped silica radioluminescence dosimetry," *Radiat. Phys. Chem.*, vol. 154, pp. 46–52, Jan. 2019, doi: 10.1016/j.radphyschem.2018.04.019.

[8] S. Girard *et al.*, "Radiation effects on silica-based preforms and optical fibers—I: Experimental study with canonical samples," *IEEE Trans. Nucl. Sci.*, vol. 55, no. 6, pp. 3473–3482, Dec. 2008, doi: 10.1109/TNS.2008.2007297.

[9] A. V. Ishchenko *et al.*, "Radiation optical effects in commercial SiO_2: Ge fibers," *J. Phys., Conf. Ser.*, vol. 552, Nov. 2014, Art. no. 012036, doi: 10.1088/1742-6596/552/1/012036.

[10] I. Reghioua *et al.*, "Cathodoluminescence characterization of point defects in optical fibers," *IEEE Trans. Nucl. Sci.*, vol. 64, no. 8, pp. 2318–2324, Aug. 2017, doi: 10.1109/TNS.2016.2644981.

[11] A. K. M. Mizanur Rahman *et al.*, "Germanium-doped optical fiber for real-time radiation dosimetry," *Radiat. Phys. Chem.*, vol. 116, pp. 170–175, Nov. 2015, doi: 10.1016/j.radphyschem.2015.04.018.

[12] A. K. M. M. Rahman *et al.*, "Ge-doped silica optical fibres as RL/OSL dosimeters for radiotherapy dosimetry," *Sens. Actuators A, Phys.*, vol. 264, pp. 30–39, Sep. 2017, doi: 10.1016/j.sna.2017.07.038.

[13] A. Basaif *et al.*, "Ge-doped silica optical fibre for time resolved radiation dosimetry," *Radiat. Phys. Chem.*, vol. 189, Dec. 2021, Art. no. 109669, doi: 10.1016/j.radphyschem.2021.109669.

[14] M. Benabdesselam, F. Mady, and S. Girard, "Assessment of Ge-doped optical fibre as a TL-mode detector," *J. Non-Crystalline Solids*, vol. 360, pp. 9–12, Jan. 2013, doi: 10.1016/j.jnoncrysol.2012.10.016.

[15] M. Benabdesselam *et al.*, "Performance of Ge-doped optical fiber as a thermoluminescent dosimeter," *IEEE Trans. Nucl. Sci.*, vol. 60, no. 6, pp. 4251–4256, Dec. 2013, doi: 10.1109/TNS.2013.2284289.

[16] M. Benabdesselam, F. Mady, J. B. Duchez, Y. Mebrouk, and S. Girard, "The opposite effects of the heating rate on the TSL sensitivity of Ge-doped fiber and TLD500 dosimeters," *IEEE Trans. Nucl. Sci.*, vol. 61, no. 6, pp. 3485–3490, Dec. 2014, doi: 10.1109/TNS.2014.2354512.

[17] S. Girard, Y. Ouerdane, C. Marcandella, A. Boukenter, S. Quenard, and N. Authier, "Feasibility of radiation dosimetry with phosphorus-doped optical fibers in the ultraviolet and visible domain," *J. Non-Cryst. Solids*, vol. 357, nos. 8–9, pp. 1871–1874, Apr. 2011, doi: 10.1016/j.jnoncrysol.2010.11.113.

[18] D. A. Bradley *et al.*, "Radioluminescence sensing of radiology exposures using P-doped silica optical fibres," *Appl. Radiat. Isot.*, vol. 141, pp. 176–181, Nov. 2018, doi: 10.1016/j.apradiso.2018.02.025.

[19] W. Miniscalco, "Erbium-doped glasses for fiber amplifiers at 1500 nm," *J. Lightw. Technol.*, vol. 9, no. 2, pp. 234–250, Feb. 1991, doi: 10.1109/50.65882.

[20] C. Campanella *et al.*, "Combined temperature and radiation effects on radiation-sensitive single-mode optical fibers," *IEEE Trans. Nucl. Sci.*, vol. 67, no. 7, pp. 1643–1649, Jul. 2020, doi: 10.1109/TNS.2020.2982280.

[21] I. Reghioua. (2018). *Cathodoluminescence Characterization Study of Point Defects in Silica-Based Materials: Optical Fibers and Nanoparticles*. Accessed: Oct. 6, 2021. [Online]. Available: https://www.theses.fr/2018LYSES002

[22] S. Girard *et al.*, "Recent advances in radiation-hardened fiber-based technologies for space applications," *J. Opt.*, vol. 20, no. 9, Aug. 2018, Art. no. 093001, doi: 10.1088/2040-8986/aad271.

[23] A. Darafsheh, R. Taleei, A. Kassaee, and J. C. Finlay, "Proton therapy dosimetry using the scintillation of the silica fibers," *Opt. Lett.*, vol. 42, no. 4, pp. 847–850, Feb. 2017, doi: 10.1364/OL.42.000847.

[24] J. Bahout *et al.*, "Remote measurements of X-rays dose rate using a cerium-doped air-clad optical fiber," *IEEE Trans. Nucl. Sci.*, vol. 67, no. 7, pp. 1658–1662, Jul. 2020, doi: 10.1109/TNS.2020.2972043.

[25] M. Cieslikiewicz-Bouet *et al.*, "Investigation of the incorporation of cerium ions in MCVD-silica glass preforms for remote optical fiber radiation dosimetry," *Sensors*, vol. 21, no. 10, Art., no. 3362, Jan. 2021, doi: 10.3390/s21103362.

[26] N. Kerboub *et al.*, "Temperature effect on the radioluminescence of Cu-, Ce-, and CuCe-doped silica-based fiber materials," *IEEE Trans. Nucl. Sci.*, vol. 68, no. 8, pp. 1782–1787, Aug. 2021, doi: 10.1109/TNS.2021.3075481.

[27] I. Reghioua *et al.*, "Cathodoluminescence investigation of Ge-point defects in silica-based optical fibers," *J. Lumin.*, vol. 179, pp. 1–7, Nov. 2016, doi: 10.1016/j.jlumin.2016.06.041.

[28] A. Alessi *et al.*, "Coupled irradiation-temperature effects on induced point defects in germanosilicate optical fibers," *J. Mater. Sci.*, vol. 52, no. 18, pp. 10697–10708, Sep. 2017, doi: 10.1007/s10853-017-1244-x.

[29] P. J. Alonso, L. E. Halliburton, E. E. Kohnke, and R. B. Bossoli, "X-ray-induced luminescence in crystalline SiO_2," *J. Appl. Phys.*, vol. 54, no. 9, p. 5369, Jun. 1998, doi: 10.1063/1.332715.

[30] M. A. Stevens-Kalceff, "Cathodoluminescence microanalysis of silica and amorphized quartz," *Mineral. Petrol.*, vol. 107, no. 3, pp. 455–469, Jun. 2013, doi: 10.1007/s00710-013-0275-5.

[31] E. Vano *et al.*, "Dosimetric quantities and effective dose in medical imaging: A summary for medical doctors," *Insights Imag.*, vol. 12, no. 1, Jul. 2021, Art. no. 99, doi: 10.1186/s13244-021-01041-2.

IEEE TRANSACTIONS ON NUCLEAR SCIENCE, VOL. 70, NO. 4, APRIL 2023 583

Toward an Embedded and Distributed Optical Fiber-Based Dosimeter for Space Applications

Arnaud Meyer, *Student Member, IEEE*, Adriana Morana, *Member, IEEE*, Luca Weninger, *Student Member, IEEE*, Nicolas Balcon, Gilles Mélin, Julien Mekki, Thierry Robin, André Champavère, *Member, IEEE*, Frédéric Saigné, Jérôme Boch, Tadec Maraine, Aomer Aït-Ali-Saïd, Emmanuel Marin, Youcef Ouerdane, Aziz Boukenter, and Sylvain Girard, *Senior Member, IEEE*

***Abstract*— We investigated the performance under γ- and X-rays of an optical-fiber-based distributed dosimeter consisting of an embedded optical time-domain reflectometry (OTDR) interrogator operating at 1610 nm and a phosphorus-doped, single-mode, size-reduced optical fiber (OF). Results show a linear response from 10^{-3} to 10^{2} Gy(SiO_2), a proper functioning of the interrogator at least up to doses of 80 Gy(SiO_2), and performances comparable with standard-sized distributed dosimetry systems found in the literature.**

***Index Terms*— Dosimetry, optical fiber (OF), optical time-domain reflectometry (OTDR), radiation.**

I. Introduction

OPTICAL FIBER (OF)-based measurement systems offer many advantages for space applications, including a very low weight and size footprint and the ability to perform distributed, i.e., spatially-resolved measurements. A variety of OF-based applications is commonly found in spacecraft, ranging from datalink signal transportation to environment sensing, inertial navigation systems, lasers, and amplifiers for free space optical communication [1].

Dosimetry is of special interest for space applications because of the complex and evolving nature of the space radiation environment, which involves various types of particles, broad energy spectra, strong influence of solar activity, and a high dependence on the location, especially in terrestrial orbit [1], [2], [3]. As the same OF can be used both for sensing and carrying the measurement signal, OF-based distributed dosimetry potentially enables more compact and lightweight solutions to monitor dose and dose rate, simultaneously at several key locations of a spacecraft, using only one sensing element and one interrogation device.

Distributed dosimetry has been studied for applications on the ground, particularly in the context of particle accelerators and large irradiation facilities. Previous works on this topic include monitoring of the TESLA Test Facility TTF1 in DESY Hamburg [4] and of Proton Synchrotron Booster [5], Large Hadron Collider [6], and CHARM facility [7] in CERN.

These distributed dosimetry applications rely on optical time-domain reflectometry (OTDR) technology, which is typically used to monitor the optical losses of OF lines in telecommunication networks, with the advantage of needing to connect only one end of the scanned OF. Their measuring principle is to send a very short laser pulse in the scanned OF; then, Rayleigh scattering, originating from random microscopic fluctuations of the OF density typically in the order of a tenth of the laser wavelength, causes part of the incoming pulse to be redirected back to the sender. By monitoring the intensity of this backscattered signal as a function of a time-of-flight measurement, a map of the signal along the fiber can be obtained. The spatial resolution Δz of this measurement is usually determined by the duration τ of the incoming laser pulse, through the following formula:

$$\Delta z = \frac{v_g}{2}\tau.$$

With v_g the group velocity of the pulse in the OF. Δz is in the order of 1 m for a typical pulsewidth of 10 ns [8].

Phosphorus (P)-doped OF is another component of interest for OF-based dosimetry applications, especially because of its radiation-induced attenuation (RIA) behavior. In particular, the RIA response of P-doped fibers in the near-infrared region is mainly dictated by P1 defects, having an optical absorption band peaking at ~1550 nm [6]. It is characterized by a mostly linear (within 5%) response to total ionizing dose (TID) up to 500 Gy(SiO_2) [6], low sensitivity to temperature, with a 15% deviation of the sensitivity within −120 °C to 80 °C [9], and its dependence to ionizing dose only, making it able to reliably detect different natures of radiation, including X-rays

Manuscript received 7 November 2022; accepted 29 November 2022. Date of publication 1 December 2022; date of current version 18 April 2023. This work was supported in part by the Occitanie Region and in part by the EU via ERDF Funds for PRESERVE Platform.

Arnaud Meyer, Adriana Morana, Luca Weninger, Emmanuel Marin, Youcef Ouerdane, Aziz Boukenter, and Sylvain Girard are with Laboratoire Hubert Curien, Université Jean Monnet, 42000 Saint-Étienne, France (e-mail: sylvain.girard@univ-st-etienne.fr).

Nicolas Balcon and Julien Mekki are with CNES, 31400 Toulouse, France.

Gilles Mélin and Thierry Robin are with iXblue Photonics, 22300 Lannion, France.

André Champavère is with GuidOptix, 42330 Saint-Bonnet-les-Oules, France.

Frédéric Saigné, Jérôme Boch, and Tadec Maraine are with IES, Université de Montpellier, CNRS, 34090 Montpellier, France.

Aomer Aït-Ali-Saïd is with TRAD, 31670 Labège, France.

Color versions of one or more figures in this article are available at https://doi.org/10.1109/TNS.2022.3226194.

Digital Object Identifier 10.1109/TNS.2022.3226194

[9], [10], γ rays [5], [6], 480-MeV protons [6], atmospheric neutrons [10], and mixed field at the CHARM facility [7].

However, porting such a distributed dosimetry technology to space applications involves asserting the reliability of the whole sensing chain, including its resilience to radiation effects and capacity to provide an accurate measurement over the whole range of doses and dose rates considered for the target application. This study preliminarily explores these two topics by testing under γ- and X-ray radiation a distributed dosimetry system consisting of a miniaturized OTDR device along with a phosphorus-doped, single-mode, and size-reduced OF.

Embedded OTDR devices are reduced in size, mass, and power consumption compared to common OTDR interrogators, in order to enable easier integration in telecommunication network equipment. Because the conventional wavelength for OF-based telecommunication is typically around 1550 nm (C-band), these embedded OTDRs operate around 1610–1625 nm (L-band) to be able to scan an OF line without disturbing communications [11].

As this working wavelength range is different from previous studies on P-doped fiber, that focused on its response at a wavelength of 1550 nm [6], [9], [12], the first objective of this work is to confirm the capacity demonstrated in [10] of such embedded devices to perform RIA measurements on a P-doped OF for dosimetry purposes, as well as to assert their capability to operate under ionizing radiation.

Also, to further characterize the whole dosimetry system, we aim to evaluate the dosimetric properties of this interrogator coupled with a miniaturized P-doped OF, with decreased dimensions, especially regarding cladding and coating diameters, resulting in a reduction of $\sim$75% of its volume footprint. We also aim to assert the variability between samples from different preforms (used for example to build calibration, engineering, or flight models), and the ability to measure different types of radiation in order to enable further calibration in easily accessible X- or γ-rays facilities.

It should be noted that the ambition of this article is not to investigate all aspects related to space qualification of a distributed fiber dosimeter but to provide a first start to identify areas of potential for this technology in space through the reported experiments and results. Several crucial aspects regarding such a qualification are not covered in this work, regarding the sensitivity of the OTDR device to single-event effects (SEE), as well as its reliability after launch conditions. After future investigations of these topics, it will be possible to suggest dosimeter implementation architectures adapted to different space mission profiles.

II. Materials and Methods

To assess the proper functioning of this distributed dosimetry system under a variety of radiation environments, we conducted two experiments involving two different types of radiation (γ- and X-rays) and different dose rates.

In all experiments, the used OTDR devices were Viavi Solutions Micro iOTDR, operating at a wavelength of 1610 nm, and having a size footprint of 190 × 170 × 16.5 mm and a weight of 200 g [13], about 9× smaller and 15× lighter than a standard OTDR unit. The devices were remotely controlled by an embedded computer (Raspberry Pi Model 4B) to initiate measurements as well as to retrieve and store results.

TABLE I
OF Samples Used for These Experiments

Name	Core dopant	Core diameter	Cladding diameter	Coating diameter	Manufacturer
A	Phosphorus	6.6 µm	80 µm	127 µm	iXblue
B	Phosphorus	6.6 µm	80 µm	127 µm	iXblue

Two different OF samples, A and B, were investigated. Both samples share the same specifications, as shown in Table I, but were drawn from different preforms.

A. γ Ray Irradiation

The first experiment was conducted at the PRESERVE facility in IES, Université de Montpellier (France), which uses a ^{60}Co source emitting γ rays at 1.17 and 1.33 MeV. The source is placed inside a large room, enabling a wide range of dose rates thanks to the inverse-square law of exposure rate as a function of distance to the source [14].

Two almost identical measurement lines were installed in this experiment, each one probed by its own OTDR device, with a pulsewidth of 5 ns and an integration time of 180 s.

Each measurement line was composed of coils of the same OF, but having different lengths, spliced together. A schematic of the experiment including length and applied dose rate to each coil is given in Fig. 1(a). All measurements were performed at room temperature (between 19 °C and 25 °C).

B. X-Ray Irradiations

An additional set of experiments was carried out at the MOPERIX facility in Laboratoire Hubert Curien, Université Jean Monnet (France), involving a COMET MXR-165 X-ray tube supplied with a voltage of 100 kV, producing an X-ray spectrum with a mean energy of 40 keV.

As shown in Fig. 1(b), a single piece of OF sample A or B, coiled as a flat spiral, was placed inside the irradiator and spliced into a radiation-hard transport fiber. The other end of the transport fiber was connected to the OTDR device placed outside of the irradiation chamber, configured with a pulsewidth of 5 ns and an integration time of 30 s. This integration time was lower than in the previous experiment in order to increase the time resolution, and therefore record the evolution of dose with a greater detail, because of the higher dose rates involved in our X-ray setup.

Two runs were performed in this setup, using OF sample A: one at a dose rate of 5 mGy(SiO_2)/s and sample length of 20 m, and another, using a new, pristine sample, at a dose rate of 430 mGy(SiO_2)/s and a length of 40 m. All irradiations were performed at room temperature (between 19 °C and 23 °C).

Finally, an experiment to demonstrate the spatially-resolved nature of this measurement technique was set up as shown in

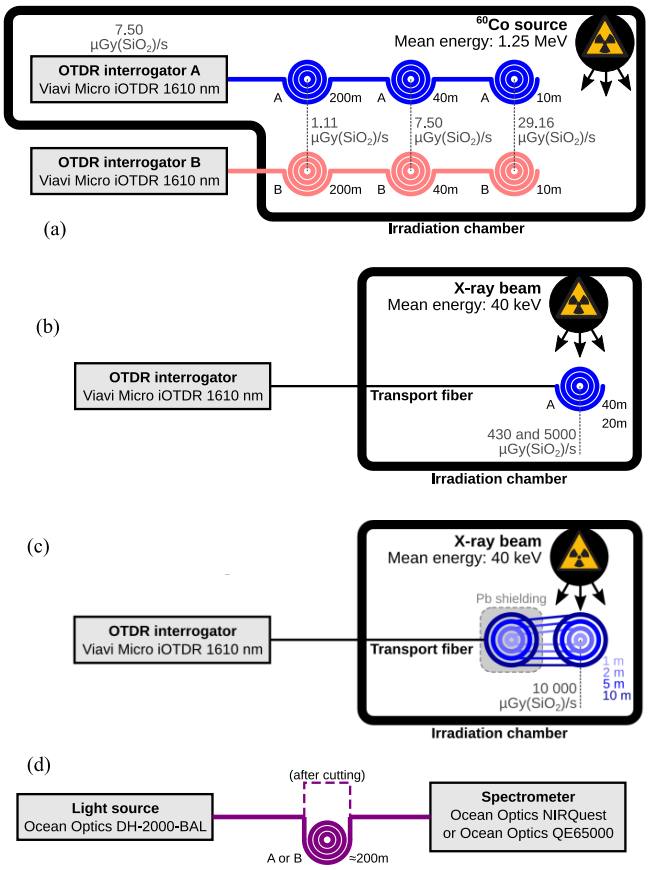

Fig. 1. Setup for (a) γ rays irradiation, (b) X-rays irradiations, (c) alternating X-ray-irradiated and non-irradiated segments, and (d) attenuation spectroscopy.

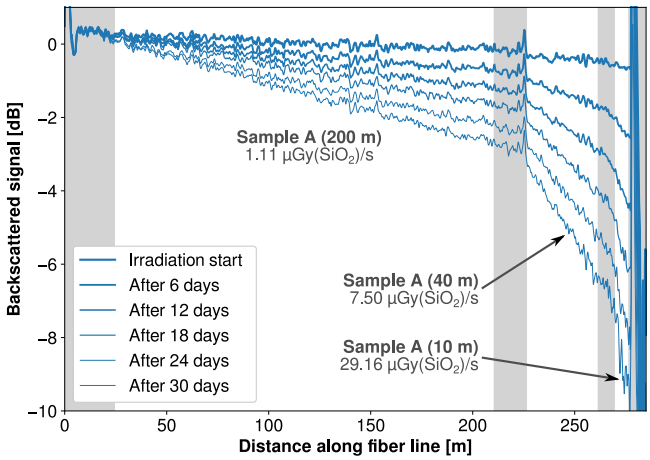

Fig. 2. OTDR traces (1610 nm) of measurement line A irradiated under γ rays during the first month of irradiation. Areas shown on a white background are the ones taken into account for RIA calculation.

Fig. 1(c), using a single measurement line divided between two flat coils, each containing segments of increasing length from 1 to 10 m. One coil was shielded using a 3-mm-thick Pb plate and the other one was irradiated at a dose rate of 10 mGy(SiO_2)/s, giving as a result an alternation of irradiated and non-irradiated segments of increasing lengths along the OF.

The dosimetry was performed in Gy(H_2O) with a PTW 23 344 plane-parallel ionization chamber connected to a Unidos E reading unit, with a relative uncertainty of 10%, and converted to Gy(SiO_2) in the data shown hereafter.

C. Attenuation Spectroscopy

The attenuation spectrum of OF samples was measured using a spectral cutback method, illustrated in Fig. 1(d). It involves an Ocean Optics DH-2000-BAL halogen-deuterium light source, emitting a continuous spectrum from 210 to 2500 nm, and two spectrometers: for the near-infrared range, an Ocean Optics NIRQuest measuring from 900 to 2100 nm, and for the visible range, an Ocean Optics QE65000 measuring from 200 to 980 nm.

The cutback method is a destructive method that consists in comparing the transmission spectra between two different lengths of the same sample, with all other parts of the measurement chain remaining unchanged [15]. The intrinsic spectral attenuation of the sample $A(\lambda)$ (in dB/km) is then obtained using the following formula:

$$A(\lambda) = -\frac{10}{\Delta L}\log_{10}\left(\frac{I_s(\lambda) - I_{\text{dark}}(\lambda)}{I_l(\lambda) - I_{\text{dark}}(\lambda)}\right)$$

where $I_{\text{dark}}(\lambda)$ is the dark spectrum, i.e., the spectrum measured with the light source switched off, $I_s(\lambda)$ and $I_l(\lambda)$ are the spectra transmitted through, respectively, short and long sample lengths, and ΔL is the length difference between long and short samples.

III. Results and Discussion

A. Calculation of RIA From OTDR Traces

The measurement produced by the OTDR device is a 1D vector containing the intensity of the backscattered signal for each location along the measurement line.

To compute RIA values based on these data, the whole length of the measurement line is split into one or several segments of interest. The OTDR trace of measurement line A under γ rays and its evolution over time is shown in Fig. 2. In this figure, there are three segments of interest, corresponding to each sample coil placed at a defined dose rate [see Fig. 1(a)].

Then, the slope of the OTDR trace of each segment is computed over time using a linear fit algorithm. The result is the evolution of attenuation over time, which, when subtracted with its value measured at the start of irradiation, gives the RIA over time for each sample. Time information is then converted into dose according to dosimetry readings of each facility, to obtain as a final result the evolution of RIA as a function of dose.

B. Dosimetry Properties Under γ Rays

An example of RIA evolution according to dose, measured for sample A under γ rays at three different dose rates,

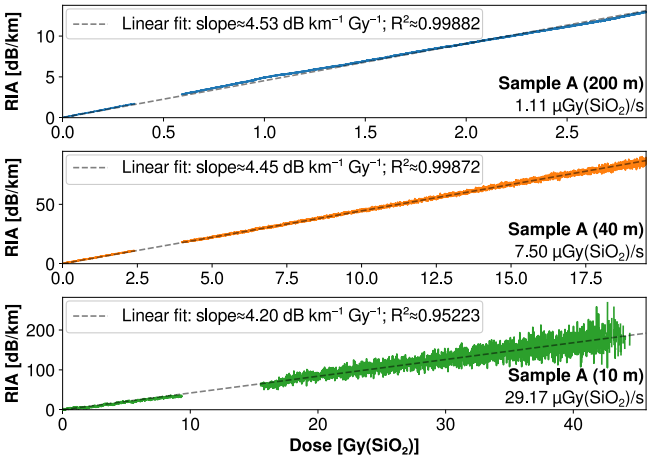

Fig. 3. Evolution of RIA (at 1610 nm) of sample A according to dose at different γ rays dose rates, during the first month of irradiation. A linear fit is applied on each curve (dashed lines) to visually highlight the linearity of these measurements.

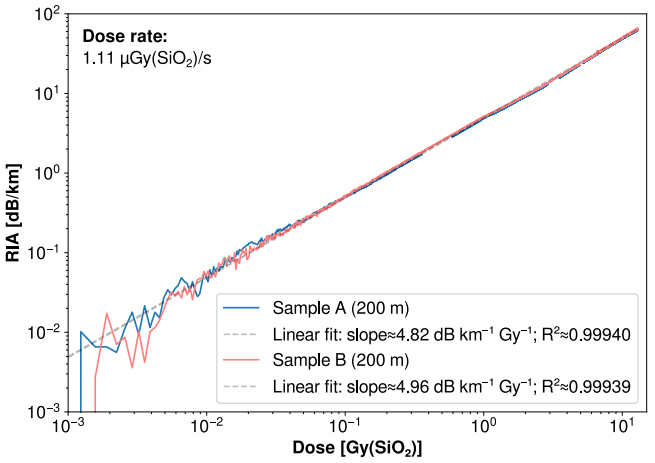

Fig. 4. Log–log plot of the compared evolution of RIA (at 1610 nm) of samples A and B according to dose at a γ ray dose rate of 1.11 μGy(SiO$_2$)/s. A linear fit is applied on each set of results to retrieve the sensitivity of each fiber.

is shown in Fig. 3. Missing data are explained by breakage of the measurement line during irradiation.

These acquisition stoppages did however not affect the total dose measurement, as the physical processes producing RIA were still taking place in the OFs under radiation. This behavior highlights the passive nature of the measuring OF highlighted in [16], with the advantage of being readable on-line, while accumulating dose.

Results of the linear fits applied to these data, indicated by the gray dashed line in each plot in Fig. 3, show a good linearity of these measurements and enable the extraction of the sensitivity of each measurement line, reported in the legend of each plot.

These calculated sensitivities are globally in the same order of magnitude as the generally used value of $\sim$4 dB km^{-1} Gy^{-1} at a wavelength of 1550 nm for P-doped fibers [6].

Interestingly, the values measured in this work are slightly greater than the ones given in the latter, despite operating at a wavelength of 1610 nm where RIA response is supposed to be lower in the order of 0.6%, according to RIA spectrum of P-doped fiber in the near-infrared region (see [6] and Section III-H). These differences could be explained by a small dependence on dose and dose rate that should be the object of a dedicated study.

C. Variability Between of Samples

As a similar setup was used for measuring A and B samples under γ rays, the variability between both samples can be established by comparing the evolution of their RIA according to dose, for the same dose rate, as shown in Fig. 4, with RIA of A and B fibers for the minimum dose rate of 1.11 μGy(SiO$_2$)/s during the whole duration of the γ rays irradiation. Missing data are explained by various events (fiber breakage, device, power failure, etc.) during this long irradiation period.

These results are in good accordance with each other, as shown both graphically and by estimation of their sensitivity coefficient through linear fit: a factor of 4.82 and 4.96 dB km^{-1} Gy^{-1} is measured, respectively, for samples A and B, amounting to a deviation of only $\sim$3%. These results hint toward a low batch-to-batch variability of dosimetric properties of these OFs drawn from different preforms but with the same set of specifications.

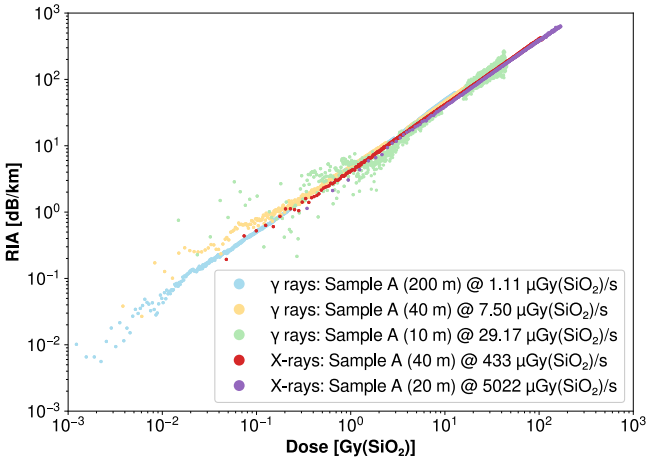

Fig. 5. Log–log plot of the compared evolution of RIA (at 1610 nm) of sample A according to dose, at different dose rates under γ- and X-rays. γ rays data are displayed in a lighter color in order to emphasize X-ray data.

D. Comparison of X- and γ-Ray Responses

In order to extend the domain of doses investigated under γ rays, we performed additional measurements under X-rays, enabling higher dose rates and, therefore, access to higher amounts of dose within a short time.

In particular, two lengths of OF sample A, respectively, 40 and 20 m long, were irradiated at, respectively, 430 μGy(SiO$_2$)/s and 5 mGy(SiO$_2$)/s and interrogated with a shorter integration time of 30 s to increase time resolution, and therefore dose resolution, while keeping an overall good measurement quality.

Fig. 5 compiles RIA measured under γ- and X-rays for sample A over four decades of dose rate, ranging from

1.11×10^{-6} to 5×10^{-3} Gy(SiO_2)/s. This graph shows that measurements taken under X- and γ-rays for the same OF sample are in excellent accordance, as long as dose calculation is performed in Gy(SiO_2), whatever the nature of radiation.

E. Performance of Embedded OTDR Device

The key parameter of an OTDR device is its dynamic range, i.e., its capability to measure low signals compared to the highly backscattered signal from the first few meters. Fig. 2 shows that in our application, the dynamic range can be estimated to ~10 dB. This value is slightly lower than the dynamic range of 15 dB reported in [4] with a standard OTDR, but it should be noted that this value is usually given for the largest available pulsewidth of the device [17], whereas we used here the shortest pulsewidth in order to have the best spatial resolution.

In terms of dosimetry, the accuracy of this system is given by its minimum measurable dose, which can be roughly evaluated to 10^{-2} Gy(SiO_2) from Fig. 4 with 200 m of OF. This relation between minimum measurable dose and sample length is comparable with data from [6], meaning that the length of OF needed to achieve a comparable accuracy in dose is globally in the same order of magnitude in both cases.

Also, as stated in Section II-A, the OTDR device used to perform measurements on line A during γ rays irradiation was placed inside the irradiation chamber during the whole run, totalizing to a TID of 81.05 Gy(SiO_2).

This device did noticeably not show any sign of failure, neither on its computing part (communication, status report, triggering, and retrieval of measurements) nor on its measurement part (increase of measurement noise).

F. Discussion of Measurement Uncertainties

The RIA measurements are subject to uncertainties, which mainly originate from two parameters: the noise of the OTDR measurements themselves and the uncertainties in the slope estimation on segments of interest.

The OTDR noise typically increases as the backscattered signal decreases. This is usually the case when the OF is highly attenuating, which means that the measurement accuracy decreases as RIA increases. An increased noise is particularly noticeable at the end of the measurement line, whose signal is reduced by attenuation from all previous segments.

Slope estimation uncertainties are calculated by the linear fit algorithm. They are influenced by the OTDR measurement noise, but also by the length of the considered segment of interest; the variance V_{slope} of the estimated slope can be expressed with the following formula:

$$V_{\text{slope}} = \frac{V_{\text{meas}}}{\sum_i (x_i - \bar{x})^2}$$

where V_{meas} is the variance of the OTDR measurements on the considered segment, and $\bar{x}$ is the mean of the positions x_i corresponding to each measurement point [18].

Methods to decrease these uncertainties, and therefore increase the signal-to-noise ratio of RIA measurements, include increasing integration time, reducing OTDR measurement noise, and considering greater segment lengths to decrease slope estimation uncertainties.

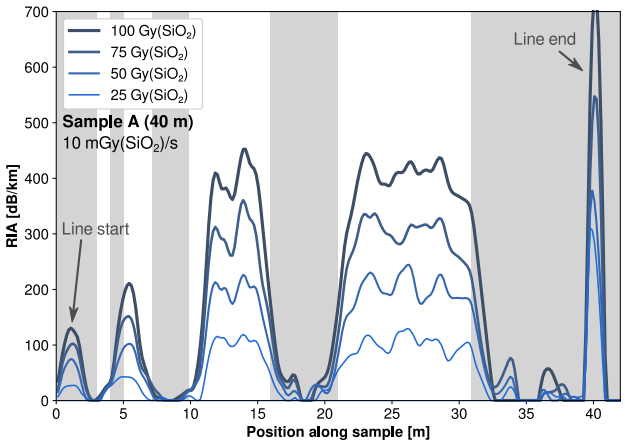

Fig. 6. Evolution of RIA measurement under X-rays (10 mGy(SiO_2)/s) over the length of a 40-m sample of OF A, with portions successively shielded and unshielded to show the spatially-resolved character of the measurement. Grayed areas show the approximate locations of shielded segments.

The influence of these parameters on measurement noise is particularly visible in Fig. 3, where RIA measurements on the 10-m sample are visibly noisier than the other samples, both because of the comparatively short sample length and the low amount of backscattered signal. The latter is the result of cumulated attenuation along the whole measurement line, and of the higher dose rate at which this segment is exposed. The magnitude of signal attenuation on this segment is especially noticeable at the end of irradiation period, as shown in Fig. 2.

G. Illustration of the Distributed Nature of the Measurement

To demonstrate the capability of this technique to produce a spatially-resolved dose measurement along an OF, a measurement line made of 40 m of OF sample A was irradiated under X-rays, as shown in Fig. 1(c), alternating between exposed segments under the X-ray beam, and non-exposed segments under Pb shielding.

By applying the RIA computation method explained in Section III-A to a sliding segment of 2-m length, we obtain the results shown in Fig. 6, illustrating that the measurement setup is able to detect, without special guidance, which parts of the OF were irradiated and which ones were not.

This figure also highlights several limitations of this measurement technique: the use of a slope calculation window of 2 m, significantly smaller than other calculations performed in this article, causes less data points to be considered for slope calculation, leading to increased uncertainties as explained in Section III-F. Moreover, this length window is at the same time too large in order to properly resolve the dose profile of the shorter segments of 1 and 2 m at the beginning of the measurement line. These results indicate that there is a balance to be kept between spatial resolution, time resolution, and accuracy of dose measurement, between which a satisfying operating point needs to be defined for each application.

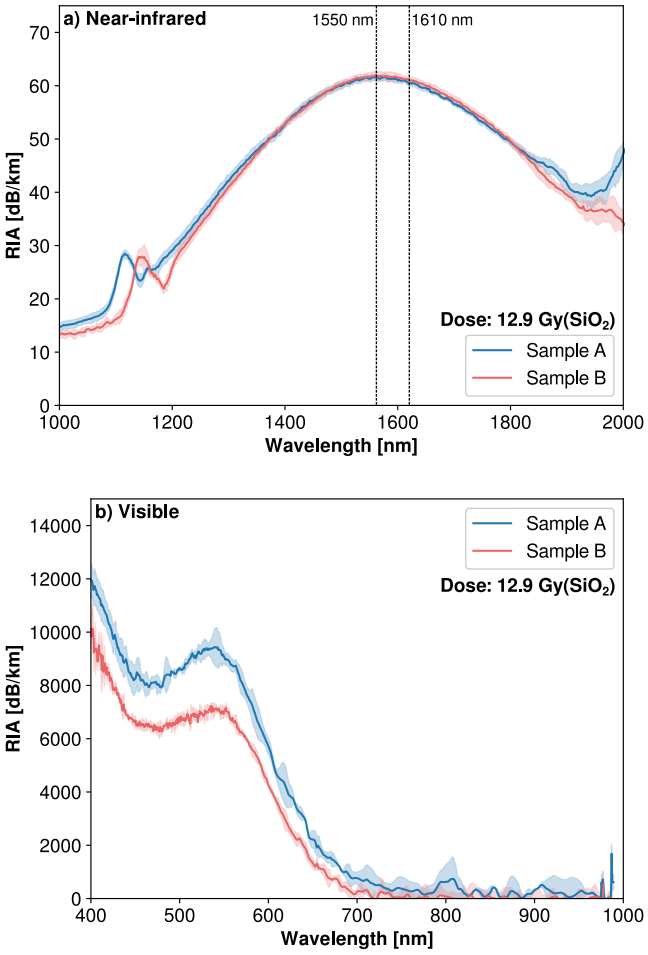

Fig. 7. RIA spectra in (a) near-infrared domain and (b) visible domain of OF samples A and B irradiated under γ rays at a dose of 12.9 Gy(SiO_2). Filled areas in lighter color show uncertainties at $\pm 2\ \sigma$.

The peaks at the left and right of Fig. 6 graph are caused by optical reflections at the air/glass interface at both ends of the OF. Whereas such peaks are typically encountered in OTDR measurement, these locations cannot be reliably considered for dose measurement, as their attenuation appears to increase despite being shielded. Therefore, a small dead zone of ± 5 m needs to be observed at the beginning and end of the measurement line to exclude such artifacts.

H. Spectrum of RIA

The optical losses of the samples irradiated under γ rays were analyzed using the cut-back method illustrated in Fig. 1(d) and subtracted with the same measurements performed on non-irradiated samples in order to compute the RIA spectrum of each fiber sample.

The resulting RIA spectra, for the near-infrared and visible spectral domains, are shown in Fig. 7. The near-infrared RIA spectrum stands in very good accordance with other occurrences in the literature [7], [9], except for the peaks located in the 1100–1150-nm spectral range which correspond to the cutoff wavelength of these OFs. These peaks appear typically in cutback measurements [15], but not in the online RIA measurements performed in the cited references.

At the OTDR interrogation wavelength of 1610 nm, the RIA is caused by the P1 defect [19] that is associated with an optical absorption band at 0.9 eV (full width at half maximum (FWHM) of 0.29 eV [20]). This defect is known to be stable at room temperature [9].

The visible RIA spectrum also matches very well other references in the literature [21], especially for the overwhelmingly larger RIA observed at shorter wavelengths, which were measured in practice by removing much shorter sample lengths during cutback operation (about 1 m, compared to the $\sim$200 m removed for near-infrared measurements).

In this spectral domain, RIA of P-doped fibers is driven by phosphorus oxygen hole centers (POHCs) and their absorption bands at 2.2 eV (FWHM = 0.35 eV), 2.5 eV (FWHM = 0.63 eV), and 3.1 eV (FWHM = 0.73 eV) [19], [22].

These spectral RIA measurements confirm that measurements performed at 1610 nm by the OTDR devices used in this study are performed in the optimal area of radiosensitivity of P-doped OFs, and only differ by less than 1% from measurements performed at 1550 nm otherwise found in literature. They also highlight the very high potential of visible-light-based measurement techniques to produce highly sensitive dosimeters using P-doped OFs, as discussed in more detail in [21].

IV. Conclusion

We have explored the potential of systems made of embedded OTDR devices coupled with P-doped, single-mode, and size-reduced OF to enable spatially-resolved and radiation-tolerant dosimetry measurements.

They have been investigated at dose rates ranging from 10^{-6} to 10^{-2} Gy(SiO_2)/s and TID up to 80 Gy(SiO_2), and have shown a dose detection threshold down to 10^{-2} Gy(SiO_2) with an OF length of 200 m.

The use of a phosphorus-doped OF reduced in size compared to standard single-mode fiber enables to produce a size and weight-optimized solution for distributed dosimetry measurement, along with the advantage offered by its low cross section to enable low-energy and/or weakly penetrating particles to reach the fiber core and, therefore, be detected. This study shows that such an OF presents comparable properties to standard-sized OFs used in dosimetry. Moreover, a comparison between samples of OF drawn from different preforms hints toward a low batch-to-batch variability.

Experiments conducted under γ- and X-rays showed that this measurement system can function under different types of radiation, providing that the dosimetry is scaled according to the dose in the material. For further studies, this approach could be generalized for a wider range of particles, including charged particles (protons and electrons) and heavy ions.

Whereas this dosimetry system is capable of spatially-resolved measurements, its spatial resolution is constrained by increasing uncertainties on dose measurement as shorter segments of the OF are evaluated. A more in-depth study on the relation between these two parameters, as well as the

definition of an optimal functioning point, could be the subject of further research.

Finally, the embedded OTDR device has been shown to display properties comparable to standard-sized devices, as well as to function properly under irradiation, at doses up to 80 Gy(SiO_2). To further assess the radiation tolerance of this system, more diverse radiation environments could also be considered, along with its sensitivity to SEE and its ability to recover from such effects.

ACKNOWLEDGMENT

The authors would like to thank the company Viavi Solutions France SAS for lending the OTDR devices for this research.

REFERENCES

[1] S. Girard et al., "Recent advances in radiation-hardened fiber-based technologies for space applications," *J. Opt.*, vol. 20, no. 9, Aug. 2018, Art. no. 093001, doi: 10.1088/2040-8986/aad271.

[2] E. R. Benton and E. V. Benton, "Space radiation dosimetry in low-Earth orbit and beyond," *Nucl. Instrum. Methods Phys. Res. B, Beam Interact. Mater. At.*, vol. 184, nos. 1–2, pp. 255–294, Sep. 2001, doi: 10.1016/S0168-583X(01)00748-0.

[3] J. L. Barth, "Space and atmospheric environments: From low Earth orbits to deep space," in *Protection of Materials and Structures From Space Environment* (Space Technology Proceedings), vol. 5, J. I. Kleiman and Z. Iskanderova, Eds. Dordrecht, The Netherlands: Springer, 2004, doi: 10.1007/1-4020-2595-5_2.

[4] H. Henschel, M. Körfer, J. Kuhnhenn, U. Weinand, and F. Wulf, "Fibre optic radiation sensor systems for particle accelerators," *Nucl. Instrum. Methods Phys. Res. A, Accel. Spectrom. Detect. Assoc. Equip.*, vol. 526, no. 3, pp. 537–550, Jul. 2004, doi: 10.1016/j.nima.2004.02.030.

[5] D. Di Francesca et al., "Distributed optical fiber radiation sensing in the proton synchrotron booster at CERN," *IEEE Trans. Nucl. Sci.*, vol. 65, no. 8, pp. 1639–1644, Aug. 2018, doi: 10.1109/TNS.2018.2818760.

[6] D. Di Francesca et al., "Qualification and calibration of single-mode phosphosilicate optical fiber for dosimetry at CERN," *J. Lightw. Technol.*, vol. 37, no. 18, pp. 4643–4649, Sep. 2019.

[7] D. Di Francesca et al., "Dosimetry mapping of mixed-field radiation environment through combined distributed optical fiber sensing and FLUKA simulation," *IEEE Trans. Nucl. Sci.*, vol. 66, no. 1, pp. 299–305, Jan. 2019, doi: 10.1109/TNS.2018.2882135.

[8] A. H. Hartog, *An Introduction to Distributed Optical Fibre Sensors*. Boca Raton, FL, USA: CRC Press, 2017, doi: 10.1201/9781315119014.

[9] A. Morana et al., "Operating temperature range of phosphorous-doped optical fiber dosimeters exploiting infrared radiation-induced attenuation," *IEEE Trans. Nucl. Sci.*, vol. 68, no. 5, pp. 906–912, May 2021, doi: 10.1109/TNS.2021.3053164.

[10] S. Girard et al., "Atmospheric neutron monitoring through optical fiber-based sensing," *Sensors*, vol. 20, no. 16, p. 4510, Jan. 2020, doi: 10.3390/s20164510.

[11] M. Pellegatta, M. Monguzzi, A. Mazzarese, and A. Zucchetti, "Fiber networks maintenance in the all-optical network era," in *Proc. IEEE/IFIP Netw. Oper. Manage. Symp. Manage. Solutions New Commun. World (NOMS)*, Apr. 2002, pp. 855–868, doi: 10.1109/NOMS.2002.1015629.

[12] S. Girard et al., "Transient and steady-state radiation response of phosphosilicate optical fibers: Influence of H_2 loading," *IEEE Trans. Nucl. Sci.*, vol. 67, no. 1, pp. 289–295, Jan. 2020, doi: 10.1109/TNS.2019.2947583.

[13] *Viavi Solutions, Nano and Micro iOTDR Cards Datasheets*. Accessed: Feb. 1, 2022. [Online]. Available: https://www.viavisolutions.com/en-us/literature/nano-and-micro-iotdr-cards-data-sheets-en.pdf

[14] F. Ravotti, "Dosimetry techniques and radiation test facilities for total ionizing dose testing," *IEEE Trans. Nucl. Sci.*, vol. 65, no. 8, pp. 1440–1464, Aug. 2018, doi: 10.1109/TNS.2018.2829864.

[15] W. Heitmann, "Precision single-mode fiber spectral attenuation measurements," *J. Opt. Commun.*, vol. 8, no. 1, pp. 2–8, Jan. 1987, doi: 10.1515/JOC.1987.8.1.2.

[16] D. Di Francesca, K. Kandemir, G. Li Vecchi, R. G. Alia, Y. Kadi, and M. Brugger, "Implementation of optical-fiber postmortem dose measurements: A proof of concept," *IEEE Trans. Nucl. Sci.*, vol. 67, no. 1, pp. 140–145, Jan. 2020, doi: 10.1109/TNS.2019.2946583.

[17] J. Brendel, "High-resolution photon-counting OTDR for PON testing and monitoring," in *Proc. Conf. Opt. Fiber Commun., Nat. Fiber Optic Eng. Conf. (OFC/NFOEC)*, Feb. 2008, pp. 1–5, doi: 10.1109/OFC.2008.4528296.

[18] D. C. Montgomery and G. C. Runger, *Applied Statistics and Probability for Engineers*. Hoboken, NJ, USA: Wiley, 2010.

[19] D. L. Griscom, E. J. Friebele, K. J. Long, and J. W. Fleming, "Fundamental defect centers in glass: Electron spin resonance and optical absorption studies of irradiated phosphorus-doped silica glass and optical fibers," *J. Appl. Phys.*, vol. 54, no. 7, pp. 3743–3762, Jul. 1983, doi: 10.1063/1.332591.

[20] S. Girard et al., "Overview of radiation induced point defects in silica-based optical fibers," *Rev. Phys.*, vol. 4, Nov. 2019, Art. no. 100032, doi: 10.1016/j.revip.2019.100032.

[21] S. Girard, Y. Ouerdane, C. Marcandella, A. Boukenter, S. Quenard, and N. Authier, "Feasibility of radiation dosimetry with phosphorus-doped optical fibers in the ultraviolet and visible domain," *J. Non-Cryst. Solids*, vol. 357, nos. 8–9, pp. 1871–1874, Apr. 2011, doi: 10.1016/j.jnoncrysol.2010.11.113.

[22] D. Di Francesca et al., "Combined temperature radiation effects and influence of drawing conditions on phosphorous-doped optical fibers," *Phys. Status Solidi A*, vol. 216, no. 3, 2019, Art. no. 1800553, doi: 10.1002/pssa.201800553.

radiation

MDPI

Article

Simulation and Optimization of Optical Fiber Irradiation with X-rays at Different Energies

Arnaud Meyer [1], Damien Lambert [2], Adriana Morana [1], Philippe Paillet [2], Aziz Boukenter [1] and Sylvain Girard [1,*]

[1] Laboratoire Hubert Curien, UMR-CNRS 5516, Université Jean Monnet, F-42000 Saint-Etienne, France; arnaud.meyer@univ-st-etienne.fr (A.M.); adriana.morana@univ-st-etienne.fr (A.M.); aziz.boukenter@univ-st-etienne.fr (A.B.)
[2] CEA, DAM, DIF, 91297 Arpajon, France; damien.lambert@cea.fr (D.L.); philippe.paillet@cea.fr (P.P.)
* Correspondence: sylvain.girard@univ-st-etienne.fr

Simple Summary: We investigated the influence of modifying the voltage of an X-ray tube, and therefore its photon energy spectrum, on the Total Ionizing Dose deposited in a single-mode, radiation sensitive, optical fiber. Simulation data, obtained using a toolchain combining SpekPy and Geant4 software, are compared to experimental results and demonstrate an increase of the deposited dose with operating voltage, which is mainly caused by low-energy photons below 30 keV.

Abstract: We investigated the influence of modifying the voltage of an X-ray tube with a tungsten anode between 30 kV and 225 kV, and therefore its photon energy spectrum (up to 225 keV), on the Total Ionizing Dose deposited in a single-mode, phosphorus-doped optical fiber, already identified as a promising dosimeter. Simulation data, obtained using a toolchain combining SpekPy and Geant4 software, are compared to experimental results obtained on this radiosensitive optical fiber and demonstrate an increase of the deposited dose with operating voltage, at a factor of 4.5 between 30 kV and 225 kV, while keeping the same operating current of 20 mA. Analysis of simulation results shows that dose deposition in such optical fibers is mainly caused by the low-energy part of the spectrum, with 90% of the deposited energy originating from photons with an energy below 30 keV. Comparison between simulation and various experimental measurements indicates that phosphosilicate fibers are adapted for performing X-ray dosimetry at different voltages.

Keywords: optical fibers; X-ray tubes; Geant4; radiation effects; dosimetry

Citation: Meyer, A.; Lambert, D.; Morana, A.; Paillet, P.; Boukenter, A.; Girard, S. Simulation and Optimization of Optical Fiber Irradiation with X-rays at Different Energies. *Radiation* **2023**, *3*, 58–74. https://doi.org/10.3390/radiation3010006

Academic Editor: Leonardo Abbene

Received: 14 February 2023
Revised: 6 March 2023
Accepted: 15 March 2023
Published: 20 March 2023

1. Introduction

1.1. Interest of X-rays for Radiation Testing

Radiation testing can involve a variety of ionizing radiation sources, such as photons, protons, electrons, neutrons, or heavy ions. The choice of a certain type of radiation source depends on multiple factors, including conformity to a target environment, emphasis on certain physical processes, and observation of standard practices.

Availability and ease of use are other factors that play a role in the actual planning of such radiation testing. In this regard, X-ray tests have significant advantages over other kinds of radiation sources. X-ray tubes, in particular, have been used for over a century for various applications, ranging from medical imaging [1] to material characterization [2]. These sources of high-energy photons, typically up to several hundreds of keV, are available commercially and therefore relatively easy to procure, install and manipulate safely, compared, for instance, to radioisotope sources.

A typical X-ray tube contains a cathode and an anode, both sealed in a vacuum. The cathode is typically a filament through which a very small electrical current circulates, on the order of several mA. A very high voltage, on the order of tens to hundreds of kV, is

applied between the cathode and the anode, causing electrons extracted from the cathode to be accelerated at very high velocity towards the anode, effectively forming an electron beam. Finally, the anode, typically a thick layer of a high-Z material like tungsten, causes the conversion of part of the incoming electron beam to photons through two physical processes: bremsstrahlung, generating a continuous energy spectrum until a threshold determined by the tube voltage; and characteristic emission, generating very intense and narrow energy peaks characteristic of the anode material. The beam exiting the X-ray tube is therefore a combination of these two processes: a continuous energy spectrum along with sharp characteristic peaks [1–3]. This beam is emitted in every direction in space, but practical limitations, such as the orientation of the anode and the presence of an output window on the X-ray tube, cause it to be limited to a cone of radiation originating from the anode.

Between the X-ray source itself and the sample being irradiated, several interceding elements cause a modification of both the energy spectrum and intensity of the X-ray beam. First, as the anode can be assimilated to a point source, the intensity of the beam decreases naturally with increasing distance from the tube, following a reverse square law. Second, there are numerous materials between the point of emission and the sample, including the window of the X-ray tube, typically made of a low-Z material such as beryllium, and a layer of air, both significantly absorbing very-low-energy photons. Additional filtration, typically from materials like aluminum, can also be considered to reduce even more the low-energy part of the spectrum, causing the mean energy of the beam to increase, which can optimize dose deposition in thick samples [4].

1.2. Importance of Dosimetry and Its Accuracy

Absorbed dose is a key quantity in applications that involve the presence of ionizing radiation, and dosimetry is the measurement of this quantity. The International Commission on Radiation Units and Measurements (ICRU) defines absorbed dose as the quotient between the mean energy imparted by ionizing radiation to a sample of matter and the mass of this sample. The unit of absorbed dose is J/kg, which is also given the special name Gray (Gy) [5]. Because radiation interacts in different ways and intensities with different materials, it is common in dosimetry to specify the material for which a quantity of absorbed dose is applicable by including the name of the material in the unit of the result, appearing as Gy(material).

In the domain of radiation damage applied to materials, the absorbed dose is usually categorized in two different families of processes: the Total Ionizing Dose (TID) relates to the dose due to ionization events [4,6], whereas the Displacement Damage Dose (DDD) refers to the dose due to the displacement of atoms, and is of particular significance in crystalline materials like semiconductors [7,8].

Improvement of the accuracy of dosimetry is an important topic in all applications where such measurements are needed, despite the variety of radiation environments and types of dosimetry devices involved. Research towards more accurate dosimetry crosses many scientific fields and applications, including radiotherapy [9,10], radiation protection [11], radiation testing of electronic devices [4,6–8], space missions [12,13], and even large physics instruments [14–16].

Because the physical framework of dosimetry involves particle interaction at the atomic level, the need to improve the understanding and accuracy of the dose deposition process and its measurement brought forward simulation tools to reproduce as accurately as possible these physical processes. Because of their ability to simulate individual particles and events, Monte-Carlo codes have become one of the tools of reference due to their efficiency and consistency to perform dosimetry calculations [17–19].

1.3. Use of Optical Fibers as Dosimeters

Silica-based optical fibers (OFs) are passive waveguides that operate at optical wavelengths, typically between the ultraviolet (~300 nm) and infrared (~2000 nm) domains [20].

Their functioning principle relies on a difference of refractive index between the central element of the fiber, named *core*, and its surrounding element, named *cladding*. In practice, both these elements are covered by a protective, polymer-type material, named *coating*, that does not play a role in its guiding properties. The typical base material of such OFs is amorphous silica SiO_2, doped differently between core and cladding in order to achieve the desired refractive index contrast [21]. In terms of radiation behavior, these dopants play an important role, and can make the OF range anywhere between radiation-hardened to radiation-sensitive [22]. Radiation effects on optical fiber are usually categorized in three areas: Radiation-Induced Attenuation (RIA) causing the transmitted signal to decrease under radiation; Radiation-Induced Emission (RIE) causing light to be emitted inside the OF under radiation; and Radiation-Induced Refractive Index Change (RIRIC) causing the refractive index of the fiber material to be modified under radiation [23].

OFs have emerged as a promising technology for dosimetry because of their relative immunity to external electromagnetic radiation, their ability to be used both as a sensitive element and a means to transport signal, as well as for their low dimensions which enable space-resolved measurements or access to space-constrained applications. The use of OF probes for dosimetry in radiation therapy is an increasing domain of research, using different interrogation techniques [24,25] as well as different types of OFs.

Phosphorus (P)-doped OFs in particular exhibit strong radiation sensitivity and have been the object of ample research to assess their dosimetric properties [15,16,26–28]. More specifically, the RIA of P-doped OFs in the 1550 nm wavelength region—caused by the absorption band of P_1 defects induced in phosphosilicate glasses by high-energy radiation [20,29]—was shown to be mostly linear (within 5%) up to doses of 500 Gy [15], lowly sensitive (within 15%) to temperature between −120 and 80 °C [27], and stable in time after irradiation [15]. Therefore, numerous studies have considered using P-doped OFs as dosimeters, especially combined with interrogation techniques allowing to map attenuation of an OF through its length, effectively resulting in distributed dosimeters [14,15]. Moreover, various radiation tests have shown that this RIA response scales very well over a wide variety of radiation sources, including steady-state X-rays [15,16,26–28,30,31], pulsed X-rays [30], γ rays [32–34], protons [15], neutrons [31,32], and mixed field such as the CHARM facility in CERN [35].

These previous experimental results overall indicate that P-doped OFs are only sensitive to TID effects and relatively unaffected by DDD effects [31]. Although such a statement could be challenged in very high neutron fluence environments such as in-core instrumentation, for most cases, these previous research works hint towards the possibility of investigating and qualifying the radiation properties of OFs interchangeably between different radiation environments. In regard to the advantages described above, the use of X-ray generators for such preliminary research offers therefore a strong advantage in terms of accessible dose and dose rate ranges, budget, flexibility, reliability and safety.

1.4. Influence of X-ray Voltage on Optical Fiber Dosimetry

Despite the long-standing practice of X-ray irradiation, several practical questions remain regarding the use of such irradiators for qualifying the radiation response of OFs. Dosimetry, in particular, is a key element that depends on multiple factors, such as distance from the source, voltage and current of the X-ray tube, and material or geometry of the irradiated sample. The use of dosimetry devices, like ionization chambers, helps in providing an in situ measurement of the dose or dose rate at a certain functioning point. However, such dosimeters do not deliver a measurement directly corresponding to the irradiated sample, but rather use a standardized unit, such as dose in water or air kerma. In order to properly understand and optimize the irradiation process using X-rays, the correspondence between ionization chamber dosimetry and the actual dosimetry of the irradiated sample needs to be properly understood and modeled, especially regarding the wide range of energy spectra enabled by setting different X-ray tube voltages. The particular geometry of OFs—being long and extremely thin compared to ionization chambers that are

only able to provide measurements averaged through their sensitive volume—is another key difference that requires proper evaluation.

This study aims to explore and model the dosimetry of OFs irradiated using X-ray tubes in order to properly understand and optimize the irradiation process of such elements, as well as the influence of key parameters such as X-ray tube voltage, on the actual dosimetry of the samples.

2. Materials and Methods

2.1. Optical Fiber Irradiation

The actual OF irradiation experiments were carried out in the LabHX facility of Laboratoire Hubert Curien of Université Jean Monnet Saint-Étienne, France. This irradiator is equipped with a COMET MXR-225/26 X-ray tube operating up to 225 kV and a current up to 30 mA (20 mA at the highest voltage). This X-ray tube includes a tungsten anode with an angle θ of 30°, which center is located 4.3 cm above a 2 mm-thick sealing window made of beryllium, resulting in a nominal irradiation cone with an angle α of 40°.

A simplified schematic of the X-ray tube is shown in Figure 1, along with the definition of the coordinate system used in this paper, which is the same as the software SpekPy (cf. Section 2.2): x is orientated in the anode-cathode direction and positive towards the cathode, and z is the central axis and positive in the X-ray beam propagation direction. The direction and orientation of the y axis can be determined using the right-hand rule.

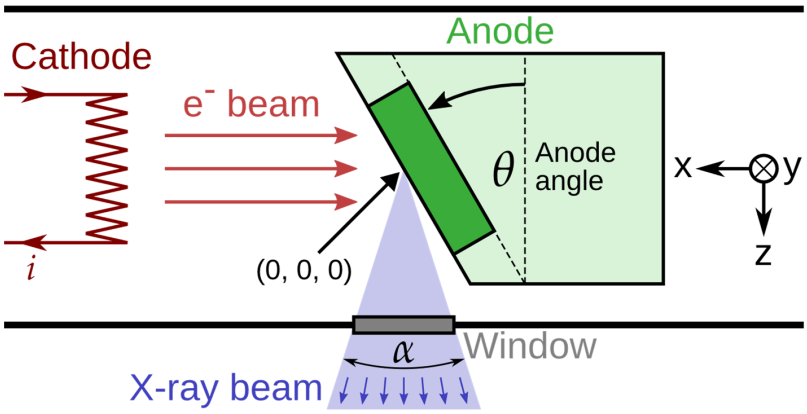

Figure 1. Simplified schematic of a typical X-ray tube and of the coordinate system of this study.

The irradiation setup is summarized in Figure 2. Each irradiated sample was taken from a P-doped OF manufactured by iXblue. Every OF sample was cut to a length of 1 m and coiled in a flat spiral of 5 cm internal radius in order to reduce as much as possible its size, and therefore beam deviation, while keeping a high enough bending radius to ensure good guiding of the signal inside the OF.

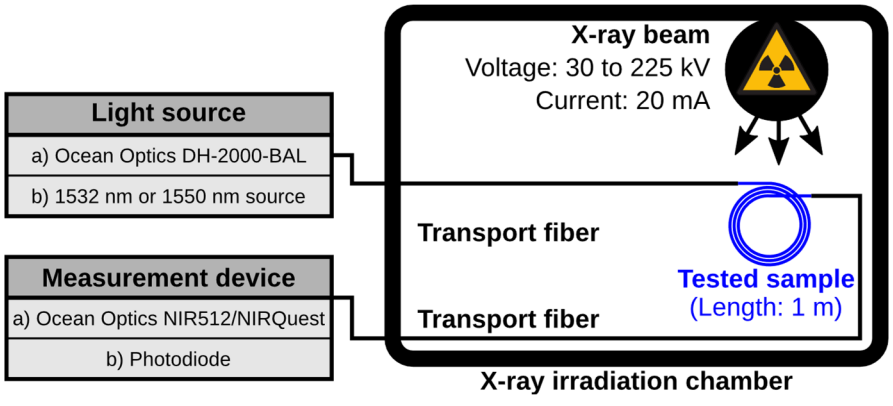

Figure 2. Experimental setup of OF irradiation with an X-ray tube at different voltages.

Each OF sample was spliced at both ends to a transport, radiation-hardened OF, connecting it to instrumentation placed outside of the irradiation chamber. One end was connected to a light source, the other end to a measurement device.

Two kinds of measurements were performed in this setup: spectral measurements were acquired using an Ocean Optics DH-2000-BAL deuterium-halogen light source, covering a continuous spectrum between wavelengths of 210 nm and 2500 nm; and two models of compact infrared spectrometers: Ocean Optics NIR512, operating between 856 nm and 1735 nm, and Ocean Optics NIRQuest, operating between 900 nm and 2137 nm. Further RIA measurements were performed using an optical source at either 1532 nm or 1550 nm and a photodiode to measure the transmitted optical power.

The samples were centered around the following coordinates: (y = 0, z = 42.5 cm), and were positioned on the x-axis to be centered around the beam maximum as described in Section 3.1. They were irradiated at room temperature (between 18 °C and 28 °C) at five different X-ray tube voltages between 30 kV and 225 kV, and a constant X-ray tube current of 20 mA, for a time period between 900 s and 3600 s for each OF sample.

Dosimetry was performed using a PTW 23344 ionization chamber connected to a UNIDOS E reading unit, which is calibrated for dose in water and therefore delivers a dose rate reading in $Gy(H_2O)/s$. The plane-parallel ionization chamber we used has a sensitive volume diameter of 15.9 mm, which only enables a coarse spatial resolution. Its documentation also states that this ionization chamber is optimized for use with X-ray tube voltages from 15 kV to 70 kV, although in this study we evaluated the raw, uncorrected measurement of the dosimetry system from 30 kV to 225 kV.

2.2. Simulation of X-ray Spectrum and Fluence Rate

In order to determine the X-ray spectrum and fluence rate as it reaches the irradiated OF, we programmed a simulation based on the SpekPy software.

SpekPy [36] is a Python library that models the spectrum of X-ray tubes. It is the successor of the stand-alone software SpekCalc [37]. SpekPy is able to calculate the spectrum, but also key parameters like fluence, half-value layer or air kerma, at any position from a defined X-ray source. It handles tungsten (W) anodes operated at voltages between 30 and 300 kV, as well as molybdenum (Mo) and rhodium (Rh) between 20 and 50 kV. It also features the functionality to accurately simulate the filtration of materials standing between the source and the sample, which takes into account the increase of filtration path observed for off-axis measurements. The accuracy of SpekPy was verified against standard NIST X-ray spectra [38].

In this work, we used SpekPy v2.0.8 (last updated in May 2022) with the *kqp* physics model, which is described by SpekPy authors to be the most accurate, especially regarding off-axis estimations [36]. The use of this physics model had notably a strong influence on the results of Section 3.1.

2.3. Simulation of Deposited Dose in Optical Fiber

In order to obtain the dose deposited by X-rays in the different parts of the irradiated OF, we programmed a simulation based on the Geant4 software.

Geant4 [39–41] is a C++ toolkit that provides all the necessary elements to build a Monte-Carlo simulation of particle physics over a wide domain of energies, scales and applications. It was first developed by CERN and is now maintained by an international collaboration [39], which provides regular updates to its core and physics engines.

In this work, we used Geant4 v11.1 (released in December 2022), along with the *QBBC_EMZ* physics package, which is the recommended package for the simulation of radiation effects in a space environment [42]. It includes the *G4EmStandardPhysics_option4* physics module, which uses the most accurate electromagnetic models and tracking of charged particles, especially at low energies [43].

The P-doped OF was modeled by three cylinders (*G4Tubs* objects) for the core, cladding and coating, respectively, using the diameters mentioned in Figure 3 and a common length

of 1 mm. Each layer was modeled by a different material: SiO_2 with 6.6 wt% concentration of phosphorus and density 2.21 g/cm^3 for the core, pure SiO_2 with density 2.20 g/cm^3 for the cladding, and acrylate $C_5H_3N_1$ with density 1.18 g/cm^3 for the coating.

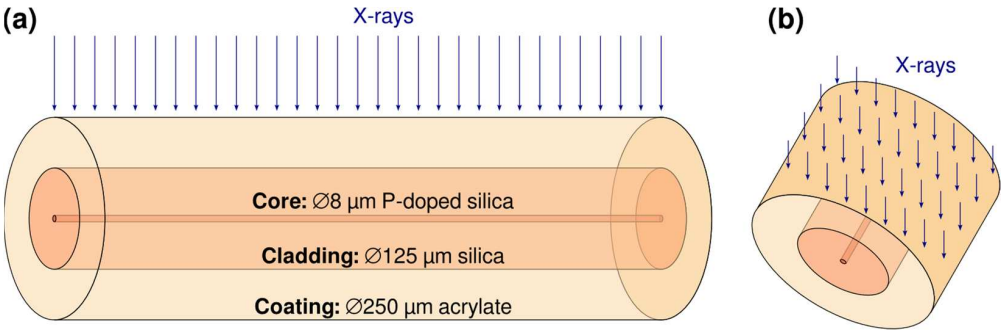

Figure 3. Geometry of the Monte-Carlo simulation of dose deposition in the irradiated OF, viewed (**a**) from the side, (**b**) from the top.

The incoming particles were configured using the *G4GeneralParticleSource* module, with a particle type set to photons, a rectangular source of dimensions 250 µm × 1 mm (the projected surface of the OF on a horizontal plane) placed 1 mm above the simulated OF, and a direction set vertically towards the OF. The spectrum of the particles was either monoenergetic from 1 keV to 2000 keV, or using the spectrum simulated by SpekPy, as described further in this article.

Dose deposition was determined using the *G4PSDoseDeposition* primitive scorer, which divides the energy deposited in a volume, determined by the physical processes implemented in the physics libraries, by the mass of this volume. Energy deposition is simulated discretely at every step of a *cut in range* (set to 1 nm in our case), and continuously in-between [39,41].

Each simulation was run for 1,000,000 photons, corresponding to a photon fluence of 4×10^8 cm^{-2} per run, and the dose deposited in the core, cladding and coating of the OF were totalized for each run. Each of these runs was repeated 100 times with different random number generator seeds in order to evaluate the statistical deviation, and therefore the uncertainty, of the results.

3. Results and Discussion

3.1. Shape of the X-ray Beam and Position of the Maximum

A first important parameter to consider with X-ray tubes is an offset of the beam, typically observed towards the anode to cathode direction. This offset, called the *heel effect* in the medical domain [44], is caused by the fact that physical phenomena causing the conversion of electrons to photons take place inside the anode material, and therefore newly produced photons need to go through different thicknesses of this material depending on their direction, resulting in an angular spectrum with a privileged direction. This direction of maximum beam intensity is typically off-axis, and can be estimated by simulation.

Figure 4a depicts the normalized X-ray fluence simulated by SpekPy according to the position on the x-axis, for 5 different operating voltages between 30 kV and 225 kV. It highlights a maximum that is always located off-axis, i.e., at an x position different than 0. As the X-ray tube voltage increases, the beam maximum moves even further from the axis.

Figure 4b shows a two-dimensional map of the simulated fluence rate for a single voltage of 100 kV. This image shows that although the beam is shifted several centimeters in the x-axis from the vertical of the X-ray anode (x = 0), it is symmetrical in the y-axis because the X-ray tube geometry is entirely symmetric in this axis. The composition of the heel effect in the x-axis and symmetry in the y-axis brings an elliptical shape to the actual beam spot. This figure also features the limit of the 40° emission cone of our setup, beyond which the fluence should be negligible in practice. For later reference, an outline of the dimensions of an irradiated OF is shown in the solid line, along with the location of the

four dosimetry points that will be considered in the rest of the document, each located 5 cm from the OF center.

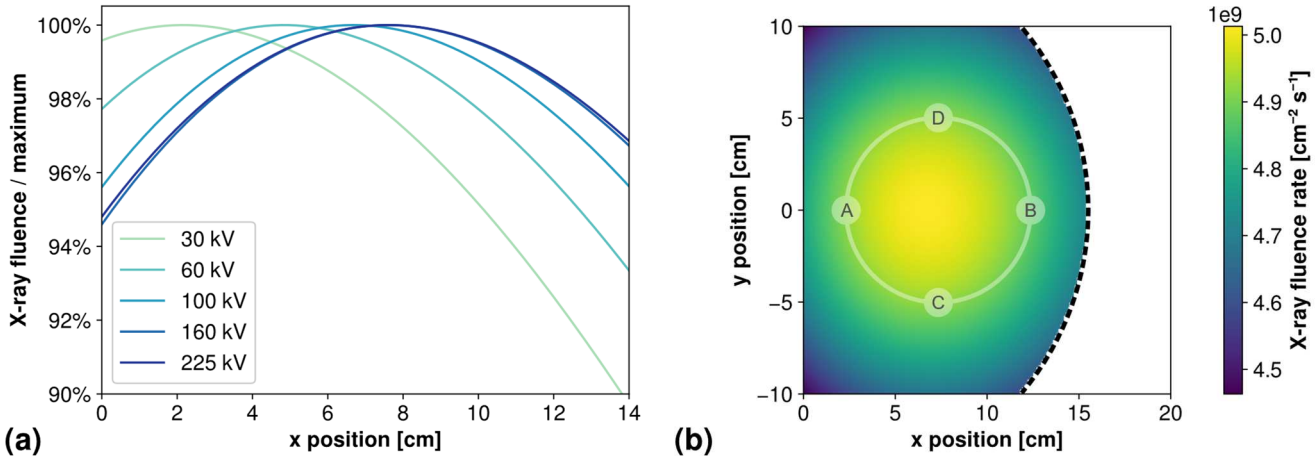

Figure 4. (**a**) Simulated fluence (normalized by maximum) of the X-ray beam according to position on the x-axis and X-ray tube voltage, at vertical position z = 42.5 cm. (**b**) Simulated fluence rate map of the X-ray beam at a position of z = 42.5 cm, tube voltage of 100 kV and current of 20 mA. Dashed contour shows the limits of the X-ray beam 40° cone, and solid contour shows the outline of an OF sample, with the location of the four dosimetry points A, B, C and D, each drawn inside a circle indicating the size of the ionization chamber sensitive surface.

Table 1 shows the simulated position of this beam maximum for the five investigated operating voltages, along with the experimental positions at which the OFs were placed, determined by ionization chamber measurements (with an uncertainty of ±1 cm). Both these measurements are in quite good agreement, except for the highest voltages at which the experimental position was set a few centimeters further than the simulated one. This could be due to an incorrect experimental estimation of the beam maximum position, also evidenced in the off-centering of ionization chamber measurements exposed in Section 3.6.

Table 1. Simulated x position of the X-ray beam maximum, and location of the irradiated OF sample, according to operating voltage.

X-ray Tube Voltage	30 kV	60 kV	100 kV	160 kV	225 kV
Simulated x position of beam maximum [cm]	2.2	4.9	6.7	7.6	7.6
Experimental x position of OF coil center [cm]	2	5	7	9	10

3.2. X-ray Energy Spectrum, Mean Energy and Fluence at Different Tube Voltages

Using SpekPy we simulated the X-ray beam spectrum at the location of the optical fiber sample. Because of the circular shape of the sample, we considered four locations placed at 5 cm, as introduced in Section 3.1. The spectrum was simulated at these four locations, and we calculated the average of these four spectra to obtain the average spectrum and fluence observed by the irradiated OF. Uncertainty was calculated from the standard deviation between these four sets of data.

After inputting parameters corresponding to the COMET MXR-225/26 source, X-ray spectra were simulated in these conditions with tube voltage varying between 30 kV and 225 kV with a step of 5 kV, and a constant tube current of 20 mA. Filtration from the beryllium window of the X-ray tube and the layer of air between the window and the sample was considered in the simulation.

An excerpt of the resulting spectra is shown in Figure 5a, for five voltages between 30 kV and 225 kV. Both features of the X-ray spectrum are easily identifiable: the continuous background caused by the bremsstrahlung effect, with a cut-off energy corresponding to the operating voltage, and the sharp characteristic peaks of the tungsten anode. These main

characteristic peaks are identified on the figure by their X-ray emission spectroscopy line names, summarized in Table 2. Through all investigated voltages, characteristic emission accounts for between 27% and 38% of the total fluence.

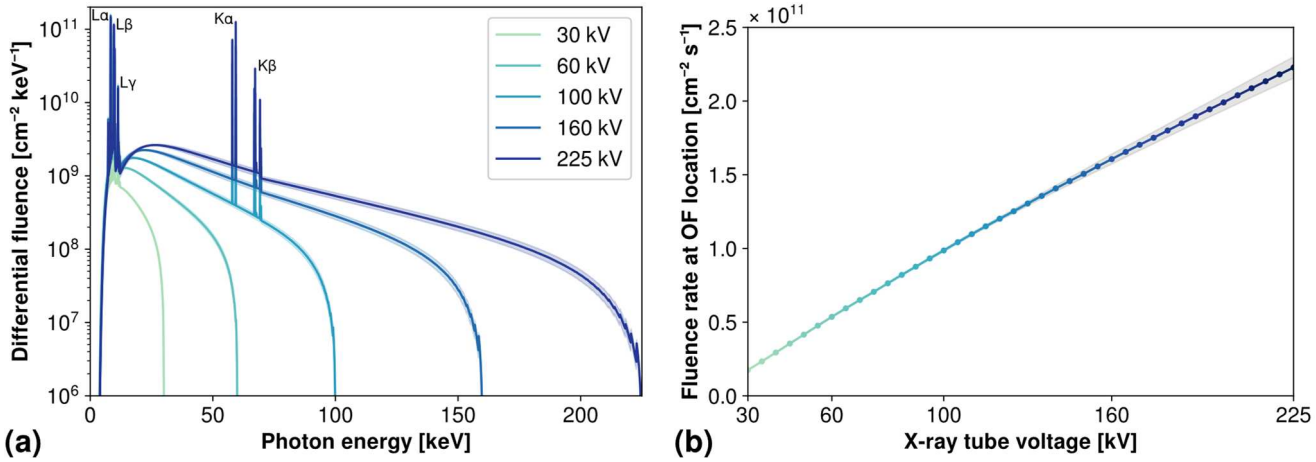

Figure 5. (**a**) Simulated energy spectra of the X-ray beam for five different source voltages from 30 kV to 225 kV at a location corresponding to the irradiated OF, with a constant current of 20 mA. The names of the main characteristic X-ray emission lines of tungsten are given next to the corresponding peaks. (**b**) Simulated fluence rate of the X-ray beam for 40 different voltages from 30 kV to 225 kV at locations corresponding to the irradiated OFs, with a constant current of 20 mA. Filled areas indicate uncertainties at $\pm 2\sigma$.

Table 2. Main characteristic X-ray emission lines for element tungsten (W) [45].

X-ray Line Name	Kα	Kβ	Lα	Lβ	Lγ
Main electronic transitions	KL_3 ($K\alpha_1$) KL_2 ($K\alpha_2$)	KM_3 ($K\beta_1$) $KN_{2/3}$ ($K\beta_2$)	L_3M_5 ($L\alpha_1$) L_3M_4 ($L\alpha_2$)	L_2M_4 ($L\beta_1$) L_3N_5 ($L\beta_2$)	L_2N_4 ($L\gamma_1$)
Mean energy [keV]	58.8	67.7	8.4	9.7	11.3

As the operating voltage increases, the spectrum shifts towards higher energies because of bremsstrahlung; but it should also be noted that the overall intensity increases with increasing voltage, even at lower energies, despite the operating current remaining at the same value of 20 mA.

Calculating the integral of such an energy spectrum gives the total fluence ϕ simulated at a considered location for a given operating voltage. This operation can be conveniently performed by SpekPy, which can also take into account the operating exposure, given in the unit mA·s. In the following calculations, we input an exposure of 20 mA·s so that the fluence calculated by SpekPy corresponds to the fluence delivered by our setup during one second, also known as fluence rate $\dot{\phi}$, in $cm^{-2}\ s^{-1}$, as per the ICRU definition [5]. Note that in some communities, this quantity is sometimes referred to as *flux*, or *flux density*, although ICRU prefers the use of the term *fluence rate*, to avoid confusion with other physical quantities [5].

This overall increase of fluence with operating voltage is also illustrated in Figure 5b, which depicts the evolution of the total fluence rate integrated over the whole spectrum with the operating voltage of the X-ray tube. As the graph indicates, the relation between voltage and fluence rate is almost linear, and can be roughly approximated in these conditions as voltage [kV] $\times\ 10^9$ [$cm^{-2}\ s^{-1}\ kV^{-1}$].

Using these simulated spectra, we can also determine their mean energy, which is a useful characteristic to compare different kinds of irradiation beams. This quantity can be calculated by considering the energy spectrum $\phi(E)$ as a continuous and unnormalized probability density function. Its mean energy $\bar{E}$ and mean energy-fluence $\bar{\psi}$ (considering

$\psi = \phi E$) are therefore the expected value of the corresponding distributions, which are given by Equations (1) and (2), and give the results shown in Table 3.

$$\bar{E} = \frac{\int E\phi(E)dE}{\int \phi(E)dE} \quad \text{for mean energy} \tag{1}$$

$$\bar{\psi} = \frac{\int E^2\phi(E)dE}{\int E\phi(E)dE} \quad \text{for mean energy-fluence} \tag{2}$$

Table 3. Mean energy and energy-fluence of the simulated X-ray beam at different voltages.

X-ray Tube Voltage	30 kV	60 kV	100 kV	160 kV	225 kV
Mean energy $\bar{E}$ [keV]	12.2	17.2	25.1	37.4	49.5
Mean energy-fluence $\bar{\psi}$ [keV]	14.3	24.4	40.1	60.3	79.4

3.3. Dose Sensitivity of Optical Fiber According to Energy or X-ray Tube Voltage

Using the Monte-Carlo simulation process described in Section 2.2, we determined the dose/fluence response of the optical fiber and the ionization chamber by running simulations with two different types of source spectra. In the first case, we simulated a monoenergetic source, varying between 1 keV and 2000 keV with 50 energies spaced evenly in a logarithmic scale. In the second case, we considered an X-ray photon spectrum, taking as input the spectrum simulated by SpekPy (described in Section 3.2), with 40 voltages from 30 kV to 225 kV with a step of 5 kV. An important parameter to consider is that Geant4 normalizes any given source spectrum, and therefore the fluence determined by SpekPy has no influence on these results.

The energy response of the OF, in the form of the simulated dose over fluence calculated separately for core, cladding and coating, is shown in Figure 6a for monoenergetic photons and Figure 6b for X-ray tube spectra at different operating voltages. For these two figures, uncertainties at $\pm 2\sigma$ are lesser than 10%, which corresponds approximately to the thickness of the plot line with the chosen log scale of these graphs.

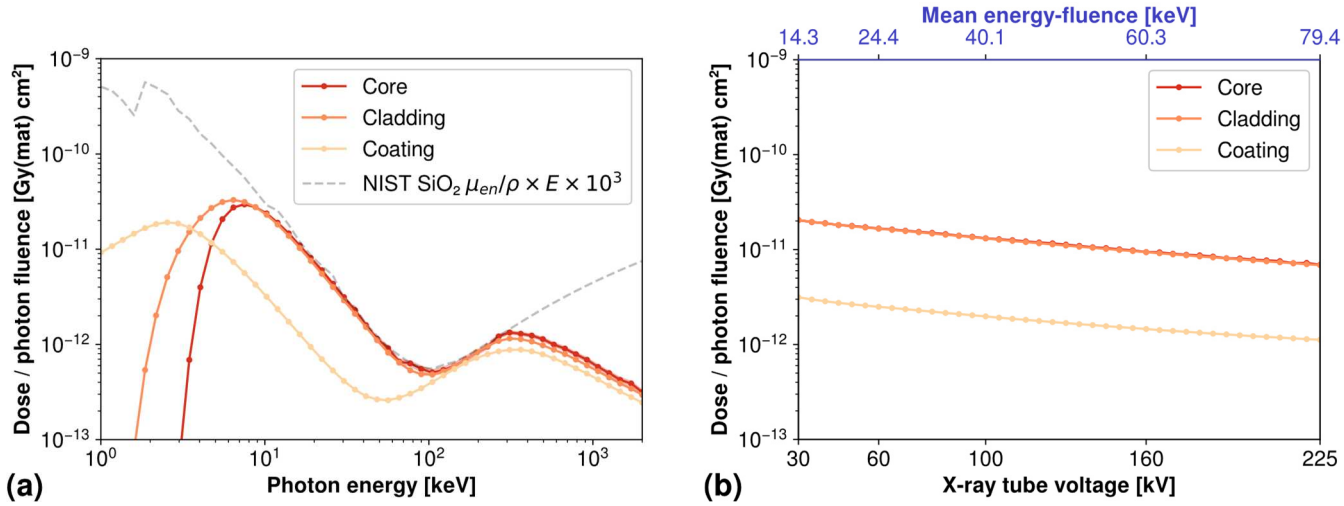

Figure 6. (**a**) Simulated dose/fluence of the OF for monoenergetic photons from 1 keV to 2 MeV. (**b**) Simulated dose/fluence of the OF for X-ray tube spectra at different operating voltages.

The monoenergetic response shown in Figure 6a features a high sensitivity to low energies around the 10 keV region, then a decreasing sensitivity with increasing energy, with the exception of a local maximum around the 300 keV region. The coating response appears overall lower than those of the core and cladding, except for very low energies,

which can be explained by the lower density and less interacting material simulated for the OF coating.

Core and cladding share a similar energy response, except for energies lower than 10 keV for which the cladding receives more dose than the core. This difference in very low energies between core, cladding and coating can be explained by the geometry of the OF (cf. Figure 3), and the fact that very-low energy particles are mostly stopped by the coating, then by the cladding, and are converted to deposited dose in these regions. On the other side of the graph, the decrease of deposited dose at higher energies, above 300 keV, is explained by the fact that secondary particles are generated with a high kinetic energy, enabling them to travel far beyond the limits of the OF without losing all their energy in the form of deposited dose.

These hypotheses are supported by the superimposition of the mass-energy absorption coefficient μ_{en}/ρ for silica (with ρ the material density), calculated from the tabulated values given by NIST for single elements, in the unit cm^2/g [46] and multiplied by the energy (in J) to give the theoretical kerma, i.e., the energy of released secondary particles per unit of mass [5]. This value is further multiplied by a factor of 10^3 to consider the conversion from grams (from the unit used in the NIST data) to kilograms (as per the definition of the kerma unit in J/kg). As it appears in Figure 6a, the simulated dose/fluence ratio in the OF core and cladding matches perfectly the theoretical kerma between 10 keV and 300 keV, meaning that all energy released in the form of secondary particles ends up being deposited in these parts of the OF, whereas the differences in lower and higher energies are explained by the statements presented above.

The response of the OF as a function of X-ray tube voltage shown in Figure 6b is comparatively less structured, and can be thought as a weighted average of the monoenergetic values; as a result, core and cladding dose sensitivities are identical over the whole investigated range of X-ray tube voltages. The data show an overall decreasing sensitivity of the OF with increasing voltage, by a factor of approximately 3 between the dose/fluence ratio simulated at 30 kV and the one simulated at 225 kV.

3.4. Dose Sensitivity Spectrum of the Optical Fiber under X-rays

Combining the X-ray spectra simulated in Section 3.2 with the OF core monoenergetic dose response simulated in Section 3.3, we obtain the graph in Figure 7a showing the contribution of each photon energy to the total dose deposition in the OF. Uncertainties are estimated from both SpekPy and Geant4 simulations, and amount to approximately 10% over the whole spectrum.

Because the OF is more sensitive in the low-energy region around 10 keV (cf. Figure 6a), the contribution of the low-energy region of the X-ray spectrum is significantly enhanced compared to higher energies. In particular, the series of L characteristic lines appear to predominate the contribution to the total amount of dose deposited in the OF for all investigated X-ray voltages.

To further highlight this contribution of the low-energy part of the X-ray spectrum to dose deposition, Figure 7b shows the cumulative integral of the dose response spectrum in Figure 7a, normalized by the integral of this whole spectrum. Figure 7c shows the same data in a stacked bar plot format to further highlight the contribution of each energy bin to total dose deposition.

For all investigated voltages, at least 90% of the dose deposited in the OF is caused by photons with an energy lower or equal to 30 keV (respectively, 75% below 15 keV). Moreover, the contribution of the characteristic X-ray emission peaks is also very significant, with Lα contributing from 26% to 30% to the total dose deposition, and Lβ between 20% and 30%.

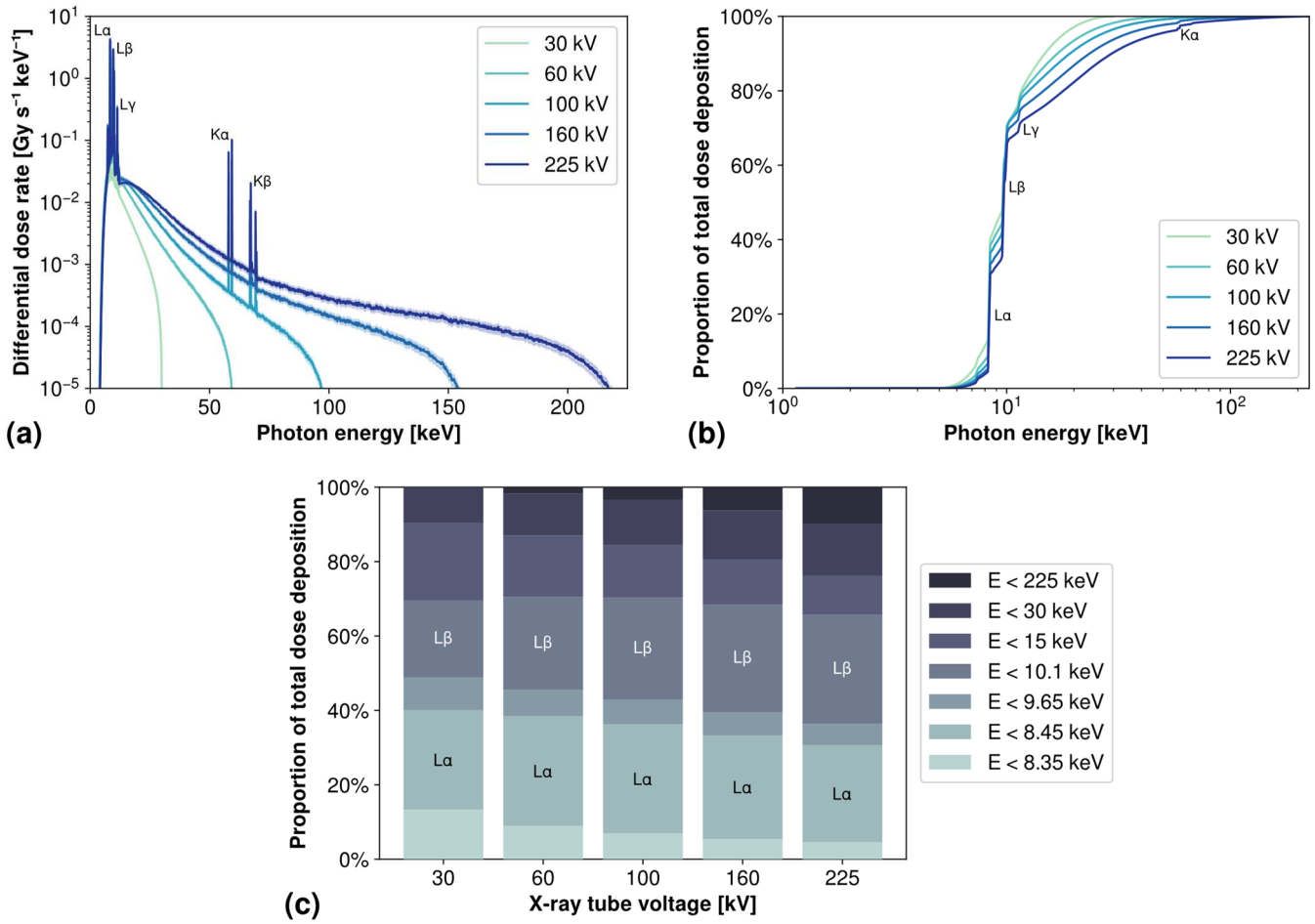

Figure 7. For five different source voltages between 30 kV and 225 kV: (**a**) Simulated dose deposition spectra of the X-ray beam inside the OF. The names of the main characteristic X-ray emission lines of tungsten are given next to the corresponding peaks. Filled areas indicate uncertainties at $\pm 2\sigma$. (**b**) Simulated cumulative dose deposition spectra of the X-ray beam, in an energy interval up to 30 keV. The name of the tungsten characteristic X-ray lines contributing the most to dose deposition are shown next to the corresponding sharp increases. (**c**) Stacked bar plot of simulated cumulative dose response showing the contribution of each energy interval to the total dose. Contributions due solely to characteristic tungsten X-ray lines Lα and Lβ are indicated inside the corresponding bins.

3.5. Dosimetry Measurements Using Optical Fiber

Using the experimental setup described in Section 2.1, we acquired the intensity transmitted through OF samples using different types of measurements, and calculated the RIA by applying the following formula:

$$\mathrm{RIA} = -10 \log_{10}\left(\frac{I - I_{\mathrm{dark}}}{I_0 - I_{\mathrm{dark}}}\right)$$

with I the measured intensity at each instant, I_0 the intensity at irradiation start, and I_{dark} the intensity with the light source switched off.

Figure 8a shows the spectral RIA, in the infrared range, of the OF acquired after irradiating up to 3000 s with an operating voltage of 100 kV. It features a clearly defined band around the 1550 nm region, which is known to be the signature of the P_1 defects of P-doped OFs, that present an optical absorption band peaking at 0.79 eV [20] and offer a great interest for dosimetry, as introduced in Section 1. As shown in the inset, RIA varies very little between 1500 nm and 1600 nm, and the deviation between values measured hereafter at 1532 nm and 1550 nm is lesser than 0.5%.

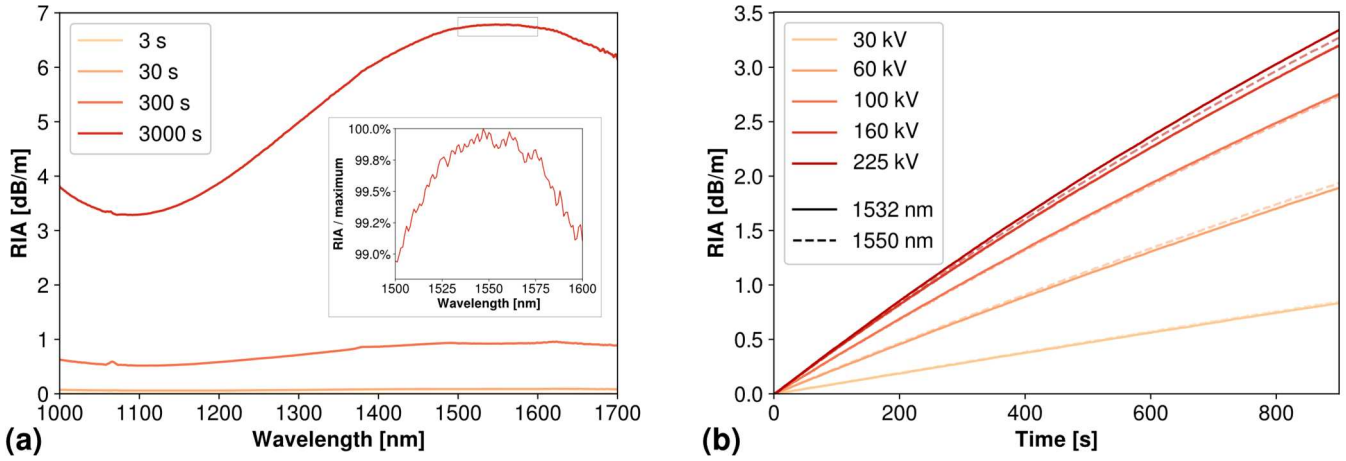

Figure 8. (**a**) Spectral RIA of the optical fiber irradiated during 3, 30, 300 and 3000 s with a tube voltage of 100 kV. Inset magnifies the framed area at 3000 s between 1500 nm and 1600 nm, normalized by maximum. (**b**) Evolution of optical fiber RIA at 1532 nm and 1550 nm according to irradiation time, at different X-ray tube voltages.

Figure 8b shows the evolution of the RIA measured at 1532 nm and 1550 nm according to irradiation time, for five operating voltages between 30 kV and 225 kV. Evolution of RIA with time is close to linear, and shows a very similar trend between different operating voltages. By performing a linear fit on the first 100 s of each of these RIA measurements, we obtain the rate of OF RIA increase for each investigated operating voltage, summarized in Table 4.

Table 4. Experimental RIA rates of OF samples at 1532 nm and 1550 nm over the first 100 s of irradiation, for investigated X-ray tube voltages. Uncertainty is estimated to be less than ±1%.

X-ray Tube Voltage	30 kV	60 kV	100 kV	160 kV	225 kV
RIA rate at 1532 nm [dB m^{-1} s^{-1}]	0.93	2.32	3.52	4.20	4.41
RIA rate at 1550 nm [dB m^{-1} s^{-1}]	0.97	2.35	3.49	4.20	4.32

For both investigated wavelengths, because of the high linearity of the measurements and the high number of measurement points, the uncertainty in the values given in Table 4 is estimated to be less than 1%.

3.6. Dosimetry Measurements Using Ionization Chamber

To check the response of a conventional dosimetry system with different X-ray energies, we placed the ionization chamber described in Section 2.1 at four locations placed 5 cm around the center of the irradiated OF for each voltage (see Figure 4b).

The results of the dose rate measurements using this method are shown in solid lines on Figure 9, in the unit $Gy(H_2O)/s$ which is the one displayed by the dosimetry device. These data show a clear increase of the dose rate perceived by the ionization chamber with increasing tube voltage, consistent with the simulated increase of beam fluence rate reported in Figure 5a. However, the rate of increase at higher energies is visibly reduced for the ionization chamber, whereas beam fluence appears to follow a more linear trend through all investigated voltages.

Measurements taken through the four dosimetry locations are in good accordance, and show a good beam homogeneity at the locations corresponding to the irradiated OFs. However, point B stands out as its data significantly deviates from the other points at higher operating voltages, whereas point A, which stands symmetrical to point B in the x-axis, appears relatively unaffected. This deviation can first be explained by a slightly incorrect estimation of the experimental location of the beam center, along with the practical

uncertainty of ±1 cm, considering the positioning inaccuracy of the ionization chamber given its large dimensions.

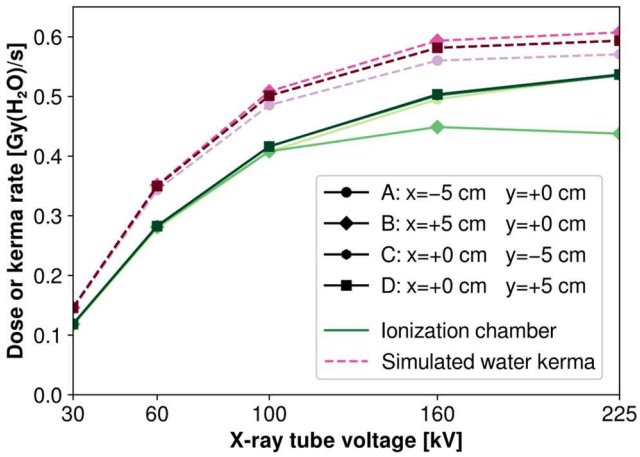

Figure 9. Dose rate measured by the ionization chamber (solid line) and simulated water kerma rate (dashed line) at five tube voltages and four points in a radius of 5 cm around locations corresponding to the center of the irradiated OFs.

Another parameter to take into account is the global decrease of beam homogeneity in the x-axis at higher voltages, as the beam takes a more elliptical shape (cf. Section 3.1). By calculating the theoretical water kerma rate from the simulated spectra at each voltage and location, along with the NIST μ_{en}/ρ data for water [46], we can reproduce to an extent the deviation observed on the x-axis, as shown in dashed lines on Figure 9, for a center of the dosimetry locations perfectly located on the beam maximum.

Comparison between experimental and simulated dosimetry values shows a systematic over-estimation of the dose rate by simulation compared to the experiment. Because the dose rate in water given by the ionization chamber is supposed to be at electronic equilibrium and therefore equal to kerma, both these quantities should be comparable.

This observed deviation can be explained by the difference between the fluence simulated by SpekPy and our actual experimental setup, and we can therefore estimate a factor k_{simul} = 0.83 (±10%) cm^{-2}/cm^{-2} to take this difference into account.

3.7. Comparison between Simulation, Optical Fiber and Ionization Chamber

Figure 10 summarizes all measurements and simulations performed in this work by displaying side-by-side the dose rate estimated by three different means.

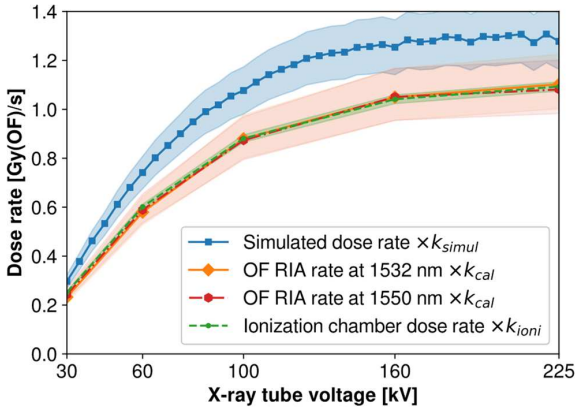

Figure 10. Comparison between dose rate determined by three different means: simulation, scaling of RIA rate and scaling of ionization chamber measurements; for X-ray tube voltages between 30 kV and 225 kV. Filled areas show uncertainties at ±2σ.

The simulated dose/fluence in the OF core obtained in Section 3.1 was multiplied by the fluence rate of the X-ray beam (as shown in Figure 5a) to obtain the simulated dose rate in the OF core for each operating voltage. This simulated dose rate was further multiplied by the factor k_{simul}, determined in Section 3.6, to consider the difference between simulated and experimental fluences in our setup.

The OF RIA rates determined in Section 3.5 were multiplied by the calibration factor $k_{cal} = 4.0 \times 10^{-3}$ ($\pm$10%) dB km^{-1} Gy^{-1}, determined under γ rays in a previous experiment involving the same type of OF [15], to obtain an estimated dose rate as measured by the OF at the different experimented voltages.

Finally, to compare the dose rate in water measured locally by the ionization chamber in Section 3.6 with these other results specific to the dose deposited in the OF, we used a fit algorithm to determine a simple relation between displayed ionization chamber dose rate and dose rate estimated by OF RIA. These calculations show that a very simple linear relation exists between these two measurements, with a constant scaling factor defined here as k_{ioni} = 2.14 ($\pm$10%) Gy(OF)/Gy(H_2O) for all investigated voltages. The very good accordance between both these measurements is further highlighted by the superimposition of these two trends in Figure 10.

We observe that although all experimental results show a very good agreement when scaled as described above, simulation results appear to be systematically overestimated, by a factor of approximately 1.2, slightly varying with voltage. As this discrepancy cannot be explained by the difference between simulated and experimental fluences which is already taken into account by the factor k_{simul}, other factors can be considered to explain these deviations, such as uncertainties on OF positioning, OF sample lengths, OF dimensions and composition, and/or specifications of the X-ray tube.

4. Conclusions

By combining simulation tools and experimental work, we investigated the effects of varying the operating voltage of an X-ray tube on the dose deposition in a radiosensitive P-doped OF.

A first important effect of modifying the tube voltage is a shift of the X-ray beam center along the x-axis, with a span of about 5.5 cm over the investigated range of voltages, between 30 kV and 225 kV. This parameter has to be taken into account to properly position irradiated samples around the actual center of the beam.

Simulated X-ray spectra using SpekPy show the relative weights of bremsstrahlung and characteristic emission, and highlight the increase of X-ray photon fluence with increasing operating voltage over the whole spectrum, even at lower energies.

Monte-Carlo simulations of the monoenergetic dose/fluence response spectrum of the OF using Geant4 show that both core and cladding are most sensitive to photons around 10 keV, and reach electronic equilibrium between 10 keV and 300 keV. Photons of energy lower than 10 keV are unable to penetrate the fiber coating, and photons of energy higher than 300 keV release secondary electrons of too high a velocity to have their energy fully converted to deposited dose. Polyenergetic dose/fluence response shows that due to this higher contribution of the low-energy part of the spectrum to dose deposition, X-ray spectra of lower voltages tend to deposit more dose inside the OF; although this phenomenon is largely counterbalanced by the observed increase of fluence with operating voltage described above.

The important contribution of the low-energy part of the spectrum to OF dose deposition is further highlighted by combining both simulation results, which show that 90% of the dose is deposited by photons under 30 keV. These results also emphasize the very significative influence of tungsten characteristic X-ray emission peaks Lα and Lβ, which, combined, amount to between 47% and 57% of the total deposited dose through all investigated voltages.

These simulation results were compared with experimental work to assess the fidelity and reliability of the proposed simulation toolchain. Two kinds of measurements were

acquired: RIA of P-doped OF and water dose rate using an ionization chamber. All these experimental measurements scale very well, and we determined a scaling factor of 2.14 ($\pm$10%) Gy(OF)/Gy(H_2O), practically constant for all investigated voltages, to convert the ionization chamber dose rate to the actual dose rate perceived by the OF, which demonstrates the ability of phosphosilicate OFs to be used accurately as X-ray dosimeters through different tube voltages. Overall, simulation and experimental results estimate a factor of approximately 4.5 between dose rates at 30 kV and 225 kV, for the same operating current. This shows that in the case of OF irradiation, the range of available dose rates for a given X-ray irradiator can be extended by proper adjustment of the operating voltage. Moreover, dosimetry performed using conventional tools, such as the ionization chamber studied here, appears to deliver consistent results over the whole investigated range of voltages, and therefore the use of a single scaling factor for all voltages appears to be appropriate.

Dose rate estimated by simulation displays the same increasing trend with operating voltage as experimental results, but is still slightly over-estimated by a factor of approximately 1.2. This shows the ability and limitations of the proposed simulation toolchain to estimate, to some extent, the absolute value of experimental results.

Investigations on the causes of inaccuracy in the estimation of the experimental dose rate could be a subject for further research, so that a complete dosimetry model could be produced for a given X-ray irradiator, enabling an efficient planning and optimization of sample irradiation.

Moreover, the overwhelming influence of the low-energy photons on OF dose deposition suggests that beam filtering—using for example aluminum which is known to attenuate the lower part of the spectrum—could produce very significant changes in the dosimetry. This could be used both to reach lower dose rates and to favor certain physical processes, such as Compton scattering, because of the higher mean energy of the X photons in this case. The effects of such filtering at different X-ray voltages could be the topic of further research, along with an exploration of higher voltages and photon energies.

Overall, these results broaden the knowledge of the sensitivity of P-doped OF dosimeters under X-ray beams, and outline their practical advantages and limits. The present work has shown that such devices can be used with a reliability comparable to conventional ionization chambers at X-ray tube voltages from 30 kV to 225 kV. On the other hand, their high sensitivity to the low-energy part of the spectrum may deviate their response from standard dosimetry units, such as dose in water, in case of higher energy beams. This behavior at higher energies could be further assessed and investigated, although the good accordance demonstrated here between simulation results and ^{60}Co γ ray calibration performed in [35] hints toward the reliability of this dosimetry technique at photon energies in the MeV range, at least when the low-energy part of the spectrum is negligible. Finally, the use of optical attenuation as a means of measurement involves an appropriate length of OF, especially when a high sensitivity is required, which can circumvent the dimensional advantages of using an OF to perform localized dosimetry; in which case, more localized techniques such as radioluminescence-based fiber dosimeters could provide an advantage.

Author Contributions: Conceptualization, S.G., A.M. (Adriana Morana) and A.M. (Arnaud Meyer); methodology, S.G., A.M. (Adriana Morana), D.L. and A.M. (Arnaud Meyer); software, A.M. (Arnaud Meyer); formal analysis, A.M. (Arnaud Meyer); writing—original draft preparation, A.M. (Arnaud Meyer); writing—review and editing, A.M. (Arnaud Meyer), S.G., A.M. (Adriana Morana) and D.L.; supervision, S.G., D.L., P.P. and A.B. All authors have read and agreed to the published version of the manuscript.

Funding: This research received no external funding.

Institutional Review Board Statement: Not applicable.

Informed Consent Statement: Not applicable.

Data Availability Statement: The data supporting the findings of this study are available from the corresponding authors upon reasonable request.

Conflicts of Interest: The authors declare no conflict of interest.

References

1. Seibert, J.A. X-ray Imaging Physics for Nuclear Medicine Technologists. Part 1: Basic Principles of X-ray Production. *J. Nucl. Med. Technol.* **2004**, *32*, 139–147. [PubMed]
2. Ladd, M.; Palmer, R. X-rays and X-ray Diffraction. In *Structure Determination by X-ray Crystallography: Analysis by X-rays and Neutrons*; Ladd, M., Palmer, R., Eds.; Springer: Boston, MA, USA, 2013; pp. 111–159, ISBN 978-1-4614-3954-7.
3. Poludniowski, G.G. Calculation of X-ray Spectra Emerging from an x-Ray Tube. Part II. X-ray Production and Filtration in x-Ray Targets. *Med. Phys.* **2007**, *34*, 2175–2186. [CrossRef] [PubMed]
4. Lambert, D.; Gaillardin, M.; Raine, M.; Paillet, P.; Duhamel, O.; Marcandella, C.; Martinez, M.; Rostand, N.; Lagutère, T.; Aubert, D.; et al. TID Effects Induced by ARACOR, 60Co, and ORIATRON Photon Sources in MOS Devices: Impact of Geometry and Materials. *IEEE Trans. Nucl. Sci.* **2021**, *68*, 991–1001. [CrossRef]
5. Seltzer, S.M.; Bartlett, D.T.; Burns, D.T.; Dietze, G.; Menzel, H.-G.; Paretzke, H.G.; Wambersie, A. Fundamental Quantities and Units for Ionizing Radiation. *ICRU J.* **2011**, *11*, 1. [CrossRef]
6. Ravotti, F. Dosimetry Techniques and Radiation Test Facilities for Total Ionizing Dose Testing. *IEEE Trans. Nucl. Sci.* **2018**, *65*, 1440–1464. [CrossRef]
7. Srour, J.R.; Marshall, C.J.; Marshall, P.W. Review of Displacement Damage Effects in Silicon Devices. *IEEE Trans. Nucl. Sci.* **2003**, *50*, 653–670. [CrossRef]
8. Ohshima, T.; Onodaa, S. Radiation Resistance of Semiconductors. In *Radiation Applications*; Kudo, H., Ed.; An Advanced Course in Nuclear Engineering; Springer: Singapore, 2018; pp. 81–116, ISBN 978-981-10-7350-2.
9. Thwaites, D. Accuracy Required and Achievable in Radiotherapy Dosimetry: Have Modern Technology and Techniques Changed Our Views? *J. Phys. Conf. Ser.* **2013**, *444*, 012006. [CrossRef]
10. Kron, T.; Lehmann, J.; Greer, P.B. Dosimetry of Ionising Radiation in Modern Radiation Oncology. *Phys. Med. Biol.* **2016**, *61*, R167–R205. [CrossRef]
11. McDonald, J.C. Calibration Measurements and Standards for Radiation Protection Dosimetry. *Radiat. Prot. Dosim.* **2004**, *109*, 317–321. [CrossRef]
12. Berger, T. Radiation Dosimetry Onboard the International Space Station ISS. *Z. Für Med. Phys.* **2008**, *18*, 265–275. [CrossRef]
13. Caffrey, J.A.; Hamby, D.M. A Review of Instruments and Methods for Dosimetry in Space. *Adv. Space Res.* **2011**, *47*, 563–574. [CrossRef]
14. Henschel, H.; Körfer, M.; Kuhnhenn, J.; Weinand, U.; Wulf, F. Fibre Optic Radiation Sensor Systems for Particle Accelerators. *Nucl. Instrum. Methods Phys. Res. Sect. A Accel. Spectrometers Detect. Assoc. Equip.* **2004**, *526*, 537–550. [CrossRef]
15. Di Francesca, D.; Vecchi, G.L.; Girard, S.; Morana, A.; Reghioua, I.; Alessi, A.; Hoehr, C.; Robin, T.; Kadi, Y.; Brugger, M. Qualification and Calibration of Single-Mode Phosphosilicate Optical Fiber for Dosimetry at CERN. *J. Light. Technol.* **2019**, *37*, 4643–4649. [CrossRef]
16. Paillet, P.; Girard, S.; Goiffon, V.; Duhamel, O.; Morana, A.; Lambert, D.; De Michele, V.; Campanella, C.; Mélin, G.; Robin, T.; et al. Phosphosilicate Multimode Optical Fiber for Sensing and Diagnostics at Inertial Confinement Fusion Facilities. *IEEE Sens. J.* **2022**, *22*, 22700–22706. [CrossRef]
17. Papadimitroulas, P. Dosimetry Applications in GATE Monte Carlo Toolkit. *Phys. Med.* **2017**, *41*, 136–140. [CrossRef]
18. Andreo, P. Monte Carlo Simulations in Radiotherapy Dosimetry. *Radiat. Oncol.* **2018**, *13*, 121. [CrossRef]
19. Czarnecki, D.; Zink, K.; Pimpinella, M.; Borbinha, J.; Teles, P.; Pinto, M. Monte Carlo Calculation of Quality Correction Factors Based on Air Kerma and Absorbed Dose to Water in Medium Energy X-ray Beams. *Phys. Med. Biol.* **2020**, *65*, 245042. [CrossRef]
20. Girard, S.; Alessi, A.; Richard, N.; Martin-Samos, L.; De Michele, V.; Giacomazzi, L.; Agnello, S.; Francesca, D.D.; Morana, A.; Winkler, B.; et al. Overview of Radiation Induced Point Defects in Silica-Based Optical Fibers. *Rev. Phys.* **2019**, *4*, 100032. [CrossRef]
21. Lingle, R.; Peckham, D.W.; McCurdy, A.; Kim, J. Light-Guiding Fundamentals and Fiber Design. In *Specialty Optical Fibers Handbook*; Méndez, A., Morse, T.F., Eds.; Academic Press: Burlington, MA, USA, 2007; pp. 19–68, ISBN 978-0-12-369406-5.
22. Tomashuk, A.L.; Golant, K.M. Radiation-Resistant and Radiation-Sensitive Silica Optical Fibers. In Proceedings of the Advances in Fiber Optics, SPIE, Whistler, BC, Canada, 14–17 May 2000; Volume 4083, pp. 188–201.
23. Girard, S.; Morana, A.; Ladaci, A.; Robin, T.; Mescia, L.; Bonnefois, J.-J.; Boutillier, M.; Mekki, J.; Paveau, A.; Cadier, B.; et al. Recent Advances in Radiation-Hardened Fiber-Based Technologies for Space Applications. *J. Opt.* **2018**, *20*, 093001. [CrossRef]
24. O'Keeffe, S.; Fitzpatrick, C.; Lewis, E.; Al-Shamma'a, A.I. A Review of Optical Fibre Radiation Dosimeters. *Sens. Rev.* **2008**, *28*, 136–142. [CrossRef]
25. Zubair, H.T.; Begum, M.; Moradi, F.; Rahman, A.K.M.M.; Mahdiraji, G.A.; Oresegun, A.; Louay, G.T.; Omar, N.Y.M.; Khandaker, M.U.; Adikan, F.R.M.; et al. Recent Advances in Silica Glass Optical Fiber for Dosimetry Applications. *IEEE Photonics J.* **2020**, *12*, 1–25. [CrossRef]

26. Girard, S.; Ouerdane, Y.; Marcandella, C.; Boukenter, A.; Quenard, S.; Authier, N. Feasibility of Radiation Dosimetry with Phosphorus-Doped Optical Fibers in the Ultraviolet and Visible Domain. *J. Non-Cryst. Solids* **2011**, *357*, 1871–1874. [CrossRef]
27. Morana, A.; Campanella, C.; Marin, E.; Mélin, G.; Robin, T.; Li Vecchi, G.; Di Francesca, D.; Boukenter, A.; Ouerdane, Y.; Mady, F.; et al. Operating Temperature Range of Phosphorous-Doped Optical Fiber Dosimeters Exploiting Infrared Radiation-Induced Attenuation. *IEEE Trans. Nucl. Sci.* **2021**, *68*, 906–912. [CrossRef]
28. Girard, S.; De Michele, V.; Alessi, A.; Marcandella, C.; Di Francesca, D.; Paillet, P.; Morana, A.; Vidalot, J.; Campanella, C.; Agnello, S.; et al. Transient and Steady-State Radiation Response of Phosphosilicate Optical Fibers: Influence of H2 Loading. *IEEE Trans. Nucl. Sci.* **2020**, *67*, 289–295. [CrossRef]
29. Griscom, D.L.; Friebele, E.J.; Long, K.J.; Fleming, J.W. Fundamental Defect Centers in Glass: Electron Spin Resonance and Optical Absorption Studies of Irradiated Phosphorus-doped Silica Glass and Optical Fibers. *J. Appl. Phys.* **1983**, *54*, 3743–3762. [CrossRef]
30. Girard, S.; Baggio, J.; Bisutti, J. 14-MeV Neutron, γ-Ray, and Pulsed X-ray Radiation-Induced Effects on Multimode Silica-Based Optical Fibers. *IEEE Trans. Nucl. Sci.* **2006**, *53*, 3750–3757. [CrossRef]
31. Girard, S.; Morana, A.; Hoehr, C.; Trinczek, M.; Vidalot, J.; Paillet, P.; Bélanger-Champagne, C.; Mekki, J.; Balcon, N.; Li Vecchi, G.; et al. Atmospheric Neutron Monitoring through Optical Fiber-Based Sensing. *Sensors* **2020**, *20*, 4510. [CrossRef]
32. Borgemans, P.; Brichard, B. Dose Reconstruction with Multiple Wavelength Analysis in Irradiated Optical Fibres. *Radiat. Prot. Dosim.* **1999**, *85*, 497–500. [CrossRef]
33. Paul, M.C.; Bohra, D.; Dhar, A.; Sen, R.; Bhatnagar, P.K.; Dasgupta, K. Radiation Response Behavior of High Phosphorous Doped Step-Index Multimode Optical Fibers under Low Dose Gamma Irradiation. *J. Non-Cryst. Solids* **2009**, *355*, 1496–1507. [CrossRef]
34. Tomashuk, A.L.; Grekov, M.V.; Vasiliev, S.A.; Svetukhin, V.V. Fiber-Optic Dosimeter Based on Radiation-Induced Attenuation in P-Doped Fiber: Suppression of Post-Irradiation Fading by Using Two Working Wavelengths in Visible Range. *Opt. Express* **2014**, *22*, 16778–16783. [CrossRef]
35. Di Francesca, D.; Infantino, A.; Vecchi, G.L.; Girard, S.; Alessi, A.; Kadi, Y.; Brugger, M. Dosimetry Mapping of Mixed-Field Radiation Environment Through Combined Distributed Optical Fiber Sensing and FLUKA Simulation. *IEEE Trans. Nucl. Sci.* **2019**, *66*, 299–305. [CrossRef]
36. Poludniowski, G.; Omar, A.; Bujila, R.; Andreo, P. Technical Note: SpekPy v2.0—A Software Toolkit for Modeling X-ray Tube Spectra. *Med. Phys.* **2021**, *48*, 3630–3637. [CrossRef]
37. Poludniowski, G.; Landry, G.; DeBlois, F.; Evans, P.M.; Verhaegen, F. SpekCalc: A Program to Calculate Photon Spectra from Tungsten Anode X-ray Tubes. *Phys. Med. Biol.* **2009**, *54*, N433–N438. [CrossRef]
38. Bujila, R.; Omar, A.; Poludniowski, G. A Validation of SpekPy: A Software Toolkit for Modelling X-ray Tube Spectra. *Phys. Med.* **2020**, *75*, 44–54. [CrossRef]
39. Agostinelli, S.; Allison, J.; Amako, K.; Apostolakis, J.; Araujo, H.; Arce, P.; Asai, M.; Axen, D.; Banerjee, S.; Barrand, G.; et al. Geant4—A Simulation Toolkit. *Nucl. Instrum. Methods Phys. Res. Sect. A Accel. Spectrometers Detect. Assoc. Equip.* **2003**, *506*, 250–303. [CrossRef]
40. Allison, J.; Amako, K.; Apostolakis, J.; Araujo, H.; Arce Dubois, P.; Asai, M.; Barrand, G.; Capra, R.; Chauvie, S.; Chytracek, R.; et al. Geant4 Developments and Applications. *IEEE Trans. Nucl. Sci.* **2006**, *53*, 270–278. [CrossRef]
41. Allison, J.; Amako, K.; Apostolakis, J.; Arce, P.; Asai, M.; Aso, T.; Bagli, E.; Bagulya, A.; Banerjee, S.; Barrand, G.; et al. Recent Developments in Geant4. *Nucl. Instrum. Methods Phys. Res. Sect. A Accel. Spectrometers Detect. Assoc. Equip.* **2016**, *835*, 186–225. [CrossRef]
42. Ivanchenko, V.; Dondero, P.; Fioretti, V.; Ivantchenko, A.; Lei, F.; Lotti, S.; Mantero, A.; Mineo, T. Validation of Geant4 10.3 Simulation of Proton Interaction for Space Radiation Effects. *Exp. Astron.* **2017**, *44*, 437–450. [CrossRef]
43. Ivanchenko, V.; Bagulya, A.; Bakr, S.; Bandieramonte, M.; Bernard, D.; Bordage, M.-C.; Brown, J.; Burkhardt, H.; Dondero, P.; Elles, S.; et al. Progress of Geant4 Electromagnetic Physics Developments and Applications. *EPJ Web Conf.* **2019**, *214*, 02046. [CrossRef]
44. Fung, K.K.; Gilboy, W.B. "Anode Heel Effect" on Patient Dose in Lumbar Spine Radiography. *BJR* **2000**, *73*, 531–536. [CrossRef]
45. Thompson, A.; Attwood, D.; Gullikson, E.; Howells, M.; Kim, K.J.; Kirz, J.; Kortright, J.; Lindau, I.; Pianetta, P.; Robinson, A. *X-ray Data Booklet*; Lawrence Berkeley National Laboratory: Berkeley, CA, USA, 2009. Available online: https://xdb.lbl.gov (accessed on 27 January 2023).
46. Hubbell, J.H.; Seltzer, S.M. X-ray Mass Attenuation Coefficients. *NIST Stand. Ref. Database 126* **2009**. [CrossRef]

List of scientific communications

This part exhaustively lists the scientific communications produced during this thesis, in terms of published scientific articles as the main author, in collaboration with other authors, or in terms of participation in scientific conferences.

Articles published as the main author

1. A. Meyer *et al.*, "X-Ray Radioluminescence in Diversely Doped Multimode Silica-Based Optical Fibers," *IEEE Transactions on Nuclear Science*, vol. 69, no. 7, pp. 1625–1632, Jul. 2022, ISSN: 1558-1578. DOI: 10.1109/TNS.2022.3140392
2. A. Meyer *et al.*, "Simulation and Optimization of Optical Fiber Irradiation with X-rays at Different Energies," *Radiation*, vol. 3, no. 1, pp. 58–74, 1 Mar. 2023, ISSN: 2673-592X. DOI: 10.3390/radiation3010006
3. A. Meyer *et al.*, "Toward an Embedded and Distributed Optical Fiber-Based Dosimeter for Space Applications," *IEEE Transactions on Nuclear Science*, vol. 70, no. 4, pp. 583–589, Apr. 2023, ISSN: 1558-1578. DOI: 10.1109/TNS.2022.3226194

Articles published as a collaborating author

1. T. Allanche *et al.*, "In Situ Optical Characterization of Bulk Optical Glasses Under Protons and X-Rays," *IEEE Transactions on Nuclear Science*, vol. 69, no. 7, pp. 1492–1499, Jul. 2022, ISSN: 1558-1578. DOI: 10.1109/TNS.2022.3151964
2. J. Harb *et al.*, "Femtosecond Direct Laser Writing of Silver Clusters in Phosphate Glasses for X-ray Spatially-Resolved Dosimetry," *Chemosensors*, vol. 10, no. 3, p. 110, 3 Mar. 2022, ISSN: 2227-9040. DOI: 10.3390/chemosensors10030110
3. P. Paillet *et al.*, "Phosphosilicate Multimode Optical Fiber for Sensing and Diagnostics at Inertial Confinement Fusion Facilities," *IEEE Sensors Journal*, vol. 22, no. 23, pp. 22 700–22 706, Dec. 2022, ISSN: 1558-1748. DOI: 10.1109/JSEN.2022.3217436
4. C. Campanella *et al.*, "Influence of Ambient Light on the Radiation-Induced Attenuation of Germanosilicate Optical Fibers in the Visible and Near-Infrared Domains," *IEEE Transactions on Nuclear Science*, vol. 70, no. 4, pp. 562–567, Apr. 2023, ISSN: 1558-1578. DOI: 10.1109/TNS.2022.3228099
5. M. Gaillardin *et al.*, "Investigations on Ionizing Dose Deposition in Thin-Layered Devices: Sample-to-Sample Variability and Electronic Equilibrium Dependence," *IEEE Transactions on Nuclear Science*, vol. 70, no. 8, pp. 2027–2033, Aug. 2023, ISSN: 1558-1578. DOI: 10.1109/TNS.2023.3239950

Oral presentations in international scientific conferences

1. A. Meyer, "X-Ray Radioluminescence in Diversely Doped Multimode Silica-based Optical Fibers," presented at the Radiation Effects on Components and Systems Conference (RADECS), in collab. with A. Morana *et al.*, Sep. 15, 2021
2. A. Meyer, "Influence of X-ray energy on dosimetry using phosphorus-doped optical fiber," presented at the Workshop on Radiation Effects on Optoelectronics and Photonics Technologies (RADOPT), in collab. with A. Morana *et al.*, Nov. 16, 2021
3. A. Meyer, "Towards an Embedded and Distributed Optical Fiber-based Dosimeter for Space Applications," presented at the IEEE Nuclear & Space Radiation Effects Conference (NSREC), in collab. with A. Morana *et al.*, Jul. 21, 2022

Optical-fiber-based distributed dosimetry for space applications

Abstract

Dosimetry for the space environment requires sensors that are sensitive to a wide range of particles and energies, while keeping low volume and mass footprints. Optical fibers provide a suitable solution for these applications, along with the unique property of enabling *distributed* dosimetry, i.e. access to the dose received by virtually any location along the sensing fiber.

Such distributed dosimetry systems were reported in the literature for ground-based applications, especially in particle accelerators. This work explores the performance of distributed dosimetry systems based on miniaturized, phosphorus-doped optical fibers, interrogated around 1550 nm by embedded Optical Time-Domain Reflectometers (OTDRs).

These systems were characterized using γ ray, X-ray and proton beam irradiation, as well as offline measurements for the assessment of their measurement uncertainties. Results concluded to a linear evolution of the Radiation-Induced Attenuation (RIA) at the interrogation wavelength, with a sensitivity coefficient between ~3.8 $\mathrm{dB\,km^{-1}\,Gy(SiO_2)^{-1}}$ and 4.9 $\mathrm{dB\,km^{-1}\,Gy(SiO_2)^{-1}}$, depending on the type of optical fiber and the maximum dose involved, up to 40.16 $\mathrm{Gy(SiO_2)}$.

Dosimétrie répartie par fibre optique pour les applications spatiales

Résumé

La dosimétrie pour l'environnement spatial nécessite des capteurs sensibles à une large gamme de particules et d'énergies, tout en conservant des empreintes réduites de volume de et masse. Les fibres optiques fournissent une solution appropriée à ces applications, ainsi que la propriété unique de permettre une dosimétrie *répartie*, c'est-à-dire l'accès à la dose reçue par virtuellement n'importe quel point le long de la fibre sensible.

De tels systèmes de dosimétrie répartie ont été documentés dans la littérature pour des applications au sol, notamment pour des accélérateurs de particules. Ce travail explore les performances de systèmes de dosimétrie répartie basés sur des fibres optiques miniaturisées et dopées au phosphore, interrogées autour de 1550 nm par des réflectomètres optiques (OTDRs) embarqués.

Ces systèmes ont été caractérisés par irradiation γ, X et proton, ainsi que par des mesures hors ligne pour évaluer leurs incertitudes de mesure. Les résultats ont conclu à une évolution linéaire de l'atténuation radio-induite (RIA) à la longueur d'onde d'interrogation, avec un coefficient de sensibilité entre ~3,8 $\mathrm{dB\,km^{-1}\,Gy(SiO_2)^{-1}}$ et 4,9 $\mathrm{dB\,km^{-1}\,Gy(SiO_2)^{-1}}$, selon le type de fibre optique et la dose maximale reçue, jusqu'à 40,16 $\mathrm{Gy(SiO_2)}$.